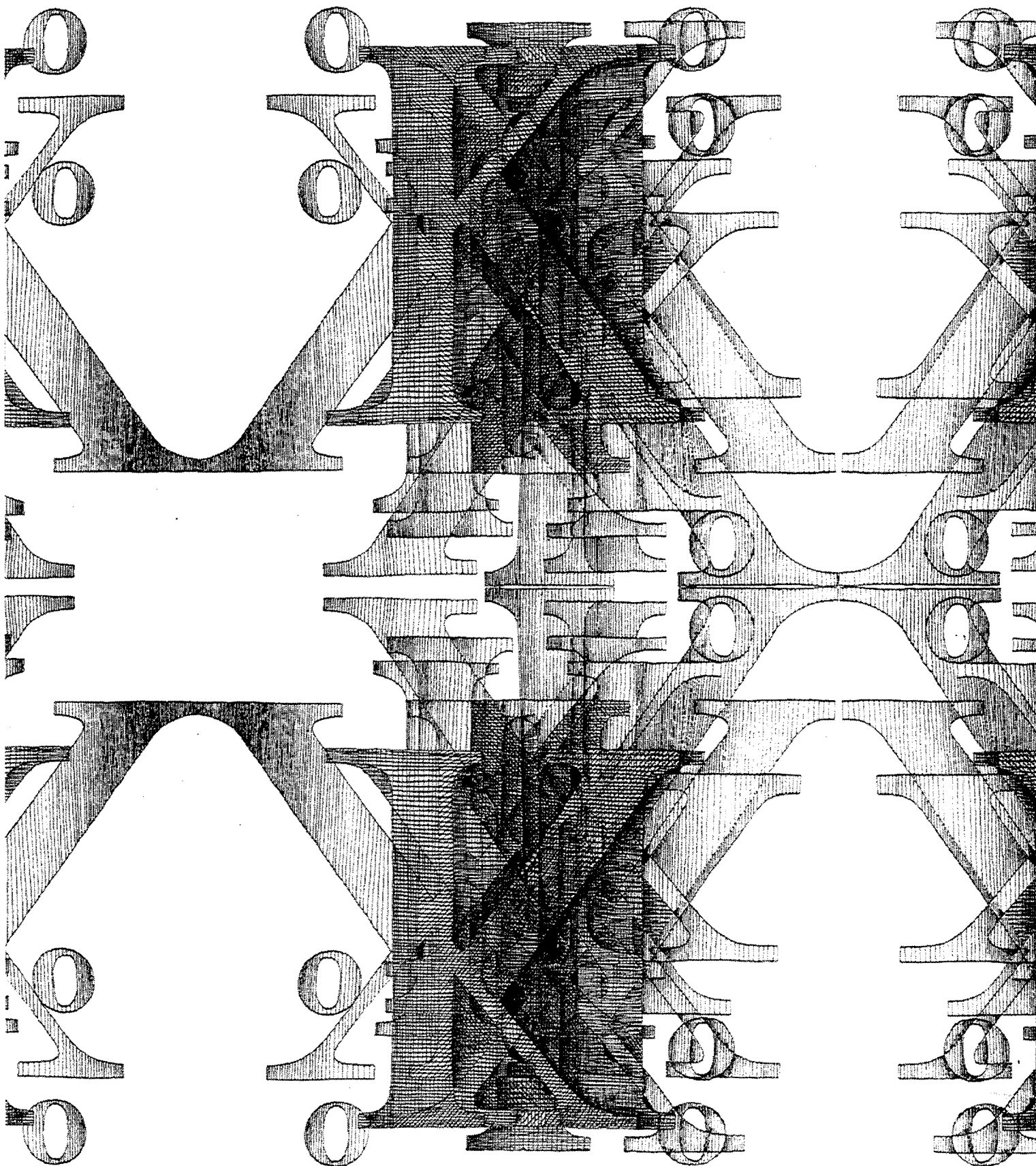# Results from the Neutral Kaon Program at Fermilab's Meson Center Beamline (1985-1997)

**Fermi National Accelerator Laboratory**

# Results from the Neutral Kaon Program at Fermilab's Meson Center Beamline 1985 - 1997

Erik Ramberg, Editor

Published on behalf of the E731, E773 and E799 Collaborations

*Fermi National Accelerator Laboratory*
*P.O. Box 500, Batavia, Illinois 60510*

January 1998

# Table of Contents

# Introduction

This volume contains reprints of all articles reporting physics results from the Fermilab E731, E773, and E799 experiments. This series of experiments concentrated on studies of CP violating and rare neutral kaon decays. This collection is due to the efforts of Erik Ramberg.

The data for the experiments was obtained in four distinct running periods in the M-Center beam line. These experiments followed a path whose origins can be traced to the early days of Fermilab, and which continues today.

E731 was a new experiment in a new beam with the primary purpose of studying CP violation in the neutral kaon system. The detector was designed with the sole criterion of having maximal acceptance for the $K_L \rightarrow 2\pi^\circ$ decay-the decay which statistically limits such studies. The double beam arrangement that had been employed in earlier Fermilab experiments was used to minimize some key systematic uncertainties. Originally, it was not planned that any other physics would be done with the beam and detector.

E731 was proposed in 1983; the authors of the proposal were G. Gollin, K. Nishikawa, B. Winstein (spokesman), Chicago; G. Bock, Fermilab; and B. Peyaud, R. Turlay, A. Zylberstejn, Saclay. E731 had an initial 6-week "test" run which ended in June of 1985. One measurement, that of $\epsilon'/\epsilon$, resulted from this run (p1).

Between 1985 and 1987, the detector was upgraded, particularly the trigger and read-out. A run began in August of 1987; its end was extended to February of 1988.

A set of data taken in a 5-week period at the end of the run was the source of the first publications from this run. The technique, now used by all $\epsilon'/\epsilon$ experiments, of collecting all four $K_L$ and $K_S$ to $2\pi$ modes simultaneously, was first employed in this data set. A new value for $\epsilon'/\epsilon$ (p12), a study of CPT symmetry in the neutral kaon system (p18), and two other studies that capitalized upon the large multi-body acceptance (p5, p9) resulted from this data set.

When the full data sample was analyzed, 9 more papers resulted (p16, p22-54). These included more accurate values for the quantities measured in the earlier analyses and some quite different studies. The first search for the $K_L \rightarrow \pi^\circ \nu \bar{\nu}$ decay was published. Accurate values for the lifetime of the $K_S$, the $K_L$, $K_S$ mass difference and the phase

of the $2\pi$ transition amplitudes were obtained. An important finding was that the mass difference, which had not been measured for many years, had a value significantly below the accepted average. When previous measurements of the phases of the $2\pi$ amplitudes were accordingly re-evaluated, they then came into agreement with CPT symmetry. And a new, third manifestation of CP violation (in addition to the $2\pi$ decay and the semi-leptonic charge asymmetry) was seen for the first time in the interference between $K_L$ and $K_S$ into the $\pi^+\pi^-\gamma$ channel. A full description of the beam, detector, and analysis techniques in E731 (based upon the PhD thesis of L. Gibbons) was also written (p114).

The detector was modified for a two month run which began in September of 1991 as a dedicated study of CPT symmetry. This data set (E773, G. Gollin, spokesman) produced several measurements in 3 publications (p98-109). The experiment used two regenerators and a significant advance in the understanding of the regeneration phenomenon was made. The phases of the $2\pi$ transition amplitudes and the $K_L$, $K_S$ mass difference were better measured, and the interference in the $\pi^+\pi^-\gamma$ mode was determined even more precisely.

A dedicated rare kaon decay search (E799, Y. Wah and T. Yamanaka, spokesmen) immediately followed E773 for an additional 2 months. The primary purpose of this run was to extend the search for the CP violating $K_L \rightarrow \pi^\circ e^+ e^-$ decay. This was done to the level of $10^{-9}$ (p63). Ten additional papers resulted from this last run of the Meson Center detector (p55-62, p71-97, p110). These included improved limits in the closely related $\pi^\circ \nu \bar{\nu}$ and $\pi^\circ \mu^+ \mu^-$ branching ratios. A broad study of radiative decays was also performed. This included (a) enough $K_L \rightarrow 4e$ decays for the first spin-parity analysis of the final state; (b) the first high statistics study of the $\mu^+\mu^-\gamma$ decay; and, (c) the first observation of the $\mu^+\mu^-e^+e^-$ decay mode. A new technique was developed for studying rare $\pi^\circ$ decays: using the unambiguous signature of a $K_L \rightarrow 3\pi^\circ$ decay as a tag. By this means, the $\pi^\circ \rightarrow e^+e^-$ decay was observed particularly cleanly, and a limit on the flavor violating $\pi^\circ \rightarrow \mu e$ transition was established. Finally, a large improvement in the $K_L \rightarrow \pi^\circ \mu e$ limit was obtained, and measurements of the production polarization of $\Lambda$ hyperons were made.

The collaboration began with barely 10 members and ended with over 40. Nineteen students obtained their PhDs on the data collected from these experiments; of these, 14 have remained in the field, all joining other collaborations. Of the 20 postdocs who worked on these experiments, 16 remain in the field, 9 of whom are continuing in the FNAL Kaon program. These experiments were done with modest budgets in a climate where significant parts of the detector were produced by University groups with their own funding. The first author on almost every publication was chosen as the student or postdoc whose work led to the reported result.

It took a long time for all the analysis to be completed but the results were satisfying. The final error obtained on $\epsilon'/\epsilon$ was an order-of-magnitude improvement over the best prior measurement. This result and the determinations of the phases of the CP violating amplitudes, $K_S$ lifetime and $K_L$, $K_S$ mass difference have not been surpassed in the published literature to date. Because of the high acceptance and high kaon energy, the rare decay studies performed compete well with other experiments having much more kaon flux. Of all the results and studies of rare decays of this collaboration, only two have so far been bettered by groups other than our own (p22, p79).

This work is continuing, but in a new, larger collaboration at Fermilab. Again, a new beam and a new detector were constructed for KTeV, which is in the midst of data collection. It again is studying $\epsilon'/\epsilon$ and rare decays with greater sensitivity. Prospects for success look very good.

Bruce Winstein
March, 1997

# Chronological List of Results from the Fermilab K° Program (1985-1997)

*This list summarizes the complete set of physics results to come out of the kaon program in the meson center beamline of Fermilab, 1985-1997. It is arranged in chronological order and gives the title, first author, collaboration, journal reference, date of publication and page number in this volume. Each entry also includes the numerical results quoted in the abstract of the paper. Other qualitative results may be quoted in the abstract, or other quantitative results may be discussed in the body of the paper. Errors are quoted as statistical, then systematic. Limits on branching ratios are quoted for 90% confidence level.*

V. Papadimitriou, et.al. (E731); Physical Review D44, R573; 1 August, 1991

$$\Gamma(K_L \to \pi^\circ\gamma\gamma, m_{\gamma\gamma} \geq 0.280 GeV)/\Gamma(K_L \to all)$$
$$= (1.86 \pm 0.60 \pm 0.60) \times 10^{-6}$$
$$\Gamma(K_L \to \pi^\circ\gamma\gamma, m_{\gamma\gamma} < 0.264 GeV)/\Gamma(K_L \to all)$$
$$< 5.1 \times 10^{-6}$$

G.E. Graham, et.al. (E731); Physics Letters B295, 169; 26 November, 1992

$$BR(K_L \to \pi^\circ\nu\bar{\nu}) < 2.2 \times 10^{-4}$$

S.V. Somalwar, et.al. (E731); Physical Review Letters 68, 2580; 27 April, 1992

$$h(K_L \to 3\pi^\circ) = -[3.3 \pm 1.1 \pm 0.7] \times 10^{-3}$$

L.K. Gibbons, et.al. (E731); Physical Review Letters 70, 1199; 1 March, 1993

$$\tau_S = (0.8929 \pm 0.0016) \times 10^{-10}s$$
$$\Delta m = (0.5286 \pm 0.0028) \times 10^{10}\hbar s^{-1}$$
$$\Phi_{+-} = 42.2^\circ \pm 1.4^\circ$$
$$\Delta\Phi = -1.6^\circ \pm 1.2^\circ$$

L.K. Gibbons, et.al. (E731); Physical Review Letters 70, 1203; 1 March, 1993

$$Re(\epsilon'/\epsilon) = (7.4 \pm 5.2 \pm 2.9) \times 10^{-4}$$

G. Makoff, et.al. (E731); Physical Review Letters 70, 1591; 15 March, 1993

$$BR(K_{e4}) = [5.16 \pm 0.20 \pm 0.22] \times 10^{-5}$$
$$L_3 = -(3.4 \pm 0.4) \times 10^{-3}$$

E.J. Ramberg, et.al. (E731); Physical Review Letters 70, 2525; 26 April, 1993

$$\Gamma(K_L \to \pi^+\pi^-\gamma)/\Gamma(K_L \to \pi^+\pi^-)$$
$$= (23.0 \pm 0.7) \times 10^{-3}$$
$$\Gamma(K_S \to \pi^+\pi^-\gamma, E_\gamma^* > 20 MeV)/\Gamma(K_S \to \pi^+\pi^-)$$
$$= (7.10 \pm 0.22) \times 10^{-3}$$

---

‡The sign of $L_3$ was incorrectly reported as positive in this paper. It was corrected in Physical Review Letters, Errata; 4 September, 1995.

---

‡Errors in table headings and figure captions in this paper are corrected in Physical
Review Letters, Errata; 4 September, 1995.

# The E731 Collaboration

A. Barker, R.A. Briere, L.K. Gibbons, G.E. Graham, G. Makoff,
K. Nishikawa, V. Papadimitriou, J.R. Patterson, B. Schwingenheuer,
S. Somalwar, Y.W. Wah, B. Winstein, R. Winston,
M. Woods and H. Yamamoto

*The Enrico Fermi Institute and the Department of Physics,*
*The University of Chicago, Chicago, Illinois, 60637*


E.C. Swallow

*Department of Physics, Elmhurst College, Elmhurst, Illinois 60126 and*
*The Enrico Fermi Institute, The University of Chicago, Chicago, Illinois, 60637*


G.J. Bock, R. Coleman, J. Enagonio, Y. B. Hsiung, E. Ramberg,
K. Stanfield, R. Stefanski, and T. Yamanaka

*Fermi National Accelerator Laboratory, Batavia, Illinois 60510*


G. Blair, G.D. Gollin, G.L. Grazer, M. Karlsson,
J.K. Okamitsu and R. Tschirhart

*Department of Physics, Princeton University, Princeton, New Jersey 08544*


J.C. Brisson, R. Daudin, P. Debu, P. Jarry, B. Peyaud,
R. Turlay, and B. Vallage

*Department de Physique des Particules Elementaires, Centre d'Etudes*
*Nucleaires de Saclay, F-91191 Gif-sur-Yvette Cedex, France*

# The E773 Collaboration

A.R. Barker, R.A. Briere, E. Cheu, L.K. Gibbons, D.A. Harris, G. Makoff,
K.S. McFarland, A. Roodman, B. Schwingenheuer, Y.W. Wah,
B. Winstein, and R. Winston

*The Enrico Fermi Institute and the Department of Physics,*
*The University of Chicago, Chicago, Illinois, 60637*


E.C. Swallow

*Department of Physics, Elmhurst College, Elmhurst, Illinois 60126 and*
*The Enrico Fermi Institute, The University of Chicago, Chicago, Illinois, 60637*


G.J. Bock, R. Coleman, M. Crisler, J. Enagonio, R. Ford, Y.B. Hsiung,
D. Jensen, E. Ramberg, R. Tschirhart, and T. Yamanaka

*Fermi National Accelerator Laboratory, Batavia, Illinois 60510*


E.M. Collins and G.D. Gollin

*Department of Physics, University of Illinois, Urbana, Illinois 61801*


P. Gu, P. Haas, W.P. Hogan, S. Kim, J.N. Matthews, S.S. Myung,
S. Schnetzer, S.V. Somalwar, G. Thomson, and Y. Zou

*Department of Physics, Rutgers University, Piscataway, New Jersey 08855*

# The E799 Collaboration

K. Arisaka, J. Kubic, D. Roberts, W. Slater, M. Spencer, and M. Weaver

*Department of Physics, University of California at Los Angeles,*
*Los Angeles, California 90024*


R.A. Briere, E. Cheu, D.A. Harris, P. Krolak, G. Makoff,
K.S. McFarland, A. Roodman, B. Schwingenheuer, S. Somalwar,
Y.W. Wah, B. Winstein, and R. Winston

*The Enrico Fermi Institute and the Department of Physics,*
*The University of Chicago, Chicago, Illinois, 60637*


A.R. Barker

*Department of Physics, University of Colorado, Boulder, Colorado 80309*


E.C. Swallow

*Department of Physics, Elmhurst College, Elmhurst, Illinois 60126 and*
*The Enrico Fermi Institute, The University of Chicago, Chicago, Illinois, 60637*


G.J. Bock, R. Coleman, M. Crisler, J. Enagonio, R. Ford,
Y.B. Hsiung, D. Jensen, E. Ramberg, and R. Tschirhart

*Fermi National Accelerator Laboratory, Batavia, Illinois 60510*


E.M. Collins and G.D. Gollin

*Department of Physics, University of Illinois, Urbana, Illinois 61801*


T. Nakaya and T. Yamanaka

*Department of Physics, Osaka University, Toyonaka, Osaka, 560 Japan*


P. Gu, P. Haas, W.P. Hogan, S. Kim, J.N. Matthews,
S.S. Myung, S. Schnetzer, G. Thomson, and Y. Zou

*Department of Physics, Rutgers University, Piscataway, New Jersey 08855*

Plan view of the E731 detector.

25 cm

PA

VA9 VA0

VA1 VA2

DRA VA3 VA4

MA

LGA

Lead Glass

Muon
Veto
Plane

Lead
Wall

BA

Collar
Anti

$K_L$
beams

Vacuum Windows

Regenerators  Calibration magnets

Drift
Chambers

Analysis Magnet

Hadron Veto

C,B Trigger Planes

110  120  130  140  150  160  170  180  190

Distance from Target (m)

Plan view of the E773 detector.

Plan view of the E799 detector.

Collaborators inspect the Meson Center enclosure before installation of the beamline and detector.

A view of the 804 lead glass blocks that made up the calorimeter for E731, E773 and E799.

The four drift chambers after being refurbished for the new kaon program at KTeV.



Looking upstream in the Meson Center enclosure with the vacuum decay vessel and its veto arrays.

The upstream regenerator in E773.



The last shift of E799 celebrates the end of the kaon program in Meson Center beamline.

# First Result on a New Measurement of $\epsilon'/\epsilon$ in the Neutral-Kaon System

M. Woods, K. Nishikawa,[a] J. R. Patterson, Y. W. Wah, B. Winstein, R. Winston, and H. Yamamoto

*The Enrico Fermi Institute and the Department of Physics, The University of Chicago, Chicago, Illinois 60637*

E. C. Swallow

*Department of Physics, Elmhurst College, Elmhurst, Illinois 60126, and*
*The Enrico Fermi Institute, The University of Chicago, Chicago, Illinois 60637*

G. J. Bock, R. Coleman, Y. B. Hsiung, K. Stanfield, R. Stefanski, and T. Yamanaka

*Fermi National Accelerator Laboratory, Batavia, Illinois 60510*

G. D. Gollin, G. L. Grazer, and J. K. Okamitsu

*Department of Physics, Princeton University, Princeton, New Jersey 08544*

and

P. Jarry, R. Daudin, P. Debu, B. Peyaud, and R. Turlay

*Département de Physique des Particules Elémentaires, Centre d'Etudes Nucléaires de Saclay,*
*F-91191 Gif-sur-Yvette Cedex, France*
(Received 8 February 1988)

A new beam line and detector were constructed to increase statistical precision and greatly reduce systematic uncertainty on the ratio of the *CP*-nonconserving parameters $\epsilon'/\epsilon$. Major improvements are discussed together with a result from a first run: $\epsilon'/\epsilon = 0.0032 \pm 0.0028$ (statistical) $\pm 0.0012$ (systematic). The precision is better than earlier measurements yet the result is still consistent with the superweak mechanism (which predicts zero) and that due to Kobayashi and Maskawa. Significantly more data are being collected.

*CP* nonconservation was first[1] observed in the $\pi^+\pi^-$ decay of the long-lived neutral kaon $(K_L)$; this and many subsequent measurements point to a very small asymmetry in the mixing of $K^0$ and $\bar{K}^0$, parametrized by $|\epsilon| \simeq 2.3 \times 10^{-3}$.

A natural way of incorporating the asymmetry into the charged current weak interaction was advanced by Kobayashi and Maskawa[2] and, especially since the subsequent discovery[3] of the bottom quark, this has provided increased motivation for further studies. The Kobayashi-Maskawa mechanism has as one consequence a second manifestation of *CP* nonconservation in the $K^0(\bar{K}^0) \rightarrow 2\pi$ decay itself, parametrized[4] by the ratio $\epsilon'/\epsilon$. This is in contrast to the superweak[5] model. However, the effect is small (in the range $0.001 \lesssim |\epsilon'/\epsilon| \lesssim 0.007$) and the theoretical uncertainty is considerable.[6]

This experiment seeks to isolate such an effect by the measurement of the decay rates of $K_L$ and $K_S$ to charged and neutral pions:

$$\frac{\Gamma(K_L \rightarrow \pi^+\pi^-)/\Gamma(K_S \rightarrow \pi^+\pi^-)}{\Gamma(K_L \rightarrow \pi^0\pi^0)/\Gamma(K_S \rightarrow \pi^0\pi^0)} \simeq 1 + 6\,\mathrm{Re}\,\epsilon'/\epsilon.$$

Recent published experiments[7,8] had sensitivities to the above double ratio in the range of 0.03 to 0.04 and found no deviation from unity.

The technique which our group[7] has adopted in experiments at Fermilab allows simultaneous detection of $K_L$ and $K_S$ decays with a double neutral beam derived symmetrically from a single target; the $K_S$ are provided by coherent regeneration from material (the regenerator) placed in one of the $K_L$ beams. The experiment is run in two distinct modes: charged, where $\pi^+\pi^-$ are detected, and neutral, where $2\pi^0$ are detected. This approach provides good control of systematic uncertainties:

(a) Since $K_L$ and $K_S$ decays are detected simultaneously, time-dependent losses cancel. Such losses come from triggering, accidental vetoing (e.g., from short-term intensity variations), electronic drifts, and resolution changes.

(b) The momentum dependence of regeneration at high energies[9] results in nearly identical spectra for decaying $K_L$'s and $K_S$'s.

(c) Acceptance and intensity differences for decays from the two beams are negligible as the regenerator is frequently moved from one to the other.

$K_L$ and $K_S$ decays then differ *only* in the decay distribution along the beam so that good knowledge of the acceptance is needed. Background in $K_L$ decays and contamination from diffractive and inelastic regeneration in $K_S$ decays must be small and understood.

The experiment was performed in the new Meson

FIG. 1. Detector schematic, elevation view.

Center beam line at the Fermilab Tevatron. The neutral beams ($0.5 \times 0.5$ mrad$^2$) were defined at 4.8 mrad from a Be target. A component of soft neutrons, common in previous neutral beams, was greatly reduced by an appropriate configuration of collimation and sweeping.

The detector is shown schematically in Fig. 1. The regenerator was about 123 m from the production target and the end of the decay region was defined by two closely spaced 1-mm scintillators between which an 0.1-radiation-length lead sheet, serving as a converter for the neutral mode, could be placed ("conversion plane" in Fig. 1).

The regenerator was constructed of four identical sections each consisting of 19 cm of B$_4$C, 1.76 cm of Pb, and six anticoincidence counters. The lead provided a sharp cutoff to the spatial distribution of $K_S \rightarrow 2\pi^0$ decays. The anticounters signaled inelastic events: Corrections for these dominated the systematic uncertainty in our previous effort.[7]

Charged tracks were measured with a 2000-wire, 16-plane drift-chamber spectrometer. Electrons and photons were identified with a circular array of 804 lead-glass blocks.

In the charged mode, a signal at the conversion plane and a two-track signature in the $A$ and $B$ hodoscopes were required. A 2-radiation-length lead sheet upstream of the $B$ hodoscope (only used in the charged mode) suppressed $K_{e3}$ decays with a pulse-height requirement. The hodoscope after 3 m of steel provided $K_{\mu3}$ rejection.

In the neutral mode, a 30-GeV electromagnetic energy and two tracks in the $A$ and $B$ hodoscopes consistent with a photon conversion were required—the magnet currents were chosen to separate and then recombine the pair at the lead glass. Background in this mode is dominated by $K_L \rightarrow 3\pi^0$ decays where photons miss, or merge with others in, the lead glass. Ten planes of anticoincidence with sensitivity above about 100 MeV were employed. One, placed in the beams, signaled photons with $E > 5$ GeV; another recognized photons close to the beam holes through the lead glass.

The events were reconstructed[10] similarly to Ref. 7. The chambers had plane resolutions of approximately 150 $\mu$m, and the $K^0 \rightarrow \pi^+ \pi^-$ mass resolution was 3.5 MeV (rms). High-statistics lead-glass calibration was done periodically with electron pairs; the resolution was $\sigma/E \cong 1.5\% + 5\%/\sqrt{E}$ and $2\pi^0$ mass resolution was 6.1

TABLE I. Event total, mass cut, and background summary for each mode.

| Mode | Events[a] | Mass cut | Background[b] (%) | Improvement[c] factor | Systematic error(%) |
|---|---|---|---|---|---|
| $K_L \rightarrow 2\pi^0$ | 6747 | $\pm 3.3\sigma$ | 1.56 | 5.4 | 0.30 |
| $K_S \rightarrow 2\pi^0$ | 21788 | $\pm 3.3\sigma$ | 2.90 | 5.0 | 0.20 |
| $K_L \rightarrow \pi^+\pi^-$ | 35838 | $\pm 3.9\sigma$ | 1.23 | 2.5 | 0.18 |
| $K_S \rightarrow \pi^+\pi^-$ | 130025 | $\pm 3.9\sigma$ | 0.30 | 5.7 | 0.03 |

[a]After subtractions.

[b]Residual non-$\pi\pi$ background for $K_L$ modes: diffractive and inelastic contribution for $P_T^2 < 250$ (4000) (MeV/$c$)$^2$ for $\pi^+\pi^-$ ($2\pi^0$) $K_S$ modes.

[c]With respect to Ref. 7.

MeV.

Table I gives the event totals and background levels; significant improvement over Ref. 7 was obtained. The improved suppression of inelastic regeneration reduced the contamination under the coherent $K_S$ peak in the neutral mode by a factor of about 5. Figure 2 shows the $K_L \rightarrow 2\pi^0$ invariant-mass distribution; the array of photon vetos reduced the background in this mode by more than a factor of 5.

Background subtractions were made in each 10-GeV/$c$ momentum bin (13 charged bins from 30 GeV/$c$ and 11 neutral bins from 40 GeV/$c$). The ratios of $K_S$ to $K_L$ decays, after correction for acceptance, were simultaneously fitted for three parameters: the $B_4C$ regeneration amplitude, its power-law momentum dependence, and $\epsilon'/\epsilon$. The fit gave $|(f-\bar{f})/k| \propto p^{-0.596 \pm 0.009}$, consistent with past work.[9,11] The result[12] is $\epsilon'/\epsilon = 0.0032 \pm 0.0028$ where the (statistical) error is nearly a factor of 2 better than in Ref. 7; $\chi^2$ was 0.98 per degree of freedom.

The sources of systematic uncertainty are associated with the accidental activity in the detector, the relative energy calibration between the two modes, the background subtractions, and the acceptance corrections.

The integration time for the lead-glass signals was 250 ns; as a result, the neutral mode was the one most affected by accidental activity: Nearly 10% of otherwise good decays were lost. Since the distributions of photons in the lead glass for $K_L$ and $K_S$ are not exactly the same and the accidental hits are not perfectly uniform, the combined effect could in principle give an asymmetry in the loss. From a study of accidental events superimposed on Monte Carlo data, however, it was determined that the asymmetry was less than 2% itself. The resulting systematic error was 0.20% in the double ratio.

The $\pi^+\pi^-$ energy scale was determined with the well-known values for the $K^0$ and $\Lambda$ masses. A neutral-mode energy-scale error will shift the vertex; however, as no vertex cut was made, the corresponding systematic error was greatly reduced. The energy scale was initially determined for each block with only the electron calibration data. A final correction of $\approx 0.5\%$ was made to adjust the edges of the vertex distributions; the residual uncertainty was estimated at 0.2%, leading to an uncertainty in the double ratio of 0.21%.

The sources of uncertainties in the backgrounds were as follows (see Table I): The $3\pi^0$ contamination (Fig. 2) was determined by the fit of the background shape from a Monte Carlo simulation; the major uncertainty came from imperfectly known efficiencies of some veto planes. The backgrounds in $K_L \rightarrow \pi^+\pi^-$ were well understood semileptonic decays ($\approx 85\%$) and a small ($\approx 15\%$) non-kaon-decay component.

The diffractive and inelastic components under the coherent peaks in the $K_S$ samples were rejected by a cut on the momentum transfer $P_t^2$ at the regenerator. (Of course the identical cut was applied to the $K_L$ samples.) The distributions in this variable were very well understood for both decay modes and in fact they are the same in principle. The remaining background in the neutral
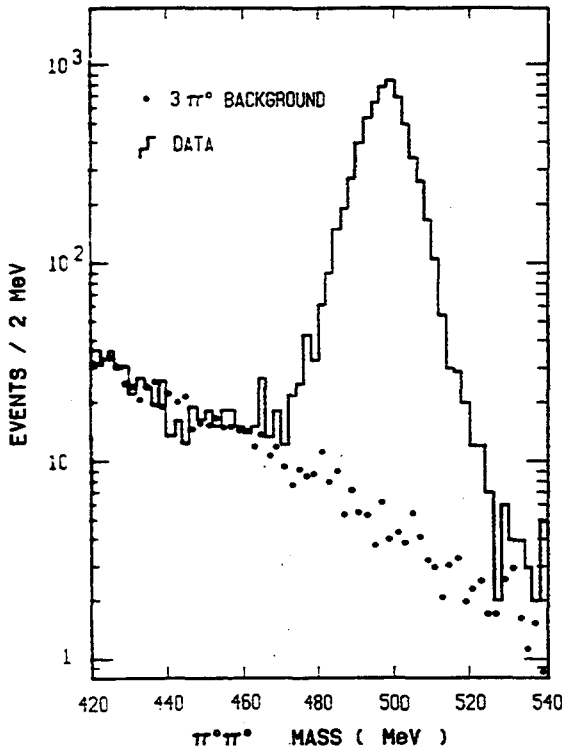


FIG. 2. Reconstructed $\pi^0\pi^0$ invariant mass for $K_L$. The $3\pi^0$ background shape determined from Monte Carlo is superimposed.



FIG. 3. Reconstructed decay-vertex distribution for $K_{L,S} \rightarrow 2\pi^0$, data and Monte Carlo simulation.

mode was larger because of the poorer resolution [1500 $(\text{MeV}/c)^2$] of the coherent peak; the error in the subtraction was dominated by resolution uncertainties.

The remaining systematic error comes from uncertainties in the acceptances for charged and neutral decays. Very important checks were provided by consistency in the acceptance-corrected momentum spectra and regeneration power laws between the two modes. In the charged mode, where the resolution on the reconstructed vertex is excellent (15 cm rms), the data can be analyzed in small bins with little statistical loss, and by our fitting the ratios of regenerated to vacuum events, acceptance corrections are reduced significantly. For example, with 1.5-m bins the overall correction is only 0.48%. From such studies the systematic error in the charged acceptance is estimated to be 0.25%.

In the neutral mode, the poorer vertex resolution (1.1 m rms) and energy-scale uncertainty complicate the use of small bins. Figure 3 shows the vertex distributions compared with the Monte Carlo simulation; agreement is excellent but an independent check is desired. There were only three apertures for photons so that the acceptance could be readily understood: the lead-glass array (including the hardware-defined inner edge around the beam holes), a lead mask just upstream of the regenerator (see Fig. 1), and a thick lead aperture surrounding the conversion plane. In a typical momentum bin, the acceptance downstream of the mask varied with vertex by only about 1% per meter, the mean decay position for $K_L$ and $K_S$ events differed by less than 2 m, and the acceptance correction was about 2%. For the region upstream of the mask ($\approx 10\%$ of the $K_L$ data), the acceptance varied more sharply (by design). Both regions were studied with over 500000 $3\pi^0$ decays having even greater acceptance variations; there was no disagreement with the Monte Carlo simulation outside statistics. Furthermore, a consistent result was obtained when we discarded the upstream events although then the error from an energy scale uncertainty increased to about 0.4%. From these studies, the uncertainty in the neutral-mode acceptance correction was estimated at 0.50%.

The total systematic error on the double ratio is given by our combining all the above (uncorrelated) uncertainties in quadrature yielding an error of 0.75%. The result is $\epsilon'/\epsilon = 0.0032 \pm 0.0028$ (statistical) $\pm 0.0012$ (systematic). Combining these errors in quadrature gives $\epsilon'/\epsilon = 0.0032 \pm 0.0030$. This is consistent with previous measurements while being more precise by nearly a factor of 2; however, the superweak and Kobayashi-Maskawa models are both still viable. The experiment is running with upgrades and a significant increase in statistical precision is expected.[13]

(a)Present address: Institute for Nuclear Study, University of Tokyo, Tokyo, Japan.

[1]J. H. Christenson, J. W. Cronin, V. L. Fitch, and R. Turlay, Phys. Rev. Lett. 13, 138 (1964).

[2]M. Kobayashi and T. Maskawa, Prog. Theor. Phys. 49, 652 (1973).

[3]S. Herb et al., Phys. Rev. Lett. 39, 252 (1977).

[4]Since $\arg(\epsilon') = \arg(\epsilon)$, $\text{Re}\,\epsilon'/\epsilon = \epsilon'/\epsilon$; see J. W. Cronin, Rev. Mod. Phys. 53, 373 (1981).

[5]L. Wolfenstein, Phys. Rev. Lett. 13, 569 (1964).

[6]See L. Wolfenstein, Annu. Rev. Nucl. Part. Sci. 36, 137 (1986), for a discussion of the predictions.

[7]R. H. Bernstein et al., Phys. Rev. Lett. 54, 1631 (1985).

[8]J. K. Black et al., Phys. Rev. Lett. 54, 1628 (1985).

[9]See A. Gsponer et al., Phys. Rev. Lett. 42, 13 (1979).

[10]For a full description of the analysis and detector see P. Jarry, Ph.D. thesis, Université de Paris-Sud, 1987 (unpublished); M. Woods, Ph.D. thesis, University of Chicago, 1988 (unpublished).

[11]Here $f$ ($\bar{f}$) is the forward $K^0$ ($\bar{K}^0$) scattering amplitude and $k$ is the kaon wave number. The fit included interference with $K_L$ decays.

[12]A preliminary result was given by B. Winstein, in Proceedings of the Salt Lake City Meeting, edited by Carleton DeTar and James Ball (World Scientific, Singapore, 1987), pp. 37-58.

[13]Another experiment with a different technique at CERN has the preliminary result $\epsilon'/\epsilon = 0.0035 \pm 0.0007$ (statistical) $\pm 0.0012$ (systematic) $\pm 0.0004$ (Monte Carlo), and it also will acquire more data. See the review by I. Mannelli, in Proceedings of the International Symposium on Lepton and Photon Interactions at High Energies, Hamburg, West Germany, 1987 (to be published).

# New Limits on $K_{L,S} \to \pi^0 e^+ e^-$

L. K. Gibbons, V. Papadimitriou, J. R. Patterson, Y. W. Wah, B. Winstein, R. Winston, M. Woods, [(a)] and
H. Yamamoto

*The Enrico Fermi Institute and the Department of Physics, The University of Chicago, Chicago, Illinois 60637*

E. C. Swallow

*Department of Physics, Elmhurst College, Elmhurst, Illinois 60126, and*
*The Enrico Fermi Institute, The University of Chicago, Chicago, Illinois 60637*

G. J. Bock, R. Coleman, Y. B. Hsiung, K. Stanfield, R. Stefanski, and T. Yamanaka

*Fermi National Accelerator Laboratory, Batavia, Illinois 60510*

G. Blair, [(b)] G. D. Gollin, M. Karlsson, and J. K. Okamitsu

*Department of Physics, Princeton University, Princeton, New Jersey 08544*

P. Debu, B. Peyaud, R. Turlay, and B. Vallage

*Department de Physique des Particules Elementaires, Centre d'Etudes Nucleaires de Saclay,*
*F-91191 Gif-sur-Yvette CEDEX, France*

Data taken in a Fermilab experiment designed to measure the $CP$-violation parameter $\epsilon'/\epsilon$ from a study of $K \to 2\pi$ decays were used to look for the as yet unseen decay modes $K_{L,S} \to \pi^0 e^+ e^-$. The detector was optimized for the detection of kaon decays with four electromagnetic showers in the final state. The results (90% confidence) are branching ratios $< 4.2 \times 10^{-8}$ and $< 4.5 \times 10^{-5}$ for $K_L \to \pi^0 e^+ e^-$ and $K_S \to \pi^0 e^+ e^-$, respectively.

PACS numbers: 13.20.Eb

The $\pi^0 e^+ e^-$ decay of the long-lived neutral kaon ($K_L$) is an attractive avenue for the observation of $CP$ violation in a decay amplitude, particularly should detailed studies of the $2\pi$ decays of the neutral kaon ($\epsilon'/\epsilon$) prove inconclusive. The $CP$-violating amplitude is expected[1] to be comparable to or larger than the $CP$-conserving one. The leading $CP$-conserving amplitude proceeds through two-photon exchange while the $CP$-violating one may proceed via one-photon exchange. Within the framework of the standard model where $CP$ violation comes from the phase $\delta$ in the Kobayashi-Maskawa matrix,[2] $K_L \to \pi^0 e^+ e^-$ may have a sizable $\Delta S = 1$ $CP$-violating effect. Theoretical estimates[1] of the branching ratio are in the $10^{-11}$ range, while the current experimental limit[3] is $< 2.3 \times 10^{-6}$ at 90% confidence. There has been no $K_S \to \pi^0 e^+ e^-$ measurement, while predictions[1] range from $5 \times 10^{-9}$ to $5 \times 10^{-10}$.

Fermilab experiment E-731, which was performed in the Meson Center beam line at the Tevatron, had as its primary goal the determination of the $K \to 2\pi$ $CP$-violation parameter $\epsilon'/\epsilon$. The present search is based upon the analysis of a special data set in which $K_{L,S} \to \pi^0 \pi^0$ and $K_{L,S} \to \pi^+ \pi^-$ were recorded simultaneously.

Two neutral $K_L$ beams ($\frac{1}{2} \times \frac{1}{2}$ mrad$^2$) were created at 4.8 mrad by 800-GeV protons striking a Be target. A regenerator which moved alternately between the beams every proton spill was used to provide $K_S$. The detector

was employed in an earlier test run and it is shown schematically in Fig. 1; it has been described elsewhere[4,5] in detail. Charged particles were measured and momentum analyzed with a 2000-wire drift-chamber spectrometer which consisted of eight $x$ planes and eight $y$ planes with 0.635-cm maximum drift distance. These planes had a position resolution of about 110 $\mu$m and were 98% efficient. Energies and positions of photons and electrons were measured with an 804-block lead-glass array stacked circularly. Each block measured 5.82 cm ($H$) by 5.82 cm ($W$) by 60 cm ($L$), giving a depth of 20 radiation lengths. There were two holes (11.6 cm × 11.6 cm) separated vertically by 11.6 cm at the center of the array for the beams to pass. A common pulsed light source illuminated every block once every second to provide short-term gain tracking. The pulse heights were digitized with effectively 15-bit analog-to-digital converters using a 150-ns gate.

Several improvements have been made to the detector since the previous data taking period. The most important one was the instrumentation of each of the lead-glass phototube outputs with a 60-MHz flash analog-to-digital converter. These were the front-end electronics for a two-dimensional cluster-finding trigger processor, and they also served to suppress out-of-time photons. A cluster was defined as a "neighbor-connected" island of lead-glass blocks each with more than 1 GeV. The trigger processor contributed less than 2% dead time and

FIG. 1. Detector schematic, elevation view.

a FASTBUS-based data-acquisition system was implemented to increase the data taking capability as well.

There were two triggers relevant to the data set used in this search. The first ("four cluster") required exactly four clusters, 30 GeV or more energy deposited in the lead-glass, and no hit in the trigger plane (see Fig. 1). Hence this trigger recorded $\pi^0 e^+ e^-$ candidates in the downstream decay region as well as $\pi^0 \pi^0$ candidates from both upstream and downstream decay regions. The second trigger ("two track") required one or more hits at the trigger plane and



FIG. 2. (a) Distribution of $E/P$ in the lead-glass from the electron calibration data. The resolution is about 4% rms; (b) distribution of the $\pi^0$ mass reconstructed from $K_L \rightarrow \pi^+ \pi^- \pi^0$ decays.

two tracks in the spectrometer, and hence was sensitive to $\pi^0 e^+ e^-$ decays from the upstream decay region; however, this trigger was prescaled by a factor of 8.

Because the trigger processor used signals from the lead-glass directly, the relative gains of all lead-glass blocks were monitored and adjusted to within 5% over the entire data taking period. Calibration data with $e^+ e^-$ pairs produced in a thin upstream foil were taken periodically to provide high-statistics calibration for the lead-glass; the resolution was $\sigma/E \approx 1.5\% + 5\%/\sqrt{E}$ ($E$ in GeV). Chamber-alignment data were also recorded daily.

The momenta of the $e^+$ and $e^-$ and the decay vertex of $K_L \rightarrow \pi^0 e^+ e^-$ candidates were determined by the drift-chamber spectrometer. The $e^+$ and $e^-$ were identified by matching the tracks with the clusters, and requiring $0.85 < E/P < 1.15$, where $E$ is the cluster energy and $P$ is the momentum. Figure 2(a) shows the $E/P$ distribution for electrons from the calibration data (which is essentially identical to the same distribution of electrons from $K_{e3}$ decays taken during the main data run). From a study of $K_L \rightarrow \pi^+ \pi^- \pi^0$ decays, the $\pi^0$

mass resolution was determined to be about 4 MeV/$c^2$ [see Fig. 2(b)]. The $\gamma\gamma$ mass was required to be within 10 MeV/$c^2$ of the nominal $\pi^0$ value. By then constraining the $\gamma\gamma$ mass to the nominal value, the reconstructed kaon mass ($M_{\pi ee}$) would have a resolution of about 4.5 MeV/$c^2$. The square of the transverse momentum ($P_t^2$) of the $\pi^0 e^+ e^-$ system with respect to the line connecting the decay vertex and the production target had a resolution of about 50 MeV$^2$/$c^2$. The candidates are displayed in a two-dimensional $M_{\pi ee}$ vs $P_t^2$ plot as shown in Fig. 3(b). A candidate is defined to have $P_t^2 < 200$ MeV$^2$/$c^2$ and $489 < m_K < 507$ MeV/$c^2$; these cuts would include about 95% of the signal. No candidate is found in the signal region. Figure 3(a) shows the equivalent region for $K_L \rightarrow \pi^+ \pi^- \pi^0$ decays. Given the timing and energy resolution of the detector, the background of $K \rightarrow 2\pi^0$ with Dalitz decays is insignificant; the very few remaining events are consistent with radiative $K_{e3}$ with an accidental photon.

Figure 4 shows the relative acceptance for Monte Carlo–generated $K_L \rightarrow \pi^0 e^+ e^-$ decays as a function of the $e^+ e^-$ effective mass. Because of the loose cuts, the



FIG. 3. Reconstructed kaon mass vs the square of the transverse momentum for (a) $K_L \rightarrow \pi^+ \pi^- \pi^0$ and (b) $K_L \rightarrow \pi^0 e^+ e^-$. There are 24 events above the top of the plot in (b). The events in the plots were selected with a $\pi^0$ mass cut of $2.5\sigma$ and the boxes represent the signal region. There are no background events for the $K_S$ decay.

FIG. 4. The relative acceptance vs the $e^+e^-$ invariant mass of the $K_L \rightarrow \pi^0 e^+ e^-$ decay for the four-cluster trigger.

$\rightarrow \pi^+\pi^-$ decays from the two-track trigger as normalization, the 90%-confidence limits from that trigger are $<4.1\times10^{-7}$ and $<4.5\times10^{-5}$, respectively.

By the combination of the above, the results are $B(K_L \rightarrow \pi^0 e^+ e^-) < 4.2\times10^{-8}$ and $B(K_S \rightarrow \pi^0 e^+ e^-) < 4.5 \times 10^{-5}$ (90% confidence). This is the first limit of any significance for the $K_S$ decay. The $K_L$ limit is an improvement of more than a factor of 50 over the previous limit[3]; while still far from the level predicted by the standard model, it serves to constrain the parameters of light scalar particles coupling to $e^+ e^-$. The result is consistent with $B(K_L \rightarrow \pi^0 e^+ e^-) < 3.2\times10^{-7}$, recently obtained by Jastrzembski et al.[6]

effect of internal radiation is expected to be small; external radiation is properly treated. For the four-cluster trigger, the acceptance is 9.5% for a fiducial downstream decay volume of 22.2 m and for the two-track trigger, the acceptance is about 10% for an upstream decay volume of 14 m for kaon energy between 30 and 150 GeV, assuming a uniform three-body phase space distribution.

The upper limit $B(K_L \rightarrow \pi^0 e^+ e^-) < 4.7\times10^{-8}$ (90% confidence) is obtained by normalizing to a sample of $58.8\times10^3$ $K_L \rightarrow 2\pi^0$ decays observed simultaneously in the four-cluster trigger. The normalization data do not require track reconstruction; however, the relative branching ratios of $\pi^+\pi^-$ to $\pi^0\pi^0$ from both $K_L$ and $K_S$ were also determined from the same data set and they agree with the published values to within 5%. With the use of $71.3\times10^3$ $K_L \rightarrow \pi^+\pi^-$ and $2.24\times10^5$ $K_S$

(a)Present address: SLAC, Stanford, CA 94305.

(b)Present address: Department of Nuclear Physics, Oxford University, Oxford, United Kingdom.

[1]J. F. Donoghue, B. R. Holstein, and G. Valencia, Phys. Rev. D 35, 2769 (1987), and references within; L. M. Sehgal, Phys. Rev. D 38, 808 (1988); G. Ecker, A. Pich, and E. deRafael, Nucl. Phys. B303, 665 (1988).

[2]M. Kobayashi and T. Maskawa, Prog. Theor. Phys. 49, 652 (1973).

[3]A. S. Carroll et al., Phys. Rev. Lett. 46, 525 (1980).

[4]M. Woods et al., Phys. Rev. Lett. 60, 1695 (1988).

[5]For a complete description of the detector see P. Jarry, Ph.D. thesis, Université de Paris-Sud, 1987 (unpublished); M. Woods, Ph.D. thesis, University of Chicago, 1988 (unpublished).

[6]E. Jastrzembski et al., Phys. Rev. Lett. 61, 2300 (1988).

# Search for $K_L \to \pi^0 \gamma \gamma$

V. Papadimitriou, L. K. Gibbons, J. R. Patterson, Y. W. Wah, B. Winstein, R. Winston, M. Woods,[a] and
H. Yamamoto

*The Enrico Fermi Institute and the Department of Physics, The University of Chicago,
Chicago, Illinois 60637*

E. C. Swallow

*Department of Physics, Elmhurst College, Elmhurst, Illinois 60126
and The Enrico Fermi Institute, The University of Chicago, Chicago, Illinois 60637*

G. J. Bock, R. Coleman, Y. B. Hsiung, K. Stanfield, R. Stefanski, and T. Yamanaka

*Fermi National Accelerator Laboratory, Batavia, Illinois 60510*

G. D. Gollin, M. Karlsson, and J. K. Okamitsu

*Department of Physics, Princeton University, Princeton, New Jersey 08544*

P. Debu, B. Peyaud, R. Turlay, and B. Vallage

*Department de Physique des Particules Elementaires, Centre d'Etudes Nucleaires de Saclay,
F-91191 Gif-sur-Yvette CEDEX, France*
(Received 20 April 1989)

A search for the rare decay mode $K_L \to \pi^0 \gamma \gamma$ was performed using a data set from Fermilab experiment E-731. The decay is of interest in the context of chiral perturbation theory and for its contribution to the decay $K_L \to \pi^0 e^+ e^-$. The result is $B(K_L \to \pi^0 \gamma \gamma) < 2.7 \times 10^{-6}$ (90% confidence level) which is nearly a two-order-of-magnitude improvement over the previous best limit.

The as yet unobserved decay $K_L \to \pi^0 \gamma \gamma$ is of current interest for at least three reasons. First, it provides an opportunity to test the standard model in the context of chiral symmetry: At the one-loop level in chiral perturbation theory,[1] the decay has a branching ratio of $6.8 \times 10^{-7}$ with a characteristic $\gamma\gamma$ invariant-mass $(m_{\gamma\gamma})$ distribution having a peak at about 325 MeV.[2] Second, this decay provides a *CP*-conserving intermediate state for the $K_L \to \pi^0 e^+ e^-$ decay which has been the subject of recent experimental[3-5] and theoretical[6] attention as a possible avenue for the observation of direct *CP* nonconservation; its magnitude will greatly affect the interpretation of the results of such experimental efforts. Third, this mode could be a background to the $K_L \to 2\pi^0$ decay for precision experiments[7,8] measuring $\epsilon'/\epsilon$, especially if its branching ratio were at the level of the current limit,[9,10] $2.4 \times 10^{-4}$.

The principal background for this mode is the $K_L \to 3\pi^0$ decay occurring $3 \times 10^5$ times more frequently than the signal. The challenge in observing such a signal at the predicted level is the effective rejection of the $3\pi^0$ decays; in addition, the understanding of the residual background after the necessarily stringent analysis cuts allows better sensitivity.[11]

This experiment, E-731 at Fermilab, collected data with the primary goal of determining $\epsilon'/\epsilon$. The search reported here is based upon an analysis of a subset of the data that was particularly suited for this analysis. Some characteristics of the detector have been described previously;[3,7] here, we summarize the essential features relevant to the decay mode in question. Energies and positions of photons were measured with an 804-block lead-glass array having transverse block dimensions of $5.82 \times 5.82$ cm$^2$. The energy resolution for photons was given approximately by $\sigma_E/E = (2.5 + 5.0/\sqrt{E})\%$ ($E$ in GeV) and the corresponding $\pi^0$ mass resolution was about 3 MeV. Events with the desired number of electromagnetic showers were selected on line by a trigger processor[12] which counted clusters in the lead-glass array. Eleven planes of photon-veto counters situated between 75 m upstream and 2 m downstream of the lead glass were employed to reject the background arising from $K_L \to 3\pi^0$ decays where one or two photons miss the lead-glass calorimeter. A drift-chamber system was used to reject $K_L$ decays with charged particles in the final state.

Candidates for the $K_L \to \pi^0 \gamma \gamma$ decay were required to have exactly four clusters in the lead-glass array and total energy between 40 and 150 GeV. The decay vertex was determined with the measured cluster energies and positions by assuming that the invariant mass of the four photons was that of the neutral kaon. To determine the pairing of the photons, the pair with invariant mass closest to that of the neutral pion $(m_{\pi^0})$ was chosen as the candidate $\pi^0$; this pair is labeled (12) and it was required that $|m_{12} - m_{\pi^0}| < 5$ MeV. Up to this point the

cuts were also satisfied by $2\pi^0$ decays which would usually have both pair masses, $m_{12}$ and $m_{34}$, consistent with $m_{\pi^0}$. The rejection of the $2\pi^0$ decays was done in two steps. First, it was required that $|m_{34}-m_{\pi^0}| > 12$ MeV; this resulted in a suppression of a factor of about 25. Second, some $2\pi^0$ events with their photons paired as (13)(24) or (14)(23) would still remain; if either of these alternative pairings was consistent with the $2\pi^0$ hypothesis,[7] the event was also discarded. This latter requirement provided an additional rejection factor of about 40.

$K_L \rightarrow 3\pi^0$ decays can become background four-cluster



FIG. 1. (a) $\gamma\gamma$ invariant mass for $K_L \rightarrow \pi^0\gamma\gamma$ decay events. The histograms are the candidate events and the solid curve represents the distribution predicted by chiral perturbation theory for a branching ratio of $10^{-5}$. The arrow indicates the position of the cut (300 MeV). (b) $\gamma\gamma$ invariant mass for data and background Monte Carlo simulation. The dots correspond to the data [the same as in (a) with coarser binning]; the shaded histogram corresponds to the $K_L \rightarrow 2\pi^0$ contribution to the background; the unshaded histogram corresponds to the sum of the backgrounds from $K_L \rightarrow 2\pi^0$ and from $K_L \rightarrow 3\pi^0$ decays. The background Monte Carlo simulation (twice the statistics as the data) is absolutely normalized.

events either when photons are undetected or when they overlap in the lead glass so that they are unresolvable as separate clusters. The veto counters were effective in detecting photons escaping from the fiducial volume of the detector and events with substantial energy deposit in these counters were rejected from the sample. In addition, the transverse center of energy of the four photons was required to be in the $K_L$ beam region ($11.2 \times 11.2$ $cm^2$).[13] The number of events with unresolved overlapping clusters was substantially reduced by rejecting those with cluster shapes inconsistent with that of a single photon. The $3\pi^0$ background was further reduced by considering only decays in the upstream 14-m region of the decay volume ending 57 m upstream of the glass array. The reconstructed decay vertex in events with missing photons is artificially shifted downstream; also, photons are more likely to overlap when the decay occurs near the lead-glass array. The selection of this region of the decay region was made on the basis of a Monte Carlo study to optimize the experimental sensitivity in the presence of this background. These criteria provide a rejection factor for $3\pi^0$ decays relative to $\pi^0\gamma\gamma$ decays of about $10^4$.

Figure 1(a) shows the $\gamma\gamma$ effective mass for the "non $\pi^0$" photon pair. A characteristic feature in this distribution is a prominent "double fusion" peak appearing at about $m_{\gamma\gamma} = 270$ MeV which arises when two $\pi^0$s in $K_L \rightarrow 3\pi^0$ decays are superimposed: Each photon from one $\pi^0$ overlaps with a photon from the other $\pi^0$ with an invariant-mass threshold of twice the $\pi^0$ mass. The solid curve indicates the $K_L \rightarrow \pi^0\gamma\gamma$ signal shape predicted by chiral perturbation theory;[1] $(60.0 \pm 1.2)\%$ of the $\pi^0\gamma\gamma$ events have $m_{\gamma\gamma}$ greater than 300 MeV and we have chosen this region for our search to have good discrim-



FIG. 2. Acceptance vs the $\gamma\gamma$ invariant mass for $K_L \rightarrow \pi^0\gamma\gamma$ decays. The dip around 135 MeV is due to the cut that excludes $\gamma\gamma$ masses near the $\pi^0$ mass.

FIG. 3. The decay-vertex distribution, in meters from the $K_L$ production target, for $K_L \rightarrow \pi^0\gamma\gamma$ candidates and background Monte Carlo events with $m_{\gamma\gamma} > 300$ MeV. The dots correspond to the data, while the histogram corresponds to the sum of the backgrounds from $K_L \rightarrow 2\pi^0$ and from $K_L \rightarrow 3\pi^0$ decays. The background Monte Carlo simulation is absolutely normalized. The arrow indicates the position of the cut (124 m).

ination against background. The acceptance is relatively flat for $m_{\gamma\gamma}$ above 160 MeV, as shown in Fig. 2. Figure 1(b) shows the Monte Carlo predictions of the backgrounds to $\pi^0\gamma\gamma$ decay coming from the $3\pi^0$ and $2\pi^0$ modes. The Monte Carlo distributions are normalized by means of a sample of fully reconstructed $K_L \rightarrow 2\pi^0$ decays observed simultaneously. The contribution from accidental clusters is found to be negligible. Figure 3 shows agreement in the reconstructed vertex distributions for the signal and expected background events with $m_{\gamma\gamma} > 300$ MeV, including the region downstream of the fiducial cut.

For the high-mass sample ($m_{\gamma\gamma} > 300$ MeV), we have 24 candidate events with a predicted background of 20.8 events (18.2 from $3\pi^0$'s and 2.6 from $2\pi^0$'s). From studies of the $3\pi^0$ background in this mode and in the $K_L \rightarrow 2\pi^0$ mode, we assign a 20% error to the estimate of the background in the high-mass region which is a combination of the statistical error in the Monte Carlo simulation (15%) and our estimate of the systematic error (12%). The systematic uncertainty comes largely from lack of precise knowledge of the efficiencies of the photon-veto planes. The 90%-confidence-allowed signal is 13.9 events, calculated with the maximum-likelihood method. The $\pi^0\gamma\gamma$ acceptance is 2.4% and the normalization is provided by $11.1 \times 10^3$ $K_L \rightarrow 2\pi^0$ decays observed simultaneously and selected with similar criteria as the $\pi^0\gamma\gamma$ candidates where appropriate, including photon-veto, cluster-shape, decay-region, and total-energy cuts. The corresponding acceptance for $K_L \rightarrow 2\pi^0$ is 5.8%. Using world average values[10] for the $K_L \rightarrow 2\pi^0$ and for $K_L \rightarrow 3\pi^0$ branching ratios we con-

clude that $B(K_L \rightarrow \pi^0\gamma\gamma) < 2.7 \times 10^{-6}$ (90% confidence level). We have assumed that the $m_{\gamma\gamma}$ spectrum follows that predicted in chiral perturbation theory; if instead a uniform phase space for the decay is assumed, the limit becomes $4.4 \times 10^{-6}$ (90% confidence level) where the whole mass range except the region of the double fusion peak (264–292 MeV) is used.

Our result is nearly a factor of 90 improvement over the current experimental limit[9,10] which was also calculated using a distribution in $m_{\gamma\gamma}$ similarly peaked at high values. It is consistent with the predictions of chiral perturbation theory although another factor of about 4 in sensitivity would be required to confirm the prediction. The CP-conserving contribution to $K_L \rightarrow \pi^0 e^+ e^-$ has now been better constrained and we have shown that this decay should not be a serious background to the $K_L \rightarrow 2\pi^0$ mode.

---

(a)Present address: SLAC, Stanford, CA 94305.

[1]G. Ecker, A. Pich, and E. De Rafael, Phys. Lett. B 189, 363 (1987).

[2]Alternative theoretical approaches to this decay, predicting similar branching ratios, have also been considered: One of them assumed a $\pi^+\pi^-\pi^0$ intermediate state where the charged pions annihilate to two photons: P. Ko and J. Rosner, Enrico Fermi Institute Report No. EFI 89-13, 1989 (to be published); L. M. Sehgal, Phys. Rev. D 6, 367 (1972). Another applied the vector-dominance model: T. Morozumi and H. Iwasaki, KEK Report No. KEK-TH-206, 1988 (unpublished).

[3]L. K. Gibbons et al., Phys. Rev. Lett. 61, 2661 (1988).

[4]G. D. Barr et al., Phys. Lett. B 214, 303 (1988).

[5]E. Jastrzembski et al., Phys. Rev. Lett. 61, 2300 (1988).

[6]See, for example, C. O. Dib, I. Dunietz, and F. Gilman, Phys. Rev. D 39, 2639 (1989), and references therein.

[7]M. Woods et al., Phys. Rev. Lett. 60, 1695 (1988).

[8]H. Burkhardt et al., Phys. Lett. B 206, 169 (1988).

[9]M. Banner, J. W. Cronin, J. K. Liu, and J. E. Pilcher, Phys. Rev. 188, 2033 (1969).

[10]Particle Data Group, G. P. Yost et al., Phys. Lett. B 204, 1 (1988).

[11]We point out that quantitative understanding of the background in the $\pi^0\gamma\gamma$ mode will also give increased confidence in the background estimate in the better constrained $\pi^0\pi^0$ mode.

[12]H. Sanders, V. Papadimitriou, J. Ting, Y. W. Wah, and E. Weatherhead, IEEE Trans. Nucl. Sci. 36, 358 (1988).

[13]The regenerated $K_S$ beam is not used in this analysis.

# Determination of Re(ε'/ε) by the Simultaneous Detection of the Four $K_{L,S} \to \pi\pi$ Decay Modes

J. R. Patterson, A. Barker, R. A. Briere, L. K. Gibbons, G. Makoff, V. Papadimitriou, S. Somalwar,
Y. W. Wah, B. Winstein, R. Winston, M. Woods,[a] and H. Yamamoto
*The Enrico Fermi Institute and the Department of Physics, The University of Chicago, Chicago, Illinois 60637*

E. Swallow
*Department of Physics, Elmhurst College, Elmhurst, Illinois 60126
and the Department of Physics, The University of Chicago, Chicago, Illinois 60637*

G. J. Bock, R. Coleman, J. Enagonio, Y. B. Hsiung, K. Stanfield, R. Stefanski, and T. Yamanaka
*Fermi National Accelerator Laboratory, Batavia, Illinois 60510*

G. Blair,[b] G. D. Gollin,[c] M. Karlsson, J. K. Okamitsu,[d] and R. Tschirhart
*Department of Physics, Princeton University, Princeton, New Jersey 08544*

J. C. Brisson, P. Debu, B. Peyaud, R. Turlay, and B. Vallage
*Département de Physique des Particules Élémentaires, Centre d'Etudes Nucléaires de Saclay,
F-91191 Gif-sur-Yvette CEDEX, France*
(Received 18 December 1989)

The E731 experiment at Fermilab has searched for direct CP violation in $K^0 \to \pi\pi$, which is parametrized by ε'/ε. For the first time all four of the $K_{L,S} \to \pi\pi$ modes were collected simultaneously, which greatly facilitated studies of systematic uncertainty. We find Re(ε'/ε) = −0.0004 ± 0.0014(stat) ± 0.0006(syst). The result provides no evidence for direct CP violation.

This paper presents a new determination of the CP-violation parameter Re(ε'/ε). Since a result[1] from the first run of this experiment was reported, the detector has been improved and substantially more data have been collected.

The six-quark model[2] of Cabibbo, Kobayashi, and Maskawa (CKM) provides the most natural way of incorporating CP violation into the weak interaction. Until very recently, the only observed CP-nonconserving effects were consistent with asymmetric $K^0$-$\bar{K}^0$ mixing, parametrized by ε. This is a second-order effect in the CKM framework, but could also signal a new $\Delta S = 2$ interaction (e.g., superweak[3]). Within the CKM framework, first-order ("direct") CP nonconservation in $K^0 \to \pi\pi$ decays, parametrized by ε'/ε, is also expected, and searches for it in the predicted range provide an important test of the model. Recently, the NA31 group at CERN reported[4] evidence for such an effect.

As is well known, Re(ε'/ε) can be determined from the double ratio R of the $\pi\pi$ decay rates of the $K_L$ and $K_S$ mesons:

$$R \equiv \frac{\Gamma(K_S \to \pi^+\pi^-)/\Gamma(K_L \to \pi^+\pi^-)}{\Gamma(K_S \to \pi^0\pi^0)/\Gamma(K_L \to \pi^0\pi^0)} \approx 1 - 6\,\mathrm{Re}(\epsilon'/\epsilon).$$

It is important to minimize systematic uncertainty in the collection and analysis of the four decay modes. In our experiment, the $K_S$ are provided by coherent regeneration, ensuring an angular divergence identical to that of the $K_L$, and very similar momentum spectra for $\pi\pi$

events. Decays of $K_S$ and $K_L$ to a given final state (charged or neutral) are collected at the same time by means of side-by-side $K_L$ and $K_S$ beams, so electronic drifts, accelerator instabilities, and phototube gain shifts affect them virtually identically. Furthermore, the regenerator alternates between the beams, rendering the effect of asymmetries in the beams or the detector response negligible. The analysis[5] reported here is based on about 20% of the data collected during a fixed-target run at Fermi National Accelerator Laboratory. These are distinguished in that, for the first time, decays from all four modes were collected simultaneously.

As a function of proper time $t$ from the regenerator, the $\pi\pi$ decay rates in the vacuum and regenerated beams are proportional to $|\eta|^2$ and $|\rho\exp(-t/2\tau_S + i\Delta m\, t) + \eta|^2$, respectively; $\rho$ is the coherent regeneration amplitude, $\tau_S$ is the $K_S$ lifetime, $\Delta m$ is the $K_L$-$K_S$ mass difference, and $\eta$ is the appropriate ratio of $K_L$-to-$K_S$ decay amplitudes. Because $|\rho| \gg |\eta|$, the ratio of the total number of regenerated to vacuum charged (neutral) decays $R_{+-(00)}$ is proportional to $|\rho/\eta_{+-(00)}|^2$. Thus, $R \approx R_{+-}/R_{00}$.

Kaons were produced by 800-GeV protons incident at 5 mrad on a beryllium target. The regenerator, instrumented to detect inelastic regeneration, was located 123 m downstream of the target.

An 804-block lead-glass calorimeter 181 m from the target determined the energies and positions of photons and electrons. Its energy resolution was roughly 1.5%

FIG. 1. Invariant-mass distribution for $K_L \rightarrow \pi^0\pi^0$ events. The histogram is data; the solid circles are from a Monte Carlo simulation for the residual $K_L \rightarrow \pi^0\pi^0\pi^0$ background, absolutely normalized. A very small nonkaon contribution, seen here at high mass, is also subtracted. The arrows indicate the positions of the cuts.

FIG. 2. Event density in equal-area concentric rings around the $K_L$ beam for $\pi^0\pi^0$ events. The histogram is data; the solid circles show the expected size and shape of incoherent events from the regenerator as determined from $\pi^+\pi^-$. The arrow indicates the position of the cut.

$(2.5\%) + 5\%/\sqrt{E}$ ($E$ in GeV) for electrons (photons). The neutral trigger required greater than 28 GeV in the calorimeter and either four or six isolated electromagnetic clusters,[6] accepting $\pi^0\pi^0\pi^0$ as well as $\pi^0\pi^0$ decays. Eleven planes of photon veto counters were employed to reduce background from $\pi^0\pi^0\pi^0$ decays with photons missing the lead glass.

The decay vertex for $K_{L,S} \rightarrow \pi^0\pi^0$ decays was found by pairing the photons using the known $\pi^0$ mass as a constraint. The $\pi^0\pi^0$ invariant mass is shown in Fig. 1 for $K_L$ decays, differentiated from $K_S$ decays by means of the center of energy of the four photons in the calorimeter. The residual background from $K_L \rightarrow \pi^0\pi^0\pi^0$ decays was $(0.37 \pm 0.07)\%$, and was well reproduced by a Monte Carlo simulation.

Charged tracks were reconstructed (typically with 1% momentum resolution) using a 16-plane drift-chamber spectrometer with 100-$\mu$m resolution per plane. A (prescaled) two-track trigger was formed using hodoscopes at 137.8 and 179.5 m; $K_{\mu3}$ decays were rejected using a muon filter. Thus, $\pi e\nu$ and $\pi^+\pi^-\pi^0$ as well as $\pi^+\pi^-$ decays were accepted.

For $K_{L,S} \rightarrow \pi^+\pi^-$ decays the invariant-mass resolution was about 3.5 MeV/$c^2$; the cut was $\pm 14$ MeV/$c^2$ around the nominal kaon mass. Background from $\pi e\nu$ decays was reduced with cuts on $E/p$ and the kaon transverse momentum ($P_t^2 < 250$ MeV$^2/c^2$). The residual $K_L$ background was $(0.32 \pm 0.06)\%$.

To extract the coherently regenerated $K_S$ signals, the diffractive and inelastic contributions must be subtracted. After the $P_t^2$ cut, we found a $(0.13 \pm 0.01)\%$ contribution to $K_S \rightarrow \pi^+\pi^-$ from such incoherent events; this

is 2.3 times smaller than in Ref. 1, largely because of the removal of 1.5 in. of lead from the regenerator. For neutral decays, only the center of energy at the calorimeter was available to identify incoherently regenerated $K_S$, which scattered into both the $K_L$ and $K_S$ beams. Their contributions were accurately predicted from the $P_t^2$ distribution for simultaneously observed $\pi^+\pi^-$ decays (Fig. 2), and were $[4.70 \pm 0.14(\text{syst})]\%$ and $[2.56 \pm 0.07(\text{syst})]\%$ for the $K_L$ and $K_S$ samples, respectively.

Acceptance corrections, necessary because of the difference in $K_S$ and $K_L$ vertex distributions, were made using a detailed Monte Carlo simulation of the beam and detector. The nonlinear and non-Gaussian response of the lead glass to photons, important for neutral decays, was reproduced with no free parameters, using results from EGS[7] simulations of electromagnetic showers together with the effective attenuation length of Cherenkov light in each block. The restriction that the same detector and beam parameters be used in the simulation of all four modes, applicable since all were collected simultaneously, provided a powerful check of the Monte Carlo simulation as a whole.

The $K_L \rightarrow \pi^+\pi^-$ decay-vertex distribution is well reproduced by a Monte Carlo simulation, as shown in Fig. 3. The agreement is equally good for the other decays.

The final sample included kaons with energy between 40 and 150 GeV decaying in the region from 120 to 137 m from the target. The raw numbers of events passing all cuts and the background and acceptance corrections are given in Table I with the value of $R_{+-}/R_{00}$ at each stage. The acceptance was similar for $K_S$ and $K_L$: It

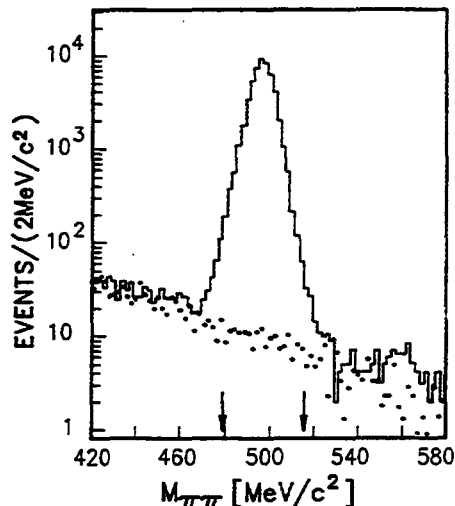FIG. 3. (a) Decay-vertex distribution for $K_L \rightarrow \pi^+\pi^-$ events. The histogram is data and the solid circles are from a Monte Carlo simulation. (b) Ratio of data to a Monte Carlo simulation. The dashed line corresponds to an acceptance error that would shift the $K_S$-to-$K_L$ ratio by 2%, the size of the NA31 effect. The arrows indicate the positions of the cuts.

varied slowly with decay vertex, the mean of which differed for $K_S$ and $K_L$ decays by less than 1.5 m. The total change in the double ratio from raw data to final acceptance-corrected samples is 7%; the final double ratio indicates a small value of $\mathrm{Re}(\epsilon'/\epsilon)$.

To extract $\mathrm{Re}(\epsilon'/\epsilon)$, we fit $R_{+-}$ and $R_{00}$ for $|\rho/\eta|$ in the two modes in 10-GeV/$c$ bins of kaon momentum. The momentum dependence, common to the neutral and charged modes, is expected to obey a power law,[8] while a magnitude difference is proportional to $\mathrm{Re}(\epsilon'/\epsilon)$. The best-fit power for the charged (neutral) mode was $-0.602 \pm 0.010$ ($-0.605 \pm 0.010$) with $\chi^2 = 11.5$ (10.7)

TABLE I. Event totals and corrections.

| | Neutral | Charged | $R_{+-}/R_{00}$ |
|---|---|---|---|
| Raw events | | | |
| $K_L$ | 52 226 | 43 357 | |
| $K_S$ | 201 332 | 178 803 | 1.0698 |
| | | | |
| Background fractions | | | |
| $K_L$ | 0.0507 | 0.0032 | |
| $K_S$ | 0.0256 | 0.0013 | 1.0442 |
| | | | |
| Acceptance | | | |
| $K_L$ | 0.1884 | 0.5041 | |
| $K_S$ | 0.1813 | 0.5064 | 1.0003 |

for nine degrees of freedom; the two are consistent with each other and with previous determinations.[9] The combined fit yielded $\mathrm{Re}(\epsilon'/\epsilon) = -0.0004 \pm 0.0014$ (stat).

Systematic errors were associated with background subtractions, detector and beam variations with time, accidental activity in the detector, energy calibration and resolution, and acceptance.

Uncertainty in the backgrounds is dominated by those in the incoherent contributions to neutral decays, which are expected to partially cancel in $R_{00}$. As a conservative estimate of the total uncertainty on the double ratio all background errors are added in quadrature, yielding a total of 0.18%.

All decays to a common final state were analyzed together; this and the use of loose cuts (the reconstruction efficiency was more than 90% for all $\pi\pi$ decays satisfying the geometrical requirements) reduced sensitivity to time variations: $R_{+-}$ and $R_{00}$ were stable throughout even though the intensity, targeting, and detector efficiencies varied.

Accidental activity, concentrated near the vacuum beam, could have changed the relative $K_L$ and $K_S$ efficiencies. Accidental events, collected with the $\pi\pi$ data at a rate proportional to the instantaneous beam intensity, contained a photon cluster 2.7% of the time and an average of 8.5 chamber hits. When overlaid on $\pi\pi$ Monte Carlo events they correctly reproduced the small intensity dependence of our selection criteria; however, no bias between $K_L$ and $K_S$ was seen within the statistical error of the simulation (0.07%) for either mode.

The energy scale for the charged mode was determined sufficiently accurately using the known $K^0$ and $\Lambda$ masses. For the neutral mode, after electron calibration of the individual lead-glass blocks, the overall scale was adjusted ($\approx 0.5\%$) using the sharp edge in the $K_S$ decay vertex at the regenerator, leaving a residual uncertainty of 0.1%. By choice of the fiducial region,[10] this resulted in only 0.03% uncertainty in $R_{00}$. Uncertainty in the energy resolution, however, led to an 0.2% uncertainty in $R_{00}$.

Acceptances were extensively studied using $10^7$ $\pi ev$ and $6 \times 10^6$ $\pi^0\pi^0\pi^0$ decays taken with the $\pi\pi$ events; the agreement in vertex and other distributions with Monte Carlo simulation over the chosen fiducial region was excellent. Also, when $\mathrm{Re}(\epsilon'/\epsilon)$ was extracted using small vertex bins, almost eliminating the need for acceptance corrections, a consistent result was obtained (with increased systematic error from resolution uncertainty).

In the same analysis, we fit[11] for $\tau_S$ and $\Delta m$. Separate neutral and charged fits were consistent and the combined results were $\tau_S = [0.8902 \pm 0.0021 \, (\text{stat})] \times 10^{-10}$ sec and $\Delta m = [0.534 \pm 0.009 \, (\text{stat})] \times 10^{10}\hbar$ sec$^{-1}$, in agreement with the accepted values.[12] These studies, together with the stability of $R_{+-}$ and $R_{00}$ when selection criteria, beam profiles, and detector apertures and efficiencies were varied in the Monte Carlo simulation,

led to the assignment of 0.25% systematic uncertainty due to acceptance.

Combining these uncertainties in quadrature, the total systematic error on the double ratio is then 0.38%. The final result is

$$\text{Re}(\epsilon'/\epsilon) = -0.0004 \pm 0.0014(\text{stat}) \pm 0.0006(\text{syst}).$$

The accurate determinations of $\tau_S$, $\Delta m$, and the regeneration momentum dependence for both modes attest to the soundness of the technique.

The result is consistent with the superweak model;[3] it does not confirm recent evidence[4] for direct CP violation. The CKM standard model may also account for such a small value of $\text{Re}(\epsilon'/\epsilon)$ with a heavy top quark[13] or with the incorporation of electroweak corrections which could be important.[14]

We thank H. Sanders and J. Ting at The University of Chicago, the ACP group and E. Beck at FNAL, and G. L. Grazer and P. Jarry for their contributions. This work was supported in part by DOE, NSF, and the French Atomic Energy Commission. Two of us (G.D.G. and Y.W.W.) are recipients of DOE Outstanding Junior Investigator grants. One of us (J.R.P.) submitted this work in partial fulfillment of the requirements for the Ph.D. degree at The University of Chicago.

---

(a)Current address: Stanford Linear Accelerator Center, P.O. Box 4349, Stanford, CA 94309.

(b)Current address: Department of Nuclear Physics, University of Oxford, Oxford OX1 3RH, United Kingdom.

(c)Current address: Department of Physics, University of Illinois, Urbana, IL 61801.

(d)Current address: Princeton Combustion Research Laboratories, Monmouth Junction, NJ 08852.

[1]M. Woods et al., Phys. Rev. Lett. **60**, 1695 (1988).

[2]M. Kobayashi and T. Maskawa, Prog. Theor. Phys. **49**, 652 (1973).

[3]L. Wolfenstein, Phys. Rev. Lett. **13**, 569 (1964).

[4]H. Burkhardt et al., Phys. Lett. B **206**, 169 (1988), find $\text{Re}(\epsilon'/\epsilon) = 0.0033 \pm 0.0007(\text{stat}) \pm 0.0008(\text{syst})$.

[5]For a detailed description of the analysis, see J. R. Patterson, Ph.D. thesis, University of Chicago, 1990.

[6]H. Sanders, V. Papadimitriou, J. Ting, Y. W. Wah, and E. Weatherhead, IEEE Trans. Nucl. Sci. **36**, 358 (1988).

[7]W. R. Nelson, H. Hirayama, and D. W. O. Rogers, SLAC Report No. SLAC-265, 1985 (unpublished).

[8]See, for example, J. Roehrig et al., Phys. Rev. Lett. **38**, 1116 (1977).

[9]A. Gsponer et al., Phys. Rev. Lett. **42**, 13 (1979); also, R. H. Bernstein et al., Phys. Rev. Lett. **54**, 1631 (1985); Woods et al., Ref. 1.

[10]When the $\gamma$ energies are decreased, approximately the same number of $K_L$ leave at the downstream boundary as enter at the upstream boundary; essentially all $K_S$ are included.

[11]The CPT-violating phase difference $(\Delta\Phi)$ between $\eta_{+-}$ and $\eta_{00}$ was also fit and found consistent with zero [M. Karlsson et al. (unpublished)]. Here we assume $\Delta\Phi = 0$.

[12]Particle Data Group, G. P. Yost et al., Phys. Lett. B **204**, 1 (1988).

[13]A. Buras and J. M. Gerard, Phys. Lett. B **203**, 272 (1988); C. S. Kim, J. L. Rosner, and C. P. Yuan, University of Durham Report No. DTP-89-52 (to be published).

[14]J. M. Flynn and L. Randall, Phys. Lett. B **224**, 221 (1989); G. Buchalla, A. J. Buras, and M. K. Harlander, Technische Universitat Munchen Report No. TUM-T31-3/89, 1989 (to be published).

# New limit on $K_L \to \pi^0 e^+ e^-$

A. Barker, R. A. Briere, L. K. Gibbons, G. Makoff, V. Papadimitriou, J. R. Patterson, S. Somalwar,
Y. W. Wah, B. Winstein, R. Winston, M. Woods,* and H. Yamamoto
*The Enrico Fermi Institute and the Department of Physics, The University of Chicago, Chicago, Illinois 60637*

E. C. Swallow
*Department of Physics, Elmhurst College, Elmhurst, Illinois 60126
and The Enrico Fermi Institute, The University of Chicago, Chicago, Illinois 60637*

G. J. Bock, R. Coleman, J. Enagonio, Y. B. Hsiung, R. Tschirhart, K. Stanfield, R. Stefanski, and T. Yamanaka
*Fermi National Accelerator Laboratory, Batavia, Illinois 60510*

G. D. Gollin,† M. Karlsson, and J. K. Okamitsu‡
*Department of Physics, Princeton University, Princeton, New Jersey 08544*

P. Debu, B. Peyaud, R. Turlay, and B. Vallage
*Department de Physiques des Particules Elementaires, Centre d'Etudes Nucleaires de Saclay,
F-91191 Gif-sur-Yvette CEDEX, France*
(Received 12 March 1990)

Based upon the analysis of the complete data set of Fermilab experiment E-731, we report a new limit on the branching ratio of $K_L \to \pi^0 e^+ e^-$ which is $< 7.5 \times 10^{-9}$ (90% confidence).

The decay $K_L \to \pi^0 e^+ e^-$ has raised considerable interest theoretically[1] and experimentally[2-4] for its ability to elucidate direct $CP$ violation. Within the standard model, this decay mode is likely to have a ratio of direct $CP$ violation to that from mixing ($\epsilon'/\epsilon$) of order one, unlike the one measured[5] through the $K \to 2\pi$ decay modes. Earlier, we reported[2] a limit $B(K_L \to \pi^0 e^+ e^-) < 4.2 \times 10^{-8}$ based on a special data set collected in Fermilab experiment E-731, which had its primary goal to determine $\epsilon'/\epsilon$ from $K \to 2\pi$ modes. Here we update the limit using the entire data sample.

The apparatus and event reconstruction are described elsewhere.[2,6] The momenta of the $e^+$ and $e^-$ and the decay vertex of $K_L \to \pi^0 e^+ e^-$ candidates were determined by the drift-chamber spectrometer. The energies and positions of all the final-state particles were measured by an 804-block lead-glass calorimeter. Each of the showers (clusters) observed in the lead glass was required to be consistent with an isolated photon or $e^+$ or $e^-$ (the "shape" cut). The $e^+$ and $e^-$ were identified by matching the reconstructed tracks with the calorimeter clusters, and requiring $0.85 < E/P < 1.15$, where $E$ is the cluster energy deposited in the lead glass and $P$ is the track momentum. We further required that the invariant mass of the $e^+$ and $e^- (M_{ee})$ be greater than 100 MeV/$c^2$. From a study of $K_L \to \pi^+ \pi^- \pi^0$ decays, the $\pi^0$ mass resolution was determined to be about 4 MeV/$c^2$. The $\gamma\gamma$ mass was required to be within 10 MeV/$c^2$ of the nominal $\pi^0$ value. By then constraining the $\gamma\gamma$ mass to the nominal value, the expected kaon mass $(M_{\pi ee})$ resolution is about 4.5 MeV/$c^2$. The square of the transverse momentum $(P_t^2)$ of the $\pi^0 e^+ e^-$ system with respect to the line connecting the decay vertex and the production target has an expected resolution of about 50 MeV$^2$/$c^2$.

The candidates from the entire data set are displayed in a two-dimensional $M_{\pi ee}$ vs $P_t^2$ plot as shown in Fig. 1. A candidate is defined to have $P_t^2 < 200$ MeV$^2$/$c^2$, 489 $< M_{\pi ee} < 507$ MeV/$c^2$, and $M_{ee} > 100$ MeV/$c^2$; these cuts would include about 90% of the signal. No candidate is found in the signal region.

The "shape" and $M_{ee}$ cuts were not applied for our previous result.[2] The "shape" requirement suppressed background events from $K_{e3}$ decay with an accidental $\pi^0$ (or radiative $K_{e3}$ decay with a single accidental photon) when the pion showered in the calorimeter and satisfied the $E/P$



FIG. 1. Reconstructed kaon mass vs the square of the transverse momentum for $K_L \to \pi^0 e^+ e^-$. The box represents the signal region.

cut. The $M_{ee}$ cut retained 95% of the signal while rejecting events with $\pi^0$s decayed to $\gamma e^+ e^-$ where the $\pi^0$ came from a neutral-kaon decay. The sparsely distributed events outside the box in Fig. 1 are consistent[4] with the residual $K_{e3}$ plus accidental $\pi^0$ background.

The limit is obtained with data from two types of triggers. The "four-cluster" trigger required four electromagnetic showers and 30 GeV or more energy deposited in the lead-glass calorimeter. The "two-track" trigger required two tracks in the tracking spectrometer. For kaon energy between 30 and 160 GeV and assuming a uniform three-body phase-space distribution, the acceptance is 9.0% for a fiducial decay volume of 18 m for the "four-cluster" trigger and is 10% for a fiducial decay

volume of 17 m for the "two-track" trigger. The "two-track" data, unlike those collected in the special data set,[2] were not prescaled.

The upper limit is obtained by normalizing to samples of more than $10^5$ $K_L \rightarrow \pi^0\pi^0$ and $K_L \rightarrow \pi^+\pi^-$ decays observed simultaneously. The limits obtained from the "two-track" and "four-cluster" data are $< 3.6 \times 10^{-8}$ and $< 9.5 \times 10^{-9}$ (90% confidence), respectively. The combined result $B(K_L \rightarrow \pi^0 e^+ e^-) < 7.5 \times 10^{-9}$ (90% confidence) is an improvement of about factor of 6 from our previous result. This limit is also consistent with the recent result obtained by a Brookhaven experiment[7] and helps to limit the possible contribution from direct $CP$ violation.

*Present address: SLAC, Stanford, CA 94305.

†Present address: Department of Physics, University of Illinois, Urbana, IL 61801.

‡Present address: Princeton Combustion Research Laboratories, Monmouth Junction, NJ 08852.

[1]J. F. Donoghue, B. R. Holstein, and G. Valencia, Phys. Rev. D 35, 2769 (1987); L. M. Sehgal, ibid. 38, 808 (1988); G. Ecker, A. Pich, and E. deRafael, Nucl. Phys. B303, 665 (1988); C. O. Dib, I. Dunitz, and F. Gilman, Phys. Rev. D 39, 2639 (1989); J. Flynn and L. Randall, Phys. Lett. B 216, 221 (1989).

[2]L. K. Gibbons et al., Phys. Rev. Lett. 61, 2661 (1988).

[3]G. D. Barr et al., Phys. Lett. B 214, 303 (1988).

[4]A. Barker et al., Fermilab Proposal No. E-799, 1989 (unpublished). This document describes in detail the calculation of the possible backgrounds.

[5]J. R. Patterson et al., Phys. Rev. Lett. 64, 1491 (1990); H. Burkhardt et al., Phys. Lett. B 206, 169 (1988).

[6]For a complete description of the detector, see J. R. Patterson, Ph.D. thesis, University of Chicago, 1990.

[7]The result from the BNL-Vassar-Yale experiment (AGS-845) is $B(K_L \rightarrow \pi^0 e^+ e^-) < 5.5 \times 10^{-9}$ (90% C.L.). See M. Schmidt et al., in Proceedings of the Meeting of the APS Division of Particles and Fields, Houston, Texas, 1990 (unpublished); K. E. Ohl et al., Yale University report (unpublished).

# Test of *CPT* Symmetry through a Determination of the Difference in the Phases of $\eta_{00}$ and $\eta_{+-}$ in $K \to 2\pi$ Decays

M. Karlsson, G. D. Gollin,[a] J. K. Okamitsu,[b] and R. Tschirhart[c]

*Department of Physics, Princeton University, Princeton, New Jersey 08544*

A. Barker, R. A. Briere, L. K. Gibbons, G. Makoff, V. Papadimitriou, J. R. Patterson, S. Somalwar,
Y. W. Wah, B. Winstein, R. Winston, M. Woods,[d] and H. Yamamoto

*The Enrico Fermi Institute and Department of Physics, The University of Chicago, Chicago, Illinois 60637*

E. Swallow

*Department of Physics, Elmhurst College, Elmhurst, Illinois 60126
and Department of Physics, The University of Chicago, Chicago, Illinois 60637*

G. J. Bock, R. Coleman, J. Enagonio, Y. B. Hsiung, K. Stanfield, R. Stefanski, and T. Yamanaka

*Fermi National Laboratory, Batavia, Illinois 60510*

P. Debu, B. Peyaud, R. Turlay, and B. Vallage

*Département de Physique des Particules Elémentaires, Centre d'Etudes Nucléaires de Saclay,
F 91191 Gif-sur-Yvette CEDEX, France*

(Received 22 January 1990)

Data collected by the E731 experiment at Fermilab were used to search for *CPT* violation in $K^0 \to \pi\pi$ decays by measuring the difference $\Delta\phi$ between the phases of the *CP*-violating parameters $\eta_{00}$ and $\eta_{+-}$. Our result, $\Delta\phi = -0.3° \pm 2.4° \pm 1.2°$, where the first error is statistical and the second systematic, is consistent with *CPT* symmetry.

*CPT* symmetry is a natural consequence of local quantum field theory[1] and guarantees the equality of masses and lifetimes of particles and antiparticles. It is conceivable, however, that a small violation of *CPT* symmetry could occur in extensions of quantum field theory (e.g., string theory[2]); thus, it is imperative to check *CPT* symmetry wherever possible. The neutral-kaon system provides some of the most sensitive tests of *CPT* symmetry. The ratio of the decay amplitudes $\eta \equiv \text{amp}(K_L \to \pi\pi)/\text{amp}(K_S \to \pi\pi)$ can be written as[3] $\eta_{+-} \equiv |\eta_{+-}|e^{i\phi_{+-}} = (\epsilon - \Delta + a) + \epsilon'$ for the $\pi^+\pi^-$ final state and $\eta_{00} \equiv |\eta_{00}|e^{i\phi_{00}} = (\epsilon - \Delta + a) - 2\epsilon'$ for the $\pi^0\pi^0$ final state (Fig. 1). Here $\epsilon$ is a measure of *CP* violation without *CPT* violation in $K^0$-$\bar{K}^0$ mixing, and $\Delta$ is similarly a measure of *CPT* violation without *T* violation. Direct *CP* and *CPT* violations in the decay amplitudes are parametrized by $a \equiv (A_0 - \bar{A}_0)/(A_0 + \bar{A}_0)$ (chosen to be real[4]) and

$$\epsilon' = \frac{1}{\sqrt{2}} \frac{A_2 - \bar{A}_2}{A_0 + \bar{A}_0} e^{i(\delta_2 - \delta_0)}, \tag{1}$$

where $A_I$ ($\bar{A}_I$) is the $2\pi$ decay amplitude of $K^0$ ($\bar{K}^0$) to isospin-$I$ final state with corresponding phase shift $\delta_I$ from final-state interactions. *CPT* symmetry results in two constraints that can be tested by experiment: First, *CPT* symmetry implies that the phase of $2\eta_{+-} + \eta_{00}$ be within a few degrees of the "natural angle" $\phi_\epsilon \equiv \arg(\Gamma_S/2 + i\Delta m) = 43.7° \pm 0.2°$, where $\Gamma_S$ is the $K_S$

decay rate and $\Delta m \equiv M_{K_L} - M_{K_S}$. Second, using the experimental value[5] $\delta_2 - \delta_0 = -45° \pm 10°$ in Eq. (1), the *CPT* relation $\bar{A}_I = A_I^*$ leads to $\arg\epsilon' \approx \phi_\epsilon$. This, together with the current knowledge[6,7] of $|\text{Re}(\epsilon'/\epsilon)|$, requires the phase difference $\Delta\phi \equiv \phi_{00} - \phi_{+-}$ to be much less than $1°$. With the accepted value[8] of $\phi_{+-} = 44.6° \pm 1.2°$,



CP and CPT violating parameters

FIG. 1. Relationship among the *CPT*-violating parameters $a$, $\Delta$, and the directly measurable quantities $\eta_{+-}$, $\eta_{00}$. Since *CPT* symmetry predicts $\epsilon'$ to be parallel to $\epsilon$, a nonzero value of $\Delta\phi = \phi_{00} - \phi_{+-}$ also indicates *CPT* violation. The magnitudes of $a$, $\Delta$, and $\epsilon'$ are exaggerated for clarity.

however, the most recent published measurement[9] of $\phi_{00}=55.7° \pm 5.8°$ corresponds to a phase difference about 2 standard deviations away from the prediction of $CPT$ symmetry;[10] this has generated considerable interest and speculation.[3]

In our experiment, the phase difference is measured using two parallel neutral-kaon beams, one of which passes through a regenerator located 123 m downstream of the production target. The $\pi\pi$ decay rate in the regenerated beam as a function of proper time $t$ is sensitive to the phase $\phi_\eta$ ($=\phi_{+-},\phi_{00}$) in the interference term:

$$\frac{d^2 I_{\pi\pi}}{dP_K dt} \propto F(P_K)e^{-X}[|\rho|^2 e^{-t/\tau_S} + |\eta|^2 e^{-t/\tau_L} + 2|\rho||\eta|e^{-t/2\tau_S}\cos(\Delta m\, t + \phi_\rho - \phi_\eta)] , \tag{2}$$

where $\tau_S$ ($\tau_L$) is the $K_S$ ($K_L$) lifetime, $\Delta m$ the mass difference between $K_L$ and $K_S$, $\rho=|\rho|e^{i\phi_\rho}$ the coherent regeneration amplitude, and $F(P_K)$ the incident kaon momentum spectrum. The incident flux is normalized to the other vacuum beam whose $\pi\pi$ rate is simply $F(P_K) \times |\eta|^2 e^{-t/\tau_L}$. The factor $e^{-X}$ accounts for absorption in the regenerated beam. As can be inferred from Eq. (2), the values extracted for $\phi_{+-}$ and $\phi_{00}$ individually depend on $\phi_\rho$ and $\Delta m$, but the difference $\Delta\phi \equiv \phi_{00} - \phi_{+-}$ is insensitive to both parameters.

A description of the experimental setup can be found in Refs. 6 and 11, and only a brief account of the essential features is given here. The $\pi^0\pi^0$ decays were detected with a lead-glass calorimeter having an energy resolution for photons of $2.5\% + 5\%/\sqrt{E}$ ($E$ in GeV). The $\pi^+\pi^-$ decays were reconstructed using a magnet and a sixteen-plane drift-chamber system with a typical momentum resolution of 1%. All four decay modes, $K_{S,L} \rightarrow \pi^+\pi^-, \pi^0\pi^0$, were collected simultaneously and the regenerator alternated frequently between the two beams. This minimizes sensitivity to differences in intensity and momentum spectrum between the beams as well as to reconstruction inefficiencies, dead-time effects, and calibration changes with time.

The phase-difference result presented here is based on the same data set that was recently used to determine $\mathrm{Re}(\epsilon'/\epsilon)$,[6] and the event-reconstruction and background-subtraction techniques employed are the same as for that analysis. For neutral decays, however, the length of the decay region is extended downstream by 13 m to increase sensitivity to the phase in the interference term. Most of the phase information is provided by decays at the lower end of the energy range where a larger proper-time region can be sampled. For $\pi^+\pi^-$ decays, the length of the decay region is 14 m (6.5 $K_S$ lifetimes at 40 GeV), and for $\pi^0\pi^0$ decays, it is 29 m (14 $K_S$ lifetimes at 40 GeV). It is not possible to extend the decay region for the charged mode since it is hardware defined by a thin trigger hodoscope.

The $2\pi^0$ mass distribution for the regenerated beam has a small (0.04%) background which is dominated by $3\pi^0$ decays from the $K_L$ beam transmitted through the regenerator. A $3\pi^0$ decay can fake a $2\pi^0$ signal when two out of the six photons are lost either by escaping the detector or by merging with other photons in the lead-glass calorimeter. Figure 2 shows the vertex distributions for signal and backgrounds in the regenerated beam. For the vacuum beam, the level of $3\pi^0$ back-

ground is higher (0.99%); its vertex distribution has the same shape as that of the regenerated beam. Another source of background arises from incoherently produced kaons that emerge with nonzero scattering angle from the regenerator. This amounts to 2.7% in the regenerated beam, and its vertex distribution is also shown in Fig. 2. The corresponding background level for the vacuum beam is 2.8%. There is also a background due to nuclear interactions at the regenerator ($z=123$ m) and at the 2-mm-thick trigger hodoscope ($z=138$ m). In the charged mode, the background in the vacuum beam (0.32%) is dominated by $K_{e3}$ decays, whereas the background in the regenerated beam (0.13%) comes from incoherent regeneration.

In order to extract $\phi_{+-} - \phi_\rho$ and $\phi_{00} - \phi_\rho$ from the shapes of the vertex distributions in the regenerated beam, the acceptance as a function of decay vertex must be well understood. Accurate knowledge of the accep-



FIG. 2. The vertex distribution of reconstructed $2\pi^0$ decays in the regenerated beam together with the background contributions from incoherently regenerated $K_S$ (triangles) and $3\pi^0$ decays and nuclear interactions (squares). The incoherent background under the coherent peak is measured from the data by the extrapolation to zero scattering angle (see text). The $3\pi^0$+ nuclear interaction backgrounds are estimated by the fit of the mass distribution where the $3\pi^0$ component is obtained from the Monte Carlo simulation.

tance is essential for the determination of $\text{Re}(\epsilon'/\epsilon)$, and is discussed in detail in Ref. 6. The fit is done by comparing the background-subtracted and acceptance-corrected $z$ distributions with the predicted rate $I_{\pi\pi}$ of Eq. (2), constrained by the total number of events in the vacuum beam. In the fit for $\phi_{+-}$ and $\phi_{00}$, the kaon parameters $\tau_S$, $\tau_L$, and $\Delta m$ are fixed to their world-average values.[8] The parameter $\text{Re}(\epsilon'/\epsilon)$, which is a measure of the difference in magnitude between $\eta_{+-}$ and $\eta_{00}$, is allowed to float in the fit.[12] The assumptions made for the regeneration amplitude[13] are the following: (a) The difference in the forward-scattering amplitudes[14] between $K^0$ and $\bar{K}^0$ has a power-law dependence on the kaon momentum; namely, $|(f-\bar{f})/k| \propto P_K^{-\alpha}$; (b) the phase of $(f-\bar{f})/k$ is given by the analyticity condition $\arg[(f-\bar{f})/k] = -(2-\alpha)\pi/2$. The absorption factor $e^{-X}$ is measured to better than 1% of itself from $K_L \rightarrow \pi^+\pi^-\pi^0$ and $K_L \rightarrow \pi^0\pi^0\pi^0$ decays in the two beams. This uncertainty has a negligible effect on $\Delta\phi$.

The result of the fit is $\phi_{+-} = 47.7° \pm 2.0°$, $\phi_{00} = 47.4° \pm 1.4°$, and $\Delta\phi \equiv \phi_{00} - \phi_{+-} = -0.3° \pm 2.4°$. The errors are statistical and $\chi^2 = 316$ for 340 degrees of freedom. Figure 3 shows the quality of the fit to the data for both modes. As a check of our understanding of the acceptance, we have also fitted for $\tau_S$ and $\Delta m$, and we have obtained $\tau_S = (0.8882 \pm 0.0030) \times 10^{-10}$ s (charged mode), $\tau_S = (0.8929 \pm 0.0033) \times 10^{-10}$ s (neutral mode), $\Delta m = (0.5377 \pm 0.0098) \times 10^{10} \hbar$ s$^{-1}$ (both modes combined), where the errors are statistical only. These results are in good agreement with the corresponding world averages.[8]

The systematic errors on $\Delta\phi$ come from various sources. When the parameters $\tau_S$ and $\Delta m$ are varied by 1 standard deviation around their world-average values, the value of $\Delta\phi$ changes by 0.2° for $\tau_S$ and 0.1° for $\Delta m$. Similarly the value of $\Delta\phi$ changes by $+0.8°$ for a change of $+10^{-3}$ on $\text{Re}(\epsilon'/\epsilon)$. The acceptance was carefully studied using high-statistics modes ($10^7$ $K_{e3}$ events for charged mode and $6\times10^6$ $3\pi^0$ for neutral mode). The remaining uncertainty in the acceptance corresponds to an error in $\Delta\phi$ of 0.9°. The uncertainty in the absolute energy calibration (0.1%) is determined from the sharp upstream edge of the decay distribution in the regenerated beam. The resulting error in $\Delta\phi$ is 0.6°. The subtraction of the $3\pi^0$ and incoherent backgrounds in neutral mode contributes an error of 0.3°. Accidental overlaps in the detector have a negligible effect on the result. The combined systematic error on $\Delta\phi$ is thus 1.2°. Excluding the regeneration phase uncertainty, the systematic error on $\phi_{+-}$ is 0.9° (dominated by acceptance uncertainty) and the systematic error on $\phi_{00}$ is 0.8° (dominated by absolute energy calibration).

The final result is then $\Delta\phi \equiv \phi_{00} - \phi_{+-} = -0.3° \pm 2.4°(\text{stat}) \pm 1.2°(\text{syst})$. This result is consistent with zero and thus with the prediction of $CPT$ symmetry. With the world average of $\phi_{+-}$, our measurement of $\Delta\phi$

leads to a value for $\arg(2\eta_{+-} + \eta_{00})$ of $44.5° \pm 1.5°$, which is well within 1 standard deviation of the natural angle $\phi_\epsilon = 43.7°$. Our measurement of $\phi_{+-}$ is consistent with the world average. This supports the assumptions made for the regeneration amplitude in the fit. In conclusion, our measurement shows no indication of $CPT$ violation. Further confirmation is provided by a recent experiment[15] which finds $\Delta\phi = 0.2° \pm 2.9°$.

The limit on $\Delta\phi$ also leads to a limit on the component of $\epsilon'$ perpendicular to $\epsilon$ using the relation $\text{Im}(\epsilon'/\epsilon) = -\Delta\phi/3$ which can be easily seen from Fig. 1. With the measured value of $\Delta\phi$, we obtain a 95%-confidence limit on $\text{Im}(\epsilon'/\epsilon)$ without any assumption of $CPT$ invariance: $-0.03 < \text{Im}(\epsilon'/\epsilon) < 0.03$.



FIG. 3. The vertex distributions in the regenerated beam after background subtractions and acceptance corrections for the (a) neutral and (b) charged modes. The solid curves are the result of the fit described in the text. The momentum cuts on the kaon energy are (a) [40,50] GeV and (b) [30,40] GeV.

---

[a] Current address: Department of Physics, Loomis Laboratory of Physics, University of Illinois, 1110 West Green Street, Urbana, IL 61801.

[b] Current address: Princeton Combustion Laboratories, 4275 U.S. Highway 1, Monmouth Junction, NJ 08852.

[c] Current address: Fermi National Laboratory, Batavia, IL 60510.

[d] Current address: Stanford Linear Accelerator Center, P.O. Box. 4349, Stanford, CA 94309.

[1] G. Lüders, Dansk. Mat. Fys. Medd. 28, 17 (1954); W. Pauli, *Niels Bohr and the Development of Physics* (Pergamon, New York, 1955); R. Jost, Helv. Phys. Acta 30, 409 (1957).

[2] E. Witten, Commun. Math. Phys. 109, 525 (1987); H. Sonoda, Nucl. Phys. B326, 135 (1989).

[3] N. W. Tanner and R. H. Dalitz, Ann. Phys. (N.Y.) 171, 463 (1986); V. V. Barmin et al., Nucl. Phys. B247, 293 (1984); J. W. Cronin, Acta Phys. Pol. B 15, 419 (1984), and references therein.

[4] The relative phase of $K_0$ and $\bar{K}_0$ is chosen such that $\arg A_0 = \arg \bar{A}_0$ (Wu-Yang phase convention).

[5] T. J. Devlin and J. O. Dickey, Rev. Mod. Phys. 51, 237 (1979).

[6] M. Woods et al., Phys. Rev. Lett. 60, 1695 (1988); J. R. Patterson et al., ibid. 64, 1491 (1990).

[7] H. Burkhardt et al., Phys. Lett. B 206, 169 (1988).

[8] Particle Data Group, G. P. Yost et al., Phys. Lett. B 204, 1 (1988).

[9] J. H. Christenson et al., Phys. Rev. Lett. 43, 1209 (1979).

[10] The discrepancy between $\arg(2\eta_{+-} + \eta_{00})$ and $\phi_\epsilon$ is also about $2\sigma$ if it is assumed that the $\Delta S = \Delta Q$ rule holds and that there is no anomalously large CP or CPT violations in $3\pi^0$ and semileptonic modes; Barmin et al., Ref. 3.

[11] For a detailed discussion of the analysis, see the M. Karlsson, Ph.D. thesis, Princeton University, 1990.

[12] In the determination of $\mathrm{Re}(\epsilon'/\epsilon)$ in Ref. 6, the phase difference was fixed at zero. The value obtained for $\mathrm{Re}(\epsilon'/\epsilon)$ in this analysis is consistent with that given in Ref. 6.

[13] J. Roehrig et al., Phys. Rev. Lett. 38, 1116 (1977).

[14] The regeneration amplitude $\rho$ is related to $(f-\bar{f})/k$ by $\rho = \pi i N L g(f-\bar{f})/k$, where $N$ is the density of scatterers, $L$ is the length of the regenerator, and $g = (1-e^{-x})/x$ is a geometrical factor with $x = (\frac{1}{2} - i\Delta m/\Gamma_S)L/\Lambda_S$ with $\Lambda_S$ the $K_S$ decay length. For a thin regenerator $g$ is unity, and $|g-1|$ is always less than 0.2 in our case.

[15] R. Carosi et al. (NA31 experiment), CERN Report No. CERN-EP/90-06 (to be published).

# Measurement of the branching ratio of the decay $K_L \to \pi^0\gamma\gamma$

V. Papadimitriou,* A. Barker, R. A. Briere, L. K. Gibbons, G. Makoff, J. R. Patterson,[†] S. Somalwar,
Y. W. Wah, B. Winstein, R. Winston, M. Woods,[‡] and H. Yamamoto
*The Enrico Fermi Institute and the Department of Physics, The University of Chicago, Chicago, Illinois 60637*

E. C. Swallow
*Department of Physics, Elmhurst College, Elmhurst, Illinois 60126
and The Enrico Fermi Institute, The University of Chicago, Chicago, Illinois 60637*

G. J. Bock, R. Coleman, J. Enagonio, Y. B. Hsiung, E. Ramberg, K. Stanfield, R. Tschirhart, and T. Yamanaka
*Fermi National Accelerator Laboratory, Batavia, Illinois 60510*

G. D. Gollin,[§] M. Karlsson,** and J. K. Okamitsu[††]
*Department of Physics, Princeton University, Princeton, New Jersey 08544*

P. Debu, B. Peyaud, R. Turlay, and B. Vallage
*Department de Physique des Particules Elementaires, Centre d'Etudes Nucleaires de Saclay,
F-91191 Gif-sur-Yvette CEDEX, France*
(Received 19 February 1991)

Using the complete Fermilab E731 data set, we find $\Gamma(K_L \to \pi^0\gamma\gamma, \ m_{\gamma\gamma} \geq 0.280 \ \text{GeV})/\Gamma(K_L \to \text{all}) = (1.86 \pm 0.60 \pm 0.60) \times 10^{-6}$, in good agreement with a recent report of the first observation of this decay. For the low $\gamma\gamma$ mass region we find $\Gamma(K_L \to \pi^0\gamma\gamma, \ m_{\gamma\gamma} < 0.264 \ \text{GeV})/\Gamma(K_L \to \text{all}) < 5.1 \times 10^{-6}$ (90% confidence).

The decay $K_L \to \pi^0\gamma\gamma$ is of current interest [1-6] within the context of both chiral perturbation theory and the vector-meson-dominance model, and also for its contribution to the decay $K_L \to \pi^0 e^+e^-$ as a CP-conserving intermediate state. Predictions for its branching ratio vary from $6.3 \times 10^{-7}$ to $6.2 \times 10^{-6}$, and predicted $\gamma\gamma$ mass distributions differ markedly. At the one-loop level in chiral perturbation theory [1], the branching ratio is estimated to be $6.8 \times 10^{-7}$ with a characteristic $\gamma\gamma$ invariant-mass distribution $(m_{\gamma\gamma})$ peaking at about 0.325 GeV.

Earlier we reported [7] an upper limit for the branching ratio of this decay of $2.7 \times 10^{-6}$ (90% confidence) assuming the $\gamma\gamma$ invariant-mass distribution expected by chiral

perturbation theory. That result was based on a subset of our data; here we report results from the entire data sample which therefore supersede the earlier results. In the meantime, CERN experiment NA31 has recently reported [8] an observation of the decay: They have found a signal primarily at high $\gamma\gamma$ invariant mass and a branching ratio significantly greater than that predicted by chiral perturbation theory. They find

$$\frac{\Gamma(K_L \to \pi^0\gamma\gamma, \ m_{\gamma\gamma} \geq 0.280 \ \text{GeV})}{\Gamma(K_L \to \text{all})} = (2.1 \pm 0.6) \times 10^{-6}.$$

The primary goal of experiment E731 is the determination of the CP-violation parameter $\epsilon'/\epsilon$ [9]. The characteristics of the detector and the event reconstruction have

been described in detail elsewhere [7,10]; here we summarize the essential features of the analysis and its differences from that used in our previous publication. Energies and positions of photons were measured with an 804-block lead-glass calorimeter. Candidates for the $K_L \rightarrow \pi^0 \gamma\gamma$ decay were required to have exactly four electromagnetic showers (clusters) in the lead glass, each with an energy of at least 1 GeV, and total energy between 40 and 150 GeV. The decay vertex was determined from the measured cluster energies and positions by assuming that the invariant mass of the four photons was that of the neutral kaon. The two photons, labeled (12), with invariant mass closest to the nominal neutral-pion mass ($m_{\pi^0}$) were taken to be the decay products of the candidate $\pi^0$. The $\pi^0$ mass resolution was about 3 MeV and it was required that $|m_{12} - m_{\pi^0}| \leq 5$ MeV.

Background rejection is critical since the signal is poorly constrained. The rejection of the $K_L \rightarrow 2\pi^0$ background was done in two steps. First, it was required that the mass of the non-$\pi^0$ pair ($m_{\gamma\gamma}$ or $m_{34}$) differ from $m_{\pi^0}$ by at least 14 MeV. Second, the candidate event was reconstructed as a $K_L \rightarrow 2\pi^0$ decay by constraining the invariant masses of each pair of photons to the nominal $\pi^0$ mass, and if it satisfied the criteria described in Refs. [7] and [10], it was rejected as a mispaired $2\pi^0$ decay. $K_L \rightarrow 3\pi^0$ decays, which are the dominant remaining background, can masquerade as four-cluster events either when photons escape the detector or when multiple photons fuse in the lead glass to form a single cluster. This background was considerably reduced (1) by using the many photon veto counters for the detection of escaping photons, (2) by requiring that the transverse center of energy of the four photons be in the $K_L$ beam region, and (3) by considering only decays in the upstream part of the decay region, starting at 110 m and ending at 128 m from the target. The selection of the downstream edge of this decay region was made on the basis of a Monte Carlo study to maximize the sensitivity to a signal in the presence of known amounts of $3\pi^0$ and $2\pi^0$ backgrounds; the data themselves were not used. In fact, the sensitivity is relatively independent on the position of the downstream edge. The background with overlapping clusters was substantially reduced by rejecting events with cluster shapes inconsistent with that of a single photon. Additional suppression of the $3\pi^0$ background came from kinematically rejecting events with two superimposed $\pi^0$ (double fusion events) where each photon from one $\pi^0$ overlaps with a photon from the other $\pi^0$ so that $m_{\gamma\gamma} > 2m_{\pi^0}$. For this background, these fused clusters are the $\gamma\gamma$ pair about 70% of the time according to the Monte Carlo simulations; in addition, the energies of the photons which fuse tend to be high. By analyzing each candidate event as though these clusters are so fused, the individual photon energies could be kinematically determined. A cut on a combination of these energies reduced the background by about 28% while reducing the expected signal by about 6.5% (see Ref. [10]). The drift-chamber spectrometer and four scintillation hodoscopes were used to reject $K_L$ decays with charged particles in the final state (e.g., $K_L \rightarrow \pi^+\pi^-\pi^0$) or events with photon conversions. The contribution from accidental clusters in our data sample is

found to be negligible. Finally, we rejected events with photons projecting outside the holes of the lead-mask photon veto which is located at about 122 m from the target and is one of our defining apertures.

Figure 1 shows the comparison of data and background Monte Carlo simulation for the $\gamma\gamma$ effective mass. A characteristic feature in this distribution is the prominent double fusion peak appearing at about $m_{\gamma\gamma} = 0.270$ GeV. The background coming from the $3\pi^0$ and $2\pi^0$ modes is absolutely normalized to the data by means of a sample of fully reconstructed $K_L \rightarrow 2\pi^0$ decays observed simultaneously and selected with criteria similar to those used for the $\pi^0\gamma\gamma$ candidates. Although for low $\gamma\gamma$ mass the data–Monte Carlo agreement is good within statistics, at high masses there is a significant excess of data. The background in the high-mass region consists predominantly of events where both $\gamma$'s are fused clusters. The Monte Carlo simulation correctly reproduces the prominent double fusion peak, which is important in establishing that the excess at higher values is indeed a signal. Figure 2 shows the comparison of data and background Monte Carlo simulation for the reconstructed $z$ decay vertex distributions with $m_{\gamma\gamma} \geq 0.280$ GeV, including the region downstream of the fiducial cut. The data excess is uniformly distributed over the decay region as is expected for a signal.

In Fig. 3 we show the data–Monte Carlo comparison for the $m_{12}$ distribution for $m_{\gamma\gamma} \geq 0.280$ GeV. The excess



FIG. 1. Data–Monte Carlo comparison of the $\gamma\gamma$ mass distribution for $\pi^0\gamma\gamma$ candidates and background events based on the full data set. The normalization is absolute. The error bars correspond to the data, the shaded histogram to the $2\pi^0$ background Monte Carlo simulation, and the dashed histogram to the sum of the $3\pi^0$ and $2\pi^0$ background Monte Carlo simulations.

FIG. 2. Data–Monte Carlo comparison for the $z$ decay vertex distribution for $\pi^0\gamma\gamma$ candidates and background events with $m_{\gamma\gamma} \geq 0.280$ GeV. The normalization is absolute. The error bars correspond to the data, the shaded histogram to the $2\pi^0$ background Monte Carlo simulation, and the dashed histogram to the sum of the $3\pi^0$ and $2\pi^0$ background Monte Carlo simulations. The arrow indicates the position of the cut.

FIG. 3. Data–Monte Carlo comparison for the $m_{12}$ ($\pi^0$ candidate) distribution for $\pi^0\gamma\gamma$ candidates and background events including $\pi^0\gamma\gamma$ signal Monte Carlo simulation, for $m_{\gamma\gamma} \geq 0.280$ GeV. The error bars correspond to the data; the diagonally shaded histogram to the sum of the $3\pi^0$ and $2\pi^0$ background Monte Carlo simulations; the horizontally shaded histogram to the $\pi^0\gamma\gamma$ signal normalized with the branching ratio of $1.86 \times 10^{-6}$, and the dashed histogram to the sum of the background and the signal. The normalization is absolute.

over the background Monte Carlo simulation is peaked at the nominal $\pi^0$ mass with a width consistent with the prediction of a $\pi^0\gamma\gamma$ Monte Carlo simulation. (It should be noted that the background also peaks near, but not at, the nominal neutral-pion mass. This happens because the background often has a true $\pi^0$ but, because of the overlaps of the other two clusters, its mass is somewhat shifted and broadened due to the nonlinearity in the lead-glass response.) The $\pi^0\gamma\gamma$ signal is normalized at a branching ratio $1.86 \times 10^{-6}$ (see below). The agreement is good and gives additional confidence that the excess of data at high $m_{\gamma\gamma}$ is $\pi^0\gamma\gamma$ signal.

For the high-mass sample ($m_{\gamma\gamma} \geq 0.280$ GeV) we have 232 candidate events from which 104 come from a data set with a 0.09-radiation-length lead sheet inserted in the beams 137.8 m from the target. The effect of the lead sheet is that it will sometimes convert one (or more) of the photons causing both signal and background events to be lost. The Monte Carlo simulation properly accounts for this and the total predicted background is $(171.9 \pm 11.5)$ events (150.7 from $3\pi^0$s and 21.2 from $2\pi^0$s). Based on background studies and many comparisons of data with Monte Carlo distributions, we assign an 11% systematic error to the estimate of the background in the high mass region. There are three sources to this systematic uncertainty which are added in quadrature. The first is due to imperfect knowledge of the efficiencies of the photon vetoes (exclusive of the lead mask, itself a photon veto discussed later) and this is estimated to result in 5% uncertainty. The second arises from possible errors in the understanding of the photon energy resolution and this is estimated to result in a 3% uncertainty. The third, which is the largest, is associated with the discarding of a few remaining events with photons projecting outside the aperture of the lead mask. These events are not well simulated and this is estimated to result in a 9% uncertainty. The $\pi^0\gamma\gamma$ acceptance is 3.4% (4.4%) for data with (without) the lead sheet inserted and the normalization is provided by $45000$ $K_L \to 2\pi^0$ decays taken simultaneous-

ly. Using the world average value [11] for the $K_L \to 2\pi^0$ branching ratio we conclude that

$$\frac{\Gamma(K_L \to \pi^0\gamma\gamma, \, m_{\gamma\gamma} \geq 0.280 \text{ GeV})}{\Gamma(K_L \to \text{all})}$$

$$= (1.86 \pm 0.60 \pm 0.60) \times 10^{-6},$$

where the first error is statistical and the second is systematic. If we assume the $m_{\gamma\gamma}$ distribution predicted by chiral perturbation theory we then have

$$\frac{\Gamma(K_L \to \pi^0\gamma\gamma)}{\Gamma(K_L \to \text{all})} = (2.2 \pm 0.7 \pm 0.7) \times 10^{-6}.$$

We have also looked for a signal at lower $\gamma\gamma$ masses. Our acceptance for masses below the double fusion peak is smooth and averages [7,10] about 5%, except for the narrow region excluded around the nominal $\pi^0$ mass. For the region $m_{\gamma\gamma} < 0.264$ GeV we have $367 \pm 19.2$ data events and $377.5 \pm 18.4$ expected background events. This gives

$$\frac{\Gamma(K_L \to \pi^0\gamma\gamma, \, m_{\gamma\gamma} < 0.264 \text{ GeV})}{\Gamma(K_L \to \text{all})} < 5.1 \times 10^{-6}$$

(90% confidence)

where we have used a phase-space distribution for $m_{\gamma\gamma}$ and have included a 15% systematic error on the background prediction.

We thus confirm both the substantial branching ratio and the peaking at high mass first reported by the NA31 group. Our analysis uses less stringent kinematic cuts so that our acceptance is smooth and substantial over the entire mass region, leading to a limit at lower mass values. The central value for the branching ratio is a factor of three higher than the chiral perturbation theory prediction. More statistics and better background rejection will be necessary for additional studies of this decay mode.

---

*Current address: Fermi National Accelerator Laboratory, Batavia, IL 60510.

†Current address: Cornell University, Ithaca, NY 14853.

‡Current address: SLAC, Stanford, P.O. Box 4349, CA 94305.

§Current address: Department of Physics, University of Illinois, Urbana, IL 61801.

**Current address: CERN, CH-1211, Geneva 23, Switzerland.

††Current address: Princeton Combustion Research Laboratories, Monmouth Junction, NJ 08852.

[1] G. Ecker, A. Pich, and E. De Rafael, Phys. Lett. B **189**, 363 (1987).

[2] P. Ko and J. L. Rosner, Phys. Rev. D **40**, 3775 (1989).

[3] T. Morozumi and H. Iwasaki, in *Physics at TeV Scale*, Proceedings of the Second Meeting, Tsukuba, Japan, 1988, edited by K. Hidaka and K. Hikasa (KEK, Tsukuba, 1988).

[4] L. M. Sehgal, Phys. Rev. D **41**, 161 (1990).

[5] P. Ko, Phys. Rev. D **41**, 1531 (1990).

[6] G. Ecker, A. Pich, and E. De Rafael, Report Nos. UWThPh-1989-65, FTUV/89-44 (unpublished).

[7] V. Papadimitriou *et al.*, Phys. Rev. Lett. **63**, 28 (1989).

[8] G. D. Barr *et al.*, Phys. Lett. B **242**, 523 (1990).

[9] J. R. Patterson *et al.*, Phys. Rev. Lett. **64**, 1491 (1990).

[10] V. Papadimitriou, Ph.D. thesis, University of Chicago, 1990.

[11] Particle Data Group, G. P. Yost *et al.*, Phys. Lett. B **204**, 1 (1988).

# Search for the decay $K_L \rightarrow \pi^0 \nu \bar{\nu}$

G.E. Graham, A.R. Barker, R.A. Briere, L.K. Gibbons, G. Makoff, V. Papadimitriou [1],
J.R. Patterson [2], S.V. Somalwar, Y.W. Wah, B. Winstein, R. Winston, H. Yamamoto [3]

*Enrico Fermi Institute and Department of Physics, University of Chicago, Chicago, IL 60637, USA*

E.C. Swallow

*Department of Physics, Elmhurst College, Elmhurst, IL 60126, USA*
*and Enrico Fermi Institute, University of Chicago, Chicago, IL 60637, USA*

G.J. Bock, R. Coleman, J. Enagonio, Y.B. Hsiung, E. Ramberg, K. Stanfield, R. Tschirhart,
T. Yamanaka [4]

*Fermi National Accelerator Laboratory, Batavia, IL 60510, USA*

G.D. Gollin [5], M. Karlsson [6]

*Department of Physics, Princeton University, Princeton, NJ 08544, USA*

P. Debu, B. Peyaud, R. Turlay and B. Vallage

*Department de Physique des Particules Elementaires, Centre d'Etudes Nucleaires de Saclay,*
*F-91191 Gif-sur-Yvette Cedex, France*

Data collected in Fermilab experiment E731 was used to perform the first search for the decay $K_L \rightarrow \pi^0 \nu \bar{\nu}$. This decay is dominated by short distance effects and is almost entirely direct $CP$ violating within the standard model. Cuts were developed to reject the background processes $\Lambda \rightarrow n\pi^0$ and $K_L \rightarrow \pi^+ e^- \gamma \nu$. No candidate events were seen. We find BR $(K_L \rightarrow \pi^0 \nu \bar{\nu}) < 2.2 \times 10^{-4}$ at the 90% confidence level.

The decay $K_L \rightarrow \pi^0 \nu \bar{\nu}$ is uniquely well suited to the study of direct $CP$ violation within the standard model. It is one of four related processes in which a kaon decays to a pion and a light lepton pair. These are (i) $K^+ \rightarrow \pi^+ e^+ e^-$ ($K^+_{\pi ee}$); (ii) $K^+ \rightarrow \pi^+ \nu \bar{\nu}$ ($K^+_{\pi\nu\nu}$); (iii) $K^0 \rightarrow \pi^0 e^+ e^-$ ($K^0_{\pi ee}$); and (iv) $K^0 \rightarrow \pi^0 \nu \bar{\nu}$ ($K^0_{\pi\nu\nu}$).

The first of these, $K^+_{\pi ee}$, has been observed [1] with a branching ratio measured to be $2.75 \times 10^{-7}$. Unlike the other three, this process is dominated by long distance effects.

The branching ratio limit [2] for the second process, $K^+_{\pi\nu\nu}$, is $< 3.4 \times 10^{-8}$ at the 90% confidence level. This decay mode is dominated by short distance effects [3] described by one-loop diagrams involving virtual charm or top quarks. The top quark term is proportional to the magnitude of the as yet undetermined $V_{td}$ element of the CKM matrix. The standard model predicts that the branching fraction for this decay will be around $10^{-10}$.

For the third process, $K^0_{\pi ee}$, the branching ratio [4] is $< 3.5 \times 10^{-9}$ for $K_L$ and the limit [5] is $< 4.5 \times$

$10^{-5}$ for $K_S$, at the 90% confidence level. The $K_L$ decay mode has both direct and indirect $CP$ violating contributions [6]. The interesting direct piece is primarily a short-distance effect which can be fairly reliably calculated. However, this term can be extracted from a measurement of $K_L \to \pi^0 e^+ e^-$ only after the indirect piece has been determined from a measurement of $\Gamma(K_S \to \pi^0 e^+ e^-)$. It will be necessary to subtract the $CP$-conserving amplitude arising from the $\pi^0 \gamma^* \gamma^*$ intermediate state [7] and measurements [8] of $K_L \to \pi^0 \gamma\gamma$ has been made. Experimentally a substantial background [9] from radiative Dalitz decays, $K_L \to e^+ e^- \gamma\gamma$, also needs to be subtracted.

In this paper, we report the results of a search for the fourth mode, $K^0 \to \pi^0 \nu\bar{\nu}$. This process has been considered theoretically [10], but because of the formidable experimental difficulties, no search for this mode has previously been performed. The major attraction of this mode is its potential for the study of direct $CP$ violation in the standard model. There is no significant long-distance contribution to $K_L \to \pi^0 \nu\bar{\nu}$ and, based on existing upper limits for the $K^+_{\pi\nu\nu}$ mode, the amplitude from indirect $CP$ violation is negligible compared to direct $CP$ violating effects. The dominant, direct $CP$ violating, contribution to the decay is proportional to the imaginary part of $V_{td}$. In the Wolfenstein [11] parametrization of the CKM matrix, $V_{td} = A\lambda^3(1-\rho-i\eta)$ and the standard model predicts

$$\mathrm{BR}(K_L \to \pi^0 \nu\bar{\nu}) = 1.5 \times 10^{-10} (M_t/100\ \mathrm{GeV})^2 A^4 \eta^2,$$

where $M_t$ is the mass of the top quark. In the standard model, the magnitude of $\eta$ can be related to the known value of $\epsilon$: it is estimated [12] that $\eta$ lies somewhere between about 0.1 and 0.6. Based on the value [12] $A = 0.85 \pm 0.09$, and the mass of the top quark determined indirectly from LEP data [13] to be $157 \pm 40$ GeV/$c^2$, the branching fraction for $K_L \to \pi^0 \nu\bar{\nu}$ could be as large as $2 \times 10^{-10}$.

The experimental signature for $K_L \to \pi^0 \nu\bar{\nu}$ is an observed single $\pi^0$ with unbalanced transverse momentum. Two decay modes of the neutral pion, $\pi^0 \to \gamma\gamma$ and $\pi^0 \to e^+ e^- \gamma$, could be used for detection, each with its own experimental difficulties. If the $\gamma\gamma$ final state is used, the transverse position of the decay vertex within the neutral beam cannot be accurately determined, and a very hermetic photon veto system is required in order to reject background from $K_L \to 2\pi^0$

decays. Using the $e^+ e^- \gamma$ final state (Dalitz decays) permits the determination of the decay vertex so that the invariant mass and transverse momentum of the $e^+ e^- \gamma$ system can be calculated, allowing considerable background rejection. We have therefore elected for this first search to require a Dalitz decay, even though the Dalitz decay branching fraction is only about $\frac{1}{80}$ of that for $\pi^0 \to \gamma\gamma$. With this technique, we found that the most important backgrounds in this experiment were due to the decays $\Lambda \to n\pi^0(\pi^0 \to e^+ e^- \gamma)$ and $K_L \to \pi^+ e^- \gamma\nu$ (and its charge conjugate) when the pion is misidentified as an electron. It was necessary to develop cuts to identify and reject events from each of these processes.

Here we describe briefly the features of the experimental apparatus relevant to this search. Two neutral $K_L$ beams (each $\frac{1}{2} \times \frac{1}{2}$ mrad$^2$) were created at 4.8 mrad by 800 GeV protons striking a Be target. One of the two neutral beams hit a regenerator in order to produce a $K_S$ flux, but only decays from the other (vacuum) beam were used in this search. The trajectories and momenta of charged particles were reconstructed using four drift chambers and an analyzing magnet which imparted a horizontal transverse momentum ($P_t$) kick of about 200 MeV/$c$. Each drift chamber consisted of two $X$ planes and two $Y$ planes; each plane had a resolution of approximately 100 μm. A roughly circular array of 804 lead glass blocks was used to measure the energies and positions of electrons and photons. Each block measured 5.82 cm by 5.82 by 60 cm long, this depth being equal to about 19 radiation lengths. We obtained photon energy and position resolutions of $\sigma/E \cong 2.5\% + 5\%/\sqrt{E}$ and $\sim 3$ mm, respectively. In the lead glass array, there were two 11.6 cm by 11.6 cm beam holes whose centers were 11.6 cm above and below the center of the array, through which the neutral beams passed. These two beam holes were viewed by a beam hole calorimeter which was about 30 radiation lengths (1.3 interaction lengths) long. There were altogether twelve planes of photon veto counters at different positions in the spectrometer which were used to detect decay products outside the chamber and calorimeter acceptances. In this search we used $K_L$ decays occurring in a region 31 m long. Further characteristics of the E731 detector have been described elsewhere [14].

The trigger used to collect the events analyzed here required two or more charged particles, one each on

the left and right sides of the second drift chamber (1.63 m wide×1.42 m high located about 3 meters upstream of the analyzing magnet). It also required charged particle hits in opposite quadrants of a scintillator hodoscope just in front of the lead glass calo-rimeter, with some overlap between quadrants near the center of the detector. These requirements were only rarely satisfied by $\pi^0$ Dalitz decays since the electron–positron pair usually has a very small opening angle [15].

In the analysis, a signal event candidate is required to have two charged tracks and one photon, where a photon is defined as an energy cluster in the lead glass not matched to either track. Both tracks were identified as electrons by the requirement that $0.925 < E/p < 1.075$, where $E$ is the total energy of the calo-rimeter cluster matched to the track, and $p$ is the track momentum measured in the drift chamber system. All three clusters' shapes were required to be consistent with the shape expected for electromagnetic showers. The $E/p$ and shape cuts together gave a $\pi/e$ rejection of about 100 for track momentum in the range of 2–20 GeV/$c$. Radiative $K_{e3}$ ($K_L \to \pi e \gamma \nu$) background events in which the pion was misidentified as electron were reconstructed by assuming that one of the two tracks was a pion. The neutrino is not observed, but using mass and $P_t$ constraints, its momentum (and therefore that of the decaying kaon) can be calculated up to a two-fold ambiguity in the longitudinal component. The cosine of the angle between the electron and photon in the kaon center-of-mass frame is then calculated based on the assumption that the smaller of the two kaon energy solutions is correct. The resulting distribution of cosines, shown in fig. 1, is not sensitive to this assumption. The distribution peaks sharply near +1 since the photons in $\pi e \gamma \nu$ background events are produced by internal or external bremsstrahlung, and so tend to be collinear with the electron. Events were rejected if $\cos \theta_{e\gamma} > 0.95$ for either possible assignment of one track as an electron and the other as a pion.

The energy of the photon was required to be greater than 5 GeV in order to reject the usually softer photons which were accidentally coincident with $K_{e3}$ events. To reject events with radiative external conversion and backgrounds resulting from accidental activity, we required $12 < M_{ee} < 48$ MeV/$c^2$, $M_{\pi e \gamma} < 500$ MeV/$c^2$, and $P_t^{ee} < 17$ MeV/$c$ where $M_{ee}$



Fig. 1. The histogram is the distribution of $\cos \theta_{e\gamma}$ for events surviving all other cuts. The peak at +1 is from radiative $K_{e3}$ decays. This background is removed by discarding events with $\cos \theta_{e\gamma} > 0.95$. The curve shows the distribution predicted by a Monte Carlo simulation of $K_L \to \pi^0 \nu \bar{\nu}$ with $\pi^0 \to e^+ e^- \gamma$.

and $M_{\pi e \gamma}$ are the invariant masses of the assumed $ee$ pair and $\pi e \gamma$ system, and $P_t^{ee}$ is the transverse momentum of the $ee$ pair relative to the kaon flight direction. Although the $M_{ee}$ value for a real $\pi^0$ Dalitz decay could be higher than 48 MeV/$c^2$, the cut was set to further reject the remaining $K_{e3}$ background with the misidentified pion as electron. This misidentification shifted the reconstructed $M_{ee}$ invariant mass down by the pion mass value, however due to the characteristics [15] of the $M_{ee}$ distribution of $\pi^0$ Dalitz decay, the signal sensitivity suffers only a small loss. These cuts reduced the acceptance by about 8% in a Monte Carlo signal simulation while reducing the number of events of the data sample by a factor of 18.

To normalize the total exposure of the experiment, we reconstructed $K_L \to e^+ e^- \gamma$ events from the same data sample. Fig. 2 shows the invariant $e^+ e^- \gamma$ mass distribution. Forty-nine events are seen. Based on the measured branching ratio for this mode [16] and the Monte Carlo calculated acceptance of $4.75 \times 10^{-3}$, the total number of kaon decays to which the detector was exposed is about $1.08 \times 10^9$. This agrees to within 5% with the result of an independent flux calculation based on a sample of about $3.3 \times 10^5$ $K_L \to \pi^+ \pi^-$ events collected simultaneously.

Fig. 2. Distribution of the reconstructed kaon mass for $K_L \to e^+e^-\gamma$ candidates. There are 49 events lying between 480 and 520 MeV/$c^2$. The width of the gaussian fit is 9.5 MeV/$c^2$.

Even though the beam production target was about 100 meters upstream of the decay volume, some very high energy (250–350 GeV) $\Lambda$ hyperons produced at the target lived long enough to enter the fiducial volume. The neutron from the decay $\Lambda \to n\pi^0 (\pi^0 \to e^+e^-\gamma)$ usually went into the beam holes. To reduce background from this source, we rejected any event in which more than 10 GeV was deposited in the beam hole calorimeter. Because sufficient accidental activity in the beam hole calorimeter would cause good events to be discarded, this cut reduced the effective flux by about 5%. The $P_t$ spectrum of reconstructed $\pi^0$s from $\Lambda \to n\pi^0$ peaks just below 100 MeV/$c$, near the kinematic limit of 104 MeV/$c$ for this decay. Fig. 3 shows the distribution of reconstructed $e^+e^-\gamma$ invariant mass versus $P_t$ after all cuts. The empty box in the figure contains the region within which we search for $K_L \to \pi^0 \nu\bar{\nu}$ events. The events below the box are the remaining $\Lambda \to n\pi^0 (\pi^0 \to e^+e^-\gamma)$ background. Events outside the sensitivity box but away from the $\pi^0$ peak are from the small fraction of radiative $K_{e3}$ decays surviving all cuts.

The search region is defined by the cuts $115 < M_{ee\gamma} < 155 \text{ MeV}/c^2$ and $140 < P_t^{ee\gamma} < 240 \text{ MeV}/c$. The high limit of $P_t^{ee\gamma}$ is the largest possible $P_t$ of the $\pi^0$ from $K_L \to \pi^0 \nu\bar{\nu}$ could have attained with resolution effect (231 MeV/$c$ is the kinematical limit with no resolution effect). Fig. 4 shows the distribution of re-



Fig. 3. Reconstructed $e^+e^-\gamma$ invariant mass versus the transverse momentum for events surviving all cuts. The box represents the $\pi^0\nu\bar{\nu}$ search region as described in the text. The vertical axis projection clearly shows the residual $\Lambda \to n\pi^0$ events. The remaining backgrounds are due to radiative $K_{e3}$ decays, and $K_{e3}$'s in accidental coincidence with photons, both with misidentified pions.

constructed $e^+e^-\gamma$ invariant mass versus $P_t$ from Monte Carlo simulated data of $K_L \to \pi^0 \nu\bar{\nu} (\pi^0 \to e^+e^-\gamma)$ after all other cuts. Assuming a matrix element with a pure vector form factor, about 40% of $K_L \to \pi^0 \nu\bar{\nu} (\pi^0 \to e^+e^-\gamma)$ events lie within the defined search region (the box shown in fig. 4). Including this factor, the Monte Carlo calculated acceptance for $K_L \to \pi^0 \nu\bar{\nu} (\pi^0 \to e^+e^-\gamma)$ is $8.2 \times 10^{-4}$ for kaon energies between 20 and 220 GeV and decay vertices between 106 and 137 meters downstream of the target. We see no events within the search region, and therefore conclude with 90% confidence that the branching fraction for the decay $K_L \to \pi^0 \nu\bar{\nu}$ is less than $2.2 \times 10^{-4}$.

Searches with far greater sensitivity will be required in order to observe this process at the level predicted by the standard model.

This work partially fulfilled the requirements of a

# Results from the Neutral Kaon Program
# at Fermilab's Meson Center Beamline (1985-1997)

**Fermi National Accelerator Laboratory**

# Results from the Neutral Kaon Program at Fermilab's Meson Center Beamline 1985 - 1997

Erik Ramberg, Editor

Published on behalf of the E731, E773 and E799 Collaborations

*Fermi National Accelerator Laboratory*
*P.O. Box 500, Batavia, Illinois 60510*

January 1998

# Table of Contents

# Introduction

This volume contains reprints of all articles reporting physics results from the Fermilab E731, E773, and E799 experiments. This series of experiments concentrated on studies of CP violating and rare neutral kaon decays. This collection is due to the efforts of Erik Ramberg.

The data for the experiments was obtained in four distinct running periods in the M-Center beam line. These experiments followed a path whose origins can be traced to the early days of Fermilab, and which continues today.

E731 was a new experiment in a new beam with the primary purpose of studying CP violation in the neutral kaon system. The detector was designed with the sole criterion of having maximal acceptance for the $K_L \to 2\pi^\circ$ decay-the decay which statistically limits such studies. The double beam arrangement that had been employed in earlier Fermilab experiments was used to minimize some key systematic uncertainties. Originally, it was not planned that any other physics would be done with the beam and detector.

E731 was proposed in 1983; the authors of the proposal were G. Gollin, K. Nishikawa, B. Winstein (spokesman), Chicago; G. Bock, Fermilab; and B. Peyaud, R. Turlay, A. Zylberstejn, Saclay. E731 had an initial 6-week "test" run which ended in June of 1985. One measurement, that of $\epsilon'/\epsilon$, resulted from this run (p1).

Between 1985 and 1987, the detector was upgraded, particularly the trigger and read-out. A run began in August of 1987; its end was extended to February of 1988.

A set of data taken in a 5-week period at the end of the run was the source of the first publications from this run. The technique, now used by all $\epsilon'/\epsilon$ experiments, of collecting all four $K_L$ and $K_S$ to $2\pi$ modes simultaneously, was first employed in this data set. A new value for $\epsilon'/\epsilon$ (p12), a study of CPT symmetry in the neutral kaon system (p18), and two other studies that capitalized upon the large multi-body acceptance (p5, p9) resulted from this data set.

When the full data sample was analyzed, 9 more papers resulted (p16, p22-54). These included more accurate values for the quantities measured in the earlier analyses and some quite different studies. The first search for the $K_L \to \pi^\circ \nu \bar{\nu}$ decay was published. Accurate values for the lifetime of the $K_S$, the $K_L$, $K_S$ mass difference and the phase

of the $2\pi$ transition amplitudes were obtained. An important finding was that the mass difference, which had not been measured for many years, had a value significantly below the accepted average. When previous measurements of the phases of the $2\pi$ amplitudes were accordingly re-evaluated, they then came into agreement with CPT symmetry. And a new, third manifestation of CP violation (in addition to the $2\pi$ decay and the semi-leptonic charge asymmetry) was seen for the first time in the interference between $K_L$ and $K_S$ into the $\pi^+\pi^-\gamma$ channel. A full description of the beam, detector, and analysis techniques in E731 (based upon the PhD thesis of L. Gibbons) was also written (p114).

The detector was modified for a two month run which began in September of 1991 as a dedicated study of CPT symmetry. This data set (E773, G. Gollin, spokesman) produced several measurements in 3 publications (p98-109). The experiment used two regenerators and a significant advance in the understanding of the regeneration phenomenon was made. The phases of the $2\pi$ transition amplitudes and the $K_L$, $K_S$ mass difference were better measured, and the interference in the $\pi^+\pi^-\gamma$ mode was determined even more precisely.

A dedicated rare kaon decay search (E799, Y. Wah and T. Yamanaka, spokesmen) immediately followed E773 for an additional 2 months. The primary purpose of this run was to extend the search for the CP violating $K_L \to \pi^\circ e^+e^-$ decay. This was done to the level of $10^{-9}$ (p63). Ten additional papers resulted from this last run of the Meson Center detector (p55-62, p71-97, p110). These included improved limits in the closely related $\pi^\circ\nu\bar{\nu}$ and $\pi^\circ\mu^+\mu^-$ branching ratios. A broad study of radiative decays was also performed. This included (a) enough $K_L \to 4e$ decays for the first spin-parity analysis of the final state; (b) the first high statistics study of the $\mu^+\mu^-\gamma$ decay; and, (c) the first observation of the $\mu^+\mu^-e^+e^-$ decay mode. A new technique was developed for studying rare $\pi^\circ$ decays: using the unambiguous signature of a $K_L \to 3\pi^\circ$ decay as a tag. By this means, the $\pi^\circ \to e^+e^-$ decay was observed particularly cleanly, and a limit on the flavor violating $\pi^\circ \to \mu e$ transition was established. Finally, a large improvement in the $K_L \to \pi^\circ\mu e$ limit was obtained, and measurements of the production polarization of $\Lambda$ hyperons were made.

The collaboration began with barely 10 members and ended with over 40. Nineteen students obtained their PhDs on the data collected from these experiments; of these, 14 have remained in the field, all joining other collaborations. Of the 20 postdocs who worked on these experiments, 16 remain in the field, 9 of whom are continuing in the FNAL Kaon program. These experiments were done with modest budgets in a climate where significant parts of the detector were produced by University groups with their own funding. The first author on almost every publication was chosen as the student or postdoc whose work led to the reported result.

It took a long time for all the analysis to be completed but the results were satisfying. The final error obtained on $\epsilon'/\epsilon$ was an order-of-magnitude improvement over the best prior measurement. This result and the determinations of the phases of the CP violating amplitudes, $K_S$ lifetime and $K_L$, $K_S$ mass difference have not been surpassed in the published literature to date. Because of the high acceptance and high kaon energy, the rare decay studies performed compete well with other experiments having much more kaon flux. Of all the results and studies of rare decays of this collaboration, only two have so far been bettered by groups other than our own (p22, p79).

This work is continuing, but in a new, larger collaboration at Fermilab. Again, a new beam and a new detector were constructed for KTeV, which is in the midst of data collection. It again is studying $\epsilon'/\epsilon$ and rare decays with greater sensitivity. Prospects for success look very good.

Bruce Winstein
March, 1997

# Chronological List of Results from the Fermilab K° Program (1985-1997)

*This list summarizes the complete set of physics results to come out of the kaon program in the meson center beamline of Fermilab, 1985-1997. It is arranged in chronological order and gives the title, first author, collaboration, journal reference, date of publication and page number in this volume. Each entry also includes the numerical results quoted in the abstract of the paper. Other qualitative results may be quoted in the abstract, or other quantitative results may be discussed in the body of the paper. Errors are quoted as statistical, then systematic. Limits on branching ratios are quoted for 90% confidence level.*

$$\Gamma(K_L \to \pi^\circ\gamma\gamma, m_{\gamma\gamma} \geq 0.280 GeV)/\Gamma(K_L \to all)$$
$$= (1.86 \pm 0.60 \pm 0.60) \times 10^{-6}$$
$$\Gamma(K_L \to \pi^\circ\gamma\gamma, m_{\gamma\gamma} < 0.264 GeV)/\Gamma(K_L \to all)$$
$$< 5.1 \times 10^{-6}$$

$$BR(K_L \to \pi^\circ\nu\bar{\nu}) < 2.2 \times 10^{-4}$$

$$h(K_L \to 3\pi^\circ) = -[3.3 \pm 1.1 \pm 0.7] \times 10^{-3}$$

$$\tau_S = (0.8929 \pm 0.0016) \times 10^{-10}s$$
$$\Delta m = (0.5286 \pm 0.0028) \times 10^{10}\hbar s^{-1}$$
$$\Phi_{+-} = 42.2^\circ \pm 1.4^\circ$$
$$\Delta\Phi = -1.6^\circ \pm 1.2^\circ$$

$$Re(\epsilon'/\epsilon) = (7.4 \pm 5.2 \pm 2.9) \times 10^{-4}$$

$$BR(K_{e4}) = [5.16 \pm 0.20 \pm 0.22] \times 10^{-5}$$
$$L_3 = -(3.4 \pm 0.4) \times 10^{-3}$$

$$\Gamma(K_L \to \pi^+\pi^-\gamma)/\Gamma(K_L \to \pi^+\pi^-)$$
$$= (23.0 \pm 0.7) \times 10^{-3}$$
$$\Gamma(K_S \to \pi^+\pi^-\gamma, E_\gamma^* > 20 MeV)/\Gamma(K_S \to \pi^+\pi^-)$$
$$= (7.10 \pm 0.22) \times 10^{-3}$$

---

‡The sign of $L_3$ was incorrectly reported as positive in this paper. It was corrected in Physical Review Letters, Errata; 4 September, 1995.

$$|\eta_{+-\gamma}| = (2.15 \pm 0.26 \pm 0.20) \times 10^{-3}$$
$$\phi_{+-\gamma} = (72 \pm 23 \pm 17)°$$
$$|\epsilon'_{+-\gamma}|/\epsilon < 0.3$$

$$BR(\pi° \rightarrow e^+ e^-, (m_{ee}/m_{\pi°})^2 > 0.95)$$
$$= [7.6^{+3.9}_{-2.8} \pm 0.5] \times 10^{-8}$$

$$BR(K_L \rightarrow \pi°\mu^+\mu^-) < 5.1 \times 10^{-9}$$

$$BR(K_L \rightarrow \pi°e^+e) < 4.3 \times 10^{-9}$$

$$\tfrac{1}{2}[BR(\pi° \rightarrow \mu^+e^-) + BR(\pi° \rightarrow \mu^-e^+)] < 8.6 \times 10^{-9}$$

$$BR(K_L \rightarrow e^+e^-e^+e^-) = [3.96 \pm 0.78 \pm 0.32] \times 10^{-8}$$

$$BR(K_L \rightarrow \pi°\nu\bar{\nu}) < 5.8 \times 10^{-5}$$

$$BR(K_L \rightarrow \pi°\pi°\gamma) < 2.3 \times 10^{-4}$$

$$BR(K_L \rightarrow e^+e^-\gamma\gamma, E_{\gamma}^* > 5MeV) = [6.5 \pm 1.2 \pm 0.6] \times 10^{-7}$$

$$BR(K_L \rightarrow \mu^+\mu^-\gamma) = [3.23 \pm 0.23 \pm 0.19] \times 10^{-7}$$

$$\phi_{\pm} = 43.53° \pm 0.97°$$
$$\phi_{\circ\circ} - \phi_{\pm} = 0.62° \pm 1.03°$$

$$|\eta_{+-\gamma}| = (2.359 \pm 0.062 \pm 0.040) \times 10^{-3}$$
$$\phi_{+-\gamma} = (43.8 \pm 3.5 \pm 1.9)°$$

$$BR(K_L \rightarrow e^+e^-\mu^+\mu^-) = (2.9^+6.7_{-2.4}) \times 10^{-9}$$
$$BR(K_L \rightarrow e^{\mp}e^{\mp}\mu^{\pm}\mu^{\pm}) < 6.1 \times 10^{-9}$$

---

‡Errors in table headings and figure captions in this paper are corrected in Physical Review Letters, Errata; 4 September, 1995.

# The E731 Collaboration

A. Barker, R.A. Briere, L.K. Gibbons, G.E. Graham, G. Makoff,
K. Nishikawa, V. Papadimitriou, J.R. Patterson, B. Schwingenheuer,
S. Somalwar, Y.W. Wah, B. Winstein, R. Winston,
M. Woods and H. Yamamoto

*The Enrico Fermi Institute and the Department of Physics,
The University of Chicago, Chicago, Illinois, 60637*

E.C. Swallow

*Department of Physics, Elmhurst College, Elmhurst, Illinois 60126 and
The Enrico Fermi Institute, The University of Chicago, Chicago, Illinois, 60637*

G.J. Bock, R. Coleman, J. Enagonio, Y. B. Hsiung, E. Ramberg,
K. Stanfield, R. Stefanski, and T. Yamanaka

*Fermi National Accelerator Laboratory, Batavia, Illinois 60510*

G. Blair, G.D. Gollin, G.L. Grazer, M. Karlsson,
J.K. Okamitsu and R. Tschirhart

*Department of Physics, Princeton University, Princeton, New Jersey 08544*

J.C. Brisson, R. Daudin, P. Debu, P. Jarry, B. Peyaud,
R. Turlay, and B. Vallage

*Department de Physique des Particules Elementaires, Centre d'Etudes
Nucleaires de Saclay, F-91191 Gif-sur-Yvette Cedex, France*

# The E773 Collaboration

A.R. Barker, R.A. Briere, E. Cheu, L.K. Gibbons, D.A. Harris, G. Makoff,
K.S. McFarland, A. Roodman, B. Schwingenheuer, Y.W. Wah,
B. Winstein, and R. Winston

*The Enrico Fermi Institute and the Department of Physics,
The University of Chicago, Chicago, Illinois, 60637*


E.C. Swallow

*Department of Physics, Elmhurst College, Elmhurst, Illinois 60126 and
The Enrico Fermi Institute, The University of Chicago, Chicago, Illinois, 60637*


G.J. Bock, R. Coleman, M. Crisler, J. Enagonio, R. Ford, Y.B. Hsiung,
D. Jensen, E. Ramberg, R. Tschirhart, and T. Yamanaka

*Fermi National Accelerator Laboratory, Batavia, Illinois 60510*


E.M. Collins and G.D. Gollin

*Department of Physics, University of Illinois, Urbana, Illinois 61801*


P. Gu, P. Haas, W.P. Hogan, S. Kim, J.N. Matthews, S.S. Myung,
S. Schnetzer, S.V. Somalwar, G. Thomson, and Y. Zou

*Department of Physics, Rutgers University, Piscataway, New Jersey 08855*

# The E799 Collaboration

K. Arisaka, J. Kubic, D. Roberts, W. Slater, M. Spencer, and M. Weaver

*Department of Physics, University of California at Los Angeles,*
*Los Angeles, California 90024*


R.A. Briere, E. Cheu, D.A. Harris, P. Krolak, G. Makoff,
K.S. McFarland, A. Roodman, B. Schwingenheuer, S. Somalwar,
Y.W. Wah, B. Winstein, and R. Winston

*The Enrico Fermi Institute and the Department of Physics,*
*The University of Chicago, Chicago, Illinois, 60637*


A.R. Barker

*Department of Physics, University of Colorado, Boulder, Colorado 80309*


E.C. Swallow

*Department of Physics, Elmhurst College, Elmhurst, Illinois 60126 and*
*The Enrico Fermi Institute, The University of Chicago, Chicago, Illinois, 60637*


G.J. Bock, R. Coleman, M. Crisler, J. Enagonio, R. Ford,
Y.B. Hsiung, D. Jensen, E. Ramberg, and R. Tschirhart

*Fermi National Accelerator Laboratory, Batavia, Illinois 60510*


E.M. Collins and G.D. Gollin

*Department of Physics, University of Illinois, Urbana, Illinois 61801*


T. Nakaya and T. Yamanaka

*Department of Physics, Osaka University, Toyonaka, Osaka, 560 Japan*


P. Gu, P. Haas, W.P. Hogan, S. Kim, J.N. Matthews,
S.S. Myung, S. Schnetzer, G. Thomson, and Y. Zou

*Department of Physics, Rutgers University, Piscataway, New Jersey 08855*

Plan view of the E731 detector.

Plan view of the E773 detector.

25 cm

Lead Glass

Muon Trigger Plates

Lead Wall

Photon Veto Counters

Transition Radiation Detectors

Photon Veto Counters

$K_L$ beams

Vacuum Window

Calibration magnets

Drift Chambers

Analysis Magnet

Hadron Veto

Trigger Planes

120   130   140   150   160   170   180   190

Distance from Target (m)

Plan view of the E799 detector.

Collaborators inspect the Meson Center enclosure before installation of the beamline and detector.

A view of the 804 lead glass blocks that made up the calorimeter for E731, E773 and E799.

The four drift chambers after being refurbished for the new kaon program at KTeV.



Looking upstream in the Meson Center enclosure with the vacuum decay vessel and its veto arrays.

The upstream regenerator in E773.



The last shift of E799 celebrates the end of the kaon program in Meson Center beamline.

# First Result on a New Measurement of $\epsilon'/\epsilon$ in the Neutral-Kaon System

M. Woods, K. Nishikawa,[a] J. R. Patterson, Y. W. Wah, B. Winstein, R. Winston, and H. Yamamoto

*The Enrico Fermi Institute and the Department of Physics, The University of Chicago, Chicago, Illinois 60637*

E. C. Swallow

*Department of Physics, Elmhurst College, Elmhurst, Illinois 60126, and*
*The Enrico Fermi Institute, The University of Chicago, Chicago, Illinois 60637*

G. J. Bock, R. Coleman, Y. B. Hsiung, K. Stanfield, R. Stefanski, and T. Yamanaka

*Fermi National Accelerator Laboratory, Batavia, Illinois 60510*

G. D. Gollin, G. L. Grazer, and J. K. Okamitsu

*Department of Physics, Princeton University, Princeton, New Jersey 08544*

and

P. Jarry, R. Daudin, P. Debu, B. Peyaud, and R. Turlay

*Département de Physique des Particules Elémentaires, Centre d'Etudes Nucléaires de Saclay,*
*F-91191 Gif-sur-Yvette Cedex, France*
(Received 8 February 1988)

A new beam line and detector were constructed to increase statistical precision and greatly reduce systematic uncertainty on the ratio of the *CP*-nonconserving parameters $\epsilon'/\epsilon$. Major improvements are discussed together with a result from a first run: $\epsilon'/\epsilon = 0.0032 \pm 0.0028$ (statistical) $\pm 0.0012$ (systematic). The precision is better than earlier measurements yet the result is still consistent with the superweak mechanism (which predicts zero) and that due to Kobayashi and Maskawa. Significantly more data are being collected.

*CP* nonconservation was first[1] observed in the $\pi^+\pi^-$ decay of the long-lived neutral kaon $(K_L)$; this and many subsequent measurements point to a very small asymmetry in the mixing of $K^0$ and $\bar{K}^0$, parametrized by $|\epsilon| \approx 2.3 \times 10^{-3}$.

A natural way of incorporating the asymmetry into the charged current weak interaction was advanced by Kobayashi and Maskawa[2] and, especially since the subsequent discovery[3] of the bottom quark, this has provided increased motivation for further studies. The Kobayashi-Maskawa mechanism has as one consequence a second manifestation of *CP* nonconservation in the $K^0(\bar{K}^0) \rightarrow 2\pi$ decay itself, parametrized[4] by the ratio $\epsilon'/\epsilon$. This is in contrast to the superweak[5] model. However, the effect is small (in the range $0.001 \lesssim |\epsilon'/\epsilon| \lesssim 0.007$) and the theoretical uncertainty is considerable.[6]

This experiment seeks to isolate such an effect by the measurement of the decay rates of $K_L$ and $K_S$ to charged and neutral pions:

$$\frac{\Gamma(K_L \rightarrow \pi^+\pi^-)/\Gamma(K_S \rightarrow \pi^+\pi^-)}{\Gamma(K_L \rightarrow \pi^0\pi^0)/\Gamma(K_S \rightarrow \pi^0\pi^0)} \simeq 1 + 6\,\mathrm{Re}\,\epsilon'/\epsilon.$$

Recent published experiments[7,8] had sensitivities to the above double ratio in the range of 0.03 to 0.04 and found no deviation from unity.

The technique which our group[7] has adopted in experiments at Fermilab allows simultaneous detection of $K_L$ and $K_S$ decays with a double neutral beam derived symmetrically from a single target; the $K_S$ are provided by coherent regeneration from material (the regenerator) placed in one of the $K_L$ beams. The experiment is run in two distinct modes: charged, where $\pi^+\pi^-$ are detected, and neutral, where $2\pi^0$ are detected. This approach provides good control of systematic uncertainties:

(a) Since $K_L$ and $K_S$ decays are detected simultaneously, time-dependent losses cancel. Such losses come from triggering, accidental vetoing (e.g., from short-term intensity variations), electronic drifts, and resolution changes.

(b) The momentum dependence of regeneration at high energies[9] results in nearly identical spectra for decaying $K_L$'s and $K_S$'s.

(c) Acceptance and intensity differences for decays from the two beams are negligible as the regenerator is frequently moved from one to the other.

$K_L$ and $K_S$ decays then differ *only* in the decay distribution along the beam so that good knowledge of the acceptance is needed. Background in $K_L$ decays and contamination from diffractive and inelastic regeneration in $K_S$ decays must be small and understood.

The experiment was performed in the new Meson

FIG. 1. Detector schematic, elevation view.

Center beam line at the Fermilab Tevatron. The neutral beams $(0.5\times0.5$ mrad$^2)$ were defined at 4.8 mrad from a Be target. A component of soft neutrons, common in previous neutral beams, was greatly reduced by an appropriate configuration of collimation and sweeping.

The detector is shown schematically in Fig. 1. The regenerator was about 123 m from the production target and the end of the decay region was defined by two closely spaced 1-mm scintillators between which an 0.1-radiation-length lead sheet, serving as a converter for the neutral mode, could be placed ("conversion plane" in Fig. 1).

The regenerator was constructed of four identical sections each consisting of 19 cm of $B_4C$, 1.76 cm of Pb, and six anticoincidence counters. The lead provided a sharp cutoff to the spatial distribution of $K_S \to 2\pi^0$ decays. The anticounters signaled inelastic events: Corrections for these dominated the systematic uncertainty in our previous effort.[7]

Charged tracks were measured with a 2000-wire, 16-plane drift-chamber spectrometer. Electrons and photons were identified with a circular array of 804 lead-glass blocks.

In the charged mode, a signal at the conversion plane and a two-track signature in the $A$ and $B$ hodoscopes were required. A 2-radiation-length lead sheet upstream of the $B$ hodoscope (only used in the charged mode) suppressed $K_{e3}$ decays with a pulse-height requirement. The hodoscope after 3 m of steel provided $K_{\mu3}$ rejection.

In the neutral mode, a 30-GeV electromagnetic energy and two tracks in the $A$ and $B$ hodoscopes consistent with a photon conversion were required—the magnet currents were chosen to separate and then recombine the pair at the lead glass. Background in this mode is dominated by $K_L \to 3\pi^0$ decays where photons miss, or merge with others in, the lead glass. Ten planes of anticoincidence with sensitivity above about 100 MeV were employed. One, placed in the beams, signaled photons with $E > 5$ GeV; another recognized photons close to the beam holes through the lead glass.

The events were reconstructed[10] similarly to Ref. 7. The chambers had plane resolutions of approximately 150 $\mu$m, and the $K^0 \to \pi^+\pi^-$ mass resolution was 3.5 MeV (rms). High-statistics lead-glass calibration was done periodically with electron pairs; the resolution was $\sigma/E \cong 1.5\% + 5\%/\sqrt{E}$ and $2\pi^0$ mass resolution was 6.1

TABLE I. Event total, mass cut, and background summary for each mode.

| Mode | Events[a] | Mass cut | Background[b] (%) | Improvement[c] factor | Systematic error(%) |
|---|---|---|---|---|---|
| $K_L \to 2\pi^0$ | 6747 | $\pm 3.3\sigma$ | 1.56 | 5.4 | 0.30 |
| $K_S \to 2\pi^0$ | 21788 | $\pm 3.3\sigma$ | 2.90 | 5.0 | 0.20 |
| $K_L \to \pi^+\pi^-$ | 35838 | $\pm 3.9\sigma$ | 1.23 | 2.5 | 0.18 |
| $K_S \to \pi^+\pi^-$ | 130025 | $\pm 3.9\sigma$ | 0.30 | 5.7 | 0.03 |

[a]After subtractions.

[b]Residual non-$\pi\pi$ background for $K_L$ modes: diffractive and inelastic contribution for $P_T^2 < 250$ (4000) (MeV/$c$)$^2$ for $\pi^+\pi^-$ $(2\pi^0)$ $K_S$ modes.

[c]With respect to Ref. 7.

MeV.

Table I gives the event totals and background levels; significant improvement over Ref. 7 was obtained. The improved suppression of inelastic regeneration reduced the contamination under the coherent $K_S$ peak in the neutral mode by a factor of about 5. Figure 2 shows the $K_L \rightarrow 2\pi^0$ invariant-mass distribution; the array of photon vetos reduced the background in this mode by more than a factor of 5.

Background subtractions were made in each 10-GeV/$c$ momentum bin (13 charged bins from 30 GeV/$c$ and 11 neutral bins from 40 GeV/$c$). The ratios of $K_S$ to $K_L$ decays, after correction for acceptance, were simultaneously fitted for three parameters: the $B_4C$ regeneration amplitude, its power-law momentum dependence, and $\epsilon'/\epsilon$. The fit gave $|(f-\bar{f})/k| \propto p^{-0.596 \pm 0.009}$, consistent with past work.[9,11] The result[12] is $\epsilon'/\epsilon = 0.0032 \pm 0.0028$ where the (statistical) error is nearly a factor of 2 better than in Ref. 7; $\chi^2$ was 0.98 per degree of freedom.

The sources of systematic uncertainty are associated with the accidental activity in the detector, the relative energy calibration between the two modes, the background subtractions, and the acceptance corrections.

The integration time for the lead-glass signals was 250 ns; as a result, the neutral mode was the one most affected by accidental activity: Nearly 10% of otherwise good decays were lost. Since the distributions of photons

in the lead glass for $K_L$ and $K_S$ are not exactly the same and the accidental hits are not perfectly uniform, the combined effect could in principle give an asymmetry in the loss. From a study of accidental events superimposed on Monte Carlo data, however, it was determined that the asymmetry was less than 2% itself. The resulting systematic error was 0.20% in the double ratio.

The $\pi^+\pi^-$ energy scale was determined with the well-known values for the $K^0$ and $\Lambda$ masses. A neutral-mode energy-scale error will shift the vertex; however, as no vertex cut was made, the corresponding systematic error was greatly reduced. The energy scale was initially determined for each block with only the electron calibration data. A final correction of $\approx 0.5\%$ was made to adjust the edges of the vertex distributions; the residual uncertainty was estimated at 0.2%, leading to an uncertainty in the double ratio of 0.21%.

The sources of uncertainties in the backgrounds were as follows (see Table I): The $3\pi^0$ contamination (Fig. 2) was determined by the fit of the background shape from a Monte Carlo simulation; the major uncertainty came from imperfectly known efficiencies of some veto planes. The backgrounds in $K_L \rightarrow \pi^+\pi^-$ were well understood semileptonic decays ($\approx 85\%$) and a small ($\approx 15\%$) non-kaon-decay component.

The diffractive and inelastic components under the coherent peaks in the $K_S$ samples were rejected by a cut on the momentum transfer $P_T^2$ at the regenerator. (Of course the identical cut was applied to the $K_L$ samples.) The distributions in this variable were very well understood for both decay modes and in fact they are the same in principle. The remaining background in the neutral



FIG. 2. Reconstructed $\pi^0\pi^0$ invariant mass for $K_L$. The $3\pi^0$ background shape determined from Monte Carlo is superimposed.



FIG. 3. Reconstructed decay-vertex distribution for $K_{L,S} \rightarrow 2\pi^0$, data and Monte Carlo simulation.

mode was larger because of the poorer resolution [1500 (MeV/$c$)$^2$] of the coherent peak; the error in the subtraction was dominated by resolution uncertainties.

The remaining systematic error comes from uncertainties in the acceptances for charged and neutral decays. Very important checks were provided by consistency in the acceptance-corrected momentum spectra and regeneration power laws between the two modes. In the charged mode, where the resolution on the reconstructed vertex is excellent (15 cm rms), the data can be analyzed in small bins with little statistical loss, and by our fitting the ratios of regenerated to vacuum events, acceptance corrections are reduced significantly. For example, with 1.5-m bins the overall correction is only 0.48%. From such studies the systematic error in the charged acceptance is estimated to be 0.25%.

In the neutral mode, the poorer vertex resolution (1.1 m rms) and energy-scale uncertainty complicate the use of small bins. Figure 3 shows the vertex distributions compared with the Monte Carlo simulation; agreement is excellent but an independent check is desired. There were only three apertures for photons so that the acceptance could be readily understood: the lead-glass array (including the hardware-defined inner edge around the beam holes), a lead mask just upstream of the regenerator (see Fig. 1), and a thick lead aperture surrounding the conversion plane. In a typical momentum bin, the acceptance downstream of the mask varied with vertex by only about 1% per meter, the mean decay position for $K_L$ and $K_S$ events differed by less than 2 m, and the acceptance correction was about 2%. For the region upstream of the mask ($\approx 10\%$ of the $K_L$ data), the acceptance varied more sharply (by design). Both regions were studied with over 500000 $3\pi^0$ decays having even greater acceptance variations; there was no disagreement with the Monte Carlo simulation outside statistics. Furthermore, a consistent result was obtained when we discarded the upstream events although then the error from an energy scale uncertainty increased to about 0.4%. From these studies, the uncertainty in the neutral-mode acceptance correction was estimated at 0.50%.

The total systematic error on the double ratio is given by our combining all the above (uncorrelated) uncertainties in quadrature yielding an error of 0.75%. The result is $\epsilon'/\epsilon = 0.0032 \pm 0.0028$ (statistical) $\pm 0.0012$ (systematic). Combining these errors in quadrature gives $\epsilon'/\epsilon = 0.0032 \pm 0.0030$. This is consistent with previous measurements while being more precise by nearly a factor of 2; however, the superweak and Kobayashi-Maskawa models are both still viable. The experiment is running with upgrades and a significant increase in statistical precision is expected.[13]

We are happy to acknowledge important technical contributions by R. Armstrong, H. Sanders, E. Beck, H. Edwards, S. Sobczynski, J. M. Garin, and D. Gauthereau. M. Asner, D. Burkeen, D. Cinabro, L. Gibbons, and G. Wright helped with chamber construction and V. Papadimitriou with analysis. The support of the Fermilab staff is gratefully acknowledged. The work was supported in part by the National Science Foundation, the Department of Energy, and the French Atomic Energy Commission. One of us (M.W.) submitted this work in partial fulfillment of the requirement for the Ph.D. degree at The University of Chicago.

[a] Present address: Institute for Nuclear Study, University of Tokyo, Tokyo, Japan.

[1] J. H. Christenson, J. W. Cronin, V. L. Fitch, and R. Turlay, Phys. Rev. Lett. 13, 138 (1964).

[2] M. Kobayashi and T. Maskawa, Prog. Theor. Phys. 49, 652 (1973).

[3] S. Herb et al., Phys. Rev. Lett. 39, 252 (1977).

[4] Since arg($\epsilon'$)=arg($\epsilon$), Re$\epsilon'/\epsilon$=$\epsilon'/\epsilon$; see J. W. Cronin, Rev. Mod. Phys. 53, 373 (1981).

[5] L. Wolfenstein, Phys. Rev. Lett. 13, 569 (1964).

[6] See L. Wolfenstein, Annu. Rev. Nucl. Part. Sci. 36, 137 (1986), for a discussion of the predictions.

[7] R. H. Bernstein et al., Phys. Rev. Lett. 54, 1631 (1985).

[8] J. K. Black et al., Phys. Rev. Lett. 54, 1628 (1985).

[9] See A. Gsponer et al., Phys. Rev. Lett. 42, 13 (1979).

[10] For a full description of the analysis and detector see P. Jarry, Ph.D. thesis, Université de Paris-Sud, 1987 (unpublished); M. Woods, Ph.D. thesis, University of Chicago, 1988 (unpublished).

[11] Here $f$ ($\bar{f}$) is the forward $K^0$ ($\bar{K}^0$) scattering amplitude and $k$ is the kaon wave number. The fit included interference with $K_L$ decays.

[12] A preliminary result was given by B. Winstein, in Proceedings of the Salt Lake City Meeting, edited by Carleton DeTar and James Ball (World Scientific, Singapore, 1987), pp. 37-58.

[13] Another experiment with a different technique at CERN has the preliminary result $\epsilon'/\epsilon = 0.0035 \pm 0.0007$ (statistical) $\pm 0.0012$ (systematic) $\pm 0.0004$ (Monte Carlo), and it also will acquire more data. See the review by I. Mannelli, in Proceedings of the International Symposium on Lepton and Photon Interactions at High Energies, Hamburg, West Germany, 1987 (to be published).

# New Limits on $K_{L,S} \to \pi^0 e^+ e^-$

L. K. Gibbons, V. Papadimitriou, J. R. Patterson, Y. W. Wah, B. Winstein, R. Winston, M. Woods, [a] and
H. Yamamoto

*The Enrico Fermi Institute and the Department of Physics, The University of Chicago, Chicago, Illinois 60637*

E. C. Swallow

*Department of Physics, Elmhurst College, Elmhurst, Illinois 60126, and*
*The Enrico Fermi Institute, The University of Chicago, Chicago, Illinois 60637*

G. J. Bock, R. Coleman, Y. B. Hsiung, K. Stanfield, R. Stefanski, and T. Yamanaka

*Fermi National Accelerator Laboratory, Batavia, Illinois 60510*

G. Blair, [b] G. D. Gollin, M. Karlsson, and J. K. Okamitsu

*Department of Physics, Princeton University, Princeton, New Jersey 08544*

P. Debu, B. Peyaud, R. Turlay, and B. Vallage

*Department de Physique des Particules Elementaires, Centre d'Etudes Nucleaires de Saclay,*
*F-91191 Gif-sur-Yvette CEDEX, France*
(Received 22 September 1988)

Data taken in a Fermilab experiment designed to measure the CP-violation parameter $\epsilon'/\epsilon$ from a study of $K \to 2\pi$ decays were used to look for the as yet unseen decay modes $K_{L,S} \to \pi^0 e^+ e^-$. The detector was optimized for the detection of kaon decays with four electromagnetic showers in the final state. The results (90% confidence) are branching ratios $<4.2\times10^{-8}$ and $<4.5\times10^{-5}$ for $K_L \to \pi^0 e^+ e^-$ and $K_S \to \pi^0 e^+ e^-$, respectively.

PACS numbers: 13.20.Eb

The $\pi^0 e^+ e^-$ decay of the long-lived neutral kaon ($K_L$) is an attractive avenue for the observation of CP violation in a decay amplitude, particularly should detailed studies of the $2\pi$ decays of the neutral kaon ($\epsilon'/\epsilon$) prove inconclusive. The CP-violating amplitude is expected[1] to be comparable to or larger than the CP-conserving one. The leading CP-conserving amplitude proceeds through two-photon exchange while the CP-violating one may proceed via one-photon exchange. Within the framework of the standard model where CP violation comes from the phase $\delta$ in the Kobayashi-Maskawa matrix,[2] $K_L \to \pi^0 e^+ e^-$ may have a sizable $\Delta S = 1$ CP-violating effect. Theoretical estimates[1] of the branching ratio are in the $10^{-11}$ range, while the current experimental limit[3] is $<2.3\times10^{-6}$ at 90% confidence. There has been no $K_S \to \pi^0 e^+ e^-$ measurement, while predictions[1] range from $5\times10^{-9}$ to $5\times10^{-10}$.

Fermilab experiment E-731, which was performed in the Meson Center beam line at the Tevatron, had as its primary goal the determination of the $K \to 2\pi$ CP-violation parameter $\epsilon'/\epsilon$. The present search is based upon the analysis of a special data set in which $K_{L,S} \to \pi^0 \pi^0$ and $K_{L,S} \to \pi^+ \pi^-$ were recorded simultaneously.

Two neutral $K_L$ beams ($\frac{1}{2} \times \frac{1}{2}$ mrad$^2$) were created at 4.8 mrad by 800-GeV protons striking a Be target. A regenerator which moved alternately between the beams every proton spill was used to provide $K_S$. The detector

was employed in an earlier test run and it is shown schematically in Fig. 1; it has been described elsewhere[4,5] in detail. Charged particles were measured and momentum analyzed with a 2000-wire drift-chamber spectrometer which consisted of eight $x$ planes and eight $y$ planes with 0.635-cm maximum drift distance. These planes had a position resolution of about 110 $\mu$m and were 98% efficient. Energies and positions of photons and electrons were measured with an 804-block lead-glass array stacked circularly. Each block measured 5.82 cm ($H$) by 5.82 cm ($W$) by 60 cm ($L$), giving a depth of 20 radiation lengths. There were two holes (11.6 cm×11.6 cm) separated vertically by 11.6 cm at the center of the array for the beams to pass. A common pulsed light source illuminated every block once every second to provide short-term gain tracking. The pulse heights were digitized with effectively 15-bit analog-to-digital converters using a 150-ns gate.

Several improvements have been made to the detector since the previous data taking period. The most important one was the instrumentation of each of the lead-glass phototube outputs with a 60-MHz flash analog-to-digital converter. These were the front-end electronics for a two-dimensional cluster-finding trigger processor, and they also served to suppress out-of-time photons. A cluster was defined as a "neighbor-connected" island of lead-glass blocks each with more than 1 GeV. The trigger processor contributed less than 2% dead time and

FIG. 1. Detector schematic, elevation view.

a FASTBUS-based data-acquisition system was implemented to increase the data taking capability as well.

There were two triggers relevant to the data set used in this search. The first ("four cluster") required exactly four clusters, 30 GeV or more energy deposited in the lead-glass, and no hit in the trigger plane (see Fig. 1). Hence this trigger recorded $\pi^0 e^+ e^-$ candidates in the downstream decay region as well as $\pi^0 \pi^0$ candidates from both upstream and downstream decay regions. The second trigger ("two track") required one or more hits at the trigger plane and



FIG. 2. (a) Distribution of $E/P$ in the lead-glass from the electron calibration data. The resolution is about 4% rms; (b) distribution of the $\pi^0$ mass reconstructed from $K_L \rightarrow \pi^+\pi^-\pi^0$ decays.

two tracks in the spectrometer, and hence was sensitive to $\pi^0 e^+ e^-$ decays from the upstream decay region; however, this trigger was prescaled by a factor of 8.

Because the trigger processor used signals from the lead-glass directly, the relative gains of all lead-glass blocks were monitored and adjusted to within 5% over the entire data taking period. Calibration data with $e^+ e^-$ pairs produced in a thin upstream foil were taken periodically to provide high-statistics calibration for the lead-glass; the resolution was $\sigma/E \simeq 1.5\% + 5\%/\sqrt{E}$ ($E$ in GeV). Chamber-alignment data were also recorded daily.

The momenta of the $e^+$ and $e^-$ and the decay vertex of $K_L \rightarrow \pi^0 e^+ e^-$ candidates were determined by the drift-chamber spectrometer. The $e^+$ and $e^-$ were identified by matching the tracks with the clusters, and requiring $0.85 < E/P < 1.15$, where $E$ is the cluster energy and $P$ is the momentum. Figure 2(a) shows the $E/P$ distribution for electrons from the calibration data (which is essentially identical to the same distribution of electrons from $K_{e3}$ decays taken during the main data run). From a study of $K_L \rightarrow \pi^+ \pi^- \pi^0$ decays, the $\pi^0$

mass resolution was determined to be about 4 MeV/$c^2$ [see Fig. 2(b)]. The $\gamma\gamma$ mass was required to be within 10 MeV/$c^2$ of the nominal $\pi^0$ value. By then constraining the $\gamma\gamma$ mass to the nominal value, the reconstructed kaon mass ($M_{\pi ee}$) would have a resolution of about 4.5 MeV/$c^2$. The square of the transverse momentum ($P_t^2$) of the $\pi^0 e^+ e^-$ system with respect to the line connecting the decay vertex and the production target had a resolution of about 50 MeV$^2$/$c^2$. The candidates are displayed in a two-dimensional $M_{\pi ee}$ vs $P_t^2$ plot as shown in Fig. 3(b). A candidate is defined to have $P_t^2 < 200$ MeV$^2$/$c^2$ and $489 < m_K < 507$ MeV/$c^2$; these cuts would include about 95% of the signal. No candidate is found in the signal region. Figure 3(a) shows the equivalent region for $K_L \rightarrow \pi^+ \pi^- \pi^0$ decays. Given the timing and energy resolution of the detector, the background of $K \rightarrow 2\pi^0$ with Dalitz decays is insignificant; the very few remaining events are consistent with radiative $K_{e3}$ with an accidental photon.

Figure 4 shows the relative acceptance for Monte Carlo–generated $K_L \rightarrow \pi^0 e^+ e^-$ decays as a function of the $e^+ e^-$ effective mass. Because of the loose cuts, the



FIG. 3. Reconstructed kaon mass vs the square of the transverse momentum for (a) $K_L \rightarrow \pi^+ \pi^- \pi^0$ and (b) $K_L \rightarrow \pi^0 e^+ e^-$. There are 24 events above the top of the plot in (b). The events in the plots were selected with a $\pi^0$ mass cut of 2.5$\sigma$ and the boxes represent the signal region. There are no background events for the $K_S$ decay.

FIG. 4. The relative acceptance vs the $e^+e^-$ invariant mass of the $K_L \rightarrow \pi^0 e^+ e^-$ decay for the four-cluster trigger.

effect of internal radiation is expected to be small; external radiation is properly treated. For the four-cluster trigger, the acceptance is 9.5% for a fiducial downstream decay volume of 22.2 m and for the two-track trigger, the acceptance is about 10% for an upstream decay volume of 14 m for kaon energy between 30 and 150 GeV, assuming a uniform three-body phase space distribution.

The upper limit $B(K_L \rightarrow \pi^0 e^+ e^-) < 4.7 \times 10^{-8}$ (90% confidence) is obtained by normalizing to a sample of $58.8 \times 10^3$ $K_L \rightarrow 2\pi^0$ decays observed simultaneously in the four-cluster trigger. The normalization data do not require track reconstruction; however, the relative branching ratios of $\pi^+\pi^-$ to $\pi^0\pi^0$ from both $K_L$ and $K_S$ were also determined from the same data set and they agree with the published values to within 5%. With the use of $71.3 \times 10^3$ $K_L \rightarrow \pi^+\pi^-$ and $2.24 \times 10^5$ $K_S$

$\rightarrow \pi^+\pi^-$ decays from the two-track trigger as normalization, the 90%-confidence limits from that trigger are $< 4.1 \times 10^{-7}$ and $< 4.5 \times 10^{-5}$, respectively.

By the combination of the above, the results are $B(K_L \rightarrow \pi^0 e^+ e^-) < 4.2 \times 10^{-8}$ and $B(K_S \rightarrow \pi^0 e^+ e^-) < 4.5 \times 10^{-5}$ (90% confidence). This is the first limit of any significance for the $K_S$ decay. The $K_L$ limit is an improvement of more than a factor of 50 over the previous limit[3]; while still far from the level predicted by the standard model, it serves to constrain the parameters of light scalar particles coupling to $e^+e^-$. The result is consistent with $B(K_L \rightarrow \pi^0 e^+ e^-) < 3.2 \times 10^{-7}$, recently obtained by Jastrzembski et al.[6]

(a)Present address: SLAC, Stanford, CA 94305.

(b)Present address: Department of Nuclear Physics, Oxford University, Oxford, United Kingdom.

[1] J. F. Donoghue, B. R. Holstein, and G. Valencia, Phys. Rev. D 35, 2769 (1987), and references within; L. M. Sehgal, Phys. Rev. D 38, 808 (1988); G. Ecker, A. Pich, and E. deRafael, Nucl. Phys. B303, 665 (1988).

[2] M. Kobayashi and T. Maskawa, Prog. Theor. Phys. 49, 652 (1973).

[3] A. S. Carroll et al., Phys. Rev. Lett. 46, 525 (1980).

[4] M. Woods et al., Phys. Rev. Lett. 60, 1695 (1988).

[5] For a complete description of the detector see P. Jarry, Ph.D. thesis, Université de Paris-Sud, 1987 (unpublished); M. Woods, Ph.D. thesis, University of Chicago, 1988 (unpublished).

[6] E. Jastrzembski et al., Phys. Rev. Lett. 61, 2300 (1988).

# Search for $K_L \to \pi^0 \gamma \gamma$

V. Papadimitriou, L. K. Gibbons, J. R. Patterson, Y. W. Wah, B. Winstein, R. Winston, M. Woods,[a] and
H. Yamamoto

*The Enrico Fermi Institute and the Department of Physics, The University of Chicago,
Chicago, Illinois 60637*

E. C. Swallow

*Department of Physics, Elmhurst College, Elmhurst, Illinois 60126
and The Enrico Fermi Institute, The University of Chicago, Chicago, Illinois 60637*

G. J. Bock, R. Coleman, Y. B. Hsiung, K. Stanfield, R. Stefanski, and T. Yamanaka

*Fermi National Accelerator Laboratory, Batavia, Illinois 60510*

G. D. Gollin, M. Karlsson, and J. K. Okamitsu

*Department of Physics, Princeton University, Princeton, New Jersey 08544*

P. Debu, B. Peyaud, R. Turlay, and B. Vallage

*Department de Physique des Particules Elementaires, Centre d'Etudes Nucleaires de Saclay,
F-91191 Gif-sur-Yvette CEDEX, France*
(Received 20 April 1989)

A search for the rare decay mode $K_L \to \pi^0 \gamma \gamma$ was performed using a data set from Fermilab experiment E-731. The decay is of interest in the context of chiral perturbation theory and for its contribution to the decay $K_L \to \pi^0 e^+ e^-$. The result is $B(K_L \to \pi^0 \gamma \gamma) < 2.7 \times 10^{-6}$ (90% confidence level) which is nearly a two-order-of-magnitude improvement over the previous best limit.

The as yet unobserved decay $K_L \to \pi^0 \gamma \gamma$ is of current interest for at least three reasons. First, it provides an opportunity to test the standard model in the context of chiral symmetry: At the one-loop level in chiral perturbation theory,[1] the decay has a branching ratio of $6.8 \times 10^{-7}$ with a characteristic $\gamma\gamma$ invariant-mass ($m_{\gamma\gamma}$) distribution having a peak at about 325 MeV.[2] Second, this decay provides a CP-conserving intermediate state for the $K_L \to \pi^0 e^+ e^-$ decay which has been the subject of recent experimental[3-5] and theoretical[6] attention as a possible avenue for the observation of direct CP nonconservation; its magnitude will greatly affect the interpretation of the results of such experimental efforts. Third, this mode could be a background to the $K_L \to 2\pi^0$ decay for precision experiments[7,8] measuring $\epsilon'/\epsilon$, especially if its branching ratio were at the level of the current limit,[9,10] $2.4 \times 10^{-4}$.

The principal background for this mode is the $K_L \to 3\pi^0$ decay occurring $3 \times 10^5$ times more frequently than the signal. The challenge in observing such a signal at the predicted level is the effective rejection of the $3\pi^0$ decays; in addition, the understanding of the residual background after the necessarily stringent analysis cuts allows better sensitivity.[11]

This experiment, E-731 at Fermilab, collected data with the primary goal of determining $\epsilon'/\epsilon$. The search reported here is based upon an analysis of a subset of the data that was particularly suited for this analysis. Some

characteristics of the detector have been described previously;[3,7] here, we summarize the essential features relevant to the decay mode in question. Energies and positions of photons were measured with an 804-block lead-glass array having transverse block dimensions of $5.82 \times 5.82$ cm$^2$. The energy resolution for photons was given approximately by $\sigma_E/E = (2.5 + 5.0/\sqrt{E})\%$ ($E$ in GeV) and the corresponding $\pi^0$ mass resolution was about 3 MeV. Events with the desired number of electromagnetic showers were selected on line by a trigger processor[12] which counted clusters in the lead-glass array. Eleven planes of photon-veto counters situated between 75 m upstream and 2 m downstream of the lead glass were employed to reject the background arising from $K_L \to 3\pi^0$ decays where one or two photons miss the lead-glass calorimeter. A drift-chamber system was used to reject $K_L$ decays with charged particles in the final state.

Candidates for the $K_L \to \pi^0 \gamma \gamma$ decay were required to have exactly four clusters in the lead-glass array and total energy between 40 and 150 GeV. The decay vertex was determined with the measured cluster energies and positions by assuming that the invariant mass of the four photons was that of the neutral kaon. To determine the pairing of the photons, the pair with invariant mass closest to that of the neutral pion ($m_{\pi^0}$) was chosen as the candidate $\pi^0$; this pair is labeled (12) and it was required that $|m_{12} - m_{\pi^0}| < 5$ MeV. Up to this point the

cuts were also satisfied by $2\pi^0$ decays which would usually have both pair masses, $m_{12}$ and $m_{34}$, consistent with $m_{\pi^0}$. The rejection of the $2\pi^0$ decays was done in two steps. First, it was required that $|m_{34}-m_{\pi^0}| > 12$ MeV; this resulted in a suppression of a factor of about 25. Second, some $2\pi^0$ events with their photons paired as (13)(24) or (14)(23) would still remain; if either of these alternative pairings was consistent with the $2\pi^0$ hypothesis,[7] the event was also discarded. This latter requirement provided an additional rejection factor of about 40.

$K_L \rightarrow 3\pi^0$ decays can become background four-cluster



events either when photons are undetected or when they overlap in the lead glass so that they are unresolvable as separate clusters. The veto counters were effective in detecting photons escaping from the fiducial volume of the detector and events with substantial energy deposit in these counters were rejected from the sample. In addition, the transverse center of energy of the four photons was required to be in the $K_L$ beam region ($11.2\times11.2$ cm$^2$).[13] The number of events with unresolved overlapping clusters was substantially reduced by rejecting those with cluster shapes inconsistent with that of a single photon. The $3\pi^0$ background was further reduced by considering only decays in the upstream 14-m region of the decay volume ending 57 m upstream of the glass array. The reconstructed decay vertex in events with missing photons is artificially shifted downstream; also, photons are more likely to overlap when the decay occurs near the lead-glass array. The selection of this region of the decay region was made on the basis of a Monte Carlo study to optimize the experimental sensitivity in the presence of this background. These criteria provide a rejection factor for $3\pi^0$ decays relative to $\pi^0\gamma\gamma$ decays of about $10^4$.

Figure 1(a) shows the $\gamma\gamma$ effective mass for the "non $\pi^0$" photon pair. A characteristic feature in this distribution is a prominent "double fusion" peak appearing at about $m_{\gamma\gamma}=270$ MeV which arises when two $\pi^0$s in $K_L \rightarrow 3\pi^0$ decays are superimposed: Each photon from one $\pi^0$ overlaps with a photon from the other $\pi^0$ with an invariant-mass threshold of twice the $\pi^0$ mass. The solid curve indicates the $K_L \rightarrow \pi^0\gamma\gamma$ signal shape predicted by chiral perturbation theory;[1] $(60.0\pm1.2)\%$ of the $\pi^0\gamma\gamma$ events have $m_{\gamma\gamma}$ greater than 300 MeV and we have chosen this region for our search to have good discrim-



FIG. 1. (a) $\gamma\gamma$ invariant mass for $K_L \rightarrow \pi^0\gamma\gamma$ decay events. The histograms are the candidate events and the solid curve represents the distribution predicted by chiral perturbation theory for a branching ratio of $10^{-5}$. The arrow indicates the position of the cut (300 MeV). (b) $\gamma\gamma$ invariant mass for data and background Monte Carlo simulation. The dots correspond to the data [the same as in (a) with coarser binning]; the shaded histogram corresponds to the $K_L \rightarrow 2\pi^0$ contribution to the background; the unshaded histogram corresponds to the sum of the backgrounds from $K_L \rightarrow 2\pi^0$ and from $K_L \rightarrow 3\pi^0$ decays. The background Monte Carlo simulation (twice the statistics as the data) is absolutely normalized.

FIG. 2. Acceptance vs the $\gamma\gamma$ invariant mass for $K_L \rightarrow \pi^0\gamma\gamma$ decays. The dip around 135 MeV is due to the cut that excludes $\gamma\gamma$ masses near the $\pi^0$ mass.

FIG. 3. The decay-vertex distribution, in meters from the $K_L$ production target, for $K_L \rightarrow \pi^0 \gamma\gamma$ candidates and background Monte Carlo events with $m_{\gamma\gamma} > 300$ MeV. The dots correspond to the data, while the histogram corresponds to the sum of the backgrounds from $K_L \rightarrow 2\pi^0$ and from $K_L \rightarrow 3\pi^0$ decays. The background Monte Carlo simulation is absolutely normalized. The arrow indicates the position of the cut (124 m).

ination against background. The acceptance is relatively flat for $m_{\gamma\gamma}$ above 160 MeV, as shown in Fig. 2. Figure 1(b) shows the Monte Carlo predictions of the backgrounds to $\pi^0 \gamma\gamma$ decay coming from the $3\pi^0$ and $2\pi^0$ modes. The Monte Carlo distributions are normalized by means of a sample of fully reconstructed $K_L \rightarrow 2\pi^0$ decays observed simultaneously. The contribution from accidental clusters is found to be negligible. Figure 3 shows agreement in the reconstructed vertex distributions for the signal and expected background events with $m_{\gamma\gamma} > 300$ MeV, including the region downstream of the fiducial cut.

For the high-mass sample ($m_{\gamma\gamma} > 300$ MeV), we have 24 candidate events with a predicted background of 20.8 events (18.2 from $3\pi^0$'s and 2.6 from $2\pi^0$'s). From studies of the $3\pi^0$ background in this mode and in the $K_L \rightarrow 2\pi^0$ mode, we assign a 20% error to the estimate of the background in the high-mass region which is a combination of the statistical error in the Monte Carlo simulation (15%) and our estimate of the systematic error (12%). The systematic uncertainty comes largely from lack of precise knowledge of the efficiencies of the photon-veto planes. The 90%-confidence-allowed signal is 13.9 events, calculated with the maximum-likelihood method. The $\pi^0 \gamma\gamma$ acceptance is 2.4% and the normalization is provided by $11.1 \times 10^3$ $K_L \rightarrow 2\pi^0$ decays observed simultaneously and selected with similar criteria as the $\pi^0 \gamma\gamma$ candidates where appropriate, including photon-veto, cluster-shape, decay-region, and total-energy cuts. The corresponding acceptance for $K_L \rightarrow 2\pi^0$ is 5.8%. Using world average values [10] for the $K_L \rightarrow 2\pi^0$ and for $K_L \rightarrow 3\pi^0$ branching ratios we con-

clude that $B(K_L \rightarrow \pi^0 \gamma\gamma) < 2.7 \times 10^{-6}$ (90% confidence level). We have assumed that the $m_{\gamma\gamma}$ spectrum follows that predicted in chiral perturbation theory; if instead a uniform phase space for the decay is assumed, the limit becomes $4.4 \times 10^{-6}$ (90% confidence level) where the whole mass range except the region of the double fusion peak (264–292 MeV) is used.

Our result is nearly a factor of 90 improvement over the current experimental limit [9,10] which was also calculated using a distribution in $m_{\gamma\gamma}$ similarly peaked at high values. It is consistent with the predictions of chiral perturbation theory although another factor of about 4 in sensitivity would be required to confirm the prediction. The $CP$-conserving contribution to $K_L \rightarrow \pi^0 e^+ e^-$ has now been better constrained and we have shown that this decay should not be a serious background to the $K_L \rightarrow 2\pi^0$ mode.

---

(a)Present address: SLAC, Stanford, CA 94305.

[1]G. Ecker, A. Pich, and E. De Rafael, Phys. Lett. B 189, 363 (1987).

[2]Alternative theoretical approaches to this decay, predicting similar branching ratios, have also been considered: One of them assumed a $\pi^+ \pi^- \pi^0$ intermediate state where the charged pions annihilate to two photons: P. Ko and J. Rosner, Enrico Fermi Institute Report No. EFI 89-13, 1989 (to be published); L. M. Sehgal, Phys. Rev. D 6, 367 (1972). Another applied the vector-dominance model: T. Morozumi and H. Iwasaki, KEK Report No. KEK-TH-206, 1988 (unpublished).

[3]L. K. Gibbons et al., Phys. Rev. Lett. 61, 2661 (1988).

[4]G. D. Barr et al., Phys. Lett. B 214, 303 (1988).

[5]E. Jastrzembski et al., Phys. Rev. Lett. 61, 2300 (1988).

[6]See, for example, C. O. Dib, I. Dunietz, and F. Gilman, Phys. Rev. D 39, 2639 (1989), and references therein.

[7]M. Woods et al., Phys. Rev. Lett. 60, 1695 (1988).

[8]H. Burkhardt et al., Phys. Lett. B 206, 169 (1988).

[9]M. Banner, J. W. Cronin, J. K. Liu, and J. E. Pilcher, Phys. Rev. 188, 2033 (1969).

[10]Particle Data Group, G. P. Yost et al., Phys. Lett. B 204, 1 (1988).

[11]We point out that quantitative understanding of the background in the $\pi^0 \gamma\gamma$ mode will also give increased confidence in the background estimate in the better constrained $\pi^0 \pi^0$ mode.

[12]H. Sanders, V. Papadimitriou, J. Ting, Y. W. Wah, and E. Weatherhead, IEEE Trans. Nucl. Sci. 36, 358 (1988).

[13]The regenerated $K_S$ beam is not used in this analysis.

# Determination of Re($\epsilon'/\epsilon$) by the Simultaneous Detection of the Four $K_{L,S} \to \pi\pi$ Decay Modes

J. R. Patterson, A. Barker, R. A. Briere, L. K. Gibbons, G. Makoff, V. Papadimitriou, S. Somalwar,
Y. W. Wah, B. Winstein, R. Winston, M. Woods,[a] and H. Yamamoto

*The Enrico Fermi Institute and the Department of Physics, The University of Chicago, Chicago, Illinois 60637*

E. Swallow

*Department of Physics, Elmhurst College, Elmhurst, Illinois 60126*
*and the Department of Physics, The University of Chicago, Chicago, Illinois 60637*

G. J. Bock, R. Coleman, J. Enagonio, Y. B. Hsiung, K. Stanfield, R. Stefanski, and T. Yamanaka

*Fermi National Accelerator Laboratory, Batavia, Illinois 60510*

G. Blair,[b] G. D. Gollin,[c] M. Karlsson, J. K. Okamitsu,[d] and R. Tschirhart

*Department of Physics, Princeton University, Princeton, New Jersey 08544*

J. C. Brisson, P. Debu, B. Peyaud, R. Turlay, and B. Vallage

*Département de Physique des Particules Élémentaires, Centre d'Etudes Nucléaires de Saclay,*
*F-91191 Gif-sur-Yvette CEDEX, France*
(Received 18 December 1989)

The E731 experiment at Fermilab has searched for direct $CP$ violation in $K^0 \to \pi\pi$, which is parametrized by $\epsilon'/\epsilon$. For the first time all four of the $K_{L,S} \to \pi\pi$ modes were collected simultaneously, which greatly facilitated studies of systematic uncertainty. We find Re($\epsilon'/\epsilon$) $= -0.0004$ $\pm 0.0014$(stat)$\pm 0.0006$(syst). The result provides no evidence for direct $CP$ violation.

This paper presents a new determination of the $CP$-violation parameter Re($\epsilon'/\epsilon$). Since a result[1] from the first run of this experiment was reported, the detector has been improved and substantially more data have been collected.

The six-quark model[2] of Cabibbo, Kobayashi, and Maskawa (CKM) provides the most natural way of incorporating $CP$ violation into the weak interaction. Until very recently, the only observed $CP$-nonconserving effects were consistent with asymmetric $K^0$-$\bar{K}^0$ mixing, parametrized by $\epsilon$. This is a second-order effect in the CKM framework, but could also signal a new $\Delta S = 2$ interaction (e.g., superweak[3]). Within the CKM framework, first-order ("direct") $CP$ nonconservation in $K^0 \to \pi\pi$ decays, parametrized by $\epsilon'/\epsilon$, is also expected, and searches for it in the predicted range provide an important test of the model. Recently, the NA31 group at CERN reported[4] evidence for such an effect.

As is well known, Re($\epsilon'/\epsilon$) can be determined from the double ratio $R$ of the $\pi\pi$ decay rates of the $K_L$ and $K_S$ mesons:

$$R \equiv \frac{\Gamma(K_S \to \pi^+\pi^-)/\Gamma(K_L \to \pi^+\pi^-)}{\Gamma(K_S \to \pi^0\pi^0)/\Gamma(K_L \to \pi^0\pi^0)} \approx 1 - 6\,\mathrm{Re}(\epsilon'/\epsilon).$$

It is important to minimize systematic uncertainty in the collection and analysis of the four decay modes. In our experiment, the $K_S$ are provided by coherent regeneration, ensuring an angular divergence identical to that of the $K_L$, and very similar momentum spectra for $\pi\pi$

events. Decays of $K_S$ and $K_L$ to a given final state (charged or neutral) are collected at the same time by means of side-by-side $K_L$ and $K_S$ beams, so electronic drifts, accelerator instabilities, and phototube gain shifts affect them virtually identically. Furthermore, the regenerator alternates between the beams, rendering the effect of asymmetries in the beams or the detector response negligible. The analysis[5] reported here is based on about 20% of the data collected during a fixed-target run at Fermi National Accelerator Laboratory. These are distinguished in that, for the first time, decays from all four modes were collected simultaneously.

As a function of proper time $t$ from the regenerator, the $\pi\pi$ decay rates in the vacuum and regenerated beams are proportional to $|\eta|^2$ and $|\rho\exp(-t/2\tau_S + i\Delta m t) + \eta|^2$, respectively; $\rho$ is the coherent regeneration amplitude, $\tau_S$ is the $K_S$ lifetime, $\Delta m$ is the $K_L$-$K_S$ mass difference, and $\eta$ is the appropriate ratio of $K_L$-to-$K_S$ decay amplitudes. Because $|\rho| \gg |\eta|$, the ratio of the total number of regenerated to vacuum charged (neutral) decays $R_{+-(00)}$ is proportional to $|\rho/\eta_{+-(00)}|^2$. Thus, $R \approx R_{+-}/R_{00}$.

Kaons were produced by 800-GeV protons incident at 5 mrad on a beryllium target. The regenerator, instrumented to detect inelastic regeneration, was located 123 m downstream of the target.

An 804-block lead-glass calorimeter 181 m from the target determined the energies and positions of photons and electrons. Its energy resolution was roughly 1.5%

13



FIG. 1. Invariant-mass distribution for $K_L \to \pi^0\pi^0$ events. The histogram is data; the solid circles are from a Monte Carlo simulation for the residual $K_L \to \pi^0\pi^0\pi^0$ background, absolutely normalized. A very small nonkaon contribution, seen here at high mass, is also subtracted. The arrows indicate the positions of the cuts.

FIG. 2. Event density in equal-area concentric rings around the $K_L$ beam for $\pi^0\pi^0$ events. The histogram is data; the solid circles show the expected size and shape of incoherent events from the regenerator as determined from $\pi^+\pi^-$. The arrow indicates the position of the cut.

$(2.5\%)+5\%/\sqrt{E}$ ($E$ in GeV) for electrons (photons). The neutral trigger required greater than 28 GeV in the calorimeter and either four or six isolated electromagnetic clusters,[6] accepting $\pi^0\pi^0\pi^0$ as well as $\pi^0\pi^0$ decays. Eleven planes of photon veto counters were employed to reduce background from $\pi^0\pi^0\pi^0$ decays with photons missing the lead glass.

The decay vertex for $K_{L,S} \to \pi^0\pi^0$ decays was found by pairing the photons using the known $\pi^0$ mass as a constraint. The $\pi^0\pi^0$ invariant mass is shown in Fig. 1 for $K_L$ decays, differentiated from $K_S$ decays by means of the center of energy of the four photons in the calorimeter. The residual background from $K_L \to \pi^0\pi^0\pi^0$ decays was $(0.37\pm0.07)\%$, and was well reproduced by a Monte Carlo simulation.

Charged tracks were reconstructed (typically with 1% momentum resolution) using a 16-plane drift-chamber spectrometer with 100-$\mu$m resolution per plane. A (prescaled) two-track trigger was formed using hodoscopes at 137.8 and 179.5 m; $K_{\mu3}$ decays were rejected using a muon filter. Thus, $\pi e\nu$ and $\pi^+\pi^-\pi^0$ as well as $\pi^+\pi^-$ decays were accepted.

For $K_{L,S} \to \pi^+\pi^-$ decays the invariant-mass resolution was about 3.5 MeV/$c^2$; the cut was $\pm14$ MeV/$c^2$ around the nominal kaon mass. Background from $\pi e\nu$ decays was reduced with cuts on $E/p$ and the kaon transverse momentum ($P_t^2<250$ MeV$^2/c^2$). The residual $K_L$ background was $(0.32\pm0.06)\%$.

To extract the coherently regenerated $K_S$ signals, the diffractive and inelastic contributions must be subtracted. After the $P_t^2$ cut, we found a $(0.13\pm0.01)\%$ contribution to $K_S \to \pi^+\pi^-$ from such incoherent events; this

is 2.3 times smaller than in Ref. 1, largely because of the removal of 1.5 in. of lead from the regenerator. For neutral decays, only the center of energy at the calorimeter was available to identify incoherently regenerated $K_S$, which scattered into both the $K_L$ and $K_S$ beams. Their contributions were accurately predicted from the $P_t^2$ distribution for simultaneously observed $\pi^+\pi^-$ decays (Fig. 2), and were $[4.70\pm0.14(\text{syst})]\%$ and $[2.56\pm0.07(\text{syst})]\%$ for the $K_L$ and $K_S$ samples, respectively.

Acceptance corrections, necessary because of the difference in $K_S$ and $K_L$ vertex distributions, were made using a detailed Monte Carlo simulation of the beam and detector. The nonlinear and non-Gaussian response of the lead glass to photons, important for neutral decays, was reproduced with no free parameters, using results from EGS[7] simulations of electromagnetic showers together with the effective attenuation length of Cherenkov light in each block. The restriction that the *same* detector and beam parameters be used in the simulation of all four modes, applicable since all were collected simultaneously, provided a powerful check of the Monte Carlo simulation as a whole.

The $K_L \to \pi^+\pi^-$ decay-vertex distribution is well reproduced by a Monte Carlo simulation, as shown in Fig. 3. The agreement is equally good for the other decays.

The final sample included kaons with energy between 40 and 150 GeV decaying in the region from 120 to 137 m from the target. The raw numbers of events passing all cuts and the background and acceptance corrections are given in Table I with the value of $R_{+-}/R_{00}$ at each stage. The acceptance was similar for $K_S$ and $K_L$: It

1492

FIG. 3. (a) Decay-vertex distribution for $K_L \to \pi^+\pi^-$ events. The histogram is data and the solid circles are from a Monte Carlo simulation. (b) Ratio of data to a Monte Carlo simulation. The dashed line corresponds to an acceptance error that would shift the $K_S$-to-$K_L$ ratio by 2%, the size of the NA31 effect. The arrows indicate the positions of the cuts.

varied slowly with decay vertex, the mean of which differed for $K_S$ and $K_L$ decays by less than 1.5 m. The total change in the double ratio from raw data to final acceptance-corrected samples is 7%; the final double ratio indicates a small value of $\text{Re}(\epsilon'/\epsilon)$.

To extract $\text{Re}(\epsilon'/\epsilon)$, we fit $R_+-$ and $R_{00}$ for $|\rho/\eta|$ in the two modes in 10-GeV/$c$ bins of kaon momentum. The momentum dependence, common to the neutral and charged modes, is expected to obey a power law,[8] while a magnitude difference is proportional to $\text{Re}(\epsilon'/\epsilon)$. The best-fit power for the charged (neutral) mode was $-0.602 \pm 0.010$ ($-0.605 \pm 0.010$) with $\chi^2 = 11.5$ (10.7)

TABLE I. Event totals and corrections.

| | Neutral | Charged | $R_+-/R_{00}$ |
|---|---|---|---|
| **Raw events** | | | |
| $K_L$ | 52 226 | 43 357 | |
| $K_S$ | 201 332 | 178 803 | 1.0698 |
| | | | |
| **Background fractions** | | | |
| $K_L$ | 0.0507 | 0.0032 | |
| $K_S$ | 0.0256 | 0.0013 | 1.0442 |
| | | | |
| **Acceptance** | | | |
| $K_L$ | 0.1884 | 0.5041 | |
| $K_S$ | 0.1813 | 0.5064 | 1.0003 |

for nine degrees of freedom; the two are consistent with each other and with previous determinations.[9] The combined fit yielded $\text{Re}(\epsilon'/\epsilon) = -0.0004 \pm 0.0014$ (stat).

Systematic errors were associated with background subtractions, detector and beam variations with time, accidental activity in the detector, energy calibration and resolution, and acceptance.

Uncertainty in the backgrounds is dominated by those in the incoherent contributions to neutral decays, which are expected to partially cancel in $R_{00}$. As a conservative estimate of the total uncertainty on the double ratio all background errors are added in quadrature, yielding a total of 0.18%.

All decays to a common final state were analyzed together; this and the use of loose cuts (the reconstruction efficiency was more than 90% for all $\pi\pi$ decays satisfying the geometrical requirements) reduced sensitivity to time variations: $R_+-$ and $R_{00}$ were stable throughout even though the intensity, targeting, and detector efficiencies varied.

Accidental activity, concentrated near the vacuum beam, could have changed the relative $K_L$ and $K_S$ efficiencies. Accidental events, collected with the $\pi\pi$ data at a rate proportional to the instantaneous beam intensity, contained a photon cluster 2.7% of the time and an average of 8.5 chamber hits. When overlaid on $\pi\pi$ Monte Carlo events they correctly reproduced the small intensity dependence of our selection criteria; however, no bias between $K_L$ and $K_S$ was seen within the statistical error of the simulation (0.07%) for either mode.

The energy scale for the charged mode was determined sufficiently accurately using the known $K^0$ and $\Lambda$ masses. For the neutral mode, after electron calibration of the individual lead-glass blocks, the overall scale was adjusted ($\approx 0.5\%$) using the sharp edge in the $K_S$ decay vertex at the regenerator, leaving a residual uncertainty of 0.1%. By choice of the fiducial region,[10] this resulted in only 0.03% uncertainty in $R_{00}$. Uncertainty in the energy resolution, however, led to an 0.2% uncertainty in $R_{00}$.

Acceptances were extensively studied using $10^7$ $\pi e\nu$ and $6\times10^6$ $\pi^0\pi^0\pi^0$ decays taken with the $\pi\pi$ events; the agreement in vertex and other distributions with Monte Carlo simulation over the chosen fiducial region was excellent. Also, when $\text{Re}(\epsilon'/\epsilon)$ was extracted using small vertex bins, almost eliminating the need for acceptance corrections, a consistent result was obtained (with increased systematic error from resolution uncertainty).

In the same analysis, we fit[11] for $\tau_S$ and $\Delta m$. Separate neutral and charged fits were consistent and the combined results were $\tau_S = [0.8902 \pm 0.0021 \text{(stat)}] \times 10^{-10}$ sec and $\Delta m = [0.534 \pm 0.009 \text{(stat)}] \times 10^{10} \hbar$ sec$^{-1}$, in agreement with the accepted values.[12] These studies, together with the stability of $R_+-$ and $R_{00}$ when selection criteria, beam profiles, and detector apertures and efficiencies were varied in the Monte Carlo simulation,

led to the assignment of 0.25% systematic uncertainty due to acceptance.

Combining these uncertainties in quadrature, the total systematic error on the double ratio is then 0.38%. The final result is

$$\mathrm{Re}(\epsilon'/\epsilon) = -0.0004 \pm 0.0014(\mathrm{stat}) \pm 0.0006(\mathrm{syst}) \, .$$

The accurate determinations of $\tau_S$, $\Delta m$, and the regeneration momentum dependence for both modes attest to the soundness of the technique.

The result is consistent with the superweak model;[3] it does not confirm recent evidence[4] for direct $CP$ violation. The CKM standard model may also account for such a small value of $\mathrm{Re}(\epsilon'/\epsilon)$ with a heavy top quark[13] or with the incorporation of electroweak corrections which could be important.[14]

We thank H. Sanders and J. Ting at The University of Chicago, the ACP group and E. Beck at FNAL, and G. L. Grazer and P. Jarry for their contributions. This work was supported in part by DOE, NSF, and the French Atomic Energy Commission. Two of us (G.D.G. and Y.W.W.) are recipients of DOE Outstanding Junior Investigator grants. One of us (J.R.P.) submitted this work in partial fulfillment of the requirements for the Ph.D. degree at The University of Chicago.

---

[a]Current address: Stanford Linear Accelerator Center, P.O. Box 4349, Stanford, CA 94309.

[b]Current address: Department of Nuclear Physics, University of Oxford, Oxford OX1 3RH, United Kingdom.

[c]Current address: Department of Physics, University of Illinois, Urbana, IL 61801.

[d]Current address: Princeton Combustion Research Laboratories, Monmouth Junction, NJ 08852.

[1]M. Woods et al., Phys. Rev. Lett. 60, 1695 (1988).

[2]M. Kobayashi and T. Maskawa, Prog. Theor. Phys. 49, 652 (1973).

[3]L. Wolfenstein, Phys. Rev. Lett. 13, 569 (1964).

[4]H. Burkhardt et al., Phys. Lett. B 206, 169 (1988), find $\mathrm{Re}(\epsilon'/\epsilon) = 0.0033 \pm 0.0007(\mathrm{stat}) \pm 0.0008(\mathrm{syst})$.

[5]For a detailed description of the analysis, see J. R. Patterson, Ph.D. thesis, University of Chicago, 1990.

[6]H. Sanders, V. Papadimitriou, J. Ting, Y. W. Wah, and E. Weatherhead, IEEE Trans. Nucl. Sci. 36, 358 (1988).

[7]W. R. Nelson, H. Hirayama, and D. W. O. Rogers, SLAC Report No. SLAC-265, 1985 (unpublished).

[8]See, for example, J. Roehrig et al., Phys. Rev. Lett. 38, 1116 (1977).

[9]A. Gsponer et al., Phys. Rev. Lett. 42, 13 (1979); also, R. H. Bernstein et al., Phys. Rev. Lett. 54, 1631 (1985); Woods et al., Ref. 1.

[10]When the $\gamma$ energies are decreased, approximately the same number of $K_L$ leave at the downstream boundary as enter at the upstream boundary; essentially all $K_S$ are included.

[11]The $CPT$-violating phase difference ($\Delta\Phi$) between $\eta_{+-}$ and $\eta_{00}$ was also fit and found consistent with zero [M. Karlsson et al. (unpublished)]. Here we assume $\Delta\Phi = 0$.

[12]Particle Data Group, G. P. Yost et al., Phys. Lett. B 204, 1 (1988).

[13]A. Buras and J. M. Gerard, Phys. Lett. B 203, 272 (1988); C. S. Kim, J. L. Rosner, and C. P. Yuan, University of Durham Report No. DTP-89-52 (to be published).

[14]J. M. Flynn and L. Randall, Phys. Lett. B 224, 221 (1989); G. Buchalla, A. J. Buras, and M. K. Harlander, Technische Universitat Munchen Report No. TUM-T31-3/89, 1989 (to be published).

# New limit on $K_L \to \pi^0 e^+ e^-$

A. Barker, R. A. Briere, L. K. Gibbons, G. Makoff, V. Papadimitriou, J. R. Patterson, S. Somalwar, Y. W. Wah, B. Winstein, R. Winston, M. Woods,* and H. Yamamoto

*The Enrico Fermi Institute and the Department of Physics, The University of Chicago, Chicago, Illinois 60637*

E. C. Swallow

*Department of Physics, Elmhurst College, Elmhurst, Illinois 60126*
*and The Enrico Fermi Institute, The University of Chicago, Chicago, Illinois 60637*

G. J. Bock, R. Coleman, J. Enagonio, Y. B. Hsiung, R. Tschirhart, K. Stanfield, R. Stefanski, and T. Yamanaka

*Fermi National Accelerator Laboratory, Batavia, Illinois 60510*

G. D. Gollin,† M. Karlsson, and J. K. Okamitsu‡

*Department of Physics, Princeton University, Princeton, New Jersey 08544*

P. Debu, B. Peyaud, R. Turlay, and B. Vallage

*Department de Physiques des Particules Elementaires, Centre d'Etudes Nucleaires de Saclay,*
*F-91191 Gif-sur-Yvette CEDEX, France*
(Received 12 March 1990)

Based upon the analysis of the complete data set of Fermilab experiment E-731, we report a new limit on the branching ratio of $K_L \to \pi^0 e^+ e^-$ which is $< 7.5 \times 10^{-9}$ (90% confidence).

The decay $K_L \to \pi^0 e^+ e^-$ has raised considerable interest theoretically[1] and experimentally[2-4] for its ability to elucidate direct $CP$ violation. Within the standard model, this decay mode is likely to have a ratio of direct $CP$ violation to that from mixing ($\epsilon'/\epsilon$) of order one, unlike the one measured[5] through the $K \to 2\pi$ decay modes. Earlier, we reported[2] a limit $B(K_L \to \pi^0 e^+ e^-) < 4.2 \times 10^{-8}$ based on a special data set collected in Fermilab experiment E-731, which had its primary goal to determine $\epsilon'/\epsilon$ from $K \to 2\pi$ modes. Here we update the limit using the entire data sample.

The apparatus and event reconstruction are described elsewhere.[2,6] The momenta of the $e^+$ and $e^-$ and the decay vertex of $K_L \to \pi^0 e^+ e^-$ candidates were determined by the drift-chamber spectrometer. The energies and positions of all the final-state particles were measured by an 804-block lead-glass calorimeter. Each of the showers (clusters) observed in the lead glass was required to be consistent with an isolated photon or $e^+$ or $e^-$ (the "shape" cut). The $e^+$ and $e^-$ were identified by matching the reconstructed tracks with the calorimeter clusters, and requiring $0.85 < E/P < 1.15$, where $E$ is the cluster energy deposited in the lead glass and $P$ is the track momentum. We further required that the invariant mass of the $e^+$ and $e^-$ ($M_{ee}$) be greater than 100 MeV/$c^2$. From a study of $K_L \to \pi^+ \pi^- \pi^0$ decays, the $\pi^0$ mass resolution was determined to be about 4 MeV/$c^2$. The $\gamma\gamma$ mass was required to be within 10 MeV/$c^2$ of the nominal $\pi^0$ value. By then constraining the $\gamma\gamma$ mass to the nominal value, the expected kaon mass ($M_{\pi ee}$) resolution is about 4.5 MeV/$c^2$. The square of the transverse momentum ($P_t^2$) of the $\pi^0 e^+ e^-$ system with respect to the line connecting the decay vertex and the production target has an expected resolution of about 50 MeV$^2$/$c^2$.

The candidates from the entire data set are displayed in a two-dimensional $M_{\pi ee}$ vs $P_t^2$ plot as shown in Fig. 1. A candidate is defined to have $P_t^2 < 200$ MeV$^2$/$c^2$, $489 < M_{\pi ee} < 507$ MeV/$c^2$, and $M_{ee} > 100$ MeV/$c^2$; these cuts would include about 90% of the signal. No candidate is found in the signal region.

The "shape" and $M_{ee}$ cuts were not applied for our previous result.[2] The "shape" requirement suppressed background events from $K_{e3}$ decay with an accidental $\pi^0$ (or radiative $K_{e3}$ decay with a single accidental photon) when the pion showered in the calorimeter and satisfied the $E/P$



FIG. 1. Reconstructed kaon mass vs the square of the transverse momentum for $K_L \to \pi^0 e^+ e^-$. The box represents the signal region.

cut. The $M_{ee}$ cut retained 95% of the signal while rejecting events with $\pi^0$'s decayed to $\gamma e^+ e^-$ where the $\pi^0$ came from a neutral-kaon decay. The sparsely distributed events outside the box in Fig. 1 are consistent[4] with the residual $K_{e3}$ plus accidental $\pi^0$ background.

The limit is obtained with data from two types of triggers. The "four-cluster" trigger required four electromagnetic showers and 30 GeV or more energy deposited in the lead-glass calorimeter. The "two-track" trigger required two tracks in the tracking spectrometer. For kaon energy between 30 and 160 GeV and assuming a uniform three-body phase-space distribution, the acceptance is 9.0% for a fiducial decay volume of 18 m for the "four-cluster" trigger and is 10% for a fiducial decay

volume of 17 m for the "two-track" trigger. The "two-track" data, unlike those collected in the special data set,[2] were not prescaled.

The upper limit is obtained by normalizing to samples of more than $10^5$ $K_L \to \pi^0\pi^0$ and $K_L \to \pi^+\pi^-$ decays observed simultaneously. The limits obtained from the "two-track" and "four-cluster" data are $< 3.6 \times 10^{-8}$ and $< 9.5 \times 10^{-9}$ (90% confidence), respectively. The combined result $B(K_L \to \pi^0 e^+ e^-) < 7.5 \times 10^{-9}$ (90% confidence) is an improvement of about factor of 6 from our previous result. This limit is also consistent with the recent result obtained by a Brookhaven experiment[7] and helps to limit the possible contribution from direct $CP$ violation.

*Present address: SLAC, Stanford, CA 94305.

†Present address: Department of Physics, University of Illinois, Urbana, IL 61801.

‡Present address: Princeton Combustion Research Laboratories, Monmouth Junction, NJ 08852.

[1]J. F. Donoghue, B. R. Holstein, and G. Valencia, Phys. Rev. D 35, 2769 (1987); L. M. Sehgal, ibid. 38, 808 (1988); G. Ecker, A. Pich, and E. deRafael, Nucl. Phys. B303, 665 (1988); C. O. Dib, I. Dunitz, and F. Gilman, Phys. Rev. D 39, 2639 (1989); J. Flynn and L. Randall, Phys. Lett. B 216, 221 (1989).

[2]L. K. Gibbons et al., Phys. Rev. Lett. 61, 2661 (1988).

[3]G. D. Barr et al., Phys. Lett. B 214, 303 (1988).

[4]A. Barker et al., Fermilab Proposal No. E-799, 1989 (unpublished). This document describes in detail the calculation of the possible backgrounds.

[5]J. R. Patterson et al., Phys. Rev. Lett. 64, 1491 (1990); H. Burkhardt et al., Phys. Lett. B 206, 169 (1988).

[6]For a complete description of the detector, see J. R. Patterson, Ph.D. thesis, University of Chicago, 1990.

[7]The result from the BNL-Vassar-Yale experiment (AGS-845) is $B(K_L \to \pi^0 e^+ e^-) < 5.5 \times 10^{-9}$ (90% C.L.). See M. Schmidt et al., in Proceedings of the Meeting of the APS Division of Particles and Fields, Houston, Texas, 1990 (unpublished); K. E. Ohl et al., Yale University report (unpublished).

# Test of *CPT* Symmetry through a Determination of the Difference in the Phases of $\eta_{00}$ and $\eta_{+-}$ in $K \to 2\pi$ Decays

M. Karlsson, G. D. Gollin,[a] J. K. Okamitsu,[b] and R. Tschirhart[c]

*Department of Physics, Princeton University, Princeton, New Jersey 08544*

A. Barker, R. A. Briere, L. K. Gibbons, G. Makoff, V. Papadimitriou, J. R. Patterson, S. Somalwar,
Y. W. Wah, B. Winstein, R. Winston, M. Woods,[d] and H. Yamamoto

*The Enrico Fermi Institute and Department of Physics, The University of Chicago, Chicago, Illinois 60637*

E. Swallow

*Department of Physics, Elmhurst College, Elmhurst, Illinois 60126
and Department of Physics, The University of Chicago, Chicago, Illinois 60637*

G. J. Bock, R. Coleman, J. Enagonio, Y. B. Hsiung, K. Stanfield, R. Stefanski, and T. Yamanaka

*Fermi National Laboratory, Batavia, Illinois 60510*

P. Debu, B. Peyaud, R. Turlay, and B. Vallage

*Département de Physique des Particules Elémentaires, Centre d'Etudes Nucléaires de Saclay,
F 91191 Gif-sur-Yvette CEDEX, France*

(Received 22 January 1990)

Data collected by the E731 experiment at Fermilab were used to search for *CPT* violation in $K^0 \to \pi\pi$ decays by measuring the difference $\Delta\phi$ between the phases of the *CP*-violating parameters $\eta_{00}$ and $\eta_{+-}$. Our result, $\Delta\phi = -0.3° \pm 2.4° \pm 1.2°$, where the first error is statistical and the second systematic, is consistent with *CPT* symmetry.

*CPT* symmetry is a natural consequence of local quantum field theory[1] and guarantees the equality of masses and lifetimes of particles and antiparticles. It is conceivable, however, that a small violation of *CPT* symmetry could occur in extensions of quantum field theory (e.g., string theory[2]); thus, it is imperative to check *CPT* symmetry wherever possible. The neutral-kaon system provides some of the most sensitive tests of *CPT* symmetry. The ratio of the decay amplitudes $\eta \equiv \mathrm{amp}(K_L \to \pi\pi)/\mathrm{amp}(K_S \to \pi\pi)$ can be written as[3] $\eta_{+-} \equiv |\eta_{+-}|e^{i\phi_{+-}} = (\epsilon - \Delta + a) + \epsilon'$ for the $\pi^+\pi^-$ final state and $\eta_{00} \equiv |\eta_{00}|e^{i\phi_{00}} = (\epsilon - \Delta + a) - 2\epsilon'$ for the $\pi^0\pi^0$ final state (Fig. 1). Here $\epsilon$ is a measure of *CP* violation without *CPT* violation in $K^0$-$\bar{K}^0$ mixing, and $\Delta$ is similarly a measure of *CPT* violation without *T* violation. Direct *CP* and *CPT* violations in the decay amplitudes are parametrized by $a \equiv (A_0 - \bar{A}_0)/(A_0 + \bar{A}_0)$ (chosen to be real[4]) and

$$\epsilon' = \frac{1}{\sqrt{2}} \frac{A_2 - \bar{A}_2}{A_0 + \bar{A}_0} e^{i(\delta_2 - \delta_0)}, \qquad (1)$$

where $A_I$ ($\bar{A}_I$) is the $2\pi$ decay amplitude of $K^0$ ($\bar{K}^0$) to isospin-$I$ final state with corresponding phase shift $\delta_I$ from final-state interactions. *CPT* symmetry results in two constraints that can be tested by experiment: First, *CPT* symmetry implies that the phase of $2\eta_{+-} + \eta_{00}$ be within a few degrees of the "natural angle" $\phi_\epsilon \equiv \arg(\Gamma_S/2 + i\Delta m) = 43.7° \pm 0.2°$, where $\Gamma_S$ is the $K_S$

decay rate and $\Delta m \equiv M_{K_L} - M_{K_S}$. Second, using the experimental value[5] $\delta_2 - \delta_0 = -45° \pm 10°$ in Eq. (1), the *CPT* relation $\bar{A}_I = A_I^*$ leads to $\arg\epsilon' \approx \phi_\epsilon$. This, together with the current knowledge[6,7] of $|\mathrm{Re}(\epsilon'/\epsilon)|$, requires the phase difference $\Delta\phi \equiv \phi_{00} - \phi_{+-}$ to be much less than $1°$. With the accepted value[8] of $\phi_{+-} = 44.6° \pm 1.2°$,



FIG. 1. Relationship among the *CPT*-violating parameters $a$, $\Delta$, and the directly measurable quantities $\eta_{+-}$, $\eta_{00}$. Since *CPT* symmetry predicts $\epsilon'$ to be parallel to $\epsilon$, a nonzero value of $\Delta\phi = \phi_{00} - \phi_{+-}$ also indicates *CPT* violation. The magnitudes of $a$, $\Delta$, and $\epsilon'$ are exaggerated for clarity.

however, the most recent published measurement[9] of $\phi_{00}=55.7° \pm 5.8°$ corresponds to a phase difference about 2 standard deviations away from the prediction of $CPT$ symmetry;[10] this has generated considerable interest and speculation.[3]

$$\frac{d^2 I_{\pi\pi}}{dP_K dt} \propto F(P_K)e^{-X}[\,|\rho|^2 e^{-t/\tau_S}+|\eta|^2 e^{-t/\tau_L}+2|\rho|\,|\eta|e^{-t/2\tau_S}\cos(\Delta m\,t+\phi_\rho-\phi_\eta)]\,, \tag{2}$$

where $\tau_S$ ($\tau_L$) is the $K_S$ ($K_L$) lifetime, $\Delta m$ the mass difference between $K_L$ and $K_S$, $\rho=|\rho|e^{i\phi_\rho}$ the coherent regeneration amplitude, and $F(P_K)$ the incident kaon momentum spectrum. The incident flux is normalized to the other vacuum beam whose $\pi\pi$ rate is simply $F(P_K) \times |\eta|^2 e^{-t/\tau_L}$. The factor $e^{-X}$ accounts for absorption in the regenerated beam. As can be inferred from Eq. (2), the values extracted for $\phi_{+-}$ and $\phi_{00}$ individually depend on $\phi_\rho$ and $\Delta m$, but the difference $\Delta\phi \equiv \phi_{00}-\phi_{+-}$ is insensitive to both parameters.

A description of the experimental setup can be found in Refs. 6 and 11, and only a brief account of the essential features is given here. The $\pi^0\pi^0$ decays were detected with a lead-glass calorimeter having an energy resolution for photons of $2.5\%+5\%/\sqrt{E}$ ($E$ in GeV). The $\pi^+\pi^-$ decays were reconstructed using a magnet and a sixteen-plane drift-chamber system with a typical momentum resolution of 1%. All four decay modes, $K_{S,L}\rightarrow\pi^+\pi^-,\pi^0\pi^0$, were collected simultaneously and the regenerator alternated frequently between the two beams. This minimizes sensitivity to differences in intensity and momentum spectrum between the beams as well as to reconstruction inefficiencies, dead-time effects, and calibration changes with time.

The phase-difference result presented here is based on the same data set that was recently used to determine $\mathrm{Re}(\epsilon'/\epsilon)$,[6] and the event-reconstruction and background-subtraction techniques employed are the same as for that analysis. For neutral decays, however, the length of the decay region is extended downstream by 13 m to increase sensitivity to the phase in the interference term. Most of the phase information is provided by decays at the lower end of the energy range where a larger proper-time region can be sampled. For $\pi^+\pi^-$ decays, the length of the decay region is 14 m (6.5 $K_S$ lifetimes at 40 GeV), and for $\pi^0\pi^0$ decays, it is 29 m (14 $K_S$ lifetimes at 40 GeV). It is not possible to extend the decay region for the charged mode since it is hardware defined by a thin trigger hodoscope.

The $2\pi^0$ mass distribution for the regenerated beam has a small (0.04%) background which is dominated by $3\pi^0$ decays from the $K_L$ beam transmitted through the regenerator. A $3\pi^0$ decay can fake a $2\pi^0$ signal when two out of the six photons are lost either by escaping the detector or by merging with other photons in the lead-glass calorimeter. Figure 2 shows the vertex distributions for signal and backgrounds in the regenerated beam. For the vacuum beam, the level of $3\pi^0$ back-

ground is higher (0.99%); its vertex distribution has the same shape as that of the regenerated beam. Another source of background arises from incoherently produced kaons that emerge with nonzero scattering angle from the regenerator. This amounts to 2.7% in the regenerated beam, and its vertex distribution is also shown in Fig. 2. The corresponding background level for the vacuum beam is 2.8%. There is also a background due to nuclear interactions at the regenerator ($z=123$ m) and at the 2-mm-thick trigger hodoscope ($z=138$ m). In the charged mode, the background in the vacuum beam (0.32%) is dominated by $K_{e3}$ decays, whereas the background in the regenerated beam (0.13%) comes from incoherent regeneration.

In order to extract $\phi_{+-}-\phi_\rho$ and $\phi_{00}-\phi_\rho$ from the shapes of the vertex distributions in the regenerated beam, the acceptance as a function of decay vertex must be well understood. Accurate knowledge of the accep-



FIG. 2. The vertex distribution of reconstructed $2\pi^0$ decays in the regenerated beam together with the background contributions from incoherently regenerated $K_S$ (triangles) and $3\pi^0$ decays and nuclear interactions (squares). The incoherent background under the coherent peak is measured from the data by the extrapolation to zero scattering angle (see text). The $3\pi^0+$ nuclear interaction backgrounds are estimated by the fit of the mass distribution where the $3\pi^0$ component is obtained from the Monte Carlo simulation.

tance is essential for the determination of $\text{Re}(\epsilon'/\epsilon)$, and is discussed in detail in Ref. 6. The fit is done by comparing the background-subtracted and acceptance-corrected $z$ distributions with the predicted rate $I_{\pi\pi}$ of Eq. (2), constrained by the total number of events in the vacuum beam. In the fit for $\phi_{+-}$ and $\phi_{00}$, the kaon parameters $\tau_S$, $\tau_L$, and $\Delta m$ are fixed to their world-average values.[8] The parameter $\text{Re}(\epsilon'/\epsilon)$, which is a measure of the difference in magnitude between $\eta_{+-}$ and $\eta_{00}$, is allowed to float in the fit.[12] The assumptions made for the regeneration amplitude[13] are the following: (a) The difference in the forward-scattering amplitudes[14] between $K^0$ and $\bar{K}^0$ has a power-law dependence on the kaon momentum; namely, $|(f-\bar{f})/k| \propto P_K^{-\alpha}$; (b) the phase of $(f-\bar{f})/k$ is given by the analyticity condition $\arg[(f-\bar{f})/k] = -(2-\alpha)\pi/2$. The absorption factor $e^{-X}$ is measured to better than 1% of itself from $K_L \to \pi^+\pi^-\pi^0$ and $K_L \to \pi^0\pi^0\pi^0$ decays in the two beams. This uncertainty has a negligible effect on $\Delta\phi$.

The result of the fit is $\phi_{+-} = 47.7° \pm 2.0°$, $\phi_{00} = 47.4° \pm 1.4°$, and $\Delta\phi \equiv \phi_{00} - \phi_{+-} = -0.3° \pm 2.4°$. The errors are statistical and $\chi^2 = 316$ for 340 degrees of freedom. Figure 3 shows the quality of the fit to the data for both modes. As a check of our understanding of the acceptance, we have also fitted for $\tau_S$ and $\Delta m$, and we have obtained $\tau_S = (0.8882 \pm 0.0030) \times 10^{-10}$ s (charged mode), $\tau_S = (0.8929 \pm 0.0033) \times 10^{-10}$ s (neutral mode), $\Delta m = (0.5377 \pm 0.0098) \times 10^{10} \hbar$ s$^{-1}$ (both modes combined), where the errors are statistical only. These results are in good agreement with the corresponding world averages.[8]

The systematic errors on $\Delta\phi$ come from various sources. When the parameters $\tau_S$ and $\Delta m$ are varied by 1 standard deviation around their world-average values, the value of $\Delta\phi$ changes by 0.2° for $\tau_S$ and 0.1° for $\Delta m$. Similarly the value of $\Delta\phi$ changes by +0.8° for a change of $+10^{-3}$ on $\text{Re}(\epsilon'/\epsilon)$. The acceptance was carefully studied using high-statistics modes ($10^7$ $K_{e3}$ events for charged mode and $6 \times 10^6$ $3\pi^0$ for neutral mode). The remaining uncertainty in the acceptance corresponds to an error in $\Delta\phi$ of 0.9°. The uncertainty in the absolute energy calibration (0.1%) is determined from the sharp upstream edge of the decay distribution in the regenerated beam. The resulting error in $\Delta\phi$ is 0.6°. The subtraction of the $3\pi^0$ and incoherent backgrounds in neutral mode contributes an error of 0.3°. Accidental overlaps in the detector have a negligible effect on the result. The combined systematic error on $\Delta\phi$ is thus 1.2°. Excluding the regeneration phase uncertainty, the systematic error on $\phi_{+-}$ is 0.9° (dominated by acceptance uncertainty) and the systematic error on $\phi_{00}$ is 0.8° (dominated by absolute energy calibration).

The final result is then $\Delta\phi \equiv \phi_{00} - \phi_{+-} = -0.3° \pm 2.4°(\text{stat}) \pm 1.2°(\text{syst})$. This result is consistent with zero and thus with the prediction of $CPT$ symmetry. With the world average of $\phi_{+-}$, our measurement of $\Delta\phi$

leads to a value for $\arg(2\eta_{+-} + \eta_{00})$ of $44.5° \pm 1.5°$, which is well within 1 standard deviation of the natural angle $\phi_\epsilon = 43.7°$. Our measurement of $\phi_{+-}$ is consistent with the world average. This supports the assumptions made for the regeneration amplitude in the fit. In conclusion, our measurement shows no indication of $CPT$ violation. Further confirmation is provided by a recent experiment[15] which finds $\Delta\phi = 0.2° \pm 2.9°$.

The limit on $\Delta\phi$ also leads to a limit on the component of $\epsilon'$ perpendicular to $\epsilon$ using the relation $\text{Im}(\epsilon'/\epsilon) = -\Delta\phi/3$ which can be easily seen from Fig. 1. With the measured value of $\Delta\phi$, we obtain a 95%-confidence limit on $\text{Im}(\epsilon'/\epsilon)$ without any assumption of $CPT$ invariance: $-0.03 < \text{Im}(\epsilon'/\epsilon) < 0.03$.



FIG. 3. The vertex distributions in the regenerated beam after background subtractions and acceptance corrections for the (a) neutral and (b) charged modes. The solid curves are the result of the fit described in the text. The momentum cuts on the kaon energy are (a) [40,50] GeV and (b) [30,40] GeV.

---

(a)Current address: Department of Physics, Loomis Laboratory of Physics, University of Illinois, 1110 West Green Street, Urbana, IL 61801.

(b)Current address: Princeton Combustion Laboratories, 4275 U.S. Highway 1, Monmouth Junction, NJ 08852.

(c)Current address: Fermi National Laboratory, Batavia, IL 60510.

(d)Current address: Stanford Linear Accelerator Center, P.O. Box. 4349, Stanford, CA 94309.

[1]G. Lüders, Dansk. Mat. Fys. Medd. 28, 17 (1954); W. Pauli, *Niels Bohr and the Development of Physics* (Pergamon, New York, 1955); R. Jost, Helv. Phys. Acta 30, 409 (1957).

[2]E. Witten, Commun. Math. Phys. 109, 525 (1987); H. Sonoda, Nucl. Phys. B326, 135 (1989).

[3]N. W. Tanner and R. H. Dalitz, Ann. Phys. (N.Y.) 171, 463 (1986); V. V. Barmin et al., Nucl. Phys. B247, 293 (1984); J. W. Cronin, Acta Phys. Pol. B 15, 419 (1984), and references therein.

[4]The relative phase of $K_0$ and $\bar{K}_0$ is chosen such that $\arg A_0 = \arg \bar{A}_0$ (Wu-Yang phase convention).

[5]T. J. Devlin and J. O. Dickey, Rev. Mod. Phys. 51, 237 (1979).

[6]M. Woods et al., Phys. Rev. Lett. 60, 1695 (1988); J. R. Patterson et al., ibid. 64, 1491 (1990).

[7]H. Burkhardt et al., Phys. Lett. B 206, 169 (1988).

[8]Particle Data Group, G. P. Yost et al., Phys. Lett. B 204, 1 (1988).

[9]J. H. Christenson et al., Phys. Rev. Lett. 43, 1209 (1979).

[10]The discrepancy between $\arg(2\eta_{+-} + \eta_{00})$ and $\phi_\epsilon$ is also about $2\sigma$ if it is assumed that the $\Delta S = \Delta Q$ rule holds and that there is no anomalously large CP or CPT violations in $3\pi^0$ and semileptonic modes; Barmin et al., Ref. 3.

[11]For a detailed discussion of the analysis, see the M. Karlsson, Ph.D. thesis, Princeton University, 1990.

[12]In the determination of $\mathrm{Re}(\epsilon'/\epsilon)$ in Ref. 6, the phase difference was fixed at zero. The value obtained for $\mathrm{Re}(\epsilon'/\epsilon)$ in this analysis is consistent with that given in Ref. 6.

[13]J. Roehrig et al., Phys. Rev. Lett. 38, 1116 (1977).

[14]The regeneration amplitude $\rho$ is related to $(f-\bar{f})/k$ by $\rho = \pi i N L g (f-\bar{f})/k$, where $N$ is the density of scatterers, $L$ is the length of the regenerator, and $g = (1 - e^{-x})/x$ is a geometrical factor with $x = (\frac{1}{2} - i\Delta m/\Gamma_S)L/\Lambda_S$ with $\Lambda_S$ the $K_S$ decay length. For a thin regenerator $g$ is unity, and $|g-1|$ is always less than 0.2 in our case.

[15]R. Carosi et al. (NA31 experiment), CERN Report No. CERN-EP/90-06 (to be published).

# Measurement of the branching ratio of the decay $K_L \to \pi^0 \gamma \gamma$

V. Papadimitriou,* A. Barker, R. A. Briere, L. K. Gibbons, G. Makoff, J. R. Patterson,† S. Somalwar,
Y. W. Wah, B. Winstein, R. Winston, M. Woods,‡ and H. Yamamoto

*The Enrico Fermi Institute and the Department of Physics, The University of Chicago, Chicago, Illinois 60637*

E. C. Swallow

*Department of Physics, Elmhurst College, Elmhurst, Illinois 60126
and The Enrico Fermi Institute, The University of Chicago, Chicago, Illinois 60637*

G. J. Bock, R. Coleman, J. Enagonio, Y. B. Hsiung, E. Ramberg, K. Stanfield, R. Tschirhart, and T. Yamanaka

*Fermi National Accelerator Laboratory, Batavia, Illinois 60510*

G. D. Gollin,$^\S$ M. Karlsson,** and J. K. Okamitsu††

*Department of Physics, Princeton University, Princeton, New Jersey 08544*

P. Debu, B. Peyaud, R. Turlay, and B. Vallage

*Department de Physique des Particules Elementaires, Centre d'Etudes Nucleaires de Saclay,
F-91191 Gif-sur-Yvette CEDEX, France*

(Received 19 February 1991)

Using the complete Fermilab E731 data set, we find $\Gamma(K_L \to \pi^0 \gamma \gamma$, $m_{\gamma\gamma} \geq 0.280$ GeV)/$\Gamma(K_L \to$ all)$=(1.86 \pm 0.60 \pm 0.60) \times 10^{-6}$, in good agreement with a recent report of the first observation of this decay. For the low $\gamma\gamma$ mass region we find $\Gamma(K_L \to \pi^0 \gamma \gamma$, $m_{\gamma\gamma} < 0.264$ GeV)/$\Gamma(K_L \to$ all)$< 5.1 \times 10^{-6}$ (90% confidence).

The decay $K_L \to \pi^0 \gamma \gamma$ is of current interest [1-6] within the context of both chiral perturbation theory and the vector-meson-dominance model, and also for its contribution to the decay $K_L \to \pi^0 e^+ e^-$ as a $CP$-conserving intermediate state. Predictions for its branching ratio vary from $6.3 \times 10^{-7}$ to $6.2 \times 10^{-6}$, and predicted $\gamma\gamma$ mass distributions differ markedly. At the one-loop level in chiral perturbation theory [1], the branching ratio is estimated to be $6.8 \times 10^{-7}$ with a characteristic $\gamma\gamma$ invariant-mass distribution ($m_{\gamma\gamma}$) peaking at about 0.325 GeV.

Earlier we reported [7] an upper limit for the branching ratio of this decay of $2.7 \times 10^{-6}$ (90% confidence) assuming the $\gamma\gamma$ invariant-mass distribution expected by chiral perturbation theory. That result was based on a subset of our data; here we report results from the entire data sample which therefore supersede the earlier results. In the meantime, CERN experiment NA31 has recently reported [8] an observation of the decay: They have found a signal primarily at high $\gamma\gamma$ invariant mass and a branching ratio significantly greater than that predicted by chiral perturbation theory. They find

$$\frac{\Gamma(K_L \to \pi^0 \gamma \gamma, \; m_{\gamma\gamma} \geq 0.280 \, \text{GeV})}{\Gamma(K_L \to \text{all})} = (2.1 \pm 0.6) \times 10^{-6}.$$

The primary goal of experiment E731 is the determination of the $CP$-violation parameter $\epsilon'/\epsilon$ [9]. The characteristics of the detector and the event reconstruction have

been described in detail elsewhere [7,10]; here we summarize the essential features of the analysis and its differences from that used in our previous publication. Energies and positions of photons were measured with an 804-block lead-glass calorimeter. Candidates for the $K_L \rightarrow \pi^0 \gamma\gamma$ decay were required to have exactly four electromagnetic showers (clusters) in the lead glass, each with an energy of at least 1 GeV, and total energy between 40 and 150 GeV. The decay vertex was determined from the measured cluster energies and positions by assuming that the invariant mass of the four photons was that of the neutral kaon. The two photons, labeled (12), with invariant mass closest to the nominal neutral-pion mass $(m_{\pi^0})$ were taken to be the decay products of the candidate $\pi^0$. The $\pi^0$ mass resolution was about 3 MeV and it was required that $|m_{12} - m_{\pi^0}| \leq 5$ MeV.

Background rejection is critical since the signal is poorly constrained. The rejection of the $K_L \rightarrow 2\pi^0$ background was done in two steps. First, it was required that the mass of the non-$\pi^0$ pair $(m_{\gamma\gamma}$ or $m_{34})$ differ from $m_{\pi^0}$ by at least 14 MeV. Second, the candidate event was reconstructed as a $K_L \rightarrow 2\pi^0$ decay by constraining the invariant masses of each pair of photons to the nominal $\pi^0$ mass, and if it satisfied the criteria described in Refs. [7] and [10], it was rejected as a mispaired $2\pi^0$ decay. $K_L \rightarrow 3\pi^0$ decays, which are the dominant remaining background, can masquerade as four-cluster events either when photons escape the detector or when multiple photons fuse in the lead glass to form a single cluster. This background was considerably reduced (1) by using the many photon veto counters for the detection of escaping photons, (2) by requiring that the transverse center of energy of the four photons be in the $K_L$ beam region, and (3) by considering only decays in the upstream part of the decay region, starting at 110 m and ending at 128 m from the target. The selection of the downstream edge of this decay region was made on the basis of a Monte Carlo study to maximize the sensitivity to a signal in the presence of known amounts of $3\pi^0$ and $2\pi^0$ backgrounds; the data themselves were not used. In fact, the sensitivity is relatively independent on the position of the downstream edge. The background with overlapping clusters was substantially reduced by rejecting events with cluster shapes inconsistent with that of a single photon. Additional suppression of the $3\pi^0$ background came from kinematically rejecting events with two superimposed $\pi^0$ (double fusion events) where each photon from one $\pi^0$ overlaps with a photon from the other $\pi^0$ so that $m_{\gamma\gamma} > 2m_{\pi^0}$. For this background, these fused clusters are the $\gamma\gamma$ pair about 70% of the time according to the Monte Carlo simulations; in addition, the energies of the photons which fuse tend to be high. By analyzing each candidate event as though these clusters are so fused, the individual photon energies could be kinematically determined. A cut on a combination of these energies reduced the background by about 28% while reducing the expected signal by about 6.5% (see Ref. [10]). The drift-chamber spectrometer and four scintillation hodoscopes were used to reject $K_L$ decays with charged particles in the final state (e.g., $K_L \rightarrow \pi^+ \pi^- \pi^0$) or events with photon conversions. The contribution from accidental clusters in our data sample is

found to be negligible. Finally, we rejected events with photons projecting outside the holes of the lead-mask photon veto which is located at about 122 m from the target and is one of our defining apertures.

Figure 1 shows the comparison of data and background Monte Carlo simulation for the $\gamma\gamma$ effective mass. A characteristic feature in this distribution is the prominent double fusion peak appearing at about $m_{\gamma\gamma} = 0.270$ GeV. The background coming from the $3\pi^0$ and $2\pi^0$ modes is absolutely normalized to the data by means of a sample of fully reconstructed $K_L \rightarrow 2\pi^0$ decays observed simultaneously and selected with criteria similar to those used for the $\pi^0\gamma\gamma$ candidates. Although for low $\gamma\gamma$ mass the data–Monte Carlo agreement is good within statistics, at high masses there is a significant excess of data. The background in the high-mass region consists predominantly of events where both $\gamma$'s are fused clusters. The Monte Carlo simulation correctly reproduces the prominent double fusion peak, which is important in establishing that the excess at higher values is indeed a signal. Figure 2 shows the comparison of data and background Monte Carlo simulation for the reconstructed $z$ decay vertex distributions with $m_{\gamma\gamma} \geq 0.280$ GeV, including the region downstream of the fiducial cut. The data excess is uniformly distributed over the decay region as is expected for a signal.

In Fig. 3 we show the data–Monte Carlo comparison for the $m_{12}$ distribution for $m_{\gamma\gamma} \geq 0.280$ GeV. The excess



FIG. 1. Data–Monte Carlo comparison of the $\gamma\gamma$ mass distribution for $\pi^0\gamma\gamma$ candidates and background events based on the full data set. The normalization is absolute. The error bars correspond to the data, the shaded histogram to the $2\pi^0$ background Monte Carlo simulation, and the dashed histogram to the sum of the $3\pi^0$ and $2\pi^0$ background Monte Carlo simulations.

FIG. 2. Data–Monte Carlo comparison for the $z$ decay vertex distribution for $\pi^0\gamma\gamma$ candidates and background events with $m_{\gamma\gamma} \geq 0.280$ GeV. The normalization is absolute. The error bars correspond to the data, the shaded histogram to the $2\pi^0$ background Monte Carlo simulation, and the dashed histogram to the sum of the $3\pi^0$ and $2\pi^0$ background Monte Carlo simulations. The arrow indicates the position of the cut.

FIG. 3. Data–Monte Carlo comparison for the $m_{12}$ ($\pi^0$ candidate) distribution for $\pi^0\gamma\gamma$ candidates and background events including $\pi^0\gamma\gamma$ signal Monte Carlo simulation, for $m_{\gamma\gamma} \geq 0.280$ GeV. The error bars correspond to the data; the diagonally shaded histogram to the sum of the $3\pi^0$ and $2\pi^0$ background Monte Carlo simulations; the horizontally shaded histogram to the $\pi^0\gamma\gamma$ signal normalized with the branching ratio of $1.86 \times 10^{-6}$, and the dashed histogram to the sum of the background and the signal. The normalization is absolute.

over the background Monte Carlo simulation is peaked at the nominal $\pi^0$ mass with a width consistent with the prediction of a $\pi^0\gamma\gamma$ Monte Carlo simulation. (It should be noted that the background also peaks near, but not at, the nominal neutral-pion mass. This happens because the background often has a true $\pi^0$ but, because of the overlaps of the other two clusters, its mass is somewhat shifted and broadened due to the nonlinearity in the lead-glass response.) The $\pi^0\gamma\gamma$ signal is normalized at a branching ratio $1.86 \times 10^{-6}$ (see below). The agreement is good and gives additional confidence that the excess of data at high $m_{\gamma\gamma}$ is $\pi^0\gamma\gamma$ signal.

For the high-mass sample ($m_{\gamma\gamma} \geq 0.280$ GeV) we have 232 candidate events from which 104 come from a data set with a 0.09-radiation-length lead sheet inserted in the beams 137.8 m from the target. The effect of the lead sheet is that it will sometimes convert one (or more) of the photons causing both signal and background events to be lost. The Monte Carlo simulation properly accounts for this and the total predicted background is $(171.9 \pm 11.5)$ events (150.7 from $3\pi^0$s and 21.2 from $2\pi^0$s). Based on background studies and many comparisons of data with Monte Carlo distributions, we assign an 11% systematic error to the estimate of the background in the high mass region. There are three sources to this systematic uncertainty which are added in quadrature. The first is due to imperfect knowledge of the efficiencies of the photon vetoes (exclusive of the lead mask, itself a photon veto discussed later) and this is estimated to result in 5% uncertainty. The second arises from possible errors in the understanding of the photon energy resolution and this is estimated to result in a 3% uncertainty. The third, which is the largest, is associated with the discarding of a few remaining events with photons projecting outside the aperture of the lead mask. These events are not well simulated and this is estimated to result in a 9% uncertainty. The $\pi^0\gamma\gamma$ acceptance is 3.4% (4.4%) for data with (without) the lead sheet inserted and the normalization is provided by 45000 $K_L \rightarrow 2\pi^0$ decays taken simultaneous-

ly. Using the world average value [11] for the $K_L \rightarrow 2\pi^0$ branching ratio we conclude that

$$\frac{\Gamma(K_L \rightarrow \pi^0\gamma\gamma, m_{\gamma\gamma} \geq 0.280 \text{ GeV})}{\Gamma(K_L \rightarrow \text{all})}$$

$$= (1.86 \pm 0.60 \pm 0.60) \times 10^{-6},$$

where the first error is statistical and the second is systematic. If we assume the $m_{\gamma\gamma}$ distribution predicted by chiral perturbation theory we then have

$$\frac{\Gamma(K_L \rightarrow \pi^0\gamma\gamma)}{\Gamma(K_L \rightarrow \text{all})} = (2.2 \pm 0.7 \pm 0.7) \times 10^{-6}.$$

We have also looked for a signal at lower $\gamma\gamma$ masses. Our acceptance for masses below the double fusion peak is smooth and averages [7,10] about 5%, except for the narrow region excluded around the nominal $\pi^0$ mass. For the region $m_{\gamma\gamma} < 0.264$ GeV we have $367 \pm 19.2$ data events and $377.5 \pm 18.4$ expected background events. This gives

$$\frac{\Gamma(K_L \rightarrow \pi^0\gamma\gamma, m_{\gamma\gamma} < 0.264 \text{ GeV})}{\Gamma(K_L \rightarrow \text{all})} < 5.1 \times 10^{-6}$$

(90% confidence)

where we have used a phase-space distribution for $m_{\gamma\gamma}$ and have included a 15% systematic error on the background prediction.

We thus confirm both the substantial branching ratio and the peaking at high mass first reported by the NA31 group. Our analysis uses less stringent kinematic cuts so that our acceptance is smooth and substantial over the entire mass region, leading to a limit at lower mass values. The central value for the branching ratio is a factor of three higher than the chiral perturbation theory prediction. More statistics and better background rejection will be necessary for additional studies of this decay mode.

*Current address: Fermi National Accelerator Laboratory, Batavia, IL 60510.

†Current address: Cornell University, Ithaca, NY 14853.

‡Current address: SLAC, Stanford, P.O. Box 4349, CA 94305.

§Current address: Department of Physics, University of Illinois, Urbana, IL 61801.

**Current address: CERN, CH-1211, Geneva 23, Switzerland.

††Current address: Princeton Combustion Research Laboratories, Monmouth Junction, NJ 08852.

[1] G. Ecker, A. Pich, and E. De Rafael, Phys. Lett. B **189**, 363 (1987).

[2] P. Ko and J. L. Rosner, Phys. Rev. D **40**, 3775 (1989).

[3] T. Morozumi and H. Iwasaki, in *Physics at TeV Scale,* Proceedings of the Second Meeting, Tsukuba, Japan, 1988, edited by K. Hidaka and K. Hikasa (KEK, Tsukuba, 1988).

[4] L. M. Sehgal, Phys. Rev. D **41**, 161 (1990).

[5] P. Ko, Phys. Rev. D **41**, 1531 (1990).

[6] G. Ecker, A. Pich, and E. De Rafael, Report Nos. UWThPh-1989-65, FTUV/89-44 (unpublished).

[7] V. Papadimitriou *et al.*, Phys. Rev. Lett. **63**, 28 (1989).

[8] G. D. Barr *et al.*, Phys. Lett. B **242**, 523 (1990).

[9] J. R. Patterson *et al.*, Phys. Rev. Lett. **64**, 1491 (1990).

[10] V. Papadimitriou, Ph.D. thesis, University of Chicago, 1990.

[11] Particle Data Group, G. P. Yost *et al.*, Phys. Lett. B **204**, 1 (1988).

# Search for the decay $K_L \rightarrow \pi^0 \nu \bar{\nu}$

G.E. Graham, A.R. Barker, R.A. Briere, L.K. Gibbons, G. Makoff, V. Papadimitriou [1],
J.R. Patterson [2], S.V. Somalwar, Y.W. Wah, B. Winstein, R. Winston, H. Yamamoto [3]

*Enrico Fermi Institute and Department of Physics, University of Chicago, Chicago, IL 60637, USA*

E.C. Swallow

*Department of Physics, Elmhurst College, Elmhurst, IL 60126, USA*
*and Enrico Fermi Institute, University of Chicago, Chicago, IL 60637, USA*

G.J. Bock, R. Coleman, J. Enagonio, Y.B. Hsiung, E. Ramberg, K. Stanfield, R. Tschirhart,
T. Yamanaka [4]

*Fermi National Accelerator Laboratory, Batavia, IL 60510, USA*

G.D. Gollin [5], M. Karlsson [6]

*Department of Physics, Princeton University, Princeton, NJ 08544, USA*

P. Debu, B. Peyaud, R. Turlay and B. Vallage

*Department de Physique des Particules Elementaires, Centre d'Etudes Nucleaires de Saclay,*
*F-91191 Gif-sur-Yvette Cedex, France*

Data collected in Fermilab experiment E731 was used to perform the first search for the decay $K_L \rightarrow \pi^0 \nu \bar{\nu}$. This decay is dominated by short distance effects and is almost entirely direct $CP$ violating within the standard model. Cuts were developed to reject the background processes $\Lambda \rightarrow n\pi^0$ and $K_L \rightarrow \pi^+ e^- \gamma \nu$. No candidate events were seen. We find BR $(K_L \rightarrow \pi^0 \nu \bar{\nu}) < 2.2 \times 10^{-4}$ at the 90% confidence level.

The decay $K_L \rightarrow \pi^0 \nu \bar{\nu}$ is uniquely well suited to the study of direct $CP$ violation within the standard model. It is one of four related processes in which a kaon decays to a pion and a light lepton pair. These are (i) $K^+ \rightarrow \pi^+ e^+ e^-$ ($K^+_{\pi ee}$); (ii) $K^+ \rightarrow \pi^+ \nu \bar{\nu}$ ($K^+_{\pi \nu \nu}$); (iii) $K^0 \rightarrow \pi^0 e^+ e^-$ ($K^0_{\pi ee}$); and (iv) $K^0 \rightarrow \pi^0 \nu \bar{\nu}$ ($K^0_{\pi \nu \nu}$).

The first of these, $K^+_{\pi ee}$, has been observed [1] with a branching ratio measured to be $2.75 \times 10^{-7}$. Unlike the other three, this process is dominated by long distance effects.

The branching ratio limit [2] for the second process, $K^+_{\pi \nu \nu}$, is $< 3.4 \times 10^{-8}$ at the 90% confidence level. This decay mode is dominated by short distance effects [3] described by one-loop diagrams involving virtual charm or top quarks. The top quark term is proportional to the magnitude of the as yet undetermined $V_{td}$ element of the CKM matrix. The standard model predicts that the branching fraction for this decay will be around $10^{-10}$.

For the third process, $K^0_{\pi ee}$, the branching ratio [4] is $< 3.5 \times 10^{-9}$ for $K_L$ and the limit [5] is $< 4.5 \times$

$10^{-5}$ for $K_S$, at the 90% confidence level. The $K_L$ decay mode has both direct and indirect $CP$ violating contributions [6]. The interesting direct piece is primarily a short-distance effect which can be fairly reliably calculated. However, this term can be extracted from a measurement of $K_L \rightarrow \pi^0 e^+ e^-$ only after the indirect piece has been determined from a measurement of $\Gamma(K_S \rightarrow \pi^0 e^+ e^-)$. It will be necessary to subtract the $CP$-conserving amplitude arising from the $\pi^0 \gamma^* \gamma^*$ intermediate state [7] and measurements [8] of $K_L \rightarrow \pi^0 \gamma \gamma$ has been made. Experimentally a substantial background [9] from radiative Dalitz decays, $K_L \rightarrow e^+ e^- \gamma \gamma$, also needs to be subtracted.

In this paper, we report the results of a search for the fourth mode, $K^0 \rightarrow \pi^0 \nu \bar{\nu}$. This process has been considered theoretically [10], but because of the formidable experimental difficulties, no search for this mode has previously been performed. The major attraction of this mode is its potential for the study of direct $CP$ violation in the standard model. There is no significant long-distance contribution to $K_L \rightarrow \pi^0 \nu \bar{\nu}$ and, based on existing upper limits for the $K^+_{\pi\nu\nu}$ mode, the amplitude from indirect $CP$ violation is negligible compared to direct $CP$ violating effects. The dominant, direct $CP$ violating, contribution to the decay is proportional to the imaginary part of $V_{td}$. In the Wolfenstein [11] parametrization of the CKM matrix, $V_{td} = A\lambda^3(1 - \rho - i\eta)$ and the standard model predicts

$$\text{BR}(K_L \rightarrow \pi^0 \nu \bar{\nu}) = 1.5 \times 10^{-10} (M_t/100 \text{ GeV})^2 A^4 \eta^2 ,$$

where $M_t$ is the mass of the top quark. In the standard model, the magnitude of $\eta$ can be related to the known value of $\epsilon$: it is estimated [12] that $\eta$ lies somewhere between about 0.1 and 0.6. Based on the value [12] $A = 0.85 \pm 0.09$, and the mass of the top quark determined indirectly from LEP data [13] to be $157 \pm 40$ GeV/$c^2$, the branching fraction for $K_L \rightarrow \pi^0 \nu \bar{\nu}$ could be as large as $2 \times 10^{-10}$.

The experimental signature for $K_L \rightarrow \pi^0 \nu \bar{\nu}$ is an observed single $\pi^0$ with unbalanced transverse momentum. Two decay modes of the neutral pion, $\pi^0 \rightarrow \gamma \gamma$ and $\pi^0 \rightarrow e^+ e^- \gamma$, could be used for detection, each with its own experimental difficulties. If the $\gamma \gamma$ final state is used, the transverse position of the decay vertex within the neutral beam cannot be accurately determined, and a very hermetic photon veto system is required in order to reject background from $K_L \rightarrow 2\pi^0$

decays. Using the $e^+ e^- \gamma$ final state (Dalitz decays) permits the determination of the decay vertex so that the invariant mass and transverse momentum of the $e^+ e^- \gamma$ system can be calculated, allowing considerable background rejection. We have therefore elected for this first search to require a Dalitz decay, even though the Dalitz decay branching fraction is only about $\frac{1}{80}$ of that for $\pi^0 \rightarrow \gamma \gamma$. With this technique, we found that the most important backgrounds in this experiment were due to the decays $\Lambda \rightarrow n\pi^0 (\pi^0 \rightarrow e^+ e^- \gamma)$ and $K_L \rightarrow \pi^+ e^- \gamma \nu$ (and its charge conjugate) when the pion is misidentified as an electron. It was necessary to develop cuts to identify and reject events from each of these processes.

Here we describe briefly the features of the experimental apparatus relevant to this search. Two neutral $K_L$ beams (each $\frac{1}{2} \times \frac{1}{2}$ mrad$^2$) were created at 4.8 mrad by 800 GeV protons striking a Be target. One of the two neutral beams hit a regenerator in order to produce a $K_S$ flux, but only decays from the other (vacuum) beam were used in this search. The trajectories and momenta of charged particles were reconstructed using four drift chambers and an analyzing magnet which imparted a horizontal transverse momentum ($P_t$) kick of about 200 MeV/$c$. Each drift chamber consisted of two $X$ planes and two $Y$ planes; each plane had a resolution of approximately 100 μm. A roughly circular array of 804 lead glass blocks was used to measure the energies and positions of electrons and photons. Each block measured 5.82 cm by 5.82 by 60 cm long, this depth being equal to about 19 radiation lengths. We obtained photon energy and position resolutions of $\sigma/E \cong 2.5\% + 5\%/\sqrt{E}$ and $\sim 3$ mm, respectively. In the lead glass array, there were two 11.6 cm by 11.6 cm beam holes whose centers were 11.6 cm above and below the center of the array, through which the neutral beams passed. These two beam holes were viewed by a beam hole calorimeter which was about 30 radiation lengths (1.3 interaction lengths) long. There were altogether twelve planes of photon veto counters at different positions in the spectrometer which were used to detect decay products outside the chamber and calorimeter acceptances. In this search we used $K_L$ decays occurring in a region 31 m long. Further characteristics of the E731 detector have been described elsewhere [14].

The trigger used to collect the events analyzed here required two or more charged particles, one each on

the left and right sides of the second drift chamber (1.63 m wide × 1.42 m high located about 3 meters upstream of the analyzing magnet). It also required charged particle hits in opposite quadrants of a scintillator hodoscope just in front of the lead glass calorimeter, with some overlap between quadrants near the center of the detector. These requirements were only rarely satisfied by $\pi^0$ Dalitz decays since the electron–positron pair usually has a very small opening angle [15].

In the analysis, a signal event candidate is required to have two charged tracks and one photon, where a photon is defined as an energy cluster in the lead glass not matched to either track. Both tracks were identified as electrons by the requirement that $0.925 < E/p < 1.075$, where $E$ is the total energy of the calorimeter cluster matched to the track, and $p$ is the track momentum measured in the drift chamber system. All three clusters' shapes were required to be consistent with the shape expected for electromagnetic showers. The $E/p$ and shape cuts together gave a $\pi/e$ rejection of about 100 for track momentum in the range of 2–20 GeV/$c$. Radiative $K_{e3}$ ($K_L \to \pi e \gamma \nu$) background events in which the pion was misidentified as electron were reconstructed by assuming that one of the two tracks was a pion. The neutrino is not observed, but using mass and $P_t$ constraints, its momentum (and therefore that of the decaying kaon) can be calculated up to a two-fold ambiguity in the longitudinal component. The cosine of the angle between the electron and photon in the kaon center-of-mass frame is then calculated based on the assumption that the smaller of the two kaon energy solutions is correct. The resulting distribution of cosines, shown in fig. 1, is not sensitive to this assumption. The distribution peaks sharply near +1 since the photons in $\pi e \gamma \nu$ background events are produced by internal or external bremsstrahlung, and so tend to be collinear with the electron. Events were rejected if $\cos \theta_{e\gamma} > 0.95$ for either possible assignment of one track as an electron and the other as a pion.

The energy of the photon was required to be greater than 5 GeV in order to reject the usually softer photons which were accidentally coincident with $K_{e3}$ events. To reject events with radiative external conversion and backgrounds resulting from accidental activity, we required $12 < M_{ee} < 48$ MeV/$c^2$, $M_{\pi e \gamma} < 500$ MeV/$c^2$, and $P_t^{ee} < 17$ MeV/$c$ where $M_{ee}$



Fig. 1. The histogram is the distribution of $\cos \theta_{e\gamma}$ for events surviving all other cuts. The peak at +1 is from radiative $K_{e3}$ decays. This background is removed by discarding events with $\cos \theta_{e\gamma} > 0.95$. The curve shows the distribution predicted by a Monte Carlo simulation of $K_L \to \pi^0 \nu \bar{\nu}$ with $\pi^0 \to e^+ e^- \gamma$.

and $M_{\pi e \gamma}$ are the invariant masses of the assumed $ee$ pair and $\pi e \gamma$ system, and $P_t^{ee}$ is the transverse momentum of the $ee$ pair relative to the kaon flight direction. Although the $M_{ee}$ value for a real $\pi^0$ Dalitz decay could be higher than 48 MeV/$c^2$, the cut was set to further reject the remaining $K_{e3}$ background with the misidentified pion as electron. This misidentification shifted the reconstructed $M_{ee}$ invariant mass down by the pion mass value, however due to the characteristics [15] of the $M_{ee}$ distribution of $\pi^0$ Dalitz decay, the signal sensitivity suffers only a small loss. These cuts reduced the acceptance by about 8% in a Monte Carlo signal simulation while reducing the number of events of the data sample by a factor of 18.

To normalize the total exposure of the experiment, we reconstructed $K_L \to e^+ e^- \gamma$ events from the same data sample. Fig. 2 shows the invariant $e^+ e^- \gamma$ mass distribution. Forty-nine events are seen. Based on the measured branching ratio for this mode [16] and the Monte Carlo calculated acceptance of $4.75 \times 10^{-3}$, the total number of kaon decays to which the detector was exposed is about $1.08 \times 10^9$. This agrees to within 5% with the result of an independent flux calculation based on a sample of about $3.3 \times 10^5$ $K_L \to \pi^+ \pi^-$ events collected simultaneously.

Fig. 2. Distribution of the reconstructed kaon mass for $K_L \rightarrow e^+e^-\gamma$ candidates. There are 49 events lying between 480 and 520 MeV/$c^2$. The width of the gaussian fit is 9.5 MeV/$c^2$.

Even though the beam production target was about 100 meters upstream of the decay volume, some very high energy (250–350 GeV) $\Lambda$ hyperons produced at the target lived long enough to enter the fiducial volume. The neutron from the decay $\Lambda \rightarrow n\pi^0(\pi^0 \rightarrow e^+e^-\gamma)$ usually went into the beam holes. To reduce background from this source, we rejected any event in which more than 10 GeV was deposited in the beam hole calorimeter. Because sufficient accidental activity in the beam hole calorimeter would cause good events to be discarded, this cut reduced the effective flux by about 5%. The $P_t$ spectrum of reconstructed $\pi^0$s from $\Lambda \rightarrow n\pi^0$ peaks just below 100 MeV/$c$, near the kinematic limit of 104 MeV/$c$ for this decay. Fig. 3 shows the distribution of reconstructed $e^+e^-\gamma$ invariant mass versus $P_t$ after all cuts. The empty box in the figure contains the region within which we search for $K_L \rightarrow \pi^0 \nu\bar{\nu}$ events. The events below the box are the remaining $\Lambda \rightarrow n\pi^0(\pi^0 \rightarrow e^+e^-\gamma)$ background. Events outside the sensitivity box but away from the $\pi^0$ peak are from the small fraction of radiative $K_{e3}$ decays surviving all cuts.

The search region is defined by the cuts $115 < M_{ee\gamma} < 155$ MeV/$c^2$ and $140 < P_t^{ee\gamma} < 240$ MeV/$c$. The high limit of $P_t^{ee\gamma}$ is the largest possible $P_t$ of the $\pi^0$ from $K_L \rightarrow \pi^0 \nu\bar{\nu}$ could have attained with resolution effect (231 MeV/$c$ is the kinematical limit with no resolution effect). Fig. 4 shows the distribution of re-



Fig. 3. Reconstructed $e^+e^-\gamma$ invariant mass versus the transverse momentum for events surviving all cuts. The box represents the $\pi^0\nu\bar{\nu}$ search region as described in the text. The vertical axis projection clearly shows the residual $\Lambda \rightarrow n\pi^0$ events. The remaining backgrounds are due to radiative $K_{e3}$ decays, and $K_{e3}$'s in accidental coincidence with photons, both with misidentified pions.

constructed $e^+e^-\gamma$ invariant mass versus $P_t$ from Monte Carlo simulated data of $K_L \rightarrow \pi^0\nu\bar{\nu}(\pi^0 \rightarrow e^+e^-\gamma)$ after all other cuts. Assuming a matrix element with a pure vector form factor, about 40% of $K_L \rightarrow \pi^0\nu\bar{\nu}(\pi^0 \rightarrow e^+e^-\gamma)$ events lie within the defined search region (the box shown in fig. 4). Including this factor, the Monte Carlo calculated acceptance for $K_L \rightarrow \pi^0\nu\bar{\nu}(\pi^0 \rightarrow e^+e^-\gamma)$ is $8.2 \times 10^{-4}$ for kaon energies between 20 and 220 GeV and decay vertices between 106 and 137 meters downstream of the target. We see no events within the search region, and therefore conclude with 90% confidence that the branching fraction for the decay $K_L \rightarrow \pi^0\nu\bar{\nu}$ is less than $2.2 \times 10^{-4}$.

Searches with far greater sensitivity will be required in order to observe this process at the level predicted by the standard model.

This work partially fulfilled the requirements of a

pression no longer exists in higher orders of $\chi$PT and in fact some estimates which include higher-order effects indicate the possibility of the $CP$-conserving two-photon intermediate-state amplitude being of the same size as the $CP$-violating amplitude [8,9].

Theoretical estimates of the $K_L^0 \to \pi^0\pi^0\gamma$ branching ratio range from $1\times10^{-8}$ down to $7\times10^{-11}$, where the former is derived by relating $K_L^0 \to \pi^0\pi^0\gamma$ to $K_L^0 \to \pi^+\pi^-\gamma$ [10], and the latter is estimated by chiral dimensional analysis [11]. There exists no prior experimental information on this decay.

In this article, we report on the first published search for the decay $K_L^0 \to \pi^0\pi^0\gamma$. The data for this analysis were collected by the E799 Collaboration during the 1991 Fermilab Fixed Target run. Fermilab-E799 was a dedicated rare $K_L^0$ decay experiment whose primary emphasis was the search for direct $CP$ violation in $K_L^0 \to \pi^0 e^+ e^-$. Short periods of the data taking were devoted to searching for rare $K_L^0$ decays that exclusively contained neutral particles in the final state. It is from data taken during these special runs, referred to as the neutral runs, that we derive this result.

The $K_L^0$'s used in E799 came from interactions in a Be target of 800 GeV protons provided by the Fermilab Tevatron. Two nearly parallel $K_L^0$ beams were shaped by a set of precision collimators, and the subsequent $K_L^0$ decays were observed in the detector beginning 120 m downstream of the target. The E799 detector as it was configured during the neutral runs is shown in Fig. 1. A detailed description of the detector can be found elsewhere [12,13], so only a brief summary of the detector elements most pertinent to this analysis will be given here.

Since the $K_L^0 \to \pi^0\pi^0\gamma$ final state consists of only photons, the single most important detector element in this analysis is the electromagnetic calorimeter. The electromagnetic calorimeter used during the neutral runs consisted of a 4.5 radiation length ($X_0$) Pre-Shower Detector (PSD) [12] followed by a lead-glass array. The PSD was only used during the neutral runs. The PSD was

a lead-scintillating fiber sampling calorimeter. The first lead layer was $2.25\,X_0$ thick, and the remaining $2.25\,X_0$ of lead was composed of $\frac{1}{4}X_0$ lead sheets sampled by alternating $X$ and $Y$ measuring layers of 2 mm diameter scintillating fibers. There was a total of 10 layers of fibers (5 $X$ measuring and 5 $Y$ measuring) with a total of 8960 fibers. The fibers were read out with 32 Hamamatsu R4135 position-sensitive photomultiplier tubes. As far as we know, the PSD represents the first time that this promising technology of scintillating fibers read out with position sensitive photomultiplier tubes has been implemented in a full scale detector used in a physics experiment. The lead-glass portion of the calorimeter consisted of 804 blocks measuring $(5.8\,\mathrm{cm})^2 \times 18.7\,X_0$ deep arranged in a roughly circular array of 1 m radius. There were two holes in the calorimeter which allowed for the passage of the neutral beams. Using the PSD–lead-glass calorimeter, the $K_L^0$ mass resolution measured from $K_L^0 \to \pi^0\pi^0\pi^0$ decays was $5.9\,\mathrm{MeV}/c^2$ (see Fig. 2). Using electrons from calibration data, the measured position resolution of the calorimeter was better than 1 mm for electron energies greater than 5 GeV.

Besides being able to reconstruct the $K_L^0 \to \pi^0\pi^0\gamma$ candidates in the calorimeter, the detector also needed to be able to suppress the potentially large backgrounds coming from $K_L^0 \to \pi^0\pi^0\pi^0$ decays. To help reject background to $K_L^0 \to \pi^0\pi^0\gamma$ from $K_L^0 \to \pi^0\pi^0\pi^0$, where only five of the six photons are observed, the detector was equipped with a series of 12 planes of lead-Lucite photon veto detectors that were used to reject events with photons that missed the calorimeter. Another source of background from $K_L^0 \to \pi^0\pi^0\pi^0$ occurs when two of the six photons strike the calorimeter close enough to each other so that they cannot be resolved as two photons. We refer to this pair of photons as being "fused." The primary reason for installing the PSD during the neutral runs was to reject this fused-photon background. The fine granularity of the PSD provided by the 2 mm scintillating fibers allowed photons to be resolved at separation distances of < 1 cm. Other potential backgrounds
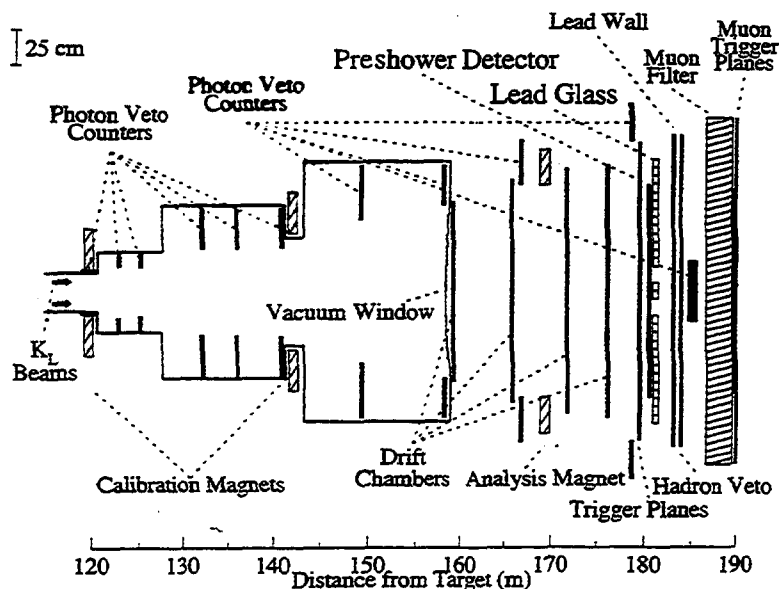


FIG. 1. The E799 Detector.
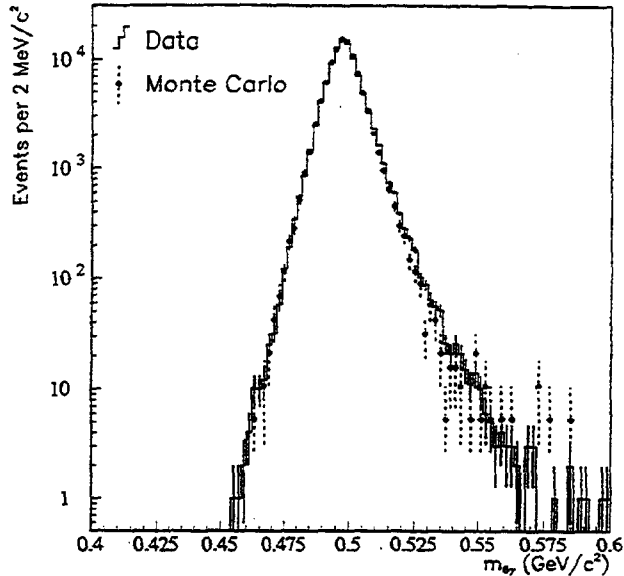
FIG. 2. The invariant mass calculated from the six photon events of the $K_L^0 \to 3\pi^0$ normalization sample for both data and Monte Carlo simulation.

from decays with charged particles in the final state were more than sufficiently rejected by the four planes of drift chambers and two planes of scintillation hodoscopes that formed part of the charged-particle spectrometer.

The on-line event selection for data used in this analysis was accomplished through the use of a multilevel hardware trigger system. The fast first-level trigger required that there be at least 55 GeV of energy deposited in the lead-glass portion of the calorimeter, no charged particles hitting any of the photon veto elements, no photons or electrons escaping through the beam holes in the lead glass, no more than one counter hit in either of the two scintillator banks just upstream of the PSD, and no activity in the hadron shower veto behind the lead glass. The second-level trigger consisted of a hardware processor that counted the number of energy clusters found in the lead glass. Clusters were required to have energy of at least 1 GeV. For the $K_L^0 \to \pi^0\pi^0\gamma$ sample, the number of clusters found by the trigger processor was required to be five, and for the $K_L^0 \to \pi^0\pi^0\pi^0$ normalization sample (which was recorded simultaneously with the $K_L^0 \to \pi^0\pi^0\gamma$ data) the number of clusters was required to equal six. The 5- and 6-cluster events were prescaled on-line by factors of 8 and 2, respectively, due to data bandwidth limitations (the primary goal of data set was to study $K_L^0 \to \pi^0\gamma\gamma$. The prescales on the 5- and 6-cluster events were necessary to optimize our sensitivity for 4-cluster events). Over the course of the 72 h run during which this data set was collected, a total of $1.6 \times 10^6$ 5-cluster events and $3.1 \times 10^6$ 6-cluster events were written to data tapes.

Off-line event selection first required that a software photon cluster-finding algorithm that used both PSD and lead-glass information find the same number of clusters as were found by the hardware processor, and that these clusters be in time with the event trigger. Photons had to

be at least 1/2 of a lead-glass block width away from the outer edge of the array and at least 1/2 of a block width away from the beam holes. Furthermore, no photon could be located in the four lead-glass blocks which separated the beam holes. Photons had to have a reconstructed energy within the range $2.0 \,\text{GeV} \leq E_\gamma \leq 60.0 \,\text{GeV}$. To reject poorly reconstructed photon showers that can occur when photons overlap in the projective readout of the PSD, it was required that the asymmetry $A$ of a photon's energy measured by the $X$ and $Y$ views of the PSD be $< 0.45$ for all showers, where $A$ is defined as

$$A = |E_x - E_y| / (E_x + E_y). \tag{1}$$

This helps reject events where a shower overlaps one shower in the $X$ view and another in the $Y$ view. This corresponds to a $4.5\sigma$ cut, based on electron showers used in calibration. It was also required that no tracks from charged particles be found in the drift chambers.

Event reconstruction involved pairing the photons into candidate $\pi^0$'s where the invariant mass of a photon pair was assumed to be the $\pi^0$ mass in order to calculate the decay $Z$ position. There are two $\pi^0$ pairs for the $K_L^0 \to \pi^0\pi^0\gamma$ candidates and three $\pi^0$ pairs for the $K_L^0 \to 3\pi^0$ candidates. In both cases, there were fifteen different pairing possibilities. The best pairing was selected based on the $\chi^2_{\text{pairing}}$ for the hypothesis that all the $\pi^0$'s shared a common decay vertex $(Z)$. Using this common $Z$ vertex position, the invariant mass of all photons $m_{n\gamma}$ defined as

$$m_{n\gamma}^2 = \frac{1}{(Z_{\text{PSD}} - Z)^2} \sum_{i>j} E_i E_j r_{ij}^2, \tag{2}$$

was calculated, where $Z_{\text{PSD}}$ is the $Z$ position of the PSD, $n$ is 5 for the $K_L^0 \to \pi^0\pi^0\gamma$ candidates and 6 for the $K_L^0 \to 3\pi^0$ candidates, $i$ and $j$ run from 1 to $n$, $E_i$ is the energy of the $i$th photon, and $r_{ij}$ is the distance between photons $i$ and $j$ as measured at the PSD. The best $\chi^2_{\text{pairing}}$ was required to be less than 3 for 5-cluster events and less than 10 for 6-cluster events. Figures 2 and 3 show the invariant mass and reconstructed $Z$ decay point of the $3\pi^0$ normalization sample.

In order to further reject $K_L^0 \to 3\pi^0$ events with missing or very low-energy photons, cuts were made requiring the reconstructed center of energy of the event to lie within the neutral beam fiducial area—no extra clusters of energy to be found in the lead glass with energy greater than 300 MeV, and no extra peaks of energy to be found in the PSD with energy greater than 300 MeV. Off-line cuts on the photon veto detectors were also made. Furthermore, events with a missing photon will have their reconstructed $Z$ vertex position shifted downstream, so only events with $Z$ upstream of 145 m from the target were kept.

To reject $K_L^0 \to 3\pi^0$ events with a fused pair of photons, all clusters were required to have a shape in the lead glass that was consistent with being from a single photon and to have rms photon shower width measured in the PSD under 9 mm. These cuts were tuned by making comparisons with well reconstructed $K_L^0 \to 3\pi^0$ decays which were free of fusions. Events were further tested
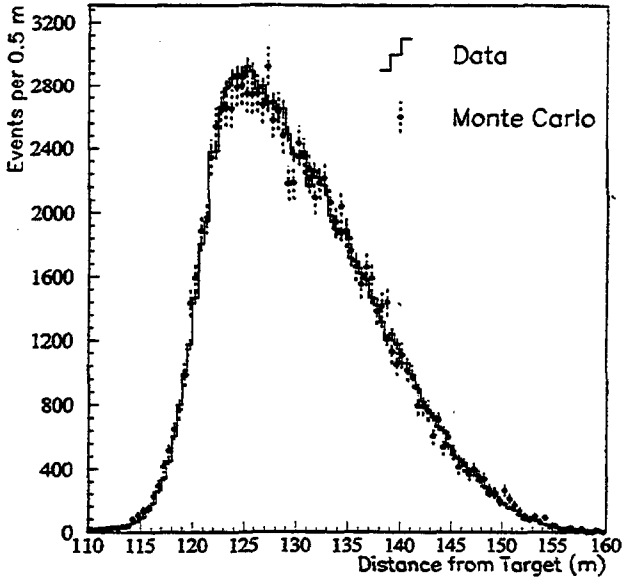
FIG. 3. The reconstructed $Z$ decay point for the $K_L^0 \to 3\pi^0$ normalization sample for both data and Monte Carlo simulation.

FIG. 4. The invariant mass of the 5-cluster data sample after all other cuts. Overlaid on the data is the $3\pi^0$ background Monte Carlo mass distribution. The dotted histogram is a mass plot after all cuts for the $K_L^0 \to \pi^0\pi^0\gamma$ Monte Carlo (arbitrary scale). The arrows indicate the signal region.

for fusions by splitting the energy of one cluster into two "photons," then reconstructing the event as a $3\pi^0$ decay. By taking three clusters and assuming one of them to be a fused pair, and that the resulting four photons come from two $\pi^0$'s, one can solve for the common $Z$ decay point $Z_{\text{fusion}}$ of the two $\pi^0$'s :

$$(Z_{\text{PSD}} - Z_{\text{fusion}})^2 = \left(\frac{1}{m_{\pi^0}}\right)^2$$

$$\times \left(\frac{1}{E_1 E_3 r_{13}^2} + \frac{1}{E_2 E_3 r_{23}^2}\right)^{-1} , \quad (3)$$

where $E_3$ is the energy of the presumed fused cluster. The two clusters which are not part of the triplet can be used to calculate another $Z$ decay point, assuming that these two photons also come from a common $\pi^0$. For real $3\pi^0$ fusion events, $Z_{\text{fusion}}$ and this second $Z$ should be roughly equal, and one can construct $\chi_{\text{fusion}}^2$ to test this hypothesis. There is a total of 30 different ways of combining clusters in this manner, and events are kept only if the smallest $\chi_{\text{fusion}}^2$ out of the 30 combinations is greater than 3.

The resulting five-cluster invariant mass distribution $m_{5\gamma}$, after all cuts except the final mass cut, is shown in Fig. 4. Also shown in Fig. 4 is an overlay of the Monte Carlo-simulated $K_L^0 \to 3\pi^0$ background that still remains after all cuts. The Monte Carlo statistics are 3.4 times that of the data, and the normalization to the data is from sidebands above and below the signal region. A fit of the Monte Carlo distribution to the data yields a $\chi^2/N_{\text{DF}}$ of 103/99, indicating that the data distribution is consistent with being purely $K_L^0 \to 3\pi^0$ background. The large hump in the distribution just below the $K_L^0$ mass is from events with one escaped photon, which forces the reconstructed invariant mass to be less than $K_L^0$ mass. The long tail that extends through the signal

region and out to high mass is from a combination of fusion events and escaped photon events where the wrong pairing out of the 15 possible was found to have the best $\chi_{\text{pairing}}^2$. This results in a misreconstructed $Z$ decay point and allows the reconstructed invariant mass to be larger than the actual $K_L^0$ mass. It should be mentioned that all cuts in this analysis were selected to optimize the experiment's sensitivity to $K_L^0 \to \pi^0\pi^0\gamma$. Tighter cuts could be made to reduce the background level and improve the signal-to-background ratio. However, the resulting loss in signal acceptance would lead to a weaker final limit on the branching ratio.

The signal region is defined from $480\,\text{MeV} \le m_{5\gamma} \le 516\,\text{MeV}$ which, in terms of the simulated $K_L^0 \to \pi^0\pi^0\gamma$ mass resolution, is a $\pm 2\sigma$ window. (The $K_L^0 \to \pi^0\pi^0\gamma$ mass resolution is worse than the $K_L^0 \to 3\pi^0$ resolution quoted earlier. The smaller number of $\pi^0$'s in the final state makes the reconstruction less constrained.) 445 events in the data sample pass all cuts. The Monte Carlo simulation predicts that 77% of these events are $K_L^0 \to 3\pi^0$ events with a missing photon, and the rest are events with a fused pair of photons. The normalized Monte Carlo simulation predicts $441.5 \pm 10.1$ (stat) $\pm$ 18.3 (syst) events in the signal region, where the systematic error is from sensitivity to the selection of the sideband regions. An absolute normalization of the Monte Carlo simulation to the data results in a prediction of the number of background events which is 21% higher than what is seen in the data. The sideband normalization yields a more conservative limit, and the discrepancy in the absolute normalization will be included in the final systematic error on the normalization. There is no indication of a signal, so we set an upper limit at a 90% confidence level for the mean number of $K_L^0 \to \pi^0\pi^0\gamma$

events to be $N_{\pi^0\pi^0\gamma} < 41.6$. This limit is calculated in the Gaussian approximation as

$$N_{\pi^0\pi^0\gamma} = (N_{\text{data}} - \mu_{\text{bkg}})$$

$$+1.282 \left(N_{\text{data}} + \sigma_{\text{stat}}^2 + \sigma_{\text{syst}}^2\right)^{1/2}, \qquad (4)$$

where $N_{\text{data}}$ is the number of observed events, $\mu_{\text{bkg}}$ is the mean number of expected background events, and the $\sigma$'s refer to the errors on the expected background level.

In order to convert this to a limit on the branching ratio, we normalize to fully reconstructed $K_L^0 \to 3\pi^0$ decays that were collected simultaneously with the $K_L^0 \to \pi^0\pi^0\gamma$ candidates, as mentioned previously. To limit possible systematic errors, we used the same cuts on the normalization sample as on the signal sample, with a few exceptions: the $\chi_{\text{pairing}}^2$ cuts were different for the two modes, no $\chi_{\text{fusion}}^2$ cut was applied to the normalization sample, and of course the normalization sample contained six photons in the final state instead of five. A total of 98 495 $K_L^0 \to 3\pi^0$ events pass all cuts.

Systematic errors on the normalization include a 3.7% error on the $K_L^0 \to 3\pi^0$ branching ratio [14]. Also considered were effects of systematic uncertainties in the understanding of the calorimeter, such as mismeasurement of the energy scale, uncertainties in the energy and position resolutions, and analogue to digital converter (ADC) pedestal shifts. The total systematic error from these sources was 1.3%. Cuts to reject fusions and to reject low-energy photons in the calorimeter contributed 7.0% to the systematic error. A Monte Carlo simulation was used to estimate the relative acceptance of $K_L^0 \to \pi^0\pi^0\gamma$ to $K_L^0 \to 3\pi^0$. This ratio, $A_{\pi^0\pi^0\gamma}/A_{3\pi^0}$, was determined to be $1.56 \pm 0.02$, where the error is the statistical er-

ror from the simulation. (In calculating $A_{\pi^0\pi^0\gamma}$, it is assumed that $K_L^0 \to \pi^0\pi^0\gamma$ is a pure electric quadrupole transition in order to generate the photon energy distribution. As a consequence of gauge invariance and Bose statistics, this is the lowest allowed multipole in the matrix element (assuming $CP$ invariance) [10]). Adding all sources of systematic error in quadrature, including the error on the Monte Carlo acceptance ratio, yields a total systematic error of 22.5%.

The single event sensitivity (SES) is then $[5.62 \pm 0.02(\text{stat}) \pm 1.23(\text{syst})] \times 10^{-6}$. Combining this with the upper limit on the number of observed $K_L^0 \to \pi^0\pi^0\gamma$ events, we set a 90% confidence level upper limit on the branching ratio of $N_{\pi^0\pi^0\gamma} \times \text{SES} = 2.3 \times 10^{-4}$. This result, while still several orders of magnitude away from theoretical predictions, represents the first published search for this decay mode. Forthcoming rare kaon experiments should be able to make significant improvements on this measurement. For example, the next generation of this experiment to be performed at Fermilab (E799-II) will have greatly improved hermetic photon detection and will use a CsI calorimeter. The superior energy resolution provided by this new calorimeter will help in both event reconstruction efficiency and background rejection. Furthermore, the statistical sensitivity will be greatly increased.

[1] For recent reviews, where earlier references can be found, see L. Littenberg and G. Valencia, Annu. Rev. Nucl. Part. Phys. **43**, 729 (1993); G. D'Ambrosio, M. Miragliuolo, and P. Santorelli, Report No. LNF-92/066 (P), 1992 (unpublished).

[2] H. Burkhardt et al., Phys. Lett. B **199**, 139 (1987).

[3] G. D. Barr et al., Phys. Lett. B **284**, 440 (1992).

[4] V. Papadimitriou et al., Phys. Rev. D **44**, R573 (1991).

[5] R. Funck and J. Kambor, Nucl. Phys. **B396**, 53 (1993).

[6] G. Ecker, A. Pich, and E. de Rafael, Phys. Lett. B **189**, 363 (1987).

[7] G. Ecker, A. Pich, and E. de Rafael, Phys. Lett. B **237**,

481 (1990).

[8] J. Flynn and L. Randall, Phys. Lett. B **216**, 221 (1989).

[9] P. Heiliger and L. M. Sehgal, Phys. Rev. D **47**, 4920 (1993).

[10] P. Heiliger and L. M. Sehgal, Phys. Lett. B **307**, 182 (1993).

[11] G. Ecker, H. Neufeld, and A. Pich, Report No. CERN-TH.6920/93, 1993 (unpublished).

[12] D. Roberts, Ph.D. thesis, UCLA, 1994.

[13] K. S. McFarland et al., Phys. Rev. Lett. **71**, 31 (1993).

[14] Particle Data Group, K. Hikasa et al., Phys. Rev. D **45**, S1 (1992).

# Measurement of the Branching Ratio of $K_L \rightarrow e^+e^-\gamma\gamma$

T. Nakaya and T. Yamanaka
*Department of Physics, Osaka University, Toyonaka, Osaka 560, Japan*

K. Arisaka, D. Roberts,* W. Slater, and M. Weaver
*University of California at Los Angeles, Los Angeles, California 90024*

R. A. Briere, E. Cheu, D. A. Harris,† K. S. McFarland,‡ A. Roodman, B. Schwingenheuer, S. V. Somalwar,§
Y. W. Wah, B. Winstein, and R. Winston
*The Enrico Fermi Institute, The University of Chicago, Chicago, Illinois 60637*

A. R. Barker
*University of Colorado, Boulder, Colorado 80309*

E. C. Swallow
*Elmhurst College, Elmhurst, Illinois 60126*
*and The Enrico Fermi Institute, The University of Chicago, Chicago, Illinois 60637*

G. J. Bock, R. Coleman, M. Crisler, J. Enagonio, R. Ford, Y. B. Hsiung,
D. A. Jensen, E. Ramberg, and R. Tschirhart
*Fermi National Accelerator Laboratory, Batavia, Illinois 60510*

E. M. Collins and G. D. Gollin
*University of Illinois, Urbana, Illinois 61801*

P. Gu, P. Haas, W. P. Hogan, S. K. Kim,∥ J. N. Matthews, S. S. Myung,∥
S. Schnetzer, G. B. Thomson, and Y. Zou
*Rutgers University, Piscataway, New Jersey 08855*
(Received 2 June 1994)

A new measurement of the $K_L \rightarrow e^+e^-\gamma\gamma$ branching ratio was carried out in Fermilab experiment E799. We observed 58 $K_L \rightarrow e^+e^-\gamma\gamma$ events. The measured branching ratio is $B(K_L \rightarrow e^+e^-\gamma\gamma, E_\gamma^* > 5 \text{ MeV}) = [6.5 \pm 1.2(\text{stat}) \pm 0.6(\text{syst})] \times 10^{-7}$.

The process $K_L \rightarrow e^+e^-\gamma\gamma$ is dominated by a $K_L$ Dalitz decay, $K_L \rightarrow e^+e^-\gamma$, with an internal bremsstrahlung photon. This radiative $K_L$ Dalitz decay provides an excellent testing ground for QED radiative corrections. These radiative corrections are particularly important for the precise measurement of the branching ratio of the parent $K_L \rightarrow e^+e^-\gamma$ decay, and for studies of the nontrivial $K_L \gamma^* \gamma$ vertex [1] which contributes to the $K_L \rightarrow e^+e^-\gamma$ form factor. In addition, the radiative $K_L$ Dalitz decay is expected to be the most serious background [2] in experiments searching for the *CP* violating decay $K_L \rightarrow \pi^0 e^+e^-$ [3] beyond the current experimental sensitivity ($\sim 10^{-9}$) [4]. The expected $K_L \rightarrow e^+e^-\gamma\gamma$ branching ratio is calculated to be $5.8 \times 10^{-7}$ with an infrared cutoff of 5 MeV in the center of mass frame of the kaon [2]. The previous measurement of $B(K_L \rightarrow e^+e^-\gamma\gamma) = (6.6 \pm 3.2) \times 10^{-7}$ is based on $17 \pm 8$ events [5]. It is important to measure this branching ratio more precisely to compare it with the expected branching ratio and to better establish the background level for $K_L \rightarrow \pi^0 e^+e^-$.

The goal of Fermilab experiment E799 was to search for the decay $K_L \rightarrow \pi^0 e^+e^-$ and other multibody rare $K_L$ decays. Two nearly parallel $K_L$ beams were produced by an 800 GeV proton beam that struck a beryllium target. After collimation the neutral beams entered the detector volume where decays were selected in the interval between 90 and 160 m from the target. A detailed description of the E799 detector can be found elsewhere [6]. Only elements of the detector used in this analysis are described here. The trajectories and momenta of charged tracks were measured with a spectrometer composed of four drift chambers and an analyzing magnet with a nominal 200 MeV/c transverse momentum kick. Each drift chamber had two horizontal and vertical planes, with a typical position resolution of 100 $\mu$m per plane. The momentum resolution was $(\sigma_p/p)^2 = (5 \times 10^{-3})^2 + \{1.4 \times 10^{-4}[p(\text{GeV}/c)]\}^2$. The energy and position of electrons and photons were measured with a lead-glass calorimeter composed of 804 blocks arranged in a circular array of 1 m radius with two beam holes in the center to allow the passage of the neutral kaon beams. Each block in the array was $(5.8 \text{ cm})^2 \times 18.7$ radiation lengths deep. The energy resolution of electrons was typically 4.4% for this data sample. The detector had two scintillator hodoscopes

between the downstream end of the spectrometer and the calorimeter, which were used for triggering. The detector also had a photon veto system used to reject events in which photons missed the calorimeter.

Two types of triggers were used for this analysis to accept both $K_L \rightarrow e^+e^-\gamma\gamma$ and $K_L \rightarrow e^+e^-\gamma$ decays. The latter decay mode is used to normalize to the total kaon flux of the experiment. Both triggers required two hits in each hodoscope, drift chamber hits consistent with two tracks, and no veto counter hits. In addition, to satisfy the $K_L \rightarrow e^+e^-\gamma\gamma$ trigger there had to be a minimum total energy in the calorimeter of 55 GeV, and four clusters of energy in the calorimeter, each cluster having an energy threshold of 2.5 GeV. Likewise, the $K_L \rightarrow e^+e^-\gamma$ trigger demanded a minimum total energy of 6 GeV and three identified clusters, and was prescaled by 14. The energy threshold for the latter trigger was set lower to search for other decay modes. The same energy threshold was used for both samples in the off-line analysis.

Off-line analysis of the data required two reconstructed tracks, each pointing to a cluster, which formed a good vertex in the detector volume. Electrons were identified by requiring the track momentum to match the calorimeter cluster energy to within 15%. Clusters not associated with tracks were considered as photon candidates. The transverse profile of each cluster was required to be consistent with that of a single electromagnetic shower. Events with exactly one (two) photon candidate(s) were used for the $K_L \rightarrow e^+e^-\gamma$ ($K_L \rightarrow e^+e^-\gamma\gamma$) sample. Kinematic quantities were then calculated assuming the photons in the event originated from the two-track vertex. Events with the square of the transverse momentum of $e^+e^-\gamma\gamma$ with respect to the $K_L$ direction ($P_t^2$) less than 1000 (MeV/$c$)$^2$ were kept. Monte Carlo simulation predicts that this cut keeps 90% of the $K_L \rightarrow e^+e^-\gamma\gamma$ signal. The $\pi^+\pi^-\gamma\gamma$ invariant mass ($M_{\pi\pi\gamma\gamma}$) was calculated by assuming that charged particles were pions, and events with this mass between 450 and 550 MeV/$c^2$ were rejected as $K_L \rightarrow \pi^+\pi^-\pi^0$ events. The acceptance loss for the decay $K_L \rightarrow e^+e^-\gamma\gamma$ was negligible.

At this stage three remaining background sources contribute to the $M_{ee\gamma\gamma}$ mass window, $466 \leq M_{ee\gamma\gamma} \leq 530$ MeV/$c^2$ ($2.3\sigma$ as determined from the Monte Carlo simulation). The first background comes from $K_L \rightarrow 2\pi^0$ decays where one $\pi^0$ Dalitz decay ($\pi^0 \rightarrow e^+e^-\gamma$) and one photon is lost or merges with other photons in the calorimeter ($K_L \rightarrow \pi^0\pi_D^0$). The second background results from misidentifying the pion as an electron in $K_L \rightarrow \pi e\nu$ decays with two extra photons from bremsstrahlung and accidental processes [$K_{e3}(2\gamma)$]. The third background is $K_L \rightarrow e^+e^-\gamma$ decays with an external bremsstrahlung photon or accidental activity [$K_L \rightarrow e^+e^-\gamma(\gamma)$].

In order to remove the $K_{e3}(2\gamma)$ background events we define the quantity

$$\min\Sigma\cos = \text{Minimum}(\cos\theta_{11} + \cos\theta_{21}, \cos\theta_{12} + \cos\theta_{22}),$$

where $\theta_{ij}$ is the angle between the $i$th electron and the $j$th photon in the center of mass frame of the kaon. This quantity distinguishes between Dalitz decays and $K_{e3}(2\gamma)$ decays since one of the photons in a Dalitz decay is usually emitted nearly opposite to the $e^+e^-$ momentum. For $K_{e3}(2\gamma)$ decays, the angles between the photons and the two charged particles are less correlated. Figure 1 shows the $\min\Sigma\cos$ distributions for both the data and the Monte Carlo simulation for $K_L \rightarrow e^+e^-\gamma\gamma$ and the major backgrounds. The Monte Carlo simulation consists of generated events overlaid with "accidental events" which correctly sampled the accidental activity in the detector. The $K_L \rightarrow e^+e^-\gamma(\gamma)$ background is included in $K_L \rightarrow e^+e^-\gamma\gamma$ events: both kinds of events have similar $\min\Sigma\cos$ distributions. In Fig. 1 the $\min\Sigma\cos$ of $K_L \rightarrow e^+e^-\gamma\gamma$ events is peaked near $-2$, well separated from the $K_{e3}(2\gamma)$ events. The $\min\Sigma\cos$ is required to be less than $-0.6$ in order to reject the $K_{e3}(2\gamma)$ background. This cut removes 93% of the $K_{e3}(2\gamma)$ background while decreasing the $K_L \rightarrow e^+e^-\gamma\gamma$ acceptance by 9%.

Another kinematic variable used to reject background is the minimum $\theta_{ij}$ angle ($\theta_{\min}$) defined above. The bremsstrahlung photon tends to be emitted in the same direction as the parent electron with a $\theta_{\min}$ of order $10^{-1}$ rad. In addition, the $\theta_{\min}$ distribution can distinguish between internal and external bremsstrahlung since the distribution for external bremsstrahlung is peaked more sharply near 0. Figure 2 shows the $\theta_{\min}$ distribution of data and Monte Carlo events after the $\min\Sigma\cos$ cut. The value of $\theta_{\min}$ is required to be larger than 0.06 rad to suppress the $K_L \rightarrow e^+e^-\gamma(\gamma)$ background, and required to be smaller than 0.5 rad mainly to suppress the $K_L \rightarrow \pi^0\pi_D^0$ background. This cut removes 87% of the $K_L \rightarrow e^+e^-\gamma(\gamma)$ background and 98% of the $K_L \rightarrow \pi^0\pi_D^0$ background while decreasing the $K_L \rightarrow e^+e^-\gamma\gamma$ acceptance by 60%.

Figure 3 shows the invariant mass distribution of the $e^+e^-\gamma\gamma$ and $e^+e^-\gamma$ events. The $e^+e^-\gamma$ events were se-
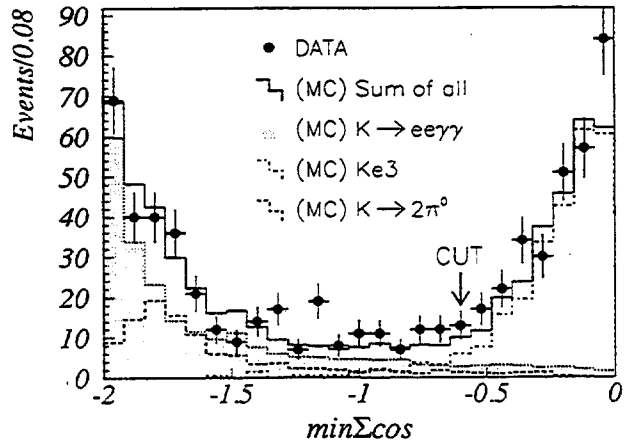


FIG. 1. The $\min\Sigma\cos$ distributions of the data and the Monte Carlo simulation. The level of the background Monte Carlo simulation was estimated by normalizing to the region of reconstructed kaon mass below the $K_L$ mass.
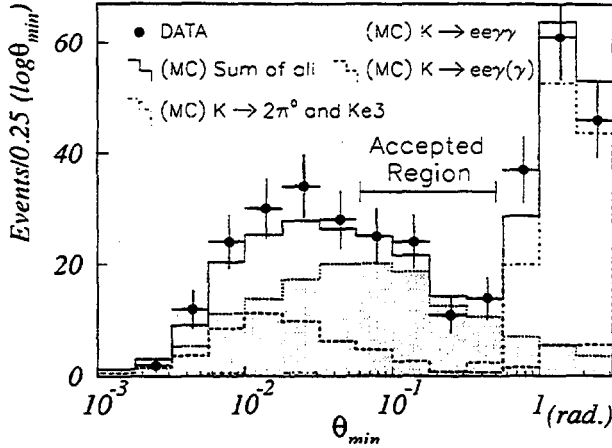
FIG. 2. The minimum angle distribution ($\theta_{min}$) between each electron, photon combination in the center of mass frame of the kaon. The normalization between the different Monte Carlo samples was based on the Monte Carlo prediction.

lected with the same cuts as the $e^+e^-\gamma\gamma$ events except for the $M_{\pi\pi\gamma\gamma}$ and the $\theta_{min}$ cuts. There is a clear peak in Fig. 3 at the kaon mass with 69 and 275 events in the kaon mass window for the $e^+e^-\gamma\gamma$ and $e^+e^-\gamma$ events, respectively. The background in the $e^+e^-\gamma\gamma$ sample consists of $K_L \to \pi^0\pi_D^0$, $K_{e3}(2\gamma)$, $K_L \to \pi^0\pi^0\pi_D^0$, and $K_L \to e^+e^-\gamma(\gamma)$ events. Other background sources such as $K_L \to \pi^+\pi^-\pi^0$, $K_L \to \pi_D^0\pi_D^0$, and $K_L \to \pi^0\pi_D^0\pi_D^0$ were negligible. We used the Monte Carlo simulation to estimate the levels of the first three sources of background. Using the reconstructed kaon mass we normalized each background to the region below the $K_L$ mass and extrapolated the number we expect in the $K_L$ mass window. The number of background events is $2.1 \pm 0.3$ events from $K_L \to \pi^0\pi_D^0$, $0.6 \pm 0.2$ events from $K_{e3}(2\gamma)$, and $0.5 \pm 0.2$ events from $K_L \to \pi^0\pi^0\pi_D^0$. The background to $e^+e^-\gamma$ events comes from $K_{e3}(\gamma)$ decays, and
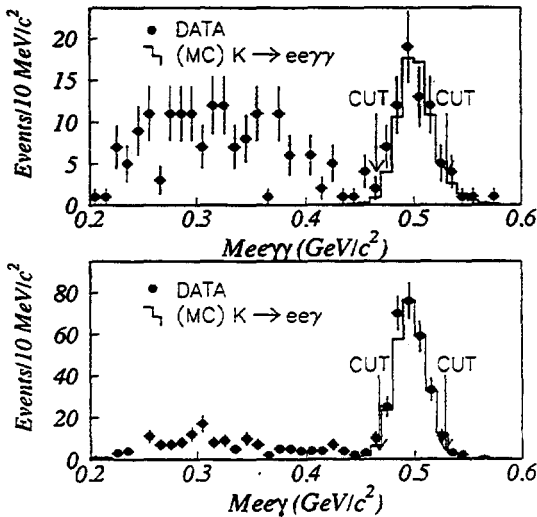


FIG. 3. The invariant mass distributions of $e^+e^-\gamma\gamma$ events and $e^+e^-\gamma$ events.

the number was estimated to be $2.3 \pm 0.9$. Correcting for these backgrounds reduces the number of $e^+e^-\gamma\gamma$ ($N_{ee\gamma\gamma}$) and $e^+e^-\gamma$ ($N_{ee\gamma}$) events to $65.8 \pm 8.3$ events and $272.7 \pm 16.6$ events, respectively.

In order to determine the $K_L \to e^+e^-\gamma\gamma$ branching ratio, it is necessary to determine the amount of $K_L \to e^+e^-\gamma(\gamma)$ background which remains in the $e^+e^-\gamma\gamma$ sample. In addition, the normalization sample, $e^+e^-\gamma$ events, consists of the radiative $K_L$ Dalitz decay with a missing photon, and the $K_L$ Dalitz decay. We use the following method to disentangle the number of radiative and nonradiative $K_L$ Dalitz decays in the $e^+e^-\gamma\gamma$ and $e^+e^-\gamma$ samples. The ratio of the number of remaining $e^+e^-\gamma\gamma$ events to $e^+e^-\gamma$ events is related to $R = B(K_L \to e^+e^-\gamma\gamma)/B(K_L \to e^+e^-\gamma)$ as

$$\frac{N_{ee\gamma\gamma}}{N_{ee\gamma}} = \frac{(1-R)A_{ee\gamma\to ee\gamma\gamma} + RA_{ee\gamma\gamma\to ee\gamma\gamma}}{(1-R)A_{ee\gamma\to ee\gamma} + RA_{ee\gamma\gamma\to ee\gamma}}, \quad (1)$$

where $B(K_L \to e^+e^-\gamma)$ is the branching ratio of the $K_L \to e^+e^-\gamma$ including the radiative decay, $e^+e^-\gamma\gamma$, and $A_{x\to y}$ is the Monte Carlo probability that an event generated as $x$ is accepted as $y$. Each acceptance, listed in Table I, was determined from a Monte Carlo simulation with energies of kaons between 35 and 220 GeV. The Monte Carlo generator for $K_L \to e^+e^-\gamma$ and $K_L \to e^+e^-\gamma\gamma$, based on Ref. [7], is divided into two parts by a cutoff parameter for $M_{\gamma\gamma}$. The value of this cutoff is fixed at $2.29$ MeV/$c^2$, the same as in Ref. [7], and it is far below the detector threshold. Above this cutoff, $K_L \to e^+e^-\gamma\gamma$ events were explicitly generated, and below it nonradiative $K_L \to e^+e^-\gamma$ events were generated. In both cases external bremsstrahlung processes were simulated.

By solving Eq. (1), $R$ is found to be $0.29 \pm 0.06$(stat). By using the numerator of Eq. (1), the number of $K_L \to e^+e^-\gamma\gamma$ events is calculated to be $57.5 \pm 8.5$(stat), and the number of $K_L \to e^+e^-\gamma(\gamma)$ events is $8.3 \pm 2.0$(stat). In the normalization sample we calculate the number of $K_L \to e^+e^-\gamma$ events to be $173.5 \pm 23.4$ and the number of $K_L \to e^+e^-\gamma\gamma$ events to be $99.2 \pm 17.0$. The calorimeter energy threshold is approximately 10 MeV in the kaon rest frame. An infrared cutoff of 5 MeV ($E_\gamma^* \geq 5$ MeV) is used to calculate the branching ratio of $K_L \to e^+e^-\gamma\gamma$, to allow direct comparison of this measurement to theoretical predictions [2] as well as the previous published measurement [5]. The Monte Carlo simulation predicts the effect of this cutoff to be $B(K_L \to e^+e^-\gamma\gamma, E_\gamma^* \geq 5$ MeV$)/B(K_L \to$

TABLE I. The acceptance for each decay mode. The numbers in the $ee\gamma\gamma*$ column are for the less restrictive $ee\gamma\gamma$ analysis as described in the text. The acceptance of observed $ee\gamma$ events includes a trigger prescale factor of $1/14$.

| Decay mode | Acceptances ($10^{-4}$) | | |
| --- | --- | --- | --- |
| | $ee\gamma$ | $ee\gamma\gamma$ | $ee\gamma\gamma*$ |
| $K_L \to ee\gamma$ | 9.2 | 0.44 | 2.8 |
| $K_L \to ee\gamma\gamma$ | 13.1 | 7.6 | 17.2 |

$e^+e^-\gamma\gamma) = 0.247$. By using the inclusive branching ratio, $B(K_L \rightarrow e^+e^-\gamma) = (9.1 \pm 0.5) \times 10^{-6}$ [1], the branching ratio of $K_L \rightarrow e^+e^-\gamma\gamma$ is measured to be $B(K_L \rightarrow e^+e^-\gamma\gamma, E_\gamma^* \geq 5 \text{ MeV}) = [6.5 \pm 1.2(\text{stat})] \times 10^{-7}$.

The main sources of systematic errors come from uncertainties in normalization, detector resolution, and background. The contribution to the total systematic from the uncertainty in the $K_L \rightarrow e^+e^-\gamma$ branching ratio is 5.5%. Uncertainties in the position resolution of extra clusters in the calorimeter introduce a systematic error through the $\theta_{min}$ cut. The position resolution of extra clusters was estimated from special electron calibration runs in the data to be 5.3 mm, while the Monte Carlo simulation predicted 4.6 mm. This disagreement leads to a 3.3% systematic error. We also found that the cuts used to isolate electromagnetic clusters introduced a systematic error of 2.2%. The total amount of material upstream of the analyzing magnet is 1.16% of a radiation length. Uncertainty in the amount of material can change the estimate of the $K_L \rightarrow e^+e^-\gamma(\gamma)$ background level. The emission probability of an external bremsstrahlung photon differed by 20% between the amount found from special calibration run data and the Monte Carlo expectation. This discrepancy results in an additional 3.5% systematic error in the branching ratio. The energy and momentum resolution couple directly into the acceptance calculation and the uncertainty in these values adds an additional 1.5% and 1.0% to the systematic error, respectively. We found that the difference between using phase space and the form factor, $\alpha_{K^*}$, resulted in a systematic error of 2.2%. The other sources of systematic error were the Monte Carlo statistics, 3.4%, and the background subtraction, 0.7%. The total systematic error was calculated to be 8.8% by adding all individual components in quadrature, leading to a final result of $B(K_L \rightarrow e^+e^-\gamma\gamma, E_\gamma^* \geq 5 \text{ MeV}) = [6.5 \pm 1.2(\text{stat}) \pm 0.6(\text{syst})] \times 10^{-7}$.

A less restrictive analysis was performed to check the above result, and to study the kinematic distributions of $K_L \rightarrow e^+e^-\gamma\gamma$ events with higher statistics. Removing the $\theta_{min}$ cut at 0.06 rad increases the number of $e^+e^-\gamma\gamma$ events to $198.8 \pm 14.3$. This less restrictive analysis gives $B(K_L \rightarrow e^+e^-\gamma\gamma, E_\gamma^* \geq 5 \text{ MeV}) = [7.7 \pm 1.4(\text{stat}) \pm 1.0(\text{syst})] \times 10^{-7}$ based on $151.6 \pm 17.4$ $K_L \rightarrow e^+e^-\gamma\gamma$ signals and $47.2 \pm 9.9$ $K_L \rightarrow e^+e^-\gamma(\gamma)$ background events. This result is consistent with the more restrictive analysis. Figure 4 shows the $M_{ee}$ and $M_{\gamma\gamma}$ distributions of the $e^+e^-\gamma\gamma$ events from the less restrictive analysis. The data distributions are consistent with the sum of the $K_L \rightarrow e^+e^-\gamma\gamma$ and the $K_L \rightarrow e^+e^-\gamma(\gamma)$ phase space Monte Carlo distributions. This is the first time these kinematic distributions were compared for the $K_L \rightarrow e^+e^-\gamma\gamma$ decay. In conclusion, we have determined the $K_L \rightarrow e^+e^-\gamma\gamma$ branching ratio to be $B(K_L \rightarrow e^+e^-\gamma\gamma, E_\gamma^* \geq 5 \text{ MeV}) = [6.5 \pm 1.2(\text{stat}) \pm 0.6(\text{syst})] \times 10^{-7}$. This measurement
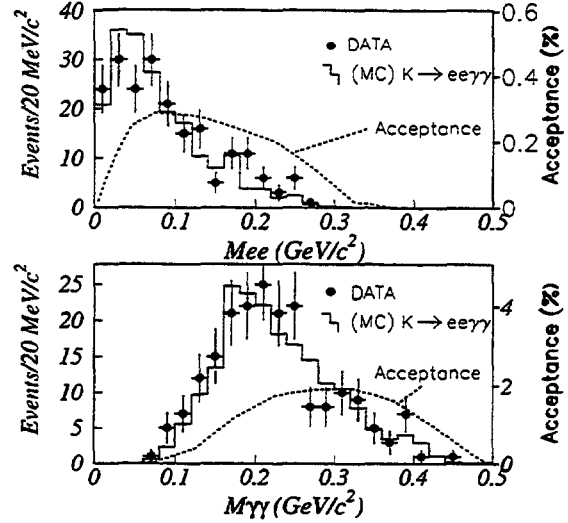


FIG. 4. The $e^+e^-$ invariant mass and the $\gamma\gamma$ invariant mass distributions without the minimum angle cut ($\theta_{min} \geq 0.06$). The Monte Carlo simulation includes the sum of the $K_L \rightarrow e^+e^-\gamma\gamma$ and $K_L \rightarrow e^+e^-\gamma(\gamma)$ samples in the proportions described in the text. Also shown is the $K_L \rightarrow e^+e^-\gamma\gamma$ acceptance as a function of $M_{ee}$ and $M_{\gamma\gamma}$.

is more precise than previous measurements, and it is consistent with theoretical expectations.

*Present address: University of California, Santa Barbara, Santa Barbara, CA 93106.

†Present address: University of Rochester, Rochester, NY 14627.

‡Present address: Fermi National Accelerator Laboratory, Batavia, IL 60510.

§Present address: Rutgers University, Piscataway, NJ 08855.

‖Present address: Seoul National University, Seoul 151-742, Korea.

[1] Particle Data Group, K.Hikasa et al., Phys. Rev. D 45, S1 (1992).

[2] H. B. Greenlee, Phys. Rev. D 42, 3724 (1990).

[3] J. F. Donoghue, B. R. Holstein, and G. Valencia, Phys. Rev. D 35, 2769 (1987).

[4] D. A. Harris et al., Phys. Rev. Lett. 71, 3918 (1993).

[5] W. M. Morse et al., Phys. Rev. D 45, 36 (1992).

[6] K. S. McFarland et al., Phys. Rev. Lett. 71, 31 (1993).

[7] L. Roberts and J. Smith, Phys. Rev. D 33, 3457 (1986).

# Polarization of $\Lambda$ and $\bar{\Lambda}$ produced by 800-GeV protons

E.J. Ramberg[a], G.J. Bock[a], R. Coleman[a], M. Crisler[a], J. Enagonio[a], R. Ford[a], Y.B. Hsiung[a],
D.A. Jensen[a], R. Tschirhart[a], K. Arisaka[b], D. Roberts[b,1], W. Slater[b], M. Weaver[b],
R.A. Briere[c], E. Cheu[c], D.A. Harris[c,2], P. Krolak[c], G. Makoff[c,3], K.S. McFarland[c,4],
A. Roodman[c], B. Schwingenheuer[c], S. Somalwar[c,5], Y.W. Wah[c], B. Winstein[c], R. Winston[c],
A.R. Barker[d], E.C. Swallow[e,f], E.M. Collins[g], G.D. Gollin[g], T. Nakaya[h], T. Yamanaka[h],
P. Gu[i], P. Haas[i], W.P. Hogan[i], S. Kim[i,6], J.N. Matthews[i], S.S. Myung[i,6], S. Schnetzer[i],
G. Thomson[i], Y. Zou[i]

[a] *Fermi National Accelerator Laboratory, Batavia, Illinois 60510, USA*
[b] *Department of Physics, University of California at Los Angeles, Los Angeles, California 90024, USA*
[c] *The Enrico Fermi Institute and the Department of Physics, The University of Chicago, Chicago, Illinois, 60637, USA*
[d] *Department of Physics, University of Colorado, Boulder, Colorado 80309, USA*
[e] *Department of Physics, Elmhurst College, Elmhurst, Illinois 60126, USA*
[f] *The Enrico Fermi Institute, The University of Chicago, Chicago, Illinois, 60637, USA*
[g] *Department of Physics, University of Illinois, Urbana, Illinois 61801, USA*
[h] *Department of Physics, Osaka University, Toyonaka, Osaka, 560 Japan*
[i] *Department of Physics, Rutgers University, Piscataway, New Jersey 08855, USA*

## Abstract

We have measured the polarization of $\Lambda$ and $\bar{\Lambda}$ hyperons produced by 800 GeV protons on a Be target at a fixed targeting angle of 4.8 mrad. Comparison with previous data at 400 GeV production energy and twice the targeting angle shows no significant energy dependence for the $\Lambda$ polarization. This is in striking contrast to the energy dependence found for $\Sigma^+$ and $\Xi^-$ polarizations. We find no evidence for $\bar{\Lambda}$ polarization at 800 GeV.

[1] Current address: Physics Department, University of California, Santa Barbara, California, 93106, USA.

[2] Current address: Physics Department, University of Rochester, Rochester, New York, 14627, USA.

[3] Current address: Solomon Brothers, New York City, New York 10048, USA.

[4] Current address: Physics Department, Fermilab, Batavia, Illinois 60510, USA.

[5] Current address: Physics Department, Rutgers University, Piscataway, New Jersey 08855, USA.

[6] Current address: Physics Department, Seoul National University, Seoul 151-742, Korea.

Although it has been known for more than 15 years that some hyperons are produced with a significant polarization in hadroproduction experiments, there is still no generally accepted mechanism [1–4] that can explain the pattern of polarizations. The recent discovery [5,6] that the anti-hyperons $\bar{\Xi}^+$ and $\bar{\Sigma}^-$ are produced polarized upsets the idea [7] that the pattern might be explained by a valence quark model. One author has suggested [4] that this discrepancy might arise from a difference in polarization between hy-
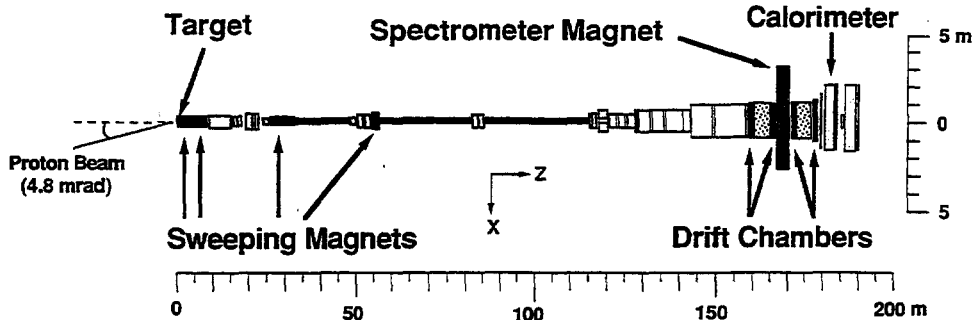
Fig. 1. Plan view of the Fermilab Meson Center beamline showing the locations of the sweeping magnets and detector elements.

peron production at 400 GeV and 800 GeV. Recently, evidence has been presented [6,8] that both $\Xi^-$ and $\Sigma^+$ hyperon polarizations differ significantly between 400 GeV and 800 GeV. Previous to these observations, it appeared [3] that high energy hyperon polarization was a function only of the hyperon transverse momentum ($p_T$) and the fraction of beam energy carried by the final state hyperon ($x_F$). The dependence of $\Lambda$ polarization on these variables has been well measured [9] at 400 GeV. An ISR experiment [10] at center of mass energies of $\sqrt{s} = 53$ and $\sqrt{s} = 62$ GeV suggests a substantial polarization increase with energy. Direct comparison is not possible, however, because of large statistical uncertainties as well as differing kinematic conditions and production processes (proton–Be versus proton–proton reactions). In this letter, we present the first measurements of $\Lambda$ and $\bar{\Lambda}$ polarization in fixed target hadroproduction at 800 GeV. In a direct comparison with 400 GeV data, we find no significant polarization difference. We also find no evidence for $\bar{\Lambda}$ polarization at this energy.

The data discussed in this letter were obtained by Fermilab Experiment 799. A secondary neutral hadron beam, including $\Lambda$ hyperons, was produced by a primary 800 GeV proton beam incident on a Be target. The targeting angle was fixed at 4.8 mrad in the horizontal plane. Since we could not vary the production angle, the $\Lambda$ spin direction was reversed by altering its precession angle in our beamline magnets.

Collimators, lead absorbers, and 4 sweeping magnets were used to create two neutral beams, separated vertically by an angle of 1.2 mrad. After the last sweeping magnet, located approximately 55 meters from the target, $\Lambda \rightarrow p\pi^-$ decays could occur without the final state particles being swept out of the

beamline. The $\Lambda$ polarization is perpendicular to the production plane, along (or opposite) the $p_P \times p_\Lambda$ direction. (For this analysis, we define the $p_P \times p_\Lambda$ direction to be the $+Y$ axis. The neutral beamline is the $+Z$ axis, and the origin of coordinates is at the production target.) The sweeping magnets all had magnetic fields in the horizontal ($X$) direction producing a precession of the $\Lambda$ spin in the $Y$–$Z$ plane. By altering the field strength and polarity of just one sweeping magnet, the $\Lambda$ spin precession was changed from $0°$ ($0.0 \pm 0.3$ T-m total field integral) to $180°$ ($16.0 \pm 0.3$ T-m). The accepted value [13] of the $\Lambda$ magnetic moment was used in calculating the required field strength. The field of this magnet was changed approximately every run, typically 8 hours. The data set used for this analysis spans 109 runs. Fig. 1 shows the locations of the sweeping magnets and detector elements along the beamline.

The decay region for $\Lambda \rightarrow p\pi^-$ decays extended from $Z = 55$ m to $Z = 160$ m. The acceptance for upstream decays was limited by a rectangular collimator at $Z = 85$ m and by the upstream beam pipe. The spectrometer began at $Z = 160$ m. The main spectrometer components were 4 drift chambers for charged particle tracking and a lead glass calorimeter for electromagnetic particle identification. Each drift chamber contained 2 $X$-measuring views and 2 $Y$-measuring views of wire planes, with each plane giving single hit resolution of approximately 100 $\mu$m. The wire spacing in the drift chamber planes was 12.7 mm, with one plane in each view offset from the other by half a wire spacing. There were 2 drift chambers on either side of an analyzing magnet whose integral transverse momentum kick was 200 MeV/c. The observed momentum resolution from the spectrometer was $(\sigma_p/p)^2 =$

$(5 \times 10^{-3})^2 + (1.4 \times 10^{-4}p)^2$, where $p$ is the momentum of the track in GeV/c. The calorimeter gave an average electron energy resolution of 4.5% for this experiment. To veto events which had additional decay products outside the acceptance of the drift chambers and calorimeter, there were veto counters at periodic stations in the region downstream of 120 meters from the target. Two hodoscopes upstream of the lead glass array were used to form the trigger for charged particles. The detector is described in greater detail elsewhere [11].

At the first level, the $\Lambda \rightarrow p\pi^-$ trigger required 2 hits in each trigger counter bank (rejecting events with 3 or more hits in both trigger banks) and the absence of energy in the various veto counters. At the second level, the trigger selected high momentum forward particles by comparing $X$-view hits in the central 10 wires of the drift chambers with patterns stored in a high-speed lookup memory module. The deflection of the selected particles by the spectrometer magnet was less than or equal to 1 wire. A further requirement of the trigger was that the number of drift chamber hits be consistent with a two track decay.

For this analysis, events with two reconstructed tracks in both the $X$ and $Y$ views and with the lower momentum track pointing toward a calorimeter cluster of energy $E > 0.5$ GeV were retained. Cuts were made to ensure good quality tracks matched to a vertex. The drift chamber hits associated with the two tracks were also required to satisfy the trigger conditions. The two tracks were required to be of opposite sign, with the higher momentum track being positively (negatively) charged for the $\Lambda$ ($\bar{\Lambda}$) sample. The lower momentum track was required to be at least 1.2 cm from the nearest calorimeter beam hole to ensure good particle identification.

Fig. 2a shows the proper lifetime ($\tau_\Lambda$) distribution for the data in the $\Lambda$ decay sample. As can be seen, the distribution is essentially flat beyond 10 lifetimes. This long-lived tail is correlated with a calorimeter response consistent with an electron signal ($E/p = 1$). These events are background from the decay $K_L \rightarrow \pi e \nu_e$ (Ke3). The level of this background is the same for the two polarization settings. Cuts of $\tau_\Lambda < 10$ and $E/p < 0.8$ were imposed on the data sample, reducing the Ke3 background to well below 1%. To ensure that each event was consistent with a $\Lambda$ or $\bar{\Lambda}$ decay, the invariant mass of the two tracks was calculated, with the
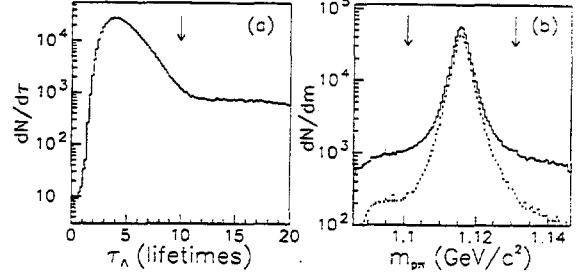


Fig. 2. For the $\Lambda$ decay sample discussed in the text, (a) is the number of proper lifetimes, $\tau_\Lambda$, from the target to the event vertex, and (b) is the reconstructed $p\pi^-$ mass in GeV/c². The solid line is before cuts on $\tau_\Lambda$, $E/p$ and transverse momentum. The dashed line is after the cuts. The arrows indicate cut values.

higher momentum track assumed to be a proton and the lower momentum track a pion. This reconstructed mass, $m_{p\pi}$, was required to be within 15 MeV/c² of the nominal [13] $\Lambda$ mass, 1115.6 MeV/c². The reconstructed momentum transverse to the $\Lambda$ line of flight from the target was required to be less than 45 MeV/c. Fig. 2b shows the $m_{p\pi}$ distribution before and after the cuts on $\tau_\Lambda$, $E/p$ and transverse momentum. The number of $\Lambda$ decay events passing all of the cuts is 379 247, of which 186 146 events have 0° polarization precession. The number of $\bar{\Lambda}$ events is 11 464, of which 5522 have 0° precession. There were approximately equal numbers of events in each beam.

Another source of background is $K^0 \rightarrow \pi^+\pi^-$ decays with the positive pion misidentified as a proton. An estimate can be made of the level of this background from the sidebands of the invariant mass spectrum: $15 < |m_{p\pi} - m_\Lambda| < 30$ MeV/c². A clear pion-pion mass peak is evident at the neutral kaon mass, 498 MeV/c². The number of $K^0$ decays in the mass sidebands that pass all other cuts is then an estimate of the background under the $\Lambda$ mass peak itself. We estimate the background from $K^0$ decays to be 0.4% (6.4%) for the $\Lambda$ ($\bar{\Lambda}$) sample.

The $\Lambda$ polarization was determined by first splitting our data into two oppositely polarized samples and then calculating the direction cosines $[\cos\theta_x, \cos\theta_y, \cos\theta_z]$ of the pion momentum vector in the $\Lambda$ rest frame. For a sample of decays where the $\Lambda$ has an average polarization $P$, the normalized direction cosine distribution [12] is

$$f_\pm(\cos\theta_i) \propto A(\cos\theta_i)[1 \pm \alpha_\pi P_i \cos\theta_i] \qquad (1)$$
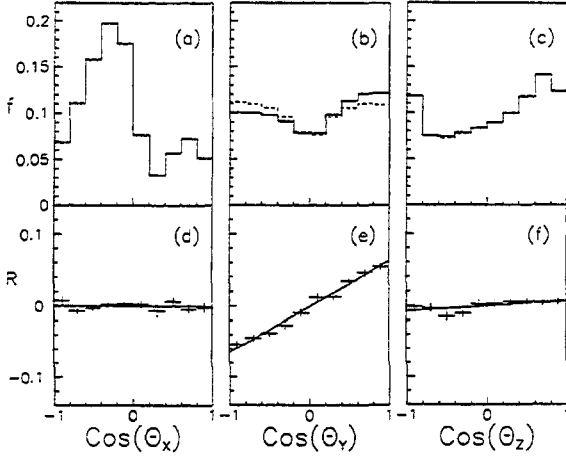
Fig. 3. Normalized direction cosine distributions $f_\pm(\cos\theta_i)$ in the (a) $X$, (b) $Y$, and (c) $Z$ directions. Solid lines are $f_+$ and dashed are $f_-$. Graphs (d), (e), and (f) show the ratio $R(\cos\theta_i)$ defined in Eq. (2). Error bars are statistical only.

for $i = x$, $y$, $z$. The currently accepted value [13] of the pion asymmetry parameter in $\Lambda \rightarrow p\pi^-$ decay is $\alpha_\pi = -0.642 \pm 0.013$. The function $A(\cos\theta_i)$ describes the experimental acceptance for $\Lambda$ decays as a function of the pion direction cosine. The quantity $f_+(\cos\theta_i)$ [$f_-(\cos\theta_i)$] is the fraction of the 0° [180°] precession sample with a given value of $\cos\theta_i$. Then the antisymmetric ratio:

$$R(\cos\theta_i) = \frac{(f_+ - f_-)}{(f_+ + f_-)} = \alpha_\pi P_i \cos\theta_i \qquad (2)$$

has a slope with respect to $\cos\theta_i$ which gives the asymmetry $\alpha_\pi P_i$, from which the polarization component $P_i$ is obtained. As long as the acceptance of the detector does not vary rapidly with time, it does not enter this calculation of the polarization because it cancels in the ratio. Backgrounds will reduce the calculated value of polarization by a factor of $(1 + B/S)$, where $B/S$ is the ratio of background events to signal events. An analysis of $K_L \rightarrow \pi^+\pi^-\pi^0$ decays, taken simultaneously with the $\Lambda$ data, shows that these kaon decays are not affected by the magnet settings. It is assumed that the kaon decays comprising our background are likewise unaffected. All polarization results presented have been corrected for background.

Fig. 3 shows a comparison between the pion direction cosine distributions for the two magnet settings. As can be seen, the pairs of distributions are essentially identical in the $X$ and $Z$ directions. In the $Y$

direction, however, the two distributions are clearly different, showing the effect of the $\Lambda$ polarization on the pion decay distribution. Also shown in Fig. 3 are plots of the ratio defined in Eq. (2). Linear fits to these graphs give average asymmetries of $\alpha_\pi P_X = -0.0002 \pm 0.0037$, $\alpha_\pi P_Y = 0.0639 \pm 0.0028$, and $\alpha_\pi P_Z = 0.0071 \pm 0.0028$. The slight deviation from zero of the average $Z$ polarization has been thoroughly investigated, and no known acceptance biases contributed to it. The data were split into separate groups of runs to look for time dependence. No significant run-to-run variation in the calculated $\Lambda$ asymmetries was found.

The $\Lambda$ data were divided into energy bins, and the polarization was calculated for each bin. Results for $P_Y$ are shown in Table 1.

There was not enough $\bar\Lambda$ data to determine polarizations for separate energy subsamples. The entire $\bar\Lambda$ data sample was analyzed using the method discussed above. A value of $\langle P_Y \rangle = 0.014 \pm 0.027$ was obtained. This sample had an average $\bar\Lambda$ energy of 252 GeV and an average transverse momentum of 1.22 GeV/c.

Our bias canceling analysis in combination with frequent polarization reversals by magnetic precession effectively eliminated most sources of systematic error. To check this we calculated $P_X$ and $P_Y$ for each $\Lambda$ energy bin and obtained values consistent with zero to within two standard deviations. We also verified that there was no significant polarization difference between events from the upper beam and the lower beam. There was likewise no significant polarization difference between upstream ($Z < 85$ m) and downstream ($Z > 85$ m) decays. Since these subsamples differed substantially in acceptance, this clearly indicates that detector acceptance effects do not significantly impact our polarization results.

The uncertainty in the accepted value [13] of $\alpha_\pi$ gives rise to a 2% polarization scale uncertainty. The 0.3 T-m uncertainty in our precession field integral would give rise to an 0.2% underestimate of the lambda polarization value. These are to be compared to our relative statistical error, which is 10% or greater for each energy bin. We have taken the view that the observed overall $Z$ asymmetry of 0.0071 provides an absolute upper limit on acceptance systematics and have conservatively assigned a corresponding systematic error for each energy bin. We also assign an

Table 1

Polarization of Λ hyperons produced at 800 GeV. The errors are statistical and systematic combined. The negative sign for $P_Y$ indicates that the polarization vector is *opposite* to $p_P \times p_\Lambda$ which defines the positive $Y$ axis.

| Energy range (GeV) | Number of Events | Average energy (GeV) | $p_T$ (GeV/c) | $x_F$ | $P_Y$ |
|---|---|---|---|---|---|
| 100–150 | 6308 | 137.5 ± 0.1 | 0.67 | 0.172 | −0.066±0.038 |
| 150–200 | 50344 | 180.5 ± 0.1 | 0.87 | 0.226 | −0.064±0.016 |
| 200–250 | 104902 | 226.2 ± 0.1 | 1.09 | 0.283 | −0.079±0.014 |
| 250–300 | 101896 | 273.7 ± 0.1 | 1.32 | 0.342 | −0.089±0.014 |
| 300–350 | 64629 | 322.5 ± 0.1 | 1.56 | 0.403 | −0.126±0.015 |
| 350–400 | 31999 | 371.5 ± 0.1 | 1.80 | 0.465 | −0.163±0.019 |
| 400–800 | 19123 | 444.2 ± 0.3 | 2.15 | 0.556 | −0.198±0.023 |
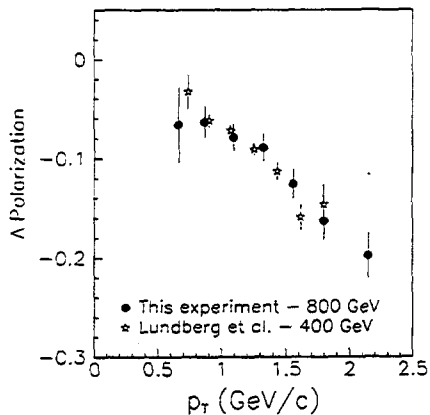


Fig. 4. Lambda polarization versus production transverse momentum $(p_T)$. For comparison, data for 400 GeV production (Ref. 10) are also shown.

uncertainty to the background estimates of 20% of their size. These systematic errors were combined in quadrature with the statistical uncertainty for each energy bin to obtain the error values given in Table 1.

Fig. 4 shows the variation of Λ polarization with production transverse momentum. On this same graph, comparable data [9] from Fermilab Experiment 555 has been superimposed. These data had a targeting angle of approximately 9.6 mrad, twice our targeting angle, and a proton beam energy of 400 GeV, half our energy. The target material for this data and for ours was Be. For a given value of $p_T$, the E555 data have the same $x_F$ value as the data presented here, and are therefore directly comparable. No significant change in Λ polarization is seen between the two production energies of 400 and 800 GeV. This contrasts markedly with the situation for $\Xi^-$ hyperons, where polariza-

tion differences are as large as a factor of two, with the 800 GeV data having the greater polarization [8]. Polarizations at these energies for $\Sigma^+$ hyperons also differ by as much as a factor of two, but with the 800 GeV data having the lower polarization [6].

In conclusion, we have determined the polarization of Λ hyperons produced by 800 GeV protons at a fixed targeting angle of 4.8 mrad. Comparing our values with those determined previously for production at 400 GeV and a targeting angle of 9.6 mrad, we find no significant energy dependence in Λ polarization at these energies. This is in clear contrast to the energy dependence observed for both $\Xi^-$ and $\Sigma^+$ polarizations at these same energies. We also find no significant $\bar{\Lambda}$ polarization at 800 GeV. These results emphasize the still puzzling nature of the polarization pattern in hadroproduction of hyperons.

References

[1] P. Skubic et al., Phys. Rev. D 18 (1978) 3115.
[2] J. Lach, Fermilab preprint CONF-91/200 (1991).
[3] L. Pondrom, Phys. Rep. 122 (1985) 58.
[4] K. Heller, Proc. of the 9th Int. Symp. on High Energy Spin Physics (Springer-Verlag, Bonn, Germany, 1990) p. 97.
[5] P. M. Ho et al., Phys. Rev. Lett. 65 (1990) 1713.

[6] A. Morelos et al., Phys. Rev. Lett. 71 (1993) 2172.

[7] T. DeGrand and H. Miettinen, Phys. Rev. D 24 (1981) 2419.

[8] J. Duryea et al., Phys. Rev. Lett. 67 (1991) 1193.

[9] B. Lundberg et al., Phys. Rev. D 40 (1989) 3557.

[10] S. Erhan et al., Phys. Lett. B 82 (1979) 301.

[11] K. McFarland et al., Phys. Rev. Lett. 71 (1993) 31;
see also K. McFarland Ph.D. thesis, University of Chicago
(1994) unpublished.

[12] C. Ankebrandt et al., Phys. Rev. Lett. 51 (1983) 863.

[13] Particle Data Group, K. Hikasa et al., Review of particle
properties, Phys. Rev. D 45 (1992) 1. This reference uses
the symbol $\alpha_-$ to denote the *proton* asymmetry parameter
in $\Lambda \rightarrow p\pi^-$ decay. Because this is a two-body decay, it is
related to the *pion* asymmetry parameter by $\alpha_\pi = -\alpha_-$.

# Measurement of the Branching Ratio and Form Factor of $K_L \to \mu^+ \mu^- \gamma$

M. B. Spencer, K. Arisaka, D. Roberts,* W. Slater, and M. Weaver

*University of California at Los Angeles, Los Angeles, California 90024*

R. A. Briere, E. Cheu, D. A. Harris,† P. Krolak, K. S. McFarland,‡ A. Roodman, B. Schwingenheuer, S. V. Somalwar,§ Y. W. Wah, B. Winstein, and R. Winston

*The Enrico Fermi Institute, The University of Chicago, Chicago, Illinois 60637*

A. R. Barker

*University of Colorado, Boulder, Colorado 80309*

E. C. Swallow

*Elmhurst College, Elmhurst, Illinois 60126*
*and The Enrico Fermi Institute, The University of Chicago, Chicago, Illinois 60637*

G. J. Bock, R. Coleman, M. Crisler, J. Enagonio,‖ R. Ford, Y. B. Hsiung, D. A. Jensen, E. Ramberg,¶ and R. Tschirhart

*Fermi National Accelerator Laboratory, Batavia, Illinois 60510*

E. M. Collins** and G. D. Gollin

*University of Illinois, Urbana, Illinois 61801*

T. Nakaya and T. Yamanaka

*Department of Physics, Osaka University, Toyonaka, Osaka 560 Japan*

P. Gu, P. Haas,†† W. P. Hogan, S. K. Kim,‡‡ J. N. Matthews, S. S. Myung,‡‡ S. Schnetzer, G. B. Thomson, and Y. Zou

*Rutgers University, Piscataway, New Jersey 08855*
(Received 5 January 1995)

We report on a measurement of the decay $K_L \to \mu^+ \mu^- \gamma$ from Fermilab experiment E799. We observe 207 candidate signal events with an estimated background of $10.5 \pm 4.0$ events and establish $B(K_L \to \mu^+ \mu^- \gamma) = [3.23 \pm 0.23(\text{stat}) \pm 0.19(\text{syst})] \times 10^{-7}$. This provides the first measurement of the $K\gamma\gamma^*$ form factor in the muonic Dalitz decay mode of the $K_L$.

PACS numbers: 13.20.Eb, 13.40.Hq, 14.40.Aq

The decay $K_L \to \mu^+ \mu^- \gamma$ is expected to be dominated by the so-called long distance contributions occurring via the $K\gamma\gamma^*$ vertex [1]. Knowledge of long distance contributions can help to determine the origin of the $\Delta I = \frac{1}{2}$ enhancement in nonleptonic weak interactions. Other rare kaon decays such as $K_L \to \mu^+ \mu^-$ depend on similar long distance contributions which must be measured in order to extract standard model parameters [2–4]. The first study of the decay $K_L \to \mu^+ \mu^- \gamma$ is an important test of the current theoretical understanding of long distance effects in neutral kaon decays.

The differential decay rate for $K_L \to l^+ l^- \gamma$ can be calculated using QED modified by a form factor $f(x)$ for the $K\gamma\gamma^*$ vertex. The result normalized to $K_L \to \gamma\gamma$ is given by

$$\Gamma_{\gamma\gamma}^{-1} \frac{d\Gamma}{dx}(K_L \to l^+ l^- \gamma) = \frac{2\alpha}{3\pi} \frac{|f(x)|^2}{x}$$
$$\times (1 - x)^3 \left(1 + \frac{2m_l^2}{x m_K^2}\right)\left(1 - \frac{4m_l^2}{x m_K^2}\right)^{1/2}, \quad (1)$$

where $x = m_{ll}^2 / m_K^2$, and the normalization is such that $f(0) = 1$. Bergström, Massó, and Singer (BMS) [1]

parametrized this form factor using a combination of a vector meson dominance model ($K_L \to \pi^0, \eta, \eta' \to \gamma^*\gamma$) and a vector-vector transition model $[K_L \to K^*\gamma \to (\rho, \omega, \phi)^*\gamma \to \gamma^*\gamma]$. In this model there is a single free parameter $\alpha_{K^*}$ and $f(x) = f_1(x) + \alpha_{K^*} f_K(x)$, where $f_1(x)$ represents the vector meson dominance amplitudes and $f_K$ is a sum over pole terms from a model of the $KK^*\gamma$ vertex. The parameter $\alpha_{K^*}$ has been inferred from studies of the decay mode $K_L \to e^+ e^- \gamma$ [5,6]. The model of Ko [4] has no free parameters and makes a definite prediction for the form factor. At this point chiral perturbation theory gives no prediction for $K_L \to \mu^+ \mu^- \gamma$ as diagrams cancel at $\mathcal{O}(p^4)$ and higher order terms have not been calculated [7].

In the decay $K_L \to l^+ l^- \gamma$ the dilepton invariant mass distribution is constrained to be between $2m_l$ and $m_K$. Together with the $1/x$ dependence of the differential rate in Eq. (1) this gives the electron mode a much larger region of decay phase space as compared to the muon mode. Thus measurements of the form factor $f(x)$ will be most sensitive to the dielectron mass spectrum (and not the $K_L \to e^+ e^- \gamma$ branching fraction) and the $K_L \to$

$\mu^+\mu^-\gamma$ branching fraction (but not the $K_L \to \mu^+\mu^-\gamma$ dimuon mass spectrum) assuming uniform experimental acceptances.

Fermilab experiment E799 was designed to search for rare $CP$ violating $K_L$ decays including $K_L \to \pi^0 e^+ e^-$ and $K_L \to \pi^0 \mu^+ \mu^-$ [8]. In the fixed target mode of the Fermilab Tevatron, 800 GeV protons were incident on a beryllium target. Two nearly parallel neutral beams were produced including $K_L$'s which then decayed in flight. The detector is described in detail elsewhere [9,10]; only those elements relevant to this analysis are mentioned here. Two hodoscope banks of vertical and horizontal counters 175 m downstream of the target were used to trigger on kaon decays with two or more charged tracks. Just downstream of these was a circular calorimeter of 804 lead-glass blocks with cross sections 5.8 cm × 5.8 cm and 18.7 radiation lengths long. The resolution for typical photon energies (12.5 GeV) in the calorimeter was 5%. Four drift chambers each with single hit resolutions of 100 $\mu$m and a magnet with a transverse momentum kick of 200 MeV/$c$ formed a spectrometer that measured charged track momenta with resolution $(\sigma_p/p)^2 = (5 \times 10^{-3})^2 + [1.4 \times 10^{-4}p/(\text{GeV}/c)]^2$. In-time energy deposits in the calorimeter were identified with a hardware cluster finder, and a fast energy sum for the entire calorimeter was used for triggering. In addition, there were several annular photon veto counters surrounding the vacuum decay volume which enabled the rejection of events with decay products outside the acceptance region of the calorimeter. Just behind the calorimeter was a 10 cm thick lead wall followed by a hodoscope bank of 45 overlapping counters designed to veto hadronic showers initiating in the calorimeter. The hadron veto was determined by an analog sum of all the individual signals from the counters. Following the hadron veto counter was a muon filter comprised of 3 m (20 interaction lengths) of steel. Muons traversing the filter steel were identified by a hodoscope bank consisting of 16 vertical, nonoverlapping counters.

In order to trigger on events with two muons we required the following elements: at least two hits in each of the trigger hodoscope banks; no hits in the photon veto counters; at least two nonadjacent hits in the muon-hodoscope bank; a sufficient number of hits in the drift chambers to be consistent with two tracks; no activity in the hadron veto counter; and a minimum energy sum of 6 GeV in the calorimeter. A two-track "minimum-bias" trigger simultaneously collected $K_L \to \pi^+\pi^-\pi^0$ events which were used for normalization. This trigger was identical to the dimuon trigger but had no muon hodoscope, hadron hodoscope, or minimum energy deposit requirements. The $K_L \to \pi^+\pi^-\pi^0$ trigger was prescaled by a factor of 3600 relative to the $K_L \to \mu^+\mu^-\gamma$ trigger.

Data were collected in the 1991 fixed target run during which $60 \times 10^6$ dimuon triggers were recorded. Data reduction began by selecting events which had two good reconstructed tracks that projected to clusters in

the calorimeter and one "photon cluster" not associated with tracks. These events were almost entirely $K_L \to \pi^\pm\mu^\mp\nu(\gamma_{\text{acc}})$ or $K_L \to \pi^+\pi^-\pi^0$ decays. In the first case the pion is misidentified as a muon or the pion decayed, and $\gamma_{\text{acc}}$ is an "accidental" photon, i.e., not associated with the $K_L$ decay. For $K_L \to \pi^+\pi^-\pi^0$ decays, both pions were misidentified as muons, and one of the photons from the decay of the $\pi^0$ escaped or overlapped a track cluster. The photon cluster was required to match a cluster found by the hardware cluster finder which had 30 ns charge integration gate as opposed to the 100 ns used to measure the energy deposited in each block. This suppressed events with out-of-time energy deposits. To further suppress contamination from accidental deposits, the photon cluster centroids were required to be at least 0.5 block from the beam holes in the calorimeter. Events with photon cluster energies below 8 GeV were rejected since accidental photons in background events typically have lower energy. This reduced the signal by 9% and rejected 42% of $K_L \to \pi^\pm\mu^\mp\nu(\gamma_{\text{acc}})$ events. Clusters not associated with tracks were required to have transverse profiles consistent with the shape expected from a photon. Track momenta were required to be above 7 GeV/$c$, greater than the 5 GeV/$c$ threshold for muons to pass through 3 m of steel. Tracks with associated energy deposits above 3 GeV in the calorimeter were rejected, thus suppressing events with hadron showers in the calorimeter. Monte Carlo studies of $K_L \to \mu^+\mu^-\gamma$ events show that the photon clusters in background events are frequently near the beamholes in the calorimeter, and are, therefore, on average closer to tracks. We use this correlation to reject background events by requiring the separation of the photon cluster and the tracks at the calorimeter to be greater than 20 cm. This cut reduces the signal by 11% and the $K_L \to \pi^\pm\mu^\mp\nu(\gamma_{\text{acc}})$ background by 33%.

For events passing these cuts, the transverse momentum squared $(P_t^2)$ versus the reconstructed invariant $\mu^+\mu^-\gamma$ mass is shown in Fig. 1. There is a clear signal in the
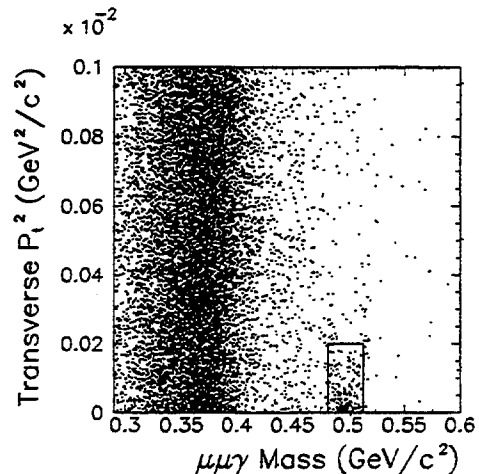


FIG. 1. $P_t^2$ vs $\mu^+\mu^-\gamma$ invariant mass distribution for events after cuts.

region near the $K_L$ mass and low $P_t^2$. The invariant mass distribution for events with $P_t^2 < 200$ MeV$^2/c^2$ is shown in Fig. 2. The region $P_t^2 < 200$ MeV$^2/c^2$ and $\mu^+\mu^-\gamma$ invariant mass in the range $0.482 < M_{\mu\mu\gamma} < 0.514$ GeV/$c^2$ was chosen so as to optimize the statistical sensitivity to the branching ratio. For the Monte Carlo simulated data that passed the previous cuts, this signal box contains 77% of the $K_L \to \mu^+\mu^-\gamma$ events, and less than 0.5% of the background events.

The large band at low $\mu^+\mu^-\gamma$ mass in Fig. 1 is consistent with $K_L \to \pi^+\pi^-\pi^0$ decays, and it falls sharply with increasing mass, producing a negligible contribution under the signal peak. We also considered the radiative process $K_L \to \pi^{\mp}\mu^{\pm}\nu\gamma$ as a potential source of background; however, it also falls rapidly with increasing mass and has negligible contribution at the kaon mass. The $K_L \to \pi^{\pm}\mu^{\mp}\nu(\gamma_{acc})$ background events produce a broad distribution in $\mu^+\mu^-\gamma$ invariant mass, and all of the background under the signal peak is consistent with having come from this process. All of the background processes considered have uniform $P_t^2$ distributions, and we determined their combined mass shape by using a region of data at $400 < P_t^2 < 1000$ MeV$^2/c^2$ (Fig. 2). The total background is estimated to be $10.5 \pm 4.0$ events out of 207 candidate signal events.

A similar analysis was performed on the minimum bias data to reconstruct $K_L \to \pi^+\pi^-\pi^0$ decays for normalization. The major difference is that now two photon clusters were required, and there was no 3 GeV track-cluster energy cut. The cut on the photon energy was relaxed to 7 GeV, thus increasing the yield. In addition, a cut of $3\sigma$ (21 MeV) around the $\pi^0$ mass was made on the reconstructed invariant mass of the two photon clusters.

High statistics Monte Carlo samples were generated for the normalization and signal modes. To properly account for activity in the detector not associated with the parent kaon decay, special "accidental" events were collected in parallel with the dimuon and minimum bias triggers. These accidental events sample the instantaneous rate of activity in the detector throughout the run, and are overlaid on the simulated decays. These simulated
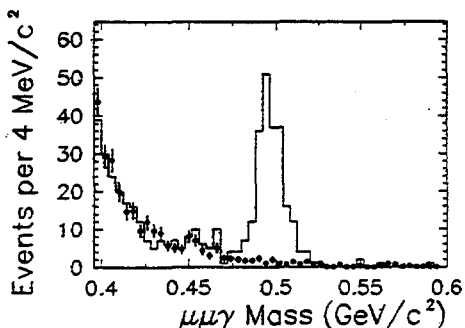
data were then passed through an identical analysis to that described above. Acceptances calculated by Monte Carlo simulations for kaons decaying in the momentum range of 20–220 GeV/$c$ and in a region 90–160 m from the target were 1.95% for $K_L \to \mu^+\mu^-\gamma$ and 1.95% for $K_L \to \pi^+\pi^-\pi^0$. With 196.5 signal events and a final sample of 20 919 $K_L \to \pi^+\pi^-\pi^0$ events, the branching ratio is $B(K_L \to \mu^+\mu^-\gamma)/B(K_L \to \pi^+\pi^-\pi^0) = [2.61 \pm 0.19(\text{stat})] \times 10^{-6}$.

The largest sources of systematic error in this ratio are due to differences between the dimuon and minimum bias triggers, the dominant contribution being from the hadron shower veto. Special muon calibration runs as well as minimum bias data were used to determine the absolute dimuon efficiency of the hadron veto to be $(55.7 \pm 2.5)\%$ [9]. The acceptance of the dimuon trigger hodoscope bank was $(65.3 \pm 1.9)\%$, which includes contributions from geometric acceptance and trigger logic. The uncertainty in the determination of background was estimated to produce at most a 2.0% change in the branching fraction. After calibrating the lead glass there were some residual nonlinearities, and this caused the branching fraction to have a small dependence on the photon cluster energy cut. The systematic uncertainty resulting from this cut was estimated to be 0.7%. Taking the branching fraction for $K_L \to \pi^+\pi^-\pi^0$ as $0.1238 \pm 0.0021$ [11] and adding all errors in quadrature the branching fraction is $B(K_L \to \mu^+\mu^-\gamma) = [3.23 \pm 0.23(\text{stat}) \pm 0.19(\text{syst})] \times 10^{-7}$. This clearly establishes the decay, while agreeing with the only previous observation of one candidate event [12].

Our result corresponds to $\Gamma_{\mu\mu\gamma}/\Gamma_{\gamma\gamma} = (5.66 \pm 0.59) \times 10^{-4}$. Using Eq. (1) with $f(x) = 1$ gives $\Gamma_{\mu\mu\gamma}/\Gamma_{\gamma\gamma} = B(K_L \to \mu^+\mu^-\gamma)/B(K_L \to \gamma\gamma) = 4.09 \times 10^{-4}$ which is $2.7\sigma$ below our measured value. This is the first indication for the presence of a form factor in the decay $K_L \to \mu^+\mu^-\gamma$. The prediction of Ko [4], $\Gamma_{\mu\mu\gamma}/\Gamma_{\gamma\gamma} = 7.45^{+0.54}_{-0.15} \times 10^{-4}$, differs from our result by $2.9\sigma$.

Assuming the model of Bergström, Massó, and Singer for the form factor, Eq. (1) can be integrated as a function of $\alpha_{K^*}$. This is shown in Fig. 3, using identical expressions for $f_1(x)$ and $f_K(x)$ as those of Ref. [6]. For this model our branching fraction corresponds to $\alpha_{K^*} = -0.018^{+0.131}_{-0.123}$.

The spectrum of dimuon invariant masses is also sensitive to the form factor. In Fig. 4 we show the dimuon mass distribution together with a Monte Carlo prediction for $f(x) = 1$. The background shape, normalized to 10.5 events, was added to the Monte Carlo data. Again the background shape was determined using high $P_t^2$ events. The assumption that the decay is dominated by the $K\gamma\gamma^*$ vertex leads directly to the dimuon invariant mass spectrum in Eq. (1), and the data in Fig. 4 follow this general shape, apart from the smaller contribution from $f(x)$. Thus the data support the assumption of $K\gamma\gamma^*$ dominance. Also shown in Fig. 4 is the ratio of data to Monte Carlo simula-



FIG. 2. Distribution of $\mu^+\mu^-\gamma$ invariant mass after cuts. Histogram is data for events with $P_t^2 < 200$ MeV$^2/c^2$ and points are data for events with $400 < P_t^2 < 1000$ MeV$^2/c^2$, and normalized to the low $P_t^2$ data.
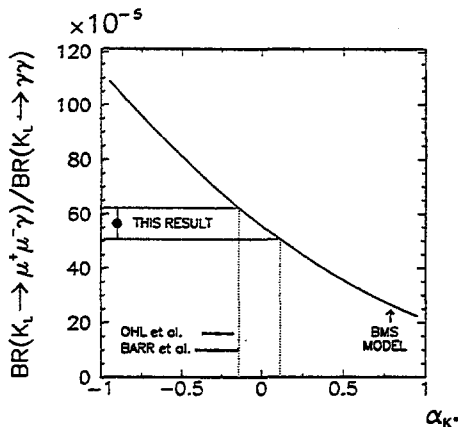
FIG. 3. This result for the branching ratio of $K_L \to \mu^+\mu^-\gamma$, normalized to $K_L \to \gamma\gamma$ (large black dot) and the extracted range of the parameter $\alpha_{K^*}$ from the model of Bergström, Massó, and Singer [1]. Also shown (horizontal error bars) are the extracted values of $\alpha_{K^*}$ from Refs. [5] and [6] for the case of $K_L \to e^+e^-\gamma$.

tion, i.e., $f(x)^2$. Using a maximum likelihood fit we obtain $\alpha_{K^*} = -0.13^{+0.21}_{-0.35}$ using the dimuon mass spectrum alone. Although less accurate, this is consistent with the value determined from the branching fraction. Together the combined best estimate is $\alpha_{K^*} = -0.028^{+0.115}_{-0.111}$. This differs by $1.8\sigma$ from the world average of $\alpha_{K^*} = -0.28 \pm 0.08$ [11], using $K_L \to e^+e^-\gamma$.

In conclusion, we have measured the branching fraction of the decay $K_L \to \mu^+\mu^-\gamma$ and the result is significantly above the prediction assuming a constant form factor.
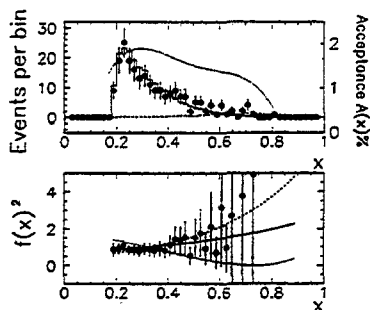


FIG. 4. Top: Dimuon mass distribution, points are data, histogram is a Monte Carlo simulation with $f(x) = 1$, dashed line is the estimated background, dotted line is the acceptance. Bottom: the ratio of data to Monte Carlo from the top plot [i.e., our measured values of $f(x)^2$]. The solid line is the result from a maximum likelihood fit. For illustration we also show predictions assuming $\alpha_{K^*} = -1$ (dashed) and $\alpha_{K^*} = +1$ (dotted). For these plots the normalization was fixed by the number of events.

This supports the BMS model and is $2.9\sigma$ away from the model of Ko. The extracted form factor shows consistency with that from $K_L \to e^+e^-\gamma$, at the $2\sigma$ level. More data, particularly copious $K_L \to e^+e^-\gamma$ with $K_L \to \mu^+\mu^-\gamma$, will better test the viability of the BMS model.

*Present address: University of California at Santa Barbara, Santa Barbara, CA 93106.

†Present address: University of Rochester, Rochester, NY 14627.

‡Present address: Fermi National Accelerator Laboratory, Batavia, IL 60510.

§Present address: Rutgers University, Piscataway, NJ 08855.

∥Present address: Colorado State University, Fort Collins, CO 80523.

¶Present address: Carnegie-Mellon University, Pittsburgh, PA 15213.

**Present address: University of West Virginia, Morgantown, WV 26506.

††Present address: Center for Neighborhood Technology, 2125 West North Ave., Chicago, IL 60647.

‡‡Present address: Seoul National University, Seoul 151-742, Korea.

‡‡Present address: Seoul National University, Seoul 151-742, Korea.

[1] L. Bergström, E. Massó, and P. Singer, Phys. Lett. 131B, 229 (1983).

[2] P. Singer, Nucl. Phys. A527, 713c (1991).

[3] G. Belánger and C. Q. Queng, Phys. Rev. D 43, 140 (1991).

[4] P. Ko, Phys. Rev. D 44, 139 (1991).

[5] G. D. Barr et al., Phys. Lett. B 240, 283 (1990).

[6] K. E. Ohl et al., Phys. Rev. Lett. 65, 1407 (1990).

[7] L. Littenberg and G. Valencia, Annu. Rev. Nucl. Part. Phys. 43, 729 (1993).

[8] D. A. Harris et al., Phys. Rev. Lett. 71, 3914 (1993); D. A. Harris et al., ibid. 71, 3918 (1993).

[9] M. B. Spencer, Ph.D. thesis, UCLA, 1995 (unpublished).

[10] K. S. McFarland et al., Phys. Rev. Lett. 71, 35 (1993).

[11] Particle Data Group, L. Montanet et al., Phys. Rev. D 50, 1173 (1994).

[12] A. S. Carroll et al., Phys. Rev. Lett. 44, 525 (1980).

# CPT Tests in the Neutral Kaon System

B. Schwingenheuer, R. A. Briere, A. R. Barker, E. Cheu, L. K. Gibbons, D. A. Harris, G. Makoff, K. S. McFarland, A. Roodman, Y. W. Wah, B. Winstein, and R. Winston

*The Enrico Fermi Institute, The University of Chicago, Chicago, Illinois 60637*

E. C. Swallow

*Elmhurst College, Elmhurst, Illinois 60126*
*and The Enrico Fermi Institute, The University of Chicago, Chicago, Illinois 60637*

G. J. Bock, R. Coleman, M. Crisler, J. Enagonio, R. Ford, Y. B. Hsiung, D. A. Jensen, E. Ramberg, R. Tschirhart, and T. Yamanaka .

*Fermi National Accelerator Laboratory, Batavia, Illinois 60510*

E. M. Collins and G. D. Gollin

*University of Illinois, Urbana, Illinois 61801*

P. Gu, P. Haas, W. P. Hogan, S. K. Kim, J. N. Matthews, S. S. Myung, S. Schnetzer, S. V. Somalwar, G. B. Thomson, and Y. Zou

*Rutgers University, Piscataway, New Jersey 08855*

Fermilab experiment E773 has measured the phases $\Phi_{+-} = 43.53° \pm 0.97°$ and $\Phi_{00} - \Phi_{+-} = 0.62° \pm 1.03°$ of the CP violating parameters $\eta_{+-}$ and $\eta_{00}$ from interference in the decay of neutral kaons into two charged or neutral pions from a pair of regenerators. New measurements of the $K_L$-$K_S$ mass difference and the $K_S$ lifetime are also given. These results test CPT symmetry and show no evidence for a violation.

CPT symmetry in particle physics follows from very general assumptions [1]; nevertheless, continued experimental tests are warranted. While C, P, and CP symmetry violations are established, no violation of CPT has been reported. The neutral kaon system has provided very stringent tests of CPT; the two most precise of these are presented in this Letter.

CP violation is parametrized by the measurable ratios of decay amplitudes:

$$\eta_{+-} = \frac{A(K_L \rightarrow \pi^+\pi^-)}{A(K_S \rightarrow \pi^+\pi^-)} = |\eta_{+-}|e^{i\Phi_{+-}}, \quad (1)$$

with a similar expression for $\eta_{00}$ in $\pi^0\pi^0$ decays. If CPT is not violated, one can show [2] that

$$\Delta\Phi = \Phi_{00} - \Phi_{+-} \approx 0. \quad (2)$$

In addition, excluding unexpectedly large CP violation in decays other than $\pi\pi$, it also follows that [2]

$$\Phi_{+-} \approx \Phi_{SW} \equiv \arctan\frac{2\Delta m}{\Delta\Gamma}, \quad (3)$$

where $\Delta m = m_L - m_S$ and $\Delta\Gamma = \Gamma_S - \Gamma_L$ are the mass and decay width differences of $K_L$ and $K_S$.

In Fermilab experiment E773, two $K_L$ beams struck two different regenerators. Downstream of its regenerator, each beam is a coherent superposition $|K_L\rangle + \rho|K_S\rangle$. Here, $\rho$ is the forward regeneration amplitude, which depends on the kaon momentum and the composition of the regenerator. The decay rate into two pions is

$$R(t) \propto |\rho e^{-it(m_S - i\Gamma_S/2)} + \eta e^{-it(m_L - i\Gamma_L/2)}|^2, \quad (4)$$

where $t$ is the proper time of the decay relative to the end of the regenerator. By measuring the decay rates into both neutral and charged pions, the phases $\Phi_\rho - \Phi_{+-}$ and $\Delta\Phi$ can be extracted from the interference terms. In addition, one can determine $\Delta m$ and $\tau_S = 1/\Gamma_S$ ($\Gamma_L$ is sufficiently well known). The regeneration amplitude $\rho$ is proportional to $(f - \bar{f})/k$, the difference of the nuclear scattering amplitudes. In our energy range, $|(f - \bar{f})/k|$ follows, to a good approximation, a power law in the kaon momentum $p = \hbar k$, and its phase is determined though a dispersion relation $(f - \bar{f})/k \propto p^{\alpha-1}\exp[-i\pi(1 + \alpha)/2]$. Elsewhere [3] the uncertainty in the extraction of the phase $\Phi_\rho$ of the regeneration amplitude from its momentum dependence is treated. This Letter, then, reports on both tests (2) and (3) of CPT symmetry.

E773 took data for three months in the 1991 fixed-target run at Fermilab. The apparatus (Fig. 1) was essentially the same as for the 1987–88 run (experiment E731 [4]) and is described in more detail elsewhere [5]. The two $K_L$ beams were produced by 800 GeV protons striking a beryllium target. The detector components were located between 115 and 190 m downstream of the target. The regenerators, which were made of plastic scintillator
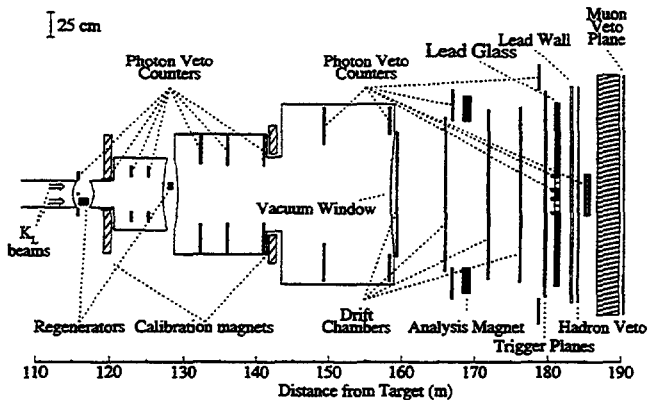
FIG. 1.   Schematic of the Fermilab E773 detector.

$(CH_{1.1})$, were placed at 117 m (the upstream regenerator, UR) and at 128 m (the downstream regenerator, DR). The UR (DR) was 1.2 (0.4) interaction lengths long. The regenerator lengths and locations were chosen to allow cross-checks of the results from the different interference patterns. They toggled between the two beams once every minute. The DR was fully active (every block was viewed by two phototubes), while only $\frac{1}{4}$ of the UR blocks were instrumented. Every block was 3.3 cm in the beam direction; the off-line cut on each was 0.2 (0.8) minimum-ionizing equivalents for the DR (UR). This vetoed almost all inelastic interactions.

The decay region for each beam extended from its regenerator to the end of the vacuum tank at 159 m. Photon vetoes for detecting particles leaving the fiducial region were located at 13 different positions inside the vacuum tank and throughout the spectrometer. The spectrometer consisted of four drift chambers and one magnet; its resolution was $\sigma_p/p = 0.50[1 \oplus p/(40\ \mathrm{GeV}/c)]\%$. After the last chamber there were two trigger scintillator hodoscopes with horizontal and vertical segmentation. Following these was a circular array of 804 lead glass blocks (each 5.8 cm $\times$ 5.8 cm $\times$ 18.7 radiation lengths deep) with two beam holes. The energy resolution varied from 3% to 6% depending on photon energy and location.

The trigger for the two-body charged decays $K \rightarrow \pi^+\pi^-$ required hits on both sides of the horizontal and vertical center lines of the drift chambers and hodoscopes (with some overlap allowed). For part of the run (set 1) there were other trigger planes at 141 m; these were removed after the drift chamber trigger was improved, increasing the charged-mode decay volume (set 2). The neutral trigger required at least 25 GeV and four or six clusters (for $2\pi^0$ and $3\pi^0$ decays) of energy in the calorimeter.

$K \rightarrow \pi^+\pi^-$ events (charged mode) were required to have two good tracks. Vertex quality and aperture cuts were applied. The ratio of cluster energy to spectrometer momentum had to be less than 0.8 to reject electrons

from $K \rightarrow \pi e \nu$. A minimum momentum requirement of 7 GeV/$c$ ensured that a muon would have penetrated a muon filter (located after the calorimeter) and fired a veto plane behind it. The $\pi^+\pi^-$ mass was required to be within 14 MeV/$c^2$ of the kaon mass; events with a $p\pi$ mass within 6 MeV/$c^2$ of the $\Lambda$ mass were rejected. Kaons that scattered in the regenerator were discarded if their transverse momentum squared $(p_T^2)$ was larger than 250 MeV$^2$/$c^2$. After all cuts, the background was small (0.2% and 0.8% for the UR and DR, respectively) and was dominated by scattered $K \rightarrow \pi^+\pi^-$ events.

For $K \rightarrow \pi^0\pi^0$ decays (neutral mode), the best pairing of the four clusters gave the decay vertex, assuming two $\pi^0$'s and a good pairing $\chi^2$. Further requirements reducing the $K \rightarrow \pi^0\pi^0\pi^0$ background were $\pi^0\pi^0$ mass between 474 and 522 MeV/$c^2$, no substantial energy in the photon vetoes, and electromagnetic cluster shapes consistent with single photons. Events with significant out-of-time energy in the calorimeter were also rejected. Kaons which scattered in the regenerators usually landed outside the profiles of the beams. For each event there were two "ring numbers," defined as $4\max[(x_E - x_C)^2, (y_E - y_C)^2]$, where the subscript $E$ ($C$) refers to the location of the center of energy (center of the given beam). These served to identify scattered kaons, as seen in Fig. 2.

The remaining background to the neutral mode had three different sources. $K_L \rightarrow \pi^0\pi^0\pi^0$ events with two photons escaping detection or overlapping were simulated and subtracted; the background fraction was 0.7% (1.3%) for the UR (DR). All significant characteristics of this background were reproduced by the simulation.

Background from beam interactions in the vacuum windows, regenerators, and air around the regenerators was small, ~0.1% for each regenerator.

The largest background was the residual from kaons scattered by the regenerators. To estimate the amount remaining after the ring number cut, a Monte Carlo simula-
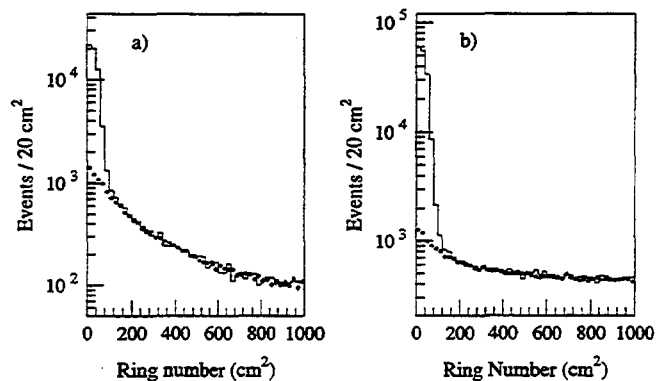


FIG. 2.   Ring number distributions of $K \rightarrow \pi^0\pi^0$ for the (a) downstream and (b) upstream regenerators. Shown are the data (histogram) and a Monte Carlo simulation (dots) of the background from scattered kaons. The cut was at 120 cm$^2$.
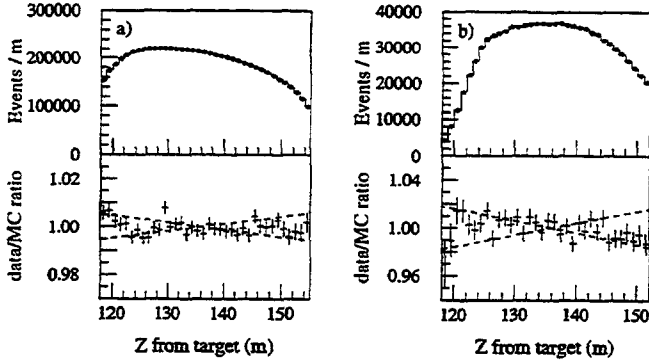
FIG. 3. Decay distributions for (a) $K_L \rightarrow \pi e \nu$ and (b) $K_L \rightarrow 3\pi^0$ decays behind the UR in set 2. The upper plots show data (histogram) and Monte Carlo results (dots), while the lower plots show the ratio of data over Monte Carlo results. Lines in each ratio plot show the possible acceptance error used in estimating systematic uncertainties. DR events showed consistent behavior.



FIG. 4. Background-subtracted, acceptance-corrected decay distributions of $K \rightarrow \pi^+\pi^-$ (set 2) and $K \rightarrow \pi^0\pi^0$ (sets 1 and 2) for upstream regenerator events in the energy bin 40–50 GeV (crosses) and the predictions from the fits with (solid line) and without (dotted line) the interference term.

tion of the scattering was used (see Fig. 2). The input to the simulation was taken from the well-determined kaon $p_T^2$ distributions for $K \rightarrow \pi^+\pi^-$. The background fractions were 2.6% for the UR and 9.0% for the DR.

Understanding the acceptance of the detector for $K \rightarrow \pi\pi$ was crucial for this analysis. It was checked by comparing the data with Mote Carlo distributions for high-statistics samples of $K_L$ decays into $3\pi^0$ and $\pi e \nu$ (Fig. 3). These decay modes were not sensitive to the regeneration parameters and provided a powerful check of our understanding of the detector. Monte Carlo simulations included an overlay of accidental activity when relevant.

Figure 4 shows the background-subtracted and acceptance-corrected decay distributions for $K \rightarrow \pi^+\pi^-$ and $K \rightarrow \pi^0\pi^0$ for one energy bin. The interference between $K_L$ and $K_S$ decays is clearly visible. Table I gives the final event totals.

The charged mode data were used to extract $\tau_S$, $\Delta m$, and $\Phi_{+-}$. Decay spectra from kaons with energies between 20 and 160 GeV and vertices from 118.5 m (130.0 m) to 154 m for the UR (DR) were fit in 10 GeV by 2 m bins. For set 1, fit was restricted to 140 m. In the fits, performed simultaneously to both regenerators in both data sets, the power law exponent $\alpha$ and the scattering amplitude $|(f - \bar{f})/k|$ at 70 GeV were floated. A total of five parameters described the normalizations

TABLE I. Background-subtracted event totals used in fits.

| Sample | UR set 1 | DR set 1 | UR set 2 | DR set 2 |
|---|---|---|---|---|
| Charged mode | 333 272 | 70 707 | 573 241 | 152 870 |
| Neutral mode | 70 362 | 24 438 | 146 869 | 50 504 |

and common energy dependence of the kaon flux on the two regenerators in the two data sets. Our choice of fits is motivated by the PDG [6] treatment of the measurements of Ref. [4].

We extract $\tau_S$ by setting $\Phi_{+-} = \Phi_{SW}$ [Eq. (3)] and floating $\Delta m$. Our result is

$$\tau_S = [0.8941 \pm 0.0014(\text{stat}) \pm 0.0009(\text{syst})] \times 10^{-10}\,\text{s}.$$

For all subsequent fits, to reduce possible biases, we fix $\tau_S$ to the world average from the PDG [6]: $(0.8926 \pm 0.0012) \times 10^{-10}$ s.

In fitting for $\Delta m$, we float $\Phi_{+-}$, with which $\Delta m$ is strongly correlated. We find

$$\Delta m = [0.5297 \pm 0.0030(\text{stat}) \pm 0.0022(\text{syst})]$$
$$\times 10^{10}\hbar\,\text{s}^{-1}.$$

This result is consistent with the value [6,7] from E731: $(0.5257 \pm 0.0049) \times 10^{10}\hbar\,\text{s}^{-1}$. The weighted average of our two measurements is $(0.5282 \pm 0.0030) \times 10^{10}\hbar\,\text{s}^{-1}$; this is nearly 2 standard deviations lower than the average of the other three results used by the PDG [6]. Note that the E731 result for $\Delta m$ was dominated by $K \rightarrow \pi^0\pi^0$ decays, while this analysis uses only $K \rightarrow \pi^+\pi^-$ decays. A lower value of $\Delta m$ brings previous measurements of $\Phi_{+-}$ into agreement with the expectation based on CPT invariance shown in Eq. (3) [4,6].

To determine $\Phi_{+-}$, we fix $\Delta m$ to the combined E731-E773 value given above. The result is

$$\Phi_{+-} = 43.53° \pm 0.58°(\text{stat}) \pm 0.49°(\text{syst}).$$

The result changes by $-0.33°$ ($0.52°$) when $\tau_S$ ($\Delta m$) is increased by $0.0012 \times 10^{-10}$ s ($0.0030 \times 10^{10}\hbar$ s). The total error, including the $\tau_S$ and $\Delta m$ dependences, is then $0.97°$. The next most precise result is from E731: $42.5° \pm 1.2°$; the central value [8] has been adjusted to consistent $\tau_S$ and $\Delta m$ values, and the systematic error is

correlated with that of the current experiment [9]. We agree well with $\Phi_{SW} = 43.37° \pm 0.17°$ ($43.64° \pm 0.17°$) derived from the PDG $\tau_S$ value and our (PDG) $\Delta m$.

The charged-mode fits have a reduced $\chi^2$ of 1.06 for 621 or 622 degrees of freedom. Correcting for hydrogen [10] in the scintillator, the nuclear scattering amplitude for carbon is $|(f - \bar{f})/k| = 1.21 \pm 0.01$ mb at 70 GeV/$c$ and varies as $p^{-0.572\pm0.007}$. Table II lists the systematic sources considered.

The fit determining $\Delta\Phi$ is similar to the $\Phi_{+-}$ fit. In addition, $\Delta\Phi$, $|\eta_{+-}/\eta_{00}|$, and normalizations for the number of $\pi^0\pi^0$ to $\pi^+\pi^-$ events in the two data sets are floated. Two parameters (found consistent with zero) for a possible energy dependence of the relative neutral to charged mode acceptance are also added. For the neutral mode the decay region extended from 120 m (130 m) to 152 m for the UR (DR) in 2 m bins and the energy range was from 40 to 150 GeV in 10 GeV bins. We find

$$\Delta\Phi = 0.62° \pm 0.71°(\text{stat}) \pm 0.75°(\text{syst}),$$

using the same values for $\tau_S$ and $\Delta m$ as in the $\Phi_{+-}$ fit. The $\chi^2$ was 1192 for 1150 degrees of freedom. This result ($0.62° \pm 1.03°$) is consistent with zero and is insensitive to the values of $\Delta m$ and $\tau_S$ used (<0.03° for one standard deviation). It is consistent with that from E731 ($-1.7° \pm 1.2°$) [4] and NA31 ($0.2° \pm 2.9°$) [11]. (Central values have been adjusted for $\tau_S$ and $\Delta m$ dependences). Averaging the E731 and E773 values (accounting for correlated systematics from the calorimeter) yields $\Delta\Phi = -0.30° \pm 0.88°$.

The systematic error for this measurement is dominated by uncertainties in the modeling of the calorimeter. The absolute energy scale was fine tuned by comparing the sharp edge in the Monte Carlo and data $z$ distributions of $K \to \pi^0\pi^0$ and $K \to 3\pi^0$ near the regenerators. The 0.08% uncertainty in the scale led to a $\pm 0.45°$ error in $\Delta\Phi$. The error contribution due to the nonlinear response of the calorimeter was estimated at 0.3°; uncertainties in the calorimeter resolution added 0.2°. Further contributions include the simulation of the background (0.4°), neutral mode acceptance (0.2°), and charged mode acceptance (0.15°).

A fit to neutral-mode data alone for $\Delta m$ and $\tau_S$ gave results consistent with those from the charged-mode fits;

the statistical power gained by adding the neutral-mode data, however, did not compensate for the additional contribution to the systematic error. The regeneration parameters were consistent in charged- and neutral-mode fits. The UR alone gave the best statistical precision (see Table I); all quantities were consistent when fitting the data from each regenerator separately.

In summary, we find that $\Delta\Phi$ is consistent with zero and that our values of $\Phi_{SW}$ and $\Phi_{+-}$ agree, consistent with $CPT$ symmetry. These results may be combined to limit the $K^0$-$\bar{K}^0$ mass difference [2], yielding

$$\frac{|m_{K^0} - m_{\bar{K}^0}|}{m_{K^0}} \approx \frac{2\Delta m}{m_{K^0}} \frac{|\eta_{+-}|}{\sin\Phi_{SW}}$$

$$\times |\Phi_{+-} - \Phi_{SW} + \Delta\Phi/3| < 1.3 \times 10^{-18}$$

at the 90% C.L.

[1] G. Lüders, K. Dan. Vidensk. Selsk. Mat. Fys. Medd. **28**, 1 (1954); W. Pauli, in *Niels Bohr and the Development of Physics* (Pergamon Press, Elmsford, NY, 1955). .

[2] V. Barmin *et al.*, Nucl. Phys. **B247**, 293 (1984); **B254**, 747(E) (1984). See also T. Nakada, in *Lepton and Photon Interactions*, edited by Persis Drell and David Rubin, AIP Conf. Proc. No. 302 (AIP, New York, 1994) for an analysis with more recent data.

[3] R.A. Briere and B. Winstein, Phys. Rev. Lett. (to be published).

[4] L.K. Gibbons *et al.*, Phys. Rev. Lett. **70**, 1199 (1993); **70**, 1203 (1993).

[5] R.A. Briere, Ph.D. thesis, University of Chicago, 1995; B. Schwingenheuer, Ph.D. thesis, University of Chicago, 1995. See also comprehensive papers by the E731 and E773 Collaborations (to be published).

[6] Particle Data Group, L. Montanet *et al.*, Phys. Rev. D **50**, 1173 (1994).

[7] L.K. Gibbons, Ph.D. thesis, University of Chicago, 1993.

[8] The 1994 PDG quotation of the E731 $\Phi_{+-}$ result has an error in the central value for the $\Delta m$ dependence. The correct result is $\Phi_{+-} = 42.21° \pm 0.9° + 189°[\Delta m - 0.5257] - 460°[\tau_S - 0.8922]$.

[9] Note that the PDG averaging of $\Phi_{+-}$ ignores the correlated $\tau_S$ and $\Delta m$ dependences, which are large.

[10] G. Bock *et al.*, Phys. Rev. Lett. **42**, 350 (1979).

[11] R. Carosi *et al.*, Phys. Lett. B **237**, 303 (1990).

TABLE II. Systematic error estimates for the charged-mode fits. The individual sources were added in quadrature to give the total error.

| | $\Phi_{+-}$ fit (deg) | $\Delta m$ fit ($10^{10}\hbar/$s) | $\tau_S$ fit ($10^{-10}$s) |
|---|---|---|---|
| Regenerator positions, sizes | 0.10 | 0.0010 | 0.0003 |
| Acceptance | 0.30 | 0.0008 | 0.0006 |
| Background subtr. | 0.15 | 0.0010 | 0.0003 |
| Regeneration phase [3] | 0.35 | 0.0008 | 0.0006 |
| $\tau_S$ dependence | — | 0.0012 | — |
| Total | 0.49 | 0.0022 | 0.0009 |

# Determining the Phase of a Strong Scattering Amplitude from Its Momentum Dependence to Better Than 1°: The Example of Kaon Regeneration

Roy A. Briere and Bruce Winstein

*The Enrico Fermi Institute, The University of Chicago, Chicago, Illinois 60637*
(Received 16 December 1994; revised manuscript received 30 March 1995)

We quantitatively study dispersion relations giving the phase of a strong scattering amplitude from its momentum dependence. We consider $C$-odd contributions to neutral kaon scattering (regeneration) where accurate measurements of both amplitudes and phases are available. We find, somewhat surprisingly, that, even including many possibly corrupting effects, the uncertainty is well below 1°. This allows an accurate determination of the phase $\phi_{+-}$ in kaon decay to test $CPT$; conversely, assuming $CPT$ symmetry, new phenomena can be limited.

Dispersion integrals relate the phase of a strong scattering amplitude at one energy to its magnitude at all energies. It is of interest to determine the accuracy with which the phase can be deduced from the momentum dependence of the magnitude. To this end, we consider primarily the scattering of neutral kaons off nuclear targets. The individual $K^0$ and $\bar{K}^0$ strong amplitudes have several contributions, but the $C$-odd piece which we treat, with opposite sign between $K^0$ and $\bar{K}^0$, is simply behaved. The weak interaction mixes $K^0$ and $\bar{K}^0$, so the scattering of the antisymmetric $K_L$ to the symmetric $K_S$ gives the $C$-odd contribution free of systematic uncertainty; this is kaon regeneration. The $K_S$ is identified by its common decay to $\pi\pi$. Furthermore, because the $K_L$ also decays to $\pi\pi$ (violating $CP$), there is interference between regenerated $K_S$ and transmitted $K_L$. The latter amplitude ($\eta_{+-}$) has been measured, allowing the determination of the phase of $\rho$, the $C$-odd scattering amplitude. Kaons also regenerate from the electric charge so that strong, weak, electromagnetic, and $CP$-violating interactions all come into play. That both the magnitude and phase of the scattering amplitude can be measured makes this system ideal for quantitative studies of dispersion relations.

Since dispersion integrals probe energies much higher than available, careful measurements can give sensitivity to new phenomena. For example, unexpected high-energy behavior in the difference between particle and antiparticle cross sections would show up at present energies in the phase of the difference amplitude. Or, neglecting such exotic possibilities, if one can determine $\phi_\rho$ from its momentum dependence, one can turn the argument around to accurately extract $\arg(\eta_{--}) = \phi_{+-}$. We use new measurements [1] with a regenerator made of scintillator ($CH_{1.1}$) to ask how well one can determine the phase of an amplitude (in this case, the regeneration amplitude) from its local momentum dependence. To our knowledge, this is the first time this question has been comprehensively addressed.

The regeneration amplitude is a combination of scattering amplitudes and a geometrical term. One finds [2] $\phi_\rho = \phi + \phi_{\text{geom}} + \pi/2$, where $\phi = \arg(f - \bar{f})$ is the phase of the difference of nuclear scattering amplitudes for $K$ and $\bar{K}$, and $\phi_{\text{geom}}$ is known.

At high energy, regeneration is dominated by the exchange of the $\omega$ Regge trajectory [3]. This by itself gives a pure power law $|(f - \bar{f})/k| \simeq p^{\alpha-1}$ (as a function of the laboratory kaon momentum, $p = \hbar k$). Analyticity of the scattering amplitudes gives the corresponding phase as $\phi = -(\pi/2)(1 + \alpha)$. Thus the momentum dependence of the modulus gives $\phi$. This "phase-power" relation (PPR) follows via standard dispersion relations independent of Regge theory. Measurements [4] of high-energy regeneration show essentially perfect power laws implying only small corrections to the deduced phase.

If the modulus only approximates a power law, the corresponding phase is nearly constant and is given, on average, by the PPR. This behavior of analytic functions is well known in electrical network engineering [5]. The key ingredient is the requirement of analyticity.

One straightforward way to analyze regeneration data involves fitting the momentum dependence of $|(f - \bar{f})/k|$ to a single power law; the PPR then gives the phase. This procedure has been used [6] and is accurate. We now explicitly consider alterations in the relationship due to multiple elements in the regenerator, multiple trajectories exchanged, possible daughter trajectories, electromagnetic regeneration, nuclear screening (elastic and inelastic), low-energy structure, and the hypothetical Odderon. The error in the extracted phase reflects uncertainties in the magnitudes of the established effects.

We first consider hydrogen, where regeneration is due to $\omega$ and $\rho$ exchange. The full expression for the amplitude is $(f - \bar{f})/k = \beta_\omega e^{i\phi_\omega} p^{\alpha_\omega - 1} - \beta_\rho e^{i\phi_\rho} p^{\alpha_\rho - 1}$. We take [7] $\alpha_\omega$ ($\alpha_\rho$) = 0.44 (0.575) and $\beta_\omega$ ($\beta_\rho$) = 11.5 (1.67). The phases $\phi_\rho = -141.8°$ and $\phi_\omega = -129.6°$ come from the PPR for each term. Over the range 20–160 GeV/$c$, the full expression follows a single power to within 1%; the phase varies from $-123.7°$ to $-120.3°$. A single-power fit gives a phase of $-122.3°$.

The single-power fit yields the average phase to better that 1° even though it differs from that of either the $\omega$ or $\rho$ alone, by more than 7°. This surprising behavior

formally arises (for sufficiently well-behaved functions) from a so-called derivative analyticity relation between the phase and the local power law [8,9] $\phi = -\pi - \tan(\frac{\pi}{2}d/d\ln p)\ln|(f - \bar{f})/k|$, with the first term holding asymptotically [10]. Threshold effects, which we limit below, can spoil this relationship [10].

Consider next $CH_{1.1}$ and assume for now regeneration off (isoscalar) C comes only from $\omega$ exchange. The deviation induced by the $\rho$ from a pure $\omega$ will be an order of magnitude smaller than for hydrogen. Uncertainties in the hydrogen parametrization have negligible effect.

Nuclear screening in carbon modifies the above assumption. Studies of $K_L$ scattering on C and Pb performed at both high and low momenta are useful [1,4,11–13]. Data with heavier nuclei (e.g., Pb), where screening effects are dominant, help validate our procedures. We treat the real part and momentum dependence of the physical Pomeron amplitude by doing a full Glauber-Franco modeling [14] of nuclear screening. With this consistent procedure we study the accuracy of the PPR. The dominant effect is multiple elastic interactions in the nucleus. Our treatment of elastic screening closely follows [15]; a full descrip-

tion, including a treatment of $p_t^2$ dependences consistent with dispersion relations, is given elsewhere [16]. The input consists of $KN$ cross sections and nuclear densities for the target nuclei. The cross sections are fit to theoretically motivated forms; this smooths the data and uses analyticity for real parts which agree with measurements. The exact functional forms are *not* important.

The four $KN$ amplitudes are written as a sum of Regge terms $F_i$ ($i = P$, $f$, $\omega$, $\rho$, and $A_2$) with the relative signs determined by charge parity and isospin. The Pomeron is parametrized as $F_P = a/p + b\pi\log p + i(c + b\log^2 p)$. (The $a/p$ term adjusts the low-energy real parts. Its magnitude is not important to our conclusions.) An equally good fit uses $F_p = a/p + b\pi/2 + i(c + b\log p)$. Our conclusions are not sensitive to the choice of $F_P$ parametrizations. Such parametrizations provide excellent fits to both the magnitude and phase of $pp$ and $p\bar{p}$ scattering up to much higher energies [17].

We now display the formula for elastic screening in a revealing form [18]. Writing $F = (4\pi/k)f$ and $F_{KN} = (F_{Kp} + F_{Kn})/2$, etc., the first few terms of the Glauber series for the forward carbon amplitudes are

$$F_{KC} \pm \bar{F}_{KC} = 12(F_{KN} \pm F_{\bar{K}N})[1 + (i/24)I_2(F_{KN}^2 \pm F_{\bar{K}N}^2)/(F_{KN} \pm F_{\bar{K}N})...]. \tag{1}$$

The coefficients $I_n$ are proportional to the probability the kaon scatters $n$ times within the nucleus; they depend on the nuclear density for which we use the harmonic-oscillator form [19].

The first term is a sum over nucleons. For the total cross section, the second term is dominated by an additional Pomeron exchange: $(F_{KC} + F_{\bar{K}C})/2 \simeq 12F_P[1 + i(I_2/24)F_P]$. For regeneration, $F_{KC} - F_{\bar{K}C} \simeq 24F_\omega[1 + i(I_2/12)F_P]$; the screening effect is twice as large. A purely imaginary, momentum-independent Pomeron would rescale the *magnitudes* of $F \pm \bar{F}$, leaving the PPR exact. A *physical* Pomeron has more complicated effects. In Table I we compare the data for carbon and lead to our full calculations, with and without elastic screening. The bulk of the observed screening is due to this easily calculated elastic effect; effects are also much larger in lead than in carbon.

To fully treat nuclear effects, we must include inelastic screening (IS) [20,21]: The incoming $K$ is scattered into inelastic intermediate states $K'$, which reform into a $K$ at a subsequent scatter. At high energies, the effect is significant, and total cross-section data [13,22] provide clear evidence. Thresholds to reach high-mass intermediate states make IS unimportant at low energies. We use the treatment of Ref. [15] where $C$-even contributions are extracted by fitting total cross-section data [4]; these also impact regeneration, whereas the $C$-odd terms essentially affect only regeneration. The latter we vary, using the new measurement of carbon regeneration [1] as a guide, and the lead data [13] rescaled to the modern value of $\eta_{+-}$. The approximations used are more accurate for carbon where the multiple scattering series converges faster.

TABLE I. Predictions and data for total cross sections and regeneration. The data are interpolations from Refs. [1,4,11–13]. Our models are based on Ref. [15] (see text) and do not make use of any regeneration data. $\Delta\sigma_{tot}$ and $\Delta\phi$ are the changes in the total cross-section and regeneration phase for the noted energy ranges. The inelastic calculations give the range as the $C$-odd inelastic term is varied from the maximum considered (from factorization) to zero; only regeneration is sensitive to these terms.

| Element | Model | $\phi_{tot}$ (mb) 70 GeV/$c$ | $\Delta\phi_{tot}$ (mb) 30–150 GeV/$c$ | $(f - \bar{f})/k$ (mb) 70 GeV/$c$ | $\Delta\phi$ (deg) 5–70 GeV/$c$ |
|---|---|---|---|---|---|
| C | No screening | 232 | 12 | 1.70 | −0.3 |
| C | Elastic screening | 194 | 9 | 1.17 | 2.5 |
| C | Inelastic screening | 182 | 3 | 1.08 → 1.21 | 5.7 → 1.4 |
| C | Data | 190(2) | 3(10) | 1.21(1) | 1.5(0.8) |
| Pb | No screening | 4024 | 203 | 32.3 | −0.3 |
| Pb | Elastic screening | 2249 | 64 | 9.3 | 8.3 |
| Pb | Inelastic screening | 2042 | −45 | 9.3 → 11.2 | 10.8 → 2.6 |
| Pb | Data | 2047(8) | −106(44) | 9.5(1) | 8.5(3.8) |

Any momentum dependence of the measured difference $\phi - \phi_{+-}$ is due to $\phi$. Our calculations are compared to the data in Table I. It is seen that the $C$-even inelastic screening term alone reproduces well the carbon phase change from 5 to 70 GeV/$c$ and that inclusion of the $C$-odd term (using factorization—see Ref. [23]) leads to several $\sigma$ disagreements. Examining the magnitude of carbon regeneration leads to the same conclusion: Only a small amount of the $C$-odd term is required. However, the lead data are better described with more $C$-odd contributions.

Using elastic screening, and adding on $C$-even and $C$-odd inelastic screening, in turn, gives three functional forms for the full amplitude. With these terms, there is a 1° to 3° change in phase across the high-energy range while $|(f - \bar{f})/k|$ deviates by $\pm 0.3\%$ from a single power. We do three fits to the high-energy carbon data [1] using these functional forms, with the amplitude and power of the $\omega$ varying. (The hydrogen is easily corrected for.) To gauge the systematic error, we examine how each fit extrapolates through the low-energy data and compare the amplitude and power to extractions independent of nuclear screening.

Figure 1 shows the results of the fits; for our nominal fit we use only elastic screening, which adequately reflects the data over the full energy range. The $\omega$ intercept is 0.437(7), in excellent agreement with a determination from scattering [0.43(1) [24]] and with a linear Chew-Frautschi plot 0.436. The amplitude from this fit agrees well with data. The fit with the $C$-odd term clearly disagrees with the low-energy data; in addition, the $\omega$
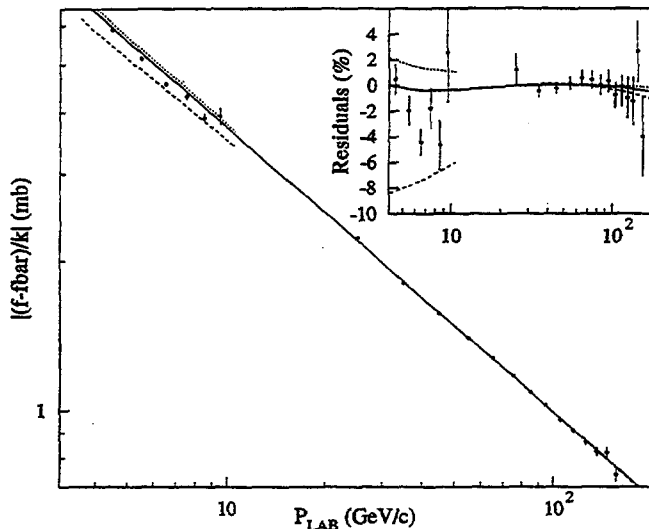


FIG. 1. The calculated magnitude of $(f - \bar{f})/k$ for carbon. The inset shows the fractional deviations relative to a single power $p^{-0.572}$. The solid curves are elastic screening only; the dotted curves include the $C$-even inelastics, fixed by the total cross-section data. The dashed curves show the effect of the maximum value of the $C$-odd inelastics considered. The data are from Ref. [15] and from a fit to the data of Ref. [5] (the errors are correlated due to common fit parameters).

intercept of 0.468(7) contradicts the other determinations. As the phase of the screening correction varies, so does its energy dependence; on average, these cancel via the PPR. The residual movement of $\phi$ with respect to our nominal fit is 0.17° (−0.24°) for the $C$-even ($C$-odd) fit. We take $\pm 0.25°$ as the systematic from nuclear screening.

In the Regge picture, subleading (daughter) trajectories may occur. We consider a sub-leading trajectory with $\alpha = \alpha_\omega - 2$ as well as $\alpha = \alpha_\omega - 1$; in the latter case, the terms differ in phase by 90°. We fit the data of Refs. [1] and [12] simultaneously. The residual shifts in the predicted phase are <0.1° with the second trajectory's amplitude statistically insignificant. Other fits give no significant evidence for a second trajectory of any $\alpha$ value.

We estimate the effects due to the detailed structure of the low-energy amplitude on the phase at our energies. The low-energy phase data [12] and the structure of the dispersion relation easily limit this to 0.2°.

For completeness, our calculations include electromagnetic regeneration which adds a constant real term (which will actually dominate regeneration, at sufficiently high energies). This gives a $(-0.10 \pm 0.05)°$ phase change; the error comes from uncertainty in the kaon mean-square charge radius [25].

The total error on the regeneration phase is then a combination in quadrature of effects summarized in the last four paragraphs: $\pm 0.35°$. The total shift in $\phi$ between a naive single-power fit and our nominal fit with the above effects was −0.04°.

We finally consider an Odderon contribution [26]. This amplitude $F_O = \cdot d + e(\ln p - i\pi/2) + f(\ln p - i\pi/2)^2$ is $C$-odd and contributes directly to $F - \bar{F}$. It can be limited by existing $pp$ and $p\bar{p}$ data. Such analyses find no evidence for the Odderon, and typically limit $|F_O/F_P| \sim 1 \times 10^{-3}$ in the 100 GeV/$c$ range [17]. Taking the Odderon parameters from the best fit of these authors, we find a shift of $-(0.2 \pm 0.6)°$ in the measured phase. Future regeneration data (assuming $CPT$ symmetry) can better limit the Odderon contribution.

While this analysis was underway, we learned of a claim [27] now published [28] that the techniques for extracting the regeneration phase at high energy in [6] have large uncertainties. The authors utilize a phase-magnitude dispersion relation; the input parametrized by $p^{\alpha-1}$ behavior for $|(f - \bar{f})/k|$ in three momentum ranges. At high energy, and low energy when available, $\alpha$ is taken from published data. Above 150 GeV, the authors introduce a large, unphysical change (kink) in the power law, the dominant source of the claimed uncertainty. The notion appears to be that, since changes in the power occurred from low to high energy, the regeneration process must not be simple and such changes may occur again. The kinks are placed just above the momentum range of the experiment, having the greatest impact on the local phase. In addition, the errors for the three regions are set fully correlated, producing the largest discrepancy. Furthermore, the error on $\alpha$ for the energy

# New Measurement of the *CP* Violation Parameter $\eta_{+-\gamma}$

J. N. Matthews, P. Gu,* P. Haas,† W. P. Hogan, S. K. Kim,‡ S. S. Myung,‡ S. Schnetzer, S. V. Somalwar,
G. B. Thomson, and Y. Zou

*Rutgers University, Piscataway, New Jersey 08855*

A. R. Barker,§ R. A. Briere, E. Cheu, D. A. Harris,‖ G. Makoff,¶ K. S. McFarland,** A. Roodman, B. Schwingenheuer,
Y. W. Wah, B. Winstein, and R. Winston

*The Enrico Fermi Institute, The University of Chicago, Chicago, Illinois 60637*

E. C. Swallow

*Elmhurst College, Elmhurst, Illinois 60126*
*and The Enrico Fermi Institute, The University of Chicago, Chicago, Illinois 60637*

G. J. Bock, R. Coleman, M. Crisler, J. Enagonio,†† R. Ford, Y. B. Hsiung, D. A. Jensen, E. Ramberg,‡‡
R. Tschirhart, and T. Yamanaka§§

*Fermi National Accelerator Laboratory, Batavia, Illinois 60510*

E. M. Collins‖‖‖‖ and G. D. Gollin

*University of Illinois, Urbana, Illinois 61801*
(Received 20 March 1995)

We have measured the *CP* violation parameter $\eta_{+-\gamma}$ in a neutral kaon experiment, E773, at Fermilab. This parameter characterizes *CP* violation in the decay $K_L \to \pi^+ \pi^- \gamma$. Kaon decays into $\pi^+ \pi^-$ collected simultaneously were used for normalization. Our result is $|\eta_{+-\gamma}| = [2.359 \pm 0.062(\text{stat}) \pm 0.040(\text{syst})] \times 10^{-3}$ with a phase $\phi_{+-\gamma} = [43.8 \pm 3.5(\text{stat}) \pm 1.9(\text{syst})]°$. The prediction that $\eta_{+-\gamma}$ should be very close to $\eta_{+-}$ is supported by our result.

The discovery of *CP* symmetry nonconservation in the weak interaction came in 1964 when the decay $K_L^0 \to \pi^+ \pi^-$ was found [1]. Within three years, the *CP*-violating decay $K_L^0 \to \pi^0 \pi^0$ was identified, as was a *CP*-violating charge asymmetry in the $K_L^0 \to \pi e \nu$ and $\pi \mu \nu$ decays [2–4]. In the subsequent time, only one additional such decay has been found: In 1993 interference between $K_S^0$ and $K_L^0$ was observed in $K^0 \to \pi^+ \pi^- \gamma$ decays by Fermilab E731 [5], proving that *CP* is violated here as well. Almost all previous measurements of *CP*-violating amplitudes are consistent with the model that *CP* violation occurs only in the $K^0/\overline{K^0}$ mass matrix and is described by one complex parameter $\epsilon$ of magnitude $\sim 2.3 \times 10^{-3}$ and phase $\sim 43°$ [6]. It is important to determine if the $\pi^+ \pi^- \gamma$ decay fits into this picture as well. The 1993 measurement was consistent with this picture within uncertainties, however, these uncertainties were relatively large when compared to the current understanding of the $\pi^+ \pi^-$ decay. The theoretical expectation is that any difference between the *CP* violation parameter describing this decay, $\eta_{+-\gamma}$, and $\eta_{+-} \approx \epsilon$ should be very small [7]. In this Letter, we report a new, more precise measurement of the $\pi^+ \pi^- \gamma$ decay amplitude.

There are two processes which contribute to the $\pi^+ \pi^- \gamma$ decay amplitude: inner bremsstrahlung (IB) and direct emission (DE). The $K_S^0$ decay is dominated by the IB process where there is a $K_S^0 \to \pi^+ \pi^-$ decay with a photon radiated by one of the final-state pions. For the $K_L^0$ decay, this process is suppressed (because the underlying $\pi^+ \pi^-$ decay violates *CP* symmetry) thereby allowing the observation of the DE process where the photon comes from the primary decay vertex. Previous experiments have found that the spectrum of photon energies in the kaon center of mass frame fits an electric dipole (*E*1) form for the IB term and a magnetic dipole (*M*1) form, modified for the effects of vector meson intermediaries, for the DE term [8–10]. The fact that the IB and DE components have different photon energy spectra allows one to determine the ratio of their contribution to the $K_L^0$ decay rate: $r = (\text{DE rate})/(\text{IB rate})$ [9–11]. Finally, the *E*1 term for the $K_S^0$ ($K_L^0$) is *CP* conserving (violating) and the modified *M*1 term for the $K_L^0$ is *CP* conserving.

Since the terms in the multipole expansion of each decay amplitude are orthogonal, interference between $K_S^0$ and $K_L^0$ will occur only for like-term multipoles. The principal contribution to the interference comes from the two IB *E*1 decays; however, higher-order multipoles contribute if present. In addition, although direct *CP* violation is expected to be small, it could present itself through a DE *E*1 transition of the $K_L^0$ interfering with the IB *E*1 transition

of the $K_S^0$. Therefore, what one measures is the ratio of decay amplitudes:

$$\eta_{+-\gamma} = \frac{A(K_L \rightarrow \pi^+\pi^-\gamma, CP \text{ violating})}{A(K_S \rightarrow \pi^+\pi^-\gamma)}.$$  (1)

In the present experiment, we used the phenomenon of coherent regeneration to study the interference between the $K_L$ and $K_S$ decay amplitudes. As a $K_L$ beam passes through material, the $K^0/\overline{K^0}$ mixture is altered, causing $K_S$ mesons to appear in the beam. The number of $\pi^+\pi^-\gamma$ decays per unit proper time observed downstream of the regenerator is

$$\frac{dN}{d\tau} = \frac{N_S B_{+-\gamma}}{|\rho|^2 \tau_S} \{|\rho|^2 e^{-\tau/\tau_S} + |\eta_{+-\gamma}|^2 e^{-\tau/\tau_L}(1 + r) + 2|\rho||\eta_{+-\gamma}|\cos(\Delta m\tau + \phi_\rho - \phi_\eta)e^{-\tau(1/\tau_s + 1/\tau_L)/2}\},$$  (2)

where $N_S$ is the number of regenerated $K_S$, $B_{+-\gamma}$ is the $K_S \rightarrow \pi^+\pi^-\gamma$ branching ratio, $\tau_S$ ($\tau_L$) is the $K_S$ ($K_L$) lifetime, and $\Delta m$ is the $K_L - K_S$ mass difference. The complex parameter $\rho$, called the regeneration amplitude, is the ratio of coherently regenerated $K_S$ to transmitted $K_L$ amplitudes and $\phi_\rho$ ($\phi_\eta$) is the phase of $\rho$ ($\eta_{+-\gamma}$).

The results quoted here come from Fermilab experiment 773, which was performed in the Meson Center beam line. Two nearly parallel $K_L$ beams were produced from an 800 GeV/$c$ primary proton beam striking a beryllium target. The $K_L$ beams themselves were incident on our apparatus which consisted of a pair of regenerators and an evacuated decay vessel followed by a magnetic spectrometer and a lead glass electromagnetic calorimeter as shown in Fig. 1.

The upstream regenerator was 1.2 interaction lengths long and was 11.28 m upstream of the shorter (0.4 interaction length) downstream regenerator. The two regenerators were composed of scintillator and instrumented with photomultiplier tubes for vetoing events in which the kaon underwent inelastic scattering within the regenerator or where the decay occurred before the downstream end of the regenerator. The regenerators were alternated between the two beams between spills to reduce systematic errors.

The spectrometer consisted of four drift chambers, two in front of and two behind the analyzing magnet. The magnet provided a transverse momentum kick of 200 MeV/$c$. Each chamber contained two horizontal and two vertical planes of wires with position resolution 80–100 $\mu$m, yielding a momentum resolution of $\sigma_p/p = $

$0.45[1 \oplus p/(40 \text{ GeV}/c)]\%$. The calorimeter was a circular array of 804 lead glass blocks, each $5.81 \times 5.81$ cm$^2$ in cross section and 18.7 radiation lengths deep, with a photon energy resolution which varied from 3% to 6% depending on photon energy and location. A more detailed description of the apparatus may be found elsewhere [12].

The trigger demanded that two oppositely charged particles traverse the detector by requiring that there be one track on either side of the horizontal and vertical midplanes of two scintillator hodoscopes downstream of the spectrometer magnet and chambers. Events were vetoed if charged particles struck any of the annular veto counters at various stations along the edges of the vacuum vessel or if there was a hit in the muon veto plane. In addition, we required there be a hit in a pair of trigger hodoscopes at 141 m. Approximately half way through the run, these planes were removed (thereby increasing the length of the decay volume) and their function in the trigger was replaced by new demands on the pattern of hits in the drift chambers. No requirement was made on information contained in the lead glass calorimeter.

The data were divided into four sets (according to which regenerator the kaon traversed and whether the hodoscope at 141 m had been removed) which were analyzed independently. In the $\pi^+\pi^-\gamma$ analysis, each event was required to have two tracks in the spectrometer coincidental with at least one cluster in the calorimeter with an energy greater than 1.5 GeV, not associated with a charged track. This photon was required to have an energy greater than 20 MeV in the kaon center of mass. To select coherently regenerated $\pi^+\pi^-\gamma$ decays, the reconstructed $\pi^+\pi^-\gamma$ invariant mass ($M_{+-\gamma}$) had to be between 484 and 512 MeV/$c^2$ and the square of the measured momentum component transverse to the incident kaon's direction ($P_T^2$) was required to be less than 150 (MeV/$c)^2$. In addition, fiducial requirements were imposed.

To eliminate $\pi\mu\nu$ decays, each track was required to have a momentum of at least 7 GeV/$c$ and to project to a point within the acceptance of the muon hodoscope. This assured that if the particle were a muon, it would have had a high probability of surviving the 3 m steel muon filter and leaving a hit in the hodoscope. $\pi e\nu$ decays were excluded by demanding that for each charged particle the ratio of energy measured in the lead glass calorimeter
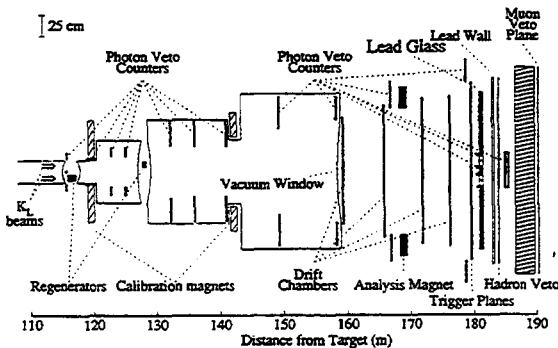


FIG. 1. Schematic of the FNAL E773 detector.

to momentum measured in the spectrometer, $E/p$, be less than 0.85. To remove $\Lambda \rightarrow p\pi$ decays, if the reconstructed $p\pi$ invariant mass was within 6 MeV/$c^2$ of the $\Lambda$ mass, we rejected events with a $p/\pi$ momentum ratio greater than 3 and a $\Lambda$ momentum greater than 100 GeV/$c$. To suppress background from $\pi^+\pi^-\pi^0$ decays, a cut was made on the variable

$$P_{\pi^0}^2 = \frac{(M_K^2 - M_{\pi^0}^2 - M_c^2)^2 - 4M_{\pi^0}^2 M_c^2 - 4M_K^2(P_T^2)_c}{4[(P_T^2)_c + M_c^2]},$$

where $M_c$ is the invariant mass of the two charged tracks and $(P_T^2)_c$ is their transverse momentum with respect to the parent kaon [13]. Events with $P_{\pi^0}^2 > -0.011$ (GeV/$c$)$^2$ were eliminated. Decays to $\pi^+\pi^-$ were removed by eliminating events with a reconstructed $\pi^+\pi^-$ invariant mass greater than 484 MeV/$c^2$. After analysis 9045 events survived, 77% of which came from the upstream regenerator.

The detector acceptance was calculated by the Monte Carlo method. The simulation included the geometry of the beams and detector elements, the efficiency and resolution of each detector element, and the known properties of kaon regeneration and decays. Figure 2 shows four histograms, typical of many, which demonstrate that the features of the data are accurately reproduced by the Monte Carlo simulation. The average overall acceptance of our detector was 14.6% (9.2%) for IB (DE) decays.

In Fig. 3 we show the decay probability for $K \rightarrow \pi^+\pi^-\gamma$ as a function of proper time, as determined from the data, and as predicted from Eq. (2). To demonstrate the effect of interference, we also show the prediction of Eq. (2) if there were no interference between the $K_L$ and $K_S$ amplitudes in this decay. It is clear that our data require the presence of $K_L$-$K_S$ interference.

The selected events for each set were put into $p$ vs $z$ distributions ($z$ being the longitudinal distance of the decay vertex from the target) in 10 GeV/$c$ × 2 m bins for fitting. The background (which included scattered, noncoherent, $K \rightarrow \pi^+\pi^-\gamma$ as well as non-$\pi\pi\gamma$ decays) was then subtracted from each $(p,z)$ bin. To estimate the total number of background events, a fit was performed

to the distribution of events in the $M_{+-\gamma}$ vs $P_T^2$ plane. The fit excluded the signal region and we interpolated to estimate the background. For the upstream (downstream) regenerator the background was 2.3% (2.5%) of the total. Events near, but outside of, the signal region were used to provide the $p$-$z$ distribution of background events. The $p$-$z$ distribution found from events to the left and right of the signal box in $M_{+-\gamma}$ was similar to the distribution of events at high $P_T^2$. The fit to the data was insensitive to the details of the background subtraction.

We performed a fit of the data to the hypothesis of $D(p,z) = S(p) \cdot f(p,z) \cdot A(p,z)$, where $S(p)$ is the momentum spectrum of kaons exiting the regenerator, $f(p,z)$ is the integral of Eq. (2) over the $(p,z)$ bin, and $A(p,z)$ is the acceptance of the detector as calculated from our Monte Carlo simulation. We determined $S(p)$ from the $\pi^+\pi^-$ data. By using the data, we find not only the shape of the spectrum, but also the absolute normalization (thereby accounting for $N_S$). The $\pi^+\pi^-$ events used the same trigger as the $\pi^+\pi^-\gamma$ data and were collected simultaneously. The analysis of the $\pi^+\pi^-$ data used many of the same cuts as the $\pi^+\pi^-\gamma$ analysis and has been described in detail elsewhere [12].

E731 had separate $K_S$ and $K_L$ beams which were used to measure $B_{+-\gamma}$ and $r$. In our fit, we constrained $B_{+-\gamma}$ and $r$ within their uncertainties to these values [9]. Our $\pi^+\pi^-$ data were used to determine $\rho$ and $\phi_{+-}$, while the $\Delta m$ used was the combined E731/E773 value [14]. The magnitudes of $\tau_L$, $\tau_S$, and $|\eta_{+-}|$ used were the Particle Data Group averages [15]. All four subsets were fit separately and checked for consistency before combining all data into one overall fit. The result of a maximum-likelihood fit to all four data sets is

$$|\eta_{+-\gamma}| = (2.359 \pm 0.062) \times 10^{-3},$$

$$\phi_{+-\gamma} = (43.8 \pm 3.5)^\circ.$$

This fit had a $\chi^2$ of 350 for 315 degrees of freedom [16].

We estimated our systematic uncertainties by varying many different elements of our analysis and observing the effect on the fit for $|\eta_{+-\gamma}|$ and $\phi_{+-\gamma}$. The result for $|\eta_{+-\gamma}|$ is $\pm 0.040 \times 10^{-3}$. The largest contributions
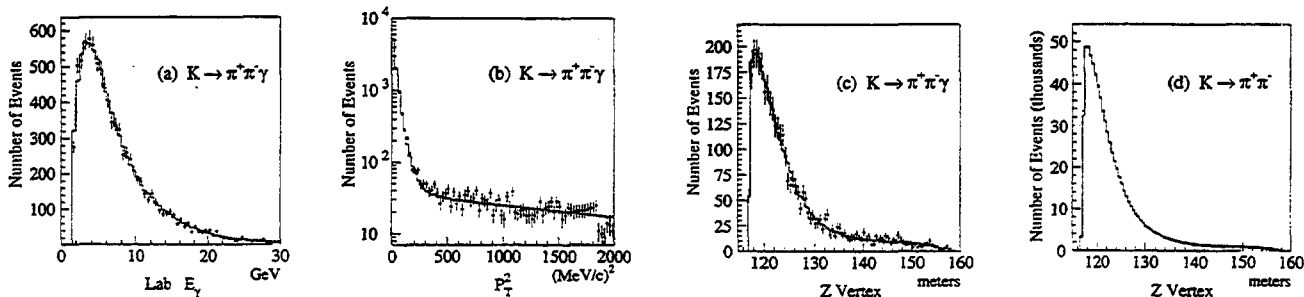


FIG. 2. Data: Monte Carlo comparisons for $K \rightarrow \pi^+\pi^-\gamma$ and $K \rightarrow \pi^+\pi^-$. Energy of the photon, transverse momentum, and longitudinal decay vertex are shown. The data are represented by the dots, while the Monte Carlo distribution is the histogram. For (a) and (b), all data sets are included, while for (c) and (d) only a subset of data from the upstream regenerator is shown. In (b), the measured background distribution, as determined from data, was added to the Monte Carlo $P_T^2$ distribution.
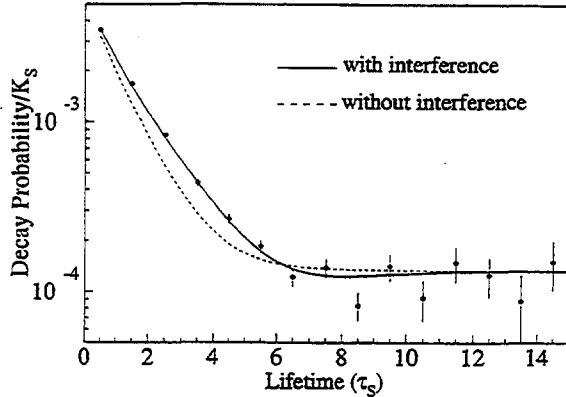
FIG. 3. The decay probability for $K \rightarrow \pi^+\pi^-\gamma$ as a function of proper time. The vertical scale is the absolutely normalized decay probability per $K_S$ exiting the regenerator. The horizontal scale is in units of $K_S$ lifetimes $(\tau_s)$. The data (corrected for acceptance and with background subtracted as described in the text) from the upstream regenerator are represented by the dots (statistical error bars are shown). The solid line shows the prediction of Eq. (2) resulting from the fit (see text), whereas the dashed line is the prediction if there were no interference between $K_L$ and $K_S$.

come from the uncertainties in background shape, flux normalization, and $|\eta_{+-}|$. These contribute 0.030, 0.021, and 0.013 (each $\times 10^{-3}$), respectively. The systematic uncertainty in $\phi_{+-\gamma}$ is $\pm 1.9°$ and is dominated by the uncertainties in normalization, $\rho$, and $|\eta_{+-}|$, which contribute $1.2°$, $0.9°$, and $0.9°$ respectively.

In summary, we have observed the interference between coherently regenerated $K_S$ and transmitted $K_L$ mesons decaying to the $\pi^+\pi^-\gamma$ final state. We collected 8836 of these decays (with a background of 209 events) and fit their distribution in $p$ and $z$ to obtain precise values for the magnitude and phase of $\eta_{+-\gamma}$. Our result is, within uncertainties, equal to $\eta_{+-}$ (in both magnitude and phase) [12,15] and is consistent with the prediction that any direct $CP$-violating contribution to $\eta_{+-\gamma}$ must be very small.

*Present address: Lawrence Berkeley Laboratory, University of California, Berkeley, CA 94720.
†Present address: Center for Neighborhood Technology, 2125 West North Avenue, Chicago, IL 60647.
‡Present address: Department of Physics, Seoul National University, Seoul 151-742, Korea.
§Present address: Department of Physics, University of Colorado, Boulder, CO 80309.
‖Present address: Department of Physics, University of Rochester, Rochester, NY 14627.
¶Present address: Solomon Brothers, New York, NY 10048.
**Present address: Fermi National Accelerator Laboratory, Batavia, IL 60510.
††Present address: Department of Atmospheric Science, Colorado State University, Fort Collins, CO 80523.
‡‡Present address: Department of Physics, Carnegie Mellon University, Pittsburgh, PA, 15213.
§§Present address: Department of Physics, Osaka University, Toyonaka, Osaka, 560 Japan.
‖‖Present address: Department of Physics, West Virginia University, Morgantown, WV 26506.

[1] J.H. Christenson et al., Phys. Rev. Lett. 13, 138 (1964).
[2] J.-M. Gaillard et al., Phys. Rev. Lett. 18, 20 (1967); J.-M. Gaillard et al., Nuovo Cimento A 59, 453 (1969).
[3] S. Bennett et al., Phys. Rev. Lett. 19, 993 (1967).
[4] D. Dorfan et al., Phys. Rev. Lett. 19, 987 (1967).
[5] E.J. Ramberg et al., Phys. Rev. Lett. 70, 2529 (1993).
[6] One possible exception would be a nonzero measurement of $\epsilon'/\epsilon$. However, the results so far from the two most sensitive experiments, Fermilab E731 and CERN NA31, are inconclusive on this point. L.K. Gibbons et al., Phys. Rev. Lett. 70, 1203 (1993); G.D. Barr et al., Phys. Lett. B 317, 233 (1993).
[7] J.F. Donoghue, B.R. Holstein, and G. Valencia, Int. J. Mod. Phys. A 2, 319 (1987), estimate that the direct $CP$ violation contribution to $\eta_{+-\gamma}$ is 5 times larger than that to $\eta_{+-}$.
[8] H. Taureg et al., Phys. Lett. 65B, 92 (1976).
[9] E.J. Ramberg et al., Phys. Rev. Lett. 70, 2525 (1993), measured $B_{+-\gamma} = (4.87 \pm 0.11) \times 10^{-3}$ and the fraction of $K_L$ decays that are DE to be 0.685 ± 0.041.
[10] A.S. Carroll et al., Phys. Rev. Lett. 44, 529 (1980).
[11] R. Rockmore and T.F. Wong, Phys. Rev. D 7, 3425 (1973); C.S. Lai and B.L. Young, Nuovo Cimento A 52, 83 (1967).
[12] B. Schwingenheuer et al., Phys. Rev. Lett. 74, 4376 (1995). See also J.N. Matthews, Ph.D. thesis, Rutgers-The State University of New Jersey, 1995 (unpublished); R.A. Briere, Ph.D. thesis, University of Chicago, 1995 (unpublished); B. Schwingenheuer, Ph.D. thesis, University of Chicago, 1995 (unpublished).
[13] D. Leurs et al., Phys. Rev. 133, B1276 (1964); A.S. Carroll et al., Phys. Rev. Lett. 44, 525 (1980).
[14] For completeness, we include the values used (see [12] above). $\rho \propto (f - \bar{f})/k$ which follows a power law in kaon momentum. Using the $\pi^+\pi^-$ data to fit a single combined (carbon + hydrogen) power law for our regenerators ($CH_{1.1}$), we find $|(f - \bar{f})/k| = 1.302 \pm 0.006$ mb at 70 GeV/$c$ and it varies as $p^{-0.574\pm0.007}$. We also find $\phi_{+-} = 43.53°$ and $\Delta m = 0.5282 \times 10^{10} \hbar s^{-1}$.
[15] Particle Data Group, L. Montanet et al., Phys. Rev. D 50, 1 (1994).
[16] As a consistency check, we fixed $|\eta_{+-\gamma}|$ and $\phi_{+-\gamma}$ to our measured values and constrained $r$ to the value from [9]. Refitting the data, we find $B_{+-\gamma} = [4.71 \pm 0.05(\text{stat})] \times 10^{-3}$.

# First Evidence for the Decay $K_L \to e^+ e^- \mu^+ \mu^-$

P. Gu, P. Haas, W. P. Hogan, S. K. Kim, J. N. Matthews, S. S. Myung, S. Schnetzer,* G. B. Thomson, and Y. Zou

*Rutgers University, Piscataway, New Jersey 08855*

K. Arisaka, D. Roberts, W. Slater, M. B. Spencer, and M. Weaver

*University of California at Los Angeles, Los Angeles, California 90024*

R. A. Briere, E. Cheu, D. A. Harris, P. Krolak, K. S. McFarland, A. Roodman, B. Schwingenheuer,
S. V. Somalwar, Y. W. Wah, B. Winstein, and R. Winston

*The Enrico Fermi Institute, The University of Chicago, Chicago, Illinois 60637*

A. R. Barker

*University of Colorado, Boulder, Colorado 80309*

E. C. Swallow

*Elmhurst College, Elmhurst, Illinois 60126*
*and The Enrico Fermi Institute, The University of Chicago, Chicago, Illinois 60637*

G. J. Bock, R. Coleman, M. Crisler, J. Enagonio, R. Ford, Y. B. Hsiung, D. A. Jensen,
V. R. O'Dell, E. Ramberg, and R. Tschirhart

*Fermi National Accelerator Laboratory, Batavia, Illinois 60510*

E. M. Collins and G. D. Gollin

*University of Illinois, Urbana, Illinois 61801*

T. Nakaya and T. Yamanaka

*Department of Physics, Osaka University, Toyonaka, Osaka, 560 Japan*
(Received 20 February 1996)

We present the first evidence for the decay $K_L \to e^+ e^- \mu^+ \mu^-$ based on the observation of one event with an estimated background of $0.067^{+0.057}_{-0.025}$ event. We determine the branching ratio to be $B(K_L \to e^+ e^- \mu^+ \mu^-) = (2.9^{+6.7}_{-2.4}) \times 10^{-9}$. In addition, we set a 90% confidence upper limit on the combined branching ratio for the lepton flavor violating decays $K_L \to e^\mp e^\mp \mu^\pm \mu^\pm$ to be $B(K_L \to e^\mp e^\mp \mu^\pm \mu^\pm) < 6.1 \times 10^{-9}$ assuming a uniform phase space distribution. [S0031-9007(96)00301-8]

We present the first evidence for the decay $K_L \to e^+ e^- \mu^+ \mu^-$. This decay is expected to proceed primarily via a two-photon intermediate state $K_L \to \gamma^* \gamma^* \to e^+ e^- \mu^+ \mu^-$ [1–4]. Because one of the virtual photons must have an invariant mass greater than $2m_\mu$, the decay is sensitive to the structure of the $K_L \gamma^* \gamma^*$ form factor. This form factor must be known accurately in order to extract the contribution of second-order weak processes to the decay $K_L \to \mu^- \mu^-$, which is sensitive to the Cabibbo-Kobayashi-Maskawa element $V_{td}$ [5–10]. Predictions for the $K_L \to e^- e^- \mu^+ \mu^-$ branching ratio are $8.0 \times 10^{-10}$ for a calculation based on a constant form factor [1] and $2.3 \times 10^{-9}$ for a calculation based on the vector meson dominance model [2]. The previous experimental 90% confidence upper limit on the branching ratio is $4.9 \times 10^{-6}$ [11].

This measurement was carried out as part of the Fermilab experiment E799 which has previously reported precision measurements of the related processes $K_L \to \gamma \gamma^* \to$ $\mu^+ \mu^- \gamma$ [12] and $K_L \to \gamma^* \gamma^* \to e^+ e^- e^+ e^-$ [13]. A detailed description of the E799 detector can be found elsewhere [14]. Two $K_L$ beams were produced by 800 GeV protons striking a Be target. A 70 m long vacuum decay volume began 90 m downstream of the target. Decay products of the $K_L$'s were detected by a spectrometer located downstream of the decay volume. The mean energy of the kaons whose decays were accepted by the trigger described below was about 80 GeV. The spectrometer included four drift chambers and a magnet for analyzing the momentum and trajectories of charged particles. The momentum resolution is given by $(\sigma_p / p)^2 = (5 \times 10^{-3})^2 + \{1.4 \times 10^{-4}(p[\text{GeV}/c])\}^2$. A lead glass calorimeter was used to measure the energies and positions of electrons and photons. The average energy resolution for accepted electrons was 4.4%. Two beam holes were symmetrically located above and below the center of the lead glass array. Seven planes of veto counters at various locations in the detector were used to detect

decay products outside the chamber and calorimeter acceptances. Two scintillator hodoscopes, used to trigger on charged particles, were located before the calorimeter. Downstream of the calorimeter was a lead wall 0.73 interaction length thick. A scintillation counter hodoscope located just downstream of the lead wall was used to veto, events with showers from charged pions hadronically interacting in the lead glass or lead wall. Finally, a muon trigger plane consisting of 16 vertically oriented, nonoverlapping scintillation counters was located just downstream of a 3 m steel muon filter.

The trigger for the $K_L \rightarrow e^+e^-\mu^+\mu^-$ events required at least two hits in each of the two trigger hodoscopes, in each of the drift chamber planes, and in nonadjacent counters in the muon trigger plane, and at least 6 GeV of energy deposit in the calorimeter. In addition, the veto counters were used to reject events with charged particles escaping the detector fiducial region. Events were also rejected if the total energy deposit in the hadron veto hodoscope located behind the lead wall was greater than that equivalent to three traversing minimum ionizing particles.

Candidate $K_L \rightarrow e^+e^-\mu^+\mu^-$ events were required to have two positively and two negatively charged tracks. The four charged particles were required to be consistent with two electrons and two muons, where electrons were identified by $0.8 < E/p < 1.2$, and muons were identified by $E < 3$ GeV and $p > 7$ GeV/$c$ where $p$ is the track momentum and $E$ is the energy of the calorimeter cluster associated with the track. Both the electron and muon pairs were required to consist of opposite sign tracks. At most, one of the four particles was allowed to pass through one of the lead glass beam holes. In this case, no identification based on the shower energy of the particle could be made for this track. The reconstructed decay vertex was required to be within the fiducial decay volume. A track separation cut required that tracks not share hits in both the horizontal and vertical views of the most upstream drift chamber in order to reject events in which a photon converted in the vacuum window immediately upstream of this chamber.

In Fig. 1, we show the $P_t^2$ vs $M_{ee\mu\mu}$ distribution of Monte Carlo $K_L \rightarrow e^+e^-\mu^+\mu^-$ events that passed the above (first stage) cuts, where $M_{ee\mu\mu}$ is the reconstructed invariant mass and $P_t$ is the component of the reconstructed $K_L$ momentum perpendicular to a vector pointing from the production target to the reconstructed decay vertex. The Monte Carlo generator included radiative corrections [15] with a low energy photon cutoff of 0.25 MeV in the $K_L$ center of mass. Radiative effects account for the scatter of events at large $P_t^2$ and low $M_{ee\mu\mu}$. We define the signal region for $K_L \rightarrow e^+e^-\mu^+\mu^-$ to be $P_t^2 < 5.0 \times 10^{-4}$ (GeV/$c$)$^2$, and $0.475 < M_{ee\mu\mu} < 0.515$ GeV/$c^2$. The signal region acceptance is 94.2% for the Monte Carlo $K_L \rightarrow e^+e^-\mu^+\mu^-$ events that passed the first stage cuts. We show the corresponding distribution for the data in Fig. 2.
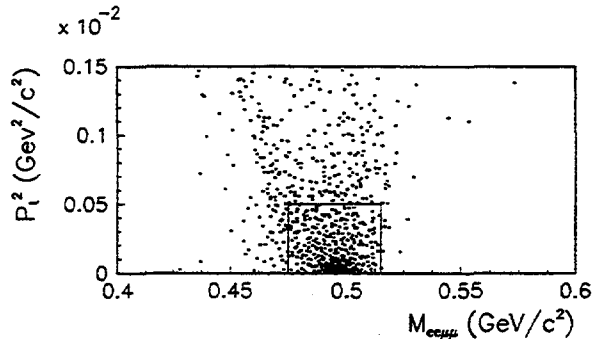


FIG. 1. The $P_t^2$ vs $M_{ee\mu\mu}$ distribution for the Monte Carlo $K_L \rightarrow e^+e^-\mu^+\mu^-$ events after the first stage cuts described in the text. The Monte Carlo generator included radiative corrections with a low energy photon cutoff of 0.25 MeV in the $K_L$ center of mass. The box is the signal region.

In searching for rare events, it is important to carefully choose cuts in an unbiased fashion. In this analysis, we blanked out the signal region and selected cuts to reject events outside of the signal region as described below. Once the signal region was examined, no further changes to the cuts were made. The events in Fig. 2 with $M_{ee\mu\mu} < 0.500$ GeV/$c^2$ are predominantly $K_L \rightarrow \pi^+\pi^-\pi^0$ decays with the $\pi^0$ undergoing Dalitz decay, $K_L \rightarrow \pi^+\pi^-\pi_D^0$ where $\pi_D^0$ represents $\pi^0 \rightarrow e^+e^-\gamma$, and in which both charged pions were misidentified as muons due to decay in flight or accidental activity in the muon counters. These events were reduced by requiring that there be no extra clusters in the calorimeter that were not associated with the charged tracks. In addition, to reduce events with a pion decay in flight, the position difference between the upstream and downstream track segments at the midplane of the magnet for muon candidate tracks was required to be less than 2 mm in the horizontal view (magnet matching cut). This cut rejected those events with tracks for which the momentum was poorly determined and which could, therefore, have a large error in the determined invariant mass. The events in Fig. 2 with $M_{ee\mu\mu} > 0.500$ GeV/$c^2$ are predominantly events with two decays consisting of combinations of $K_L \rightarrow \pi e \nu$ and $K_L \rightarrow \pi \mu \nu$ occurring within the same $\approx 2$ ns beam RF bucket and for which
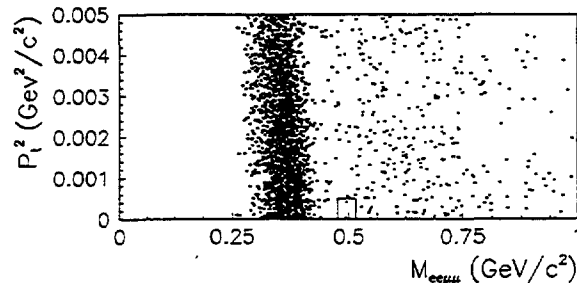


FIG. 2. The $P_t^2$ vs $M_{ee\mu\mu}$ distribution for candidate $K_L \rightarrow e^+e^-\mu^+\mu^-$ decays after the first stage cuts. The box is the signal region.

the pions were misidentified. These events were largely rejected by requiring that the $\chi^2$ of the fitted decay vertex reconstructed by extrapolation of the four tracks be less than 50 for 5 degrees of freedom. This cut accepted 90.6% of the Monte Carlo $K_L \rightarrow e^+e^-\mu^+\mu^-$ events.

The background due to events with two simultaneous $K_{l3}$ decays was estimated as follows. Since these events have a fairly flat $\chi^2$ distribution for the vertex reconstruction, they were selected from the events that passed the first stage cuts by requiring $\chi^2 > 500$. Of these, two events fall within the signal mass range. Requiring $M_{ee\mu\mu} > 0.500$ GeV/$c^2$ removes $K_L \rightarrow \pi^+\pi^-\pi_D^0$ events and yields a clean sample of events with two simultaneous $K_{l3}$ decays. Of these events, 10% fall within the $P_t^2$ signal range. Finally, an extrapolation of a linear fit to the $\chi^2$ distribution indicates that 3.8% would satisfy the $\chi^2 < 50$ cut. This background is then estimated as 2 events $\times$ 0.10 $\times$ 0.038 $= 0.008^{+0.010}_{-0.005}$ event.

In order to estimate the background from $K_L \rightarrow \pi^+\pi^-\pi_D^0$, we extrapolated the data into the signal region using an exponential fit to the data in the range $0.385 < M_{ee\mu\mu} < 0.475$ GeV/$c^2$. In order to enhance the statistical accuracy of the fit, we removed the magnet matching, the muon cluster energy, and the muon momentum cuts which increased the number of events by a factor of 2.0. The exponential fit to the data is shown in Fig. 3. For comparison, Monte Carlo $K_L \rightarrow \pi^+\pi^-\pi_D^0$ events are also shown. The fitted exponential slopes are $-72.4 \pm 14.5$ (GeV/$c^2$)$^{-1}$ for the data and $-68.0 \pm 2.8$ (GeV/$c^2$)$^{-1}$ for the Monte Carlo events. Extrapolating the fit for the data into the signal region and taking into account the factor of 2 rejection from the combined magnet matching, muon momentum, and muon cluster energy cuts, the background is estimated to be $0.021^{+0.043}_{-0.015}$ event.

Another source of background is from radiative $K_{e3}$ with internal photon conversion $K_L \rightarrow \pi^{\pm}e^{\mp}\nu(\gamma \rightarrow ee)$ and from $K_L \rightarrow \pi^{\pm}e^{\mp}\nu\pi_D^0$ with the charged pion and one of the electrons misidentified as muons. A sample of these events can be selected by choosing events with
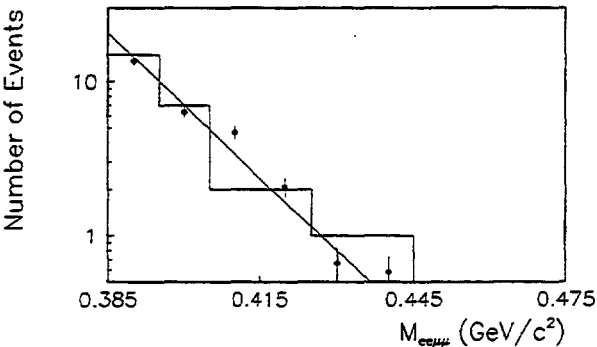
like-sign $ee$ and $\mu\mu$ pairs after applying the first stage cuts and the $\chi^2 < 50$ cut. There are 10 of these events. Of these 10 events, 2 are in the $P_t^2$ signal range, 3 are in the $M_{ee\mu\mu}$ signal range, 2 pass the extra cluster cut, and 1 passes the combined magnet matching, muon momentum, and muon shower energy cuts. We expect twice as many unlike sign pair events due to combinatorics. This background is then estimated as 10 $\times$ 0.2 $\times$ 0.3 $\times$ 0.2 $\times$ 0.1 $\times$ 2 $= 0.024^{+0.052}_{-0.020}$ event.

We also considered background from $K_L \rightarrow \mu^+\mu^-\gamma$ decays [12] with conversion of the photon in the vacuum window. The number of events expected is 1.4 without the track separation cut. The track separation cut based on hit sharing in the most upstream drift chamber reduced this background to 0.014 $\pm$ 0.004 events while accepting 85% of Monte Carlo $K_L \rightarrow e^+e^-\mu^+\mu^-$ events. Possible background from the hyperon decay $\Xi^0 \rightarrow \Lambda\pi_D^0 \rightarrow p\pi^-e^+e^-\gamma$ could be completely rejected by requiring that the reconstructed energy be less than 200 GeV due to the short proper lifetime of the hyperon.

After all the cuts, the 216 events shown in Fig. 4 remain. One event is left in the signal region with an expected combined background of $0.067^{+0.057}_{-0.025}$ event. For this event, the particle associated with the $\mu^-$ passed through one of the beam holes in the lead glass. This track projects onto one of the hit muon trigger counters. The $ee\mu\mu$, $ee$ and $\mu\mu$ invariant masses for this event are 0.494, 0.103, and 0.300 GeV/$c^2$, respectively. These along with the value of $P_t^2$ for this event are compared with Monte Carlo distributions in Fig. 5 where the Monte Carlo decays were generated using a constant $K_L\gamma^*\gamma^*$ form factor. The probability of a Monte Carlo event having an $ee$ invariant mass or a $\mu\mu$ invariant mass greater than that of the observed event are 8% and 25%, respectively. If the particle that passed through the beam hole is assigned the electron mass and the other identified muon is assigned the pion mass, the resulting $\pi eee$ invariant mass is 0.543 GeV/$c^2$. The probability of this event being either $K_L \rightarrow \pi e\nu(\gamma \rightarrow ee)$ or $K_L \rightarrow \pi e\nu\pi_D^0$ is, therefore, extremely small. Similarly, if both identified muons are assigned the pion mass, the resulting $\pi\pi ee$ mass is 0.576 GeV/$c^2$ so that the probability



FIG. 3. The $M_{ee\mu\mu}$ distributions for $0.385 < M_{ee\mu\mu} < 0.475$ MeV/$c^2$. The histogram is the data. The points are the $K_L \rightarrow \pi^+\pi^-\pi_D^0$ Monte Carlo events. The exponential fit to the data is shown.
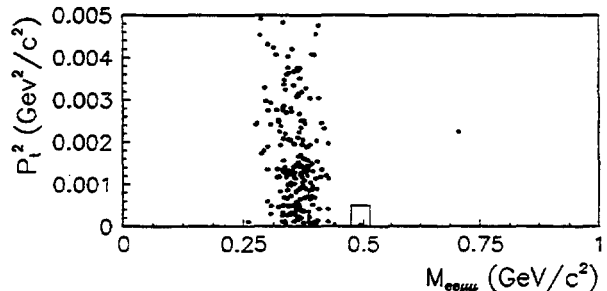


FIG. 4. The $P_t^2$ vs $M_{ee\mu\mu}$ distribution for candidate $K_L \rightarrow e^+e^-\mu^+\mu^-$ decays after all of the analysis cuts. The box is the signal region.
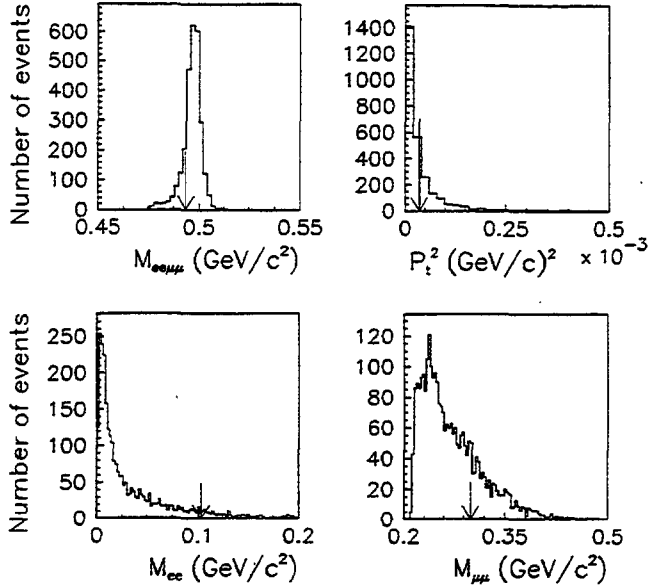
FIG. 5. The distributions of $M_{ee\mu\mu}$, $P_t^2$, $M_{ee}$, and $M_{\mu\mu}$ for accepted Monte Carlo $K_L \rightarrow e^+e^-\mu^+\mu^-$ events, where the arrows indicate the locations of the observed event.

of the event being $K_L \rightarrow \pi^+\pi^-\pi_D^0$ is also extremely small. The probability of $K_L \rightarrow \mu^+\mu^-\gamma$ with photon conversion in the vacuum window having an $ee$ mass greater than that of the observed event is 0.2%.

The four-track decay mode $K_L \rightarrow \pi^+\pi^-\pi_D^0$ was used for normalization. The trigger was the same as for the signal mode except that there were no requirements on either the muon trigger or hadron veto hodoscopes. Monte Carlo simulations based on input from muon calibration runs as well as minimum bias trigger data were used to determine the efficiency of the muon trigger hodoscope requirement for those $K_L \rightarrow e^+e^-\mu^+\mu^-$ decays that satisfied the other trigger requirements. Similar Monte Carlo studies that included event-by-event overlay of measured beam-related accidental activity showed that $(44 \pm 4)\%$ of $K_L \rightarrow e^+e^-\mu^+\mu^-$ decays were lost due to the hadron veto counter requirement [16].

Since both the signal and the normalization modes consisted of four-track events, uncertainties due to tracking tended to cancel in the ratio of their acceptances. Cuts similar to those used in the signal mode were applied. In addition, one extra cluster in the calorimeter not associated with a charged track was required due to the photon in the $\pi^0 \rightarrow ee\gamma$ decay and $M_{e^+e^-\gamma}$ was required to be in the range of 0.120 and 0.150 GeV/$c^2$. Monte Carlo study showed that 1.3% of the reconstructed $K_L \rightarrow \pi^+\pi^-\pi_D^0$ decays are from $K_L \rightarrow \pi^+\pi^-\pi^0$ with external photon conversion. Other backgrounds were negligible.

We have observed one $K_L \rightarrow e^+e^-\mu^+\mu^-$ candidate event with an estimated background of $0.067^{+0.057}_{-0.025}$ events.

A 0.067 event background has about a 7% probability of yielding one or more observed events. Based on the number of accepted $K_L \rightarrow \pi^+\pi^-\pi_D^0$ decays (233 $\pm$ 15), the $K_L \rightarrow \pi^+\pi^-\pi_D^0$ acceptance of $(1.78 \pm 0.05)\%$ with prescale factor of 3600, the $K_L \rightarrow e^+e^-\mu^+\mu^-$ acceptance of $(1.1 \pm 0.1)\%$, and the one candidate $K_L \rightarrow e^+e^-\mu^+\mu^-$ decay, the branching ratio of $K_L \rightarrow e^+e^-\mu^+\mu^-$ is calculated to be $B(K_L \rightarrow e^+e^-\mu^+\mu^-) = (2.9^{+6.7}_{-2.4}) \times 10^{-9}$. This is consistent with both the vector meson dominance model and the constant form factor predictions.

In addition, we searched for the lepton number violating decays $K_L \rightarrow e^\mp e^\mp \mu^\pm \mu^\pm$ by removing the requirement that the electron and muon pairs consist of opposite sign leptons. Assuming that the final state particles are uniformly distributed in phase space, the acceptance for these events is $(1.2 \pm 0.1)\%$. No events were seen, leading to a 90% confidence level upper limit of $6.1 \times 10^{-9}$ on the combined $K_L \rightarrow e^\mp e^\mp \mu^\pm \mu^\pm$ branching ratio.

*To whom correspondence should be addressed. Electronic address: steves@ruthep.rutgers.edu

[1] Zenaida E. S. Uy, Phys. Rev. D **43**, 802 (1991); Zenaida E. S. Uy, Phys. Rev. D **43**, 1572 (1991).

[2] C. Quigg and J. D. Jackson, UCRL Report No. 18487, 1968.

[3] T. Miyazaki, Lett. Nuovo Cimento **5**, 125 (1972).

[4] T. Miyazaki and E. Takasugi, Phys. Rev. D **8**, 2051 (1973).

[5] R. E. Shrock and M. B. Voloshin, Phys. Lett. **87B**, 375 (1979).

[6] T. Inami and C. S. Lim, Prog. Theor. Phys. **65**, 297 (1981).

[7] L. Bergström, E. Massó, P. Singer, and D. Wyler, Phys. Lett. **134B**, 373 (1984).

[8] L. Bergström, E. Massó, and P. Singer, Phys. Lett. B **249**, 141 (1990).

[9] G. Bélanger and C. Q. Geng, Phys. Rev. D **43**, 140 (1991).

[10] P. Ko, Phys. Rev. D **45**, 174 (1992).

[11] M. Ya. Balats et al., Sov. J. Nucl. Phys. **38**, 556 (1983).

[12] M. B. Spencer et al., Phys. Rev. Lett. **74**, 3323 (1995).

[13] P. Gu et al., Phys. Rev. Lett. **72**, 3000 (1994). See also G. D. Barr et al., Phys. Lett. B **259**, 389 (1991); M. R. Vagins et al., Phys. Rev. Lett. **71**, 35 (1993).

[14] K. S. McFarland et al., Phys. Rev. Lett. **71**, 31 (1993); see also P. Gu, Rutgers thesis, 1994 (unpublished).

[15] E. Barberio et al., Comput. Phys. Commun. **66**, 115 (1991).

[16] M. B. Spencer, UCLA thesis, 1995 (unpublished).

# CP and CPT symmetry tests from the two-pion decays of the neutral kaon with the Fermilab E731 detector

L. K. Gibbons,[a] A. R. Barker,[b] R. A. Briere,[c] G. Makoff,[d] V. Papadimitriou,[e] J. R. Patterson,[f] B. Schwingenheuer,[g] S. V. Somalwar,[h] Y. W. Wah, B. Winstein, R. Winston, M. Woods,[i] and H. Yamamoto[c]
*The Enrico Fermi Institute and the Department of Physics, The University of Chicago, Chicago, Illinois 60637*

G. J. Bock, R. Coleman, J. Enagonio,[j] Y. B. Hsiung, E. J. Ramberg, K. Stanfield, R. Tschirhart, and T. Yamanaka[k]
*Fermi National Accelerator Laboratory, Batavia, Illinois 60510*

E. C. Swallow
*Department of Physics, Elmhurst College, Elmhurst, Illinois 60126*
*and The Enrico Fermi Institute, The University of Chicago, Chicago, Illinois 60637*

G. D. Gollin,[l] M. Karlsson,[m] and J. K. Okamitsu[n]
*Department of Physics, Princeton University, Princeton, New Jersey 08544*

P. Debu, B. Peyaud, R. Turlay, and B. Vallage
*Department d'Astrophysique, de Physique des Particules, de Physique Nucleaire et de l'Instrumentation Associee, Centre d'Etudes de Saclay, 91191 Gif-sur-Yvette Cedex, France*

We present a comprehensive treatment of the precise determinations of the parameters $\mathrm{Re}(\varepsilon'/\varepsilon)$, $\tau_S$, $\Delta m$, $\phi_{+-}$, and $\Delta\phi$ in the neutral kaon system with the Fermilab E731 detector. Together, these determinations allow accurate studies of both $CP$ and $CPT$ symmetry. Details of the detector and its performance and the data analysis are given. The extensive Monte Carlo simulation of the detector and comparison with data are also presented. [S0556-2821(97)06311-X]

## I. INTRODUCTION

This article presents a full description of Fermilab experiment 731, focusing upon the determination of the $CP$ violation parameter $\mathrm{Re}(\varepsilon'/\varepsilon)$ in the decay of the $K_L$ and $K_S$ meson into two pions. It is largely based on the work of Gibbons [1]. After a brief review of the relevant phenomenology in the neutral kaon system, we describe the detector, beam, and analysis of the data. The Monte Carlo simulation reflecting the degree of understanding of the apparatus is

[a]Present address: Rochester University, Rochester, NY 14627.
[b]Present address: University of Colorado, Boulder, CO 80309.
[c]Present address: Harvard University, Cambridge, MA 02138.
[d]Present address: Solomon Brothers, New York, NY 10048.
[e]Present address: Fermi National Accelerator Laboratory, Batavia, IL 60510.
[f]Present address: Cornell University, Ithaca, NY 14853.
[g]Present address: Max-Planck Institute for Nuclear Physics, P.O. Box 103980, 69029 Heidelberg, Germany.
[h]Present address: Rutgers University, P.O. Box 849, Piscataway, NJ 08855.
[i]Present address: SLAC, P.O. Box 4349, Stanford, CA 94305.
[j]Present address: Department of Atomospheric Science, Colorado State University, Fort Collins, CO 80523.
[k]Present address: Physics Department, Osaka University, Toyonaka, Osaka 560, Japan.
[l]Present address: Department of Physics, University of Illinois, Urbana, IL.
[m]Present address: CERN, CH-1211, Geneva 23, Switzerland.
[n]Present address: Princeton Combustion Research Laboratories, Monmouth Junction, NJ 08852.

presented in detail. As well, calibration of the detector elements is fully treated. As a by-product, this experiment is sensitive to many of the fundamental parameters of the neutral kaon system, which also allows us to probe the validity of $CPT$ symmetry. These parameters include the $K_S$ lifetime ($\tau_S$) and the difference in mass between the $K_L$ and $K_S$ ($\Delta m \equiv m_L - m_S$). We also present the values of the phase $\phi_{+-}$ and the phase difference $\Delta\phi \equiv \phi_{00} - \phi_{+-}$, where $\phi_{+-}$ and $\phi_{00}$ are the phases of $\eta_{+-}$ and $\eta_{00}$, respectively.

## A. Kaon phenomenology and $CP$ violation

This section gives the essentials of the phenomenology of the neutral kaon system, primarily as needed for the determination of Re$(\varepsilon'/\varepsilon)$. We assume that $CPT$ symmetry holds in this section. The implications of $CPT$ symmetry violation are treated in the next section. The formalism of kaon phenomenology has been extensively treated in the literature [2–8]. The experimental status is also briefly summarized.

To study $CP$ violation and $CPT$ symmetry in the $K^0$-$\bar{K}^0$ complex, it has been traditional to describe the system by an effective $2 \times 2$ Hamiltonian [2]

$$\mathbf{H}_{\mathrm{eff}} = \mathbf{M} - i\Gamma/2, \tag{1}$$

where both the mass matrix $\mathbf{M}$ and the decay matrix $\Gamma$ are Hermitian.

The physical eigenstates $|K_{L,S}\rangle$, with definite masses $m_{L,S}$ and lifetimes $\tau_{L,S} = 1/\Gamma_{L,S}$, have time dependences

$$|K_{L,S}(t)\rangle = e^{-im_{L,S}t} e^{-\Gamma_{L,S}t/2} |K_{L,S}(0)\rangle. \tag{2}$$

The two states with definite $CP$ are

$$|K_1\rangle \sim |K^0\rangle + |\bar{K}^0\rangle \quad (CP = +1),$$

$$|K_2\rangle \sim |K^0\rangle - |\bar{K}^0\rangle \quad (CP = -1). \tag{3}$$

These would be the weak eigenstates if $CP$ symmetry were not violated.

Allowing for $CP$ violation, the eigenstates become asymmetric mixtures of the $K^0$ and $\bar{K}^0$:

$$|K_S\rangle = \frac{1}{\sqrt{2(1 - |\varepsilon|^2)}}[(1 + \varepsilon)|K^0\rangle + (1 - \varepsilon)|\bar{K}^0\rangle],$$

$$|K_L\rangle = \frac{1}{\sqrt{2(1 - |\varepsilon|^2)}}[(1 + \varepsilon)|K^0\rangle - (1 - \varepsilon)|\bar{K}^0\rangle]. \tag{4}$$

In the above expression, $\varepsilon$ is given by

$$\varepsilon = \frac{\mathrm{Im}M_{12} - \frac{1}{2}i\,\mathrm{Im}\Gamma_{12}}{i\Delta m - \frac{1}{2}(\Gamma_S - \Gamma_L)}, \tag{5}$$

where $M_{12} = \langle K^0 |\mathbf{M}| \bar{K}^0\rangle$ and $\Gamma_{12} = \langle K^0 |\Gamma| \bar{K}^0\rangle$. This expression is valid in the Wu-Yang phase convention [9]. Here $\Delta m$ is the mass difference between the long- and short-lived weak eigenstates,

$$\Delta m \equiv m_L - m_S. \tag{6}$$

There are two classes of $CP$-violating effects. In one, the $K^0$ and the $\bar{K}^0$ mix asymmetrically, resulting in a small admixture of the "wrong" $CP$ states, described as $\varepsilon$ in Eqs. (4) and (5). In the other, the $K^0$ and the $\bar{K}^0$ decay asymmetrically, from a $CP$-violating amplitude directly in the decay. The latter effect has been appropriately dubbed "direct" $CP$ violation. Over 30 years of effort have gone into establishing whether the observed $CP$ violation arises solely from mixing in the mass matrix or whether direct $CP$ violation also occurs in the decay amplitude.

### 1. CP violation from mixing

For decay modes where the final state has a definite $CP$, it is interesting to consider the ratio of $CP$-violating to $CP$-conserving amplitudes for the decay modes. In the traditional notation, we have, for the charged decay mode,

$$\eta_{+-} \equiv \frac{\langle \pi^+ \pi^- |H_W| K_L\rangle}{\langle \pi^+ \pi^- |H_W| K_S\rangle} \tag{7}$$

and, for the neutral mode,

$$\eta_{00} \equiv \frac{\langle \pi^0 \pi^0 |H_W| K_L\rangle}{\langle \pi^0 \pi^0 |H_W| K_S\rangle}. \tag{8}$$

If only the asymmetric $K^0$-$\bar{K}^0$ mixing in the mass matrix contributes to the $CP$-violating amplitudes, then

$$\eta_{+-} = \eta_{00} = \varepsilon. \tag{9}$$

Experimentally, both the phases and the magnitudes of $\eta_{+-}$ and $\eta_{00}$ are accessible. The "natural" phase for $\varepsilon$ is, then,

$$\phi_\varepsilon = \arctan\left(\frac{2\Delta m}{\Gamma_S - \Gamma_L}\right), \tag{10}$$

which follows from Eq. (5) as one can phenomenologically limit $\mathrm{Im}\Gamma_{12}$. This natural phase is often referred to as the "superweak" phase. Obviously, Eq. (9) implies that experiments should be consistent with both

$$|\eta_{+-}| = |\eta_{00}| \tag{11}$$

and

$$\phi_{+-} = \phi_{00} = \arctan\left(\frac{2\Delta m}{\Gamma_S - \Gamma_L}\right), \tag{12}$$

where $\phi_{+-}$ and $\phi_{00}$ are the phases of $\eta_{+-}$ and $\eta_{00}$, respectively. The best fit values for $|\eta_{+-}|$ and $|\eta_{00}|$ were calculated by the Particle Data Group [10],

$$|\eta_{+-}| = (2.269 \pm 0.023) \times 10^{-3},$$

$$|\eta_{00}| = (2.259 \pm 0.023) \times 10^{-3}, \tag{13}$$

which were consistent with the prediction of Eq. (11), that is, with the hypothesis that the observed $CP$ violation in $K_L$ decays was due to mixing alone.

When experiment 731 was begun in 1983, $|\eta_{+-}|$ and $|\eta_{00}|$ were consistent with each other. The phase $\phi_{+-}$ was

accurately known and a little more than two standard deviations away from the superweak phase $\phi_\varepsilon$. The phase difference $\Delta\phi \equiv \phi_{00} - \phi_{+-}$ was known only to about $6°$ and its value differed by two standard deviations from zero. In the remainder of this article, we describe how these quantities were measured in E731.

### 2. Direct CP violation in $\pi\pi$ decays

One way of isolating the mixing and decay contributions is to compare the level of $CP$ violation in two different $CP$-violating final states. The two $CP$-violating decays $K_L \to \pi^+\pi^-$ and $K_L \to \pi^0\pi^0$ allow such a comparison. Another way is to search for $CP$-violating decays, such as the rare $K_L \to \pi^0\nu\bar{\nu}$ decay, where the $CP$-conserving as well as indirect $CP$-violating decay amplitudes are highly suppressed. An observation of such a decay mode would then essentially be a signal of direct $CP$ violation. In this experiment, we use the first approach. Since this approach involved the use of an intense $K_L$ beam, we were also able to obtain limits on some rare decay modes of the $K_L$ relating to $CP$ violation [11–15].

As is customary, we define

$$\langle I | \mathbf{H}_W | K^0 \rangle = a_I \equiv A_I e^{i\delta_I}, \tag{14}$$

where $I$ denotes the isospin ($I = 0,2$) of the $\pi\pi$ final state. The overall amplitude has been separated into an amplitude $A_I$ corresponding to the weak decay process itself, and a phase shift $\delta_I$ from the final state interactions. From the assumption of $CPT$ symmetry, one also has (see, for example, Ref. [6])

$$\langle I | \mathbf{H}_W | \bar{K}^0 \rangle = \bar{a}_I \equiv A_I^* e^{i\delta_I}. \tag{15}$$

One can now explicitly adopt the Wu-Yang phase convention [9] and take $A_0$ to be real. This fixes the relative phase between the $|S| = 1$ and the $S = 0$ sectors, which are not connected by the strong and electromagnetic interactions. Of course all physical observables are independent of the choice of phase.

Allowing for direct $CP$ violation, then, yields

$$\varepsilon' \equiv \frac{i}{\sqrt{2}} e^{i(\delta_2 - \delta_0)} \frac{\mathrm{Im}A_2}{A_0}, \tag{16}$$

$$\eta_{+-} \approx \varepsilon + \varepsilon', \tag{17}$$

and

$$\eta_{00} \approx \varepsilon - 2\varepsilon'. \tag{18}$$

If there is direct $CP$ violation in the $\pi\pi$ decay of the neutral kaon, then the ratios of $CP$-violating to $CP$-conserving amplitudes are different for the $\pi^+\pi^-$ and $2\pi^0$ final states. The geometrical relation between the different $CP$-violating amplitudes is illustrated in the Wu-Yang diagram in Fig. 1.

The phase of $\varepsilon'$ follows from its definition:

$$\phi_{\varepsilon'} = \delta_2 - \delta_0 + \frac{\pi}{2}. \tag{19}$$
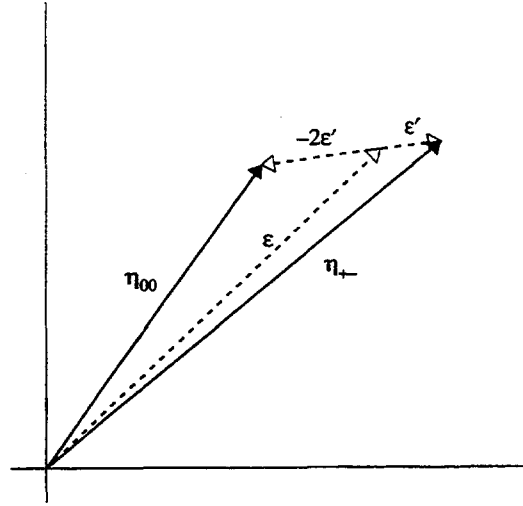


FIG. 1. The Wu-Yang phase diagram for $K \to \pi\pi$ decays. The phase and magnitude of $\varepsilon'$ relative to $\varepsilon$ have been greatly exaggerated for the sake of clarity.

The $I = 0$ and $I = 2$ final state phase shifts have been measured in other experiments, and in a recent compilation, Ochs [16] obtains $\delta_2 - \delta_0 = -43° \pm 6°$. This implies that the phase of $\varepsilon'$ is $\phi_{\varepsilon'} = 47° \pm 6°$. Comparing this phase to the phase of $\varepsilon$ obtained above, we see that $\varepsilon'$ and $\varepsilon$ are almost parallel, a convenient but accidental coincidence. To a good approximation then, we have $CP$ violation parametrized by $\mathrm{Re}(\varepsilon'/\varepsilon)$ and $CPT$ violation parametrized by $\mathrm{Im}(\varepsilon'/\varepsilon)$. The latter would result if, for example, the $K^0$-$\bar{K}^0$ mixing asymmetry were different for the $K_L$ and $K_S$.

In an experiment, one can only directly measure the decay rates for the different $K \to \pi\pi$ decays. Expressed in terms of the decay rates, a signal for direct $CP$ violation in $K \to \pi\pi$ decays is a deviation of the double ratio of rates away from unity:

$$\frac{\Gamma(K_L \to \pi^+\pi^-)/\Gamma(K_S \to \pi^+\pi^-)}{\Gamma(K_L \to \pi^0\pi^0)/\Gamma(K_S \to \pi^0\pi^0)}$$

$$= \frac{|\eta_{+-}|^2}{|\eta_{00}|^2} \approx 1 + 6\mathrm{Re}(\varepsilon'/\varepsilon). \tag{20}$$

Since $\mathrm{Re}(\varepsilon'/\varepsilon)$ is expected to be small, this deviation is approximately $6\mathrm{Re}(\varepsilon'/\varepsilon)$.

There has been quite an industry measuring $\mathrm{Re}(\varepsilon'/\varepsilon)$ over the past 30 years, and the recently published results are presented in Table I. In 1988, the NA31 group published evidence [20] for direct $CP$ violation at the three-standard-deviation level. An initial result [21] from our group based upon 20% of the data collected here was, however, consistent with no direct $CP$ violation. The analysis of the complete E731 data set, which is the focus of this article, has been published [22]; this result together with the final one from NA31 [23] is also shown in Table I for comparison. There is approximately a two-standard-deviation discrepancy between the NA31 publication and our initial result. The analysis presented here also reanalyzes the data used in Ref. [21], and so this result supersedes the previous one.

There has been considerable theoretical effort placed on the evaluation of $\mathrm{Re}(\varepsilon'/\varepsilon)$ over the last few years, with

TABLE I. Recently published measurements of $Re(\varepsilon'/\varepsilon)$. Errors listed are statistical error first and the systematic error second, otherwise the combined error.

| Collaboration | Year | $Re(\varepsilon'/\varepsilon)$ $(10^{-4})$ |
|---|---|---|
| Yale-BNL [17] | 1985 | $17 \pm 82$ |
| Chicago-Saclay (Fermilab E617) [18] | 1985 | $-46 \pm 53 \pm 24$ |
| Chicago-Elmhurst-Fermilab-Princeton-Saclay (Fermilab E731A) [19] | 1988 | $32 \pm 28 \pm 12$ |
| CERN-Dortmund-Edinburgh-Mainz-Orsay-Pisa-Siegen (CERN NA31) [20] | 1988 | $33 \pm 7 \pm 8$ |
| Chicago-Elmhurst-Fermilab-Princeton-Saclay (Fermilab E731 20%) [21] | 1990 | $-4 \pm 14 \pm 6$ |
| Chicago-Elmhurst-Fermilab-Princeton-Saclay (Fermilab E731 final result) [22] | 1993 | $7.4 \pm 5.2 \pm 2.9$ |
| CERN-Edinburgh-Mainz-Orsay-Pisa-Siegen (CERN NA31 final result) [23] | 1993 | $23 \pm 6.5$ |

results ranging from as small as $10^{-4}$ up to several $10^{-3}$. Perhaps the only hard conclusion one can draw from these calculations is that, from an experimentalist's point of view, $Re(\varepsilon'/\varepsilon)$ is expected to be *small* in the standard model. The theoretical situation has greatly improved very recently with two new calculations of $Re(\varepsilon'/\varepsilon)$ at next-to-leading order. We however defer further discussion of these results until Sec. XI.

## B. Tests of $CPT$ invariance

In the phenomenological analysis of $CP$ violation in the $\pi\pi$ decays of neutral kaons given above, many of the results we obtained rested on the assumption that the weak Hamiltonian underlying $H_{eff}$ was invariant under $CPT$. $CPT$ invariance is a very general property, arising in any local field theory which incorporates proper Lorentz transformations. However, there have been several issues recently raised which question the validity of assuming $CPT$. For example, Kobayashi and Sanda [24] question the applicability of the $CPT$ theorem to QCD because the proof of the $CPT$ theorem used the properties of asymptotically free states, while the quarks and gluons are confined and do not appear in such states. Furthermore, one might question the validity of the assumption that the world is described by a local field theory. We may well be seeing the low-energy effective interactions of some more fundamental process. If, for example, a string theory turns out to be a valid description of nature, then the nonlocal nature of such a theory could lead to $CPT$-violating phenomena. Indeed, there have even been recent speculations that such phenomena could lead to observable effects in the $K^0$-$\bar{K}^0$ system [25].

We now briefly discuss some of the tests of $CPT$ symmetry open to the kaon system and accessible by our experiment.

The phases $\phi_{+-}$ and $\phi_{00}$ can be used to test $CPT$ symmetry. Equation (12) can be divided into two different tests, and different assumptions enter each. In the first, one wishes to compare the phases $\phi_{+-}$ and $\phi_{00}$ directly, that is, to measure the phase difference $\Delta\phi \equiv \phi_{00} - \phi_{+-}$. To make such comparisons in Eq. (12), we need measurements of the mass difference $(\Delta m)$, of the $K_S$ and $K_L$ lifetimes $(\tau_S$ and $\tau_L)$,

and of the phases themselves. Using Eqs. (17) and (18), one finds that the effect of $\varepsilon'$ on the phase difference is given approximately by

$$\Delta\phi \approx 3 Re(\varepsilon'/\varepsilon)\tan(\phi_\varepsilon - \phi_{\varepsilon'}). \qquad (21)$$

Using the uncertainties in the previous measurements of $Re(\varepsilon'/\varepsilon)$ and in the $\pi\pi$ final state phase shifts, one can limit the contribution from direct $CP$ violation to the phase difference to be under $0.2°$. There were two measurements of the phase difference $\Delta\phi$, one based on a subset of the data used in this experiment [26] and another from the NA31 experiment [27] at CERN. The values obtained for $\Delta\phi$ were

$$-0.3° \pm 2.4° \pm 1.2° \quad \text{(E731 20\%, partial data set)},$$

$$+0.2° \pm 2.6° \pm 1.2° \quad \text{(NA31)}.$$

In both cases, the first errors are statistical and the second are systematic. Together, these measurements imply $\Delta\phi = -0.1° \pm 1.9°$. The experimental values for the phase above are consistent with $CPT$, but further accuracy is desired.

The other phase comparison we can make is the agreement between $\phi_{+-}$ and the superweak phase $\tan^{-1}(2\Delta m/[\Gamma_S - \Gamma_L])$. Here, we neglect the contribution of $\Gamma_{12}$ in Eq. (5) to the phase. If one assumes that the $\Delta S = \Delta Q$ law is not significantly violated and that $CP$ violation in the $3\pi$ decays is not anomalously large, then the $\pi\pi$ contribution is expected to dominate by a factor of $\Gamma_S/\Gamma_L \approx 580$. The $\pi\pi$ contribution to $Im\Gamma_{12}/\Gamma_S$ is of order $\frac{1}{22}|\varepsilon'/\varepsilon|$, and so the contribution of $\Gamma_{12}$ to the phase of $\varepsilon$ is expected to be extremely small. The phase $\phi_\varepsilon$ (and therefore the phase $\phi_{+-}$) should thus be very close to the superweak phase. The experimental data were not in the best agreement with this assertion. The phase $\phi_{+-}$ of $\eta_{+-}$ has been measured previously by studying the interference in $\pi^+\pi^-$ decays [27–29]. The world average [30] at the time we obtained our data was $\phi_{+-} = 46.6° \pm 1.2°$, over two standard deviations away from the superweak phase $43.68° \pm 0.14°$.

The latter test is, unfortunately, a somewhat model-dependent one since the assumption that the semileptonic

and $3\pi$ contributions to $\Gamma_{12}$ are small could be questioned. If one is questioning the validity of $CPT$, it is not clear that it is fair to make model-dependent assumptions about these rates. Since the $\Delta S = -\Delta Q$ amplitude is only limited at the 2% level and $CP$ violation in $3\pi$ decays is only limited at the 10% level, a completely model independent estimate of $\phi_\varepsilon$ is actually much poorer. Recent estimates [24], strictly using only the actual experimental information, have placed the value of $\phi_\varepsilon$ within the $39.5°-47.4°$ range at the 90% confidence level. It is still interesting to probe the experimental discrepancy between $\phi_{+-}$ and the superweak phase. If the discrepancy is not an artifact of the measurements, then it *is* an indication of some new physics, even if not $CPT$ violation.

A new result for $\Delta\phi$ that supersedes our previous measurement listed above has been published [31], along with a new determination of $\phi_{+-}$. These measurements are also part of the results on neutral kaon physics presented here.

### C. Overview

We have discussed many of the basic issues relevant to the measurements we can perform in this experiment. The rest of the article describes the measurement technique, data analysis, and results. In the next section, the issues affecting a measurement of $\text{Re}(\varepsilon'/\varepsilon)$ and how these issues affected the design of our experiment are discussed. Following this, we examine the detector itself and give a brief description of the data collection. Sections IV–VI present the analysis of the data, covering the calibration techniques, and the different reconstruction and background subtraction techniques in the $\pi^+\pi^-$ and $2\pi^0$ decay modes.

Our experimental method requires understanding the acceptance of the detector at a precise level. Section VII details the Monte Carlo simulation of our experiment that we used to determine the acceptance. The fitting techniques used in extracting the physical parameters are covered in Sec. VIII. Many of the issues treated are quite important as considerations for future experiments using this technique. The results of the fits for $\text{Re}(\varepsilon'/\varepsilon)$ of the kaon system are presented separately in Sec. IX.

The final part of the analysis involved the determination of the systematic uncertainty on each of the particular measurements. In Sec. X, we focus on the systematic checks and the final systematic uncertainty for our measurement of $\text{Re}(\varepsilon'/\varepsilon)$ to the uncertainty in the other parameters noted where important. With our measured parameters and systematic uncertainties all in hand, we conclude in Sec. XI by relating our findings back to the issues presented in this section.

### II. EXPERIMENTAL TECHNIQUE

A precise determination of $\text{Re}(\varepsilon'/\varepsilon)$ to better than 0.001 requires measuring the double ratio of rates [Eq. (20)] to better than 0.6%. This means collecting a large number of $K \rightarrow \pi\pi$ decays in each of the four modes and requires strict controls of biases in extracting the double ratio of rates. Here we outline the issues in measuring this double ratio and discuss how E731 techniques reduce the systematic sensitivity. Finally, we outline how these techniques allow the extraction of other parameters in the neutral kaon system. The detector

itself is described in the next section.

The origins of this technique are as follows. During the mid-1970s, some of the authors of this paper made the first successful measurement of the charge radius of the neutral kaon [32]. One needed to measure the coherent regeneration (where the contribution from atomic electrons adds to that of the nuclei) and the diffractive regeneration (where the electron contribution is incoherent); comparing the two allows isolation of the electron contribution. The problem is that the former requires a *thick* regenerator for the signal and background suppression, while the latter requires a *thin* regenerator to suppress multiple-scattering effects. Previous attempts used a compromise in the regenerator size; the choice in [32] was to use two regenerators simultaneously in two distinct kaon beams derived from the same target. By frequent alternation of the regenerators, one could assure that each saw the same incident flux.

One of the early papers on the phenomenology of $CP$ violation in the standard model was by Ellis, Gaillard, and Nanopoulos [33]. In this paper, they calculated the value of $\text{Re}(\varepsilon'/\varepsilon)$, saying that it would be in the neighborhood of 1/450 and that this "would remain outside the reach of experiments for some time to come." The subject of *direct* $CP$ violation had not been pursued for a number of years as there was no compelling indications as to its size. Now, with a possible model for the effect, it appeared at least possible to say whether the six-quark Cabibbo-Kobayashi-Maskawa (CKM) model definitively accounted for $CP$ violation. With the double-beam technique, one could see an effect of this size. This led to Fermilab experiment 617. For this effort, it was required that one photon convert in a thin conversion plane in the middle of the decay region so that the resultant $e^+e^-$ pair could be tracked, reducing background by providing a means of giving the decay vertex. The result (Bernstein *et al.* [18]) was consistent with zero with a precision of 0.006, not quite at the level predicted. (Interestingly, a BNL-YALE group [17] also performed a measurement at about the same time, with an error of 0.008.)

In 1983, we proposed a new double beam and experiment 731, to make the measurement with a precision of 0.001. E731 had a brief test run (E731A) in 1985, where again a photon conversion was required, with the result $\text{Re}(\varepsilon'/\varepsilon) = 0.0032 \pm 0.0030$ (Woods *et al.* [19]). An extensive upgrade followed the 1985 run which permitted the use of events with no conversion and thus much higher statistics. This paper treats the upgraded detector and the data it collected.

### A. Measurement

The instantaneous rate for $K^0$ decays downstream of a target is

$$\frac{d\Gamma(2\pi)}{d\tau} \propto |e^{-\tau/2\tau_S + i\Delta m \tau} + \eta e^{-\tau/2\tau_L}|^2, \qquad (22)$$

where $\tau_S$ and $\tau_L$ are the $K_S$ and $K_L$ lifetimes, $\Delta m$ is the $K_L - K_S$ mass difference, and $\tau$ is the kaon proper time. Since $|\eta|$ is small, a $2\pi$ event sample from a detector close to a target would be dominated by decays of $K_S$. In the interference region where the $K_S$ and interference terms in Eq. (22) are comparable ($\tau \approx 12\tau_S$), $\eta_{+-}$ and $\eta_{00}$ could be

extracted but this requires the relative numbers of $K^0$ and $\bar{K}^0$ to be accurately known. Using separate sources for $K_L$ and $K_S$ decays, one far from the decay volume to give a $K_L$ sample and the other close for the $K_S$ sample, is the method of choice.

Care must be taken that biases in the relative collection efficiencies of the two samples are minimized. Detector performance can change over time, but the ratio of $K_S$ and $K_L$ in either the $\pi^+\pi^-$ (charged) or $2\pi^0$ (neutral) decay mode should be robust against such changes. Differences in the relative loss of $K_S$ and $K_L$ because of spurious ("accidental") activity in the detector need to be minimized. Such activity arises from noise in the detector and readout electronics, muons from target and beam dump, neutral beam halo and interactions in detector material, and decays. Hence the number of decays collected depends nonlinearly on the primary beam intensity. Biases from changes in accidental losses need to be controlled.

The detector acceptance is a function of the decay position and energy of the kaon. The lifetime difference between the $K_L$ and $K_S$ leads to different distributions of decays and hence different acceptances. The design must provide strict control of biases in these acceptance corrections.

Other $K_L$ decay modes present backgrounds. Detection of $\pi^+\pi^-$ decays compete with $\pi^+\pi^-\pi^0$ and semileptonic ($\pi^\pm l^\mp \nu$) decays with branching ratios from 60 to 200 times larger. Similarly, the $2\pi^0$ mode has to compete with the more copious $3\pi^0$ mode. The $\pi\pi$ decays must be filtered from these more common $K_L$ decays without trigger bias. For example, in the test run for this experiment [19] we discovered that rejecting $\pi^\pm e^\mp \nu_e$ ($K_{e3}$) decays at the trigger level from eletron showers in a lead curtain in front of trigger hodoscopes introduced an uncontrollable bias in the relative loss of $\pi^+\pi^-$ decays in the $K_L$ beam relative to the $K_S$ beam. We chose to accept the $K_{e3}$ decays, eliminating them only offline.

Finally, to extract $Re(\varepsilon'/\varepsilon)$, one measures charged and neutral decays within specified fiducial regions in the center of mass. Since this requires (un)boosting the reconstructed kaons back to their rest frames, the relative energy scale between the charged and neutral modes must be very well understood.

We now describe the principles we used to control these effects.

## B. Double beams and the regenerator

Two nearly parallel beams were produced by collimating the products of an 800 GeV/$c$ proton beam striking a beryllium target. The detector was located over 100 m downstream, giving ample room for sweeping away charged particles and sufficient time for neutral hyperons to decay. Essentially all of the $K_S$ components of the $K^0$'s and $\bar{K}^0$'s produced in the target decayed, leaving two neutral $K_L$ beams (with neutron contamination).

At the upstream end of the decay volume, one of the $K_L$ beams passed through two interaction lengths of boron carbide ($B_4C$), providing coherently regenerated $K_S$. Downstream, the $\pi\pi$ decay rate at momentum $p$ is given by

$$\frac{d\Gamma_R}{dz} \propto aF(p)\{|\rho(p)|^2 e^{-z/\gamma\beta c\tau_S} + |\eta|^2 e^{-z/\gamma\beta c\tau_L}$$

$$+ 2|\rho||\eta|\cos(\Delta mz/\gamma\beta c + \phi_\rho - \phi_\eta)$$

$$\times e^{-z(1/\tau_S + 1/\tau_L)/2\gamma\beta c}\}, \tag{23}$$

where $z$ is the distance from the downstream end of the regenerator, $\rho$ is the coherent regeneration amplitude, and $a$ is the beam attenuation. The ratio $|\rho/\eta|$ was chosen in the 10–20 range (due to the momentum dependence of $\rho$), and so the $K_S$ decay term dominated. In the other (vacuum) beam, the rate is given by

$$\frac{d\Gamma_V}{dz} \propto F(p)|\eta|^2 e^{-z/\gamma\beta c\tau_L}. \tag{24}$$

In both Eqs. (23) and (24), $F(p)$ is the $K_L$ flux. The regenerator alternated between the two $K_L$ beams, making $F(p)$ nearly identical and rendering biases from detector asymmetries negligible.

Decays from both beams to a common decay mode, either $\pi^+\pi^-$ or $2\pi^0$, were detected simultaneously. (In the last 20% of the data set, all four of the $K\to\pi\pi$ modes were collected simultaneously. While collecting the $2\pi^0$ and $\pi^+\pi^-$ decays simultaneously is not crucial for the success of our technique, it does allow several more systematic cross-checks.) It is particularly important that biases in the collection and reconstruction efficiencies were kept to a minimum by keeping all triggering, reconstruction, and analysis cuts strictly independent of the beam in which a decay occurred.

Many of the advantages of simultaneously collecting the $K_L$ and $K_S$ decays to a common mode are clear. Changes in the detector response affect the $K_L$ and $K_S$ decays identically and cancel in the ratio of $K_L/K_S$ (the "single" ratio). Losses due to accidental activity cancel to first order. Intensity fluctuations in the primary proton beam also cancel in each of the single ratios.

A regenerator to produce the $K_S$ decays, rather than using a second target far downstream of the first, was chosen for the following reasons. A closer target generates backgrounds difficult to sweep away. Coherent regeneration produces a sample of $K_S$ decays with an angular spread identical to that of the $K_L$ sample. Also, the momentum distributions of the $K_S$ and $K_L$ samples are quite similar.

The use of the regenerator makes the single ratios physically meaningful. Comparing Eqs. (23) and (24), the incident kaon flux cancels in the $K_S/K_L$ ratio, leaving a measure of $|\rho/\eta|$. Since the same regenerator was used throughout the run, we have a powerful physical check (we should always measure the same regeneration amplitude) to apply to different subsets of the $\pi\pi$ decays.

The regeneration amplitude $\rho$ is related to the difference in the forward scattering amplitudes $f(0) - \bar{f}(0)$ of the $K^0$ and $\bar{K}^0$ by

$$\rho \approx \iota\pi \frac{f(0) - \bar{f}(0)}{k} Ng(L,p), \tag{25}$$

where $k = p/\hbar$ is the kaon wave number, $N$ is the density of scatterers, and $g(L,p)$ (close to unity) is a function of the length $L$ of the regenerator and the kaon momentum. Regge theory predicts [34] that the difference in the forward amplitudes is dominated by the exchange of a single trajectory, the $\omega$. This leads to the particularly simple form, for the amplitude difference,

$$\frac{f(0) - \bar{f}(0)}{k} = A p^{\alpha} e^{-\imath(\pi/2)(2+\alpha)}. \qquad (26)$$

Analyticity leads to the constraint between the power $\alpha$ and the phase of $f(0) - \bar{f}(0)$, $\phi_{f-\bar{f}} = -\pi(2+\alpha)/2$. In the high-momentum region, deviations from this power-law dependence are very small [35].

The expected power-law behavior adds one more physical constraint for controlling biases in the measurement of $\mathrm{Re}(\varepsilon'/\varepsilon)$. From the charged and neutral single ratios we obtain a measure of $\rho/\eta_{+-}$ and $\rho/\eta_{00}$ whose magnitudes will be identical only if $\varepsilon'$ is zero. However, the momentum dependences (power law) should be the same. Since essentially orthogonal elements of the detector are used for the two modes which have quite different backgrounds, a physical parameter which can be independently extracted and compared gives a powerful systematic check. This is useful in limiting biases due to nonlinear differences in the two energy scales.

There are disadvantages associated with this technique. The most serious one is additional background due to scattering in the regenerator. Diffractive regeneration, where there is a finite-momentum transfer between the kaon and a particular nucleus, is present. There are also inelastic processes where a nucleus breaks up or is excited.

Another disadvantage arises from the difference in the $K_S$ and $K_L$ lifetimes leading to different average acceptances. We use a Monte Carlo simulation to determine the corrections needed in the two modes. The acceptance function $\epsilon(p,z)$ is *identical* for the vacuum and regenerator beams. By using large bins (in $p$ and $z$) relative to the inherent detector resolution, we reduce our sensitivity to smearing effects, generally the hardest aspect of a detector to be simulated accurately.

### C. Detector design

We focus on three aspects in the design of the detector to use the double beams: (a) acceptance corrections, (b) detection of the $K \rightarrow 2\pi^0$ decays and background elimination in this mode, and (c) detection of the $K \rightarrow \pi^+\pi^-$ and elimination of the background. In both modes we need to reconstruct the momentum and decay position to compare the observed distributions to Eqs. (23) and (24) above.

#### 1. Acceptance corrections

It was important to make the acceptance calculation as simple as possible. All of the limiting geometrical apertures of the detector were defined by active veto elements. This effectively reduced the problem of determining the acceptance to measuring the edges of several planar counters at known distances from the target.

To study the detector performance and determine the acceptance, we collected high-statistics samples in the $3\pi^0$, $\pi^+\pi^-\pi^0$, and $K_{e3}$ decay modes. None of the important parameters of the detector performance, as input to the Monte Carlo simulation, was determined with the $\pi\pi$ event samples used to calculate $\mathrm{Re}(\varepsilon'/\varepsilon)$.

#### 2. $K \rightarrow 2\pi^0$ decays

For $2\pi^0$ decays, measuring the energies and positions of the four photons required a high-resolution, segmented, electromagnetic calorimeter. The calorimeter had to be sufficiently radiation hard and have a good time response. An array of lead glass crystals, measuring Čerenkov light produced by electromagnetic showers, had been used in Fermilab-E617 and was reused for this effort.

The largest background for this mode at the trigger level came from $K_L \rightarrow 3\pi^0$ decays. These could be reduced by requiring four energy clusters in the calorimeter. Because of photons escaping the detector or landing near each other ("fusing") in the calorimeter, background remained. Many planes of veto counters to detect photons escaping the lead glass aperture helped further to reduce the background.

#### 3. $K \rightarrow \pi^+\pi^-$ decays

The $\pi^+\pi^-$ decay required detecting two charged particles. For triggering, we used two hodoscope planes. The trajectories and momenta of the particles were measured using two pairs of drift chambers and a dipole analyzing magnet. The decay position of the kaon was determined by extrapolating the trajectories in the upstream chambers to a common point.

The major backgrounds to $\pi^+\pi^-$ decays, such as $\pi^+\pi^-\pi^0$ and $\pi^{\pm}l^{\mp}\nu$, were reduced by requiring two symmetric up-down and right-left signatures in hodoscope hits at the trigger level.

With a muon filter, the $\pi^{\pm}\mu^{\mp}\nu_{\mu}$ decays were vetoed at the trigger level. The $K_{e3}$ background was rejected off line using the ratio of energy from the lead glass to momentum.

Finally, the relative charged and neutral energy scales had to be well known. This was accomplished by calibrating the lead glass with tracks from electron and positron samples measured in the charged spectrometer. The samples came both from special electron calibration runs and from the $K_{e3}$ sample collected simultaneously with the $\pi^+\pi^-$ decays.

### D. Sensitivity to other kaon parameters

Examining Eq. (23) shows there is sensitivity to other important parameters of neutral kaon decay. Using the vacuum beam for normalization, we can obtain the incident flux on the regenerator. Then from the shape of the decay distribution immediately downstream, we have good sensitivity to the $K_S$ lifetime, as well as the $K_L - K_S$ interference term, allowing us to probe both the $K_L - K_S$ mass difference $\Delta m$ and the relative phase $\phi_{\rho} - \phi_{\eta}$.

### III. APPARATUS AND DATA RUN

Here we give a description of the kaon beam, the detector, and special features of the data run. Earlier descriptions and
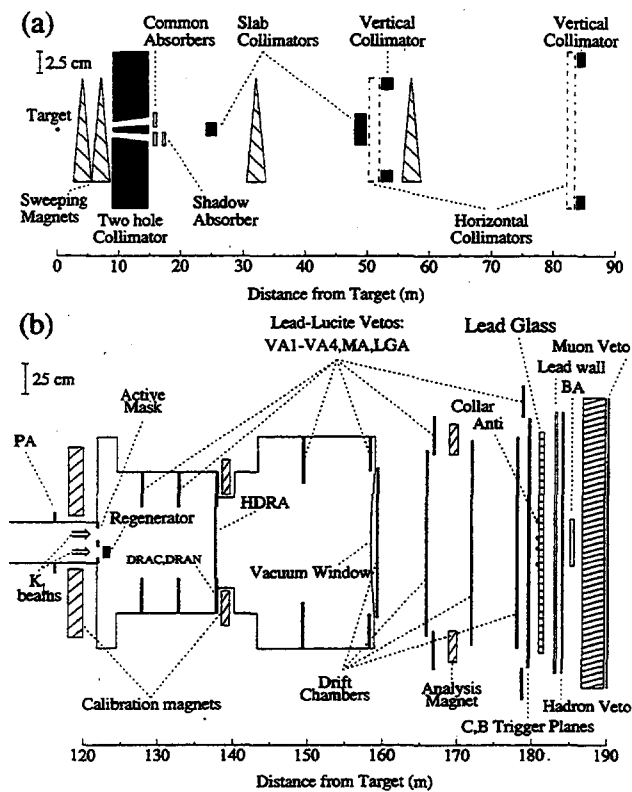
FIG. 2. Illustration of the apparatus used in this experiment. (a) is an elevation view of the layout of the collimation and sweeping system used to produce the two neutral beams. (b) shows the apparatus used to detect the kaon decay products.

illustrations of various detector elements can be found in Refs. [1,36–38].

## A. Kaon beams

The experiment was located in the Fermilab Meson Center beam line. The two kaon beams were formed by collimating secondaries produced by 800 GeV primary protons hitting a beryllium target. The primary beam was delivered in a 20 s "spill" once every minute, with intensity between $3 \times 10^{11}$ and $2 \times 10^{12}$ protons per spill. The protons arrived in $\sim 1.8$ ns "buckets" at 53 MHz; the instantaneous intensity varied by about a factor of 2 from bucket to bucket. The radio frequency (rf) timing signal, provided by the proton accelerator, gave the basic timing used in the trigger.

The target was a beryllium rod 36 cm long and 3.2 mm on a side; the proton beam profile was roughly Gaussian with a width of 0.4 mm. The beam position on the target was monitored and read out throughout each spill with a wire chamber.

The neutral beams each subtended a solid angle of 300 nsr were produced using the collimation scheme shown in Fig. 2(a). First, there was a 5.8-m-long two-hole copper collimator; it began 9 m downstream of the target and contained two tapered channels 5 mrad away from the proton beam horizontally. At the upstream end, the channels each measured $6.65 \times 6.65$ mm$^2$, centered 5.8 mm above and below the target location. The edges of neutral beams were further defined by sets of steel collimators ranging in length from 1.2 m to 1.8 m. Two slab collimators defining the inner beam edges

were located at 25 m and 49 m. The outer beam edges were defined by sets of horizontal and vertical collimators at 52 m and 83 m. Charged particles were swept out of the beams with several magnets behind the target and between the collimators.

The neutron production spectrum peaks more strongly in the forward direction than the kaon spectrum, and so the 5 mrad "targeting angle" served to decrease the $n/K$ ratio without greatly sacrificing kaon beam intensity. The ratio was further reduced by an absorber of 50.8 cm of beryllium and 7.6 cm of lead positioned just downstream of the copper collimator. This "common" absorber also converted photons, eliminating them from the beams. A second 45.7 cm beryllium "shadow absorber" only in the regenerator beam reduced the rate of interactions in the regenerator.

The entire beam path and decay volume from 17 m to 160 m was held at a vacuum under 0.015 torr. The downstream end of the vacuum was sealed by a 1.22 m diameter window, made from 0.127-mm-thick Mylar and 0.584-mm-thick Kevlar-29 mesh.

The decay region began 110 m downstream of the target. At the entrance to the decay volume, there were roughly equal numbers of $K_L$ and neutrons, and the number of $\Lambda$ particles was about 0.05% of the number of $K_L$ in the energy range 20–160 GeV/$c$ of interest. At the mean energy of 70 GeV/$c$, the residual $K_S$ component from the target was under $10^{-6}$.

A beam intensity of $3 \times 10^{11}$ protons per spill resulted in roughly $25 \times 10^6$ $K_L$ entering the decay volume in the vacuum beam with about 2% $K_L$ decaying in the decay volume.

## B. Detector

The apparatus used in this experiment is illustrated in Fig. 2(b). A list of the detector elements and their locations is given in Table II. The coordinate system used defines a $z$ axis along the beam direction. The $x$ and $y$ axes are the horizontal and vertical directions transverse to the beam, respectively. Those components which play a role common to both the $\pi^+\pi^-$ and $2\pi^0$ decay modes are described first.

### 1. Common elements

a. Regenerator. The regenerator, depicted in Fig. 3, consisted of four blocks of boron carbide (B$_4$C), each $19.0 \times 8.9 \times 8.9$ cm$^3$. It totaled two interaction lengths, which maximizes coherent regeneration. Within each 3.5 cm gap between the B$_4$C blocks were six $8.90 \times 1.74 \times 0.63$ cm$^3$ overlapping strips of scintillator. These veto counters reduced backgrounds from inelastic interactions and vetoed kaon decays within the regenerator. A 1.25-cm-thick lead piece at the very end of the regenerator converted photons from $2\pi^0$ decays within the regenerator, defining a sharp boundary for the start of the $2\pi^0$ decays in the regenerator beam. The last set of veto counters 1.75 cm downstream of the lead detected conversion products and vetoed $\pi^+\pi^-$ decays. The face of the downstream scintillator defined the start of the decay region for the $\pi^+\pi^-$ mode.

b. Upstream mask. The behavior of the acceptance in the farthest upstream region of the vacuum beam was defined by a precision veto counter [the "active mask" (AM)] located

TABLE II. The detector elements and their positions from the target.

| Detector element | z location (m) | Detector element | z location (m) |
|---|---|---|---|
| Pinching anti (PA) | 116.118 | Drift chamber 1 | 159.292 |
| Sweeper anti (SA) | 119.59 | Drift chamber 2 | 165.867 |
| Sweeper magnet | 119.59 | Magnet anti (MA) | 166.836 |
| Active mask (AM) | 121.893 | Analyzing magnet | 168.865 |
| Regenerator | 123.550 | Drift chamber 3 | 171.857 |
| Vacuum anti 1 (VA1) | 127.855 | Drift chamber 4 | 178.004 |
| Vacuum anti 2 (VA2) | 132.819 | Lead glass anti (LGA) | 178.710 |
| V hodoscope | 137.792 | C hodoscope | 179.502 |
| Lead sheet | 137.804 | B hodoscope | 179.520 |
| T hodoscope | 137.815 | Collar anti (CA) | 180.700 |
| DRAC veto counter | 137.826 | Lead glass array | 181.809 |
| DRAN veto counter | 137.866 | Lead wall | 182.7 |
| Separator magnet | 139.008 | Mu1 hadron veto | 183.996 |
| Vacuum anti 3 (VA3) | 149.309 | Back anti (BA) | 185.047 |
| Vacuum anti 4 (VA4) | 158.291 | 3.2 m steel muon filter | 186.7 |
| Vacuum window | 158.965 | Mu2 muon veto | 189.914 |

at 121.9 m from the target. The mask consisted of two layers of 2.54-cm-thick lead with scintillator behind each layer. Precise beam holes were milled in the lead and scintillator. The holes were sized and positioned such that (a) decay products from the regenerator beam occurring upstream of the regenerator would miss the regenerator (and its anti-counters) and hit the AM and (b) wide-angle decay products from upstream of the mask in the vacuum beam were detected by the mask and could not hit the "dead" material (such as the box enclosing the regenerator). The locations of the mask edges were determined with electrons from $K_{e3}$ decays.

c. HDRA. The Hodoscope and Decay Region Anticounter (HDRA) was a trigger and veto system used in both charged and neutral modes. The makeup of the HDRA is given in Fig. 4 and Table III. The hodoscopes were originally intended to flag a photon conversion. A 0.5 mm lead sheet converted one and only one photon 25% of the time, leaving a signal in the trigger (T) counters downstream of the lead and none in the veto (V) counters upstream. Both the T and V hodoscopes consisted of six 1-mm-thick staves of NE110 scintillator. A more detailed description of this conversion techinique can be found elsewhere [39]. The $\pi^+ \pi^-$ running used T and V for triggering (without the lead sheet).

Initially the $2\pi^0$ and $\pi^+ \pi^-$ events were thus collected separately. During the run we found that $2\pi^0$ events with no

photon conversion would yield a more accurate result. This allowed the removal of the lead sheet and the extension of the decay volume for $2\pi^0$. Using the downstream events does, however, require careful measurement of the materials listed in Table III to treat regeneration and conversions.

### 2. Neutral detection

a. Lead glass calorimeter. The heart of $2\pi^0$ detection was the electromagnetic calorimeter located at 181 m. It has been detailed previously in Ref. [36].

Figure 5 illustrates an event in the calorimeter. It consisted of 804 blocks of Schott F-2 lead glass arranged in a circular array with two beam holes. The blocks were $5.82 \times 5.82$ cm$^2$ by 60.17 cm long, about 18.74 radiation lengths. The radius of the array was about 0.93 m.

Ten-stage Amperex 2202 photomultiplier tubes (PMT) with bialkali photocathodes were pressure mounted to the back of each block. The tube gains were roughly $1.2 \times 10^5$. Their voltage settings were stable to within a few tenth of a volt throughout the run. A xenon flash lamp system was pulsed every 2 s throughout the run to monitor the combined effects of block transmission and PMT gain; this system worked at the 0.2% level.

Each PMT signal was delayed by 83.8 m of RG58 cable to allow time for the formation of the trigger before digiti-

Veto Counters

B$_4$C    Pb

Beam Direction
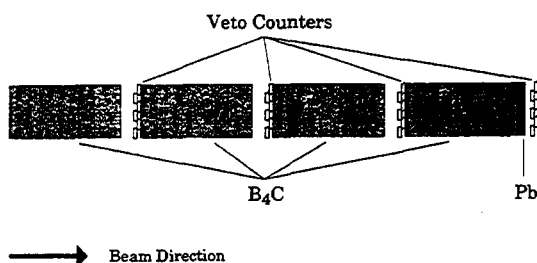
FIG. 3. The makeup of the regenerator.

V    T    Material Key

Paper
Aluminum Foil
Scintillator
Aluminized Mylar
Mylar
Lead (+ epoxy)
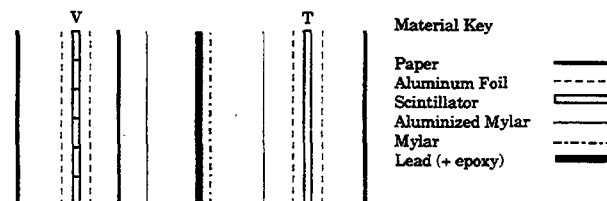
FIG. 4. An expanded view of the material contained within the HDRA. The 0.5 mm lead sheet, bonded to a Mylar sheet for support, was only in place for the neutral mode lead sheet data subsets.

zation. The signals were integrated for 150 ns and digitized in LeCroy 2280 analogue-to-digital converters (ADC's). (The long gate was necessary because of pulse broadening in the cables and the scintillation component in the lead glass.) The ADC had 12-bit accuracy but operated in a dual-range mode, extending the dynamic range to 15 bits. The crossover point of the dual range corresponded to roughly 16 GeV, and the gain ratio (nominally 8) was measured for each channel to 0.1% with the $K_{e3}$ sample. When neutral triggers were collected, the readout threshold was 5 ADC counts (about 25 MeV); when only charged events were collected, the threshold was 20 counts.

The light transmission response of the lead glass blocks was nonlinear because of absorption of the Čerenkov light. Electromagnetic showers have shower maximum increasing as the energy increases; this results in less attenuation as the light travels to the photomultiplier tube. This attenuation was the most severe and varied most rapidly for the shorter-wavelength Čerenkov light, and so Wratten 2A filters were placed before the PMT's to block light with wavelengths under 430 nm [40]. These filters (while reducing the total light by a factor of 2) improved the resolution and simplified the calibration of the glass. Typical absorptions resulted in nonlinearities of $E_{\text{true}} \propto E_{\text{measured}}^{0.97}$.

During the run, the light absorption increased because of radiation damage, particularly for blocks near the center of the array. Transmission decreased by 5% per week in the worst case. To avoid serious degradations in resolution, much of the damage was cured with ultraviolet light supplied by 400 W mercury vapor lamps. Curings were done about once a month and took about 2 days.

For each block, the absorption and gain were determined several times during the run (see Sec. IV B) from electron samples obtained from special calibration runs and from $K_{e3}$ decays.

The EM shower from an incoming electron develops across several blocks. To reconstruct the total energy in a shower, the energies from a $3 \times 3$ array of blocks (a "cluster") centered on the block of maximum energy were summed. This sum was then corrected as described in Ref. [36] for threshold effects, pedestal shifts, leakage into blocks outside of the $3 \times 3$ array, and the nonlinearity described above. These corrections were extensively studied using both EGS simulations and the electron samples.

Photon shower response is somewhat different from that for electrons because of the variation in conversion depth. A photon shower gives a response effectively as the sum of an electron and positron shower in a block shortened by the photon conversion depth $t_0$. A correction for the photon conversion depth was made on an average, but the variation added an additional contribution to the photon resolution.

The average energy resolution for electrons was described by

$$1.5\% \oplus 5\%/\sqrt{E}, \qquad (27)$$

where the energy $E$ is measured in GeV, though it varied from block to block because of variations in attenuation and quantum efficiencies. The overall photon energy resolution was

$$2.5\% \oplus 5\%/\sqrt{E}. \qquad (28)$$

The position of a photon or electron can be extracted from the pattern of energy in the $3 \times 3$ cluster. By summing the energies in each column (row) of the cluster and comparing the ratio of the edge sums to the center sum, the $x$ ($y$) position was obtained. Small corrections to the positions were made using the measured variations of the individual block dimensions from the average. This method gave an average resolution of 2.8 mm, varied from 1.5 mm for a particle near a block's edge to 4.0 mm for a particle in a block's center.

The signals from the lead glass were used for triggering purposes as well as being integrated and digitized. For this purpose, the signals from the array were viewed by two devices in addition to the ADC's.

For fast triggering, the lead glass array was subdivided into $3 \times 3$ groups of blocks, and the signals from the blocks in each $3 \times 3$ group were sent to an "adder." Each sum was integrated with a 30 ns gate. The short gate helped to identify out of time clusters. The adder outputs were summed together to give the total energy of the calorimeter.

A hardware cluster finder (HCF) counted the number of clusters in the lead glass calorimeter. A cluster refers to a contiguous island of blocks all above the HCF threshold. This led to a factor of 10 reduction in the neutral trigger rate. The signal from each block was viewed capacitively and digitized by a 30-MHz 6-bit flash ADC. A block registered a hit if its energy content was above about 1 GeV, low enough to allow high efficiency and high enough to reduce losses from photon fusions or accidental activity. Details of the HCF construction and the cluster-finding algorithm have been published elsewhere [37,41].

*b. Neutral veto systems.* A photon veto counter [the "collar anti" (CA)] covered the inner halves of the 16 blocks around the two beam holes. The counter consisted of 8 radiation lengths (4.45 cm of copper and 2.8 cm of lead) followed by scintillation counters. Its main purpose was to provide a clean and easily determined edge to the detector's photon acceptance.

The remaining photon veto counters rejected $3\pi^0$ decays and, to a lesser degree, other charged decays. The counters in most of these veto banks consisted of a scintillator plane followed by two lead-lucite sandwiches, each with five layers of lead and of lucite, totaling 3 radiation lengths. Four sets (the "vacuum antis" VA1–VA4) were arranged in rings inside the decay pipes, two on either side of the HDRA. Another set (MA), in a square ring, surrounded the aperture of the analysis magnet. A final ring was just upstream of the lead glass (LGA).

At the far upstream end there were two sets of counters used to detect photons from $3\pi^0$'s that decayed in the beam pipe preceding the decay volume. The most upstream "pinch anti" (PA) consisted of a layer of lead followed by a layer of scintillator collaring the beam pipe. The "sweeper anti" (SA) consisted of scintillator panels which lined the outside surface of the beam pipe from 117.8 m to 121.4 m. Photons that converted in this pipe section, missing the VA's, were vetoed by these scintillator panels.

A scintillator plane (DRAC) followed by 5 radiation lengths of five-layer lead and scintillator sandwich counter (DRAN) filled the area between the T and V hodoscope

TABLE III. A list of the materials in the HDRA and their physical properties. The thicknesses are averaged over the beam region, while the radiation lengths are averaged over the illuminated region. The lead sheet was not always present (see text). $(f - \bar{f})/k$ is given at 70 GeV/$c$.

| Material | Thickness (mm) | Density (g/cm$^3$) | Atomic Weight | $\dfrac{f - \bar{f}}{k}$ (mbarn) | $\dfrac{f + \bar{f}}{k}$ (mbarn) | Radiation Length (%) |
|---|---|---|---|---|---|---|
| Scintillator | 2.17 | 1.03 | 13.0 | 1.15 | 33.10 | 0.497 |
| Mylar | 0.11 | 1.39 | 96.1 | 8.29 | 239.57 | 0.044 |
| Aluminum | 0.05 | 2.70 | 27.0 | 2.07 | 59.21 | 0.058 |
| Paper | 0.38 | 0.63 | 94.1 | 10.89 | 229.51 | 0.066 |
| Lead | 0.515 | 11.35 | 207.2 | 9.71 | 326.28 | 8.9 |

planes and the vacuum pipe. Decay products outside the T and V hodoscopes struck these and vetoed the event.

Photons remaining in the beams were detected with the 28.1 radiation length "back anti" (BA) counter, made from 48 layers of 0.33 cm lead sandwiched with lucite. Hadronic showers from neutrons in the beam characteristically deposited energy deep into the BA. By comparing the energy deposit in the last one-third relative to the first two-thirds of BA, events with photons could be vetoed with tolerable loss from accidental beam neutrons.

Finally, a hodoscope plane (Mu1) downstream of the lead glass helped reject $\pi^+ \pi^- \pi^0$ decays in neutral trigger that mimicked the four photon $2\pi^0$ decays. A 21-radiation-length lead wall behind the lead glass, but immediately upstream of Mu1, together with a lead collar around the beam region prevented particles from an electromagnetic shower registering in Mu1. Hadronic showers, however, would light up Mu1 with reasonable efficiency.

### 3. Charged detection

*a. Drift chamber spectrometer.* The charged spectrometer consisted of two pairs of drift chambers to measure particle trajectories upstream and downstream of a momentum analyzing magnet. Helium bags were placed between the chambers to reduce the effects of multiple scattering.

As shown in Fig. 6, the cells of the drift chamber consisted of a sense wire located at the center of a hexagon defined by six field shaping wires. The wires in a sense plane
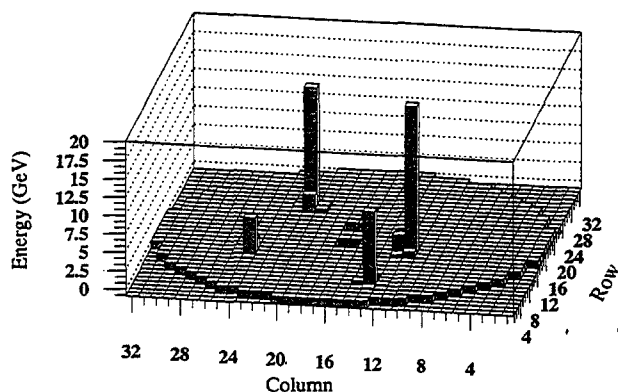


FIG. 5. A lego plot of the lead glass calorimeter with a typical $2\pi^0$ event. The two holes to pass the kaon beam can be seen in the center of the array.

were separated by 12.7 mm, and both the $x$ and $y$ views of each chamber had two sense planes offset by half that distance. This yielded a maximum drift distance of 6.35 mm perpendicular to a wire and an unambiguous determination of the side of the wire on which a particle passed. The chamber farthest upstream was the smallest, measuring $1.26 \times 1.26$ m$^2$ with 101 sense wires in each plane. The last chamber was the largest, being $1.77 \times 1.77$ m$^2$ with 140 sense wires per plane.

The field shaping wires were 100-$\mu$m gold-plated copper-beryllium and the sense wires were 25 $\mu$m gold-plated tungsten. The tolerance on wire placement was about 25$\mu$m. More details on the construction can be found in Ref. [39].

The chambers used 50% argon and 50% ethane. The drift velocity was of the order of 50 $\mu$m/ns at $-2650$ V.

The applied high voltage was ramped down to 80% of its nominal value during the 40 s between spills when the dark currents were typically 0.1–0.2 $\mu$A. Also, a small amount of alcohol (about 1%) was added to the argon-ethane as a quenching agent to help prevent breakdown and slow the chamber aging process. Ethanol was initially used, but was replaced later in the run with isopropanol.

The chamber pulses were amplified and discriminated in cards mounted on the chambers. LeCroy 4291B time-to-digital converters (TDC's) with a resolution of 1 ns were used. They were operated in *common stop* mode, where an incoming pulse would trigger a channel and a later pulse from the first level trigger would stop all triggered channels from counting further. The resulting inverted time distribution is shown in Fig. 7. The sharp edge near 240 ns corresponds to tracks hitting a sense wire. A TDC channel was dead for 250 ns after registering a hit. As described in Ref.
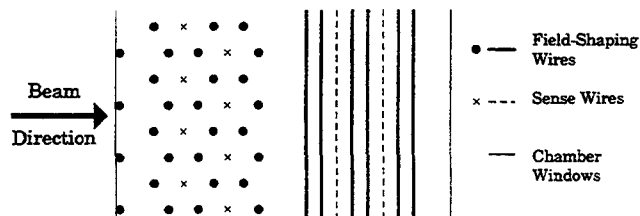


FIG. 6. Layout of the field shaping and sense wires used in all drift chambers. This is the view looking down on the chambers, with the vertical wires which measure $x$ positions in the front (left) and the horizontal wires which measure $y$ positions in the rear of the chamber.
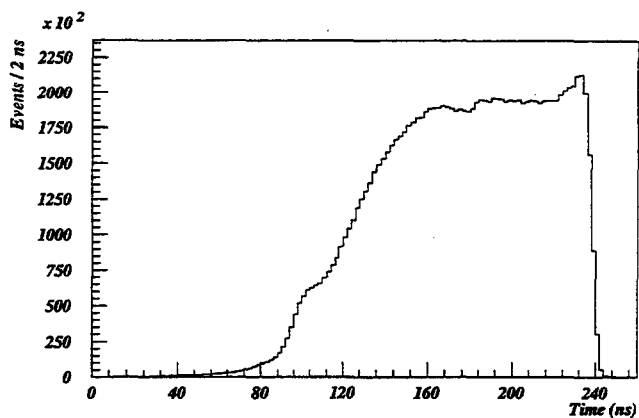
FIG. 7. Distribution of chamber drift times for in-time two-track events.



FIG. 9. Deviation of the sum of drift distances from the nominal cell size of 6.35 mm. The solid histogram is the distribution for in-time two-track events. The dot-dashed histogram is the distribution for tracks that have been identified as out of time (see text) in events with two other in-time tracks.

[38], the time distribution can be inverted to obtain a conversion from TDC time to a distance from the sense wire. The time-to-distance conversion assumed that the first drift electrons to arrive at the sense wire were those in the plane of the sense wires.

A 6 kG analysis magnet, with a 1.46 m gap, was situated between the second and third drift chambers. The transverse momentum "kick" $\Delta p_t = (q/c) \int B \, dz$ was typically 200 MeV. Values of $\int B \, dz$ were measured on a 2-in.-square grid and were interpolated between grid points. The field map is shown in Fig. 8. There was a very small horizontal field; its effect was negligible, though it did introduce a small bend in a particle's vertical trajectory.

The dipole field was negligible at the chambers, and so particles followed straight line trajectories between the upstream and downstream two chambers, greatly simplifying the track finding.

*b. Charged particle tracking.* The tracking algorithm used to reconstruct the charged particle trajectories was fairly straightforward. Tracks in the $x$ and $y$ views were found independently. An $x$ track segment candidate, either upstream or downstream, had to have at least three of the four possible planes hit. A $y$ track was accepted if it had hits on at least five of the eight possible planes. No track segments were allowed to share hits. The drift distance information from the TDC's was used to refine the location of the particle's passage. A least squares fit to the measured points

yielded direction tangents and intercepts for each of the candidate segments. The upstream and downstream segments were projected to the bend plane, and segments were paired if their projections were separated by less than 1.5 cm.

The $x$ and $y$ segments were matched by pairing the tracks using the lead glass cluster positions. After matching, the hit positions were refined once more to correct for small (of order mrad) chamber rotations and differences in signal propagation time along the sense wires (a 6 ns maximum difference). In addition, the upstream and downstream $y$ track segments were refit separately.

An inefficiency in one plane (of order 1%) meant that the "ambiguity" could not be resolved directly. In the $x$ view, the best match of the two candidate track segments (passing on either side of the unpaired wire) with a downstream segment was kept. In the $y$ view, the track fit to the other chambers was used to resolve the ambiguity.

It was useful to examine the sum of the two measured drift distances in one view of a chamber. This sum should equal the 6.35 mm separation in $x$ (or $y$) of the two wires, though a small angle correction was needed because of the 1.1 cm $z$ separation of the two planes. The deviation of the measured sum from this cell size is shown in the solid histogram in Fig. 9 for events with two valid in-time tracks (see below). The resolution of each plane can be deduced from the width of the central peak. We achieved resolutions in the 95–105 (105–115) $\mu$m range for the smaller (larger) chambers.

The low-side tail agrees very well with the expected $\delta$-ray production. The TDC's were dead immediately after a hit, and so only $\delta$ rays producing ionization arriving *earlier* than that from the primary particle were seen, making the drift distance (hence the sum of distances) appear too small. There was roughly a 0.5% chance per plane per track for a $\delta$ ray to cause a mismeasurement of the drift distance by 500 $\mu$m ($5\sigma$) or more. The high-side tail came almost exclusively from tracks passing very close to the sense wire so that the ionization is drifting longitudinally rather than transversely.

The sum of distances provides a means for identifying and throwing away out-of-time tracks. An $x$ or $y$ segment was flagged as out of time when two or more of the chambers have a sum of distance that deviates from 6.35 mm by



FIG. 8. Transverse momentum kick of the analysis magnet as a function of the $x$ and $y$ positions of a charged particle at the "bend plane" of the magnet.

more than 1 mm ($7\sigma$). The distribution of the sum of distances for out-of-time tracks identified in events with two other in-time tracks is shown as the dot-dashed histogram in Fig. 9. The expected 1.8 mm shift between the peaks can be clearly seen. The pileup and dilution of the peak structure on the high side (late buckets) are an artifact of the time-to-distance conversion which assigns a maximum drift distance of 6.35 mm to any given hit. The small central peak in the out-of-time distribution results from the small chance to have *very* early false TDC times from $\delta$ rays in two separate chambers which each cause a 1 mm mismeasurement of the sum of distance in both of the chambers. The $\delta$ rays cause this algorithm to flag in-time segments as out of time with a probability of 0.07%, resulting in a 0.28% event loss. By ridding events of the out-of-time tracks, however, there is an 8% recovery of two track events, far outweighing the small loss.

Once the particle trajectories were determined, their momenta were deduced by comparing the measured upstream ("up") and downstream ("dn") direction tangents $\theta_{x,y}$ of each measured track. Since $\theta_{x,y} = p_{x,y}/p_z$, we obtain

$$\left| \frac{\theta_x^{\mathrm{up}}}{\sqrt{1+(\theta_x^{\mathrm{up}})^2+(\theta_y^{\mathrm{up}})^2}} - \frac{\theta_x^{\mathrm{dn}}}{\sqrt{1+(\theta_x^{\mathrm{dn}})^2+(\theta_y^{\mathrm{dn}})^2}} \right| = \frac{|\Delta p_t|}{|p|},$$

where $\Delta p_t$ is the transverse momentum kick of the analysis magnet. The average momentum resolution was under 1%, with a dependence given by

$$\frac{\sigma_p}{p} = 0.45[1 \oplus p/(37.5 \text{ GeV}/c)]\%, \qquad (29)$$

where the momentum $p$ is measured in GeV/$c$. The constant term results from multiple scattering within the spectrometer.

*c. Trigger hodoscopes and veto banks.* Several planes of scintillation trigger hodoscopes were installed to provide a fast trigger. The downstream end of the charged decay volume was defined by the T and V hodoscopes, described earlier. Two more scintillation planes, the B and C hodoscopes, were located 1.5 m downstream of the last drift chamber. These were made of 1-cm-thick scintillator staves which did not overlap.

There was also a bank of scintillator counters (the Mu2 bank) located behind a 3.2 m-thick steel wall. This identified muons, both for triggering purposes in special chamber alignment runs (see Sec. IV A 2) and for rejecting $K_{\mu 3}$ ($\pi\mu\nu$) decays in normal data taking runs.

## C. Event triggers

The event triggers were kept independent of the regenerator position and of the beam from which the particle decayed. This approach resulted in triggers with minimal biases and no preference between decays from the vacuum or regenerator beam.

The first level triggers were based on information which could be obtained very quickly, such as the hit patterns in the trigger hodoscopes, the veto counter signals, and the total energy in the lead glass calorimeter. These were formed within about 450 ns of the actual decay. A successful trigger initiated the TDC counting and gated the ADC. The timing

for all first level triggers was defined by the 53 MHz rf signal synchronized to the proton bucket structure. A failure at the second level trigger aborted an event before reading it out for event building.

### 1. Neutral triggering

The neutral trigger was designed to accept four-photon ($2\pi^0$) decays as well as some six-photon ($3\pi^0$) decays, while simultaneously minimizing false triggers from $3\pi^0$ decays with missing and/or fused photons and accidental activity. The heart of the first-level neutral trigger required the total energy in the calorimeter to satisfy $E_t > 28$ GeV, greatly reducing accidental triggers. The event was vetoed with a signal in the AM, PA, SA, VA2-VA4, DRAN, MA, or LGA. Here VA1 was not used because of the activity in that counter induced by interactions in the regenerator. A BA signal vetoed events with more than 5 GeV in the first two-thirds of that counter and under 10 GeV in the last one-third. Also 25 times minimum ionizing particles (MIP's) or more in the CA vetoed events, well above the level from nearby photon showers in the calorimeter.

Hadronic events (such as $K_L \rightarrow \pi^+ \pi^- \pi^0$ decays) were rejected with an energy deposit of five MIP's or more in Mu1. Finally, any activity in the regenerator anticounters (RA's) with an energy deposit above 0.8 MIP's vetoed the event.

A factor of 10 reduction in the neutral trigger rate within 20 $\mu$s after the event, was obtained by counting isolated clusters in the lead glass with the HCF, as described above. Events with four clusters were accepted as candidate $2\pi^0$ events. We also accepted 0.05% of all first-level triggers independent of the HCF information in order to monitor its operation. Some events with six HCF clusters were accepted to obtain $3\pi^0$ decays for detector and systematic studies. These were mostly prescaled by 8 except for the last 20% of the run (which were prescaled by 1, accepted them all).

### 2. Charged triggering

A pulse height greater than 1.5 MIP's in the sum of signals from *either* the T *or* the V counters was required.

The B and C hodoscope banks defined a topological trigger which took advantage of symmetry in $\pi^+\pi^-$ decays. In the B bank, at least two distinct paddles had to be hit, with one in the left and the other in the right half. The central counter could satisfy either the left or right trigger requirement. In the C bank, it was required that hits be seen in top and bottom "halves," but again with substantial overlap.

Unwanted $K_{\mu 3}$ decays were rejected with the Mu2 scintillator bank. Vetoes from signals in the lead lucite counters of the VA4 and LGA banks helped reduce the trigger rate from $\pi^+\pi^-\pi^0$ decays. Studies at the beginning of the run and experience during the test run [39] showed it would be difficult to reject $K_{e3}$ decays in the trigger without bias in $\pi^+\pi^-$ decays.

As in the neutral trigger, the regenerator anticounters vetoed inelasticly scattered kaons. Activity in the MA or PA also vetoed an event.

The rate was reduced 30% by a second-level trigger requiring hits in the (nonoverlapping) left and right halves of the second drift chamber.

TABLE IV. The characteristics of the $\pi^+\pi^-$ and $2\pi^0$ data subsets.

| Subset | Proton beam intensity ($10^{12}$ per spill) | Pb sheet installed | $2\pi^0$ triggers to tape ($10^6$) | $\pi^+\pi^-$ triggers to tape ($10^6$) |
|---|---|---|---|---|
| C1 | 0.3 | No | – | 16 |
| N1 | 2.0 | Yes | 44 | – |
| C2 | 0.3 | No | – | 70 |
| N2 | 2.0 | Yes | 36 | – |
| C3 | 0.3 | No | – | 82 |
| N3 | 2.0 | Yes | 22 | – |
| N4 | 2.0 | No | 8 | – |
| C4 | 0.3 | No | – | 75 |
| NC | 0.8 | No | 61 | 61 |

### 3. Other triggers

There were a number of special purpose triggers collected simultaneously with the $\pi\pi$ triggers. The most important were the following.

(i) "Accidental" triggers, to study the effects of random activity in the detector. A scintillation telescope aimed at the target pile, out of the line of sight of the detector, provided a trigger proportional to the instantaneous beam intensity and independent of activity in the detector.

(ii) The "pedestal" trigger, which randomly triggered the readout of the lead glass with no readout threshold.

(iii) The "flasher" trigger, which flashed the xenon lamp used to monitor the lead-glass photomultiplier tube gains throughout the run.

(iv) The $K_{\mu3}$ trigger, identical to the $\pi^+\pi^-$ trigger, but with Mu2 bank in coincidence.

The special purpose triggers constituted 7% of the recorded triggers. The pedestal and flasher triggers were collected between spills as well as during the spill.

### D. Data collection

The data were obtained between August 1987 and February 1988. The sample occupied approximately 5000 nine-track data tapes. The details of the data-taking run and of the first data analysis pass are described in detail in Refs. [36] and [37].

The data collection was initially divided into periods with either $2\pi^0$ or $\pi^+\pi^-$ triggers. We alternated collection between charged and neutral running to ensure that we obtained an adequate sample of each mode. The proton beam intensity, the number of raw triggers recorded on tape, and the lead sheet status are summarized for each of these sets in Table IV.

At the end of neutral subset N3, one of the drift chambers had to be temporarily brought off line. Since the neutral conversion trigger (and the charged trigger) was of no use without all chambers operating, it was decided to study $2\pi^0$ collection without lead sheet (the N4 subset) and with the nonconversion trigger described above. The success of this test led us to abandon the conversion trigger in favor of collecting $2\pi^0$ and $\pi^+\pi^-$ events simultaneously in subset NC. This was the first time in any experiment that all four of the $K \rightarrow \pi\pi$ decay modes were collected simultaneously.

Our first published result [21] was based on 80% of the data in the NC sample, which we call the NCa subset. The

results of analyses of each subset are given later.

Special data samples were collected in short runs interspersed throughout the entire run. The most important ones were for calibrating the lead glass and aligning the chamber system. These are discussed in the next section.

The analysis of the data occurred in two stages. A first pass was made through all of the raw data tapes using preliminary calibrations of detector elements and analysis cuts loose enough so that minor changes to the calibrations would not change the final event sample. Candidate event types were split onto smaller sets of data summary tapes (DST's). The samples obtained included very large samples of $K_{e3}$, $3\pi^0$, $\pi^+\pi^-\pi^0$ decays, along with samples useful for searching for rare kaon decays.

### IV. CALIBRATION AND DETECTOR PERFORMANCE

A large effort went into calibrating the lead glass calorimeter and the drift chamber system. The most difficult challenge was to understand the energy scale for $2\pi^0$ relative to $\pi^+\pi^-$ to better than 0.1%. We discuss the use of $K_{e3}$ electrons for the final set of calibrations.

For the acceptance, the positions of the defining apertures had to be tracked accurately over time. A large sample of electrons, again from $K_{e3}$ decays, was used to measure the position of each aperture edge throughout the run. Since one of the apertures was almost 50 m upstream of the first chamber, the best possible resolution was required of the drift chamber system. The alignment of the drift chambers relative to each other and to fixed reference points in the detector was tracked.

#### A. Drift chamber calibration and alignment

##### 1. Review of time-to-distance conversion

The time-to-distance calibration was based on the assumption that the illumination across a cell is uniform. This is a good assumption when averaging over all the cells in a single plane. After correcting for effects like nonuniformities in the response across a drift cell [38], the time distribution (Fig. 7) can be inverted and a signal arriving $n$ nanoseconds after the earliest time corresponds to a distance $d_n$ given by

$$d_n = 0.006\,35 \times \left( \sum_{i=1}^{n} t_i \Big/ \sum_{i=1}^{N} t_i \right), \qquad (30)$$
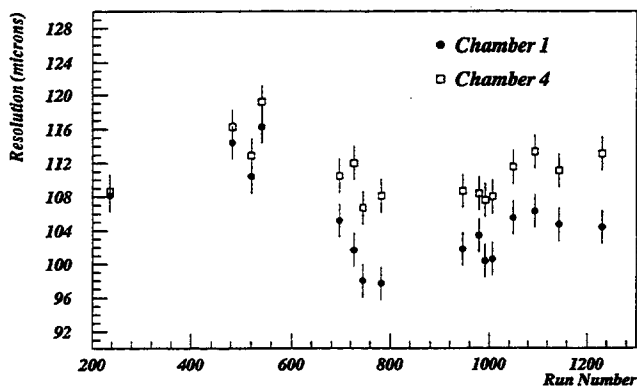
FIG. 10. Average resolution in the smallest (solid circles) and largest (open squares) drift chamber as a function of run number.

where $t_i$ is the total number of events arriving in the bin corresponding to $i$ nanoseconds after the earliest time, and $N$ is the total number of bins. This was done separately for each of the 16 wire planes once every several days of running to prevent drifts in the calibration from seriously degrading the resolution. A plot of the resolution as a function of time for the smallest (No. 1) and largest (No. 4) chambers in the $x$ view is shown in Fig. 10. When operating conditions were optimal, several planes had better than $100\mu$m resolution.

### 2. Chamber alignment

The alignment of the drift chamber system was performed in two steps. The first was internal, where the positions of the chambers were determined relative to each other. The second was an external alignment, where the positions were measured relative to the lead glass calorimeter and the production target, both taken as fixed reference points. The goal was to locate the chambers with a transverse accuracy of $10\mu$m.

The internal alignment involved two procedures: (1) to fix positions of the inner chambers in a coordinate system defined by the two outer chambers and (2) to remove any residual rotation (about the $z$ axis) between the outer chambers. The external alignment involved the measurement of, and correction for, the apparent "motion" of the production target and the calorimeter.

TABLE V. Rotation of the horizontal $y$ view sense wires away from the perpendicular $x$ view wires in each drift chamber. For a positive rotation, the horizontal $y$ wires are high on the $+x$ side of the chamber and low on the $-x$ side.

| Chamber | Rotation ($\mu$rad) |
|---------|---------------------|
| 1 | 0 |
| 2 | 47 |
| 3 | 198 |
| 4 | -150 |

The important alignment constants were the transverse offsets for each chamber and the rotation of the chamber about the $z$ axis. The complete set of constants were updated for every day of running in the $\pi^+\pi^-$ data set; the transverse offsets were adjusted two to three times a day.

The relative angles between the $x$ and $y$ planes were taken from a survey of the wires during chamber construction. The deviations from a 90° angle are listed in Table V. These values were verified for consistency with the data, but were difficult to extract. The accuracy on the survey measurements varied from 30 $\mu$rad in the smallest chamber (No. 1) to 20 $\mu$rad in the largest chamber (No. 4).

For the rest of the discussion, we assume these corrections have been made, and hence that the $x$ and $y$ measurements from a given chamber are in an orthogonal coordinate system.

*a. Internal alignment 1: Muon samples.* The first step in alignment was to orient the second and third chambers in a system defined by the two outer chambers. The procedure used muons collected with the analysis magnet off. The sample of muons illuminated each chamber fully. Roughly 50 000 muon triggers, accumulated in a few spills, provided an adequate sample for alignment.

Events with out-of-time tracks or accidental coincidences were removed. In addition, only high-quality tracks were accepted: All eight planes in each view had to have hits, and every sum of distance (which uses only drift times and hence is *independent* of the chamber offsets) had to be within 450 $\mu$m of the nominal cell size. This minimized biases from $\delta$ rays in the offsets.

A line segment in each view was defined by fitting to the $x$ and $y$ track positions measured in the first and fourth



FIG. 11. Residual between the measured and predicted position of a muon track in the downstream $y$ plane of chamber 2. (a) The residual versus the $x$ track projection. (b) The variation of the mean $y$ residual with the $x$ position, and the best fit line.
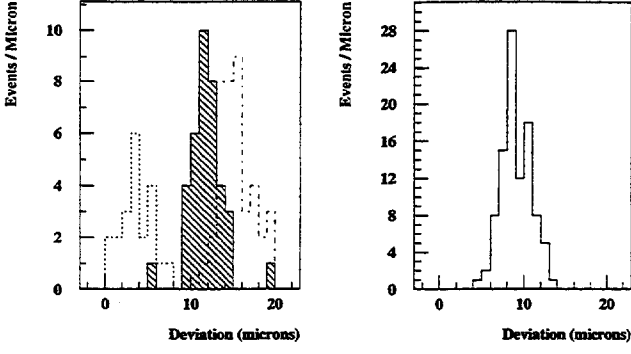
FIG. 12. Deviation of the effective separation between two $x$ planes within a chamber. Left: chamber 1, the three different histograms correspond to groups of alignment data between major chamber repair work. Right: chamber 4, little work was done on this chamber during the run.

chambers. For each plane in chambers 2 and 3, the residual between the fit and the measured hit is plotted versus the track projection in the orthogonal view. Such a plot is shown in Fig. 11(a). A linear fit to the mean residual versus position, as in Fig. 11(b), yields the offset and rotation for each plane.

In systematic studies, the reproducibility of these measurements was about 5 $\mu$m for the offsets and 10 $\mu$rad for the rotations.

For each pair of planes in one view of a chamber, the effective separation (relative to the nominal separation of 6.35 mm) can be obtained from the distribution of the difference of the offsets measured in each plane. The measured separation can have contributions both from a true separation and from a chamber rotation about the $x$ (or $y$) axis. The $x$ view distributions from the alignment data are shown in Fig. 12. The different histograms for chamber 1 correspond to time periods between work on that chamber, where changes in the $y$ chamber rotation shifted the effective offset. To refine the alignment, the two offsets for one view of a chamber were averaged, keeping the separation between the two planes at the average separation in a time period between work on that chamber.

The difference in the rotations between a plane pair can also be measured this way. There are no contributions to the measured difference aside from a true physical rotation of one plane relative to the other. The measured differences were within 8 $\mu$rad for all plane pairs, well within our desired tolerance.

*b. Internal alignment 2: Removing screw rotations.* While the above method aligns the inner chambers in a coordinate system defined by the outer ones, possible misalignments of the outer two chambers must be considered. If there is a rotation $\phi$ around the $z$ axis between the outer chambers, then the coordinate system they define leaves a "screw rotation," where the $i$th chamber is rotated out of true alignment by an angle $\phi_i = \phi(z_i - z_4)/(z_1 - z_4)$, with $z_i$ the location of the $i$th chamber. This rotation cannot be removed with single-track events. This effect also prevents the absolute measurement of the angle between the $x$ and $y$ planes mentioned above.

Decays with two charged particles defining a plane in the final state provide the sample for determining the screw rotations.

The trajectories of the tracks coming from the vertex were measured in the two chambers upstream of the magnet. Let us consider the effect due to a rotation between these chambers. Let $\vec{t}_a = (\theta_{x_a}, \theta_{y_a}, 1)$ and $\vec{t}_b = (\theta_{x_b}, \theta_{y_b}, 1)$ be the direction tangents for the two charged particles $a$ and $b$, respectively. Also let $\vec{x}_{a_i} = (x_{a_i}, y_{a_i}, z_i)$ and $\vec{x}_{b_i} = (x_{b_i}, y_{b_i}, z_i)$ be the positions of the two particles in chamber $i$ ($i = 1,2$), and let $\vec{r}_i = \vec{x}_{b_i} - \vec{x}_{a_i}$ be the separation vector of the two particles in the plane of chamber $i$. For the true trajectories, the triple product

$$d_s = \vec{t}_a \times \vec{t}_b \cdot \vec{r}_1 = 0,$$

because $\vec{r}_1$ lies in the plane defined by $\vec{t}_a$ and $\vec{t}_b$.

If chamber 2 is rotated by an angle $\phi$ relative to chamber 1 and this rotation is not corrected, then measured direction tangents become

$$\begin{pmatrix} \theta^m_{x_\alpha} \\ \theta^m_{y_\alpha} \end{pmatrix} = \begin{pmatrix} (x'_{\alpha_2} - x_{\alpha_1})/z_{21} \\ (y'_{\alpha_2} - y_{\alpha_1})/z_{21} \end{pmatrix}$$

$$= \begin{pmatrix} \theta_{x_\alpha} \\ \theta_{y_\alpha} \end{pmatrix} + \begin{pmatrix} 2\sin^2\dfrac{\phi}{2} & \sin\phi \\ -\sin\phi & 2\sin^2\dfrac{\phi}{2} \end{pmatrix} \begin{pmatrix} x_{\alpha_2}/z_{21} \\ y_{\alpha_2}/z_{21} \end{pmatrix}$$

$$\equiv \begin{pmatrix} \theta_{x_\alpha} \\ \theta_{y_\alpha} \end{pmatrix} + \begin{pmatrix} \delta\theta_{x_\alpha} \\ \delta\theta_{y_\alpha} \end{pmatrix} \tag{31}$$

for each of the tracks $\alpha = \{a, b\}$. Here $z_{21} \equiv z_2 - z_1$ is the separation between the two drift chambers. The track tangent vectors are distorted by $\vec{t}^m_\alpha = \vec{t}_\alpha + \Delta\vec{t}_\alpha$, with $\Delta\vec{t}_\alpha = (\delta\theta_{x\alpha}, \delta\theta_{y\alpha}, 0)$. This in turn changes the triple product $d_s$ to

$$d^m_s = \vec{t}^m_a \times \vec{t}^m_b \cdot \vec{r}_1$$

$$= (\vec{t}_a \times \Delta\vec{t}_b + \Delta\vec{t}_a \times \vec{t}_b) \cdot \vec{r}_1$$

$$= \frac{\vec{r}_2 \cdot \vec{r}_1}{z_{21}} \sin\phi + 2\frac{(\vec{r}_2 \times \vec{r}_1)_z}{z_{21}} \sin^2\frac{\phi}{2}, \tag{32}$$

where we have used the fact that the true triple product vanishes and that

$$(\Delta\vec{t}_a \times \Delta\vec{t}_b) \perp \vec{r}_1.$$

The chambers were surveyed into position to limit the size of $\phi$ to a few hundred $\mu$rad, and so in our sample $d^m_s \approx |\vec{r}_1||\vec{r}_2|\phi/z_{21}$. We measured the variation of $d^m_s$ with $|\vec{r}_1||\vec{r}_2|$ in the charged mode using samples of $K_{e3}$ decays obtained near the time of each muon alignment. Figure 13 shows a plot of this dependence for one of the alignments. Since $z_{21}$ is known to better than 0.02%, $\phi$ can be extracted from the slope $\phi/z_{12}$ with accuracies in the range of 5 to 10 $\mu$rad. Figure 14 is a plot of $\phi$ as a function of time through-
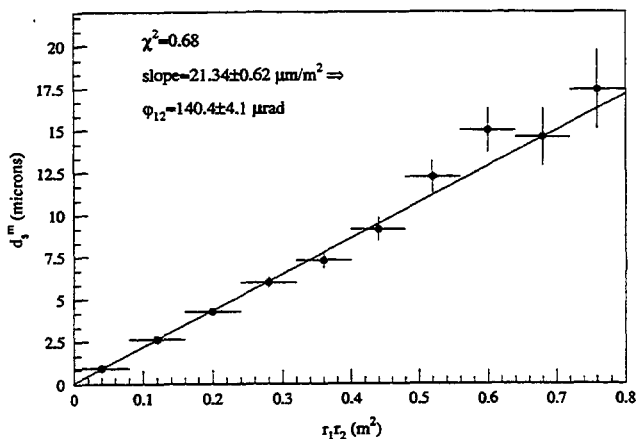
FIG. 13. Variation of the mean of $d_s^m$ with $|\vec{r}_1||\vec{r}_2|$ for one subset of $K_{e3}$ decays. The slope of the fit line is the rotation angle scaled by the separation between the first and second chambers.

out the $\pi^+\pi^-$ running. The variation is quite smooth, with occasional breaks or isolated points associated with repair work on the chambers.

A much smaller $\pi^+\pi^-\pi^0$ sample obtained during $2\pi^0$ running was used to measure $\phi$ for the remaining alignments. These measurements are also shown in Fig. 14. The chambers are not used extensively in the neutral mode, and so the poorer accuracy of the $\pi^+\pi^-\pi^0$ measurements does not pose a problem.

Once the absolute rotation $\phi$ between chambers 1 and 2 was known, the screw rotation was then removed from the entire chamber system. In principle, the measurement of the angle between the $x$ and $y$ views of a chamber could have been refined by studying the variation in $\phi$ as the decay plane varied from horizontal through vertical, but the values from the survey were sufficiently accurate for our purposes.

c. External alignment. Both the lead glass calorimeter and the target provided fixed points in $x$ and $y$, giving a line of sight for aligning the chamber centers. The lead glass also provided a reference for the chamber rotation angle about the line of sight.

The electrons from the $K_{e3}$ decays gave the position of the chamber system relative to the lead glass from the comparison of the track projection with the cluster position in the calorimeter. The average difference of the track and cluster

positions integrated over the entire calorimeter gave a very good measurement of the average offset between the chamber system and the calorimeter. The resolution on the cluster position measurement was 2.5 mm, and there was ample statistics to obtain the mean positions to better than 10 $\mu$m.

To obtain the rotation of the chamber system relative to the lead glass, the $x$ ($y$) difference was studied as a function of the row (column) of the central block. There is a bias in the reconstructed cluster position as a function of the angle of the incoming particle of order 70 $\mu$m/mrad; averaging the $x$ ($y$) track-cluster difference over a row (column) reduces this bias. From uncertainties in the true positions of the blocks, there were nonstatistical fluctuations in the measured difference from row to row and column to column of the order of 50$\mu$m. The average trend in the $x$ and $y$ views both imply a rotation of order 300 $\mu$rad, with an estimated systematic uncertainty of 50 $\mu$rad. The variation in the rotation from alignment to alignment was determined quite accurately.

A large sample of $\Lambda \rightarrow p\pi$ decays in the vacuum beam was used to align the chamber system with the target. At our energy, the $\Lambda$'s could be identified cleanly by requiring $p_p/p_\pi > 3$ and $E_\Lambda > 130$ GeV. Track quality cuts similar to those in the muon samples as well as cuts to eliminate $K$ decays were made.

The average target position measured with the $\Lambda$'s for one alignment is shown in Fig. 15. The single-event resolution was about 3 mm, and there were about 75 000 $\Lambda$ events in each alignment. The apparent horizontal and vertical motions of the target are shown in Fig. 16. The structure is real, corresponding to a shifting of the chambers. A 1 mm shift in the target position corresponds to only a 120 $\mu$m motion of the upstream chamber. During neutral mode running, the target positions were measured with $K_L \rightarrow \pi^+\pi^-\pi^0$ decays; these are also plotted in Fig. 16. There was sufficient statistics in the $\Lambda$ sample to track the motion of the chamber system on a much finer time scale than the time between muon runs.

We thus corrected the chamber system alignment once every run, roughly every 8 hours of data taking. These adjustments made a small but noticeable improvement in the measurement of the transverse momentum of coherent kaons in $K \rightarrow \pi^+\pi^-$ decays.

This completes the discussion of chamber alignment. Be-
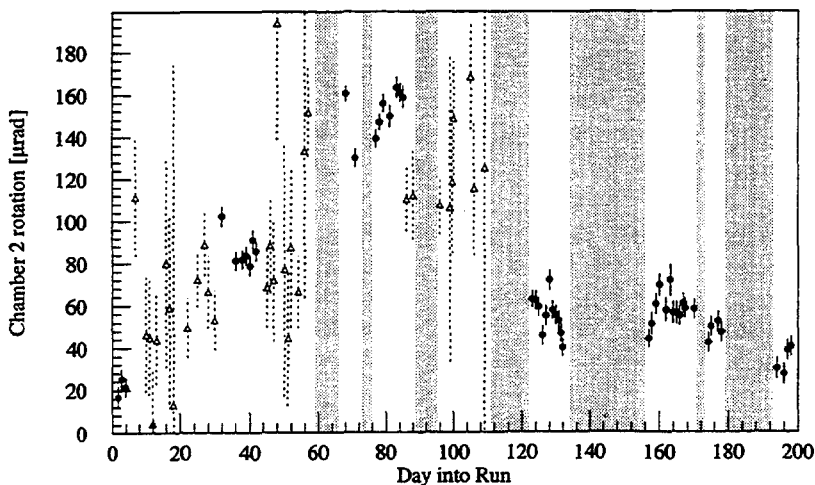


FIG. 14. Rotation of chamber 2 about the $z$ axis relative to chamber 1. The solid circles are measurements obtained with $K_{e3}$ decays accumulated in charged mode running. The open diamonds are measurements made with $\pi^+\pi^-\pi^0$ decays collected during neutral running. The gaps correspond to periods when no $\pi\pi$ data were collected due to accelerator shutdowns, etc.
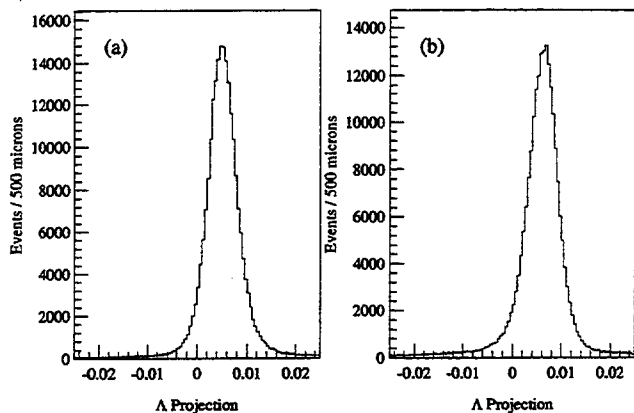
FIG. 15. Projected location of reconstructed $\Lambda$ decays from the $p\pi$ decay mode back to the plane of the target. (a) $x$ projection. (b) $y$ projection.



FIG. 17. Chamber efficiencies during several of the $\pi^+\pi^-$ runs. One of the four planes from each chamber has been plotted. These efficiencies were measured using pions. The layers shown for chambers 1 and 2 were the *most* inefficient layers (see text). The other layers in those chambers had efficiencies closer to those shown for chambers 3 and 4.

cause of the numerous large data samples that we collected using a simple, unbiased, two-track trigger, we have been able to successfully track the chamber motion versus time at the $20\mu$m level, where most of the uncertainty comes from the motion of the chambers between alignments. This was beneficial for determining the positions of the critical limiting apertures.

### 3. Chamber efficiencies

Many planes had efficiencies of 99% or greater throughout the run. Spot checks of the average efficiency for several planes during charged mode running are shown in Fig. 17.

The inner $y$ plane of chamber 1 was problematic. As seen in the figure, its efficiency degraded as the run progressed. We believe the mechanism for this was the following. This plane became increasingly sensitive to late-arriving drift hits as the rate of outgassing within the chamber decreased. The

late hits originate in the dead region between the $x$ and the $y$ high-voltage planes. As the outgassing subsided, particularly in the smallest first chamber, there were fewer impurities to trap these slowly drifting electrons. Shifting the TDC distribution to view the tail of the distribution for this plane shows a marked difference from an efficient plane (see Fig. 18). There were almost no late times in the efficient plane, while in the inefficient plane there is a broad distribution of late-arrival times which reset the TDC, making the wire inefficient in normal operation. The area under this late arrival peak relative to the area under the signal region is very close to the observed chamber inefficiency.

This problem was alleviated somewhat by bringing inhibit signals to the TDC's as fast as possible. The change in the inhibit timing resulted in the abrupt increase in efficiency in this plane. Because of the distant location of the TDC's from
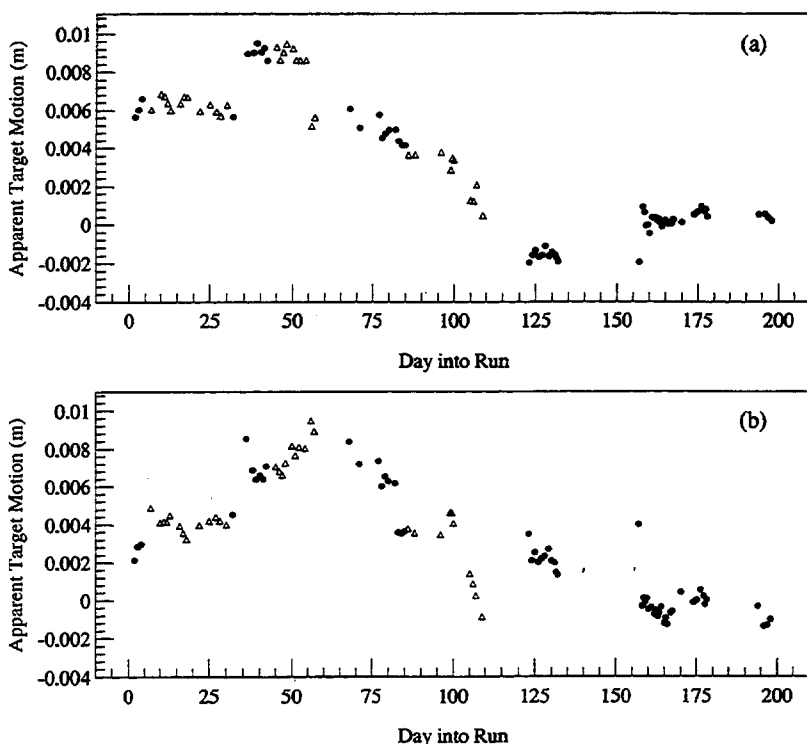




FIG. 16. Apparent motion of the target position due to the motion of the drift chamber system as a function of time into the run. The motion has been tracked with $\Lambda \to p\pi$ decays (solid circles) and $K_L \to \pi^+\pi^-\pi^0$ decays (triangles). (a) Horizontal ($x$) motion. (b) Vertical ($y$) motion.
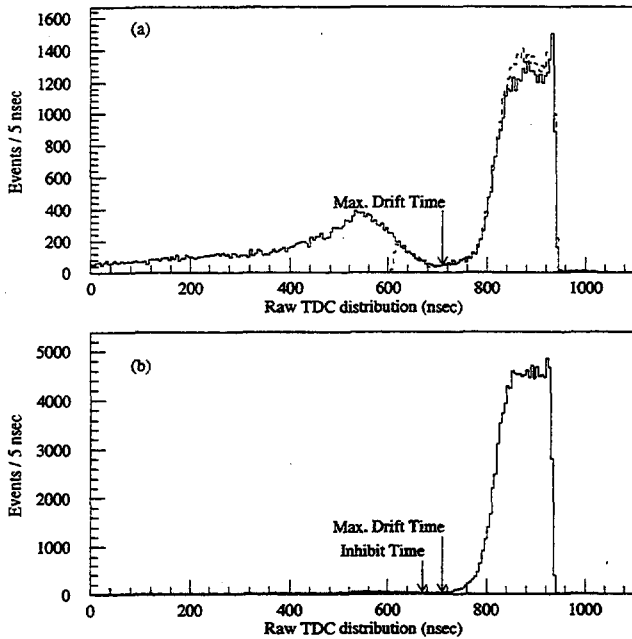
FIG. 18. Raw chamber TDC times measured using a delayed common stop. (a) Inner $y$ plane of chamber 1. The solid histogram was collected using no inhibit. The dashed histogram was collected with the standard inhibit time relative to the common stop for that chamber. The arrow indicates the position of the maximum drift time used for tracking. (b) Outer $y$ plane of chamber 4. The small arrow indicates the standard inhibit timing for this plane, and the large arrow indicates the maximum drift time used for tracking. Note the shift of this inhibit time relative to the inhibit timing in (a).

the trigger electronics, it was not possible to inhibit all of the late arrivals, and we were therefore left with a residual inefficiency in this plane. The tendencies are also visible in the inner planes of chamber 2, such as the $X$ plane plotted in Fig. 17, but have disappeared in the two chambers farthest downstream where accidental activity was lower and the inhibit timing more favorable.

The other planes in chamber 1 were not seriously affected by these late hits. The inner $x$ plane had efficiencies similar to the $x$ plane shown for chamber 2, while the outer $x$ and

$y$ planes had efficiencies better than 99.5%.

The effect of this inefficiency on $\mathrm{Re}(\varepsilon'/\varepsilon)$ turns out to be negligible. On the one hand, the tracking efficiency was not seriously affected since the only seriously degraded plane was a $y$ plane in which the tracks do not bend. Since the $y$ track finding requires that only at least five out of the eight planes and all of the other planes be very efficient, the change in the probability that we lose a track is small (on the order $10^{-4}$). On the other hand, since we collect the decays from the vacuum and regenerator beams simultaneously and the problem occurred roughly uniformly across the chamber, the inefficiency affects the $K_S$ and $K_L$ samples almost identically.

### 4. Momentum scale

The last component of the chamber calibration and alignment was the tuning of the momentum scale. While a survey of the magnetic field was able to map the shape and obtain the scale at the 0.2% level, the overall scale of the field would change slightly when the magnet polarity was reversed. During the last two charged data sets (C4 and NC), the polarity was reversed about twice per day to allow a possible measurement of the charge asymmetry in $K_{e3}$ decays.

The $\pi^+\pi^-$ mass is given, to a very good approximation, by

$$m_{\pi^+\pi^-}^2 - 2m_\pi^2 = p_1 p_2 \left( \theta^2 + \frac{2m_\pi^2}{p_1 p_2} \frac{p_1^2 + p_2^2}{p_1 p_2} \right). \qquad (33)$$

If the scale of the magnetic field shifted by a factor $\beta$, then each of the momenta would also be shifted by $\beta$. For small $\beta$, the dominant effect on the mass is to have $\Delta m_{\pi^+\pi^-}/m_K \approx \mathrm{const} \times \beta$. Hence, by monitoring the reconstructed $\pi^+\pi^-$ mass, we were able to improve the average accuracy of the momentum measurements, and map the shifts in the magnetic field strength as a function of time, as shown in Fig. 19. A clear shift of 0.1% was seen between the field strengths for the two polarities. A small correction to the assumed ratio between high-field strengths and low-field
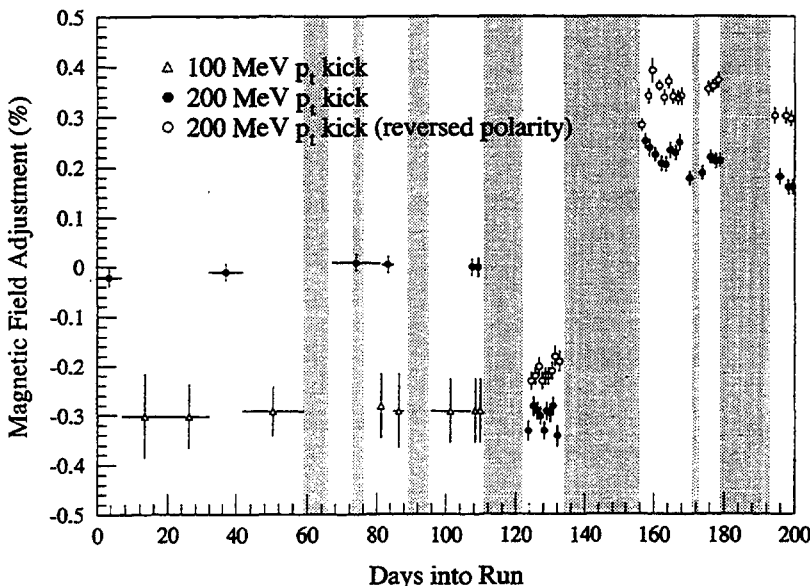


FIG. 19. Magnetic field correction factors as a function of days into run. The corrections are grouped into three magnet configurations: "normal" polarity with a 200 MeV/c $p_t$ kick (solid circles), normal polarity with a 100 MeV/c $p_t$ kick (hollow triangles), and reversed polarity with a 200 MeV/c $p_t$ kick.
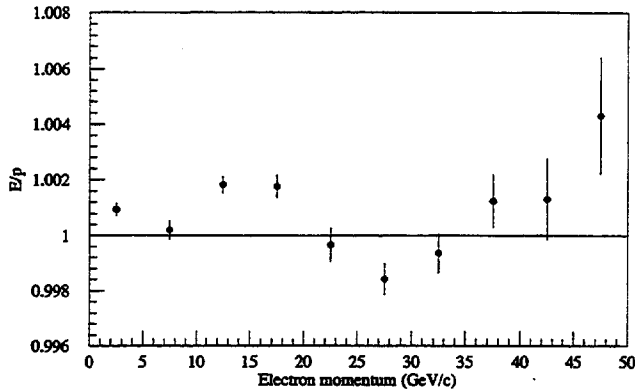
FIG. 20. Mean value of the ratio of cluster energy to track momentum $(E/p)$ versus momentum for electrons and positrons in one of the $e^+e^-$ calibration sets.



FIG. 21. Mean value of the ratio of cluster energy to track momentum $(E/p)$ versus momentum for electrons and positrons from $K_{e3}$ decays using the gains from the $e^+e^-$ calibration set of Fig. 20.

strengths was also necessary. Another step about 150 days into the run occurred after work was done on the power supplies for the magnet.

## B. Lead glass calibration

The lead glass was calibrated by comparing the momentum of an electron measured in the charged spectrometer to the energy of its shower in the calorimeter. The goal of the calibration was to understand the mean response of the calorimeter at the 0.1% level. The calibration ultimately yielded a measurement of the nonlinearity and the gain for each of the 804 blocks.

There were two types of electrons used for this calibration. The first was obtained from special runs where $e^+e^-$ pairs were created by converting photons in the beam with a copper foil. Calibration magnets upstream of the chamber system [see Fig. 2(b)] separated the $e^+e^-$ pairs vertically and horizontally so that each particle could be separately tracked in the chamber system. By adjusting the magnet settings, the electrons could be swept to illuminate the entire lead glass array.

The calibration program using these special calibration electrons allowed us to understand the overall calorimeter response within $\pm 0.2\%$ over a 50 GeV range (see Fig. 20). The drawback was a lack of statistics, particularly in the few outermost rings of blocks in the array. The outer blocks also suffered because of an insufficient momentum spread needed for the calibration to determine the block nonlinearities.

To probe the calorimeter response further, we turned to an electron sample with much higher statistics. Using the calibration electron gains, it was very simple to isolate the second sample of electrons: those from $K_{e3}$ decays in the data. Almost 40% of charged triggers were $K_{e3}$'s, leading to a total sample of $120 \times 10^6$ electrons potentially available for calibration. For the same calibration shown in Fig. 20, the electron response versus energy reveals a structure (see Fig. 21) only hinted at by the calibration electron sample.

Aside from different cuts to clean up the electron samples, the procedure to extract the two calibration constants for each block was essentially identical in both the calibration and $K_{e3}$ electron samples. The calibration procedure and the calibration electron sample are described in detail in Ref. [36]. A brief review of the model of the lead glass response
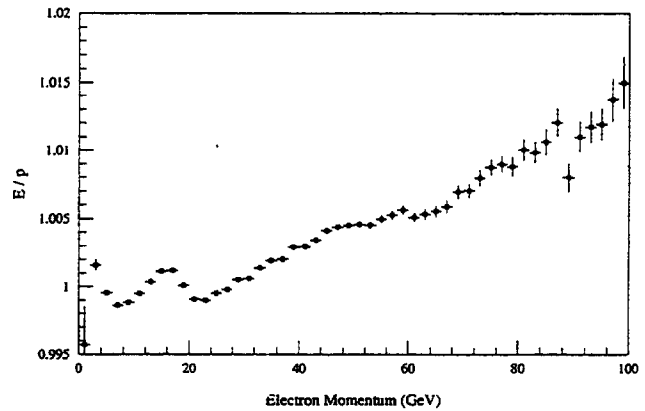
and its impact on the calibration procedure is given here.

### 1. Model of lead glass response and calibration procedure

Absorption of Čerenkov radiation as it propagates through the lead glass leads to an intrinsic nonlinear response of the calorimeter. This essentially breaks the shower reconstruction algorithm into two pieces: (1) to determine the number of Čerenkov photons present at the back of a block given the observed number $n_i$ of ADC counts in that block and (2) to determine the energy of the original showering particle given the measured number of photons present in the $3 \times 3$ cluster of blocks for that shower. The first step requires the measurement of an effective "gain" for each block. This "gain" is the result of several effects, including the quantum efficiency of the photocathode, the fraction of area of the block covered by the tube, the actual phototube gain, and the conversion constant for that ADC channel. The second step relies on knowledge of the absorption parameter, denoted $\alpha$, describing the block's absorption per radiation length and of the variation of the response function $C(E,\alpha)$ in the Čerenkov light present at the back of the block for an incoming particle of energy $E$. Here we outline the procedure used to predict the response function $C(E,\alpha)$ and then describe the $e^+e^-$ calibration procedure.

Čerenkov light is produced at an angle $\cos\theta_C = 1/\beta n$, where $n$ is the index of refraction. In the lead glass, with $n = 1.6$, the production angle is $51°$, and so most of the light produced has to be reflected at least once before reaching the back. Because neighboring blocks are optically isolated, light not reflected is lost. For particles with $\beta \approx 1$, $\theta_C$ is equal to the critical angle for total internal reflection, and so the light from shower particles traveling parallel to the longitudinal axis of the block is completely contained within the block. For shower particles produced off axis, a small amount of light is lost, but we neglect this in our model.

Assuming a uniform absorption parameter $\alpha'$ within a block, the number of Čerenkov photons present at the back of the block for an electron of incident energy $E$ is

$$N(E,\alpha) = \tilde{g}E \int_0^L \tilde{f}(E,\ell) e^{-\alpha'(L-\ell)/\cos\theta_C} d\ell, \quad (34)$$

where $L$ is the length of the block, and $\tilde{g}$ is the number of photons produced per GeV. The function $\tilde{f}(E,\ell)$ is the fractional amount of light produced at a depth $\ell$ radiation lengths into the block, normalized such that $\int_0^\infty \tilde{f}(E,\ell)d\ell = 1$. Its shape as a function of $\ell$ is similar to that of a $\Gamma$-function distribution [42]. A block's absorption is always scaled by the same factor $1/\cos\theta_C$, and so throughout the analysis we use an effective absorption parameter $\alpha = \alpha'/\cos\theta_C$.

Large numbers of electron showers were generated using the EGS [43] simulation program to study the longitudinal shower distributions $\tilde{f}(E,\ell)$ and to provide a correction table to map observed signals to true energies. The 18 energies at which showers were generated ranged from 0.25 GeV to 90.51 GeV and were evenly spaced in $\ln E$. We found [36] that the position $\ell_{max}$ of the longitudinal shower distribution maximum varied with the energy of the incoming particle according to

$$\ell_{max} = 1.022\ln(E) + 3.15, \qquad (35)$$

with $E$ measured in GeV and $\ell_{max}$ in units of radiation lengths (3.21 cm) of the lead glass.

To obtain the response function $C(E,\alpha)$, $N(E,\alpha)$ was normalized to the total number of photons ($\tilde{g}E$) produced in a shower and averaged over the ensemble of EGS showers generated at the energy $E$. The response function was then defined as

$$C(E,\alpha) = \left\langle \frac{N(E,\alpha)}{\tilde{g}E} \right\rangle \Big/ c_1(\alpha), \qquad (36)$$

where $\langle \; \rangle$ denotes the average over the ensemble of showers at energy $E$. The function $c_1(\alpha) \equiv \exp[-(L-5.157)\alpha]$ is very close to the response of a lead glass block with absorption parameter $\alpha$ to a 1 GeV electron. This response is also folded into our definition of the "gain"; that is, the gain becomes the correction needed to map the ADC counts directly to the true energy for a 1 GeV shower. The function $C(E,\alpha)$ then corrects for the different response at other energies. Most values of $\alpha$ were in the range of 3%–4% corresponding to corrections in the 1%–2% range for a typical shower.

The response function $C(E,\alpha)$ was fit reasonably well by a power law behavior $E = (\Sigma n_i/g_i)^\beta$, with the power $\beta$ given by

$$\beta = 1.0053 - 0.9106\alpha. \qquad (37)$$

Deviations of the power law from the proper correction $C(E,\alpha)$ were under 1% [36]. While the deviations were too large to allow simply using a straight power-law behavior for the cluster energy reconstruction, the near power-law behavior was still convenient to resolve the conundrum that the final nonlinearity correction depended on the energy $E$ of the original particle, while $E$ is what we need to extract. The response function $C(E,\alpha)$ tends to vary as $\ln E$, and so the approximate power-law prediction sufficed to provide an energy prediction $E_p$ that we used to obtain the proper correction $C(E_p,\alpha)$. The calibration procedures also made use of this approximate behavior.

*a. Photon calibration.* The ultimate goal of the lead glass calibration procedure is to reconstruct the energies of photons from $2\pi^0$ decays. Unfortunately, electrons begin to emit Čerenkov radiation as soon as they enter the glass, while photons do not emit radiation until after an initial conversion. If the photon converts at $\ell_0$ radiation lengths into the block, then the photon behaves effectively as the sum of an electron shower with energy $E_{e^-} = \kappa E$ and a positron shower with energy $E_{e^+} = (1-\kappa)E$, but in a "foreshortened" block of length $L - \ell_0$.

We can generalize the definition of $N(E,\alpha)$ given in Eq. (34) to depend on the conversion depth, that is,

$$N(E,\alpha,\ell_0) = \tilde{g}E \int_0^{L-\ell_0} \tilde{f}(E,\ell)e^{-\alpha'(L-\ell)/\cos\theta_C}d\ell. \qquad (38)$$

After defining $C(E,\alpha,\ell_0)$ analogously to $C(E,\alpha)$, the average electron photon correction $R(E,\alpha)$ can then be calculated as

$$R(E,\alpha) = \int_0^L d\ell_0 \int_0^1 d\kappa P(\ell_0,\kappa) \\ \times [\kappa C(\kappa E,\alpha,\ell_0) + (1-\kappa)C((1-\kappa)E,\alpha,\ell_0)]. \qquad (39)$$

The probability function $P(\ell_0,\kappa)$ is given by the Bethe-Heitler spectrum:

$$P(\ell_0,\kappa) = \left(1 + \frac{1}{42\zeta}\right)^{-1} \\ \times e^{-7/9\,\ell_0}\left[\kappa^2 + (1-\kappa)^2 + \left(\frac{2}{3} - \frac{1}{9\zeta}\right)\kappa(1-\kappa)\right], \qquad (40)$$

where $\zeta$ is the zeta function. For an absorption parameter $\alpha$ of 4%, the electron-photon difference $R$ has values from 2% to 3% over the energy range of the photons we consider. Understanding this difference between the electron and photon response is very important for the success of the experiment. We evaluate our understanding of the photon response in later sections.

*b. $e^+e^-$ electron calibration.* The procedure used to obtain the first set of calibration constants $(g_i,\alpha_i)$ for each block with the $e^+e^-$ calibration samples utilized the near-power-law behavior of the lead glass response. The procedure was an iterative one, where one first corrected the "measured energy"

$$E_m = \sum_{3\times3} n_i/g_i \qquad (41)$$

(also correcting for thresholds, etc. [36]) to a quantity $E_m'$ that should behave like a true power law, $E_{true} = E_m'^\beta$.

The momentum $p$ of the electron was measured in the charged spectrometer, and from Eqs. (34) and (36) we see that we should have $E_m/p = C(p, \alpha_i)$, where $\alpha_i$ is the current best guess for the absorption of the central block of the cluster. Using $\alpha_i$ and Eq. (37) to give the best power-law approximation, a correction factor given by

$$d = \left( \frac{C(p, \alpha_i)}{p^{1/\beta - 1}} \right)^{-1/\beta} \qquad (42)$$

was applied to $E_m$ to give $E'_m = dE_m$.

A least squares fit to $\ln E'_m$ versus $\ln p$ was then done on an event by event basis, one fit for each block. Each event was weighted with the expected smearing both from the momentum measurement and the cluster energy measurement [see Eqs. (29) and (27)]. The slope of the fit gave a corrected power law $\beta'$ from which a new absorption for the central block, $\alpha'_i$, was inferred using Eq. (37). The intercept of the plot was taken as the correction to the gain of the central block.

### 2. $K_{e3}$ electron calibration

For the final adjustment of the lead glass calibration we turned to the $K_{e3}$ sample in the vacuum beam. The $K_{e3}$ sample was initially identified by requiring that the ratio of cluster energy to track momentum satisfied $E/p > 0.85$. This left a sample of $120 \times 10^6$ events in 5 different data subsets. However, hadronic showers by pions or protons satisfied this requirement several percent of the time, leading to a contamination of several percent. Here we describe the isolation of the electron sample, the study of a structure in the glass response seen at 16 GeV, and the final calibration.

*a. $K_{e3}$ isolation.* The largest backgrounds in the $K_{e3}$ sample came from $\Lambda \to p\pi$ and $K_L \to \pi^+ \pi^- \pi^0$ decays. The $\Lambda$ decays were quite easy to eliminate. For the energies that we are interested, the proton-to-pion momentum ratio satisfied $p_p/p_\pi > 3$. The $\Lambda$'s also had to be very energetic in order to live long enough to decay in our decay volume. We are more concerned with rejecting background than preserving signal for this sample, and so we reject any event with $E_\Lambda > 100$ GeV and with a $p\pi$ mass within 15 MeV of the nominal $\Lambda$ mass, minimizing contamination from non-Gaussian tails on the $p\pi$ mass distribution.

There were several cuts applied to remove $\pi^+ \pi^- \pi^0$ decays from the sample. The most powerful was to look at the kinematics of the two tracks, assuming they were associated with charged pions. We could then examine the kinematics of these two tracks assuming that the $\pi^0$ was missing [1,44]. The majority of the $K_{e3}$ decays have an unphysical negative value for $k_{+-0}$, where

$$k_{+-0} = \frac{[(M_K^2 - M_{\pi^0}^2 - M_c^2)^2 - 4M_{\pi^0}^2 M_c^2 - 4M_K^2(P_T^2)_c]}{4M_K^2[(P_T^2)_c + M_c^2]}$$

$$= \frac{p_{0\parallel}^{*2}}{(P_T^2)_c + M_c^2}. \qquad (43)$$

Here $M_c$ is the invariant mass of the two charged tracks, $(P_T^2)_c$ is their transverse momentum with respect to the parent kaon, and $p_{0\parallel}^{*2}$ is the longitudinal $\pi^0$ momentum in the
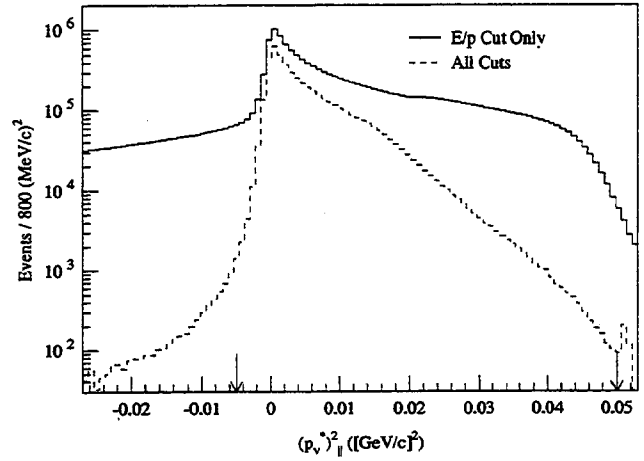


FIG. 22. $K_{e3}$ kinematic variable $p_{\nu\parallel}^{*2}$ for $K_{e3}$ candidate calibration events after a loose $E/p$ cut only (solid histogram) and after all but the kinematic cut (dashed histogram). The arrows indicate the analysis cut locations.

kaon rest frame. The $\pi^+ \pi^- \pi^0$ was effectively eliminated by removing events that simultaneously satisfied $m_{\pi\pi} < 373$ MeV and $k_{+-0} > -0.04$.

Cuts were also applied to the electron cluster shape. These included cuts on the size of the shower originally designed to eliminate two merged showers, and on the relative track and cluster positions. These reduced contamination of bremsstrahlung and were also effective at eliminating showering pions. Those $K_{e3}$ decays where one track is cleanly identified as an electron were used to show that only about 10%–15% of showering pions survived the shape cuts.

No cuts were specifically applied to reduce backgrounds from $\pi^+ \pi^-$ or $K_{\mu3}$ decays. A $K_{\mu3}$ decay has to be doubly misidentified to make it into the final sample: The pion has to shower and be identified as an electron, and the muon has to fail firing the Mu2 veto. Pions were required to have a momentum greater than 4 GeV/$c$, and the probability of this double misidentification was of order $10^{-4}$. For the $\pi^+ \pi^-$ sample there is a several percent chance for one of the two pions to shower and be identified as an electron. When combined with the difference in branching ratios, the background is again expected to be only of order $10^{-4}$ in the $K_{e3}$ sample. After the electron shape cuts, both these modes had residual contributions at the several $10^{-5}$ level.

The sample was also required to satisfy $K_{e3}$ kinematics, with $m_{\pi e} < m_{K^0}$ and $p_{\nu\parallel}^{*2} > -0.005$ (GeV/$c$)$^2$, where

$$p_{\nu\parallel}^{*2} = \frac{[(M_K^2 - M_c^2)^2 - 4M_K^2(P_T^2)_c]}{4M_K^2}, \qquad (44)$$

which is the square of the longitudinal neutrino momentum in the kaon center of mass. Some resolution smearing is allowed in the latter quantity, which is plotted in Fig. 22 before and after all of the background and misreconstruction rejection cuts (except the cut on $p_{\nu\parallel}^{*2}$).

Finally, to avoid biases in the momentum and energy measurements, cuts were applied to ensure that the electron track was cleanly reconstructed, and additional cuts were applied on the track projections to keep the electron and pion well separated.
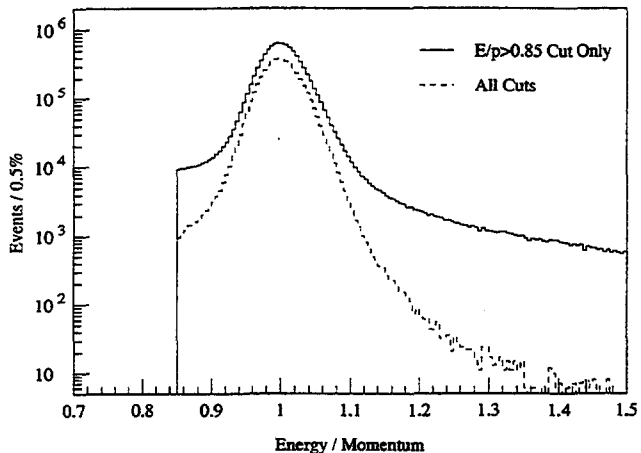
FIG. 23. $E/p$ distribution for electrons in $K_{e3}$ decays with only the initial $E/p > 0.85$ selection criterion and (solid histogram) and with all other cuts (dashed histogram).



FIG. 25. (a) $E/p$ versus ADC counts for an individual block. The effect of the high-range gain mismatch relative to the low-range gain, coupled with the nonlinearity fit, clearly stands out. The high-range gain was mismatched by 0.6% of itself. (b) The fractional high-range gain corrections for each corrected block.

The final distribution of $E/p$ before and after all cuts for the $K_{e3}$ sample from the NC set is shown in Fig. 23. The studies of the lead glass that follow relied most heavily on this set of electrons. From the reduction in the size of the tail on the high side of the distribution, we can see that the background from overlaps has been greatly reduced. The remaining tail on the low side of the $E/p$ distribution is mostly due to electrons that travel some distance down a small gap at the corner of the blocks (caused by a 2 mm bevel along each long edge of each block) before showering, and it could be reduced by rejecting tracks that project near the corners.

*b. The 16 GeV structure.* Since 16 GeV is near the low-range to high-range crossover point for the ADC modules, there was always the suspicion that a relative high-range to low-range gain mismatch was responsible for the behavior in $E/p$ versus $p$ in this region (see Fig. 21). The relative high- to low-range gain for each ADC channel was measured with a bench test and with the flasher, but it was difficult to get measurements more accurate than several tenths of a percent.

The illustration in Fig. 24 helps clarify the effect. In the



FIG. 24. Distortion introduced into $E/p$ by a 0.5% gain mismatch between the high and low ADC ranges. Left: $E/p$ versus $p$ with a gain mismatch and the best fit nonlinearity which tries to compensate. The errors are representative of those available for an individual block. Right: the difference between the distorted $E/p$ and the best fit nonlinearity. The linear fits in the high- and low-range regions yield a $0.51\% \pm 0.07\%$ measurement of the mismatch.

ideal case, with the correct high- to low-range ratio, proper absorptions, etc., the distribution of $E/p$ versus $p$ would be flat. If the absorption was known properly, but there was a gain mismatch between high and low ranges, a step would be introduced in $E/p$ versus $p$, as in part (a) of the figure. If one tried to find the best nonlinearity, it would partially compensate for the step, fitting a curve similar to the line in Fig. 24(a). When we use this new nonlinearity, a measurement of $E/p$ versus $p$ would give the residual between the measured $E/p$ and the fit curve in Fig. 24(a), yielding the tilted distributions in Fig. 24(b).

This is essentially the structure we see in Fig. 21, except that the structure is blurred by differences in the crossover region and step mismatch from block to block. Using the clean electron sample identified above, we have studied the variation of $E/p$ versus ADC counts for all blocks with electrons extending into the ADC high range. An example is shown in Fig. 25(a), with a linear fit to $E/p$ in both the high range and the low range. It is straightforward to show that the necessary fractional correction to the high-range gain is simply the difference in $E/p$ measured at the crossover point in the high- and low-range. We obtained this correction by extrapolating the high- and low-range fits to the crossover point in that block. After several iterations, the process converged. The distribution of corrections is shown in Fig. 25(b). The corrections were reproducible within 0.1% in more than one data sample of $K_{e3}$ decays.

*c. $K_{e3}$ calibration.* After the above improved measurement of the relative high-range to low-range gain, and improved measurements of the rate dependence of pedestal shifts within the ADC modules, each sample of $K_{e3}$ electrons was used to recalibrate. Since the calibration constants from the $e^+ e^-$ samples were already quite good, we did not try to make an absolute measurement of the block absorptions as described above. Instead, we assumed any residual between the electron momentum $p$ and the energy prediction $E = E_m / C(p, \alpha)$ would be very close to a residual power law $p = E^{\Delta \beta}$. The new absorptions were then given by

$$\alpha_{\text{new}} = \frac{1.0053}{0.9106} - \Delta \beta \left( \frac{1.0053}{0.9106} - \alpha_{\text{old}} \right). \tag{45}$$
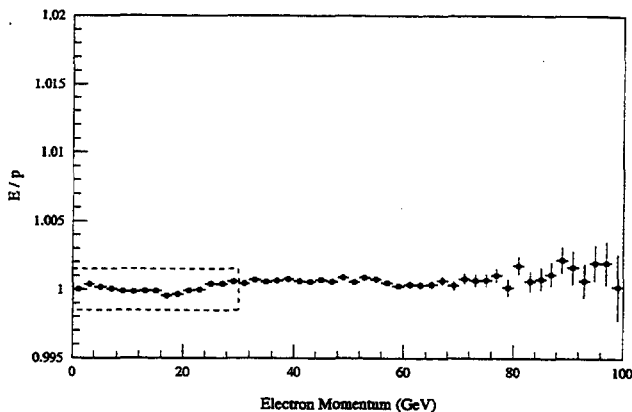
FIG. 26. Mean value of the ratio of cluster energy to track momentum $(E/p)$ versus momentum for electrons and positrons from $K_{e3}$ decays using the $K_{e3}$ calibration gains. The dashed box shows the momentum range used for the calibration.

A possible bias still existed from electron bremsstrahlung upstream of the analysis magnet and from radiative $K_{e3}$ decays. In both of these cases, when the electron momentum is above 40 GeV, the analysis magnet did not bend the electron far enough away from the photon trajectory, resulting in a merging of the photon and electron clusters in the calorimeter. Thus the cluster energy would appear higher than the measured track momentum. While the electron cluster shape cuts should largely eliminate such events, we decided to limit the maximum electron momentum for the NC set calibration to 30 GeV. The minimum momentum accepted was 2 GeV.

After calibration, the resulting distribution of the mean of $E/p$ vs $p$ in the NC set over a 100 GeV range is shown in Fig. 26. The average electron response appears to be understood within 0.1% well beyond the 30 GeV maximum electron energy used in the calibration.

In charged mode sets earlier than the NC set, the readout threshold on the lead glass was 20 counts rather than 5 counts. This made reliable calibration with the lowest-energy electrons more difficult. From studies on the NC set with a 20-count threshold simulated in software, the calibration results could be reproduced quite reliably in the inner portions of the array by changing the allowed electron momentum range to be 10–60 GeV. In addition, the higher threshold degrades the energy resolution, and so an extra resolution term was added to compensate for this when weighting the events. For the outer three rings, where radiation damage was expected to be minimal, the absorptions obtained in the NC set were simply scaled as a group. The measured scale factors were almost flat in time, increasing only slightly as the run progressed.

For neutral mode sets earlier than the NC set, we tried to make the best use of all the calibrations available to obtain the most reliable photon reconstruction. For the inner $10 \times 10$ subsection of the array, the $e^+ e^-$ samples had sufficient statistics to provide calibration constants. Because the beam intensity was highest during the $2\pi^0$ data taking, this inner portion of the array tended to suffer most from radiation damage in these sets. The $e^+ e^-$ calibrations were taken during each set, and so they provide the best measure of the absorptions at those times. For the rest of the array, the
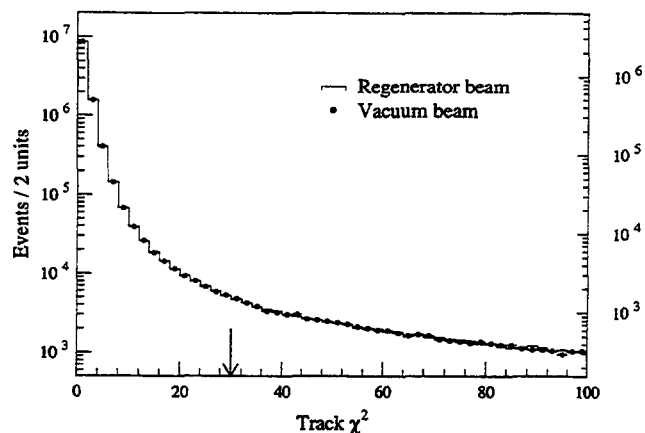


FIG. 27. Track segment $\chi^2$ (per degree of freedom) for the pion tracks from $\pi^+\pi^-$ decays. The histogram depicts the regenerator beam distribution (left scale), and the dots depict the vacuum beam distribution (right scale). The arrow indicates the position of the cut. All but the track quality cuts have been applied.

$K_{e3}$ constants were extrapolated to the neutral sets using the flasher data. The constants from the two sets agreed very well on the boundary of the $10 \times 10$ subsection.

This concludes the discussion of the calibration of the components of the detector needed to reconstruct $\pi\pi$ decays. We now turn to the discussions of reconstruction and background subtraction in the $\pi^+\pi^-$ and $2\pi^0$ decays.

## V. $\pi^+\pi^-$ ANALYSIS

In this section we describe the analysis and background subtraction for $\pi^+\pi^-$ decays. For both the $\pi^+\pi^-$ and $2\pi^0$ decay modes, the reconstruction and analysis cuts were blind both to the beam in which the decay occurred and to the position of the regenerator (in the top or bottom beam). This ensured that regenerator and vacuum beam events were treated identically and avoided a major class of biases. Only after all analysis was complete were the events divided into the regenerator beam and vacuum beam subsets for background subtractions, for comparisons to the simulations, and for fitting. No cuts were applied on decays from one beam that were not applied to decays from the other.

### A. Charge mode reconstruction

#### 1. Tracking-related cuts

The basic requirement for a $\pi^+\pi^-$ candidate was the reconstruction of two in-time tracks (see Sec. III B 3). To minimize misreconstruction, we applied several track quality cuts. The most basic one was on the track segment $\chi^2$ calculated for a linear fit to the locations of the individual hits measured in the drift chambers. A track "segment" is a trajectory measured in either upstream or downstream pair of drift chambers. The distribution of the reduced track segment $\chi^2$ (i.e., $\chi^2/n_d$, where $n_d$ is the number of degrees of freedom) is shown in Fig. 27 after all other cuts for decays from both vacuum and regenerator beams.

The long tail visible in the $\chi^2$ distribution is populated almost entirely by tracks where one hit has a drift time too small to be consistent with the other hits. This is the behavior expected from early-arriving $\delta$ rays because of TDC dead
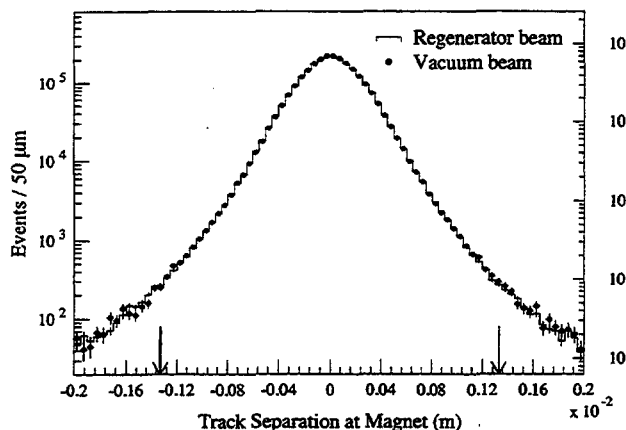
FIG. 28. Separation $d_0$ of upstream and downstream track-segment projections at the magnet bend plane for the $\pi^+\pi^-$ samples after all other cuts. The histogram depicts the regenerator beam distribution (left scale), and the dots depict the vacuum beam distribution (right scale). The arrows show the cut for an average track momentum of about 20 GeV/$c$.

time. This observed distribution agrees in absolute level (to 20%) and in shape with expectations from a simple $\delta$-ray production model.

The $\delta$-ray production probability is nearly independent of momentum for our pion momenta, and is also independent of the position in the chambers. As a result, the production probability is identical in the vacuum and regenerator beams, and so the event loss from the $\chi^2$ cut cancels in the charge mode single ratio, as shown in Fig. 27.

We also cut on the distance $d_0$ (Fig. 28) between upstream and downstream track-segment projections at the bend plane of the magnet. The resolution on $d_0$ is

$$\sigma_{d_0} \ [\mu\text{m}] = 140 \oplus \frac{3020}{p_\pi[\text{GeV}/c]}. \tag{46}$$

The first term is due to chamber resolution and the second to multiple scattering. We make a very loose cut, a momentum-dependent cut, corresponding to 6.8 standard deviations on average, though there are non-Gaussian tails present.

We require that the two tracks be consistent with originating from a common vertex by calculating their distance of closest approach $d_c$. The observed distribution for $d_c$ is shown in Fig. 29(a) for both the regenerator and vacuum beams. The small mismatch between the two beams arises because the resolution on $d_c$ varies (almost linearly) with the distance $\Delta z$ from the decay location to the first chamber. To eliminate the difference in this distribution introduced by the difference in the $z$ distributions, we cut on the scaled quantity $d_c/\Delta z$ shown in Fig. 29(b). The tail is due mostly to multiple scattering. The applied cut was $d_c/\Delta z < 4\sigma_{d_c}$, where

$$\sigma_{d_c} = 2.45 \times 10^{-5} + 8.5 \times 10^{-3}\left(\frac{1}{p_1^2} + \frac{1}{p_2^2}\right), \tag{47}$$

with the two track momenta $p_1$ and $p_2$ measured in GeV/$c$.

The decay vertex was initially defined as the midpoint of the shortest line segment joining the two tracks. We then improved the measurement of the vertex on average by using
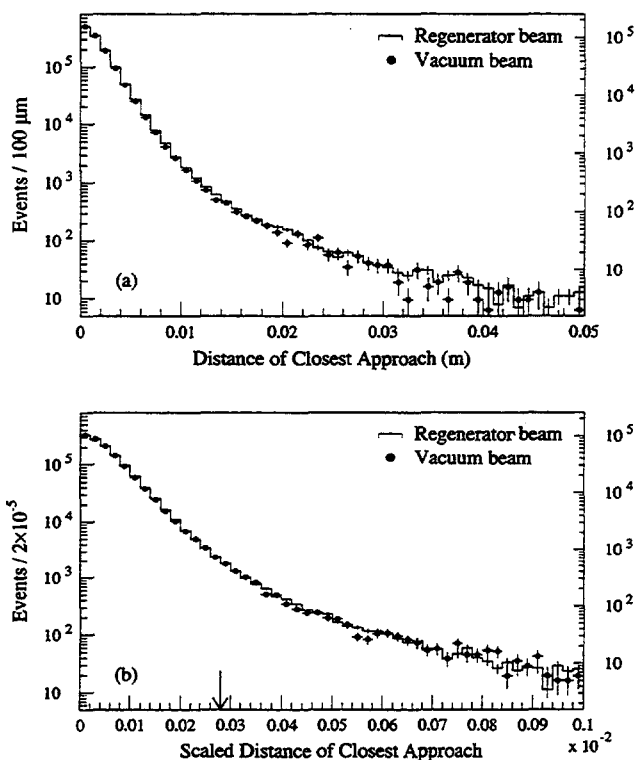




FIG. 29. Distance of closest approach $d_c$ for the two tracks measured in $\pi^+\pi^-$ decays after all other cuts. The histogram depicts the regenerator beam distribution (left scale), and the dots depict the vacuum beam distribution (right scale). (a) Raw $d_c$. (b) $d_c$ scaled by the distance from the decay location to chamber 1. The arrow marks the location of the average cut.

the fact that the higher-momentum pion in a decay suffers less from multiple scattering than the lower-momentum pion. Using our initial vertex and two upstream track trajectories as starting values, the vertex and trajectories were refit with the two pion trajectories weighted according to their multiple-scattering probabilities and measurement smearing. This led to a 10% improvement in the transverse position resolution on the vertex, for an average resolution (in the $x$ or $y$ view) of 1.0 mm. The $z$ resolution varied from 10 cm at the downstream end of the decay volume to 25 cm at the upstream end ($z = 110$ m).

The matching of the $x$ track segments to $y$ track segments was done by projecting to the appropriate cluster in the calorimeter. An ambiguity occurred when the separation of the two tracks in $x$ was small. Because of the left-right symmetry requirement of the trigger, this happened only when the pions were near the center of the array. The matching ambiguity was eliminated by requiring the $x$ separation of the projection of the two tracks to the lead glass to be larger than 2 cm when either pion projected within the two central columns of blocks.

This ambiguity was particularly important in the $x$ view because the $x$ segment carries the momentum information. A similar ambiguity did exist in the matching of the $y$ segments to clusters when a pion landed within the central two rows of lead glass blocks. A mismatch in this view, however, has little effect on the reconstruction because neither the $E/p$ calculation nor the kinematics is strongly affected (see the next section, "Kinematics and background reduction"); no cut was applied.
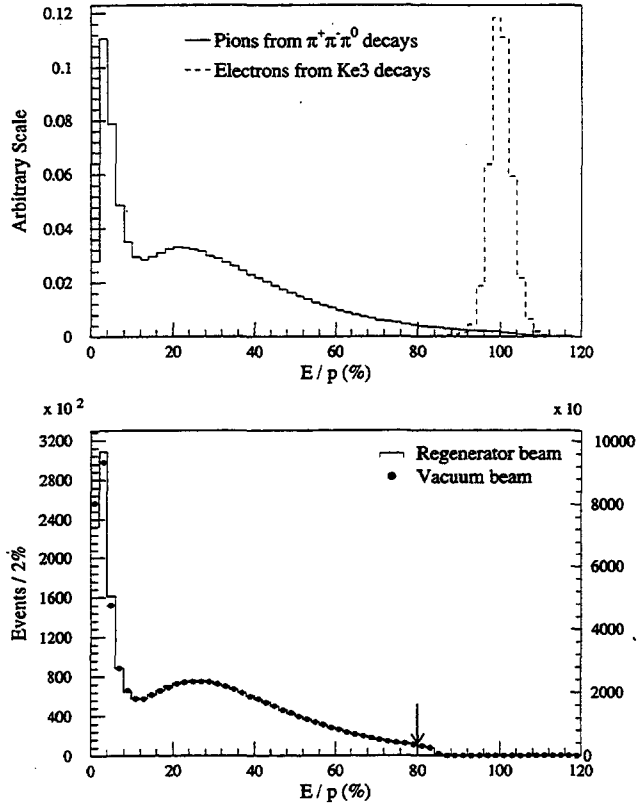
FIG. 30. Shape of the $E/p$ distribution for pions and electrons. Top: the solid histogram shows the spectrum for pions for a subset $\pi^+\pi^-\pi^0$ decays, and the dashed histogram shows the spectrum for electrons for a subset of $K_{e3}$ decays. The normalization of the two samples is arbitrary. Bottom: the $E/p$ distribution for pions from $\pi^+\pi^-$ decays after all other cuts. The histogram shows the distribution for decays in the regenerator beam (left scale), and the dots show the distribution for decays in the vacuum beam (right scale). The cutoff at 0.85 is a result of the initial loose cut in the initial data reduction analysis pass. The final cut at 0.80 is indicated by the arrow.

### 2. Kinematics and background reduction

We now turn to the identification of $K \rightarrow \pi^+\pi^-$ decays and rejection of backgrounds. Since $K_{\mu3}$ decays were largely removed by the trigger, the most copious source of two-track triggers was $K_{e3}$ decays, outnumbering $\pi^+\pi^-$ by two orders of magnitude. These were most important in the vacuum beam. There were also significant contributions from $K \rightarrow \pi^+\pi^-\pi^0$ and $\Lambda \rightarrow p\pi^-$ decays. The most serious background in the regenerator beam was from kaon scattering in the regenerator itself.

We made fiducial cuts on the tracks at the calorimeter. The resolution for projecting the $x$ or $y$ track segments to the calorimeter is of order 220 $\mu$m. Events were cut if the tracks projected beyond the inner half of the outer blocks in the array. Tracks were required to project at least 1 mm outside of the CA as well. Events with a track which projected into the beam hole, missing both the CA and the calorimeter, were also removed. We also required that both tracks project within the Mu2 veto bank and that their momentum be greater than 7 GeV/$c$ to ensure efficient rejection of $K_{\mu3}$.

The $K_{e3}$ decays could be efficiently rejected with little loss of $\pi^+\pi^-$ decays using $E/p$. The $E/p$ distribution is

shown in Fig. 30(a) for pions and for electrons. The $E/p$ for pions from $\pi^+\pi^-$ decays after all other cuts are applied is shown in Fig. 30(b). The distributions shown are after the first analysis which loosely categorized the different decays and eliminated obvious backgrounds. The $\pi^+\pi^-\pi^0$ decays could be isolated from $K_{e3}$ decays using the kinematics of the observed tracks and photons, and so no $E/p$ cut was necessary to isolate this sample from $K_{e3}$ decays. This made the $\pi^+\pi^-\pi^0$ sample useful for studying $\pi^+\pi^-$ loss due to the $E/p$ cut.

The peak at low $E/p$ corresponds to pions which do not shower. The difference between the vacuum and regenerator beams in this "minimum-ionizing" peak is due mainly to the difference in the momentum spectra. Since the minimum-ionizing peak is far from the cut, this difference does not affect the fraction of events lost. Furthermore, we generally compare the vacuum and regenerator beam distributions in small kaon momentum bins, and so the difference in the overall momentum spectra is not important.

For the final analysis, we require that both pions have $E/p < 0.80$. The electron $E/p$ resolution was about 3%, and so only the most pathological electrons survive this cut of almost seven standard deviations. On the other hand, from the $E/p$ distribution in $\pi^+\pi^-\pi^0$ decays, we find that the probability for a pion to have $E/p > 0.8$ is 3.3%. The loss of $K \rightarrow \pi^+\pi^-$ decays is then 6.5%, and the $K_{e3}$ rejection is very close to 100%. One possible way for a bias to enter into the vacuum-to-regenerator beam ratio in a momentum bin would be if the regenerator beam pions showered in blocks with a systematically different gain mismeasurement. From the $K_{e3}$ calibrations, the gains of the majority of the blocks are determined at a level of 0.2% of themselves or better. Even in the outer blocks with the least illumination, the gains are known to better than 1% of themselves. Suppose (very unrealistically) that the showering pions from the regenerator beam consistently saw blocks that were 0.3% high in calibration compared to vacuum beam events. From the level of $E/p$ near the cut, this would bias the single ratio by less than 0.01%.

After the semileptonic backgrounds had been reduced, the largest remaining backgrounds, dominated by $\Lambda$ decays, had hadronic final states. The relevant quantities are the two-pion mass

$$m_{\pi^+\pi^-} = \sqrt{(\sqrt{m_\pi^2 + |\vec{p}_1|^2} + \sqrt{m_\pi^2 + |\vec{p}_2|^2})^2 - |\vec{p}_1 + \vec{p}_2|^2} \quad (48)$$

and the $p\pi$ mass

$$m_{p\pi} = \sqrt{(\sqrt{m_p^2 + |\vec{p}_p|^2} + \sqrt{m_\pi^2 + |\vec{p}_\pi|^2})^2 - |\vec{p}_p + \vec{p}_\pi|^2}. \quad (49)$$

To reconstruct the $p\pi$ mass, the track with the greater momentum ($\vec{p}_p$) is associated with the proton (or antiproton).

Only the most energetic $\Lambda$'s live long enough to reach the decay volume. Since the decay proton carries most of the $\Lambda$ momentum, these events usually fail the cut which requires that both tracks miss the CA, collar anti. To remove the remaining $\Lambda$ decays, we use the property that the proton and pion momenta must satisfy $p_p/p_\pi > 3$. After all other
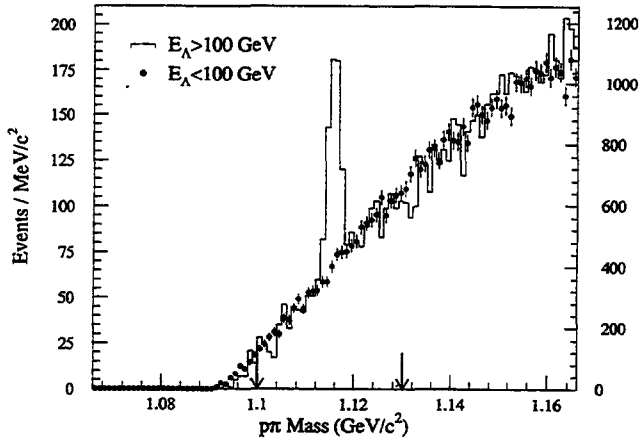
FIG. 31. Reconstructed $p\pi$ mass for all $\pi^+\pi^-$ decay candidates in the vacuum beam which are consistent with $p_p/p_\pi > 3$. All $\pi^+\pi^-$ analysis cuts except the $\Lambda$ rejection cuts have been applied. The $\Lambda$ peak is visible for $E_\Lambda > 100$ GeV (solid histogram, left scale), but not for $E_\Lambda < 100$ GeV (dots, right scale). The arrows indicate the mass cut used on events with $E_\Lambda > 100$ GeV.

cuts, 19% of the remaining $\pi^+\pi^-$ candidates have a track momentum ratio greater than 3. We plot $m_{p\pi}$ for this subsample in Fig. 31, showing separate distributions for decays with $E_\Lambda > 100$ GeV and $E_\Lambda < 100$ GeV. There is clearly no $\Lambda$ signal below 100 GeV, and in fact, the signal does not appear until the $\Lambda$ energy is above 130 GeV. Conservatively we eliminate any $\pi^+\pi^-$ candidate if it satisfies $E_\Lambda > 100$ GeV and has a mass $m_{p\pi}$ in the range from 1.10–1.13 GeV/$c^2$. The resolution of $m_{p\pi}$ measured in the $\Lambda$ sample was 2.1 MeV/$c^2$. The $\Lambda$ mass cut was left quite broad to keep background from non-Gaussian tails at a negligible level.

$\Lambda$ decays are not noticeable in the regenerator beam; nevertheless, the samples were treated identically.

Our resolution on the $\pi^+\pi^-$ mass (Fig. 32) is 3.5 MeV/$c^2$, and we isolate the sample using a cut on the mass from 484 MeV/$c^2$ to 512 MeV/$c^2$, completely eliminating $\pi^+\pi^-\pi^0$ decays. No cuts are made in the $\pi^+\pi^-$ analysis
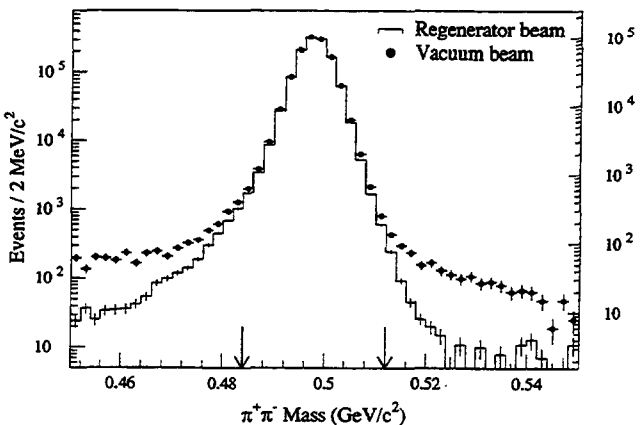


FIG. 32. Reconstructed two-pion mass for $\pi^+\pi^-$ candidates after all other cuts. The regenerator beam distribution is given by the histogram (left scale) and the vacuum beam distribution by the dots (right scale). The arrows indicate the position of the cuts used in the analysis. The radiative tail from $K \to \pi^+\pi^-\gamma$ decays is clearly visible in both beams.
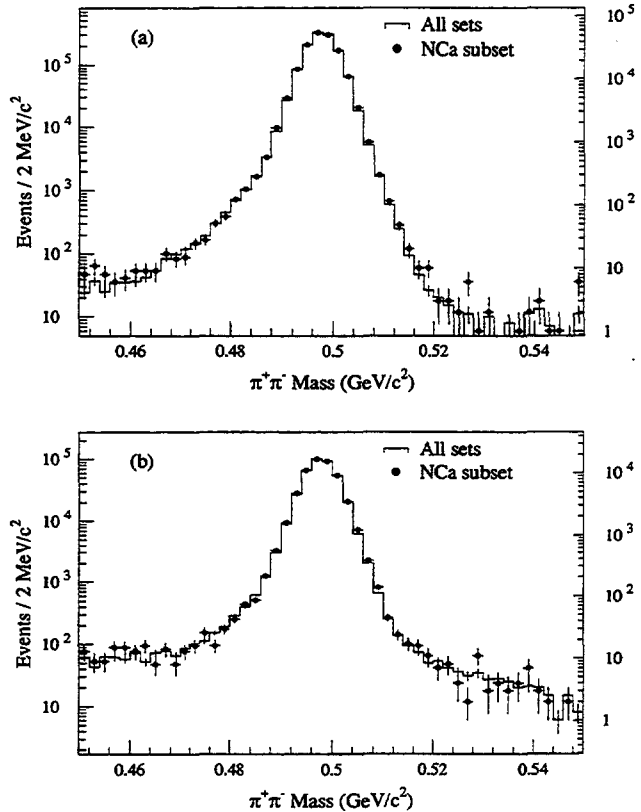


FIG. 33. Reconstructed two-pion mass for $\pi^+\pi^-$ candidates after all other cuts for the entire $\pi^+\pi^-$ data set and for the NC subset only. The histogram shows the distribution for the entire data set (left scale), and the dots show the distribution for the NCa subset (right scale). (a) Regenerator beam. (b) Vacuum beam.

on clusters in the calorimeter unassociated with tracks since hadronic showers can produce spurious clusters.

The broadening of the lower half of the $\pi^+\pi^-$ mass distribution due to the radiative decay $K \to \pi\pi\gamma$, common to both the $K_S$ and $K_L$, is clearly visible. The background in the wings of the vacuum beam distribution is from residual semileptonic decays. This is only visible in the regenerator beam distribution at high mass where it is not hidden by the radiative tail. The $K_L$ radiative decay has a contribution from decays where the photon is emitted directly from the interaction vertex as well as from inner bremsstrahlung [44,45]. The photon from the direct emission process tends to be energetic in the $K_L$ rest frame, and so the resulting $\pi^+\pi^-$ mass is shifted outside of the signal region. The remaining direct emission contribution to $\mathrm{Re}(\varepsilon'/\varepsilon)$ is quite small and is estimated to be about $0.05 \times 10^{-4}$.

In Fig. 33, the mass distributions for the entire data set are shown with the distribution from the NC set used for our initial result [21]. The shapes are quite similar even though the NC set was collected at 3 times the proton intensity of the other subsets.

The final kinematic cut requires that the reconstructed momentum of the kaon from $\pi^+\pi^-$ candidate is nearly parallel to the incident kaon trajectory. For each $\pi^+\pi^-$ candidate, the square of the transverse momentum, $p_t^2$, was calculated by assuming that the kaon had scattered in the regenerator (see Fig. 34). The scattering angle $\theta$ between the initial and final kaon trajectories is then used to calculate the
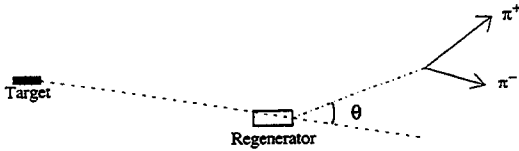
FIG. 34. Schematic representation of the method used to calculate the kaon scattering angle in the regenerator. The momenta of the two pions measured in the drift chambers (solid lines) are combined to determine the kaon trajectory. The kaon is then projected from the decay vertex to the downstream face of the regenerator (dot-dashed line). The original kaon trajectory is defined by the line connecting the projected kaon position at the regenerator to the target. The scattering angle $\theta$ is the angle between the two trajectories.

square of the transverse momentum:

$$p_t^2 = p_K^2 \sin^2 \theta. \tag{50}$$

Since the distance from the target to the regenerator is large compared to the length of the regenerator, this $p_t^2$ calculation is insensitive to the location of the scattering site inside the regenerator. This cut reduces both the residual semileptonic background in the vacuum beam and the diffractive and inelastic $\pi^+\pi^-$ backgrounds in the regenerator beam. We use the same calculation of $p_t^2$ for the vacuum and regenerator

beams to avoid bias in losses of coherent kaons due to the smearing of the measured $p_t^2$.

The $p_t^2$ distributions for the two beams are plotted in Fig. 35. In the regenerator beam, the decays with large $p_t^2$ are from kaons which regenerated inelastically. Near the coherent peak, the contribution from diffractively regenerated kaons, with a steeper $p_t^2$ spectrum than the inelastically regenerated kaons, results in the upturn in the spectrum, as seen in Fig. 35(c). The bulge in the distributions just outside the $p_t^2$ cut of 250 (MeV/$c$)$^2$ is due to the radiative decay $K \to \pi\pi\gamma$. The semileptonic decays give the steeply falling tail in the vacuum beam, as seen in Fig. 35(d). The very small, flatter component visible at larger $p_t^2$ in the vacuum beam distribution is consistent with interactions of the beam with residual gas in the decay tank.

### 3. Other cuts and summary

The final class of cuts was designed to reduce potential biases from the acceptance correction. Accidental activity in the detector could sometimes cause an event to satisfy the trigger even though the decay products themselves would not. Since accidental activity is common to the vacuum and regenerator beams, we expected the gain of events from this process to be identical in the two beams. However, to make comparisons between the data and the Monte Carlo samples
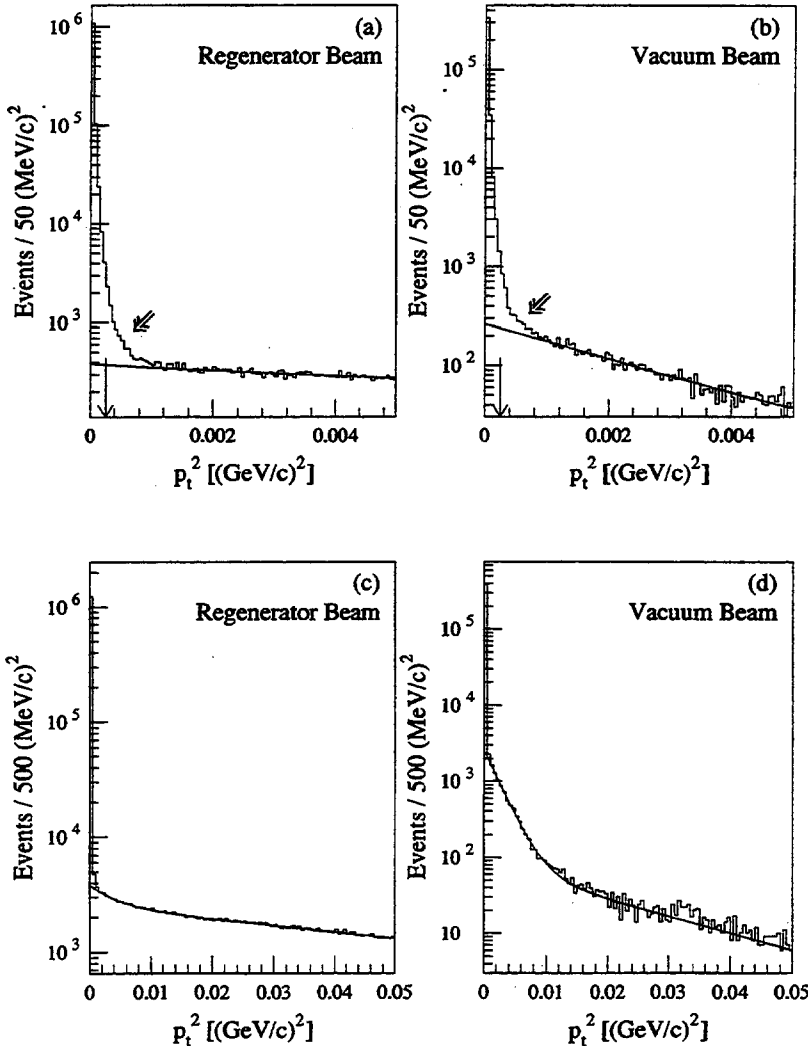


FIG. 35. The $p_t^2$ distribution for $\pi^+\pi^-$ candidates after all other cuts are applied for two different ranges of $p_t^2$. Parts (a) and (b) show the distribution for $p_t^2 < 5000$ (MeV/$c$)$^2$ for the regenerator and vacuum beams, respectively. At this scale, the structure of the coherent peak, the location of the analysis cut (vertical arrow) and the radiative tail (hollow arrow) from $\pi^+\pi^-\gamma$ decays are all visible. Parts (c) and (d) show the distribution for $p_t^2 < 50\,000$ (MeV/$c$)$^2$ for the regenerator and vacuum beams, respectively, where the contributions from different background sources (see text) are more apparent. In all four parts, the solid line is the best fit to the overall background shape.

TABLE VI. The fraction of coherent $\pi^+ \pi^-$ decays lost as each analysis cut is applied sequentially and when a cut is applied as the final cut. For the first sequential cut, the loss is relative to the number of $\pi^+ \pi^-$ events which reconstruct within the fiducial energy and $z$ region used in the fits. Each cut thereafter is normalized to the number of kaons left after the preceding cut. Here "$K_L$" and "$K_S$" have been used as shorthand for the vacuum and regenerator beams, respectively. The two momentum ranges are given in GeV/c.

| Analysis cut | Sequential loss (%) | | | | Loss as final cut (%) | | | |
|---|---|---|---|---|---|---|---|---|
| | 40–160 | | 20–160 | | 40–160 | | 20–160 | |
| | $K_L$ | $K_S$ | $K_L$ | $K_S$ | $K_L$ | $K_S$ | $K_L$ | $K_S$ |
| Pions within calorimeter | 3.77 | 4.68 | 7.12 | 7.93 | 1.09 | 1.35 | 2.14 | 2.49 |
| Vacuum window aperture | 0.04 | 0.05 | 0.15 | 0.22 | 0.02 | 0.03 | 0.11 | 0.16 |
| Analysis magnet aperture | 0.55 | 0.74 | 1.16 | 1.62 | 0.30 | 0.40 | 0.73 | 1.16 |
| HDRA aperture | 0.03 | 0.01 | 0.05 | 0.02 | 0.02 | 0.00 | 0.04 | 0.01 |
| Tracks remain in helium volume | 0.02 | 0.09 | 0.30 | 0.44 | 0.02 | 0.07 | 0.29 | 0.47 |
| $\Lambda$ cuts | 2.71 | 1.98 | 2.38 | 1.75 | 0.56 | 0.34 | 0.48 | 0.30 |
| $p_\pi > 7$ GeV/c | 3.16 | 3.38 | 4.10 | 3.87 | 0.79 | 0.91 | 1.41 | 1.13 |
| Track $\chi^2$ [a] | 0.04 | 0.05 | 0.04 | 0.05 | 0.02 | 0.02 | 0.02 | 0.02 |
| Distance of closest approach | 0.95 | 0.94 | 0.90 | 0.91 | 0.86 | 0.89 | 0.79 | 0.83 |
| Track separation at magnet | 0.04 | 0.05 | 0.06 | 0.06 | 0.03 | 0.04 | 0.05 | 0.04 |
| $\pi \rightarrow \mu\nu$ decay veto | 1.86 | 2.09 | 2.29 | 2.41 | 2.23 | 2.47 | 2.69 | 2.80 |
| Mask aperture | 1.00 | 0.01 | 0.92 | 0.01 | 1.06 | 0.00 | 0.95 | 0.00 |
| No pions in CA or beam hole | 21.99 | 21.05 | 19.68 | 18.84 | 19.38 | 18.54 | 17.23 | 16.50 |
| Chamber 2 trigger reverify | 0.01 | 0.00 | 0.01 | 0.00 | 0.01 | 0.00 | 0.01 | 0.00 |
| BC hodoscope trigger reverify | 1.89 | 1.95 | 1.92 | 1.92 | 1.74 | 1.80 | 1.77 | 1.77 |
| $\pi^+ \pi^-$ mass | 1.36 | 1.39 | 1.47 | 1.54 | 0.39 | 0.40 | 0.40 | 0.42 |
| $p_t^2$ | 0.55 | 0.48 | 0.49 | 0.43 | 0.55 | 0.48 | 0.49 | 0.43 |

[a]Without $\delta$ rays. See text for loss estimates from $\pi^+ \pi^- \pi^0$ studies.

more meaningful, we reverified the triggers using the reconstructed tracks. We required the reconstructed decay vertex to be upstream of the HDRA, the hits on the track in the second drift chamber to satisfy the east-west trigger requirement in that chamber, and the B and C hodoscope counters through which the tracks project to satisfy the trigger logic for those counter banks.

In addition to the trigger reverification, we also rejected decays where the tracks projected to within a few millimeters of the limiting apertures. This reduced the sensitivity of the charged sample to the exact location of these apertures. For decays in the vacuum beam upstream of the mask, both tracks had to pass through the mask aperture for the proper beam.

For coherent Monte Carlo events that are in our final sample, the fractional loss due to each cut is shown in Table VI. The momentum range in the table relevant to the $Re(\varepsilon'/\varepsilon)$ measurement is 40–160 GeV/c, whereas 20–160 GeV/c is used for the remaining measurements. The distribution of kaon energy after all other cuts have been made is shown in Fig. 36 for both the regenerator and vacuum beams. The similarity in the spectra for the two beams is apparent. The vertex distribution for the $K \rightarrow \pi^+ \pi^-$ decays ("$z$ distribution") from the production target after all other cuts is shown in Fig. 37. The downstream end of the regenerator is associated with the sharp edge at 123.5 m in the regenerator beam. The falloff in the rate of accepted decays upstream of 120 m in the vacuum beam is governed by the upstream active mask, which cleanly defines the acceptance in the upstream region.
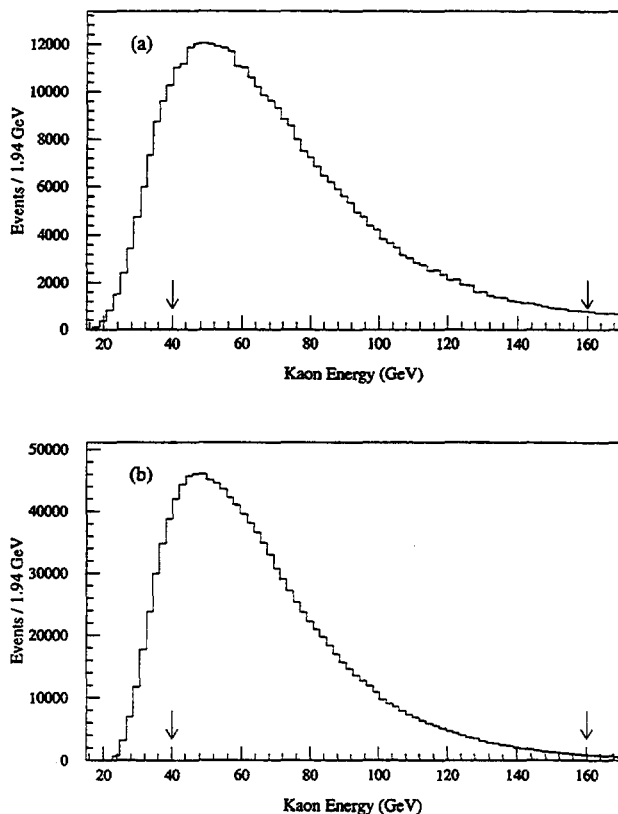


FIG. 36. Distribution of the kaon energy for the final $\pi^+ \pi^-$ sample. The arrows mark the location of the cuts used in the $Re(\varepsilon'/\varepsilon)$ analysis. (a) Vacuum beam. (b) Regenerator beam.

L. K. GIBBONS *et al.*
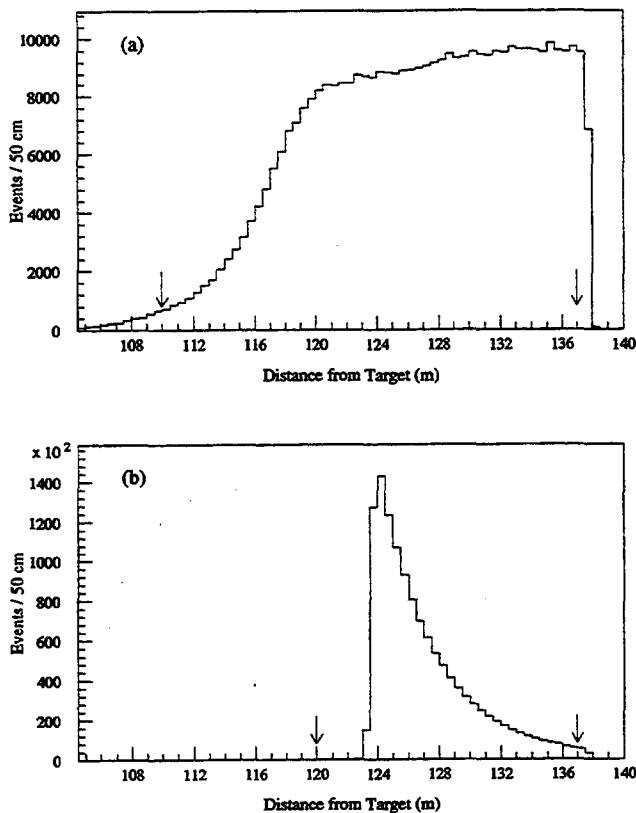




FIG. 37. Distribution of the distance of the decays from the production target for the final $\pi^+\pi^-$ sample. The arrows mark the location of the cuts used in the Re($\varepsilon'/\varepsilon$) analysis. (a) Vacuum beam. (b) Regenerator beam.

### B. $\pi^+\pi^-$ background subtraction

After applying the cuts discussed above, the residual backgrounds in the $\pi^+\pi^-$ decay mode were typically 0.1–0.3%. They could not, however, be neglected in the measure-

ment of Re($\varepsilon'/\varepsilon$). For both samples, the background is estimated by fitting the shape of the $p_t^2$ spectrum in the range 1500–20 000 (MeV/$c$)$^2$ and extrapolating underneath the coherent peak [0–250 (MeV/$c$)$^2$].

The small background from beam-gas scattering in the vacuum beam is visible at large $p_t^2$ in Fig. 35(d), where all the momentum bins have been combined. However, the low statistics of this background made a two-exponential fit in individual momentum bins difficult. In this beam, therefore, the $p_t^2$ spectrum for decays within each 10 GeV/$c$ momentum bin was fit using the form

$$\frac{dN_v(p_t^2)}{dp_t^2} = \alpha e^{-\beta p_t^2} + c, \qquad (51)$$

where $\alpha$, $\beta$, and $c$ are parameters of the fit. The exponential slopes ($\beta$) obtained in the fits are compatible with the hypothesis that the background is dominated by $K_{e3}$ decays. The constant term $c$ accommodates the average beam-interaction background.

The background level under the coherent peak in each $p$ bin and the number of coherent $K \rightarrow \pi^+\pi^-$ decays remaining after subtraction are listed in Table VII. The overall background level was 0.341%±0.010%, where the error is statistical only.

Combining all of the momentum bins, we can fit the vacuum beam $p_t^2$ spectrum to the sum of two independent exponentials for $p_t^2 < 50\,000$ (MeV/$c$)$^2$. The result of this fit is plotted as the curve in both Figs. 35(b) and 35(d). The individual semileptonic slopes measured within each momentum bin were consistent with the overall slope of $424\pm15$ (GeV/$c$)$^{-2}$. The slope obtained for the beam-interaction component of the background for this fit was $51\pm10$ (GeV/$c$)$^{-2}$.

The systematic error in the background level is dominated

TABLE VII. The number of coherent $\pi^+\pi^-$ decays after background subtraction and the total background fraction subtracted in each 10 GeV/$c$ bin. The background levels are given in percent. Indicated errors include only statistical uncertainties.

| Momentum range (GeV/$c$) | Vacuum beam Data | Vacuum beam Background (%) | Regenerator beam Data | Regenerator beam Background (%) |
|---|---|---|---|---|
| 20–30 | 11712 | 0.31±0.05 | 19059 | 0.158±0.029 |
| 30–40 | 42092 | 0.34±0.03 | 144363 | 0.165±0.011 |
| 40–50 | 59701 | 0.37±0.02 | 230593 | 0.160±0.008 |
| 50–60 | 59983 | 0.40±0.03 | 222405 | 0.157±0.008 |
| 60–70 | 52227 | 0.37±0.03 | 185010 | 0.153±0.009 |
| 70–80 | 42380 | 0.34±0.03 | 136064 | 0.150±0.010 |
| 80–90 | 32525 | 0.32±0.03 | 97159 | 0.145±0.012 |
| 90–100 | 24702 | 0.28±0.03 | 66862 | 0.144±0.015 |
| 100–110 | 17689 | 0.27±0.04 | 44144 | 0.143±0.018 |
| 110–120 | 13241 | 0.26±0.04 | 30246 | 0.143±0.022 |
| 120–130 | 9704 | 0.26±0.05 | 20461 | 0.142±0.026 |
| 130–140 | 7056 | 0.25±0.06 | 13414 | 0.142±0.033 |
| 140–150 | 5486 | 0.25±0.07 | 8656 | 0.141±0.040 |
| 150–160 | 4286 | 0.24±0.08 | 5654 | 0.141±0.050 |
| 20–160 | 382783 | 0.340±0.009 | 1224088 | 0.154±0.004 |
| 40–160 | 328980 | 0.341±0.010 | 1060667 | 0.152±0.004 |

by the uncertainty in the slope of the semileptonic background. This has been evaluated in part by varying the slope within the limits allowed by the fits to the $p_t^2$ spectra in the 1500–20 000 (MeV/$c$)$^2$ range, and also by varying the range over which the fits were performed. In addition, the background fits were modified to use a beam-interaction component with fixed exponential slopes as large as 60 (GeV/$c$)$^{-2}$. This modification introduced only small differences into the total number of events subtracted. The total systematic uncertainty in this background is 0.010%, giving a total error in the $\pi^+\pi^-$ vacuum beam background fraction of 0.014%. In Monte Carlo studies of the semileptonic background, we found that the $p_t^2$ spectrum began to deviate from a perfect exponential for $p_t^2 < 2500$ (MeV/$c$)$^2$. While this rolloff would mean we are overpredicting the background level, the mismeasurement is at most 0.003%, well within the systematic uncertainty.

We fit the $p_t^2$ spectrum in the regenerator beam after the acceptance correction with a pair of exponentials and find

$$\frac{dN}{dp_t^2} \propto e^{-5.156p_t^2} + 0.546e^{-222.78p_t^2}, \qquad (52)$$

where $p_t^2$ is measured in (GeV/$c$)$^2$. The latter, steeper, term corresponds to the diffractive regeneration background. The shallower term corresponds to the inelastic contribution, and is consistent with the inelastic slope measured in previous experiments [46]. The functional form we use to fit the momentum bin $p_t^2$ spectra fixes the inelastic and diffractive slopes to the values given in Eq. (52), but allows the relative size of the two contributions to vary. The acceptance is expected to introduce an additional exponential falloff between the true and measured $p_t^2$ spectra, and so the final functional form used in the fits was

$$\frac{dN_r(p_t^2)}{dp_t^2} = \alpha e^{-ap_t^2}(e^{-5.156p_t^2} + re^{-222.78p_t^2}), \qquad (53)$$

where $\alpha$, $a$, and $r$ are all parameters of the fits. Data in the range of 1500 (MeV/$c$)$^2 < p_t^2 < 20\,000$ (MeV/$c$)$^2$ were employed by the fit. The values for the diffractive-to-inelastic ratio $r$ obtained in the 10 GeV/$c$ momentum bin fits were statistically consistent with the value of 0.546 in the acceptance-corrected spectrum in Eq. (52).

The background levels are listed in Table VII along with the number of regenerator beam events remaining after subtraction. The total background in the regenerator beam came to 0.152% ± 0.004% for the momentum range used in the Re($\varepsilon'/\varepsilon$) analysis. The error here is statistical only.

The systematic error in the regenerator beam background level was conservatively estimated at 0.012%. If the various exponential slopes — the acceptance, diffractive and inelastic — are allowed to vary within the limits prescribed by the fits to the $p_t^2$ spectra in the range $p_t^2 > 1500$ (MeV/$c$)$^2$, the change in the background level is much smaller than this systematic estimate. Fits where the diffractive-to-inelastic ratio $r$ was fixed at 0.546 also resulted in a change much smaller than this systematic error. Finally, the spectrum in
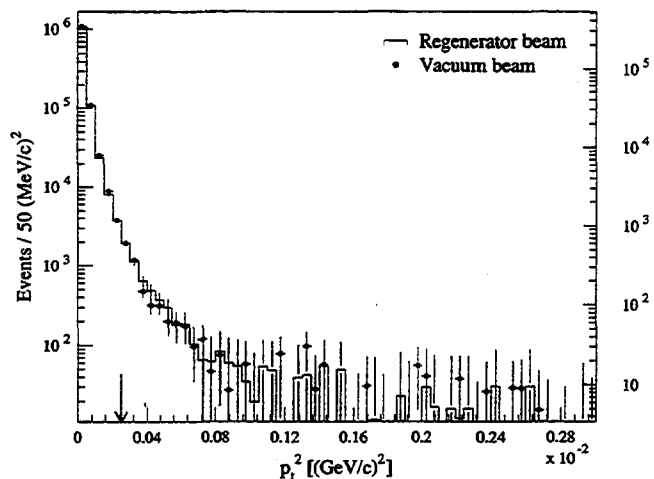


FIG. 38. Overlay of the vacuum and regenerator beam $p_t^2$ spectra after background subtraction. The arrow indicates the position of the cut used in this analysis.

each 10 GeV/$c$ momentum bin was fit to the sum of two independent exponentials. In some momentum bins, the statistical precision at high $p_t^2$ was marginal when performing a two-exponential fit. In spite of this, the backgrounds predicted using these fits differed very little in most of the momentum bins from those listed in Table VII. In the end, we increased the systematic uncertainty to a level comparable to that in the vacuum beam. Combining the statistical and systematic uncertainties, yielded a background level of 0.152 ± 0.013%.

In principle, there are contributions to the regenerator beam background from semileptonic decays as well. We can estimate this from the number of events in the high-side tail of the $K_S$ mass distribution, where the $\pi^+\pi^-\gamma$ tail does not contribute: The result is approximately $2-3 \times 10^{-5}$. This level agrees with our estimate based on the vacuum beam level of the order of $3 \times 10^{-5}$. This corresponds to a bias in Re($\varepsilon'/\varepsilon$) of $0.05 \times 10^{-4}$.

Figure 38 shows the background-subtracted $p_t^2$ spectra for the vacuum and regenerator beams. In spite of the differences in the sources which contribute to the backgrounds in the two beams, the subtracted spectra are in excellent agreement — down to the shape of the radiative tail from $\pi^+\pi^-\gamma$ decays. The agreement between the two spectra over four orders of magnitude helps to give confidence in the background systematic uncertainties estimated above.

Implicit in the above discussion of the background subtraction is the assumption that the background fraction is constant as a function of $z$ in each momentum bin. This is a good assumption in the regenerator beam, since both the background and the coherent signal are dominated by $K_S$ decays. In the vacuum beam, there are differences in, for example, the variation of the $\pi^+\pi^-$ and $K_{e3}$ acceptance as a function of $p$ and $z$, which could lead to small variations in the background as a function of $z$. Fortunately, for all of the measurements we make, our fitting technique requires only that we know the average number of events in the vacuum beam in each momentum bin. However, we still examine the $z$ shape in this beam.

Because of the low background levels, it is difficult to examine this approximation in individual 10 GeV/$c$ momen-
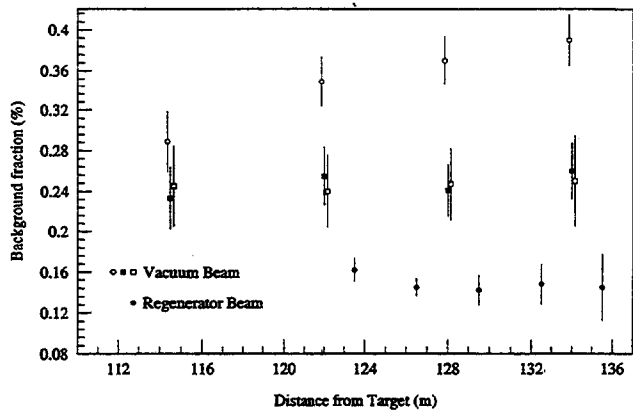
FIG. 39. Measured $\pi^+\pi^-$ background fractions as a function of $z$. The solid circles are the regenerator beam background levels. The other points are the vacuum beam levels, where the circles have been measured in the momentum range 40–80 GeV/$c$, the open squares in the range 80–120 GeV/$c$, and the solid squares in the range 120–160 GeV/$c$. The coarse binning in the vacuum beam data reflects the reduced statistical precision relative to the regenerator beam data.

tum bins. We combine the momentum bins and study in smaller $z$ bins, and the resulting $z$ dependence of the backgrounds is shown in Fig. 39.

For the regenerator beam, all of the momentum bins have been integrated together, and we see no noticeable change in the background level across the fiducial $z$ region. For the vacuum beam, we cannot combine data of all momenta together to examine the background $z$ dependence. At low momentum, the backgrounds are somewhat higher than at high momentum. However, very few low-momentum $\pi^+\pi^-$ decays are accepted upstream of the active mask. Integrating all of the momentum bins together would thus introduce an artificial step at the mask. To avoid this issue, we have examined the background fraction versus $z$ in 40 GeV/$c$ momentum bins, but have doubled the $z$ bin size relative to the regenerator beam study. The background fractions obtained in each 40 GeV/$c$ bin are also plotted in Fig. 39. Above 80 GeV/$c$, the shape is flat within our level of sensitivity. In the 40–80 GeV/$c$ range, the background tends to increase as a function of $z$. If we substitute the background levels obtained as a function of $z$ for this momentum range, the change in the background level is much less than the systematic uncertainty assigned to the background subtraction.

## C. Charge mode conclusion

For the $\mathrm{Re}(\varepsilon'/\varepsilon)$ measurement, we collected a sample of $328\,980 \pm 574 \pm 46$ $\pi^+\pi^-$ decays from the vacuum beam (after background subtraction) and $1\,060\,667 \pm 1030 \pm 138$ decays in the regenerator beam. The first errors are the statistical errors for the signal, and the second errors are the uncertainties from the background subtraction. The backgrounds in both beams were small and relatively simple to understand at the required level of precision. The overall background levels in the vacuum and regenerator beams were 0.340% and 0.152%, respectively. We estimate that these were known with fractional uncertainties of 4% and 8.5%.
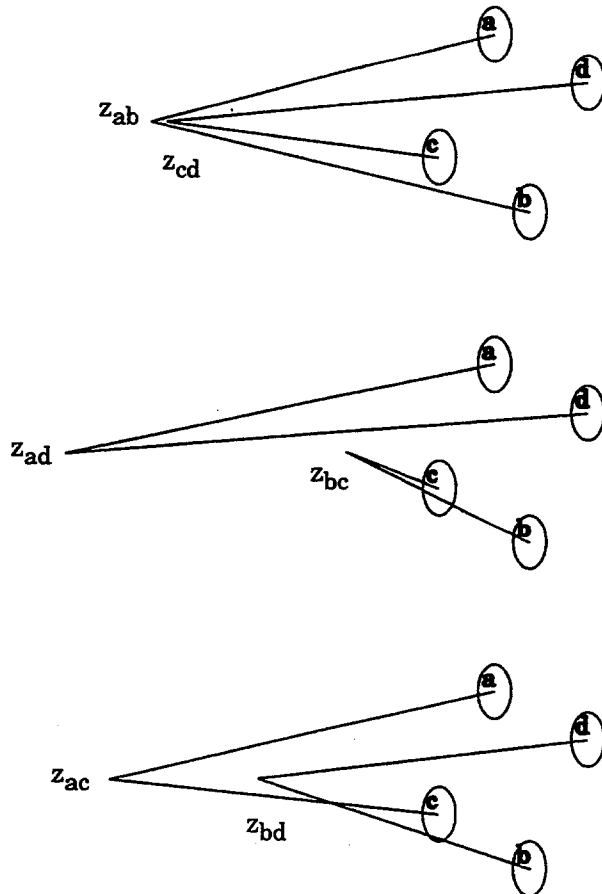


FIG. 40. The $z$ locations obtained for both $\pi^0$ decays in each of the three possible pairings of the four photons from a $K \to \pi^0\pi^0$ decay. The top pairing gives the best $\chi^2$ for $z_{ab} = z_{cd}$.

This completes the discussion of the analysis and background subtraction for the $\pi^+\pi^-$ decay samples. Details of the charged mode acceptance calculation are presented after a discussion of the $2\pi^0$ analysis.

## VI. $2\pi^0$ ANALYSIS

Here we review the reconstruction in $2\pi^0$ decays from four photons and describe the background subtraction in detail.

### A. Neutral mass and $z$ reconstruction

Reconstruction begins with the energies and positions of the four-photons measured in the calorimeter. To reconstruct the position of the kaon decay and the four-photon mass, the photons were paired using the $\pi^0$ mass as a constraint. Figure 40 illustrates the procedure. If we have paired photons $a$ and $b$, then the $z$ position $z_{ab}$ of the $\pi^0$ decay is related to the $\pi^0$ mass by

$$m_{\pi^0}^2 = 2E_a E_b(1 - \cos\theta_{ab}) \simeq E_a E_b \frac{r_{ab}^2}{(z_{\text{glass}} - z_{ab})^2}, \quad (54)$$

where $E_a$ and $E_b$ are the energies of the two photons, $\theta_{ab}$ is the angle between the two photon trajectories, and $r_{ab}$ is the
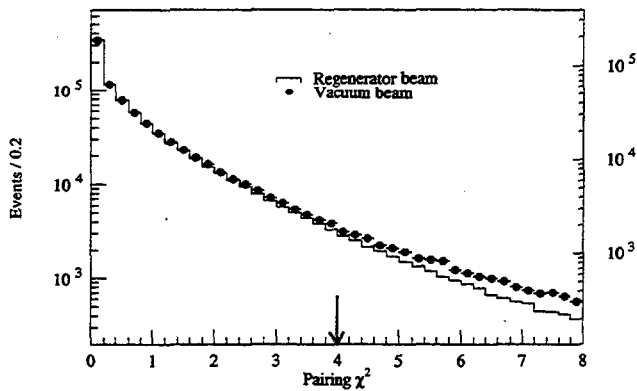
FIG. 41. The $2\pi^0$ pairing $\chi^2$ distribution for the regenerator and vacuum beams after all other cuts. The regenerator beam distribution is shown by the histogram (left axis) and the vacuum beam distribution is shown by the dots (right axis). The shapes of the two distributions differ at higher values of $\chi^2$ because of the larger $3\pi^0$ and beam interaction backgrounds in the vacuum beam. The arrow marks the location of the analysis cut.

separation of the photons in the calorimeter. We formed a second vertex position $z_{cd}$ from the other pair of photons. The $\chi^2$ for the hypothesis that $z_{ab} = z_{cd}$ is

$$\chi^2 = \frac{(z_{ab} - z_{cd})^2}{\sigma_{z_{ab}}^2 + \sigma_{z_{cd}}^2}, \tag{55}$$

taking into account the resolution for each photon's energy and position. The pairing with the best $\chi^2$ was then chosen. The resulting $\chi^2$ distribution is shown for both the regenerator and vacuum beams in Fig. 41 after all other cuts.

The $z$ of the kaon decay was taken as the weighted average of $z_{ab}$ and $z_{cd}$. The $2\pi^0$ mass was reconstructed from the four photon energies and positions using

$$m_{\pi^0\pi^0}^2 = 2\sum_{i>j} E_{\gamma_i}E_{\gamma_j}(1 - \cos\theta_{ij}). \tag{56}$$

The cosine of the angle between the two photon trajectories, $\cos\theta_{ij}$, is calculated assuming that the kaon decayed on the $z$ axis. Finite beam size has negligible effect on the mass value.

The $2\pi^0$ mass distribution for regenerator beam data and Monte Carlo is shown in Fig. 42. Residual nonlinearities in the calibration led to shifts in the reconstructed mass. We have observed such shifts in our data, and they are listed in Table VIII for each of the $2\pi^0$ subsets. Separate shifts are listed for events with and without photon clusters centered in one of the 24 "pipe blocks" surrounding the two beam holes. For comparing line shapes, we shifted the $2\pi^0$ mass
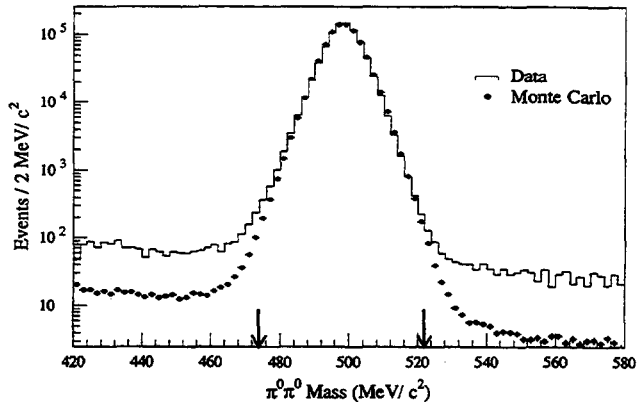
FIG. 42. Reconstructed $2\pi^0$ mass after all other cuts for regenerator beam events. The predicted signal shape from the coherent Monte Carlo simulation is overlaid. The data have been shifted set by set according to the values in Table VIII. Background has not been subtracted.

of data events by the values in the table. The Monte Carlo simulates the mass spectra quite well. The shifts were not applied as part of the standard analysis; we use them (in Sec. X) to estimate systematic effects of residual nonlinearities.

The $2\pi^0$ mass resolution is about 5.5 MeV. Our mass cut (474–522 MeV) was loose enough to be insensitive to residual nonlinearities.

Because of fluctuations in the electromagnetic showers, we occasionally chose the wrong pairing. To keep misreconstruction background to a minimum, we eliminated events if the second-best pairing had a $\chi^2$ within 8 of that of the best pairing, and a mass in the range from 470 to 526 MeV. About 1% of otherwise good kaons fail the mispairing cut.

### B. Neutral ring number

Unlike the situation in the $\pi^+\pi^-$ mode, the precise transverse location of a kaon decay could not be determined in the $2\pi^0$ mode. This means that we could not measure the $p_t^2$ of the kaon to reduce the noncoherent kaon background. Instead we considered the center of energy $(x_{CE}, y_{CE})$ of the photons in the lead glass (the location where the kaon would have passed through the calorimeter had it not decayed) given by

$$x_{CE} = \frac{\sum_{i=1}^4 E_i x_i}{\sum_{i=1}^4 E_i}, \tag{57}$$

$$y_{CE} = \frac{\sum_{i=1}^4 E_i y_i}{\sum_{i=1}^4 E_i}, \tag{58}$$

TABLE VIII. Reconstructed $2\pi^0$ mass shift $\delta m$ in MeV of data relative to Monte Carlo simulation in the five neutral subsets. Two of the subsets have been subdivided into time periods for which separate calibrations have been used. A negative shift implies the $2\pi^0$ mass in the data was lower than that in the Monte Carlo simulation.

| $2\pi^0$ subset sample | N1a | N1b | N2 | N3 | N4 | NCa | NCb |
|---|---|---|---|---|---|---|---|
| $\delta m$ (no pipe block cluster) | −0.76 | −0.83 | −0.71 | −0.74 | −0.63 | −0.43 | −0.44 |
| $\delta m$ ($\geq 1$ pipe block clusters) | −1.07 | −1.40 | −0.90 | −0.94 | −0.82 | −0.65 | −0.60 |

FIG. 45. Effect of the photon veto and fusion cuts on the vacuum beam $2\pi^0$ mass distribution. The solid histogram has all cuts but the photon veto, fusion and soft cluster cuts, the dashed histogram has the photon veto cuts added, and the dotted histogram has all cuts added. The arrows show the location of the mass cuts.

to the misidentification of a $3\pi^0$ decay as a four-cluster event when other photons also escaped or fused. Many of these fused photons were eliminated by comparing the observed cluster shape with the shape expected for an electromagnetic cluster. We used, for example, the ratio of energy in a $3\times3$ cluster to that in a $5\times5$ cluster, and the ratios of energies in the outer rows (or columns) to the cluster energy.

Very soft photons from $3\pi^0$ decays could be lost if the resulting cluster was below the hardware cluster-finding threshold of about 1 GeV. A direct search for soft clusters in the lead glass was infeasible because of remnant "clusters" from showers in other buckets in the long ADC gate. However, the "adders" had a very short gate, and hence were not affected as severely by accidental clusters. By comparing the energy observed in the adders with that in the clusters, events with extra soft clusters above roughly 600 MeV could be eliminated effectively.

The effects on the mass distribution of these cuts is shown in Fig. 45.

To reduce the inelasticly scattered kaon background (and the beam-interaction background), we use the fact that extra charged particles are often produced in such events. By cut-

ting on the number of hits in the drift chambers and the presence of activity in the B and C hodoscopes, we eliminated many inelastic events not vetoed at the trigger level. In rare cases when a photon from a $2\pi^0$ decay converted at the HDRA so that a single conversion electron cluster carried most of the photon energy, the event could have an acceptable pairing $\chi^2$ and mass. Such cases were suppressed by the cut on the number of drift chamber and hodoscope hits.

As we mentioned in Sec. III, the collar anticounter (CA) cleanly defined the inner edge of the acceptance for $2\pi^0$ decays. This counter was in veto at the trigger level, but the veto itself was quite loose. In the off-line analysis, we tightened the cut to five MIP's.

For the final sample, to give less sensitivity to the threshold behavior of the hardware cluster finder, we required the minimum photon energy to be above 1.5 GeV. We also required the photon energy to be below 60 GeV as discussed in some detail in Secs. VII and X.

The effects of the selection criteria on coherent $K \rightarrow \pi^0 \pi^0$ decays within our final fiducial volume are listed in Table X. The loss of coherent events due to the cut on the drift chamber and B and C hodoscope activity is large in the lead sheet subset because of photon conversions in the lead sheet.

The final energy distributions for the vacuum and regenerator beams are shown in Fig. 46. The two distributions are similar, though the vacuum spectrum is enhanced at the low-energy end because of the high acceptance for low-energy decays downstream of the HDRA.

### D. Neutral energy scale

The final step in neutral reconstruction was the adjustment of the energy scale of the photons relative to that of electrons in the calorimeter.

To quantify remaining nonlinearities, we took advantage of the coupling of the decay $z$ and energy scales and examined the reconstructed position of the regenerator edge as a function of the kaon energy. We transformed the shift into a photon energy correction, which we parametrized as a bilinear function of kaon energy with a knee at 80 GeV. Table XI lists the slopes (% per GeV) above and below 80 GeV, the

TABLE X. The fraction of coherent $2\pi^0$ decays in the regenerator beam lost after each analysis cut is applied as determined from the Monte Carlo simulation. In the "Sequential loss" columns, the loss of the first cut is normalized to all $2\pi^0$ events which reconstructed within the fiducial energy and $z$ region used for the $\mathrm{Re}(\varepsilon'/\varepsilon)$ fits. Each cut thereafter is normalized to the number of kaons left after the preceding cut. The precision in this table is approximately 0.03% (only a small portion of the MC simulation was used).

| Analysis cut | Sequential loss (%) | | Loss as final cut (%) | |
|---|---|---|---|---|
| | Pb sheet | No Pb sheet | Pb sheet | No Pb sheet |
| Chamber and hodoscope hits | 21.37 | 1.12 | 15.49 | 0.06 |
| Ring number | 3.28 | 2.26 | 2.74 | 1.81 |
| Photon veto | 0.00 | 0.00 | 0.00 | 0.00 |
| Minimum cluster energy | 1.35 | 1.43 | 0.89 | 1.00 |
| Maximum cluster energy | 8.81 | 8.67 | 7.77 | 7.82 |
| Cluster fusion cuts | 0.90 | 0.80 | 0.90 | 0.79 |
| Best pairing $\chi^2$ | 3.09 | 2.50 | 2.76 | 2.21 |
| Mispairing cuts | 1.74 | 1.61 | 0.99 | 0.93 |
| $2\pi^0$ mass | 0.26 | 0.21 | 0.26 | 0.21 |

FIG. 46. Kaon energy distribution for the entire $2\pi^0$ data set after all other cuts. (a) Vacuum beam. (b) Regenerator beam. The arrow marks the maximum energy used in the analysis.



FIG. 47. Data and Monte Carlo comparison of the reconstructed regenerator edge after energy scale adjustments. (a) The data have the standard adjustments. (b) The data have an additional 0.05% energy scale adjustment.

correction at 80 GeV, and the mean correction for each $2\pi^0$ subset.

A comparison of the $z$ edge in the upstream region of the regenerator beam in the data and Monte Carlo is shown in Fig. 47(a) after the correction. On average the edges match quite well. As shown in Fig. 47(b), introducing a shift in the energy scale of only 0.05% degrades the agreement noticeably: The $\chi^2$ increases by a factor of 3, and the shift is clearly visible. We estimate that the residual uncertainty in the *average* energy scale is under 0.03%. The residual uncertainty in the nonlinearity dominates the systematic error from photon reconstruction.

The coupling of the energy scale and $z$ position has some subtle effects when the lead sheet is in place. Approximately 25% of events upstream of the HDRA in the lead sheet data are lost to conversions and of course this factor must be very

well known and corrected for. But residual uncertainties and nonlinearity in the energy scale can cause decays on one side of the HDRA to reconstruct on the other side and these would be falsely corrected. To minimize the sensitivity to this effect for the lead sheet data, we eliminated decays in the $z$ region from 137 to 139 m from the final sample.

### E. Neutral mode background subtraction

There were four classes of backgrounds that had to be subtracted from the coherent $2\pi^0$ data. The largest source was $2\pi^0$ decays of scattered kaons. There were two sites producing this noncoherent background: the regenerator and the HDRA. Backgrounds from these two were treated inde-

TABLE XI. The parameters for the photon energy scale corrections and the average correction applied in each $2\pi^0$ subset.

| Subset | Slope $(E_K<80\ \mathrm{GeV})$ [% per GeV] | Slope $(E_K>80\ \mathrm{GeV})$ [% per GeV] | 80 GeV correction [%] | Average correction [%] |
|---|---|---|---|---|
| N1a | $-1.7\times10^{-3}$ | $+0.4\times10^{-3}$ | -0.094 | -0.06 |
| N1b | $-4.2\times10^{-3}$ | $,-2.9\times10^{-3}$ | -0.041 | 0.02 |
| N2 | $-4.2\times10^{-3}$ | $-6.5\times10^{-3}$ | +0.065 | 0.11 |
| N3 | $-4.3\times10^{-3}$ | $-2.8\times10^{-3}$ | +0.080 | 0.14 |
| N4 | $-4.5\times10^{-3}$ | $-7.0\times10^{-3}$ | +0.176 | 0.22 |
| NCa | $-5.0\times10^{-3}$ | $-3.3\times10^{-3}$ | +0.324 | 0.39 |
| NCb | $-3.2\times10^{-3}$ | $+0.9\times10^{-3}$ | +0.313 | 0.37 |

CP AND CPT SYMMETRY TESTS FROM THE TWO-PION ...



FIG. 48. The six regions in the vacuum $2\pi^0$ mass versus ring-number distribution used for background subtraction.

pendently. Background from $3\pi^0$ decays which reconstructed with only four clusters in the calorimeter was particularly important downstream of the HDRA. Finally, inelastic interactions of neutrons with material in the detector, particularly in the HDRA, would sometimes produce two $\pi^0$'s that reconstructed under the kaon mass peak.

The background subtraction technique used the reconstructed $2\pi^0$ mass and ring-number variables as seen in Fig. 48. The plot has been divided up into six regions; one contains the signal (region 2), while the others (region 1,3,4,5,6)—used for normalizing Monte Carlo simulations of the different backgrounds—were populated only by background. In essence, the $3\pi^0$ and beam interaction backgrounds were subtracted from the coherent and noncoherent kaons by extrapolating the sidebands under the mass peak. The noncoherent backgrounds were then extrapolated from the large ring number to the coherent peak region. The subtractions were made in individual 1 m by 10 GeV bins after the normalizations of the Monte Carlo background samples were determined globally for the entire $p$ and $z$ fiducial region.

A breakdown of the $z$ distributions (for the no lead sheet data set) of the different backgrounds is shown in Fig. 49. The contribution from each background source is summarized in Table XII.

### 1. $3\pi^0$ and beam interaction backgrounds

The $3\pi^0$ subtraction used a Monte Carlo to interpolate from the mass sidebands under the $2\pi^0$ mass peak. The simulation of the $3\pi^0$ background shape used photon veto resolutions and gains determined from $K_L \rightarrow \pi^+\pi^-\pi^0$ decays (see [38]). To obtain a background sample about 5 times that of the data required simulating $6\times10^9$ $K_L\rightarrow 3\pi^0$ decays. This was accomplished with 3 months of dedicated use of a Fermilab ACP farm of 25 computers each of 25 MIP's.

The $3\pi^0$ background Monte Carlo sample was normalized to the data using regions 1 and 3 outlined in Fig. 48. Several pitfalls had to be avoided in this normalization. First of all, beam interactions with material in the beam produced a flat background in mass. Fortunately the material in the beam is localized at the two locations, the HDRA and the regenerator. The peak from the HDRA in the vacuum beam

is clearly visible in Fig. 49. To avoid miscalculating the $3\pi^0$ normalization factor, only events reconstructing in the $z$ regions 110–122 m, 125–134 m, and 142–152 m were used.

A similar normalization problem arose from the misreconstructed signal $2\pi^0$ events that appear in the sidebands, for example, from residual mispairings. These misreconstructions occur both in data and signal Monte Carlo, and because of the way we define our acceptance, we do not want to subtract these events. The level of these misreconstructions can be seen clearly in the Monte Carlo mass distribution for the regenerator beam shown in Fig. 42, where the misreconstructions constitute a significant fraction of the events in the sidebands (this is not the case in the vacuum beam). To avoid biasing the $3\pi^0$ normalization, the signal Monte Carlo was used to predict the ratio $r$ of coherent events in the mass sidebands to coherent events in the mass peak. If $d_s$ and $d_p$ are the number of data in the signal region and in the mass sidebands, respectively, and $b_s$ and $b_p$ are the similar quantities for the $3\pi^0$ background, it is simple to show that the desired $3\pi^0$ normalization factor $a_{3\pi}$ is

$$a_{3\pi}=\frac{d_s-rd_p}{b_s-rb_p}. \tag{59}$$
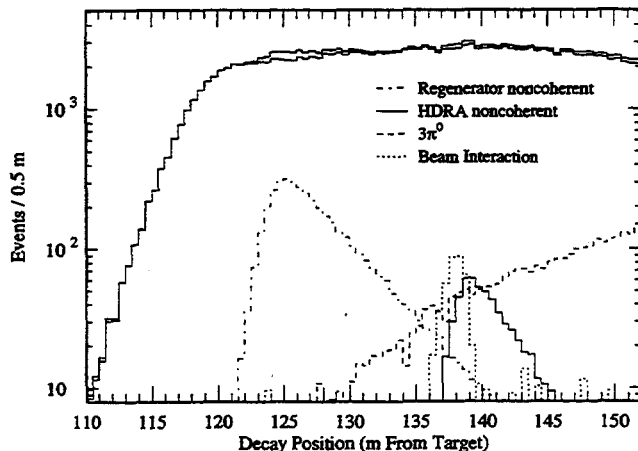


FIG. 49. The $z$ distribution of the different backgrounds to the vacuum beam $2\pi^0$ sample for the data subset with no lead sheet. Also shown are the $2\pi^0$ $z$ distributions before and after background subtraction. All cuts have been applied.

TABLE XII. The $2\pi^0$ background sources and fractions.

| Source | Vacuum beam fraction (%) | Regenerator beam fraction (%) |
|---|---|---|
| $3\pi^0$ background | 1.78±0.03 | 0.049±0.003 |
| Beam interaction | 0.21±0.02 | 0.027±0.004 |
| Regenerator noncoherent scattering | 2.26±0.04 | 2.53±0.04 |
| HDRA diffractive scattering | 0.78±0.02 | 0.027±0.002 |
| HDRA inelastic scattering | 0.13±0.02 | 0.027±0.011 |

If we had neglected this effect, the $3\pi^0$ background in the vacuum beam would have been overestimated by about 3% of itself. In the regenerator beam, however, the $3\pi^0$ background is much smaller, and had we neglected the $2\pi^0$ misreconstructions, we would have overestimated the background by almost 70% of itself. Neglecting this effect would have shifted Re($\varepsilon'/\varepsilon$) by $0.38\times10^{-4}$.

After subtracting the $3\pi^0$ background, the beam-interaction backgrounds were estimated by linearly interpolating the residual background in the mass sidebands into the signal region in each $pz$ bin. In regions of the detector with no material, this prediction should be consistent with zero as can be seen in Fig. 50. The width and position of the large peak are consistent with the $z$ resolution and HDRA location. The relative areas for the two beams are proportional to their expected hadronic content. A small background from beam interactions with the regenerator can also be seen. The only evidence of a problem in the subtraction is in the regenerator beam upstream of the regenerator; this is simply due to a small resolution mismatch between the data and the Monte Carlo, and is negligible at the $10^{-5}$ level in Re($\varepsilon'/\varepsilon$).

The mass distributions for candidate $2\pi^0$ events and the predicted background shapes are shown in Fig. 51. For the vacuum beam, the distributions for the entire $z$ region and for the normalization $z$ region are plotted. The agreement is excellent in both cases; the former checks the combination of $3\pi^0$ and beam-interaction shapes and the latter isolates the $3\pi^0$ shape. The agreement is also very good for the regenerator beam. In all three data distributions, the expected level of coherent misreconstruction in the mass sidebands has been subtracted.

The $3\pi^0$ and beam-interaction backgrounds have been studied in individual 1 m $z$ bins in the vacuum and regenera-

tor beams for both the lead sheet and no lead sheet data samples. The mass distributions for nine of these bins for the vacuum beam sample are shown in Fig. 52 where the lead sheet and no lead sheet data have been combined. Excellent agreement between the predicted and observed background shapes was found in every $z$ bin. The backgrounds were studied in 10-GeV-momentum bins, and we found good agreement there as well.

The statistical error on the $3\pi^0$ background subtraction amounted to 0.023% (0.003%) in the vacuum (regenerator) beam. It includes the errors from the number of events subtracted and the finite statistics of the $3\pi^0$ background Monte Carlo sample and the normalization. The statistical errors on the beam interaction subtraction were 0.02% and 0.004% in the vacuum and regenerator beams, respectively.

Several checks were done to estimate the systematic contribution from the mass background subtraction. We have varied the $3\pi^0$ normalization method, using, for example, different normalizations for events with photons which hit the downstream photon vetoes rather than a single overall normalization constant. We have also studied the fluctuations in the result for different $2\pi^0$ mass cuts. All studies were consistent with a limit on the systematic error for the $3\pi^0$ plus beam interaction background of 0.015%.

### 2. Noncoherent backgrounds

Since we accept $2\pi^0$ decays from downstream of the HDRA, there are two sources of scattered kaons: the regenerator and the HDRA. As Fig. 49 shows, the backgrounds from these two sources are generally well separated in $z$. The shape of the backgrounds in ring number for each source of noncoherent kaons was simulated with our Monte Carlo. The generation and normalization procedures for the two different scattering locations are described below.

*a. Regenerator noncoherent background.* The fundamental ingredient for simulating the noncoherent backgrounds was the $p_t^2$ spectrum for the scattered kaons. For the regenerator, the $p_t^2$ spectrum could be measured with the $\pi^+\pi^-$ sample. As discussed in [36], the spectrum was corrected for acceptance as a function of $p_t^2$ and parametrized as the sum of two exponentials, a steep exponential for the diffractive contribution and a shallower exponential for the inelastic contribution. The resulting spectrum for our regenerator was



FIG. 50. The $z$ distribution of the calculated beam-interaction background.

$$\frac{dN}{dp_t^2} \sim 3431e^{-5.2p_t^2} + 1875e^{-222.8p_t^2},\qquad(60)$$

where $p_t^2$ is measured in (GeV/$c$)$^2$. This parametrization was

CP AND CPT SYMMETRY TESTS FROM THE TWO-PION ...
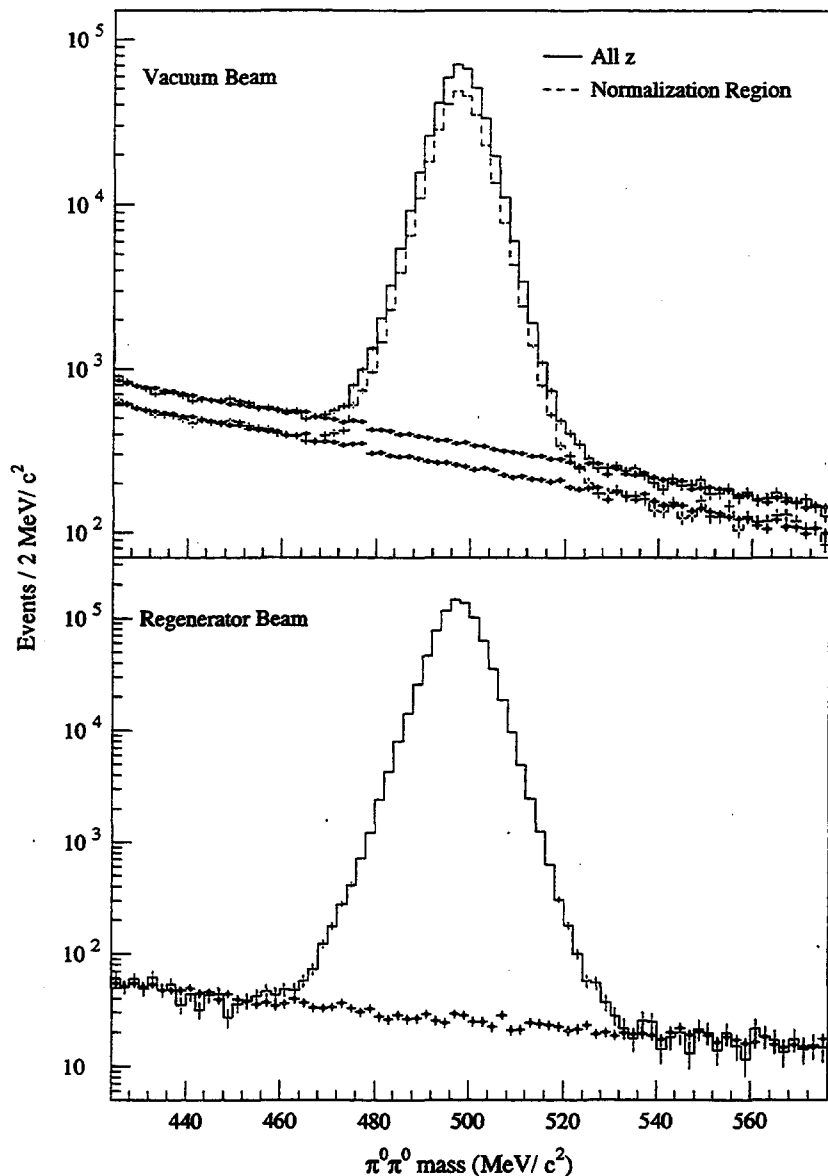


FIG. 51. The $2\pi^0$ mass distribution and the background prediction. Top: the vacuum beam distributions for the fiducial $z$ region (solid histogram) and the $3\pi^0$ background normalization $z$ region (dashed histogram). Bottom: the regenerator beam distribution for the fiducial $z$ region.

fed into the Monte Carlo simulation to generate a sample of $2\pi^0$ decays from scattered kaons.

The charged sample used to determine the $p_t^2$ spectrum was the NC set, where charged and neutral data sets were collected simultaneously. This was also the highest intensity charged subset.

The Monte Carlo background simulation was normalized to the noncoherent tail in the ring number plot (region 5 in Fig. 48). This was done using only events upstream of 134 m to avoid any contamination from the HDRA noncoherent background. The same $z$ region around the regenerator excluded in the $3\pi^0$ normalization was also excluded here, to avoid double subtracting the beam interaction background.

b. HDRA noncoherent background. Since the HDRA formed part of the charged trigger, there was not a sample of $\pi^+\pi^-$ events to give us the kaon $p_t^2$ spectrum for the HDRA. Fortunately, the forward amplitudes have been measured at the precision we need [32,47,48]. The exceptions were oxygen and nitrogen, whose forward amplitudes could be reliably obtained from that of carbon using the measured atomic number dependence $A^{-0.758}$ [49] of the kaon regeneration amplitude. Optical model calculations reproduce the

measured $p_t^2$ spectra reliably [46]. All these amplitudes were fed into the Monte Carlo and scattered kaons were generated in both the vacuum and regenerator beams with the correct amplitude and phase relative to the coherent kaons.

To normalize the diffractive sample, we subtracted from the data the regenerator noncoherent background, the $3\pi^0$ background, and the beam-interaction background in the range from 110 m to 134 m. The HDRA backgrounds do not affect this region, and so we were left with the number of coherent data events in this $z$ range. By comparing this number to the number of coherent Monte Carlo events in this region, we automatically obtained the correct normalization factor for the HDRA diffractive background Monte Carlo.

After the diffractive backgrounds were subtracted, there was a residual background from inelastic interactions of kaons in the HDRA which were not eliminated by the cuts on activity in the drift chambers and the B and C hodoscopes. To simulate the shape of this background, we use a previous measurement [46] of the $p_t^2$ spectrum of inelasticly scattered kaons. The spectrum was found to have approximately a $e^{-6p_t^2}$ dependence, independent of kaon momentum. We
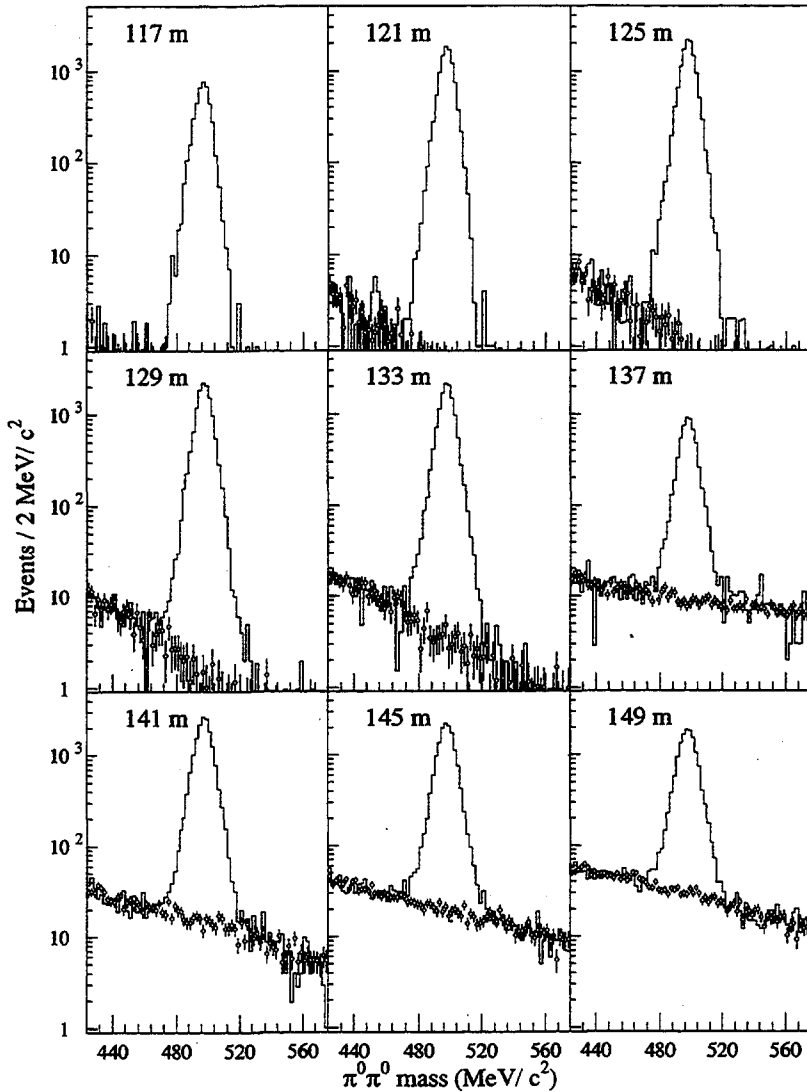
FIG. 52. Observed $2\pi^0$ mass distribution and the $3\pi^0$ and beam interaction backgrounds in nine individual 1 m $z$ bins. The $3\pi^0$ Monte Carlo normalization is common to al bins. Each plot is labeled with the upstream edge of the $z$ bin. In the 137 m bin, we only used the data from the $2\pi^0$ subset with no lead sheet.

generated a Monte Carlo sample with kaons scattered according to this spectrum at the location of the HDRA. The final result was insensitive to the exact value of the slope used. The generated sample was then normalized to the residual background in region 5 of Fig. 48 after all of the previously discussed backgrounds were subtracted. This was done in the $z$ range from 142 m to 150 m, though the final result was insensitive to the $z$ range used.

To double check the inelastic shape, a sample of inelastic events was isolated by making a tighter cut on activity in the T hodoscope. The predicted inelastic background as a function of ring number and $z$ agreed very well with the observed distribution in this sample.

*c. Noncoherent background summary and errors.* The overall agreement between data and Monte Carlo in the ring-number distribution is illustrated in Fig. 53. The predicted ring number distribution agrees very well with the data, both in the upstream region ($z < 134$ m), where only the regenerator noncoherent background contributes, and overall, where both the HDRA and regenerator backgrounds contribute. The same is true for the regenerator beam distributions, though here the contribution from kaons scattering in the HDRA is very small. The data shown here have had the $3\pi^0$ and beam-interaction backgrounds subtracted in each ring-number bin. The overall agreement is excellent.

The predicted ring-number shapes have also been studied in 1 m bins for both the vacuum and regenerator beams in the lead sheet and no lead sheet samples. Figure 54 shows the data and Monte Carlo distributions for the same nine bins in Fig. 52. The predicted and observed ring-number shapes and levels agreed well in all of the $z$ bins. The data in the 1 m $z$ bin plots shown have again had the $3\pi^0$ and beam-interaction backgrounds subtracted to allow a direct comparison of the noncoherent backgrounds. Note in particular the $z$ bin for 121–122 m. The only significant background here is the regenerator noncoherent background. The regenerator itself is located 2 m downstream of the end of this bin, and so this background is entirely from noncoherent decays which have "smeared" upstream in the reconstruction. There is excellent agreement between the predicted and observed background levels in the ring number normalization region. We have also studied these backgrounds in 10 GeV momentum bins, with similar results.

The statistical error on the number of noncoherent background events from scattering in the regenerator is 0.023% (0.018%) in the vacuum (regenerator) beam. As mentioned before, the statistical errors include contributions from the number of background events subtracted from the data, the statistical error on the Monte Carlo sample, and the normalization error. The systematic uncertainty was limited by
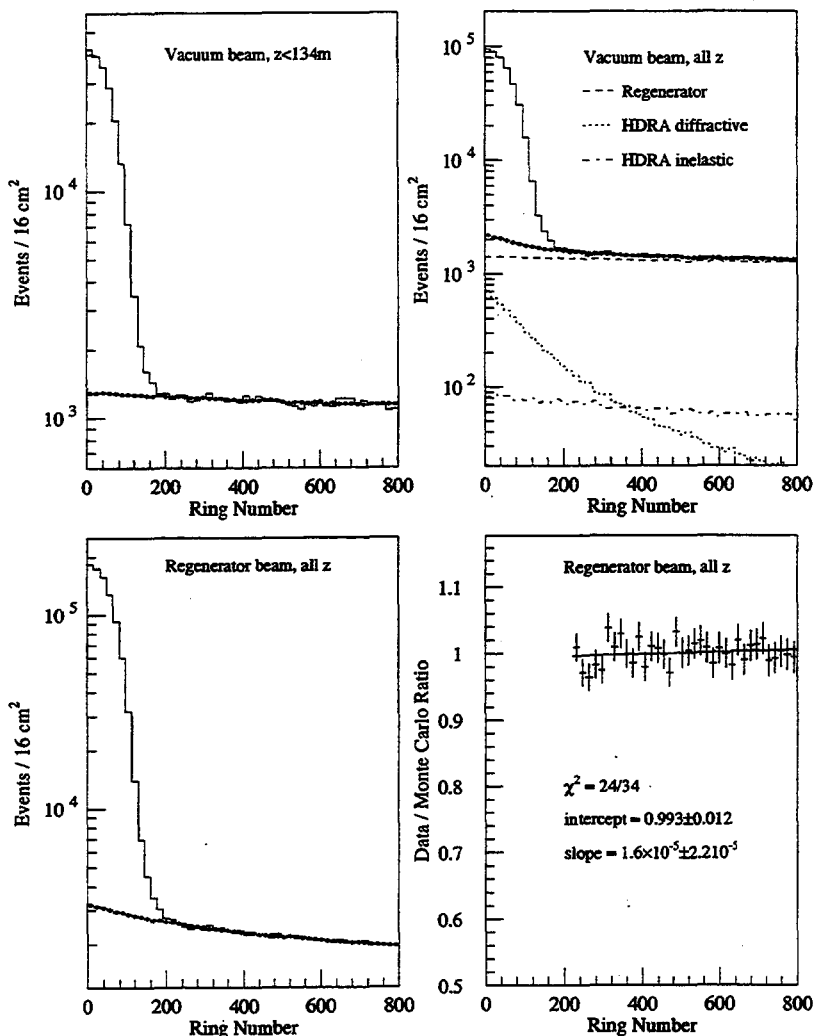
FIG. 53. Observed ring-number distributions in the $2\pi^0$ samples and the predicted backgrounds. In the first three plots, the solid histogram is data with the $3\pi^0$ and beam-interaction backgrounds subtracted, and the dots are the total predicted noncoherent background. The last plot is the ratio of the regenerator beam data to Monte Carlo simulation in the normalization range of the ring-number variable. The slope of the vacuum beam ratio is also consistent with zero.

studying the shape of the ring number distribution for the two beams and extrapolating the uncertainty to ring 0. The studies were statistically limited, and from the individual $z$ bins and the overall shape, we have limited the uncertainty on the noncoherent background level from scattering in the regenerator to 1.2% of itself. The background in the vacuum and regenerator beam from the regenerator are correlated — if the regenerator beam background fraction were smaller, the vacuum beam fraction would also be smaller. Furthermore, this background largely cancels in the vacuum-to-regenerator beam ratio. However, we have chosen to ignore this correlation when assigning a systematic error, and have taken the full 1.2% error for each of the beams.

The technique used to subtract the diffractive background from the HDRA relies upon knowledge of the regeneration amplitude and $p_t^2$ distribution for the materials in the HDRA. The uncertainty in the contributions from lead and carbon dominates, and they contribute at the level of 1.3%. Where necessary, we have corrected older amplitude measurements using the world average value for $\eta_{+-}$, and its uncertainty has been included in the background uncertainty given above. The statistical uncertainties were 0.014% (0.002%) in the vacuum (regenerator) beam.

The inelastic HDRA contribution was the most difficult to limit systematically because of its low level. The vacuum beam ring number shape agreed well, both within the total

sample and the isolated inelastic sample mentioned previously. The inelastic contribution was compared to the Monte Carlo inelastic sample by subtracting all of the other background components from the data. From studies of the shape of the tail of the ring number distribution for the inelastic samples, both overall and in 1 m bins, we have limited the uncertainty to 18% of itself.

In the regenerator beam studies of the isolated inelastic samples, we did observe a discrepancy in the overall ring number distribution at the level of two standard deviations. Since this background is so small, it was difficult to make meaningful studies in smaller $z$ bins. The exact shapes of the inelastic contributions from the HDRA are tricky to mimic, as there are comparable contributions expected from kaons which have scattered in the vacuum beam and crossed into the regenerator beam, and from kaons which have scattered within the regenerator beam itself. We have thus assigned a fairly conservative systematic uncertainty of 40% (of itself) to this background source. The statistical uncertainties on the background from inelastic scatters in the HDRA in the vacuum and regenerator beams were 0.006% and 0.002%, respectively.

### F. Neutral mode conclusion

This completes the discussion of the $2\pi^0$ reconstruction and background subtraction. Table XII shows the level of
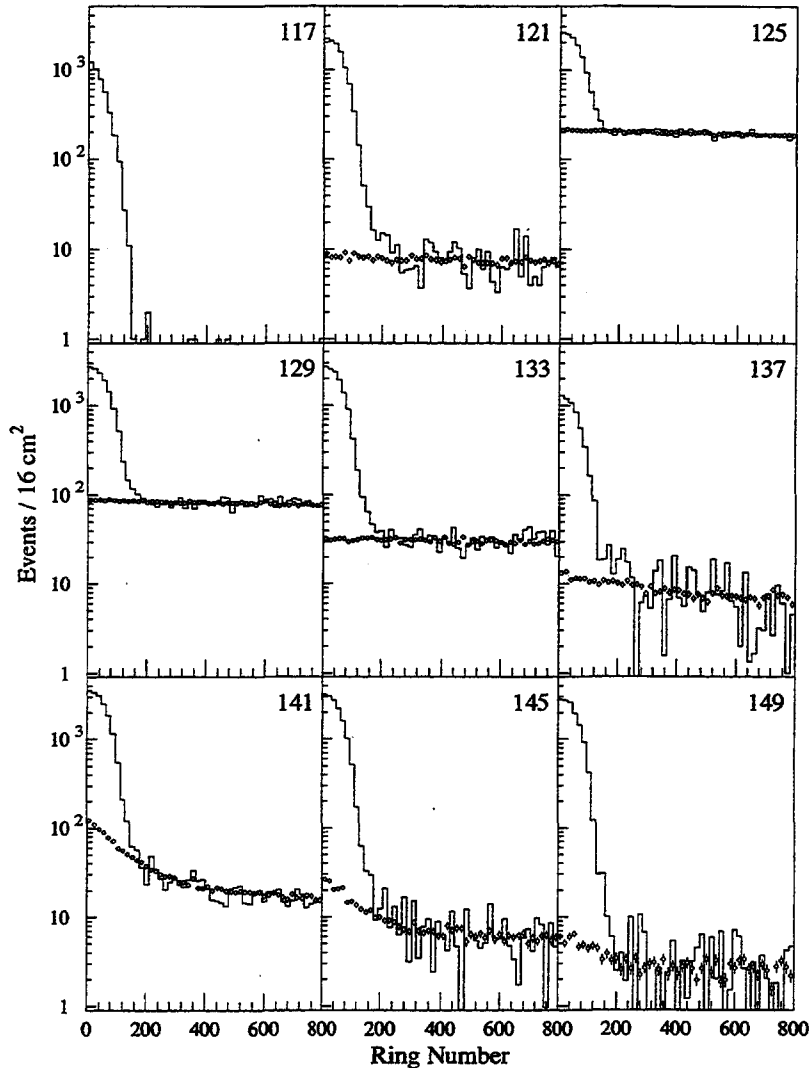
FIG. 54. Observed vacuum beam $2\pi^0$ ring-number distribution and predicted background shape in nine individual 1 m $z$ bins. Each plot is labeled with the upstream edge of the $z$ bin. In the 137 meter bin, we only used the data from the $2\pi^0$ subset with no lead sheet.

backgrounds with all errors combined. The total number of events in each of the 10 GeV momentum bins, along with the total background fraction in each bin, is summarized in Table XIII.

The final ingredient needed before we can extract the desired physics from the data samples is the acceptance for both the $\pi^+\pi^-$ and $2\pi^0$ decay modes. We now turn to a more detailed discussion of the Monte Carlo simulation and the acceptance determination.

## VII. MONTE CARLO SIMULATION

### A. Introduction

The difference in the $z$ distributions in the vacuum and regenerator beams drives the need for an understanding of the acceptance of the detector as a function of $z$. We can define two categories of acceptances: an "outer" acceptance, which is defined by the limiting apertures of the experiment, and an "inner" acceptance, which is determined by thresholds and the granularity of calorimeter and drift chambers. We devote this section to the description of the modeling of both the outer and inner acceptances.

To determine potential systematic biases in the acceptance, we use the $K_{e3}$ and $3\pi^0$ modes. These modes offer much better sensitivity to biases, both because of higher sta-

tistics and because a higher fraction of these decays probes the outer and inner acceptances.

In the Monte Carlo package the treatment of the kaon beam, propagation of the decay product, and detector response were common to all of the simulations. The only differences were the kaon decay modes and their intrinsic dynamics. Furthermore, to prevent biases in the $\pi\pi$ acceptance determinations, the tuning of the simulation hardly used the $\pi\pi$ data samples. Only the kaon production spectrum was tuned using the observed $\pi\pi$ distributions, since we bin the data in small momentum bins, which introduces negligible bias.

Important inputs to the simulation package were based on survey measurements, EGS [43] electromagnetic shower simulations, and previous experimental measurements. The high-statistics decay modes and data from muon runs were used for final tuning, including counter and drift chamber wire efficiencies ("inner" acceptance issues). For the "outer" acceptances, the locations of the limiting apertures were tracked with the electrons from $K_{e3}$ decays after the final chamber alignment (see Sec. IV A 2).

This section describes the three major components of the Monte Carlo simulation: kaon beam simulation, kaon decays and propagation of daughter particles, and detector response. A representative comparison of the simulation to the $\pi\pi$

TABLE XIII. The number of coherent $2\pi^0$ decays after background subtraction and the total background fraction in each 10 GeV bin for the lead sheet and no lead sheet data samples. The background levels are given in percent.

| Momentum range (GeV/c) | Lead | | | | No lead | | | |
|---|---|---|---|---|---|---|---|---|
| | Vacuum | | Regenerator | | Vacuum | | Regenerator | |
| | Data | Bkg (%) | Data | Bkg (%) | Data | Bkg (%) | Data | Bkg (%) |
| 40–50 | 45812 | 4.8 | 45667 | 1.6 | 30096 | 3.5 | 34700 | 1.4 |
| 50–60 | 51102 | 5.0 | 83563 | 1.7 | 34659 | 3.8 | 62948 | 1.6 |
| 60–70 | 46171 | 5.5 | 93830 | 2.2 | 31852 | 4.3 | 70311 | 2.0 |
| 70–80 | 36369 | 6.2 | 83444 | 2.7 | 25862 | 5.0 | 61841 | 2.6 |
| 80–90 | 26301 | 6.3 | 63474 | 3.2 | 18617 | 5.5 | 47401 | 3.1 |
| 90–100 | 16965 | 6.6 | 41124 | 3.9 | 12106 | 5.9 | 30694 | 3.7 |
| 100–110 | 9869 | 6.8 | 24102 | 4.5 | 7043 | 6.1 | 17605 | 4.4 |
| 110–120 | 5267 | 6.6 | 12821 | 5.2 | 3855 | 6.0 | 9360 | 5.2 |
| 120–130 | 2682 | 5.9 | 6188 | 5.8 | 1898 | 6.1 | 4383 | 6.0 |
| 130–140 | 1348 | 4.7 | 2626 | 6.4 | 941 | 4.8 | 1766 | 7.1 |
| 140–150 | 618 | 3.2 | 955 | 7.2 | 424 | 2.9 | 675 | 7.4 |
| 150–160 | 277 | 1.6 | 308 | 7.8 | 195 | 0.6 | 215 | 7.8 |
| Total | 242779 | 5.6 | 458101 | 2.7 | 167547 | 4.5 | 341897 | 2.6 |

data is shown at each stage. Finally, after all the various elements of the simulation have been discussed, the $z$ distributions of the different decay modes can be examined. First presented are the high-statistics modes, from which the limit on the systematic bias is obtained. Then, for completeness, the $\pi^+\pi^-$ and $2\pi^0$ $z$ distributions are presented.

For many of the figures, reconstructed distributions in the $\pi^+\pi^-$ and $2\pi^0$ data are presented with the Monte Carlo simulation overlaid. In these cases, the full Monte Carlo statistics (scaled to the size of the data samples) is shown. The $\pi^+\pi^-$ simulation sample size was 25 times the $\pi^+\pi^-$ data sample size and the $2\pi^0$ simulation size with (without) the lead sheet was 22 (26) times the data size.

### B. Kaon beam

We are not strongly sensitive to the details of the kaon beam for the measurement of Re($\varepsilon'/\varepsilon$) and the other parameters, but having the correct beam shape and kaon momentum spectrum helps in several ways in studies of the detector acceptance. With the correct momentum spectrum, we can compare data to the simulation integrated over a broad momentum region, increasing the sensitivity to subtle biases. Furthermore, the acceptance variation near the edges of some of the limiting apertures depends on the beam shape; having it correct simplifies the study of these edges.

Finally, though our detector was located far from the target, effects of $K^0$-$\bar{K}^0$ interference were clearly visible in the data sample, particularly at high momentum in the vacuum beam. While not a serious bias, it was very useful to directly compare the simulated and measured decay distributions, which required the incorporation of the interference effects.

The full quantum-mechanical description of the $K^0$-$\bar{K}^0$ system was used for production and propagation of the kaon beam; this was easily generalized from $\pi\pi$ to other kaon decays. Required inputs were the production spectra of $K^0$

and $\bar{K}^0$, the transport function for the propagation of the kaons through the vacuum and various absorbers in the beam, and the relative positions and orientations of the collimators which determine the final shapes of the two beams.

#### 1. Production spectrum

The basis for the energy and angular distributions of the produced kaons was the Malensek [50] parametrization of the $K^+$ and $K^-$ production spectrum for protons incident on a beryllium target.

For production of a particle with momentum $p$ into a solid angle $d\Omega$ centered at a polar angle $\theta$ and an azimuthal angle $\phi$, Malensek presents a general form for the spectrum of

$$\frac{d^2N}{dp\,d\Omega} = \frac{B}{400} x \frac{(1-x)^A(1+5e^{-Dx})}{(1+p_t^2/M^2)^4}. \quad (61)$$

In this expression, $x$ is the ratio of the produced particle's momentum $p$ to the beam energy $E_B$, $x=p/E_B$, and $p_t$ is the transverse momentum of the produced particle relative to the incident beam direction, $p_t=p\sin\theta$. Parameters $B$, $A$, $D$, and $M^2$ were then determined using experimental data at 400 GeV/c. For charged kaons, the best parametrizations had these values:

| | $B$ | $A$ | $D$ | $M^2$ |
|---|---|---|---|---|
| $K^+$ | 14.15 | 2.924 | 19.89 | 1.164 |
| $K^-$ | 12.33 | 6.107 | 17.78 | 1.098 |

We need to know how the dilution factor $d_K$, defined by

$$d_K \equiv \frac{K^0 - \bar{K}^0}{K^0 + \bar{K}^0}, \quad (62)$$

is related to the relative numbers of $K^+$ and $K^-$ produced. The dilution factor extracted by the CERN NA31 experiment
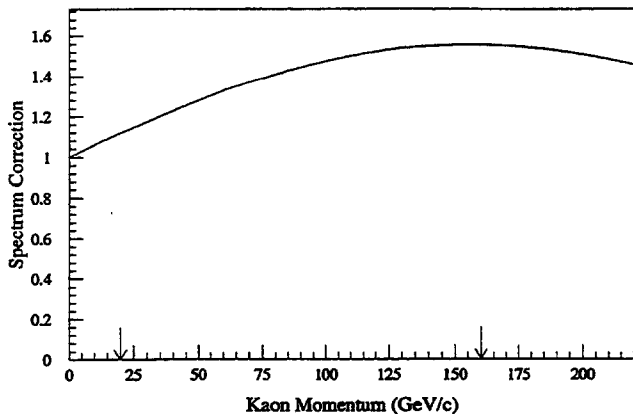
FIG. 55. Momentum-dependent correction factor needed to bring the Malensek energy spectrum into agreement with the vacuum beam spectrum observed in our $\pi^+\pi^-$ NC subset. The arrows denote the limits of the kaon momentum range used in our analyses.

as part of their dedicated $\Delta\phi$ measurement [27] indicated that a good representation is given by

$$d_K = \frac{K^+ - K^-}{K^+ + 3K^-}.\qquad(63)$$

A simple argument [51] shows that this form follows from the valence quark content of the beam particles.

Because there were uncertainties of order 10% in the data at only one beam energy used to derive this spectrum, we did not expect the Malensek spectrum to be perfect. We therefore tuned the spectrum using 80% of the vacuum beam $\pi^+\pi^-$ decays in the NC subset (about 20% of the total sample of $\pi^+\pi^-$ decays) over 20–500 GeV/c reconstructed kaon momentum range. The correction factor (which is applied to the overall rate in the beam but not to the dilution factor or to the $p_t$ spectrum) is plotted in Fig. 55. This changes by 20% from 40 to 150 GeV/c, while the spectrum itself drops by a factor of 4.5 over the same range.

The final energy spectrum in each data sets was obtained by adjusting the primary beam targeting angles. The nominal angles were 4.8 mrad in $x$ and 0 mrad in $y$. If the $y$-targeting angle were nonzero, there would be a small shift in the average kaon energy of the top beam relative to the bottom beam with a dependence of roughly

$$E_t - E_b \approx 0.5\theta_y \ \text{[mrad]},\qquad(64)$$

where $E_t$ ($E_b$) is the mean kaon energy in the top (bottom) beam in GeV, and $\theta_y$ is the $y$-targeting angle. (When $\theta_y > 0$, the proton beam falls relative to the kaon beam.) A deviation of the $x$-targeting angle from the nominal angle shifts the average kaon energy of both beams together. The targeting angles that we input to the simulation for each data subset, based on the observed kaon energies in the beams, are plotted in Fig. 56. The $x$-targeting angle is stable and independent of intensity.

The $y$-targeting angle was found to be correlated with the intensity of the proton beam which was adjusted by a vertical beam tune far upstream of the target. The beam tune for the high-intensity sets appears to have been quite similar. At
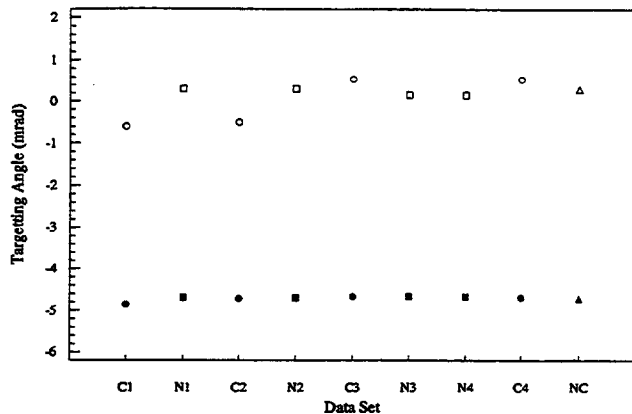


FIG. 56. Inferred $x$- and $y$-targeting angles for the nine data collection periods. The $x$- ($y$-) targeting angles are plotted as solid (open) circles. For both $x$ and $y$ angles, the highest-intensity points are the squares, the medium-intensity points are the triangles, and the lowest-intensity points are the circles.

lower intensity, a much different beam tune appears to have been used in the early data sets (C1 and C2). The last data set (NC), with an intensity between the low and high intensity, has an intermediate $y$-targeting angle.

The final energy spectra produced in the Monte Carlo simulation are compared to the observed $\pi^+\pi^-$ and $2\pi^0$ spectra in Figs. 57 and 58. The spectra agree quite well in both sets, though there is perhaps a residual bowing of a few percent in the charged mode.
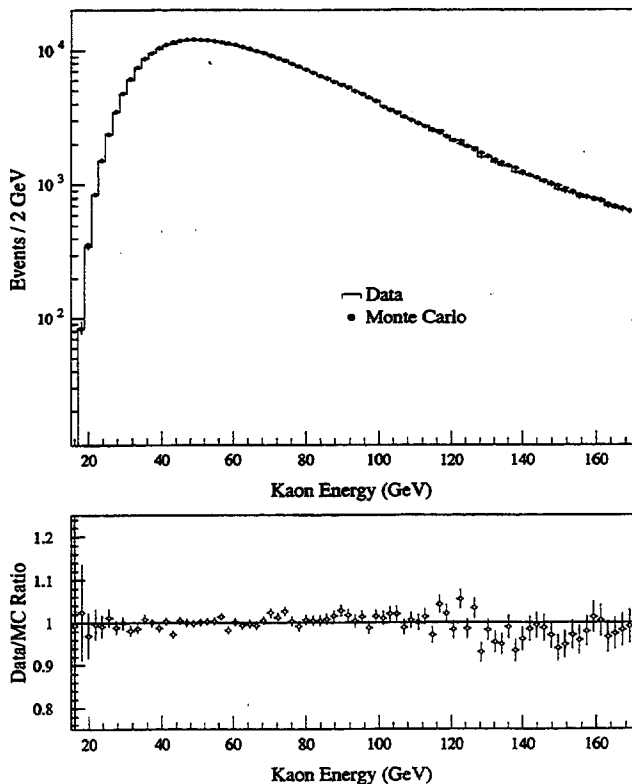


FIG. 57. Kaon energy spectrum for the $\pi^+\pi^-$ decay sample in data and Monte Carlo simulation. Top: the data spectrum is plotted as a histogram and the simulation as dots. Bottom: the ratio of data events to Monte Carlo simulation.
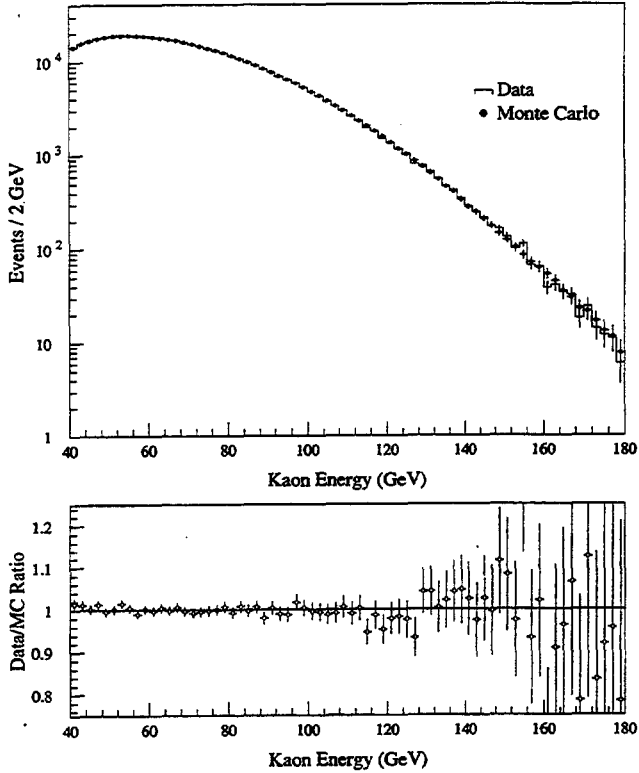
FIG. 58. Kaon energy spectrum for the $2\pi^0$ decay sample in data and Monte Carlo simulation. Top: the data spectrum is plotted as a histogram and the simulation as dots. The predicted background contributions have been added to the coherent $2\pi^0$ Monte Carlo simulation. Bottom: the ratio of data events to the Monte Carlo simulation.

## 2. Kaon transport

The $K^0$ and $\bar{K}^0$ components are written as an incoherent sum of initial $K_S$ and $K_L$ amplitudes. Given these, propagation through the vacuum is trivial:

$$\begin{pmatrix} a_S \\ a_L \end{pmatrix} \rightarrow e^{-imL} \begin{pmatrix} a_S e^{\tau(i\Delta m - \Gamma_S/2)} \\ a_L e^{-\tau\Gamma_L/2} \end{pmatrix}, \qquad (65)$$

where $a_S$ and $a_L$ are the initial $K_S$ and $K_L$ amplitudes, and the proper time $\tau$ is related to the propagation distance $\Delta z$ and the momentum $p$ by

$$\Delta z = \frac{p[\text{GeV}/c]}{m_K[\text{GeV}/c^2]} c\tau. \qquad (66)$$

The kaon passes through the remainder of the target and the common absorber. If the kaon is in the regenerator beam,

it also passes through the shadow absorber and then through the regenerator. In addition to attenuation, scattering and regeneration affect the relative $K_S$ and $K_L$ content, the final energy spectrum, and the angular spread of the beam.

Coherent regeneration of the kaons is handled exactly. The forward regeneration and overall attenuation can be incorporated into a simple matrix form:

$$\begin{pmatrix} a_S \\ a_L \end{pmatrix} \rightarrow e^{-x/2} \begin{pmatrix} T_{SS} & T_{SL} \\ T_{LS} & T_{LL} \end{pmatrix} \begin{pmatrix} a_S \\ a_L \end{pmatrix}, \qquad (67)$$

where $x$ is the total number of interaction lengths through which the kaon passes. The elements of the transformation matrix $T$ depend on the forward scattering amplitudes $f(0)$ and $\bar{f}(0)$ of the $K^0$ and $\bar{K}^0$ for the material in the kaon beam. The form for the elements of $T$ can be found in Ref. [1].

Scattered kaons essentially modify the spectrum $dN/dp\,dp_t^2$ entering the decay volume; scattering also tends to blur out the edges of the beam.

As kaons passed through the absorber materials—the lead and beryllium portions in the common absorber and the beryllium in the shadow absorber — we allowed them to have a single elastic scatter in the Monte Carlo simulation. The scatters were distributed with a $p_t^2$ spectrum of $\exp(-\alpha p_t^2)$. The slope $\alpha$ and scattering probability were taken from the $K^+$ and $K^-$ elastic scattering cross sections measured by Schiz et al. [52]. The values used are listed in Table XIV.

The scattering and coherent regeneration were included before the final spectrum tuning mentioned above was made.

## 3. Beam collimation and targeting

The last ingredient for the simulation of the beam was the fine-tuning of the collimator positions and the inclusion of the finite size of the proton beam at the target. In general, the effect of a particular collimator face could be identified in a unique region of the beam profile, allowing both the average collimator position and the angle of the collimator slab relative to the $z$ axis to be extracted.

The position of the beam spot was measured several times during each 20 s beam spill. The intensity profile of the beam itself was roughly a Gaussian with a width of 0.8 mm in $x$ and $y$. This beam jitter would blur the edges of the beam profile, just as the elastic scattering did. The beam spot movement was incorporated into the Monte Carlo simulation through these measurements.

In the charged mode, the beam shapes were studied using the projected kaon position at the regenerator. For the neutral mode, the beams shapes for a given $2\pi^0$ subset were initially

TABLE XIV. Probability and exponential slope for single elastic scattering of kaons in each of the absorber elements in the kaon beam.

| Absorber component | Single-scattering probability (%) | Exponential slope ($[\text{GeV}/c^2]^2$) |
|---|---|---|
| Beryllium, common absorber | 8.6 | 65 |
| Lead, common absorber | 17.8 | 420 |
| Beryllium, movable absorber | 7.8 | 65 |
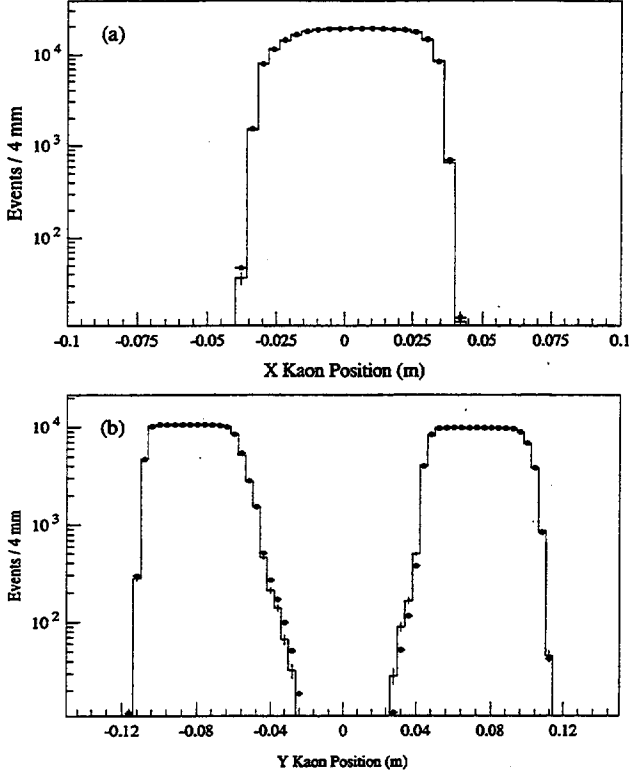
FIG. 59. Projection of the kaon trajectory to the regenerator position for all $\pi^+\pi^-$ decays collected from the vacuum beam. The $x$ projection is shown in (a), and the $y$ projection in (b). The Monte Carlo simulation (dots) has been overlaid on top of the data distribution (histogram).



FIG. 60. Center-of-energy distribution measured in the lead glass calorimeter for all $3\pi^0$ decays collected from the vacuum beam. The $x$ projection is shown in (a), and the $y$ position in (b). The Monte Carlo simulation (dots) has been overlaid on top of the data distribution (histogram).

based on the collimator positions measured in the bracketing $\pi^+\pi^-$ subsets. The final tuning was then done based on the center-of-energy distributions measured in the lead glass calorimeter for the $2\pi^0$ and $3\pi^0$ decays. The final shapes are shown for the charged mode in Fig. 59 and for the neutral beam in Fig. 60.

## C. Decays and interactions

### 1. Particle decays

The dynamics for all decay modes were fully simulated. In the $K_{e3}$ decays, the time-dependent charge asymmetry is used to decide whether the final state is $\pi^+ e^- \bar{\nu}_e$ or $\pi^- e^+ \nu_e$:

$$\delta\tau = \frac{R(\pi^- e^+ \nu) - R(\pi^+ e^- \bar{\nu})}{R(\pi^- e^+ \nu) + R(\pi^+ e^- \bar{\nu})}, \tag{68}$$

with the decay probabilities $R$ given in terms of the $K_S$ and $K_L$ amplitudes $a_S(\tau)$ and $a_L(\tau)$ by

$$R(\pi^- e^+ \nu) = \frac{|1+\varepsilon|^2}{2(1+|\varepsilon|^2)} |a_S(\tau) + a_L(\tau)|^2,$$

$$R(\pi^+ e^- \bar{\nu}) = \frac{|1-\varepsilon|^2}{2(1+|\varepsilon|^2)} |a_S(\tau) - a_L(\tau)|^2. \tag{69}$$

The form factor governing this decay is included. Similarly, the decay probabilities for the $\pi\pi$ and $\pi\pi\pi$ decays also included the $CP$-violating amplitudes,

$$R(\pi\pi) = |a_S(\tau) + \eta a_L(\tau)|^2,$$

$$R(\pi\pi\pi) = |\eta a_S(\tau) - a_L(\tau)|^2. \tag{70}$$

For $\pi^+\pi^-$ and $K_{e3}$ decays, the $\pi^+\pi^-\gamma$ and $K_{e3\gamma}$ radiative decay modes were included at the proper level, with 5 MeV and 1 MeV center-of-mass photon energy cutoffs, respectively.

The decays of daughter particles are also implemented. Of particular importance were decays in flight of the charged pions from $\pi^+\pi^-$ decays. Most muons produced in pion decay hit the muon veto bank or introduced a substantial kink in the flight path, causing the parent $\pi^+\pi^-$ decay to be rejected. About 5% of the pions decay before the lead glass calorimeter with momentum above the 7 GeV/$c$ cut (Sec. V.A.2.). But because of the difference in the $z$ distributions, there is only about 0.2% greater loss in regenerator beam than in vacuum beam. Including the decay in flight in the simulation correctly compensates this asymmetry.

### 2. Interactions with the detector material

Interactions of daughter particles with material in the detector were also simulated, including multiple scattering, bremsstrahlung, and conversions, the latter producing "grandaughter" particles. The characteristics of the material

CP AND CPT SYMMETRY TESTS FROM THE TWO-PION ...

TABLE XV. Scattering and photon conversion locations and the thickness of material in radiation lengths.

| Detector element | Location from target (m) | Thickness (radiation lengths) |
|---|---|---|
| V hodoscope | 137.792 | $3.23 \times 10^{-3}$ |
| Pb sheet[a] | 137.804 | $9.36 \times 10^{-2}$ |
| T hodoscope | 137.815 | $3.43 \times 10^{-3}$ |
| Vacuum window | 158.965 | $2.50 \times 10^{-3}$ |
| Drift chamber 1 | 159.292 | $3.42 \times 10^{-3}$ |
| Drift chamber 2 | 165.867 | $3.86 \times 10^{-3}$ |
| Drift chamber 3 | 171.857 | $3.63 \times 10^{-3}$ |
| Drift chamber 4 | 178.004 | $2.10 \times 10^{-3}$ |
| Chamber field wires[b] | — | $5.70 \times 10^{-3}$ |
| Chamber sense wires[c] | — | $6.43 \times 10^{-3}$ |
| C hodoscope | 179.502 | $4.0 \times 10^{-2}$ |
| B hodoscope | 179.520 | $4.0 \times 10^{-2}$ |

[a]Used only in $2\pi^0$ lead sheet subsets. Average radiation length is listed.
[b]This contribution is identical in all four chambers. Only the 9.9% of the tracks which hit these wires (per chamber) see this contribution.
[c]This contribution is identical in all four chambers. Only the 0.7% of the tracks which hit these wires (per chamber) see this contribution.

in the detector are given in Table XV. It was sufficient to group helium and helium bag windows with the closest drift chamber, and to collapse each chamber to a single plane.

Photon conversions at the HDRA were particularly important, since the HDRA is near the center of the $2\pi^0$ decay volume, and there are different fractions of $K \rightarrow \pi^0\pi^0$ decays in the vacuum and regenerator beams which occur upstream of the lead sheet. A straightforward calculation shows that if $c$ is the *average* probability for at least one of the four photons to convert at the HDRA, $f_v$ ($f_r$) is the fraction of $2\pi^0$ decays upstream of the HDRA in the vacuum (regenerator) beam, and there is a bias of $\Delta$ in the conversion probability in the Monte Carlo ($c_{\mathrm{MC}} = c[1+\Delta]$); then, the bias introduced into the vacuum to regenerator beam ratio $R_{00}$ is

$$ R_{00} \rightarrow R_{00} \left\{ 1 + (f_r - f_v)\frac{c}{1-c}\Delta \right\}. \tag{71} $$

Here $f_r$ and $f_v$ are 92% and 66%, respectively. About 23.7% of $K \rightarrow \pi^0\pi^0$ decays upstream of the Pb sheet have at least one conversion. Only 2% of the decays have conversion from the rest of the material. The lead sheet was present for 65% of the data taking, making the average probability for one or more conversion to be 17.1%. A mismeasurement $\Delta$ in the conversion probability would therefore bias $R_{00}$ by $0.054\Delta$. To keep the bias in $\mathrm{Re}(\varepsilon'/\varepsilon)$ under $10^{-4}$, we have to keep $\Delta < 1.1\%$. As we discuss in Sec. X E, we have achieved this by using a combination of a direct measurement of the sheet over its entire surface, and measuring the step in the $3\pi^0$ $z$ distribution at the HDRA. The simulation included the measured variation in the sheet thickness and the energy dependence of the photon cross section in lead calculated by Hubbell, Gimm, and Øverbø [53].

### 3. Limiting apertures

The fractional loss of events near the edge of an aperture is generally compensated twice in the measurement of $\mathrm{Re}(\varepsilon'/\varepsilon)$, once in the vacuum-to-regenerator beam ratio and again when comparing the $\pi^+\pi^-$ mode to the $2\pi^0$ mode. To ensure that the biases would be minimal, we measured the effective aperture edges as precisely as possible, using a large sample of electrons from $K_{e3}$ decays.

The components of the detector serving to limit the acceptance were the active mask, the HDRA, the vacuum window aperture, and the collar anti. The limiting apertures were adjusted in size and transverse location by comparing illuminations of electrons from $K_{e3}$ decays in a portion of the NC subset to those from simulated decays for that subset. Then, the sizes of the apertures were fixed and their locations were tracked by comparing the $K_{e3}$ data from different subsets to the reference subset. The $z$ positions of the apertures were measured directly in a survey at the completion of the run.

For the aperture farthest upstream at the mask anti, the space resolution for the $x$ or $y$ projection was of order 1.2 mm for a typical track, where about 0.6 mm (1 mm) comes from chamber resolution (multiple scattering). For the collar anti, the resolution was closer to 0.2 mm, with roughly equal contributions from chamber resolution and scattering in the trigger hodoscopes. These two apertures were the most critical. The $K_{e3}$ electron illumination at one edge of each of these locations is shown in Fig. 61 before the final adjustment.

To determine the relative position of a given aperture edge between the data and Monte Carlo simulation, the Monte Carlo illumination is shifted in 100 $\mu$m steps relative to the data, and a $\chi^2$ by comparing both to come from the same parent distribution is calculated.

When the illumination is plotted with a binning small relative to the (single event) resolution and the shift is small, $\chi^2$ depends quadratically on the shift. For the mask edge illumination pictured in Fig. 61, this quadratic behavior is clear in the plot of $\chi^2$ versus shift in Fig. 62. When the shift is much larger than the resolution, $\chi^2$ behaves linearly.
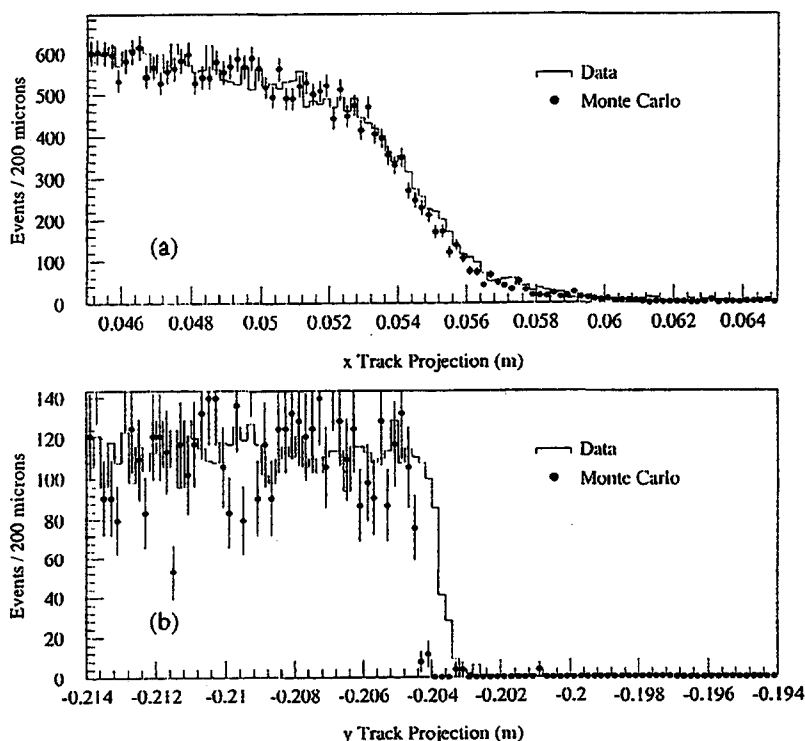
FIG. 61. Illumination of two of the aperture edges by electrons from $K_{e3}$ decays in the NC subset. The histogram shows the data illumination, while the dots show the MC prediction before the final tuning of the aperture positions. (a) Horizontal edge of the active mask. (b) East half of the bottom edge of the collar anti surrounding the lower beam. These edges showed the largest misalignment of their respective apertures before the final position adjustment. The mask edge is shifted about $230\mu$m, and the collar anti edge by about $700\mu$m.

The shifts were determined, with a quadratic fit at the minimum, statistically to better than 10 $\mu$m for the mask and the collar anti. This procedure relies on the shape of the illumination in the Monte Carlo simulation and data agreeing. To evaluate the systematic uncertainty, the procedure was repeated with windows of different sizes around each edge, with different ranges of fits, and by fitting to the expected linear behavior farther from the edge rather than to the quadratic behavior near the edge. From these studies, we have limited the systematic uncertainty on each measured edge to under 50 $\mu$m.

This systematic error does not include the position uncertainty from the chamber alignment. This uncertainty cancels in determining the *size* of the aperture, since the bias is identical for all edges of the aperture and cancels when looking at the difference between the left and right or top and bottom

edges of an aperture. It enters only when tracking the edges as a function of time. As we discuss in Sec. X D 1, there is an additional uncertainty of 60 $\mu$m from chamber alignment for each measurement of the mask anti shift, but only 15 $\mu$m for the collar anti.

The shifts measured for the mask and the collar anti are plotted in Fig. 63. The collar anti position was stable since it was rigidly attached to the lead glass which defined one end of the coordinate system. The mask anti appears to have drifted on the order of 800 $\mu$m in $y$ and 600 $\mu$m in $x$ over the course of the run. This is an artifact of tying the global coordinate system to the target. The entire target pile was sinking over the course of the run, dropping several millimeters. The apparent shift of the mask and other apertures and collimators were consistent with the target pile motion.

After all the fine-tunings based on the $K_{e3}$, it is interesting to compare the illuminations of some of the apertures in $\pi^+\pi^-$ and $2\pi^0$ decays. The mask illuminations for the two
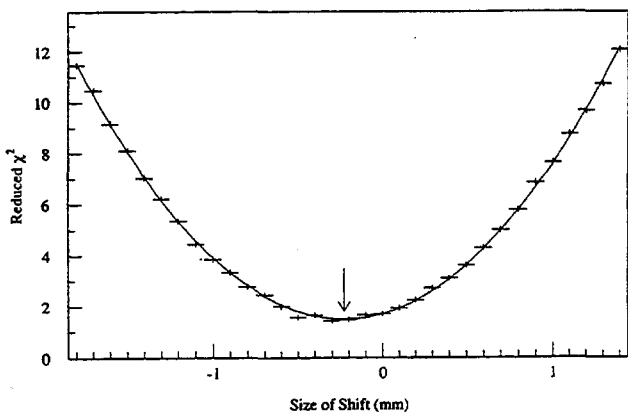


FIG. 62. Distribution of the reduced $\chi^2$ for the data and Monte Carlo $+x$ mask edge illuminations to come from the same parent distribution versus the Monte Carlo shift. The curve is the best quadratic fit, and the arrow indicates the minimum at $-226\pm7\mu$m.
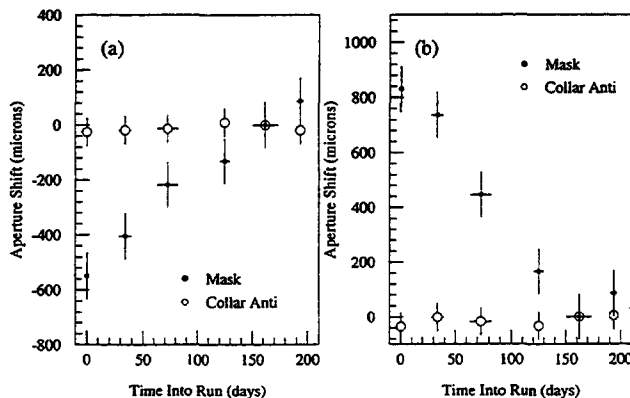


FIG. 63. Apparent motion of the collar anti and mask apertures with time. (a) Horizontal motion. (b) Vertical motion. The shifts are measured relative to the NCa subset (fifth data point).
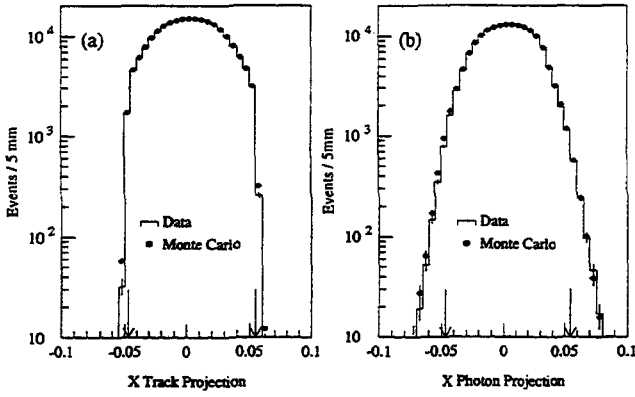
FIG. 64. Vacuum beam $\pi^+\pi^-$ track illumination and $2\pi^0$ photon illumination in the $x$ view at the plane of the active mask for the data and Monte Carlo simulation. (a) $\pi^+\pi^-$ track projection. (b) $2\pi^0$ photon projection. The arrows indicate the locations of the mask edges.

decay modes are shown in Fig. 64 (the $x$ view) and Fig. 65 (the $y$ view). Only the vacuum beam illuminates the mask. Overall, the agreement is excellent in both modes except for the small excess in the Monte Carlo simulation over the data at the $-x$ edge in the neutral mode. This mismatch is consistent with a small mismatch in the $2\pi^0$ beam shape at that edge. If attributed to an incorrect mask aperture, a mismatch of $650\mu$m at one edge shifts the vacuum-to-regenerator beam ratio (after acceptance corrections) by $-0.030\%$, and
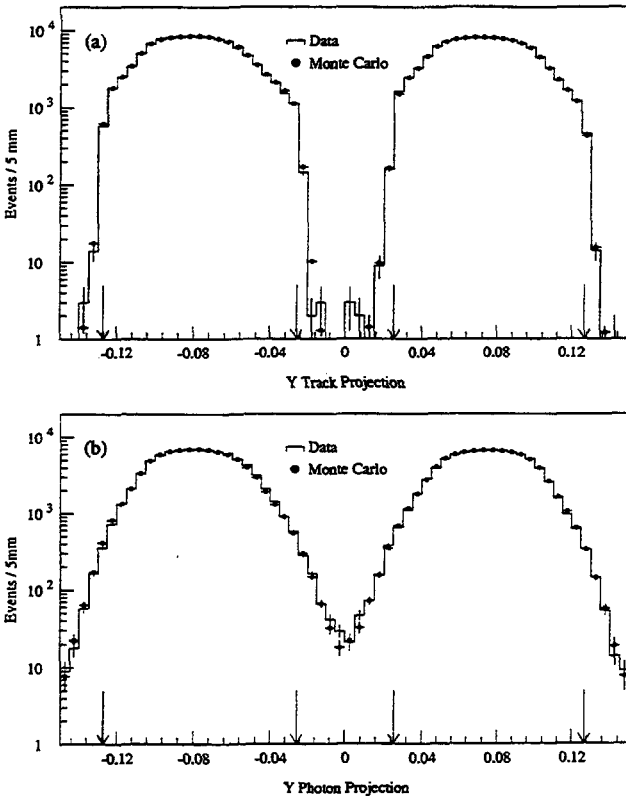


FIG. 65. Vacuum beam $\pi^+\pi^-$ track illumination and $2\pi^0$ photon illumination in the $y$ view at the plane of the active mask for the data and Monte Carlo simulation. (a) $\pi^+\pi^-$ track projection. (b) $2\pi^0$ photon projection. The arrows indicate the locations of the mask edges. Only the vacuum beam illuminations are shown.
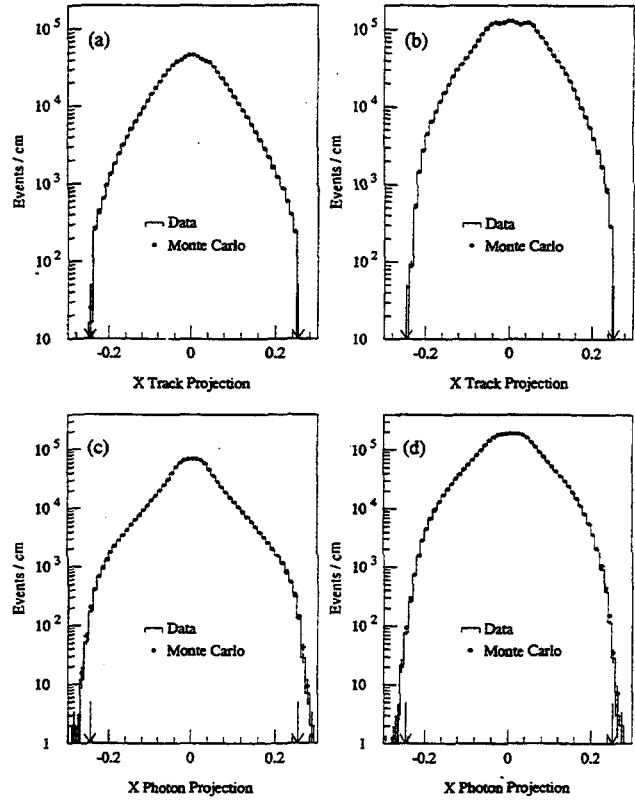


FIG. 66. The $\pi^+\pi^-$ track illumination and $2\pi^0$ photon illumination in the $x$ view at the plane of the HDRA for the data and Monte Carlo simulation. (a) Vacuum beam $\pi^+\pi^-$ track projection. (b) Regenerator beam $\pi^+\pi^-$ track projection. (c) Vacuum beam $2\pi^0$ photon projection. (d) Regenerator beam $2\pi^0$ photon projection. The arrows indicate the locations of the HDRA edges.

hence biases $\mathrm{Re}(\varepsilon'/\varepsilon)$ by $-0.50\times10^{-4}$.

The vacuum and regenerator beam illuminations at the HDRA are shown in Figs. 66 and 67 for the $x$ and $y$ views, respectively. Finally, the illuminations at the lead glass are pictured in Figs. 68 and 69 for the $x$ and $y$ views.

With the apertures under control, the "outer" acceptance has been defined. We now examine our modeling of the response of the detector elements, which determines the "inner" acceptance of the detector.

## D. Detector response

We describe in this section the simulation of the detector elements, in particular, the lead glass calorimeter response, the drift chamber response, and the response of scintillator and veto hodoscopes.

### 1. Simulation of the lead glass calorimeter response

For each electron or photon striking the lead glass calorimeter, we did not simulate a complete electromagnetic shower. Instead the response of the lead glass was parametrized as a function of electron energy, Čerenkov light absorption coefficient $\alpha$ (see Sec. IV B), and depth of photon conversion based on a stand-alone study of lead glass using the EGS4 [43] shower simulation package. The model for the attenuation length was described in Sec. IV B 1, and, along with the EGS cluster generation, in Ref. [36].
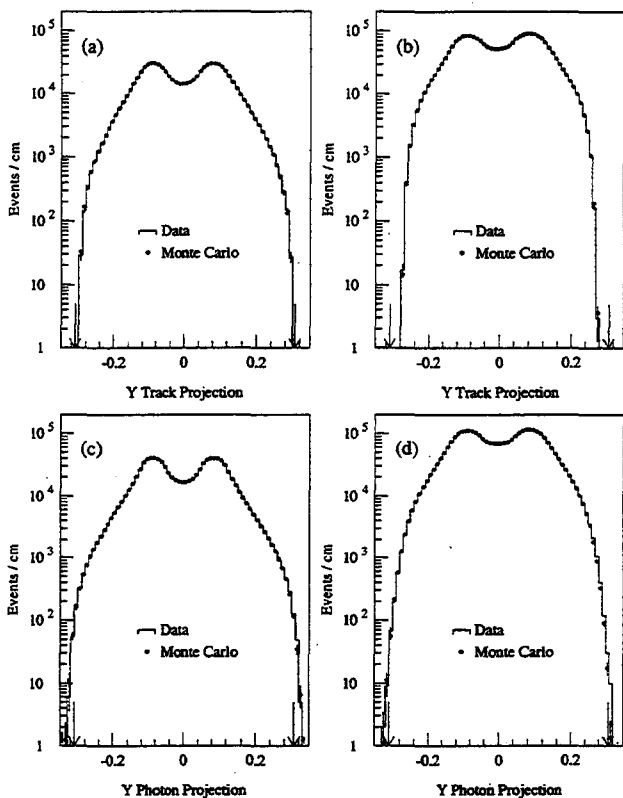
FIG. 67. The $\pi^+\pi^-$ track illumination and $2\pi^0$ photon illumination in the $y$ view at the plane of the HDRA for the data and Monte Carlo simulation. (a) Vacuum beam $\pi^+\pi^-$ track projection. (b) Regenerator beam $\pi^+\pi^-$ track projection. (c) Vacuum beam $2\pi^0$ photon projection. (d) Regenerator beam $2\pi^0$ photon projection. The arrows indicate the locations of the HDRA edges.

FIG. 68. The $\pi^+\pi^-$ track illumination and $2\pi^0$ photon illumination in the $x$ view at the plane of the lead glass for the data and Monte Carlo simulation. (a) Vacuum beam $\pi^+\pi^-$ track projection. (b) Regenerator beam $\pi^+\pi^-$ track projection. (c) Vacuum beam $2\pi^0$ photon position. (d) Regenerator beam $2\pi^0$ photon position.

*a. Parametrization of the lead glass response to electrons.* The response of the lead glass to electron showers was modeled by assuming that the absorption of Čerenkov light is uniform through the length of the block. We have calibrated the lead glass with this assumption, and from each electron calibration we have extracted an average absorption coefficient $\alpha$ (typically 3%–4% per radiation length) for each block. We expect the variations in response of the lead glass to be dominated by the depth $t_{max}$ of the maximal energy deposition. Since $t_{max}$ depends logarithmically on $E_i$ [42,54], we used the EGS4 package to generate showers with energies spaced uniformly in $\ln E_i$, from 0.25 GeV to 90.51 GeV. For each shower, the track length of each charged particle was weighted by the number of Čerenkov photons that the particle would radiate, $N_c = 1 - 1/n^2\beta^2$, where $n$ is the index of refraction. The sum of the total weighted track length was then recorded in cells measuring $0.36\times0.36\times0.5$ radiation lengths, covering a volume of 30 radiation lengths deep and $7\times7$ block widths wide transversely.

For each generated electron shower, the Čerenkov light in each cell was attenuated using a given absorption coefficient to the back of a block of a given length. (For the modeling of photons, it was useful to calculate the response for blocks of different lengths.) The response of the block to that shower was defined by the ratio of the total Čerenkov light reaching the back of the block to the total Čerenkov light produced. For each shower we calculated the response using a set of

attenuation coefficients which spanned the range of coefficients measured in the various electron calibrations. As discussed in Sec. IV B 1, we treat a photon by having it first convert at a depth $t_0$ in the block, and then treat the photon shower as two independent electron showers in a block of length $18.7 - t_0$ radiation lengths.

The block response was accumulated for each pair of absorption coefficient and block-length parameters. It was then parametrized with a simple functional form depending upon the absorption coefficient, the electron energy, and the conversion depth. This parametrization was used as the parent distribution in the Monte Carlo simulation.

For our earlier result [21,36] based on the NC subset, the responses were parametrized by a simple Gaussian using the means and rms widths of the shower distributions. Unfortunately, there are sizable tails in many of the response distributions: tails on the high side from showers fluctuating deeper into the block, and hence having less attenuation of the Čerenkov radiation, and tails on the low side from showers which lose many of the charged particles out the back of the block. From studies of electrons from $K_{e3}$ decays, we found that this parametrization resulted in slightly poorer resolution in the Monte Carlo simulation than we observed in the data since the tails had inflated the rms width.

For this simulation, we have incorporated the tails explicitly into the parametrization. For each distribution of shower responses, we first fit a Gaussian form. If over 1.25% of the distribution fell higher (lower) than 2.5 times the width of this Gaussian, then a high- (low-) side tail was added to the
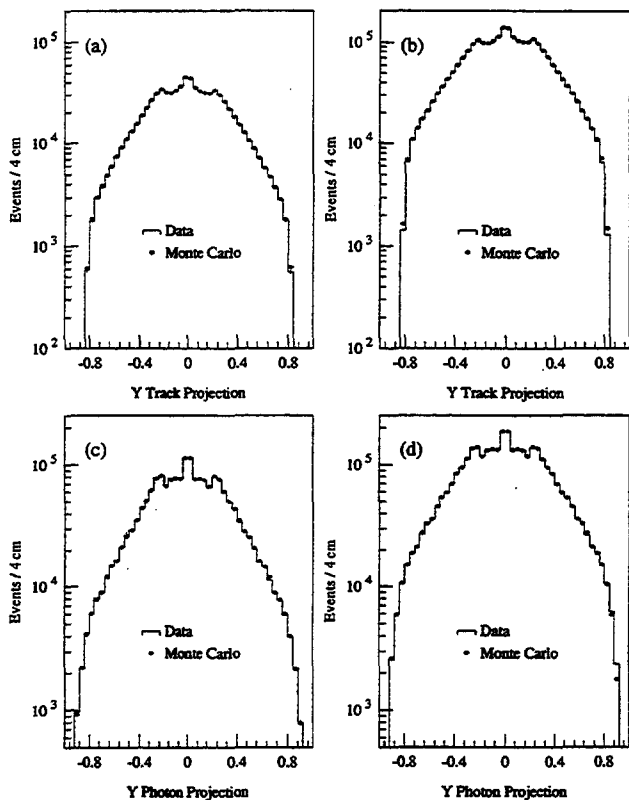
FIG. 69. The $\pi^+\pi^-$ track illumination and $2\pi^0$ photon illumination in the $y$ view at the plane of the lead glass for the data and Monte Carlo simulation. (a) Vacuum beam $\pi^+\pi^-$ track projection. (b) Regenerator beam $\pi^+\pi^-$ track projection. (c) Vacuum beam $2\pi^0$ photon position. (d) Regenerator beam $2\pi^0$ photon position.

parametrization. If one or both tails were needed, the distribution was refit simultaneously to the sum of the Gaussian +tail(s). The parametrization for the high side tail we used was

$$\frac{dN}{df} = \begin{cases} \gamma(f-f_0)e^{-\beta(f-f_0)}, & f>f_0, \\ 0, & f<f_0. \end{cases} \quad (72)$$

Here, $f$ is the response, and $f_0$, $\beta$, and $\gamma$ were parameters for each of the distributions. An analogous parametrization was used for the low-side tail. This parametrization was successful over the range of absorption coefficients, block lengths, and energies of interest as shown in Fig. 70.

The fits generally resulted in a smooth variation of the parameters as a function of the absorption coefficient and block length. For electron energies $E$ between the EGS shower energies, the parameters were interpolated linearly in $\ln E$.

The above procedure parametrizes the smearing of the calorimeter response due to electromagnetic shower fluctuations. Additional smearing occurs due to random fluctuations in the number of photoelectrons liberated from the photocathode. This term was determined using a flasher system; the average number of photoelectrons obtained in each of the 804 blocks for a 1 GeV electron is plotted in Fig. 71.

   b. *Generating a cluster from shower response.* To properly simulate the energy sharing, we accumulated a large cluster library using a clean sample of electrons from the

$e^+e^-$ calibration samples where no minimum readout threshold was used. For each cluster in the library, we have stored the pattern of the energy distribution within a $5\times5$ array of blocks centered on the block struck by an electron. The clusters are grouped according to the incident electron energy and the position in the block where the electron landed, both of which were measured with the charged spectrometer. The details of this library are given in Ref. [37].

For photons, the signal in each block from the shower simulated for each conversion electron is summed. Similarly, the signals in any overlapping blocks for two nearby showers are summed. To complete the simulation, the signal in each block of the array is converted to ADC counts using the block gain measured in electron calibration, and the readout threshold is applied.

The final stage of the simulation of the lead glass array involved simulating the hardware cluster finder (HCF). The correct threshold for each block above which the HCF would register a "hit" could be found in [37]. Once the pattern of hit blocks was obtained, the software simulation of the cluster-finding algorithm was straightforward.

To compensate for remaining effects in the modeling of the electron response, we needed to make small adjustment to the parametrization for absorption coefficients $\alpha>0.032$. The width and the exponential slope of the high-side tail were changed linearly as a function of $\alpha-0.032$, such that for a block with $\alpha=0.04$, which was fairly common near the center of the array, the Gaussian width was reduced by 4% of itself and the area under the high-side tail was halved. The two parameters that accomplished this were the only tunable parameters introduced into the electron response simulation. The agreement between the data and Monte Carlo electron resolution as a function of energy and absorption was reasonable as seen in Fig. 72. For the data, the resolution contribution on the track momentum $p$ was subtracted using Eq. (29). The worsening of the resolution at low energies results from finite photostatistics. The effect of the damaged blocks was to increase the resolution at high momentum from about 2% to 2.6%.

   c. *Photons, $\pi^+\pi^-\pi^0$ data, and Monte Carlo simulation.* To check the photon response, we studied the reconstructed $\pi^0$ mass in $\pi^+\pi^-\pi^0$ decays. We found that the simulated photon resolution was slightly wider than the resolution in the data. The difference can be understood with a model where the absorption increases toward the back of the block. The deeper a photon converts in a block, the less the Čerenkov light from its shower is attenuated. If the absorption is increasing from front to back, the spread of absorptions is smaller than for a block with uniform absorption. Hence, for photons (as well as electrons), we expect the radiation damage to compensate the fluctuations into the block. Since we cannot directly measure the absorption profile, we allowed one tunable parameter in the photon simulation. Assuming that the absorption is increasing into the block, the average absorption $\alpha_t$ seen by the $e^+e^-$ pair from the photon conversion varies with the conversion depth, $t_0$. We parametrize this change as

$$\alpha_t = \alpha(1+0.03t_0), \quad (73)$$

where $\alpha$ is the absorption coefficient of the block measured

L. K. GIBBONS *et al.*
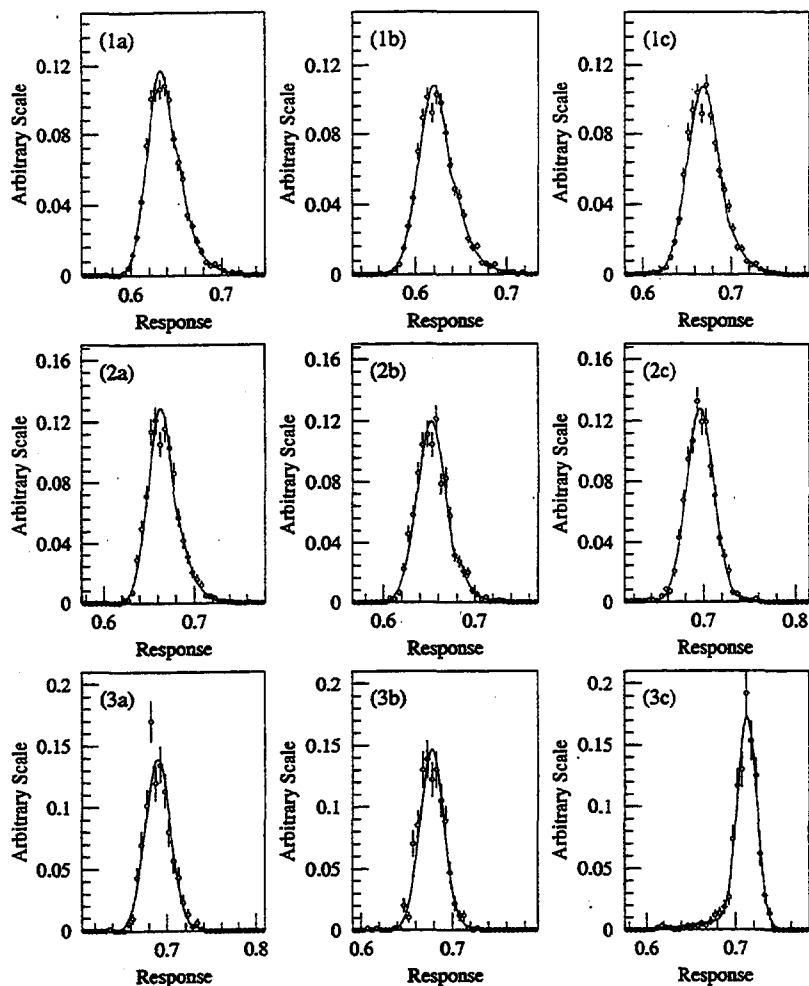


FIG. 70. Distribution of the fractional response for EGS electron showers. Rows 1–3 correspond to energies of 2 GeV, 8 GeV, and 32 GeV, respectively. The absorption coefficient $\alpha$ and block length $L$ in radiation lengths for each column are (a) $\alpha = 0.034$, $L = 18.7$, (b) $\alpha = 0.040$, $L = 17.2$, and (c) $\alpha = 0.038$, $L = 15.7$. In each plot, the curve is the best fit parametrization.

in calibration. The 3% per radiation length constant was determined from the study of the reconstructed $\gamma\gamma$ mass width in $\pi^+\pi^-\pi^0$ decays.

The $\gamma\gamma$ mass in $\pi^+\pi^-\pi^0$ decays was quite useful for studying photons in the lead glass. Since the $z$ location of the kaon can be measured directly from the charged pions in the drift chamber system, the $\gamma\gamma$ mass obtained from Eq. (54) is directly related to the two measured photon energies. We compared the $\gamma\gamma$ mass distributions for $\pi^+\pi^-\pi^0$ decays in the data and Monte Carlo simulation as a function of the average of absorption coefficients of the two photon clusters.

The $\gamma\gamma$ mass distribution for four different ranges of the average absorption coefficient is plotted in Fig. 73. Tuning was done using only the NC set, yet the Monte Carlo simulation described the data quite well in earlier subsets as well. For example, the $\gamma\gamma$ mass resolution as a function of the



FIG. 72. $K_{e3}$ electron energy resolution versus incident electron energy for three different ranges of the lead glass absorption coefficient $\alpha$. The resolution is measured using the events in all blocks within a quoted range of $\alpha$ to obtain adequate statistics. The data electrons are the solid symbols; the Monte Carlo electrons are the open symbols. The three absorption coefficient ranges (in percent per radiation length) are squares, 3.4–3.6; triangles, 3.8–4.0; and circles, 4.2–4.4.



FIG. 71. Average number of photoelectrons obtained from the shower of a 1 GeV electron for each of the 804 blocks.

CP AND CPT SYMMETRY TESTS FROM THE TWO-PION ...
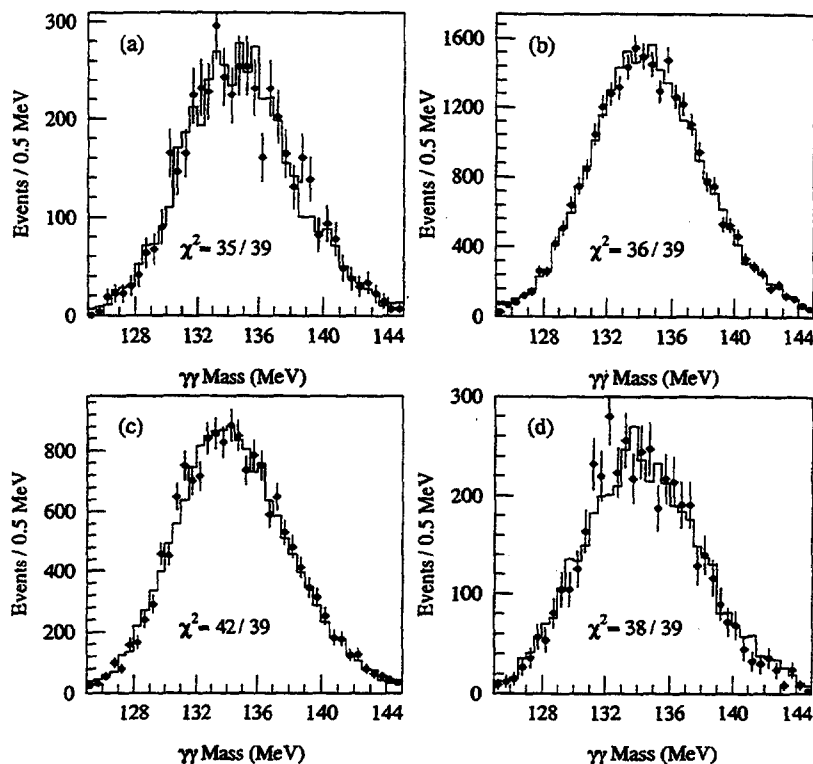


FIG. 73. The $\gamma\gamma$ mass for $\pi^+\pi^-\pi^0$ decays from the NC subset. The Monte Carlo simulation (dots) has been overlaid on top of the data distribution (histogram) with reduced $\chi^2$ for comparison. The events have been divided into different ranges of the average absorption coefficient $\bar{\alpha}=(\alpha_1+\alpha_2)/2$ of the two photon clusters. (a) $0.032\leqslant\bar{\alpha}<0.033$. (b) $0.035\leqslant\bar{\alpha}<0.036$. (c) $0.038\leqslant\bar{\alpha}<0.039$. (d) $0.040\leqslant\bar{\alpha}<0.041$.

average absorption is plotted for the NC subset and the C2 subset in Fig. 74. The data and Monte Carlo simulation agree well in both subsets in the region $\alpha>0.032$, where we tuned. In the earlier subsets, the Monte Carlo resolution seems somewhat better at very low values of $\alpha$ than we observe in the data. These low absorptions occur at the outside of the array where photon illumination is low, and have little effect on the average resolution. The overall effect of an average resolution mismatch is discussed in Sec. X.

*d. What about $2\pi^0$ decays?* The energy and overall photon illumination are well simulated, as we have seen earlier in this section. We have also seen in Sec. VI A that the line shapes of the $2\pi^0$ mass distributions match well, aside from an overall shift due to the residual nonlinearity in the data. In Sec. X later, we see that a small difference in the $2\pi^0$ mass shape for decays from the vacuum beam and the regenerator

beam, due to the differences in the energy spectra of the two beams, is also faithfully reproduced by the simulation.

The pairing $\chi^2$ for combining the four photons into two $\pi^0$'s is plotted for $2\pi^0$ data and simulation in Fig. 75. The overall shape agrees well over the bulk of the distribution, with the data showing some excess for badly reconstructed events; some of this is expected from accidental activity in the detector.

Directly related to the cluster simulation is the distribution of cluster separation (see Fig. 76) in the $2\pi^0$ data and Monte Carlo simulation. The shape of this distribution is affected by the cluster shape cuts used to reduce the $3\pi^0$ background and by the remaining $3\pi^0$ background in the $2\pi^0$ sample. The agreement between the two distributions extends over four orders of magnitude in both beams, including the region where clusters overlap.
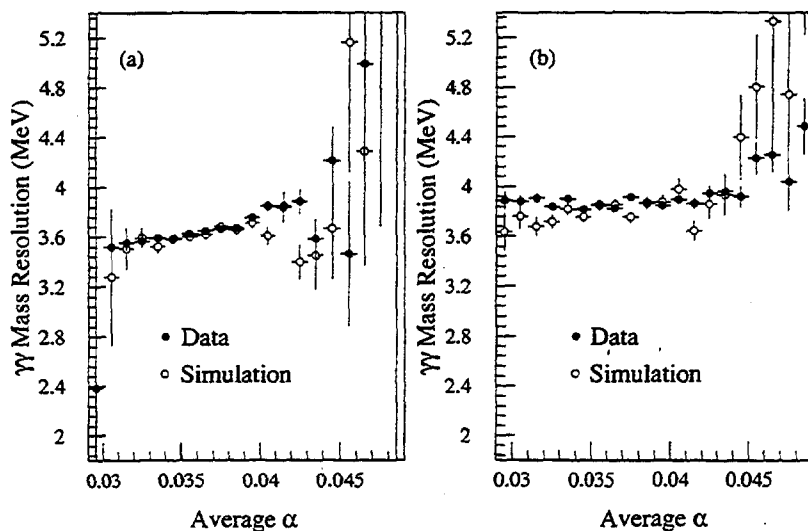


FIG. 74. Resolution on the $\gamma\gamma$ mass in the $\pi^+\pi^-\pi^0$ data and Monte Carlo simulation. The resolution is plotted as a function of the average absorption coefficient $\bar{\alpha}=(\alpha_1+\alpha_2)/2$ of the two photon clusters. (a) NC subset. (b) C2 subset.

L. K. GIBBONS *et al.*
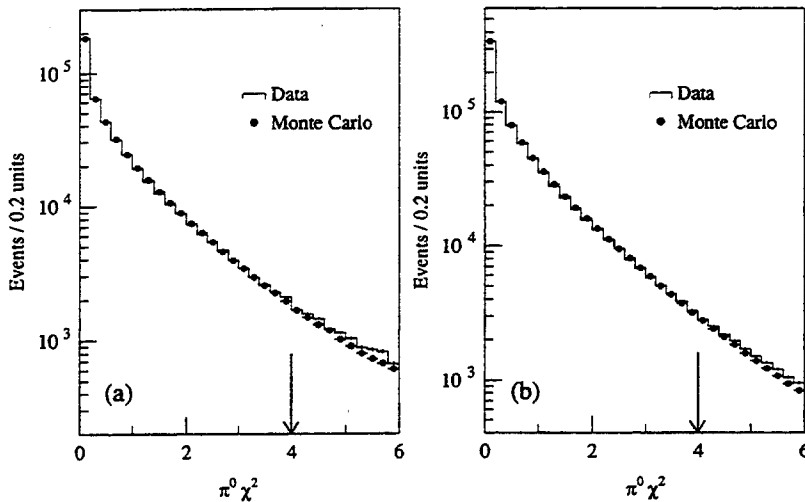


FIG. 75. Pairing $\chi^2$ for $2\pi^0$ decays in the data and Monte Carlo simulation. (a) Vacuum beam. (b) Regenerator beam. The expected background contribution has been added to the Monte Carlo prediction. The arrow in each plot marks the position of the analysis cut.

The individual cluster energies are also interesting to examine. The one distribution where the simulation failed to precisely describe the data was in the maximum cluster energy distribution. This distribution is shown in Fig. 77 for the entire $2\pi^0$ sample in both vacuum and regenerator beams. Also shown are the regenerator beam distributions for the subsets with and without the lead sheet. The change in the vacuum beam distributions for these two sets is identical to the change in the regenerator beam. While the Monte Carlo simulation describes the data quite well below energies of about 60 GeV, the data show a higher acceptance on average



FIG. 76. Cluster separation for $2\pi^0$ decays in the data and Monte Carlo simulation. The arrow indicates the minimal separation for each of the standard $3\times3$ block clusters to be distinct (complete separated). No cut is made on this variable. (a) Vacuum beam. (b) Regenerator beam. The predicted background level has been add to the $2\pi^0$ Monte Carlo simulation.

than the Monte Carlo simulation at high photon energy. This discrepancy is time dependent, appearing at a much reduced level in later subsets.

The bulk of the discrepancy comes from the blocks surrounding the beam pipe, with the remainder from the ring of blocks just outside of these pipe blocks. The discrepancy seems to be related to the actual acceptance of high-energy photons and not an effect due to smearing, since the smearing required to mimic this problem would make the $2\pi^0$ mass distribution extremely broad. Excess smearing would also distort the low end of the maximum cluster energy distribution, which agrees with the data without such a smearing.

We decided to restrict ourselves to the subsample of $2\pi^0$ decays where the maximum cluster energy was under 60 GeV/$c$. This has the further advantage of limiting the $2\pi^0$ cluster energy to the kinematic regime which is occupied by $3\pi^0$ sample. Since we used the $3\pi^0$ decays to limit the systematic error for the neutral mode acceptance, this seemed like the most conservative course. We later return to this issue as part of our systematic discussion in Sec. X B. This problem was "solved" in a subsequent experiment and we comment later on the implications for the analysis in question.

### 2. Drift chamber simulation

Relative to the lead glass, the drift chamber simulation was simple. The TDC distribution was simulated by inverting the measured time to distance function (see Sec. IV A 1) for the time period used in the data. The chamber resolution was included by first smearing the true position of the particle in the drift chamber sense plane using a Gaussian distribution whose width was determined from data. This smeared distance was then converted to a TDC time using the inverted time-to-distance function.

The measured drift chamber efficiencies were also included. The individual wire efficiencies were quite uniform across a plane (see Fig. 78). This was true even in the most inefficient plane, allowing us to characterize the efficiency for each plane with a single number. Roughly 25 wires that were missing, disconnected, or had efficiencies significantly lower than the average were handled individually. If such wires were at the edge of the chamber, where the illumina-
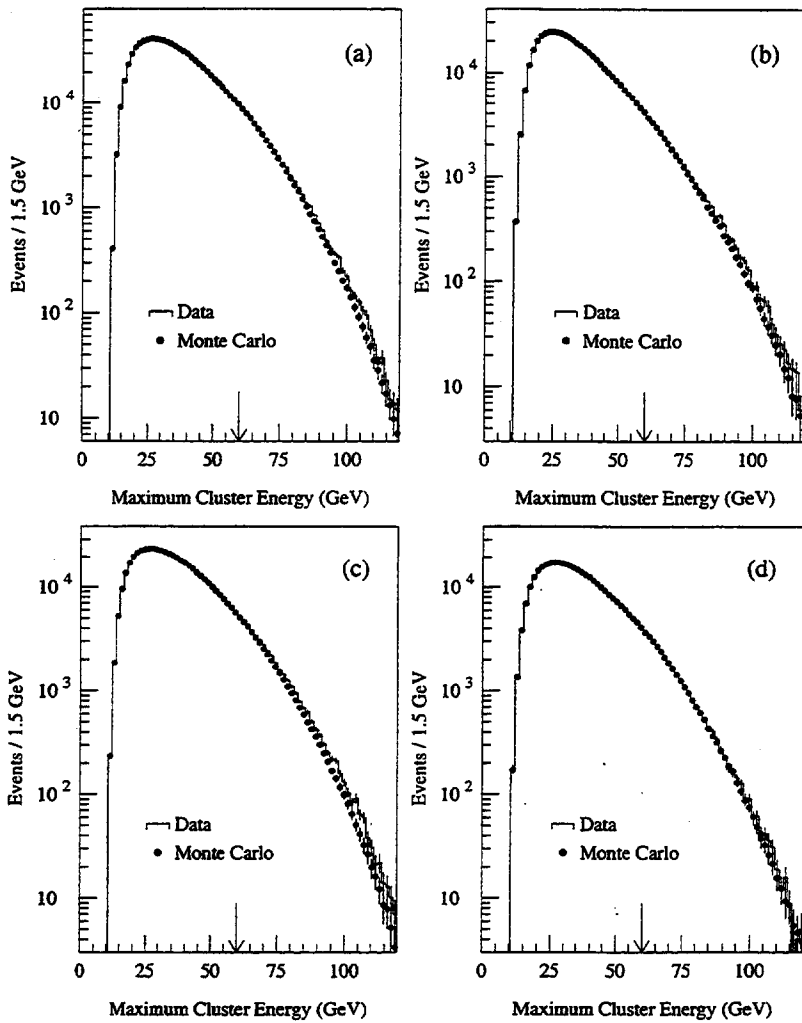
FIG. 77. Distribution of the maximum cluster energy for $2\pi^0$ decays in the data and Monte Carlo simulation. The arrow indicates the position of the analysis cut. (a) Vacuum beam distributions for the entire data set. (b) Regenerator beam distributions for the entire data set. The regenerator beam distributions are plotted separately for (c) the $2\pi^0$ subset with the lead sheet and (d) the subset without the lead sheet. Background contributions have been included in all of the Monte Carlo overlays.

tion was low, they were required to be more than 5% away from the mean; however, in the central regions this figure was 0.5%. The efficiency measured individually for each of these wires was used in the simulation, and this wire was excluded from measurement of the average efficiency of the sense plane to which it belonged.

Only three of the inefficient wires were in a high-rate region of the chamber system. The tracking algorithm was forgiving of missing hits, particularly in the $y$ view, and very few tracks were seriously misreconstructed or missed en-



FIG. 78. Individual wire efficiency for the downstream $y$ plane in chamber 2 measured with the $K_{e3}$ data in the NC subset.

tirely because of these inefficient wires. Hence these few wires had little affect on the acceptance. The illumination before and after an $x$-view sense wire broke in a fairly high-rate region is shown in Fig. 79. There is not a great change in the illumination near this wire, but the deficit in the NC set is visible.

The track separation is shown for one plane in Fig. 80. The simulation accounts for the acceptance change as the pion track separation decreases to the size of a drift cell.

One shortcoming of the simulation was the lack of $\delta$ rays. Broad tails in track quality variables were thus not simulated, but as we have seen in Sec. V, $\delta$ rays affect the decays in the vacuum beam and regenerator beam identically; we further investigate our sensitivity in Sec. X.

### 3. Hodoscope and photon veto response

The simulations of the hodoscope banks and photon veto counters were elementary. The average trigger and latch efficiencies, the former over 99.9% and the latter over 99% efficient, were determined with muon tracks. In addition, the cracks between counters were mapped using the chamber alignment muon samples and the gaps were included in the Monte Carlo simulation. In Sec. X, we examine the insensitivity of $\mathrm{Re}(\varepsilon'/\varepsilon)$ to the efficiency of the individual counters.

The photon veto responses were important for the

FIG. 79. Chamber-2 $x$ illumination by pions from $\pi^+\pi^-$ decays in data before and after one $x$-view sense wire broke. (a) The data collected before the wire broke (dots) overlaid on the NC subset data collected after the wire broke (histogram) and (b) the ratio of these distributions. (c) Monte Carlo simulation for the NC $\pi^+\pi^-$ data subset (dots) overlaid on the data for that set (histogram) and (d) the ratio of these distributions. The arrows indicate the position of the wire in question.

simulation of the four cluster $3\pi^0$ background. A technique [38] that utilized $\pi^+\pi^-\pi^0$ decays with one photon detected in the calorimeter was employed to map the response of these counters. The direction and energy of the missing photon could be inferred from the kinematics of the charged pions and reconstructed photon. By comparing the observed signals in the veto counters to the predicted energy of the "undetected" photon, the gains and resolution of the counters were extracted. A mismeasurement of the photon

veto response would be seen in the distribution of the $3\pi^0$ background. The predicted and observed $z$ shapes of the $3\pi^0$ background agree well (Sec. VI).

### E. Z comparisons

We now examine the distribution most crucial to the $\mathrm{Re}(\varepsilon'/\varepsilon)$ analysis, the $z$ distribution of kaon decays. When we fit for $\mathrm{Re}(\varepsilon'/\varepsilon)$, we integrate the contents of each 10
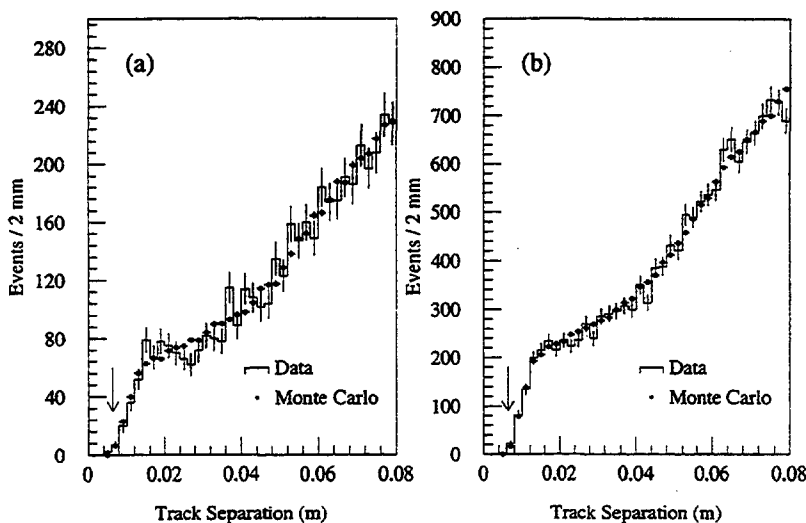


FIG. 80. Separation of the two pion tracks in the $x$ view at chamber 4 for the $\pi^+\pi^-$ data and Monte Carlo simulation. (a) Vacuum beam. (b) Regenerator beam. The arrows indicate a separation the size of one drift cell. No cut is made on this variable.
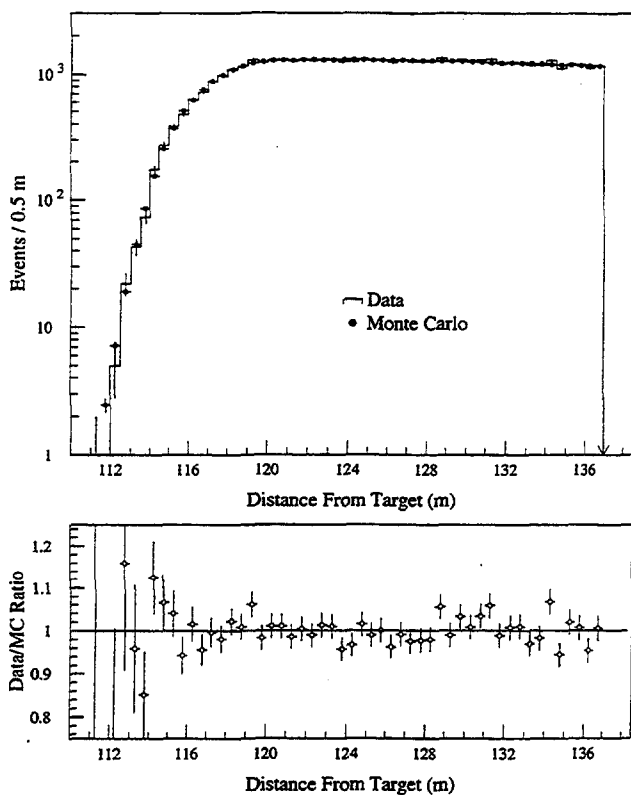
FIG. 81. Vacuum beam $z$ distribution for the $\pi^+\pi^-$ data and Monte Carlo simulation in the 60–70 GeV/$c$ bin momentum bin. All final cuts have been made. Top: the $z$ distribution for the two event samples, with the simulation statistics normalized to the data statistics. Bottom: the ratio of data events to simulated events in each 0.5 m bin.

FIG. 82. Vacuum beam $z$ distribution for the lead-sheet subset of the $2\pi^0$ data and Monte Carlo simulation in the 60–70 GeV/$c$ bin momentum bin. All final cuts have been made. Top: the $z$ distribution for the two event samples, with the simulation statistics normalized to the data statistics. Bottom: the ratio of data events to simulated events in each 0.5 m bin.

GeV/$c$ momentum bin over the entire $z$ range. A bias in the acceptance versus $z$, coupled with the difference in the vacuum and regenerator beam $z$ distributions, would lead to a bias in the ratio of events in the vacuum and regenerator beams.

From the plots already shown, it is clear that our simulation of the apparatus mocks up the data quite well. We therefore expect that any bias in the acceptance is small and expect the $z$ distributions to match well. For most problems that would affect the acceptance, such as a misplaced aperture edge, a bias in resolving closely spaced tracks, or closely spaced clusters, we expect the acceptance to either increase or decrease fairly uniformly in $z$, when comparing data to Monte Carlo simulations. For example, if an aperture is too wide, $2\pi^0$ decays near the $z$ location of the aperture are not affected, while $2\pi^0$ decays farther upstream, whose photons have had a chance to spread and approach the aperture's edges, are accepted more often in the simulation than they should. We therefore look for a linear bias as a function of $z$. In all of the studies we have done, the $\chi^2$ for a linear fit to the ratio of the data to Monte Carlo simulation have been excellent, indicating that higher order terms are not necessary.

We display, in Figs. 81 and 82 and in Figs. 83 and 84, the distributions in the vacuum beam for the 60–70 GeV/$c$ bin (near the mean kaon energy for both modes) and the 110–120 GeV/$c$ bin (picked randomly). The $\chi^2$ comparing the data and simulation are all very good.

When fitting for a linear bias in the ratio of the data to Monte Carlo simulation, the observed slopes were consistent with what one might expect from statistical fluctuations. For example, for the 48 momentum bins in the two neutral subsets, the slopes in 24 bins had significances under one standard deviation $(\sigma)$, 15 between $1\sigma$ and $2\sigma$, and 9 over $2\sigma$. Many of the slopes over $2\sigma$ occurred in bins with low statistics. The relative numbers of positive and negative slopes observed were also consistent with expected statistical fluctuations.

To probe any residual biases at a much more sensitive level, it is convenient to combine all of the momentum bins and also to use the $K_{e3}$ and $3\pi^0$ data. Because the energy spectrum and beam shapes are well simulated, the $z$ distribution in the Monte Carlo simulation integrated over all momenta should match the observed $z$ distribution in the data well. This is particularly true in the modes with charged final states. In the neutral mode, we must be more careful because of the coupling between the measured $z$ position of the kaon decay and the measured photon energies. A bias in the photon energy measurement can mimic an acceptance problem.

In the case of the $3\pi^0$ decays, the photons in the lead glass have a higher probability to overlap than photons from $2\pi^0$ decays. Hence the $3\pi^0$ decays are also more sensitive to problems with the cluster simulation than the $2\pi^0$ decays. With the increased sensitivity of the high-statistics modes to potential biases, limits on the acceptance for $\pi\pi$ decays ob-
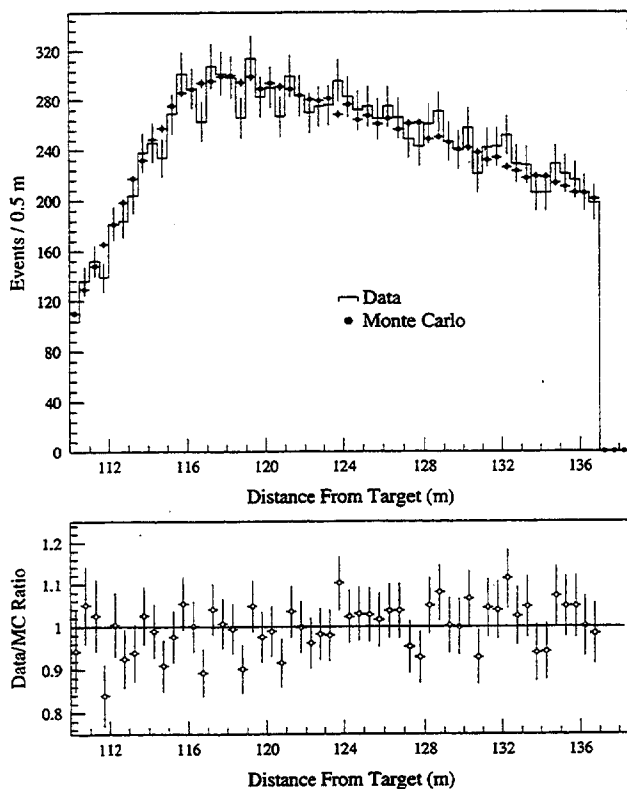
FIG. 83. Vacuum beam $z$ distribution for the $\pi^+\pi^-$ data and Monte Carlo simulation in the 110–120 GeV/$c$ bin momentum bin. All final cuts have been made. Top: the $z$ distribution for the two event samples, with the simulation statistics normalized to the data statistics. Bottom: the ratio of data events to simulated events in each 0.5 m bin.



FIG. 84. Vacuum beam $z$ distribution for the subset of the $2\pi^0$ data and Monte Carlo simulation without the lead sheet in the 110–120 GeV/$c$ bin momentum bin. All final cuts have been made. Top: the $z$ distribution for the two event samples, with the simulation statistics normalized to the data statistics. Bottom: the ratio of data events to simulated events in each 0.5 m bin.

tained using the high-statistics modes are fairly conservative estimates.

The $K_{e3}$ $z$ distribution for one of the data subsets is shown in Fig. 85. The $z$ distributions in the data and in the simulation agree very well over the entire decay volume, even upstream of the 110 m $\pi^+\pi^-$ analysis cut, where simulation keeps track of an order of magnitude drop in acceptance over 5 m reliably. We have conservatively estimated the acceptance bias in the charged mode at the level of 0.03% per meter, while the $K_{e3}$ samples had slopes which were consistent with being flat at the 0.02% per meter level.

In order to bound the acceptance bias for the $2\pi^0$ mode, the $3\pi^0$ sample we used was limited to a region away from the active mask, where the rapid change in the $3\pi^0$ acceptance shape coupled with residual uncertainties in the photon energy reconstruction might yield misleading discrepancies that do not affect Re($\varepsilon'/\varepsilon$). For the subset with no lead sheet, the $z$ distribution in the data and Monte Carlo simulation is shown in Fig. 86; the agreement is excellent and places a 0.074% per meter limit on the acceptance bias for $2\pi^0$. Upstream, the acceptance changes shape rapidly, and there is a dip in the ratio of the data to Monte Carlo simulation, about 1% at 120 m. A few more meters upstream, the data to Monte Carlo simulation ratio is again consistent with 1 when the accepted decay distribution is relatively flat. An overall energy scale shift of about 0.02% would cause this effect.

It is interesting to note that at our mean kaon energy, we would have introduced a slope of the order of 0.04% per meter into the overlay had we ignored the $K_L$ lifetime in the simulation.

Finally, we have the $\pi^+\pi^-$ and $2\pi^0$ distributions themselves. The distribution of vacuum $\pi^+\pi^-$ decays (Fig. 87) is simulated well over the entire decay volume. The vacuum distributions for $2\pi^0$ decays without the lead sheet are shown in Fig. 88 and with the lead sheet in Fig. 89. The simulation is again good; the $z$ region from 137 m to 139 m was excluded because of the sensitivity of that area to biases in the photon energy scale. There does appear to be an excess of the data over Monte Carlo simulation in part of that region, consistent with an energy scale shift of under 0.03%.

The shape of the regenerator beam distribution depends on physics parameters, such as $\rho$ and $\Delta m$, which are used in the Monte Carlo simulation. The $\pi^+\pi^-$ $z$ distribution for this beam is shown in Fig. 90, and the $2\pi^0$ distribution in Fig. 91. The simulated regenerator beam distributions agree fairly well with the data. In particular, the agreement in the $z$ shape at the sharp turn on of decays at the regenerator is very good; this is determined by the resolution function, yet even in the $2\pi^0$ mode the Monte Carlo simulation predicts the number of data events at the 10% level at three orders of magnitude down from the peak.

### F. Summary of the Monte Carlo simulation

The most apt summary of the Monte Carlo simulation is the plot of the vacuum beam $z$ overlays for the five different
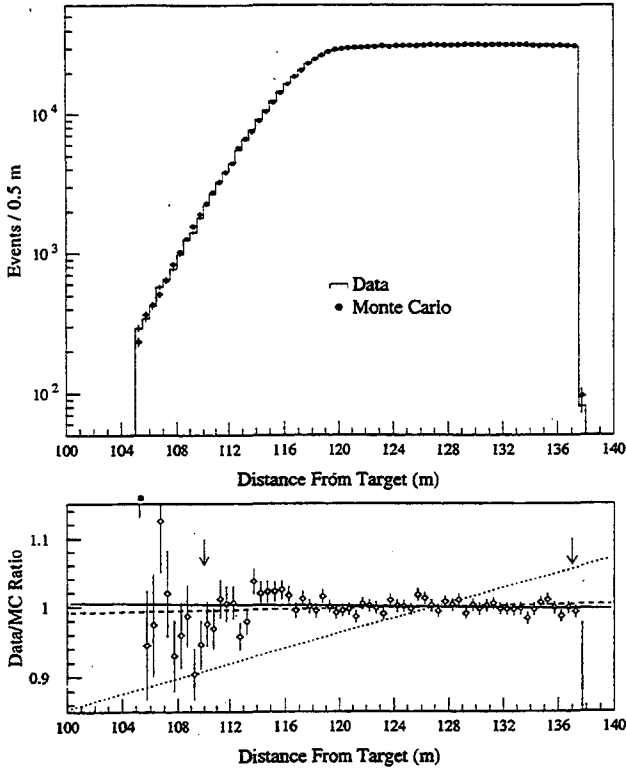
FIG. 85. Vacuum beam $z$ distribution for $K_{e3}$ decays in the data and Monte Carlo simulation after all other cuts. The sample shown is a portion of the NC subset. Top: the $z$ distribution for the two event samples, with the simulation statistics normalized to the data statistics. Bottom: the ratio of data events to simulated events in each 0.5 m bin. The solid line is the best fit slope of $-0.021\% \pm 0.018\%$ per meter. The dashed line is the slope used for the systematic estimate, 0.03% per meter. The dotted line is the slope required to shift the final result for $\text{Re}(\varepsilon'/\varepsilon)$ by $10^{-3}$. The arrows in the ratio plot indicate the $z$ fiducial region used in the $\pi^+\pi^-$ analysis.

data sets considered in this experiment (see Fig. 92). The $3\pi^0$ plot shows agreement even upstream of the mask.

In all but the $3\pi^0$ case, the $\chi^2$ values are within about one-standard-deviation fluctuation. In the neutral mode plots, both $2\pi^0$ and $3\pi^0$, the excess in the $\chi^2$ tends to come from the upstream region right at the rolloff in acceptance, where the $z$ distribution is the most sensitive to residual problems with the photon energy scale. This is particularly true for the $3\pi^0$ case, where 52 units of $\chi^2$ come from the four bins in the range 116–120 m.

The $\pi\pi$ data samples shown range in size from 150 000 to 350 000 events, and the Monte Carlo samples from about $4\times10^6$ to $8\times10^6$ events. The $K_{e3}$ sample shown has about $1\times10^6$ events in both the data and Monte Carlo samples. The $3\pi^0$ sample has about $5\times10^6$ data events and $6\times10^6$ Monte Carlo events.

In spite of the different characteristics of the decay modes, the Monte Carlo simulation reproduces the data, not only for the $z$ distributions, but also for many of the other distributions. We now take the accepted and generated $\pi\pi$ distributions from the Monte Carlo simulation and use these to extract values for $\text{Re}(\varepsilon'/\varepsilon)$ and other parameters of the neutral kaon system. We turn to the description of the techniques used to determine these parameters.
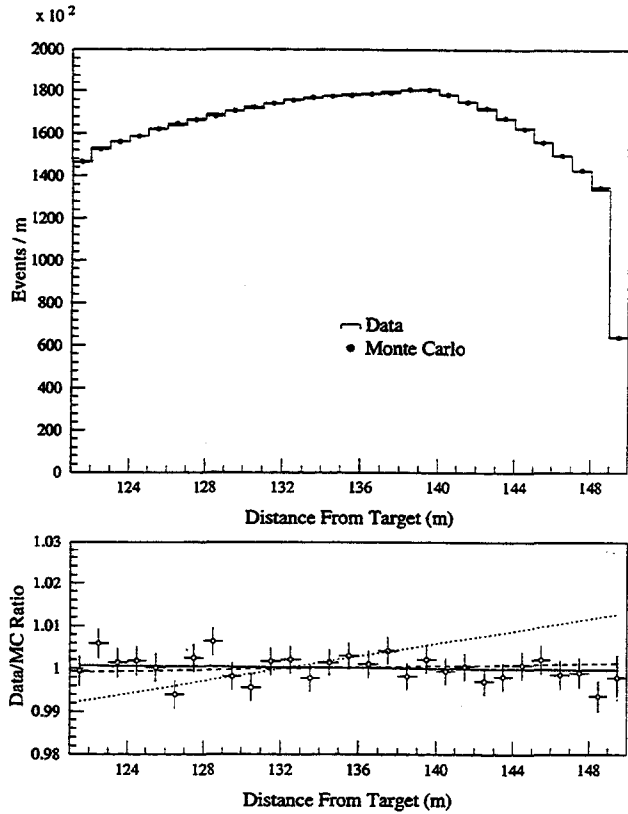
FIG. 86. The $z$ distribution for $3\pi^0$ decays in the data and Monte Carlo simulation after all other cuts. The sample shown had no lead sheet installed. Top: the $z$ distribution for the two event samples, with the simulation statistics normalized to the data statistics. Bottom: the ratio of data events to simulated events in each 1 m bin. The solid line is the best fit slope of $-0.0036\% \pm 0.0074\%$ per meter. The dashed line is the slope used for the systematic estimate, 0.074% per meter. The dotted line is the slope required to shift the final result for $\text{Re}(\varepsilon'/\varepsilon)$ by $10^{-3}$.

## VIII. FITTING PROCEDURES

We used two distinct fitting techniques in the analysis of $\pi\pi$ data sets. The first, refered to as the "constrained" fit, was used to determine the values of parameters which characterize the shape of the regenerator beam $z$ distribution: $\Delta m$, $\tau_S$, $\phi_{+-}$, and $\Delta\phi$. The vacuum beam data in each 10 GeV/$c$ bin, corrected for acceptance in a single, large-$z$ bin, was used to determine the incident flux. The second, "unconstrained" fit, was used for fitting $\text{Re}(\varepsilon'/\varepsilon)$. For the measurement of $\text{Re}(\varepsilon'/\varepsilon)$, it is the total number of decays in each beam, rather than their shape, that matters. Effectively, the incident kaon flux cancels when the ratio of the two beams is taken in each 10 GeV/$c$ momentum bin.

We now describe in detail how the prediction for either the number of events in a $pz$ bin in the regenerator beam or for the vacuum to regenerator beam ratio in a $p$ bin is determined.

### A. Functional and general fit procedure

A fit compares the observed number of events in bins of reconstructed kaon momentum $p$ and decay position $z$ in the vacuum and regenerator beams to the number expected, given a set of decay parameters. Suppose that for a $pz$ bin

L. K. GIBBONS *et al.*
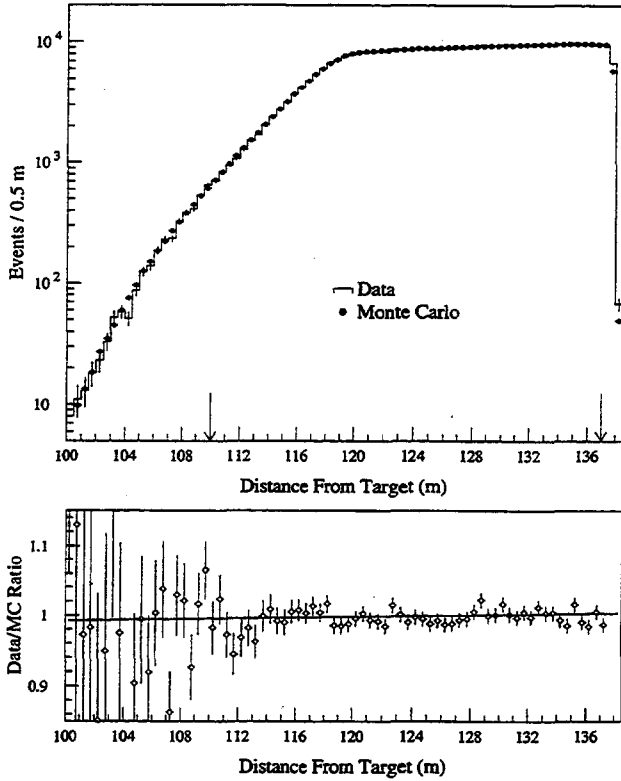


FIG. 87. The $z$ distribution for vacuum beam $\pi^+\pi^-$ decays in the data and Monte Carlo simulation after all other cuts. The sample shown is a portion of the NC subset. Top: the $z$ distribution for the two event samples, with the simulation statistics normalized to the data statistics. The arrows indicate the fiducial $z$ region used in the analysis. Bottom: the ratio of data events to simulated events in each 0.5 m bin. The solid line is the best fit slope of $0.025\% \pm 0.022\%$ per meter.

with the momentum range $p_i$ to $p_i + \Delta p$ and $z$ range $z_j$ to $z_j + \Delta z$, we observe $d_{ij}$ events in one of the beams. The number of events $d_{ij}$ is given by

$$d_{ij} = \int_{p_i}^{p_i + \Delta p} dp \int_{z_i}^{z_i + \Delta z} dz \int dp' \, F(p') \int dz'$$

$$\times s(p,z;p',z') \, a(p',z') \, r(p',z'). \qquad (74)$$

In this expression, the primed quantities $p'$ and $z'$ represent the true momentum and the true decay position. The function $F(p')$ is the flux of $K_L$ entering the decay volume with momentum $p'$. The detector acceptance and response functions are given by $a(p',z')$ and $s(p,z;p',z')$, respectively. The function $a(p',z')$ is the probability that a kaon of momentum $p'$ decaying at $z'$ reconstructs in the final sample, independent of what $p$ and $z$ are reconstructed. The function $s(p,z;p',z')$ incorporates all of the resolution and misreconstruction effects, giving the probability that a kaon with momentum in the range $p'$ to $p' + \delta p'$ and decaying in the range from $z'$ to $z' + \delta z'$ reconstructs in the ranges from $p$ to $p + \delta p$ and $z$ to $z + \delta z$.

All of the physics of the decay process is incorporated in Eq. (74) via the decay rate function $r(p',z')$. Each of these functions are discussed in detail after we treat the general fitting procedure.
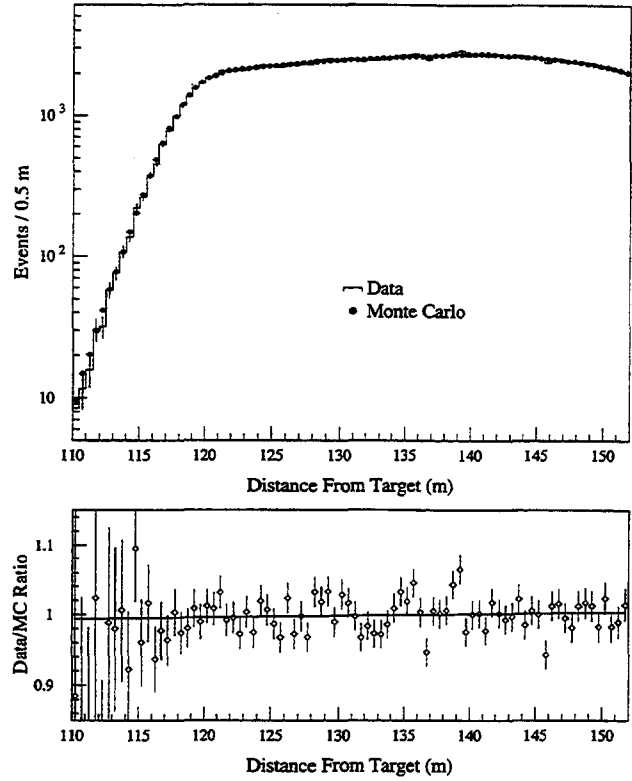
FIG. 88. The $z$ distribution for vacuum beam $2\pi^0$ decays after all other cuts from the data and simulation subsets with no lead sheet. Top: the $z$ distribution for the two event samples, with the simulation statistics normalized to the data statistics. Bottom: the ratio of data events to simulated events in each 0.5 m bin. The solid line is the best fit slope of $0.024\% \pm 0.028\%$ per meter.

### 1. General fitting procedures

*a. Binning.* In all fits, the momentum bins were 10 GeV/$c$ wide. For fits depending upon the shape of the decay distribution in a beam, we subdivided it into several $z$ regions; otherwise, a single $z$ bin was used.

In the fits, we used the rate in one beam either to constrain the incident kaon flux in the other beam or to predict the ratio of the rates in the two beams in each $pz$ bin. Were the incident kaon flux in the two beams identical, the decay rates in the vacuum and regenerator beams would be independent of the regenerator up or down position.

We now analyze the effect of slightly differing intensities for the two beams. Let the flux in the top beam be greater than that in the bottom beam, $I_t > I_b$. The trigger rate is dominated by (non-$\pi\pi$) kaon decays in the vacuum beam, and so it would be higher with the regenerator in the lower beam position, leading to a difference in the live times $L_u$ and $L_d$ for the up and down regenerator positions. The different intensities will lead to configuration-dependent accidental rates in the detector and hence a difference in the efficiency of reconstructing $\pi\pi$ decays for the two configurations. Let the fractional loss of events due to accidental activity be $(1 - \varepsilon_u)$ when the regenerator is up, and $(1 - \varepsilon_d)$ when the regenerator is down.

Finally, the relative number of decays collected in the two configurations depends on the fraction of time $f_d$ that the regenerator spends in the lower beam. The incident kaon flux in the top beam was about 8% higher than that in the bottom
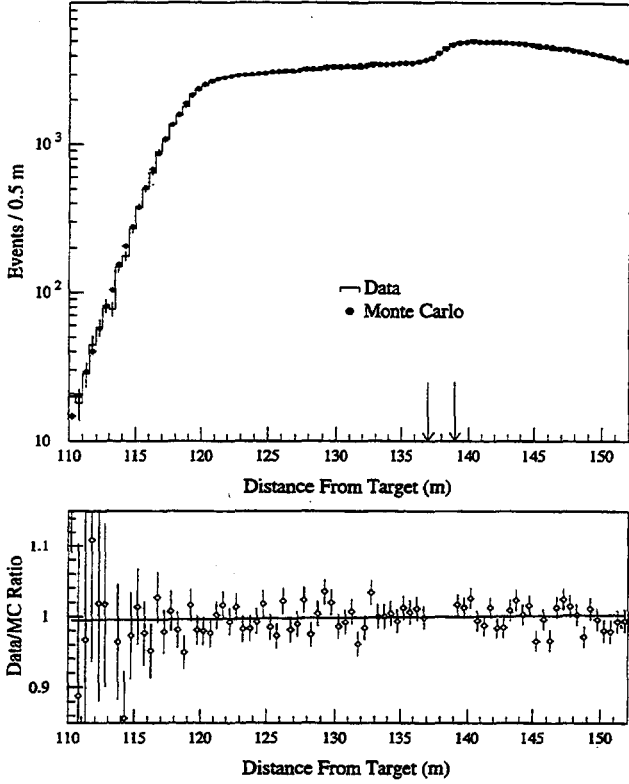
FIG. 89. The $z$ distribution for vacuum·beam $2\pi^0$ decays after all other cuts from the data and simulation subsets with the lead sheet. Top: the $z$ distribution for the two event samples, with the simulation statistics normalized to the data statistics. The arrows mark the region around the HDRA excluded from the fits. Bottom: the ratio of data events to simulated events in each 0.5 m bin. The solid line is the best fit slope of $0.018\% \pm 0.021\%$ per meter.

FIG. 90. The $z$ distribution for regenerator beam $\pi^+\pi^-$ decays after all other cuts for the data and Monte Carlo simulation. Top: the $z$ distribution for the two event samples, with the simulation statistics normalized to the data statistics. Bottom: the ratio of data events to simulated events in each 0.5 m bin. The solid line at one is for reference only.

beam, and $f_d$ differed from 50% by of order 1%, varying over the data sets.

Let $n_v$ $(n_r)$ be the probability for a kaon entering the decay region to decay and be reconstructed in a given $pz$ bin in the vacuum (regenerator) beam. Then the number of events we would collect for the regenerator sample in the top (bottom) beam would be $N_r^t = f_u L_u \varepsilon_u I_t n_r$ ($N_r^b = f_d L_d \varepsilon_d I_b n_r$), while for the vacuum beam we would have $N_v^t = f_d L_d \varepsilon_d I_t n_v$ ($N_v^b = f_u L_u \varepsilon_u I_b n_v$). The arithmetic mean of the data samples from the top and bottom beams gives

$$\frac{N_v^t + N_v^b}{N_r^t + N_r^b} = \frac{(f_d L_d \varepsilon_d I_t + f_u L_u \varepsilon_u I_b) n_v}{(f_u L_u \varepsilon_u I_t + f_d L_d \varepsilon_d I_b) n_r}. \quad (75)$$

In general, this differs from the "true" ratio $n_v/n_r$ that we need to obtain.

The factors depending on the different intensities of the two beams cancel in the geometric mean:

$$\frac{(N_v^t N_v^b)^{1/2}}{(N_r^t N_r^b)^{1/2}} = \frac{(f_d L_d \varepsilon_d I_t)^{1/2}(f_u L_u \varepsilon_u I_b)^{1/2} n_v}{(f_u L_u \varepsilon_u I_t)^{1/2}(f_d L_d \varepsilon_d I_b)^{1/2} n_r} = \frac{n_v}{n_r}. \quad (76)$$

We therefore combined the information from the two beams using the geometric mean.

We used the program MINUIT to perform $\chi^2$ minimizations.

b. *Unconstrained fitting.* The unconstrained fit was used to extract $\mathrm{Re}(\varepsilon'/\varepsilon)$. The data were binned in momentum only and the functional was used to predict the ratio $q = N_v/(N_r + N_v)$, in each momentum bin. The $\chi^2$ in this fit is then given by

$$\chi^2 = \sum_{i=1}^{n_p} \frac{(q_i - q_i')^2}{\sigma_i^2}, \quad (77)$$

where $n_p$ is the number of momentum bins, $q_i$ is the observed ratio, and $q_i'$ is the predicted ratio, containing the acceptance corrections to the decay rates in the two beams. The error $\sigma_i$ appearing in Eq. (77) is

$$\sigma_i^2 = \frac{q_i'(1 - q_i')}{N_{r_i} + N_{v_i}} + \sigma_{q_i'}^2, \quad (78)$$

where the first term is the binomial error on the predicted ratio and the second term is the error from the acceptance correction.

c. *Constrained fitting.* Here, the entire vacuum beam sample was used to predict the flux of kaons incident on the regenerator in each momentum bin by constraining the shape of the vacuum beam momentum spectrum. In the unconstrained fit, the regenerator beam was normalized to the vacuum beam in each individual momentum bin, which essentially allowed the kaon flux to float independently from momentum bin to momentum bin. The constrained technique
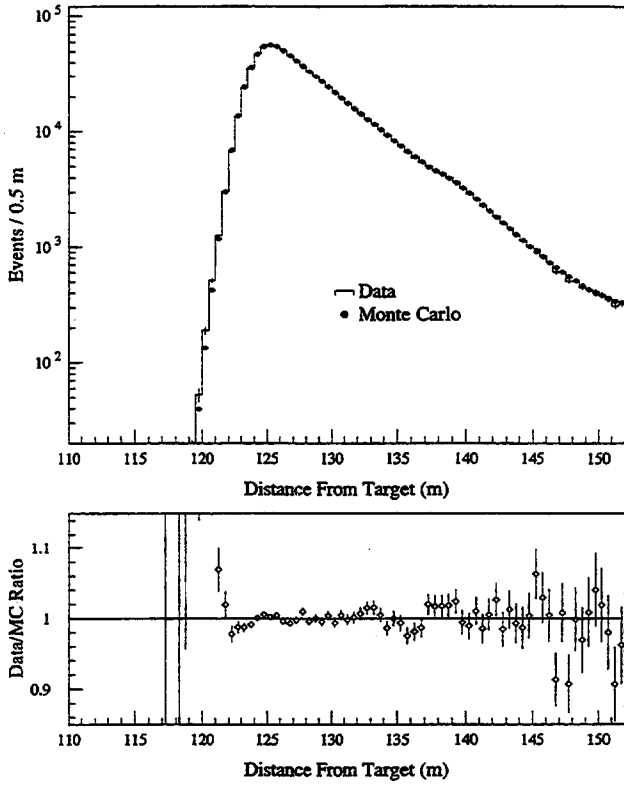
FIG. 91. The $z$ distribution for regenerator beam $2\pi^0$ decays after all other cuts for the data and simulation with the lead-sheet and no-lead-sheet subsets combined. Top: the $z$ distribution for the two event samples, with the simulation statistics normalized to the data statistics. *Bottom:* the ratio of data events to simulated events in each 0.5 m bin. The solid line at one is for reference only.

has the advantage of enhancing the sensitivity to the kaon parameters $\tau_S$, $\Delta m$, $\phi_{+-}$, and $\Delta\phi$. On the other hand, it depends on knowing the kaon energy spectrum well.

If the spectrum in the Monte Carlo simulation describes the data perfectly, then the normalization would be simple—we would simply fit for a scale factor $\alpha$ to make the number of vacuum beam decays in the data and Monte Carlo simulation match. However, there are small discrepancies between the kaon spectra in the data and Monte Carlo (Fig. 57) vacuum samples. We therefore include two additional parameters $\beta_1, \beta_2$ for a correction $c(p; \beta_1, \beta_2)$ to the Monte Carlo spectrum. If $F_{MC}(p)$ is the kaon spectrum in the Monte Carlo simulation, then the normalization factor $n_i$ for the $i$th momentum bin is given by

$$n_i = \alpha \frac{\int_{p_i}^{p_i + \Delta p} dp \; F_{MC}(p) \int_{z_u}^{z_d} dz \; r_v(p,z) \; c(p; \beta_1, \beta_2)}{\int_{p_i}^{p_i + \Delta p} dp \; F_{MC}(p) \int_{z_u}^{z_d} dz \; r_v(p,z)}, \tag{79}$$

where $r_v(p,z)$ is the vacuum beam decay rate and $z_u$ and $z_d$ are the upstream and downstream limits of the decay volume used for the normalization. We use both quadratic and piecewise linear correction functions.

There are two separate contributions to the total $\chi^2$ in this type of fit. The first one is the implementation of the vacuum beam constraint as a "soft" constraint through the term
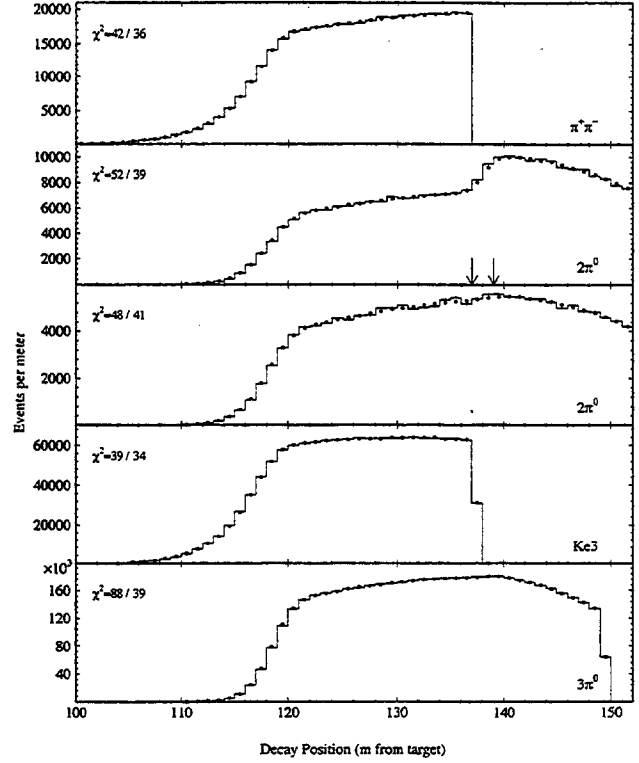
FIG. 92. Vacuum beam $z$ distributions in the data and Monte Carlo simulation for the $\pi^+\pi^-$, $2\pi^0$, $K_{e3}$, and $3\pi^0$ kaon decay modes. The two $2\pi^0$ subsets with and without the lead sheet are shown separately. The $\chi^2$ for the $z$ overlay is listed for each distribution. All other cuts have been applied. For the $3\pi^0$ overlay, 52 units of $\chi^2$ come from the four $z$ bins at 116–120 m, where the data are most sensitive to an energy scale mismatch. The arrows shown for the $2\pi^0$ lead-sheet subset indicate the $z$ region excluded from the analysis.

$$\chi^2_{constraint} = \sum_{i=1}^{n_p} \frac{(N_{v_i} - n_i D^{MC}_{v_i} \bar{\varepsilon}_{v_i})^2}{(1 + n_i) N_{v_i}}. \tag{80}$$

$N_{v_i}$ is the total number of vacuum beam events in the $i$th momentum bin in the data sample, while $D^{MC}_{v_i}$ is the total number of kaon decays, whether accepted or not, in the Monte Carlo sample. Here $\bar{\varepsilon}_{v_i}$ is the average vacuum beam acceptance for that momentum bin. The $n_i$ term in the denominator arises from the combination of statistical errors from $D^{MC}_{v_i}$ and $\bar{\varepsilon}_{v_i}$.

The functional for this type of fits was the expected number of accepted kaon decays, $N'_{r_{ij}}$, in a $pz$ bin of the regenerator beam. For the $i$th momentum bin and $j$th $z$ bin, we have

$$N'_{r_{ij}} = \frac{n_i D^{MC}_{v_i}}{d_{v_i}} p_{r_{ij}}. \tag{81}$$

Here $p_{r_{ij}}$ is the probability for this $pz$ bin of accepting a kaon decay in the regenerator beam, and $d_{v_i}$ is the probability of a kaon decaying in the vacuum beam in this momentum bin. The fraction on the right-hand side is simply the
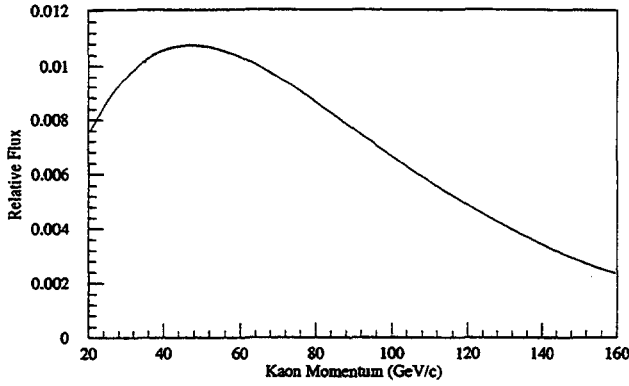
FIG. 93. Monte Carlo prediction for the momentum spectrum of kaons incident at $z = z_{reg}$ in the vacuum beam.

number of kaons incident on the regenerator beam. The total $\chi^2$ for a constrained fit is then

$$\chi^2 = \chi^2_{\text{constraint}} + \sum_{i=1}^{n_p} \sum_{j=1}^{n_z} \frac{(N_{r_{ij}} - N'_{r_{ij}})^2}{N'_{r_{ij}} + (N'_{r_{ij}} \sigma_{\bar{\varepsilon}_{r_{ij}}} / \bar{\varepsilon}_{r_{ij}})^2}. \quad (82)$$

### 2. Kaon flux F(p)

In both types of fits, the final results were quite insensitive to the exact shape of the kaon flux used in the functional approximating Eq. (74). What was more important was the difference in the $K_L$ flux between the vacuum and regenerator beams. There are small deviations of the regenerator beam flux shape from the vacuum shape because of kaon interactions with the additional material in the regenerator beam. The flux shape modifications due to kaon interactions in the common absorber were implicitly accommodated by the direct measurement of the vacuum beam $\pi^+\pi^-$ spectrum. The modifications to the regenerator beam spectrum arose from three distinct effects, primary $K_S \rightarrow K_L$ regeneration in the shadow absorber, elastic scattering in the shadow absorber, and the energy dependence of the kaon absorption in the shadow absorber and regenerator.

The spectrum of kaons predicted by our final Monte Carlo simulation to enter the decay volume in the vacuum beam is shown in Fig. 93. The corrections to the spectrum were small perturbations on this shape.

*a. Primary $K_S \rightarrow K_L$ regeneration.* Regeneration works both ways, and the primary $K_S \rightarrow K_L$ regeneration slightly modified the shape of the final $K_L$ spectrum incident on the regenerator. This effect was easily calculated; the relative shape change included was at most a few tenths of a percent.

*b. Kaon scattering in the absorbers.* Some kaons which elastically scattered in the shadow absorber remained in the beam and this effect is momentum dependent. The fraction was as large as 3% at the highest momentum and was readily included in the functional. While not affecting the extraction of $\text{Re}(\varepsilon'/\varepsilon)$, it was important to include this effect so as to obtain the proper regeneration power law.

Because of a small misalignment of the collimators, it was possible for a kaon to scatter, survive collimation, and miss the regenerator. The fraction of such incident kaons was at most 0.3% and was also included in the functional.

*c. Kaon absorption in the absorber and regenerator.* The final modification to the shape of the regenerator spectrum is due to the small energy dependence of the kaon-nucleus total cross section and, hence, of the kaon absorption in the shadow absorber and regenerator. The average transmission has been accurately measured by comparing the vacuum and regenerator beam samples in the $3\pi^0$ and $\pi^+\pi^-\pi^0$ modes. The measurements were made using kaons in the momentum range from 40 GeV/c to 150 GeV/c, and yielded $(6.33 \pm 0.03)\%$ for the $3\pi^0$ mode and $(6.43 \pm 0.06)\%$ for the $\pi^+\pi^-\pi^0$ mode. Combining these, we get average kaon transmission of $(6.35 \pm 0.03)\%$, but we need to incorporate the energy dependence.

The kaon-nucleon total cross sections are fairly well understood [55] and predictions are in good agreement with the measured energy dependence of the cross sections. The largest uncertainty in the calculation of the cross section is in the size of the correction due to inelastic screening. The uncertainty in the correction is estimated at 30% of itself.

Because of the small piece of lead at the end of the regenerator, we also need to know the total cross section for kaon-lead scattering. This cross section is well measured and predictions are again in good agreement with the measurements [55].

To implement the energy dependence of the absorption, the shape of the total cross section for carbon (given by a Glauber-Franco model) was scaled to boron-carbite and beryllium using the measured average cross sections. Because of the uncertainty in the inelastic screening correction, we introduce a correction parameter $\mu$ for each of the fits i.e., allowed it to float in the fit. The rise in the cross sections at high energy is roughly quadratic, and the correction is parametrized as a quadratic with the same minimum, having the form $\mu(p-56)^2$ [1]. The lead cross section (and its shape again from a Glauber-Franco model) is used without modification. The fits yield a small correction (up to 1.5%) to the kaon-carbon cross section of $-2.8 \pm 1.1$ mbarn at 156 GeV/c, to maintain the measured average cross section.

In summary, the kaon flux in the regenerator beam relative to the vacuum beam is given by

$$F_r(p) = \bar{t} F_v(p) c(p), \quad (83)$$

with the bulk of the difference incorporated in the average kaon transmission $\bar{t} = 6.35\%$ and $c(p)$ a small correction factor for momentum-dependent effects, of order 0.4% at our average kaon energy.

### B. Decay rates

All of the kaon physics in which we are interested is embodied in the $2\pi$ decay rates $r_v(p,z)$ and $r_r(p,z)$ for the vacuum beam and regenerator beam, respectively. For a pure $K_L$ beam, the $2\pi$ decay rate is given by

$$r_v(p,z) = \frac{dN_v}{dp \, dz} = |\eta_{+-(00)}|^2 e^{-(z-z_{reg})/\gamma\beta c \tau_L}, \quad (84)$$

where $\gamma\beta = p/m_K c^2$. The $K_L$ amplitude has been normalized to one at $z = z_{reg}$, the downstream end of the regenerator.

L. K. GIBBONS *et al.*

The $2\pi$ decay rate in the regenerator beam depends on the regeneration amplitude $\rho(p)$. For a pure incoming $K_L$, the regenerator beam decay rate is

$$r_r(p,z) = \frac{dN_r}{dp\,dz} = |\rho(p)|^2 e^{-(z-z_{reg})/\gamma\beta c\tau_S}$$

$$+ |\eta_{+-(00)}|^2 e^{-(z-z_{reg})/\gamma\beta c\tau_L}$$

$$+ 2|\rho(p)||\eta_{+-(00)}|\cos[\Delta m(z-z_{reg})/\gamma\beta c + \phi_\rho$$

$$- \phi_{+-(00)})]e^{-(z-z_{reg})/\gamma\beta c\tau_{av}}. \tag{85}$$

The quantity $\tau_{av}$ is defined by

$$\frac{1}{\tau_{av}} = \frac{1}{2}\left(\frac{1}{\tau_S} + \frac{1}{\tau_L}\right), \tag{86}$$

and $\phi_\rho = \arg(\rho)$. Recall that $|\rho/\eta|$ is of order 15, and so the $K_S$ decay term dominates the total decay rate.

We use the thick regeneration approximation, ignoring higher-order regeneration effects, such as the secondary regeneration of $K_S$ back to $K_L$, and the only normalization term in the regenerator beam relative to the vacuum beam is the kaon attenuation. This approximation gives the $K_S$ regeneration amplitude at the end of the regenerator as

$$\rho(p) = \iota\pi\gamma\beta cn\frac{f(0) - \bar{f}(0)}{k}\left(\frac{p}{70}\right)^\alpha g(L), \tag{87}$$

with

$$n = \frac{N_A d}{A}. \tag{88}$$

The parameters in the above expressions are defined as follows: $n$, density of scattering sites; $N_A$, Avogadro's number; $d$, density of the regenerator material; $A$, atomic number of the regenerator material; $f(0)$, $\bar{f}(0)$, $K^0$ and $\bar{K}^0$, forward scattering amplitude at 70 GeV/$c$; $k$, kaon wave number; $\alpha$, slope of momentum power-law dependence; and $g(L)$, geometric factor dependent on the length $L$ of the regenerator.

The function $g(L)$ is a complex geometric factor originating in the kaon propagation through the regenerator. It is given by

$$g(L) = \frac{1 - \exp[-L(1/2\tau_S - \iota\Delta m)/\gamma\beta c]}{(1/2\tau_S - \iota\Delta m)}. \tag{89}$$

In both the fitting program and Monte Carlo simulation, we actually use the full propagation treatment of the kaon amplitude through the regenerator [2]. [We have also used the thick regenerator approximation in fitting, and, for $\mathrm{Re}(\varepsilon'/\varepsilon)$, it gives identical results within $2\times10^{-5}$.] However, the important issues are more transparent in a discussion using the thick regenerator formulation.

In Eq. (87), we have explicitly incorporated the expected power-law momentum dependence of the difference of the $K^0$ and $\bar{K}^0$ forward scattering amplitudes:

$$\left|\frac{f(0) - \bar{f}(0)}{k}(p)\right| = \left|\frac{f(0) - \bar{f}(0)}{k}(70)\right|\left(\frac{p\ [\mathrm{GeV}/c]}{70}\right)^\alpha. \tag{90}$$

This dependence results from the difference in scattering being dominated by the exchange of the $\omega$ trajectory (see, for example, [34]).

To measure $\Delta m$ and $\phi_{+-}$, it is clear from Eq. (85) that we need to know the regeneration phase $\phi_\rho$. There are two contributions to this phase, $\phi_\rho = \pi/2 + \phi_g + \phi_{f-\bar{f}}$. The geometric phase $\phi_g \equiv \arg[g(L)]$ can be trivially calculated, which leaves the phase contribution from the forward scattering amplitude, $\phi_{f-\bar{f}} \equiv \arg\{[f(0) - \bar{f}(0)]/k\}$. Fortunately, the dispersion relations which result from requiring analytic behavior of the forward scattering amplitudes determine this phase. For a power-law dependence as in Eq. (90), the phase is related to the power-law slope $\alpha$ via

$$\phi_{f-\bar{f}} = -\frac{\pi}{2}(2+\alpha). \tag{91}$$

To calculate the regeneration amplitude, we need to take into account the compound structure of the regenerator. The regenerator consists of four separate blocks of boron-carbide of length $L_{B_4C} = 19.00$ cm separated by vacuum gaps of length $L_v = 3.75$ cm each. At the end of the regenerator is a piece of lead which is $L_{Pb} = 1.25$ cm thick. If $\rho_{B_4C}$ is the regeneration amplitude for one of the boron-carbide blocks and $\rho_{Pb}$ is that for the lead piece, then the total regeneration at the end of the regenerator is

$$\rho_{total} = \rho_{B_4C}[e^{-3(L_{B_4C}+L_v)\Lambda_S} + e^{-2(L_{B_4C}+L_v)\Lambda_S}$$

$$+ e^{-(L_{B_4C}+L_v)\Lambda_S} + 1]e^{-L_{Pb}\Lambda_S} + \rho_{Pb}, \tag{92}$$

with

$$\Lambda_S \equiv \frac{1}{\gamma\beta c}\left(\frac{1}{2\tau_S} - \iota\Delta m\right). \tag{93}$$

In each of our standard fits, the power-law dependence $\alpha_{B_4C}$ and scattering amplitude difference at 70 GeV/$c$, $|(f(0) - \bar{f}(0)/k)|_{70}$, for boron-carbide are parameters of the fit. The scattering phase for the boron-carbide is obtained from the analyticity relation [Eq. (91)]. For the parameters of lead we use the values obtained in a previous experiment [46]. The values of the regeneration parameters used in the fits are summarized in Table XVI. For typical values of the boron-carbide parameters, the lead piece accounts for 3.3% of the regeneration amplitude at 70 GeV/$c$.

These are the basic concepts that we implement in calculating the decay rates. There are two issues that complicate the fitting procedure beyond what we have discussed. The first complication involves the assumption made above that the beams arriving at the decay volume are pure $K_L$ beams. The second involves the modification of the decay rate to

TABLE XVI. Regeneration parameters for the boron-carbide and lead in the regenerator used in the fits. For the boron-carbide, values of regeneration parameters which float in the fitting are presented.

| Material | Atomic weight | Density $(g/cm^3)$ | $(f - \bar{f})/k$ (mbarn) | Power-law slope | Phase (deg) |
|---|---|---|---|---|---|
| $B_4C$ | 55.26 | 2.52 | 5.791[a] | −0.604[a] | − 125.6[b] |
| Pb | 207.19 | 11.35 | 9.71±0.14[c] | −0.654±0.018[d] | − 122.2±1.8[d] |

[a]Always extracted as a parameter in the fits. This is a typical value.
[b]Always obtained via analyticity from the current value of $\alpha_{B_4C}$ in the fits. This is a typical value.
[c]Value obtained using the data in [46], with a correction for the change in $\eta_{+-}$. The error includes the error quoted in [46] added in quadrature with the contribution from the uncertainty of $\eta_{+-}$.
[d]From [46]. Although the analyticity of lead is only good to a few degrees, the lead is only a small contribution here.

accommodate the material in the HDRA. The former affects all fits, while the latter affects only neutral mode data downstream of the HDRA.

### 1. Primary $K_S$ corrections

The absolute primary $K_S$ correction was small and easy to account for, as the largest fractional correction was only $10^{-4}$ at which we had the fewest data: the far upstream $z$ region and high kaon momentum. The fraction of the total number events in the momentum ranges from 40 GeV/$c$ to 160 GeV/$c$, and the $z$ range from 110 m to 137 m was corrected as a function of momentum and $z$. The total correction in the charged sample in this range is −0.62% (+0.0013%) for the vacuum (regenerator) beam sample. Almost half of the vacuum correction comes from the 160 GeV/$c$ momentum bin alone. For the same $z$ and $p$ range in the neutral sample. the correction is −0.14% (+0.0035%). The size of the correction is under 0.002% for both beams in the neutral sample downstream of 137 m.

Good checks are done when fitting for $\Delta m$ and $\tau_S$. We have found that fits using this correction technique in the Monte Carlo test samples yield the proper values of $\Delta m$ and $\tau_S$ to within 10% of the statistical precisions that we can obtain in this experiment. Fits to Re($\varepsilon'/\varepsilon$) are even less sensitive to this correction. with the level of discrepancy well below $10^{-5}$, when the values for $\Delta m$, $\tau_S$, and the $K^0$-$\bar{K}^0$ dilution factor are varied over ranges commensurate with their uncertainties.

### 2. Regeneration in the HDRA

In all of our fits involving the neutral mode, the data came from a $z$ region extending beyond the HDRA. For any portion of a $z$ bin upstream of the HDRA, the decay rate given

in the previous discussion is still correct. For the $z$ region downstream of the HDRA, however, the $K_S$ and $K_L$ amplitudes have to be modified to include regeneration and attenuation in the HDRA.

The components of the HDRA (see Table III) are very thin. To give an idea of the effect of the HDRA material on the measured parameters, if one neglected the regeneration, Re($\varepsilon'/\varepsilon$) would shift by $-4 \times 10^{-4}$. Since the physical properties of the material in the HDRA are known at the percent level, the uncertainty in Re($\varepsilon'/\varepsilon$) from the HDRA material is negligible.

The other measurements affected most in principle are the mass difference and phase measurements, which depend on the shape of the downstream decay distribution. For the typical kaon momentum of 70 GeV/$c$, the $K_S$ amplitude contributed from regeneration in the HDRA is under 2% of the $K_S$ amplitude from the regenerator propagated to the HDRA. In any of the fits, the regeneration parameters and thicknesses of the materials in the HDRA are known well enough that the uncertainty from the HDRA regeneration is negligible.

### C. Acceptance corrections

The last ingredient needed for our prediction functional is the acceptance. The physical parameters [$\Delta m$, $\tau_S$, $(f - \bar{f})/k$ for $B_4C$, etc.], used in the Monte Carlo simulation, were very close to the parameters derived in the final fit. The average acceptance over a certain range in momentum and $z$ is defined as the ratio of events *reconstructed* in this range to the number of actual decays in this range. In the terms of Eq. (74), the acceptance $\bar{\varepsilon}_{v(r)_{ij}}$ in the vacuum (regenerator) beam for the $pz$ bin starting at momentum $p_i$ and decay position $z_j$ is

$$\bar{\varepsilon}_{v(r)_{ij}} = \frac{\int_{p_i}^{p_i + \Delta p} dp \int_{z_i}^{z_i + \Delta z} dz \int dp' \ F_{v(r)}(p') \int dz' \ s(p,z;p',z') \ a(p',z') \ r_{v(r)}(p',z')}{\int_{p_i}^{p_i + \Delta p} dp' \ F_{v(r)}(p') \int_{z_i}^{z_i + \Delta z} dz' \ r_{v(r)}(p',z')}.$$

(94)

L. K. GIBBONS *et al.*
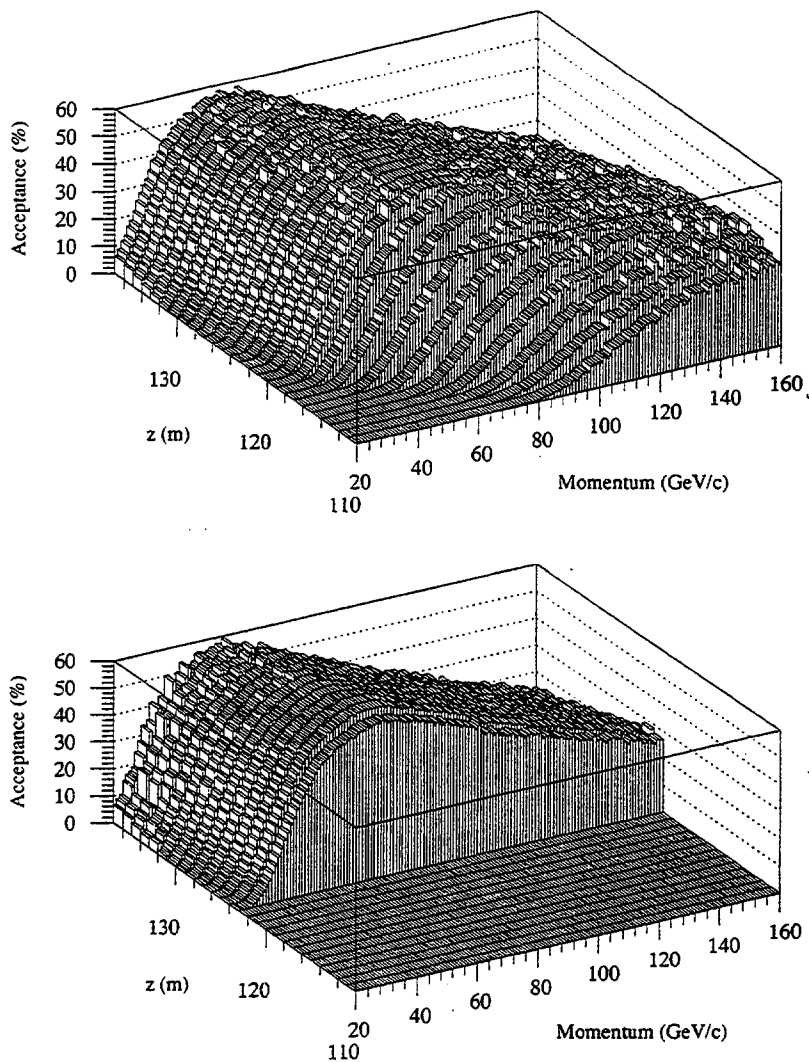


FIG. 94. Acceptance as a function of momentum and $z$ for $K \to \pi^+ \pi^-$ decays. The acceptance for the vacuum (regenerator) beam is the top (bottom) plot. The upstream acceptance in the vacuum beam is limited by the mask anti. The regenerator is located at 123.5 m.

As before, if the integration variables are unprimed, they refer to reconstructed quantities, and if primed, to true quantities.

The acceptances are shown for the two charged mode beams in Fig. 94 and the two neutral mode beams (no lead sheet) in Fig. 95. The bin sizes are 1 GeV/$c$ in momentum and 1 m (3 m) in $z$ in the charged (neutral) figure. On a $p$ and $z$ scale of 1 GeV/$c$ by 0.5 m, the vacuum and regenerator beam acceptances are nearly identical. Even at 20 GeV/$c$, where both the acceptance and decay distributions change most rapidly as a function of $p$ and $z$, the decay distribution is locally flat enough that the effect of smearing in and out of the bin is very similar in both beams.

The similarity of the vacuum and regenerator beam acceptances is demonstrated in Fig. 96, where the average acceptances as a function of $z$ in four different 10 GeV/$c$ momentum bins are shown. The regenerator and vacuum beam acceptances are noticeably different in the 20 GeV/$c$ momentum bin, slightly different at 40 GeV/$c$, and virtually identical above 60 GeV/$c$. These differences arise because the change in the decay rate across a 10 GeV/$c$ momentum bin is much larger in the regenerator beam than in the vacuum beam at the lowest momenta. Since the acceptance also varies quite rapidly across the lowest two momentum bins, the acceptance *weighted* by the decay rate is different in

the two beams. In the 20 GeV/$c$ and 40 GeV/$c$ bins, the regenerator beam acceptances from the Monte Carlo simulation have been overlaid with the acceptances predicted by weighting the vacuum acceptance calculated in 1 GeV/$c$ bins with the shape of the regenerator beam decay rate across the momentum bin; the agreement is excellent.

### D. Prediction functional

We have discussed all of the ingredients entering the prediction functional we used in our fits. We finish this section by mentioning a few additional small factors.

For $z$ bins which begin upstream of $z_{\text{reg}}$, the $z$ integral for the regenerator beam in the charged mode begins at $z = z_{\text{reg}}$. In the neutral mode, there is a small probability for all four of the photons to pass through the lead piece at the end of the regenerator without converting. The Monte Carlo simulation begins all decays at the downstream edge of the regenerator and we correct for this in the fit. The convolution of this survival probability with $K_S$ regeneration is easily calculated. The resulting rate corresponds to an effective increase in the decay volume of 1.8 mm; that is, the integral for a $z$ bin containing the regenerator begins at $z = z_{\text{reg}} - 0.0018$ for the neutral mode. The only fit using a $z$ region upstream of the regenerator is the fit for $\text{Re}(\varepsilon'/\varepsilon)$,

CP AND CPT SYMMETRY TESTS FROM THE TWO-PION ...
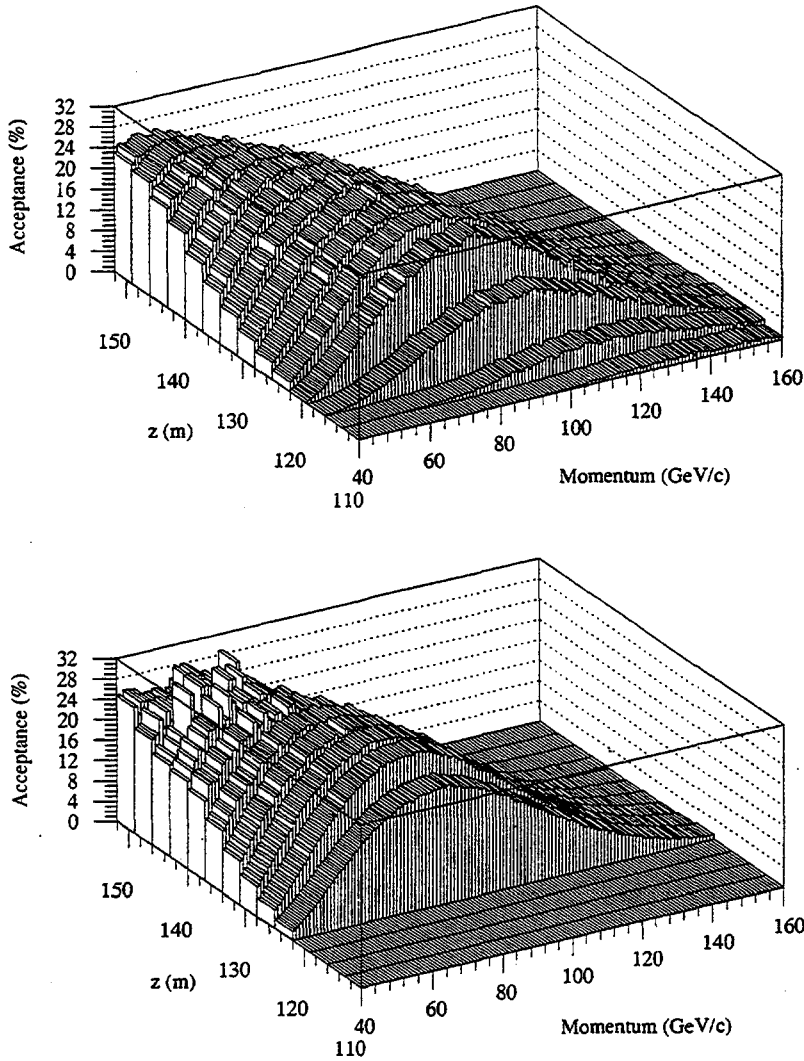


FIG. 95. Acceptance as a function of momentum and $z$ for $K \rightarrow \pi^0 \pi^0$ decays with the lead sheet removed. The acceptance for the vacuum (regenerator) beam is the top (bottom) plot. The upstream acceptance in the vacuum beam is limited by the mask anti. The regenerator is located at 123.5 m.

and the correction in this case shifts the final result by $\Delta \text{Re}(\varepsilon'/\varepsilon) = -0.8 \times 10^{-4}$.

In $z$, the average acceptance is calculated in the bin size used in the fit. Acceptances are calculated in 1 GeV/$c$ bins in momentum largely because the decay rate and acceptance vary fairly rapidly across the momentum range from 20 to 30 GeV/$c$ in the regenerator beam, and are sensitive to the values of $\Delta m$ and $\tau_S$. To avoid biases, we acceptance-correct the predicted decay rates on a scale insensitive to the fit parameters. No difference was found between fits using 1 GeV/$c$ and 0.5 GeV/$c$ bins for the acceptance correction.

Finally, because of the step introduced by photon conversions in the lead sheet in the middle of the decay volume, the two subsets were treated independently: For each $pz$ bin we obtained a prediction in each of the two subsets independently, and each subset added an independent contribution to the total $\chi^2$.

This ends the discussion of all of the details used in our fits to the $2\pi$ data samples. We now move on to discuss the results of the fits themselves.

## IX. RESULTS OF THE FITS

This section gives the final results for $\text{Re}(\varepsilon'/\varepsilon)$, the measurement for which this experiment was designed, and for $\Delta m$, $\tau_S$, $\Delta \phi$, and $\phi_{+-}$.

### A. Fitting for $\text{Re}(\varepsilon'/\varepsilon)$

In the fits for $\text{Re}(\varepsilon'/\varepsilon)$, the momentum range 40–160 GeV/$c$ was used for both charged and neutral samples.

We initially determined the power-law behavior in the individual subsets, performing unconstrained fits with $\text{Re}(\varepsilon'/\varepsilon)$ fixed at zero. The three parameters for which we fit in all cases are $[f(0) - \bar{f}(0)]/k$ at 70 GeV/$c$ (which we call $\Delta f|_{70}$), the regeneration slope $\alpha$, and the cross section correction $\mu$. One fit was to the entire charged sample one to the entire neutral sample, and to the two individual neutral subsets. For the charged mode fits, the $z$ range used was 110–137 m, and for the neutral fits, the range was 110–152 m.

Since $\text{Re}(\varepsilon'/\varepsilon)$ is fixed at zero in these fits, a nonzero value for $\text{Re}(\varepsilon'/\varepsilon)$ would force $\rho$ away from its true value, and shift $\Delta f|_{70}$. Since $\varepsilon'$ shifts $\eta_{+-}$ and $\eta_{00}$ in opposite directions, we would see a shift in $\Delta f|_{70}$ in the charged and neutral fits. On the other hand, the measured power $\alpha$ should not be biased. Only one regenerator was used so the same power $\alpha$ should be measured in all subsets.

The results of these fits are summarized in Table XVII and in Fig. 97. The $\chi^2$ for each fit is excellent, as is the agreement in the powers. From the figure, it is clear that $\text{Re}(\varepsilon'/\varepsilon)$ is small. The fractional deviations from a common power (a simultaneous fit to the $\pi^+ \pi^-$ and $2\pi^0$ data) show no obvious bias vs momentum.
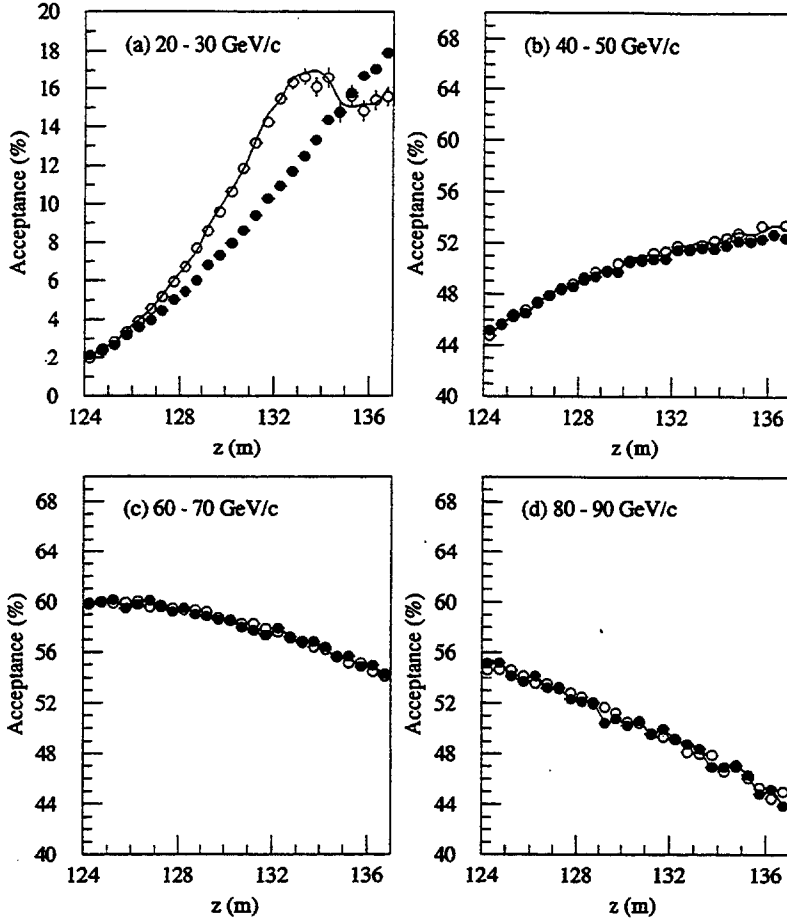
FIG. 96. The $\pi^+\pi^-$ acceptance as a function of $z$ in four of the 10 GeV/$c$ momentum bins. The vacuum (regenerator) acceptance is shown as solid (open) circles. The lines are the regenerator beam acceptances predicted by weighting the vacuum beam acceptances in 1 GeV/$c$ momentum bins with the regenerator beam decay rates.

We fit the charged and neutral data simultaneously to extract $\text{Re}(\varepsilon'/\varepsilon)$ with common regeneration and absorption parameters. The result is

$$\text{Re}(\varepsilon'/\varepsilon) = [7.4 \pm 5.2(\text{stat})] \times 10^{-4}, \qquad (95)$$

with a $\chi^2$ of 26 for 32 degrees of freedom. The remaining parameters are listed in Table XVII. The $\chi^2$ contours for $\text{Re}(\varepsilon'/\varepsilon)$ versus each of the three other parameters are well behaved as shown in Fig. 98.

The values of the fixed parameters, their precision, and influence on $\text{Re}(\varepsilon'/\varepsilon)$ in the fit are listed in Table XVIII. It is clear that $\text{Re}(\varepsilon'/\varepsilon)$ is quite insensitive to these parameters. We used values of $\Delta m$ and $\tau_S$ obtained from our data (see Sec. IX B), comparable in precision to current world averages. For $|\varepsilon|$, we used the Particle Data Group average of $|\eta_{+-}|$ [30]. Also $CPT$ symmetry is implicit in our use of the natural phase [9,3] for the phase of $\varepsilon$, $\phi_\varepsilon = \tan^{-1}[2\Delta m/(\Gamma_S - \Gamma_L)]$. The phase of $\varepsilon'$ is derived from the $\pi\pi$ phase shift analysis of Ochs [16].

As a final check, we relax the power-law assumption for the momentum dependence of $[f(0) - \bar{f}(0)]/k$, and fit for $\text{Re}(\varepsilon'/\varepsilon)$ and the regeneration amplitude in each momentum bin. $\text{Re}(\varepsilon'/\varepsilon)$ as a function of momentum is shown in Fig. 99. The average from these fits is only $0.15 \times 10^{-4}$ larger than the "standard" fit.

Measuring $\text{Re}(\varepsilon'/\varepsilon)$ by taking the momentum bin average has the advantage of being insensitive to the energy dependence of the absorption cross section. In tests of the fit-

TABLE XVII. Results of the unconstrained fits used to determine $\text{Re}(\varepsilon'/\varepsilon)$ which is fixed at 0 in the first four fits to the charged and neutral subsets so that the regeneration parameters from these sets may be compared. The cross section correction is quoted in terms of the correction to the carbon cross section at 156 GeV/$c$.

| Fit | $\text{Re}(\varepsilon'/\varepsilon)$ ($\times 10^{-4}$) | $\Delta f\|_{70}$ (mbarn) | $\alpha$ | $\Delta\sigma_T$ (mbarn) | $\chi^2/N_{DF}$ |
|---|---|---|---|---|---|
| $\pi^+\pi^-$ | 0[a] | $5.786 \pm 0.008$ | $-0.605 \pm 0.007$ | $-3.1 \pm 1.4$ | 8.9/9 |
| $2\pi^0$(Pb Sheet) | 0[a] | $5.799 \pm 0.009$ | $-0.598 \pm 0.010$ | $-2.4 \pm 2.8$ | 8.2/9 |
| $2\pi^0$(No Pb Sheet) | 0[a] | $5.801 \pm 0.011$ | $-0.609 \pm 0.011$ | $-1.8 \pm 3.2$ | 6.2/9 |
| $2\pi^0$(Combined) | 0[a] | $5.800 \pm 0.007$ | $-0.603 \pm 0.007$ | $-2.1 \pm 2.1$ | 16.8/21 |
| Simultaneous $\pi^+\pi^-$ and $2\pi^0$ | $7.4 \pm 5.2$ | $5.791 \pm 0.005$ | $-0.604 \pm 0.005$ | $-2.8 \pm 1.1$ | 25.8/32 |

[a]Fixed at this value for this fit.

*CP* AND *CPT* SYMMETRY TESTS FROM THE TWO-PION ...



FIG. 97. Regeneration amplitude versus kaon momentum. (a) The average amplitude in each momentum bin for the $\pi^+\pi^-$ (open circles) and $2\pi^0$ (open squares) data. The solid line is the best fit power to the $\pi^+\pi^-$ data. The best fit power for the $2\pi^0$ data is just visible as a dashed line above the $\pi^+\pi^-$ power. (b),(c) The fractional deviation of the average amplitude in each momentum bin from the simultaneous fit to the $\pi^+\pi^-$ and $2\pi^0$ data. The line is the average deviation.



FIG. 98. Contours of equal $\chi^2$ in the fit for $\mathrm{Re}(\varepsilon'/\varepsilon)$. The contours are plotted in steps of 1/2 standard deviations. (a) $[f(0)-\bar{f}(0)]/k|_{70\,\mathrm{GeV}/c}$ versus $\mathrm{Re}(\varepsilon'/\varepsilon)$. (b) $\alpha$ versus $\mathrm{Re}(\varepsilon'/\varepsilon)$. (c) Kaon-carbon total cross-section correction parameter (at 156 GeV/c) versus $\mathrm{Re}(\varepsilon'/\varepsilon)$.

ting procedure, the observed sensitivity to the energy dependence of the absorption cross section was an order of magnitude smaller for the bin average than for the power law fit. For this result, the power law constraint does not increase the statistical sensitivity; we report the value using the power law for consistency with the remaining fits that rely more heavily on the power law to obtain the regeneration phase.

### 1. Re(ε'/ε) and accidental biases

While the double-beam technique leads to a cancellation of accidental effects to first order, there are second-order effects that could potentially bias the result. The determination of such effects, using random triggers overlaid on Monte Carlo $\pi\pi$ decays, is detailed in the next section. Here we present the results.

In the charged mode sample, the highest-intensity subset was NC subset. Here the change in the vacuum to regenerator ratio was $-0.04\%\pm0.07\%$, consistent with zero. We therefore made no correction in the charged sample.

In the highest-intensity neutral samples, accidentals do introduce a shift in the relative vacuum and regenerator beam acceptances. The correction is $-0.17\%(-0.15\%)\pm0.06\%$ for the high intensity subsets with (without) the lead sheet. We can compare this result to the accidental study in the

lower-intensity NC subset presented in Ref. [36] by scaling the high-intensity result by the ratio of intensities. This scaling implies we should have a correction in the NC subset of $-0.06\%$, consistent with [36], where a correction of $-0.04\%\pm0.07\%$ was found. When the high- and low-intensity accidental corrections are applied, the final result for $\mathrm{Re}(\varepsilon'/\varepsilon)$ shifts by $\Delta\mathrm{Re}(\varepsilon'/\varepsilon)=+2.5\times10^{-4}$. This correction has already been made in the fits presented in the previous section.

### 2. Summary of Re(ε'/ε) fit results

The value extracted for $\mathrm{Re}(\varepsilon'/\varepsilon)$ from our entire data sample is $\mathrm{Re}(\varepsilon'/\varepsilon)=(7.4\pm5.2)\times10^{-4}$. This is the result from the power-law fit, and it includes the very small corrections for both accidental biases and for photons which do not convert within the regenerator.

We have also refit the data subset used to obtain our previously published value [21] of $\mathrm{Re}(\varepsilon'/\varepsilon)=(-4\pm14\pm6)\times10^{-4}$. There were many improvements in analysis, Monte Carlo simulation, and fitting technique since that publication. The systematic error for that result was dominated by uncertainty in the energy scale, and as Figs. 21 and 26 demonstrate, our understanding has improved substantially. The new central value for this subset is $-2.4\times10^{-4}$; the shift is well within the systematic uncertainty, and indicates the robustness of the technique.

TABLE XVIII. Variation of the extracted value for $\text{Re}(\varepsilon'/\varepsilon)$ with the values of physical constants in the fit. The units assumed for each of the constants is given in square brackets in the first column. Here $\Delta\text{Re}(\varepsilon'/\varepsilon)$ is the change in $\text{Re}(\varepsilon'/\varepsilon)$ for an increase in the constant by one standard deviation. The correction to $\text{Re}(\varepsilon'/\varepsilon)$ as a function of the physical constants is presented in the last column.

| Parameter | Value | Error | $10^4 \times \Delta\text{Re}(\varepsilon'/\varepsilon)$ ($+1\sigma$ variation) | $10^4 \times \text{Re}(\varepsilon'/\varepsilon)$ dependence |
|---|---|---|---|---|
| $\Delta m\ [10^{10}\hbar\ \text{s}^{-1}]$ | 0.5286 | 0.0028 | $+0.41$ | $77.2\left(\dfrac{\Delta m - 0.5286}{0.5286}\right)$ |
| $\tau_S\ [10^{-10}\ \text{s}]$ | 0.8929 | 0.0016 | $-0.26$ | $-147\left(\dfrac{\tau_S - 0.8929}{0.8929}\right)$ |
| $\tau_L\ [10^{-8}\ \text{s}]$ | 5.17 | 0.004 | $+0.05$ | $5.8\left(\dfrac{\tau_L - 5.17}{5.17}\right)$ |
| $|\varepsilon|\,[10^{-3}]$ | 2.279 | 0.022 | $-0.11$ | $-11.4\left(\dfrac{|\varepsilon| - 2.279}{2.279}\right)$ |
| $\phi_\varepsilon$ | 43.4° | 0.2° | $-0.15$ | $-0.75(\phi_\varepsilon - 43.4°)$ |
| $\phi_{\varepsilon'}$ | 47° | 6° | $-0.11$ | $-0.018(\phi_{\varepsilon'} - 47°)$ |

This ends the discussion of the fit for $\text{Re}(\varepsilon'/\varepsilon)$. The systematic evaluation is treated after we give the results of the constrained fits for the other kaon parameters.

### B. $\Delta m$ and $\tau_S$ fits

In fitting for $\Delta m$ and $\tau_S$, we extract values for the charged and neutral mode data separately.

The fits assumed no direct $CP$ violation: $\text{Re}(\varepsilon'/\varepsilon)=0$. We also assumed $CPT$ symmetry by using the natural phase $\tan^{-1}[2\Delta m/(\Gamma_S-\Gamma_L)]$ for the phase of $\varepsilon$. For $|\varepsilon|$, we use the same value as in the $\text{Re}(\varepsilon'/\varepsilon)$ fits (see Table XVIII). Then $\Delta m$, $\tau_S$, $\Delta f|_{70}$, and $\alpha$ are the parameters to be fit. In addition, there are three vacuum beam constraint parameters and the cross-section correction parameter (Sec. VIII A 1). The charged sample and two neutral samples have separate constraint parameters to allow for flux variations from set to set.
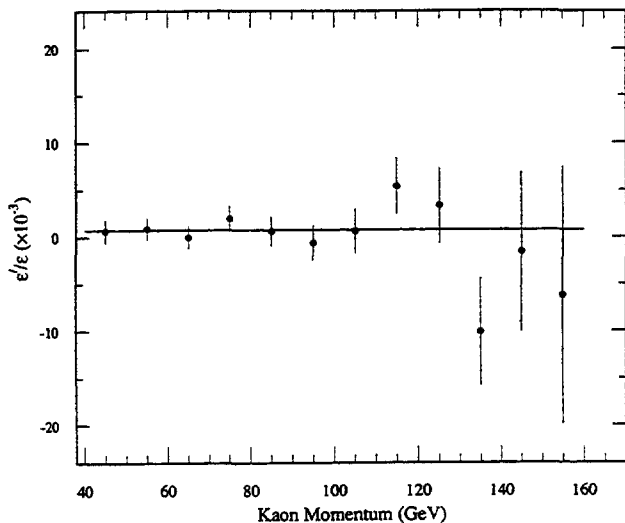


FIG. 99. Momentum dependence of $\text{Re}(\varepsilon'/\varepsilon)$. The values of $\text{Re}(\varepsilon'/\varepsilon)$ in each momentum bin (dots) have been determined independently, with no regeneration power-law constraint. The line is the weighted average of the points.

From Monte Carlo studies, we have found that systematic biases in the measurement of $\Delta m$ and $\tau_S$ are exacerbated when trying to use the $z$ region including the regenerator edge. Thus we use only the $z$ region in the regenerator beam downstream of 124.5 m (125 m) in the charged (neutral) mode fits.

The $z$ bin sizes used for these fits were chosen to be commensurate with the $z$ resolution of the individual mode. For $\pi^+\pi^-$ decays, the $z$ resolution varied from 10 cm (downstream) to 25 cm (upstream), and so the $z$ bin sizes used in the fits were at least 1 m. For the neutral mode, the resolution was closer to 1 m, and so the $z$ bins used in the fit were at least 2 m.

For increased sensitivity, the charged mode fits began at 20 GeV/$c$. This has systematic ramifications because the momentum dependence of $(f-\bar{f})/k$ may begin to deviate from a pure power law—increasing the uncertainty in the associated regeneration phase—and the decay rate, acceptance, and incident kaon flux all vary rapidly in the 20–30 GeV/$c$ range. This latter problem is most severe at the downstream end of the $\pi^+\pi^-$ decay volume, and for this reason, the $z$ range was restricted to 135 m in the charged mode fits. In spite of these limitations, the overall sensitivity was enhanced by using lower-momentum events.

The lower limit of the momentum range used in the neutral mode is limited by the $E_T$ trigger threshold, and so the fits again used 40–160 GeV/$c$. Even so, the extended $z$ range available in the $2\pi^0$ mode resulted in the $2\pi^0$ sample yielding the best statistical precision.

A summary of the results for the two modes with different binnings is shown in Table XIX. For $\Delta m$ in the charged mode, we average the values for the two binnings, giving $\Delta m = (0.5311\pm0.0044)\times10^{10}\hbar\ \text{s}^{-1}$. For $\tau_S$ in the charged mode, we find $\tau_S = (0.8952\pm0.0015)\times10^{-10}$ s. The results from neutral fits with 2 m and 3 m binnings were close, and we take the 3 m results, this binning being better matched to the 1 m resolution. The two neutral subsets give consistent results. The combined average values for $\Delta m$ and $\tau_S$ are then $\Delta m = (0.5286\pm0.0025)\times10^{10}\hbar\ \text{s}^{-1}$ and $\tau_S = (0.8929\pm0.0011)\times10^{-10}$ s with statistical error only. Be-

CP AND CPT SYMMETRY TESTS FROM THE TWO-PION ...

TABLE XIX. Summary of fits for $\Delta m$ and $\tau_S$ for both the $\pi^+\pi^-$ and $2\pi^0$ modes. Numbers in parentheses are the statistical errors to the least significant figure.

| Sample | $z$ bin size | $\Delta m$ $(10^{10}\hbar\ s^{-1})$ | $\tau_S$ $(10^{-10}\ s)$ | $\Delta f\|_{70}$ (mbarn) | $\alpha$ | $\chi^2/N_{DF}$ |
|---|---|---|---|---|---|---|
| $\pi^+\pi^-$ | 1 m | 0.5302(44) | 0.8952(15) | 5.774(9) | $-0.590(3)$ | 157/160 |
| $\pi^+\pi^-$ | 2 m | 0.5319(45) | 0.8953(15) | 5.773(9) | $-0.590(3)$ | 92/90 |
| $2\pi^0_{all}$ | 2 m | 0.5277(30) | 0.8911(16) | 5.804(11) | $-0.602(7)$ | 335/302 |
| $2\pi^0_{all}$ | 3 m | 0.5274(30) | 0.8912(17) | 5.802(11) | $-0.603(7)$ | 221/203 |
| $2\pi^0_{Pb}$ | 3 m | 0.5289(39) | 0.8904(22) | 5.803(15) | $-0.604(10)$ | 118/99 |
| $2\pi^0_{no\ Pb}$ | 3 m | 0.5251(47) | 0.8920(25) | 5.803(17) | $-0.601(11)$ | 100/99 |

fore the charged and neutral mode results can be compared directly, however, the systematic contributions must be determined.

The absorption correction parameters obtained in these fits were consistent with those in the $Re(\varepsilon'/\varepsilon)$ fits. As for the shape corrections to the Monte Carlo vacuum flux, the neutral mode needed no correction while charged data preferred the flux at the extremes of the momentum range to be several percent lower than in the center, consistent with overlays given in the previous section.

Elliptical $\chi^2$ contours showing correlations between the most important parameters of the fit are given in Fig. 100 for charged and Fig. 101 for neutral modes.

The values of $\tau_S$ and $\Delta m$ are insensitive to most of the fixed parameters in the fit. The one exception is the phase of $\phi_{+-}$; for $\tau_S$, this variation is $-0.09\%$/deg, and for $\Delta m$, it is $+0.59\%$/deg.

Fixing $\tau_S$ and the regeneration, absorption, and flux parameters at the values from one of the above fits, one can extract the average value of the cosine term in Eq. (85) in each $pz$ bin. Similarly, by fixing $\Delta m$ one can extract the average value of the $K_S$ decay term. We have done this in both the neutral and charge data using 1 m by 10 GeV/$c$ bins. The results (choosing kaon momenta under 90 GeV/$c$) are plotted against the average proper time for that bin in Figs. 102 (charged mode) and 103 (neutral mode). The proper
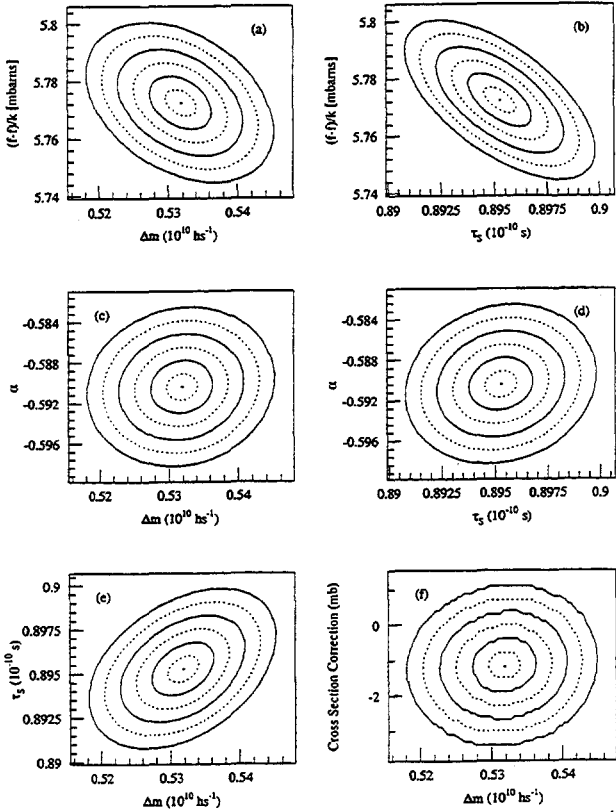


FIG. 100. Contours of equal $\chi^2$ in 1/2 standard deviation intervals in the fit (with 2 m bins) for $\Delta m$ and $\tau_S$ to the $\pi^+\pi^-$ data. (a) $\Delta f\|_{70}$ versus $\Delta m$. (b) $\Delta f\|_{70}$ versus $\tau_S$. (c) Power-law slope $\alpha$ versus $\Delta m$. (d) Power-law slope $\alpha$ versus $\tau_S$. (e) $\tau_S$ versus $\Delta m$. (f) Kaon-carbon cross-section correction (at 156 GeV/$c$) versus $\Delta m$.
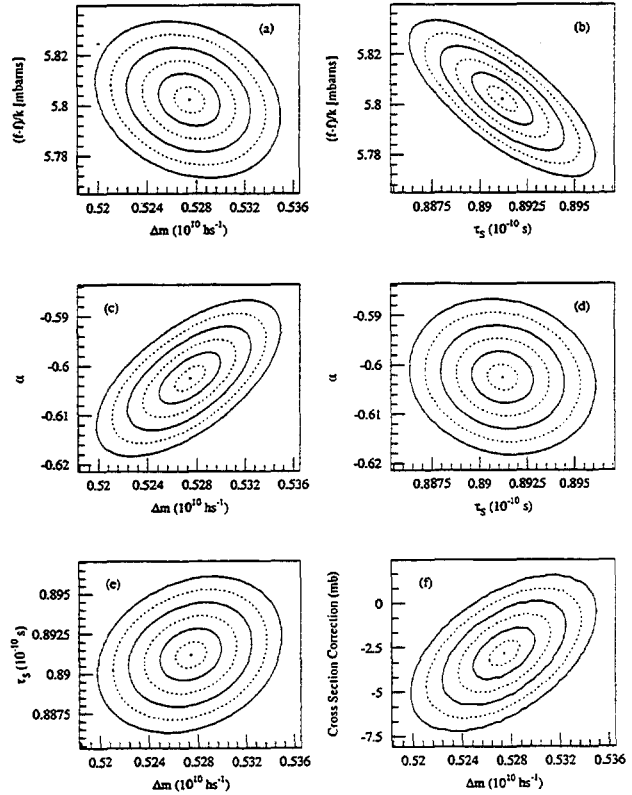
FIG. 101. Contours of equal $\chi^2$ in 1/2 standard deviation intervals in the fit for $\Delta m$ and $\tau_S$ to the $2\pi^0$ data. (a) $\Delta f\|_{70}$ versus $\Delta m$. (b) $\Delta f\|_{70}$ versus $\tau_S$. (c) Power-law slope $\alpha$ versus $\Delta m$. (d) Power-law slope $\alpha$ versus $\tau_S$. (e) $\tau_S$ versus $\Delta m$. (f) Kaon-carbon cross-section correction (at 156 GeV/$c$) versus $\Delta m$.

L. K. GIBBONS *et al.*
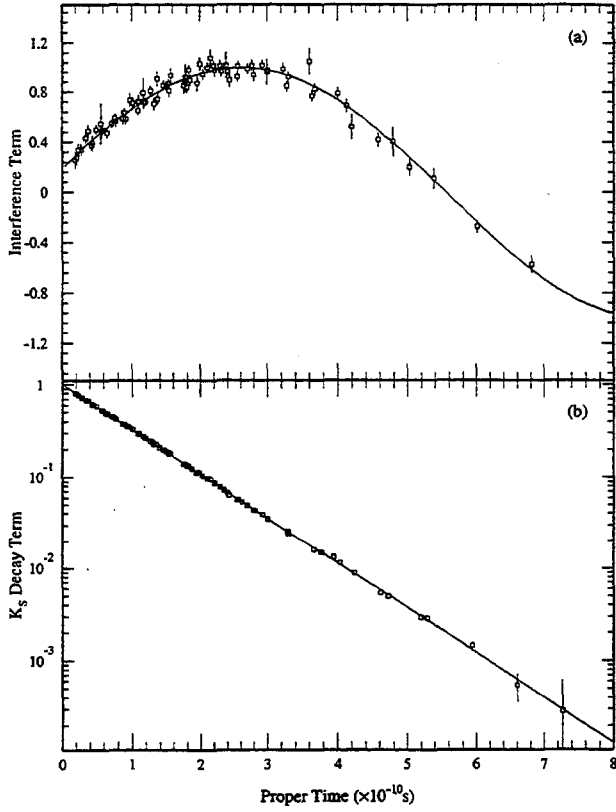


FIG. 102. The interference and $K_S$ decay curves measured for $\pi^+\pi^-$ decays with momentum under 90 GeV/$c$. (a) The interference versus the proper time in 1 m by 10 GeV/$c$ bins. (b) The $K_S$ decay term versus proper time. Both measured at the center of the 1 m by 10 GeV/$c$ bin. The $\Delta m$ and $\tau_S$ results from the grand fit to the $\pi^+\pi^-$ data are shown as the curves.

time $\tau = 0$ corresponds to the downstream face of the regenerator.

## C. Extracting the phases

The fitting methods used to extract $\Delta\phi$ and $\phi_{+-}$ are in essence identical to those used to extract $\Delta m$ and $\tau_S$. We need to measure the intercept of the interference curve at proper time $\tau = 0$. The value of the intercept for $\pi^+\pi^-$ ($2\pi^0$) decays is $\cos(\phi_\rho - \phi_{+-(00)})$. The regeneration phase $\phi_\rho$ cancels when comparing the two modes. To isolate $\phi_{+-}$, however, we must use analyticity to obtain the regeneration phase.

In extracting the phases, we make no assumptions regarding either $CPT$ or $CP$ symmetry—Re$(\varepsilon'/\varepsilon)$, $\Delta\phi$, and $\phi_{+-}$ all float. The $z$ and momentum ranges are the same as those used in the $\Delta m$ and $\tau_S$ fits. In the fit for $\Delta\phi$, $\Delta m$, and $\tau_S$ are fixed to the average values reported in Sec. IX B. Since we assumed that $\phi_{+-}$ had its natural value of $\tan^{-1}(2\Delta m/[\Gamma_S - \Gamma_L])$ in obtaining $\Delta m$ and $\tau_S$, we then should not use those $\Delta m$ and $\tau_S$ values to obtain $\phi_{+-}$ because of the inherent bias in the assumption of $CPT$. We set $\tau_S$ to the world average of $0.8922 \times 10^{-10}$ s [30] and float $\Delta m$ in the $\phi_{+-}$ fits.

We extracted $\Delta\phi$ using different bin sizes. The results are summarized in Table XX. The fits using the 1 m and 2 m bins again show a small shift, and we again average them,

obtaining $\Delta\phi = -1.6° \pm 1.0°$. The dependence on $\Delta m$ and $\tau_S$ is given by

$$\Delta\phi = -1.6° \pm \left( 190° \frac{\tau_S \times 10^{10} \text{ s} - 0.8929}{0.8929} \right.$$
$$\left. + 32° \frac{\Delta m \times 10^{-10} \hbar^{-1} \text{ s} - 0.5286}{0.5286} \right). \quad (96)$$

The results of the fit for $\phi_{+-}$ with $\Delta m$ as an additional parameter are also summarized in Table XX. The value of $\Delta m = (0.5257 \pm 0.0049) \times 10^{10} \hbar$ s$^{-1}$ obtained in this fit is consistent with the earlier results.

In both fits, Re$(\varepsilon'/\varepsilon)$ is consistent with the result of the unconstrained fit, but since these fits begin downstream of the regenerator, there would be large systematics coming from resolution smearing.

The $\chi^2$ contours of $\Delta\phi$ and $\phi_{+-}$ versus several of the other parameters are graphed in Figs. 104 and 105, respectively.

### 1. Analyticity check

Analyticity, Eq. (91), has been checked before using regenerators of different materials [32,56]. Of course $\phi_{+-}$ must be taken from elsewhere. The measured regeneration phases agreed with the analyticity prediction, Eq. (91), within errors of order $1°-2°$ from the measurment of the power-law slope $\alpha$.

We extract the regeneration phase $\phi_{f-\bar{f}}$ directly using a technique similar to that used in extracting $\Delta m$ and $\tau_S$. The regeneration phase becomes an independent parameter of the fit, with $\Delta m$ and $\tau_S$ fixed, and we fit the $\pi^+\pi^-$ and $2\pi^0$ data simultaneously. The fit results using our own value for $\Delta m$ or the world average $\Delta m$ are summarized in Table XXI. Using our own $\Delta m$, the uncertainty in $\Delta m$ corresponds to an additional uncertainty in $\phi_{f-\bar{f}}$ of $0.71°$. Using the world average, the uncertainty in $\Delta m$ corresponds to an uncertainty in $\phi_{f-\bar{f}}$ of $0.61°$. Adding these in quadrature with the statistical uncertainties on $\alpha$ and $\phi_{f-\bar{f}}$, the predicted and measured phases agree to within an uncertainty of $0.9°$. With $\Delta m$ floating, the phases agree within $1.3°$.

The regenerator used in Ref. [56] was carbon, and we expect it and boron-carbide to have similar power laws. The regeneration phase in that experiment was $-124.7° \pm 1.7°$, in good agreement with the values shown in Table XXI.

### D. Summary of the fit results

The results of the physics measurements of interest, with statistical errors only, are given below:

$$\text{Re}(\varepsilon'/\varepsilon) = (7.4 \pm 5.2) \times 10^{-4},$$

$$\Delta m_{+-} = (0.5311 \pm 0.0044) \times 10^{10} \hbar \text{ s}^{-1},$$

$$\tau_{S_{+-}} = (0.8952 \pm 0.0015) \times 10^{-10} \text{ s},$$

$$\Delta m_{00} = (0.5274 \pm 0.0030) \times 10^{10} \hbar \text{ s}^{-1},$$

CP AND CPT SYMMETRY TESTS FROM THE TWO-PION ...
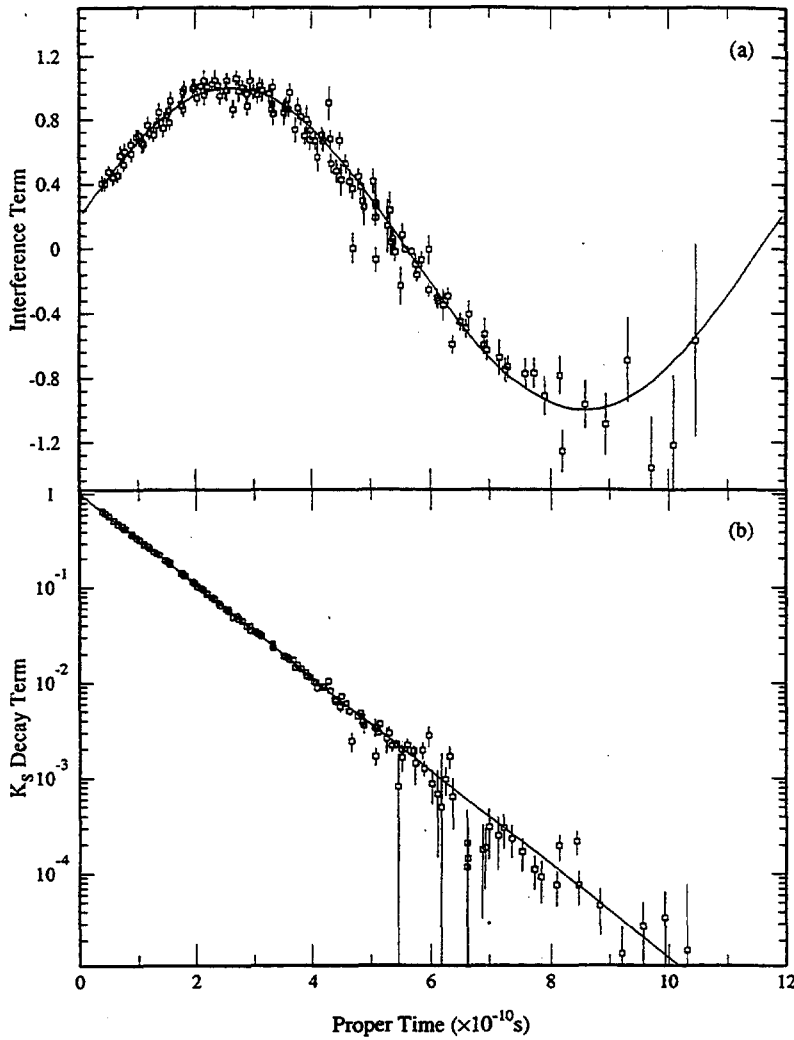


FIG. 103. The interference and $K_S$ decay curves measured for $2\pi^0$ decays with momentum under 90 GeV/c. (a) The interference versus the proper time in 1 m by 10 GeV/c bins. (b) The $K_S$ decay term versus proper time. Both measured at the center of the 1 m by 10 GeV/c bin. The $\Delta m$ and $\tau_S$ results from the grand fit to the $\pi^+\pi^-$ data are shown as the curves.

$$\tau_{S_{00}} = (0.8912 \pm 0.0017) \times 10^{-10} \text{ s},$$

$$\Delta\phi = -1.6° \pm 1.0°,$$

$$\phi_{+-} = 42.2° \pm 1.3°.$$

The next section presents the systematic uncertainties, with a focus on $\text{Re}(\varepsilon'/\varepsilon)$.

## X. SYSTEMATICS

There are five major issues which affect this measurement of $\text{Re}(\varepsilon'/\varepsilon)$: the neutral mode energy reconstruction, detector acceptance, the treatment of the HDRA material, accidental biases, and assumptions in the fitting procedure. The uncertainty in the energy reconstruction dominates. After presenting some general consistency checks we then treat each of the five issues.

TABLE XX. Results of the fits for $\Delta\phi$ and $\phi_{+-}$. Numbers in parentheses are the statistical errors to the least significant figure.

| Fit | $\Delta\phi$ | $\phi_{+-}$ | $\text{Re}(\varepsilon'/\varepsilon)$ $(10^{-4})$ | $\Delta f\vert_{70}$ (mbarn) | Power $\alpha$ | $\Delta m$ $(10^{10}\hbar \text{ s}^{-1})$ |
|---|---|---|---|---|---|---|
| $\Delta\phi$ (1 m bins) | $-1.7° \pm 1.0°$ | $44.1° \pm 0.9°$[a] | $3.2 \pm 6.7$ | $5.787(7)$ | $-0.592(3)$ | $0.5286$[b] |
| $\Delta\phi$ (2 m bins) | $-1.4° \pm 1.0°$ | $43.8° \pm 0.9°$[a] | $4.7 \pm 6.7$ | $5.785(7)$ | $-0.592(3)$ | $0.5286$[b] |
| $\phi_{+-}$ | $-1.7° \pm 1.0°$ | $42.2° \pm 1.3°$ | $8.8 \pm 6.7$ | $5.781(9)$ | $-0.592(3)$ | $0.5257(49)$ |

[a]Correlated with assumed values of $\Delta m$ and $\tau_S$ (see text).
[b]Held constant in this fit.

FIG. 104. Contours of equal $\chi^2$ in the fit for $\Delta\phi$ in 1/2 standard deviation intervals. (a) Power-law slope $\alpha$ versus $\Delta\phi$. (b) Re($\varepsilon'/\varepsilon$) versus $\Delta\phi$. (c) $\Delta f|_{70}$ versus $\Delta\phi$. (d) $\phi_{+-}$ versus $\Delta\phi$. The contours are from the fits using a 2 m $z$ binning for the $\pi^+\pi^-$ decays.

FIG. 105. Contours of equal $\chi^2$ in the fit for $\phi_{+-}$ in 1/2 standard deviation intervals. (a) $\Delta m$ versus $\phi_{+-}$. (b) $\Delta\phi$ versus $\phi_{+-}$. (c) Re($\varepsilon'/\varepsilon$) versus $\phi_{+-}$. (d) Power-law slope $\alpha$ versus $\phi_{+-}$. (e) $\Delta f|_{70}$ versus $\phi_{+-}$.

## A. Consistency checks

The variation of Re($\varepsilon'/\varepsilon$) when kinematic cuts are changed or when different data sets are fit should be consistent with the expected statistical fluctuation; significant departures could point to unresolved problems in the background subtraction, photon energy reconstruction, etc.

Over 1000 different fits have been performed, checking for any inconsistency in the fitting routine, between data subsets, between different fiducial regions, between different analysis cuts, and with various defects embedded into the Monte Carlo simulation. The most important checks are presented here.

The results of the more important studies are summarized in Table XXII, grouped into two categories. The first comprises studies changing characteristics of the fit for Re($\varepsilon'/\varepsilon$). The second consists of studies changing kinematic or event quality cuts. The latter were computationally intensive, as they require a reanalysis of the final data, signal Monte Carlo and background Monte Carlo event samples, totaling over $3.6\times10^7$ events in the neutral sample alone.

### 1. Varying the fitting technique and fiducial cuts

We have changed the binning for the $2\pi^0$ data, using 3 m in $z$ rather than 42 m. The events upstream of the regenerator position can no longer be used; this statistical loss, combined with different weighting of the events, can lead to a sizable shift in the result. This was estimated with ten different Monte Carlo samples the same size as the data statistics; it

was found to be $(2.21\pm0.49)\times10^{-4}$. The observed shift of $-2.48\times10^{-4}$ is then consistent with expectations.

If we limit the momentum range to 150 GeV/$c$, we reduce the size of the primary $K_S$ correction (Sec. VIII B) from $-0.62\%$ ($-0.07\%$) in the charged (neutral) vacuum beam to $-0.33\%$ ($-0.04\%$). The corresponding shift in the result is consistent with arising from the small loss of statistics.

We have also restricted the neutral $z$ range to match that of the charged mode; this has several small systematic advantages. For example, the dependence of Re($\varepsilon'/\varepsilon$) on the $K_L$ lifetime (see Table XVIII) virtually disappears, and there is more cancellation of the primary $K_S$ corrections between the two decay modes. In the neutral mode, the momentum distributions in the two beams match even more closely than with our standard $2\pi^0$ $z$ cut so that the mass distributions match almost exactly. In turn, Re($\varepsilon'/\varepsilon$) becomes less sensitive to the mass cut when there are residual nonlinearities in the photon energy. Finally, this $z$ range is upstream of the HDRA and the photon conversion probability now cancels in the neutral ratio.

We use the larger decay volume, however, because these small systematic advantages are heavily outweighed by the doubling of the vacuum beam statistics. Furthermore, the "crossover" background from inelastic kaon scattering in the regenerator beam is reduced by a factor of 2 relative to the vacuum signal.

When we restrict the size of the neutral decay volume, the shift in Re($\varepsilon'/\varepsilon$) is $+0.42\times10^{-4}$, within the expected range from the change in statistics. This result is $1.8\times10^{-4}$ higher than our preliminary result for Re($\varepsilon'/\varepsilon$) presented in 1991

## CP AND CPT SYMMETRY TESTS FROM THE TWO-PION ...

TABLE XXI. The measured regeneration phase and corresponding analyticity predictions in simultaneous fits to the $\pi^+\pi^-$ and $2\pi^0$ data. Numbers in parentheses are the statistical errors to the least significant figure.

| $\Delta m$ $(10^{10}\hbar\ s^{-1})$ | $\alpha$ | $\phi_{pred}$ (analyticity) | $\phi_{f-\bar{f}}$ (measured) | $\phi_{f-\bar{f}} - \phi_{pred}$ |
|---|---|---|---|---|
| 0.5286[a] | −0.5922(25) | −126.70°±0.23° | −125.92°±0.45° | 0.78°±0.51° |
| 0.5351[a] | −0.5912(24) | −126.79°±0.23° | −127.56°±0.45° | −0.77°±0.51° |
| 0.5275(47) | −0.5925(26) | −126.68°±0.23° | −125.6° ±1.3° | 1.1°±1.3° |

[a]Fixed.

[57] with the same fiducial regions. That shift is dominated by the increase in Monte Carlo statistics for determining the acceptance. The statistical uncertainty in the older, smaller Monte Carlo sample corresponded to a one-standard-deviation uncertainty of $1.9\times10^{-4}$ in $\text{Re}(\varepsilon'/\varepsilon)$.

The final check involved a change in the fitting procedure, by relaxing the assumption of analyticity to obtain the regeneration phase. Instead, the regeneration phase was set to the previously measured phase for carbon (see Sec. IX C 1). The shift of $-0.22\times10^{-4}$, was expected, given the dependence of $\text{Re}(\varepsilon'/\varepsilon)$ on the phase (Table XVIII).

### 2. Trial analysis cuts

The stability of $\text{Re}(\varepsilon'/\varepsilon)$ under changes in the background subtraction is discussed here. Some of the differences between the data and Monte Carlo simulation are also relevant.

For the first study, we have relaxed the ring-number cut from 112 to 128. This increases the noncoherent kaon background (see Fig. 44) by 12.6% (13.3%) in the vacuum (regenerator) beam, while the signal increases by only 1.2% (1.3%).

There are other important issues related to this cut. As the plots of the background subtracted ring-number distributions in Fig. 106 show, the regenerator beam is overall marginally wider than the vacuum beam because of kaons scattering in the shadow absorber. In the bottom beam, the broadening of the vacuum beyond the regenerator beam at high ring number is due to kaons which scatter in the common absorber. This is the tail of kaons that can miss the regenerator when it is in the lower beam—the "sneak-by" kaons discussed in the Sec. VIII. Since the regenerator beam $\pi\pi$ samples are

dominated by regenerated $K_S$ decays, this beam tail is suppressed by a factor of $|\rho/\eta|^2$ (i.e., by 100–200). There is no such suppression of this tail in the vacuum beam; the Monte Carlo simulation mimics this small effect well.

With the looser ring-number cut, we probe the region where the regenerator and vacuum beam shapes deviate. Since the Monte Carlo simulation reproduces this deviation, we do not expect to observe any significant bias. We observe a change in $\text{Re}(\varepsilon'/\varepsilon)$ of $0.46\times10^{-4}$, consistent with statistics.

If we turn now to studies with different $2\pi^0$ mass cuts, we do not expect as clean a situation because of the residual nonlinearities which shift $2\pi^0$ mass distributions of data relative to the Monte Carlo simulation. Since we collect the $K_S$ and $K_L$ decays simultaneously, the resolutions for the two samples are very close, as shown in Fig. 107. However, the vacuum beam $2\pi^0$ mass is somewhat wider than the regenerator beam; this is from the contribution of the lower-energy kaons in the vacuum beam downstream of the HDRA.

With our standard mass cut of $(498\pm24)$ MeV/$c^2$, the number of signal events is small at the cut position. If we tighten the cut to $(498\pm18)$ MeV/$c^2$, the signal size increases by an order of magnitude at the cut boundary. The expected bias due to $2\pi^0$ mass shift and tighter mass cut is of the order of $+0.8\times10^{-4}$. When we reanalyze with this tighter mass cut, we observe a shift of $+1.28\times10^{-4}$. The change in statistics allows a fluctuation of $0.32\times10^{-4}$ so that the observed shift is consistent with expectations.

When we broaden the mass cut, we increase the background, particularly in the vacuum beam (see Figs. 51 and 52). For example, with a mass cut of $(498\pm28)$ MeV/$c^2$ in Fig. 107, the $2\pi^0$ vacuum event total increases by 200 while

TABLE XXII. Shifts in $\text{Re}(\varepsilon'/\varepsilon)$ for changes in the fitting technique and for changes in the fiducial cuts. For the studies involving the change of a cut, the "allowed" shifts are the one-standard-deviation shifts expected from the change in statistics alone. For a change in methodology, the shift was predicted using Monte Carlo studies. The shift observed with the mass cut is discussed in the text.

| Analysis change or fit modification | $\Delta\text{Re}(\varepsilon'/\varepsilon)$ $(\times10^{-4})$ | "Allowed" shift |
|---|---|---|
| Bin $2\pi^0$ data in 3 m × 10 GeV/$c$ $p_z$ bins | −2.48 | 2.21 |
| Reduce momentum range to 40–150 GeV/$c$ | +0.21 | 0.27 |
| Reduce neutral $z$ range to 110–137 m | +0.42 | 2.65 |
| Relax analyticity assumption | −0.22 | — |
| Loosen ring cut from 112 to 128 | +0.46 | 0.47 |
| Tighten mass cut from ±24 MeV/$c^2$ to ±18 MeV/$c^2$ | +1.28 | 0.32 |
| Loosen mass cut from ±24 MeV/$c^2$ to ±28 MeV/$c^2$ | −0.30 | 0.19 |
| Loosen charged mode cuts | −0.25 | 1.01 |

FIG. 106. Regenerator beam and vacuum beam ring-number distributions in the top and bottom beams for the background-subtracted $2\pi^0$ data sample and the coherent Monte Carlo sample. In all plots, the histogram shows the distribution for the regenerator beam (left scale) and the dots show the distribution for the vacuum beam. The solid arrow indicates the cut for the standard analysis, while the dashed arrow indicates the looser cut used in the systematic study. (a) Data, top beam. (b) Data, bottom beam. (c) Monte Carlo simulation, top beam. (d) Monte Carlo simulation, bottom beam.

the $3\pi^0$ and beam interaction backgrounds increase by 1800. The allowed statistical fluctuations are dominated by the new background events, though there is a small contribution from the signal statistics. A statistical fluctuation of $0.19 \times 10^{-4}$ is expected where we observed a $-0.30 \times 10^{-4}$ shift. The errors assigned for either the background subtraction or the

residual nonlinearity are more than adequate to account for this shift.

As a final check of the sensitivity of $\mathrm{Re}(\varepsilon'/\varepsilon)$ to the analysis cuts, we made the track quality cuts and $E/p$ cut significantly looser. The cut on the track $\chi^2$ was increased from 30 to 100. This quantity (Fig. 27) has a $\delta$-ray tail in the data but we expect this to cancel in the single charged ratio.

Cuts on the segment matching at the magnet (Fig. 28) and the distance of closest approach (Fig. 29) were loosened by a factor of 2. The $E/p$ cut was relaxed from 0.80 to 0.84, increasing the semileptonic background in the $K_L$ beam by 25%. The new backgrounds levels were determined using the procedure described in Sec. V B.

The change in statistics with these relaxed cuts was 8% in each beam, dominated by the relaxation of the $\chi^2$ cut. A one-standard-deviation statistical fluctuation would be $1.01 \times 10^{-4}$ and we observe $0.25 \times 10^{-4}$.

### B. Some benefits of the double beam technique

Collecting $K_S$ and $K_L$ decays simultaneously from nearly identical beams results in a cancellation of many of the effects of the detector. This section examines two studies where the benefits of simultaneously collecting $K_S$ and $K_L$ decays to a particular final state are very apparent. The results of the fits used in these studies are summarized in Table XXIII.

#### 1. Inefficiencies and cluster energy study

In the first of these studies, we introduced a 10% inefficiency into the Monte Carlo response of two of the B hodoscope counters which form a vertical stripe near the center of the beam, and four drift chamber wires were assigned zero efficiency. Because of the different $z$ distributions, the illuminations of the doctored counters and wires by decays from the vacuum and regenerator beams are not identical. However, when we use the doctored Monte Carlo simulation for the acceptance corrections, $\mathrm{Re}(\varepsilon'/\varepsilon)$ is shifted by only $-1.5 \times 10^{-4}$.

This situation is certainly artificial. The counter efficiencies were determined with muons and the wire efficiencies with the $K_{e3}$ sample at the subpercent level. Such efficiency mismatches are also obvious, as shown in Fig. 108.



FIG. 107. Overlay of the vacuum and regenerator beam mass distributions for the total $2\pi^0$ data sample. (a) Background-subtracted data. (b) Coherent Monte Carlo simulation. The full Monte Carlo sample is plotted, but it has been scaled to the same total area is the data. For both the data and Monte Carlo simulation, the histogram is the regenerator beam distribution (left-hand scale), and the dots show the vacuum beam distribution (right-hand). The innermost and outermost pair of arrows indicate the mass cuts used in two of the systematic studies. The dashed pair of arrows show the standard mass cut.

TABLE XXIII. Shifts in $\mathrm{Re}(\varepsilon'/\varepsilon)$ for studies demonstrating the stability of $\mathrm{Re}(\varepsilon'/\varepsilon)$ due to the simultaneous collection of $K_S$ and $K_L$ decays.

| Study | $\Delta \mathrm{Re}(\varepsilon'/\varepsilon)$ ($\times 10^{-4}$) | "Allowed" shift |
|---|---|---|
| Introduce 90% efficiency into two $B$ bank trigger counters, and 0% efficiency into four drift chamber wires, in the $\pi^+\pi^-$ Monte Carlo simulation | $-1.50$ | — |
| Loosen maximum photon energy cut in $2\pi^0$ analysis from 60 GeV to 90 GeV | $+2.00$ | 1.16 |
| Loosen maximum photon energy cut in $2\pi^0$ analysis from 90 GeV to 120 GeV | $+0.10$ | 0.27 |

The next study probes the one issue which was not fully resolved—loss of high-energy clusters in the Monte Carlo simulation that is not observed in the data. This problem is discussed previously in Sec. VII D 1. The disagreement is limited mainly to the 24 blocks surrounding the beam pipes, though there is a hint of the problem in the next ring of blocks. The pipe blocks were the blocks most seriously affected by radiation damage in the high-intensity runs.

There is an apparent time dependence in the maximum cluster-energy distributions for the $2\pi^0$ subsets with and without the lead sheet, as shown in Fig. 109(a). The lead sheet data were collected in the earlier high-intensity runs. Most of the data collection for the subset without the lead sheet occurred in the later lower-intensity runs after a long shutdown during which the calorimeter underwent a long cure.

However, each beam is affected identically. The ratios of the data to Monte Carlo simulation in the maximum cluster-energy distributions for the entire data set are similar for the two beams [Fig. 109(b)], and the bias as a function of energy disappears in the ratio of ratios [Fig. 109(c)]. The latter ratio



FIG. 108. Ratio of the data and Monte Carlo track illumination at the lead glass when a 10% inefficiency is introduced into the response of two of the B hodoscope counters in the Monte Carlo. The two counters form a vertical stripe in the hodoscope bank. The data and Monte Carlo simulation are from the $\pi^+\pi^-$ subset C4. (a) Regenerator beam ratio. (b) Vacuum beam ratio. Additional structure in the plots is due to the left-right $\pi^+\pi^-$ trigger requirement coupled with the inefficiency.

is what affects the experiment, and would not have been flat had we not collected the $K_S$ and $K_L$ decays simultaneously.

Since we accept only events where the data and Monte Carlo simulation agree, we are not significantly affected by this problem. To gauge the effect, we have relaxed the cut on the maximum cluster energy from 60 GeV to 90 GeV and 120 GeV, where the mismatch is much more severe. The change in the data sample size (about 7%, as seen in Fig. 77) allows fluctuations in $\mathrm{Re}(\varepsilon'/\varepsilon)$ at the level of $1.2\times 10^{-4}$. The observed shift is just $+1.7$ standard deviations for the case of a 90 GeV cut on the maximum cluster energy, but in the direction expected if the problem were a result of a high-energy cluster acceptance problem (since the distribution in cluster energy is slightly different for the two samples), as shown in Table XXIII.

After the results of E731 were published, the source of the cluster-energy mismatch problem was discovered in the course of the analysis of Fermilab experiment E773 [58]. The effect was due to accidental energy deposited in the calorimeter. A cut based on the amount and fraction of energy outside the $3\times 3$ nominal cluster size was used. This cut (called the "cluster fusion cut"—see Table X) was applied to both the data and Monte Carlo samples. Data events were lost due to accidental energy near to a cluster of *any* energy and also occasionally due to fluctuations in *high* energy clusters. However, Monte Carlo events were lost only by the latter mechanism, since for the E731 acceptance determination these did not have accidental events overlaid. Thus a mismatch in the energy spectrum was introduced. The higher the intensity of the data subset, the greater the mismatch is as seen in Fig. 109(a). Even so, no significant bias was introduced.

### 2. Time dependence: Individual subsets

We now turn to a useful property of our technique which allows us to check both time and intensity dependences. Since the same regenerator is used throughout the experiment, we should measure a consistent regeneration amplitude in each data subset of each decay mode.

The subsets span a range of configurations. Intensities vary by a factor of 3 between subsets (see Table IV), the lead sheet is only present in some $2\pi^0$ subsets, and radiation damage in the array varies substantially. Note that the average nonlinearities measured in the pipe blocks in different subsets vary up to 40%. In spite of these very different conditions, the regeneration amplitudes measured in each subset

L. K. GIBBONS *et al.*



FIG. 109. Ratio of the data and Monte Carlo maximum cluster-energy distribution in $2\pi^0$ decays. The predicted background contribution has been included in the Monte Carlo distribution. (a) The ratio for decays in the regenerator beam for the early $2\pi^0$ subsets with the lead sheet (solid circles) and the later sets without the sheet (open circles). (b) The ratios for the total $2\pi^0$ data set in the regenerator beam (solid circles) and vacuum beam (open circles). (c) The ratio of the two ratios in (b). The best fit line to the double ratio has been superimposed.

agree well, as shown in Fig. 110, within each decay mode.

Systematic studies of the time dependence give confidence in the stability of the result. In most tests, the observed shifts in $Re(\varepsilon'/\varepsilon)$ are consistent with expected statistical fluctuations. In the cases where there may be shifts beyond statistics, a regime affected by known problems was purposely entered, and the shifts are compatible with the expected behavior.

## C. Neutral energy reconstruction

The photon energy reconstruction in the $2\pi^0$ decay has several potential biases. For example, the lead glass energy resolution yields a $z$ resolution of about 1 m, and a resolution mismatch between the data and Monte Carlo simulation could bias the acceptance. We investigate the systematic effects from both linear and nonlinear biases in the energy reconstruction.

### 1. Resolution

We would be most sensitive to the resolution if we began our $z$ fiducial region just upstream of the regenerator where events smearing upstream are not compensated by ones smearing downstream. For both our previous result [21] and this result, the upstream $z$ cut completely contained the (smeared) regenerator edge. At the downstream end of the fiducial $z$ region, the event distribution does not change rap-

idly in either beam so that the smearing of events upstream and downstream of the cut tends to cancel.

We have introduced additional smearing in the reconstructed photon energy to study possible resolution systematics. The $2\pi^0$ $z$ distribution in Fig. 111 with 2% additional smearing shows a glaring mismatch between the data and the standard Monte Carlo simulation. However, refitting for $Re(\varepsilon'/\varepsilon)$ using the smeared data and standard acceptance corrections yields a shift of only $1.5\times10^{-4}$. By studying this distribution, we limit the resolution mismatch to 0.5% which yields a shift of $0.36\times10^{-4}$.

For the constrained fits, the choice to begin the fiducial range in $z$ downstream of the regenerator (Sec. IX B) gives a relative insensitivity to resolution effects. A 0.5% smearing gives a $0.0004\times10^{10}\hbar$ s$^{-1}$ uncertainty in $\Delta m$ and $0.0003\times10^{-10}$s to $\tau_S$ in the $2\pi^0$ data, and less than 0.01° in $\Delta\phi$.

### 2. Energy scale and nonlinearity

A large effort has gone into the refinement of calibration and simulation of the lead glass calorimeter. This is because a bias in the photon energy scale moves events past both the energy and $z$ fiducial boundaries. The electron response in $K_{e3}$ decays and the photon response in $\pi^+\pi^-\pi^0$ decays are mimicked well by the Monte Carlo simulation (see Sec. VII D 1); nevertheless shifts in the reconstructed $2\pi^0$ mass
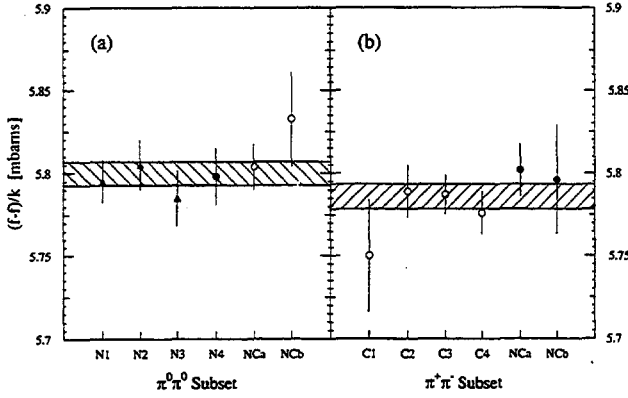
FIG. 110. The regeneration amplitude measured in individual data subsets. The $2\pi^0$ measurements are plotted in (a) and the $\pi^+\pi^-$ measurements in (b). The one-standard-deviation bands from the fits to the entire $2\pi^0$ or $\pi^+\pi^-$ sample described in Sec. IX A have been plotted as well. The highest- (lowest-) intensity data for each mode is plotted with solid (open) symbols. In part (a), the subsets with (without) the lead sheet are indicated by solid triangles (solid symbols). Small accidental corrections (see Secs. IX A 1 and X H) have been made.

(see Table VIII) imply residual nonlinearities in the reconstructed photon energy. This section evaluates the sensitivity to the energy scale.

Results from some of the studies related to the photon energy scale are summarized in Table XXIV. Most followed the same procedure. A bias was introduced into the reconstruction of photons in the data, while that in the Monte Carlo simulation was unmodified. The regenerator edge in the biased data was rematched to the regenerator edge in the Monte Carlo simulation (see Sec. VI D) as a function of kaon energy, giving a new energy scale correction. The data ere then analyzed a second time with both the bias and the new compensating scale correction. We finally fit the reanalyzed data to determine the effect on $\mathrm{Re}(\varepsilon'/\varepsilon)$.

When an average energy scale bias of 0.03% was introduced, we did not rematch the edge since this would fully compensate for this bias. The 0.03% scale change resulted in a shift of $0.93\times 10^{-4}$. However, the most troublesome effects come from nonlinear biases in the reconstruction.
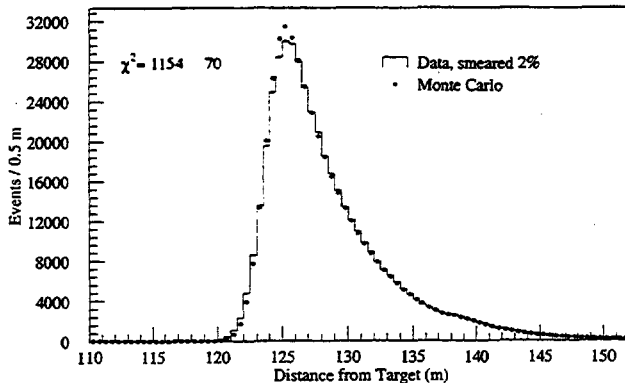


FIG. 111. The $z$ location of $2\pi^0$ decays in the regenerator beam for the data and the Monte Carlo simulation after the photon energies in the data were smeared by an additional 2%. Only the subset with the lead sheet is shown here.

TABLE XXIV. Shift in $\mathrm{Re}(\varepsilon'/\varepsilon)$ induced by some of the systematic biases introduced into the photon energy reconstruction procedure. The resolution bias was discussed in the previous section.

| Reconstruction bias | $\|\Delta\mathrm{Re}(\varepsilon'/\varepsilon)\|$ ($\times 10^{-4}$) |
|---|---|
| 0.5% energy smearing | 0.36 |
| 0.03% average energy scale change ($\Delta E = 3\times 10^{-4}E$) | 0.93 |
| Quadratic energy scale change ($\Delta E = qE^2$) | 1.57 |
| "Pedestal" shift (20 MeV per cluster) | 0.46 |

When we introduced nonlinear biases into the photon reconstruction, we indeed found that the $z$ edge matching did not completely compensate. To study pedestal shifts, we uniformly shifted the energy of every cluster by 20 MeV, which resulted in a shift in $\mathrm{Re}(\varepsilon'/\varepsilon)$ of $0.46\times 10^{-4}$. We have measured pedestal shifts using data with no minimum readout threshold, and determined them in $3\pi^0$ data with a threshold by a study of the invariant mass vs cluster energy. The pedestals measured with these two techniques agreed well, giving confidence in the pedestals measured using the $3\pi^0$ decays in data sets with a readout threshold. Typical pedestal shifts were of the order of 40–50 MeV per cluster, and these could be determined to 10 MeV or better. Corrections for the shifts are applied in the standard analysis.

To estimate the effect of remaining nonlinearities, we introduced a quadratic correction to the cluster energy, $E\rightarrow(1+qE)E$. The value of $q$ was chosen to shift the mean $2\pi^0$ mass in the data to match the Monte Carlo simulation. Typical values of $q$ were 0.000 35 (slightly higher for events with pipe block clusters).

After reanalyzing the data with the quadratic biases applied, $\mathrm{Re}(\varepsilon'/\varepsilon)$ shifted by $-1.57\times 10^{-4}$. While the mean mass is correct, the shape is distorted with large asymmetries appearing. We believe that a distortion as severe as the quadratic bias applied is not favored by the data. However, we take the full shift as an estimate of the residual bias in the energy reconstruction.

Combining the nonlinear bias with the bias from smearing, we have a total systematic contribution from photon energy reconstruction of $1.61\times 10^{-4}$. This is the largest systematic contribution to $\mathrm{Re}(\varepsilon'/\varepsilon)$.

The cluster-energy reconstruction uncertainties also dominate the systematic uncertainty in the other measurements which use the $2\pi^0$ sample. We have contributions of $0.0012\times 10^{-10}$ s in $\tau_S$, $0.0014\times 10^{10}\hbar$ s$^{-1}$ in $\Delta m$, and $0.52°$ in $\Delta\phi$.

### D. Acceptance

#### 1. Acceptance biases and Re($\varepsilon'/\varepsilon$)

As discussed in Sec. VII, the acceptance is largely governed by a few limiting apertures. The active mask and the collar anticounter were the most important since there was a significant rate at their boundaries. The lead glass, trigger counters (T and V), and other outer edges had low enough illuminations to make $\mathrm{Re}(\varepsilon'/\varepsilon)$ insensitive to their precise

TABLE XXV. Change in the single ratios and in $\mathrm{Re}(\varepsilon'/\varepsilon)$ when the size of a limiting aperture is changed in the Monte Carlo simulation. $\Delta R_{00}$ and $\Delta R_{+-}$ are the changes in the vacuum to regenerator beam ratios in the charged and neutral mode samples. In each case, the sizes of the apertures in the $x$ and $y$ were simultaneously changed by 70 $\mu$m in order to maximize the effect.

| Aperture adjustment | $\Delta R_{00}$ (percent) | $\Delta R_{+-}$ (percent) | $\|\Delta \mathrm{Re}(\varepsilon'/\varepsilon)\|$ ($\times 10^{-4}$) |
|---|---|---|---|
| Change mask size by 70 $\mu$m | −0.013 | −0.014 | 0.02 |
| Change HDRA size by 70 $\mu$m | −0.002 | Negligible | 0.03 |
| Change CA size by 70 $\mu$m | −0.021 | Negligible | 0.35 |

sizes and locations. For example, if one decreases the radius of the vacuum window by 1 mm, the single ratios change by less than 0.001%. The same is true if the lead glass edge were smaller by 1 mm.

Most important is the average effective size of an aperture rather than its exact placement. To keep the systematic uncertainty in $\mathrm{Re}(\varepsilon'/\varepsilon)$ from the acceptance correction within the $10^{-4}$ level requires knowing the average effective size of the apertures at the level of 200 $\mu$m or better. The effective size of the apertures was determined directly with electrons from $K_{e3}$ decays (Sec. VII C 3) to compensate for counter thickness, small dead regions, etc. Our systematic estimate on the position of each edge was 50 $\mu$m, and so the average aperture size is measured at the 70 $\mu$m level, well under the limit we wished to achieve. Size changes due to thermal expansion are well within this systematic estimate.

The value of $\mathrm{Re}(\varepsilon'/\varepsilon)$ is less sensitive to an aperture offset since the loss on one side is largely compensated by the gain on the other. However, if the aperture is too large (small) in the Monte Carlo simulation, we over estimate (under estimate) the acceptance.

There is an uncertainty in projecting tracks back to the aperture due to chamber misalignment. In addition, there is uncertainty in the chamber positions relative to the production target and calorimeter. The latter is at the 10–20$\mu$m level (see Sec. IV). Since we track the relative locations of two chambers to 10$\mu$m, the systematic uncertainty in the track projection is 60$\mu$m at the mask, 35$\mu$m at the HDRA, and 15$\mu$m at the collar anti. These uncertainties, as well as those from thermal expansion of the vacuum pipe stands, are within an uncertainty of approximately 70$\mu$m.

We have estimated the effects of the aperture sizes and positions by noting the event gain or loss when the aperture edges in the Monte Carlo simulation are adjusted. Table XXV outlines the effect on $\mathrm{Re}(\varepsilon'/\varepsilon)$ for the most important of these studies. We note that $\mathrm{Re}(\varepsilon'/\varepsilon)$ is insensitive, for example, to the size of the mask, which affects only the vacuum beam, but has similar effects on $\pi^+\pi^-$ and $2\pi^0$ acceptances. In the end, the result was most sensitive to the size of the collar anti, where a simultaneous decrease (or increase) of both the $x$ and $y$ sizes by 70$\mu$m induced a shift of order $0.3\times10^{-4}$ in $\mathrm{Re}(\varepsilon'/\varepsilon)$.

Regarding aperture positions, the largest change occurred when the mask was shifted in neutral mode. For a 1 mm shift, however, the bias was only $0.1\times10^{-4}$. A shift of this size would have been clearly observable (see Fig. 62).

Apertures do not solely determine the acceptance. Energy thresholds, the minimal separation of two tracks or two clus-

ters, detector resolutions, etc., all have relevance to the acceptance.

To estimate the systematic error from the acceptance, we turn to the high-statistics vacuum samples of $K_L\rightarrow 3\pi^0$ and $K_L\rightarrow \pi e \nu$ which we use to limit an acceptance bias as a function of $z$, to which the $\mathrm{Re}(\varepsilon'/\varepsilon)$ measurement is most sensitive. As with the $\pi\pi$ decay modes (Sec. VII), we have checked the track and cluster aperture illuminations, track and cluster separations, etc., in the Monte Carlo simulation relative to the data, with no surprises.

For the charged mode, we have spot checked the $z$ acceptance with $K_{e3}$ subsets, with results similar to that shown in Fig. 85. As we discussed in Sec. VII, we have limited the bias in acceptance for the $\pi^+\pi^-$ mode by determining the slope in the ratio of the $z$ distributions for the data and Monte Carlo simulation. We refer to this slope as the "acceptance bias" for the remainder of this discussion. In the charged mode, we used a fraction of the $K_{e3}$ statistics to limit the acceptance bias to 0.03% per meter; this induces a shift of $0.65\times10^{-4}$ in $\mathrm{Re}(\varepsilon'/\varepsilon)$.

The longer neutral decay region and mean separation between $K_S$ and $K_L$ decays makes the neutral mode much more sensitive to a $z$ bias. To limit the acceptance bias we have used the full sample of $3\pi^0$ decays. The lower average photon energy for $3\pi^0$ decays means a greater illumination at the detector edges than for $2\pi^0$. Also six photons probe the photon identification in the lead glass better than four photons. Thus the use of the $3\pi^0$ sample should be conservative.

We find an acceptance bias of less than 0.007% per meter (Fig. 86). [The uncertainty introduced by the lead sheet is evaluated later (Sec. X E).] This shifts $\mathrm{Re}(\varepsilon'/\varepsilon)$ by $1.00\times10^{-4}$.

Combining the charged and neutral mode values, we have a total acceptance uncertainty on $\mathrm{Re}(\varepsilon'/\varepsilon)$ of $1.19\times10^{-4}$.

### 2. Acceptance biases and the constrained fit results

Because the acceptance bias is strictly limited by the $3\pi^0$ sample, the uncertainty in the constrained fit results which use the $2\pi^0$ sample is small. For the neutral $\Delta m$ measurement, there is a $0.0001\times10^{10}\hbar s^{-1}$ contribution and, for the neutral $\tau_S$ measurement, $0.0002\times10^{-10}$ s. These include uncertainties from accidental effects (see Sec. X H). The effect on $\Delta\phi$ is negligible.

Because the acceptance was not as crucial for $\mathrm{Re}(\varepsilon'/\varepsilon)$ in the charged mode as it was in the neutral mode, we did not push as hard on limiting the acceptance bias as was possible with the $K_{e3}$ sample. One unfortunate side effect of this is a large contribution to the systematic uncertainty in the results

TABLE XXVI. Contribution to the systematic uncertainty in $\mathrm{Re}(\varepsilon'/\varepsilon)$ from backgrounds.

| | Uncertainty | |
|---|---|---|
| Background source | $\pi^+\pi^-$ | $2\pi^0$ |
| Incoherent regeneration (in regenerator) | $0.18\times10^{-4}$ | $0.84\times10^{-4}$ |
| Semileptonic decays | $0.23\times10^{-4}$ | — |
| $3\pi^0$ Decays and beam interactions | — | $0.60\times10^{-4}$ |
| Total | $0.29\times10^{-4}$ | $1.03\times10^{-4}$ |

from the constrained fits using the $\pi^+\pi^-$ sample. For the $\Delta m$ and $\tau_S$ measurements in the $\pi^+\pi^-$ sample, we have systematic contributions of $0.0009\times10^{10}\hbar$ s$^{-1}$ and $0.0020\times10^{-10}$ s. These include contributions from the shifting of the results as the $z$ bin size was varied. Similar studies for $\Delta\phi$ and $\phi_{+-}$ give $0.35°$ for the systematic error on each.

### 3. Regenerator anticounters

One acceptance detail which affects only the measurement of $\mathrm{Re}(\varepsilon'/\varepsilon)$ is the location of the last regenerator anticounter relative to the regenerator. The anticounter introduces a small asymmetry between the $\pi^+\pi^-$ and $2\pi^0$ decay modes since $\pi^+\pi^-$ decays upstream of (and inside of) the anticounter are vetoed. The uncertainty in the number of decays vetoed by this anticounter depends on its position relative to the regenerator. From direct measurements, we know this distance to about 1.2 mm. This geometrical uncertainty corresponds to a systematic error of $0.59\times10^{-4}$ in $\mathrm{Re}(\varepsilon'/\varepsilon)$.

### E. HDRA and regenerator lead piece

The thickness of the materials in the HDRA and the regeneration amplitudes are not perfectly known. To account for systematic uncertainty, the background level, acceptance, etc., are modified simultaneously for a given change in material thickness or regeneration amplitude.

### 1. Contribution of the HDRA to the systematic uncertainty on $Re(\varepsilon'/\varepsilon)$

The regeneration amplitudes from lead and carbon have been measured at the 1.4% level [46,47,49]. The regeneration amplitudes for oxygen and nitrogen were scaled from that of carbon (also scaled to the modern value for $\eta_{+-}$) using the measured $A$ dependence [49] of the regeneration amplitude. When the regeneration amplitude for lead (carbon) was varied within the uncertainty given above, the shift in $\mathrm{Re}(\varepsilon'/\varepsilon)$ observed was $0.31\times10^{-4}$ $(0.15\times10^{-4})$; these are dominated by the change in the diffractive background.

Chemical analysis shows the sheet to have been 99.9793% pure, with bismuth as the dominant impurity [59]. When we varied the lead regeneration parameters, the contribution to the regenerator beam rate from the lead in the regenerator was treated simultaneously; however, its effect was less than $0.1\times10^{-4}$.

Uncertainty in the thickness of the material in the HDRA was most important. The lead sheet had an average thickness of 518 $\mu$m, and was initially measured on a 5 cm grid to an accuracy of 10 $\mu$m. The sheet was flat horizontally within 10 $\mu$m but vertically had a taper of order 50 $\mu$m over 62 cm.

This structure was put into the Monte Carlo simulation; we then compared the size of the acceptance step in $z$ (see, for example, the lead sheet $2\pi^0$ plot in Fig. 89) in both top and bottom vacuum beams in $3\pi^0$ decays. This gives a direct measurement of the six-photon transmission probability, and we found it to be underestimated in the bottom beam by $1.1\%\pm0.2\%$ (corresponding to roughly 13 $\mu$m). The Monte Carlo simulation was adjusted accordingly.

The accuracy of the six-photon conversion probability corresponds to an accuracy on the four-photon conversion probability of 0.16% for each beam. We take this value for the *average* uncertainty for the $2\pi^0$ sample to allow for residual nonuniformities in the thickest of the sheet. The value of $\mathrm{Re}(\varepsilon'/\varepsilon)$ varies accordingly by $0.96\times10^{-4}$. The variations in backgrounds and coherent regeneration are included, but the photon transmission dominates.

The bulk of the remaining material was the 1 mm scintillator used in the T and V counters; their thicknesses were known to 25 $\mu$m. We used the equivalent of 50 $\mu$m of scintillator uncertainty to cover the remaining membranes (see Table III); $\mathrm{Re}(\varepsilon'/\varepsilon)$ changes by $0.46\times10^{-4}$, again dominated by uncertainty in photon transmission.

Regarding background, the errors quoted in Sec. VI E 2 correspond to an uncertainty in $\mathrm{Re}(\varepsilon'/\varepsilon)$ of $0.23\times10^{-4}$ from the diffractive statistical uncertainty and $0.42\times10^{-4}$ from the inelastic background.

Combining all of the errors associated with the HDRA, we have a total uncertainty in $\mathrm{Re}(\varepsilon'/\varepsilon)$ of $1.22\times10^{-4}$, one of the larger sources in this measurement.

### 2. Effect of the HDRA on the constrained fit results

In the constrained fits, the vacuum beam was used to predict the number of kaons incident on the regenerator; this depends mostly on the acceptance and background level for the vacuum beam, and on absorption in the shadow absorber and regenerator; the uncertainties in the vacuum beam from the HDRA have negligible effect.

In the regenerator beam, the dominant uncertainty comes from the HDRA inelastic background. This is a small fraction of the regenerator beam $2\pi^0$ sample, and even with the 40% uncertainty (see Sec. VI E 2), it plays a minor role in the $\mathrm{Re}(\varepsilon'/\varepsilon)$ measurement. The constrained fits, however, depend on the shape of the decay distribution and hence on the relative numbers of events upstream and downstream of the HDRA. The HDRA inelastic background is about 0.2% (0.9%) of the downstream events in the $2\pi^0$ sample without (with) the lead sheet. The uncertainty in this background contributes $0.0001\times10^{-10}$s and $0.0008\times10^{10}\hbar$s$^{-1}$ to the neutral $\tau_S$ and $\Delta m$ measurements, and $0.2°$ to the uncertainty in $\Delta\phi$. The photon conversion probability and regeneration

TABLE XXVII. Change in $\text{Re}(\varepsilon'/\varepsilon)$ for different modifications to the kaon flux shapes assumed in the fitting program. Note that these changes *are not* made in determining the acceptance; they only affect the relative contribution of the *predicted rate* of a 1 GeV/$c$ momentum bite to the total predicted rate in a 10 GeV/$c$ bin.

| Modification to beam spectrum | $\delta\text{Re}(\varepsilon'/\varepsilon)$ $(10^{-4})$ |
|---|---|
| Flat incident spectrum $[F_v(p) = \text{const}]$ | $-1.21$ |
| Quadratic distortion, both $2\pi^0$ and $\pi^+\pi^-$ samples $(F_v'(p) = F_v(p)\{1 + 0.1[(p-60)/100]^2\})$ | $+0.12$ |
| Quadratic distortion, $\pi^+\pi^-$ sample only | $+0.04$ |
| Increase average regenerator beam transmission by $1\sigma$ $(t \rightarrow 1.005t)$ | $-0.13$ |
| No shadow absorber scattering correction to regenerator beam flux | $-0.36$ |
| Use shadow absorber scattering correction determined for the $\pi^+\pi^-$ sample for all data sets[a] | $-0.27$ |
| Use shadow absorber scattering correction determined for the $2\pi^0$ lead sheet sample for all data sets | $-0.27$ |
| Change dilution factor used to calculate change in the relative flux shape between the regenerator and vacuum beam from regeneration in the shadow absorber | $+0.04$ |
| Ignore "sneak-by" rate[b] | $-0.76$ |
| Correct for "sneak-by" kaons, but ignore the rate of $K_L$ decay from these kaons | $-0.26$ |
| Use the "sneak-by" rate determined for the $\pi^+\pi^-$ set for all of the subsets | $-0.47$ |
| Use the "sneak-by" rate determined for the lead sheet $2\pi^0$ set for all of the subsets | $-0.46$ |

[a]See Sec. VIII A 2.

[b]That is, assume the entire flux of kaons observed in the vacuum beam passes through the regenerator.

amplitudes are known well enough to give negligible uncertainty.

## F. Backgrounds

Sections V B and VI E have already discussed the systematic and statistical uncertainties on the background levels for the $\pi^+\pi^-$ and $2\pi^0$ data samples. The contributions are summarized in Table XXVI. The uncertainty from the HDRA backgrounds has been included in the overall HDRA systematic contribution. The total background uncertainty in the $2\pi^0$ ($\pi^+\pi^-$) sample gives a systematic error of $1.03\times10^{-4}$ ($0.29\times10^{-4}$) to $\text{Re}(\varepsilon'/\varepsilon)$.

We have treated the regenerator background in the vacuum and regenerator beams as independent; in fact, they are largely correlated and tend to cancel. Hence, our treatment is conservative.

For the constrained fits, the largest uncertainty comes from the level of noncoherent background from the regenerator in the regenerator beam; however, this contributes only $0.000\,07\times10^{10}\hbar$ s$^{-1}$ and $0.000\,05\times10^{-10}$ s to the neutral $\Delta m$ and $\tau_S$ measurements, and under $0.02°$ to the $\Delta\phi$ measurement.

## G. Uncertainties from the fitting procedure

Some systematic issues in the fitting technique have already been discussed. For example, the bias in $\text{Re}(\varepsilon'/\varepsilon)$

from the acceptance correction is less than $10^{-5}$ when the regeneration or kaon decay parameters are varied within several percent of their nominal values. The only other inputs, apart from the decay rate distribution, are the vacuum momentum spectrum $[F_v(p)]$, the average transmission $t$, and its energy dependence $c(p)$ for the regenerator beam in Eq. (83). We now discuss the sensitivity to these input spectra and to the assumption of analyticity for the regeneration phase.

### 1. Incident kaon flux $F_v(p)$

The measurement of $\text{Re}(\varepsilon'/\varepsilon)$ is insensitive to the shape of the momentum spectrum in the fitting routine. In Table XXVII, the variation of $\text{Re}(\varepsilon'/\varepsilon)$ with modifications to the flux is given. Even a *flat* kaon spectrum (compare with Fig. 93) introduces a bias in $\text{Re}(\varepsilon'/\varepsilon)$ of only $1.21\times10^{-4}$. Note that this change affects only the calculation of the rate in a $p$ and $z$ bin in the fitting routine for a given set of test parameters. It does not change the *acceptance* calculation. Introducing a 10% bowing resulted in a $0.12\times10^{-4}$ shift when applied to both the $\pi^+\pi^-$ and $2\pi^0$ data sets, and a $0.04\times10^{-4}$ shift when applied to the $\pi^+\pi^-$ set only. Figures 57 and 58 demonstrate that the spectrum has at most a few percent bowing.

The constrained fit quantities are also insensitive to the spectrum shape; a flat spectrum induces of order-$1\sigma$ shifts in

*CP* AND *CPT* SYMMETRY TESTS FROM THE TWO-PION ...

TABLE XXVIII. Change in $\Delta m$, $\tau_S$, $\Delta\phi$, and $\phi_{+-}$ for different distortions of the vacuum and regenerator beam kaon momentum spectra.

| Modification to vacuum or regenerator beam spectrum | $\|\delta\Delta m\|$ $(10^{10}\hbar\ s^{-1})$ | $\|\delta\tau_S\|$ $(10^{-10}\ s)$ | $\|\delta\Delta\phi\|$ | $\|\delta\phi_{+-}\|$ |
|---|---|---|---|---|
| Flat incident spectrum $[F_v(p)=$ const] | 0.0038 | 0.0007 | 1.3° | 1.2° |
| Quadratic distortion $(F_v'(p)=F_v(p)\{1+0.1[(p-60)/100]^2\})$ | 0.0001 | 0.0001 | 0.3° | 0.5° |
| Change average regenerator beam transmission by one standard deviation $(t \to 1.005t)$ | 0.0004 | 0.0002 | <0.1° | 0.3° |
| No shadow absorber scattering correction to regenerator beam flux | 0.0007 | 0.0002 | 0.1° | 0.3° |
| Use the shadow absorber scattering correction determined for the $\pi^+\pi^-$ sample for all data sets | <0.0001 | <0.0001 | <0.1° | <0.1° |
| Ignore "sneak-by" rate | 0.0003 | 0.0002 | 0.5° | 0.3° |
| Use the "sneak-by" rate determined for the $\pi^+\pi^-$ set for all of the subsets | <0.0001 | <0.0001 | <0.1° | <0.1° |

the measured quantities (Table XXVIII). These arise mostly from kaons under 40 GeV/*c* in the $\pi^+\pi^-$ sample: The acceptance in this region changes more rapidly across the bin than at higher momentum. Since much of the $\Delta m$ information in the $\pi^+\pi^-$ fits comes from these low bins, the result is more sensitive to a change in the momentum distribution across the bin. The $\Delta m$ and $\tau_S$ measurements using $2\pi^0$ decays (kaons in the 40–160 GeV/*c* range) shift at most 10% of the (average) shift shown in the table.

When a 10% bowing was introduced, the shifts in $\Delta m$ and $\tau_S$ were completely negligible, and the shifts in $\Delta\phi$ and $\phi_{+-}$ were small; by this technique, an uncertainty of 0.2° is assigned to the $\phi_{+-}$ and $\Delta\phi$ measurements.

### 2. Regenerator beam flux corrections

The corrections to the regenerator beam flux—the average transmission, the shadow absorber corrections, and the correction for kaons "sneak-bys" which miss the regenerator—also introduce systematic uncertainties into the fits. Some of the studies involving variations of these corrections are listed in Tables XXVII and XXVIII.

As mentioned previously, we measured the average kaon transmission through the shadow absorber to 0.5% for the regenerator beam. At this level, all of the parameters we measured are reasonably insensitive. In the two measurements [Re($\varepsilon'/\varepsilon$) and $\Delta\phi$] where charged and neutral modes are compared, the absorption uncertainty almost exactly cancels: Re($\varepsilon'/\varepsilon$) is affected at the $0.13\times10^{-4}$ level and $\Delta\phi$ negligibly. The quantity most affected is $\phi_{+-}$, which shifts 0.3°. The values of $\Delta m$ and $\tau_S$ receive contributions of $0.0004\times10^{10}\hbar\ s^{-1}$ and $0.0002\times10^{-10}$ s, with a strong correlation between the two modes.

For the remaining corrections—shadow absorber scattering and sneak-bys—Re($\varepsilon'/\varepsilon$) is most sensitive to the *difference* between the charged and neutral data set corrections rather than to the overall flux shape. The difference in the correction for the various data sets is small relative to the overall correction, but it is that difference, not the total cor-

rection, to which the result is most sensitive. As we can see in Table XXVII, no matter which data set we chose from for the correction, the bias we observed in Re($\varepsilon'/\varepsilon$) was the same. The changes for globally applying the $\pi^+\pi^-$ corrections and the $2\pi^0$ lead sheet corrections are listed in the table. The uncertainty in the shadow absorber scattering and sneak-by corrections were dominated by uncertainties in kaon-nucleon elastic cross sections. Cross sections reported in [52] yield an uncertainty of 20%, depending mostly on how the values reported in [52] are interpreted.

The change in the correction from data set to data set is dominated by changes in beam collimation, primarily from sinking of the target pile. These changes were tracked well, but as a conservative estimate we have assigned the uncertainty on the corrections to be 50% of the difference between the most disparate pair of data sets. This corresponds to an uncertainty in Re($\varepsilon'/\varepsilon$) of $0.14\times10^{-4}$ ($0.23\times10^{-4}$) for the scattering (sneak-by) correction.

Because these corrections vary slowly across the 10 GeV/*c* bins, they do not contribute significantly to the uncertainty in the other measurements, as seen in Table XXVIII. Ignoring the corrections introduces small biases, but since they are known to about 20%, their effect on the constrained fit measurements is negligible.

### 3. Analyticity assumption

We now investigate the systematics associated with the analyticity assumption used to obtain the regeneration phase. If the regeneration amplitude deviated from a pure power behavior, then a bias in the phase extracted from the analyticity relationship could be introduced. Such could result from kaon rescattering, where there can be a Pomeron along with $\omega$ or $\rho$ exchange. The Pomeron affects the regeneration amplitude, contributing logarithmic terms that disrupt the pure power-law behavior; it also has a small real part. Since there would be no longer a pure power-law behavior, the use of analyticity to determine the regeneration phase from the "best-fit" power could lead to a small bias in this phase. We

originally argued that this could be limited to $<0.5°$ in fits which use the full momentum range down to 20 GeV/$c$. Subsequent to the publication of these results, a far more complete analysis by two of us [35] showed that this rescattering together with several other effects was limited to $<0.35°$. This paper also addresses the criticism of our technique in [60]. The key feature is that the scattering amplitudes are well enough behaved that the local power law gives an excellent approximation to the local phase even in the presence of multiple-trajectory exchange, multiple elements in the target (regenerator), and electromagnetic regeneration. Nonetheless, here we describe the original analysis.

In the fits to charged data below 40 GeV/$c$, the accuracy of the measured power-law slope $\alpha$ corresponds to an uncertainty of 0.3° in the regeneration phase and the measured parameters already reflect this uncertainty. In addition to this, we included an uncertainty of 0.5° for a nonpure power law, commensurate with both the limit on the Pomeron contribution and the change in the slope $\alpha$ when the fits are limited to momenta above 40 GeV/$c$. The contribution to the uncertainty on the charged $\tau_S$ fit is $0.0003 \times 10^{-10}$s. The $\Delta m$ measurement is more sensitive to the regeneration phase; its uncertainty contributes $0.0019 \times 10^{10} \hbar \, \mathrm{s}^{-1}$, since $\alpha$ is floating in these fits.

The $\phi_{+-}$ measurement is directly correlated with the regeneration phase $\phi_\rho$, since what is measured is the difference of phases $\phi_\rho - \phi_{+-}$ [see Eq. (85)]. Thus $\phi_{+-}$ has the 0.5° uncertainty, the dominant systematic. The regeneration phase cancels in the measurement of $\Delta \phi$.

For the neutral $\Delta m$ and $\tau_S$ measurements, the uncertainty in the regeneration phase due to the statistical uncertainty on $\alpha$ already corresponds to 0.7°. The additional uncertainty from nonpure power-law behavior is negligible. This is also true in the Re($\varepsilon'/\varepsilon$) measurement, where both the $\pi^+\pi^-$ and $2\pi^0$ samples are restricted to the momentum range above 40 GeV/$c$.

### 4. Summary of uncertainties in the fits

The measurements we make are not greatly dependent on the shape of the kaon flux in the vacuum and regenerator beams. For Re($\varepsilon'/\varepsilon$), the combination of errors due to absorption, scattering in the movable absorber, and sneak-bys amounts to $0.30 \times 10^{-4}$. For $\Delta \phi$ there is an uncertainty of 0.2° from the kaon spectrum; for $\phi_{+-}$, there is an uncertainty of 0.4° from the spectrum and transmission in the regenerator beam. These effects on $\Delta m$ and $\tau_S$ are negligible.

The uncertainty from the assumption of analyticity contributes only to fits using the charged mode data below 40 GeV/$c$. This gives a 0.5° uncertainty on $\phi_{+-}$. The corresponding uncertainty for the charged $\Delta m$ measurement is $0.0019 \times 10^{10} \hbar \, \mathrm{s}^{-1}$, and for the charged $\tau_S$ measurement it is $0.0003 \times 10^{-10}$ s.

### H. Accidental activity

The final systematic results from uncertainties in how accidental activity alters the vacuum-to-regenerator ratios for the two modes. The corrections were given in Sec. IX A 1; here, we describe the method and the uncertainty.

TABLE XXIX. Sequential change in observed $2\pi^0$ vacuum-to-regenerator beam ratio due to accidental event loss as each analysis cut is applied. Events which would not have passed cuts except for the presence of the accidental activity are *not* included in these numbers.

| Analysis cut | Change in ratio (%) |
|---|---|
| Four clusters | $+0.065 \pm 0.021$ |
| Best pairing $\chi^2 < 4$ | $-0.137 \pm 0.013$ |
| Cluster fusion | $+0.234 \pm 0.048$ |
| Second best $\chi^2$ cuts | $-0.017 \pm 0.005$ |
| Chamber, BC hodoscope hits | $+0.099 \pm 0.028$ |
| Collar anti | $-0.055 \pm 0.012$ |
| Cluster energy cuts | $-0.002 \pm 0.001$ |
| Ring number | $-0.001 \pm 0.003$ |
| $2\pi^0$ mass | $-0.032 \pm 0.004$ |
| Total energy | $-0.018 \pm 0.002$ |
| $z$ fiducial cut | $-0.051 \pm 0.002$ |
| Total | $+0.085 \pm 0.062$ |

Accidental effects are largest for the highest-intensity data samples. For $\pi^+\pi^-$, this is the NC subset; the study of the accidental effects in this data set has been detailed in [21]: For an average proton intensity of $0.8 \times 10^{12}$, the vacuum-to-regenerator ratio changes by $-0.04\% \pm 0.07\%$, requiring no correction. This statistical error, scaled to the remainder of the data (a factor of 2.7 lower in intensity), yields a total uncertainty on Re($\varepsilon'/\varepsilon$) of $0.67 \times 10^{-4}$.

For the higher-intensity $2\pi^0$ data subsets, we have determined the effect on the single ratio. We used the random triggers collected simultaneously with $\pi\pi$; these sampled the same ambient environment of kaon decays and had the same intensity distribution. A trigger was formed when a charged particle produced in the interaction of a proton in the target or dump hit a telescope located at a large angle about 50 m upstream of the regenerator. Detector activity in accidental events was overlaid on Monte Carlo coherent $\pi\pi$ events where it was important that the regenerator position for the event was determined by the overlayed accidental. A dead time effect (as in single-hit drift chamber TDC's) was fully simulated. Each event was analyzed both with and without the overlay to measure the effect on the accepted event samples.

The analysis of the overlaid Monte Carlo sample completely paralleled that of the data. For example, the $2\pi^0$ energy scale corrections based on matching the regenerator edge were applied.

What is important is the change in the vacuum-to-regenerator ratio from accidental activity. The changes after every cut which resulted in any loss (after the accidental is overlaid) are listed in Table XXIX. A positive change means a smaller fraction of events is lost in the vacuum than in the regenerator beam.

The accidental activity in the calorimeter tends to center around the more intense vacuum beam, resulting in an asymmetry for an accidental cluster to merge with a photon from $2\pi^0$. The asymmetry is apparent: For cuts that eliminate events where extra photons are apparent—the four-cluster
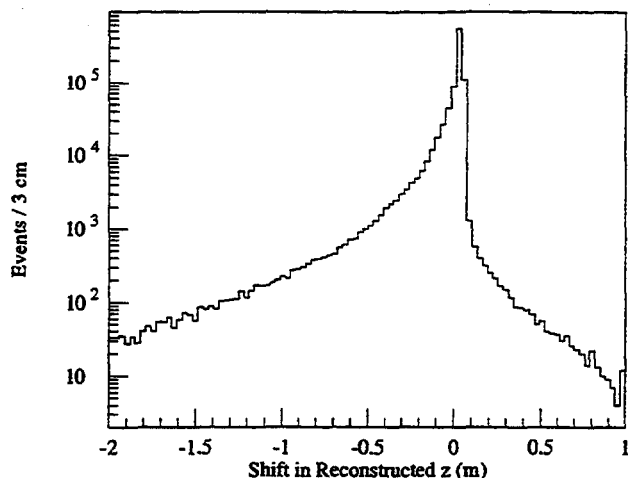
FIG. 112. Shift in the reconstructed $z$ position in $2\pi^0$ decays as a result of accidental activity in the detector. A negative value corresponds to an upstream shift away from the lead glass calorimeter.

and cluster fusion cuts—there is a greater loss of regenerator events. For cuts that discard events where a hidden accidental cluster affects the kinematics—$\chi^2$, mass, etc.—there is a greater loss of vacuum events. These losses almost compensate and the total asymmetry is quite small.

The losses are not the whole story. Accidental activity can cause events just outside of analysis cuts to satisfy those cuts after the overlay. The most important effect is a small-$z$ shift introduced by the accidental overlays (Fig. 112); it is strongly peaked at zero, but with asymmetry between upstream and downstream $z$ shifts. This is expected since extra energy tends to push the reconstructed $z$ away from the calorimeter. Since the fraction of decays near the downstream $z$ cut is larger in the vacuum beam, this asymmetry can change the vacuum-to-regenerator ratio. When both gains and losses were considered, the total change in the vacuum-to-regenerator beam ratio was $0.169\% \pm 0.060\%$. This particular study was with the lead sheet data; results without it were similar.

The absolute fraction of $2\pi^0$ events lost in the vacuum and regenerator beam samples because of accidental activity depended on cuts. For example, the event selection criteria used in $2\pi^0$ analysis, designed to minimize $3\pi^0$ back-
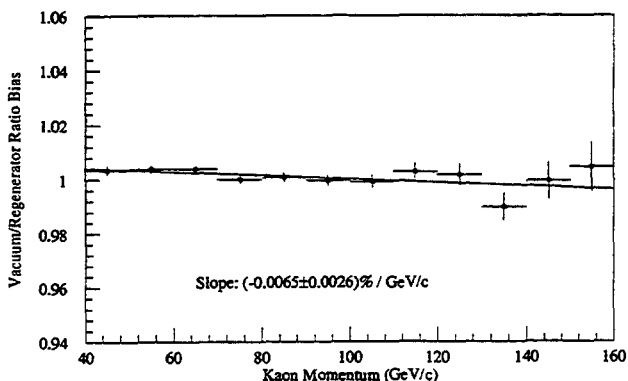


FIG. 113. Bias as a function of energy of the observed vacuum-to-regenerator beam ratio in the high-intensity $2\pi^0$ data due to accidental activity. The line drawn is the best linear fit, which has the slope listed.
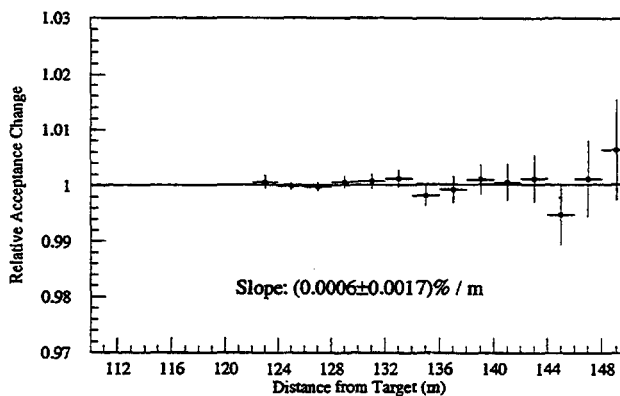


FIG. 114. Bias as a function of $z$ of the regenerator beam acceptance in the high-intensity $2\pi^0$ data due to accidental activity. The line drawn is the best linear fit, which has the slope listed.

ground, tended to remove events where activity in the lead glass was nearby (or on) a photon cluster. Systematically, it was worthwhile to tighten the cuts to reduce the $3\pi^0$ background, which was much larger in the vacuum beam, and survive with the increased loss of events. With the final cuts, the change in the sample from accidental activity was about 17% for the high-intensity running. The dominant losses came from the combination of the four-cluster requirement and the fusion and pairing $\chi^2$ cuts.

The total change in the observed vacuum-to-regenerator beam ratio is $0.169\% \pm 0.060\%$ for the high intensity data with the lead sheet present. This means the required *correction* is $-0.169\%$. The correction without the sheet is slightly smaller at $-0.154\%$. Scaling the latter value to the intensity of the NC set yields a low-intensity correction consistent with the previous study. After weighting according to the fraction of data at high intensity (about 80%) and at low intensity, the total correction to $\text{Re}(\varepsilon'/\varepsilon)$ was $+2.51\times10^{-4}$ with an uncertainty of $0.84\times10^{-4}$.

The measurements using constrained fits are not sensitive to the level of the accidental correction. The uncertainty in the vacuum-to-regenerator beam ratio is almost an order of magnitude lower than that in the kaon absorption in the regenerator beam and, hence, is negligible. Of more importance are biases in the vacuum-to-regenerator ratio vs energy (this can bias the power law) and in the regenerator beam $z$ distribution. These are plotted in Fig. 113 and Fig. 114.

The power-law shift associated with the energy dependence changes $\Delta\phi$ by about $0.1°$ and $\Delta m$ by $0.0004\times10^{10}\hbar$ s$^{-1}$. The other quantities, including $\text{Re}(\varepsilon'/\varepsilon)$, are affected negligibly.

The bias in the regenerator $z$ acceptance is consistent with zero. Its uncertainty is included in the acceptance systematic given previously.

## I. Conclusion on systematics

In general, the measurement of the $\text{Re}(\varepsilon'/\varepsilon)$ with the double-beam technique is robust. The combination of two possible cancellations—between the vacuum and regenerator beam within a decay mode, and between the regenerator samples of the two modes—tends to limit systematics from a variety of effects, such as beam absorption, accidental activity, possible aperture mismeasurements, etc. The contribu-

L. K. GIBBONS *et al.*

TABLE XXX. Summary of systematic uncertainties on Re($\varepsilon'/\varepsilon$), $\Delta m$, and $\tau_S$ measured in the $\pi^+\pi^-$ and $2\pi^0$ decay modes $\Delta\phi$ and $\phi_{+-}$.

| Systematic source | Re($\varepsilon'/\varepsilon$) $(10^{-4})$ | $\tau_S$ $(10^{-10}\text{s})$ | | $\Delta m$ $(10^{10}\hbar\text{s}^{-1})$ | | $\Delta\phi$ | $\phi_{+-}$ |
|---|---|---|---|---|---|---|---|
| | | $2\pi^0$ | $\pi^+\pi^-$ | $2\pi^0$ | $\pi^+\pi^-$ | | |
| $\gamma$ energy | 1.61 | 0.0012 | — | 0.0014 | — | 0.5° | — |
| $\pi^+\pi^-$ acceptance | 0.65 | — | 0.0020 | — | 0.0009 | 0.4° | 0.35° |
| $2\pi^0$ acceptance | 1.00 | 0.0002 | — | 0.0001 | — | — | — |
| RA4 position | 0.59 | — | — | — | — | — | — |
| HDRA material | 1.22 | 0.0001 | — | 0.0008 | — | 0.2° | — |
| $2\pi^0$ backgrounds | 1.03 | — | — | — | — | — | — |
| $\pi^+\pi^-$ backgrounds | 0.29 | — | — | — | — | — | — |
| Kaon flux | 0.30 | 0.0002 [a] | 0.0002[a] | 0.0004[a] | 0.0004[a] | 0.2° | 0.4° |
| Analyticity | — | — | 0.0003 | — | 0.0019 | — | 0.5° |
| Accidentals | 1.07 | — | — | 0.0004 | — | 0.1° | — |
| Totals | 2.87 | 0.0012 | 0.0020 | 0.0017 | 0.0021 | 0.7° | 0.7° |

[a]This error is completely correlated between the $\pi^+\pi^-$ and $2\pi^0$ samples, and is not included in the total error listed here.

tions to the systematic uncertainty on Re($\varepsilon'/\varepsilon$) are summarized in Table XXX; the total is $2.87\times10^{-4}$.

The systematic uncertainties in $\Delta m$ and $\tau_S$ and in $\Delta\phi$ and $\phi_{+-}$ are also summarized in Table XXX.

## XI. CONCLUSION

### A. Re($\varepsilon'/\varepsilon$)

Combining the results of our fits for Re($\varepsilon'/\varepsilon$) from Sec. IX A with the systematic estimate from the previous section, we have

$$\text{Re}(\varepsilon'/\varepsilon)=(7.4\pm5.2\pm2.9)\times10^{-4}, \qquad (97)$$

where the first error is the statistical uncertainty and the second error is the systematic uncertainty. A brief discussion of this result has been published [22]. Comparing this result to our earlier publication [21] based on approximately 20% of the accumulated data, this is an improvement in the statistical accuracy by a factor of 2.7 and in the systematic uncertainty by a factor of 2.1. We have improved our statistical uncertainty beyond the expected factor of $\sqrt{5}$ by extending the fiducial $z$ regions of $2\pi^0$ mode 15 m downstream. This was not possible in the $\pi^+\pi^-$ mode, which causes the $K_L\to\pi^+\pi^-$ decay to be the statistically limiting decay mode with a total of 328 980 decays after background subtraction. The dominant systematic contribution came from the uncertainty in the energy scale of the lead glass calorimeter.

Combining the statistical and systematic uncertainties in quadrature, we have

$$\text{Re}(\varepsilon'/\varepsilon)=(7.4\pm5.9)\times10^{-4}, \qquad (98)$$

which is not significantly different from zero. This result is consistent with no direct $CP$ violation in $K_L\to\pi\pi$ decays, and the superweak hypothesis cannot yet be excluded based on this measurement. At the 95% confidence level, we can place an upper limit on the value of Re($\varepsilon'/\varepsilon$) of

$$\text{Re}(\varepsilon'/\varepsilon)<17\times10^{-4}. \qquad (99)$$

This result is compared to previously published measurements of Re($\varepsilon'/\varepsilon$) in Fig. 115. After the initial publication of this result [22], a final result from CERN NA31 was published [23]. Their result, Re($\varepsilon'/\varepsilon$)=$(23\pm6.5)\times10^{-4}$, is more than $3\sigma$ from zero and does not agree very well with ours. Though the central value of the NA31 result has decreased, there is still a discrepancy at the 1.8-standard-deviation level between their result and our final result.

#### 1. Standard model predictions

The great experimental effort by both groups to improve the precision in the measurement of Re($\varepsilon'/\varepsilon$) has been paralleled by attempts to improve the precision in the calculation of Re($\varepsilon'/\varepsilon$) in the standard model. The calculation of Re($\varepsilon'/\varepsilon$) is quite difficult, particularly since the matrix elements $\langle(\pi\pi)_I|Q_i(\mu)|K\rangle$ for the decay of the neutral kaon into the $I=0,2$ $\pi\pi$ final states receive contributions from long-distance effects in QCD where perturbative approaches are not applicable. The calculation uncertainties are exacerbated by uncertainties in many of the physical parameters
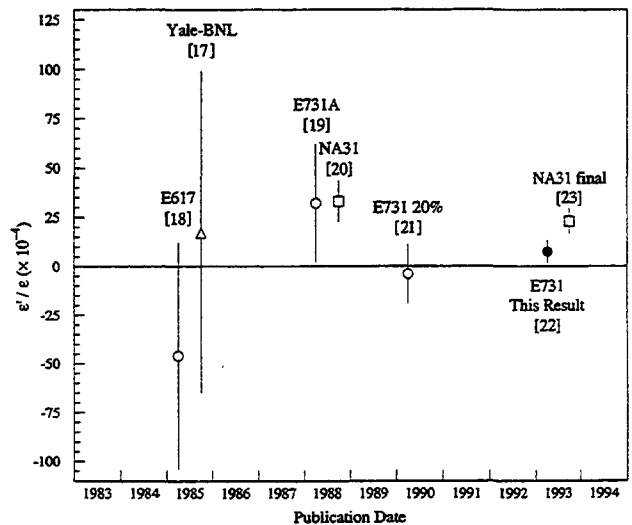


FIG. 115. The publication history of Re($\varepsilon'/\varepsilon$) measurements.

needed for the final evaluation, such as the top quark and strange quark masses $m_t$ and $m_s$, the size of CKM matrix elements $|V_{cb}|$ and $|V_{ub}|$, and the QCD scale $\Lambda_{\overline{\text{MS}}}$. While the strong penguin diagram dominates the contribution to *CP* violation for low top quark mass, Flynn and Randall [61] noticed that for higher top quark masses, the electroweak penguin diagram could provide a significant cancellation of the effect of the strong penguin. New evidence for the top quark ($m_t = 176 \pm 13$ GeV/$c^2$ from CDF [62] and $m_t = 199 \pm 30$ GeV/$c^2$ from D0 [63]) implies that this cancellation could be quite important. For top quark masses above 200 GeV/$c^2$, the cancellation could be nearly complete, making Re($\varepsilon'/\varepsilon$) hard to distinguish between the superweak models and the standard model.

In spite of the difficulties, two groups have recently finished calculations at the next-to-leading order in QCD: a Rome group which used lattice methods [64,65] and a Munich group using renormalization techniques [66]. It is very heartening that the two groups obtain fairly compatible results using different techniques. A recent summary of both of these new calculations was presented by Peccei [67], who makes a "representative prediction" of

$$\frac{\varepsilon'}{\varepsilon} = \begin{cases} (11 \pm 4) \times 10^{-4} A^2 \eta & (m_t = 140 \text{ GeV}/c^2), \\ (3 \pm 4) \times 10^{-4} A^2 \eta & (m_t = 200 \text{ GeV}/c^2), \end{cases}$$

(100)

where $A$ and $\eta$ are parameters of the CKM matrix. From the information on $\eta$ and $A$ that we have from $|\varepsilon|$, $B^0$-$\bar{B}^0$ mixing, and recent $|V_{ub}|/|V_{cb}|$ measurements, it would appear that these calculations favor values for Re($\varepsilon'/\varepsilon$) of order several times $10^{-4}$.

The Rome group has calculated the allowed range of Re($\varepsilon'/\varepsilon$) versus $\cos\delta$, where $\delta$ is the *CP*-violating phase in the CKM matrix. The central values and range for Re($\varepsilon'/\varepsilon$) do not change greatly as $|V_{ub}|$ decreases, but the allowed regions in $\cos\delta$ (or $\rho$) tend to coalesce and favor the first quadrant. The top quark mass assumed in [65] was $174 \pm 17$ GeV/$c^2$. The Munich results are for a top quark mass of $m_t = 130$ GeV/$c^2$, presented as a function of $\Lambda_{\overline{\text{MS}}}$. Both of these results are very compatible with our new measurement, and somewhat lower than the NA31 results. Unfortunately, current measurements do not have the sensitivity needed to limit the range of values allowed for parameters like $\Lambda_{\overline{\text{MS}}}$ and $m_t$. If the theoretical uncertainty continues to diminish, the next experimental efforts may well be able to provide a test of the CKM paradigm. Note that the importance of *establishing* an unambiguous signal for direct *CP* violation should not be diminished even if the theoretical uncertainties remain at their current level.

### 2. *Future for Re($\varepsilon'/\varepsilon$)*

The technique we have employed to measure Re($\varepsilon'/\varepsilon$) still holds much promise for future refinements in precision. Our current result is statistically limited, and many of the dominant contributions to the systematic uncertainty are addressable in the design of a new detector in a straightforward fashion. Our group will run a new experiment (Fermilab E832) at Fermilab, again using the double-beam technique, with a much improved beam and detector. The heart of the

new detector will be a new pure cesium-iodide (CsI) electromagnetic calorimeter that will replace the current lead glass calorimeter. Compared to our current lead glass calorimeter, the new calorimeter is expected to have much better electron and photon resolutions (of order 1%), much smaller nonlinearities, better light yields, faster timing, and (since the crystals are 27 radiation lengths long) little difference in response to electrons and photons. With this new calorimeter, it should be straightfoward to reduce the contribution of the systematic uncertainty on Re($\varepsilon'/\varepsilon$) from the $2\pi^0$ energy scale, which is the largest systematic contribution in our current measurement.

Many other areas of the experiment are also being improved. The regenerator will be fully active and hence will be able to suppress the inelastic backgrounds further. Such a regenerator has already been used successfully by this group in an experiment (Fermilab E773) dedicated to measuring $\Delta\phi$. In addition, the $3\pi^0$ background will be highly suppressed by an improved photon veto system and the finer granularity of the CsI calorimeter. All four $\pi\pi$ decay modes will be detected simultaneously in this experiment, as they were in the 20% subsample used for our first result [21]. While collecting all four modes simultaneously allows some convenient cross-checks, it is not crucial for the success of the double-beam technique.

The new experiment, slated to run in 1996, hopes to collect several $10^6$ $K_L \to \pi^0\pi^0$ and $K_L \to \pi^+\pi^-$ decays, and reach an ultimate precision of order $10^{-4}$ on Re($\varepsilon'/\varepsilon$).

The CERN NA31 experiment [68] also has a new experiment (CERN NA48), and they too are now using a double-beam method. Rather than use a regenerator to produce the $K_S$ decays, however, the CERN group will be employing two separate targets. They are also switching from a calorimetry-based charged mode detection system to a magnetic spectrometer. They hope to achieve a sensitivity approaching $10^{-4}$ on Re($\varepsilon'/\varepsilon$) as well.

### B. Other kaon parameters

#### 1. *$\Delta m$, $\tau_S$, and the superweak phase*

With the systematic contributions to the $\Delta m$ and $\tau_S$ now estimated, we can compare the results from the $\pi^+\pi^-$ and $2\pi^0$ modes, and combine the results from the two modes to compare to the current world averages. The results for $\tau_S$ are

$$\tau_S = \begin{cases} (0.8952 \pm 0.0015 \pm 0.0020) \times 10^{-10} \text{ s} & (\pi^+\pi^-), \\ (0.8912 \pm 0.0017 \pm 0.0012) \times 10^{-10} \text{ s} & (\pi^0\pi^0). \end{cases}$$

(101)

Combining the systematic and statistical errors in quadrature gives

$$\tau_S = \begin{cases} (0.8952 \pm 0.0025) \times 10^{-10} \text{ s} & (\pi^+\pi^-), \\ (0.8912 \pm 0.0021) \times 10^{-10} \text{ s} & (\pi^0\pi^0). \end{cases}$$

(102)

These numbers are in agreement with the difference at the level of 1.2 standard deviations. We therefore combine these two results, and our new measurement of $\tau_S$ becomes [31]

$$\tau_S = (0.8929 \pm 0.0016) \times 10^{-10} \text{ s},$$

(103)

which is in good agreement with previous measurements of $\tau_S$ and 25% better in precision than the PDG92 average of $(0.8922 \pm 0.0020) \times 10^{10} \hbar \, s^{-1}$ [30].

For $\Delta m$, the results from the two modes are

$$\Delta m = \begin{cases} (0.5311 \pm 0.0044 \pm 0.0020) \times 10^{10} \hbar \ s^{-1} & (\pi^+\pi^-), \\ (0.5274 \pm 0.0030 \pm 0.0017) \times 10^{10} \hbar \ s^{-1} & (\pi^0\pi^0), \end{cases}$$
(104)

and combining the errors in quadrature gives

$$\Delta m = \begin{cases} (0.5311 \pm 0.0048) \times 10^{10} \hbar \ s^{-1} & (\pi^+\pi^-), \\ (0.5274 \pm 0.0034) \times 10^{10} \hbar \ s^{-1} & (\pi^0\pi^0). \end{cases}$$
(105)

These two results are also in agreement. The consistency both of the $\Delta m$ and of the $\tau_S$ measurements, which depend on the shape of the decay distributions and hence are sensitive to biases in the acceptance, in the two different decay modes makes a powerful cross-check for our $\text{Re}(\varepsilon'/\varepsilon)$ measurement. When we combine the $\Delta m$ results from the two decay modes, our final result for $\Delta m$ is

$$\Delta m = (0.5286 \pm 0.0028) \times 10^{10} \hbar \ s^{-1}.$$
(106)

Note that this value of $\Delta m$ is the first new measure of this quantity in almost 20 years. While our result is in reasonable agreement with the previous two measurements, it is inconsistent with earliest measurements used in calculating the PDG92 average [30]. As a result, our new value is two standard deviations lower than the PDG92 average of $(0.5351 \pm 0.0024) \times 10^{10} \hbar \ s^{-1}$. Our precision is comparable to that of the PDG92 world average.

The systematic errors common to both the charged and the neutral mode (Sec. X I) have been included in the total errors for both $\Delta m$ and $\tau_S$. Even though our $\Delta m$ result is shifted lower than the PDG92 average, the value for the superweak phase we obtain using our new $\Delta m$ and $\tau_S$ results does not change significantly. We find

$$\phi_\varepsilon = \tan^{-1}(2\Delta m/[\Gamma_S - \Gamma_L]) = 43.4° \pm 0.1°.$$
(107)

Recall that the $\Delta m$ value was obtained assuming the superweak phase for $\phi_{+-}$. The dependence of $\Delta m$ to $\phi_{+-}$ is $0.0031 \times (\phi_{+-} - 43.3)\hbar \ s^{-1}$.

With $\phi_{+-}$ floating, we get $\Delta m = (0.5257 \pm 0.0049) \times 10^{10} \hbar \ s^{-1}$ (see Secs. IX B and IX C). This is still significantly lower than previous values although with larger error. Note that the PDG94 average [10] has included this result.

## C. $\Delta\phi$ and $\phi_{+-}$ measurements

### 1. Testing CPT symmetry

The first test of $CPT$ symmetry rests on the direct comparison of the phases $\phi_{+-}$ and $\phi_{00}$ of the $CP$-violating parameters $\eta_{+-}$ and $\eta_{00}$. We have found

$$\Delta\phi = -1.6° \pm 1.0° \pm 0.7°,$$
(108)

and when the statistical and systematic errors are combined in quadrature the result becomes

$$\Delta\phi = -1.6° \pm 1.2°.$$
(109)

The accuracy of our final result is a substantial improvement over that of the PDG92 average. Note that the PDG92 average for $\Delta\phi$ includes our previous result based on 20% of the data sample included in this analysis. The limit of 95% confidence level obtained from our result is $|\Delta\phi| < 3.6°$.

Let us consider the case where we have $CPT$ violation directly in $K \to \pi\pi$ decays. Following Barmin et al. [4], this can be accomplished by explicitly incorporating manifestly $CPT$-violating terms $B_I$ into the $I = 0$ and $I = 2$ decay amplitudes:

$$\langle I | H_{\text{eff}} | K^0 \rangle = (A_I + B_I) e^{i\delta_I},$$
(110)

$$\langle I | H_{\text{eff}} | \bar{K}^0 \rangle = (A_I^* - B_I^*) e^{i\delta_I}.$$
(111)

After making the same isospin decomposition as in Sec. I, the definition of $\varepsilon'$ in Eq. (16) is slightly modified:

$$\varepsilon' \to \frac{i}{\sqrt{2}} e^{i(\delta_2 - \delta_0)} \frac{\text{Im}A_2 - i\text{Re}B_2}{A_0}.$$
(112)

In this expression, we have assumed that $|\text{Im}B_0| \ll A_0$, since $A_0$ determines the rate for the dominant $K_S \to \pi\pi$ $(I = 0)$ decay rate, and it is very unlikely that a $CPT$-violating rate is this large. The $CPT$-violating component adds a term that is 90° out of phase with the previous $CP$-violating but $CPT$-conserving term. Since the final state $\pi\pi$ phase shifts place $\varepsilon'$ so close to parallel with $\varepsilon$ and since $\Delta\phi$ is so small, we can use the above expression in conjunction with Eqs. (17) and (18) to give

$$\frac{\text{Re}B_2}{\text{Re}A_2} = \frac{1}{|\omega|} \frac{\text{Re}B_2}{A_0} \approx \frac{\sqrt{2}}{3} \frac{|\varepsilon|}{|\omega|} (\phi_{+-} - \phi_{00}),$$
(113)

where $\omega \approx 1/22$ is the measured violation of the $\Delta I = 1/2$ rule. Using the PDG92 value [30] for $|\eta_{+-}|$ as the value of $|\varepsilon|$ and our new result for $\Delta\phi$, we get

$$\frac{\text{Re}B_2}{\text{Re}A_2} = (6.5 \pm 4.9) \times 10^{-4}.$$
(114)

With some reasonable assumptions about isospin, Barmin et al. [4] relate the $K^+$ and $K^-$ lifetime difference to the above ratio:

$$\frac{\tau^+ - \tau^-}{\tau^+} \approx -0.84 \frac{\text{Re}B_2}{\text{Re}A_2}.$$
(115)

This allows us to compare the strength of the $CPT$ test based on this result relative to the direct comparison of the lifetimes and place the $\Delta\phi$ $CPT$ test in a more intuitive framework:

$$\frac{\tau^+ - \tau^-}{\tau^+} = \begin{cases} (-5 \pm 4) \times 10^{-4} & (\text{our } \Delta\phi), \\ (11 \pm 9) \times 10^{-4} & (\text{from PDG [30]}). \end{cases}$$

The first result was obtained from our $\Delta\phi$ measurement and the second from the experimental measurements of the charged kaon lifetimes. In this framework, we see that the

TABLE XXXI. Our result for and previous best measurements of $\phi_{+-}$. We have corrected the previously reported value of $\phi_{+-}$ for the change in the assumed $\Delta m$ to our current result for $\Delta m$ using the reported experimental dependences.

| Experiment | $\phi_{+-}$ (deg.) | Internal error (deg.) | Assumed $\Delta m$ ($\times 10^{10} \hbar \, \mathrm{s}^{-1}$) | $\Delta \phi_{+-}$ for $+1\%$ $\delta \Delta m$ (deg.) | $\phi_{+-}$ (our $\Delta m$) (deg.) |
|---|---|---|---|---|---|
| Gjesdal et al. [28] | 45.6 | 1.0 | 0.5338 | 3.05 | 43.0 |
| Carithers et al. [29] | 45.5 | 2.8 | 0.5348 | 1.20 | 44.1 |
| Carosi et al. [27] | 46.9 | 1.6 | 0.5351 | 3.10 | 43.4 |
| This experiment [31] | 42.2 | 1.4 | Floated[a] | — | 42.2 |

[a]See Sec. IX C.

current $\Delta \phi$ measurement places stronger bounds on possible $CPT$ violation than those placed by the direct lifetime measurements.

### 2. $\phi_{+-}$ measurement

The final measurement we have made is the measurement of $\phi_{+-}$ itself, and we have found

$$\phi_{+-} = 42.2° \pm 1.3° \pm 0.7°, \qquad (116)$$

where, as usual, the first error is statistical and the second error is systematic. Combining the errors in quadrature, we have

$$\phi_{+-} = 42.2° \pm 1.5°. \qquad (117)$$

This is in excellent agreement with the superweak phase $\phi_\varepsilon = 43.4°$ (43.7°) found using our (PDG92) values for $\Delta m$ and $\tau_S$. On the other hand, this result disagrees with the previous PDG92 average [30] for $\phi_{+-}$ of $46.5° \pm 1.2°$ at slightly over the two-standard-deviation level. The value for $\phi_{+-}$ extracted from each of the previous experiments, however, depends on the value of $\Delta m$ assumed (the PDG92 average, in this case).

Since our $\Delta m$ result is lower than the previous measurements, it is interesting to compare results of different phase experiments after correcting the experiments using our value of $\Delta m$. The results of the individual corrections to $\phi_{+-}$ are listed in Table XXXI, and the previous measurements agree very well with our own. When we now average the previous results with our own, we obtain a new world average of

$$\phi_{+-} = 42.8° \pm 1.1°, \qquad (118)$$

which agrees very well with the superweak phase.

Note that no conclusions of this argument are significantly altered when we use the value of $\Delta m$ which we obtained with $\phi_{+-}$ floating.

We can again try to relate this measurement to other physical parameters of the kaon. Of particular interest is the difference between the masses of the $K^0$ and $\bar{K}^0$, which should be equal if $CPT$ is a good symmetry of nature. Let us consider for the $CPT$-violating quantity $\bar{\varepsilon}$ defined similarly to Eq. (5) as

$$\bar{\varepsilon} = \frac{\iota (M_{11} - M_{22}) + \frac{1}{2}(\Gamma_{11} - \Gamma_{22})}{2[\iota \Delta m - \frac{1}{2}(\Gamma_S - \Gamma_L)]}$$

$$= -e^{\iota \phi_\varepsilon} \frac{\iota (M_{11} - M_{22}) + \frac{1}{2}(\Gamma_{11} - \Gamma_{22})}{2 \kappa \sqrt{2} \Delta m}, \qquad (119)$$

where $\kappa \equiv [1 + 1/(2 \Delta m \tau_S)^2]^{1/2}/\sqrt{2} = 1.03$. Since we assumed $M$ and $\Gamma$ were Hermitian, $M_{11}$ and $M_{22}$ are real, and if their difference is nonzero (that is, if the $K^0$ and $\bar{K}^0$ masses are not equal), then $\bar{\varepsilon}$ adds a term common to both $\eta_{+-}$ and $\eta_{00}$ that is 90° out of phase with the contribution from $\varepsilon$. If we suppose that the $I = 0$ $\pi\pi$ decays saturate $\Gamma$ [67,69], then applying our current results for $|\eta_{00}/\eta_{+-}| \approx [1 - 3\mathrm{Re}(\varepsilon'/\varepsilon)]$ and for $\Delta \phi$ to the argument in Barmin et al. [4] implies one would not expect the second term to change the component of $\eta$ parallel to $\varepsilon$ beyond a limit of roughly 5%. For our purposes here, we therefore simply ignore this possible $CPT$-violating contribution.

Since the $CPT$-violating term from $\bar{\varepsilon}$ that arises from the mixing matrix is perpendicular to the $CP$-violating term, they form a right triangle with $\eta$ along the hypotenuse, and we therefore have

$$\tan(\phi_{+-} - \phi_\varepsilon) = \frac{1}{\varepsilon} \frac{m_{K^0} - m_{\bar{K}^0}}{2 \sqrt{2} \kappa \Delta m}. \qquad (120)$$

With our adjusted world average for $\phi_{+-}$ and our new value of the superweak phase, $\tan(\phi_{+-} - \phi_\varepsilon) = -0.010 \pm 0.019$. Combining this result with the world average of $|\eta_{+-}|$ for $|\varepsilon|$, the world average value of the neutral kaon mass, and our new value for $\Delta m$ of $(3.479 \pm 0.018) \times 10^{-12}$ MeV/$c^2$, we can limit

$$\left| \frac{m_{K^0} - m_{\bar{K}^0}}{m_{K^0}} \right| < 2.0 \times 10^{-18} \qquad (121)$$

at the 95% confidence level. This limit is about a factor of 2 better than the limit based on the PDG92 average value of $\phi_{+-}$ [30], with the improvement coming mainly from the shift in $\phi_{+-}$ towards the superweak phase.

In all, the combination of our new $\Delta m$, $\Delta \phi$, and $\phi_{+-}$ measurements further improves the limits on $CPT$ violation.

## D. Other recent measurements

Since the initial publication of these results [31], two experiments have published results concerning $\Delta m$, $\tau_S$, $\phi_{+-}$, and $\Delta\phi$. The measurements of Fermilab E773 [70], were made using essentially the same equipment described here, and a detailed article on E773 is in preparation [71]. They find $\tau_S = (0.8941 \pm 0.0014 \pm 0.0009) \times 10^{-10}$ s, $\Delta m = (0.5297 \pm 0.0030 \pm 0.0022) \times 10^{10} \hbar$ s$^{-1}$, $\phi_{+-} = 43.53°$ $\pm 0.58° \pm 0.49°$, and $\Delta\phi = 0.62° \pm 0.71° \pm 0.75°$, where the first errors quoted are statistical and the second systematic. The CERN CPLEAR experiment has measured $\Delta m$ using semileptonic neutral $K$ decays, which frees this measurement of the correlation with $\phi_{+-}$ that one has with this measument in the $\pi\pi$ decay mode. They find $\Delta m = (0.5274 \pm 0.0029 \pm 0.0005) \times 10^{10} \hbar$ s$^{-1}$ [72]. They have also measured $\phi_{+-}$ [73], finding $\phi_{+-} = 42.7° \pm 0.9°$ $\pm 0.6° \pm 0.9°$, where again the first and second errors are statistical and systematic, and the third error is from the uncertainty in their $\Delta m$ measurement.

These measurements are consistent with the findings of E731. In particular, they confirm the supposition put forward in [31] that the disagreement between $\phi_{+-}$ and $\phi_\varepsilon$ arose simply because of the bias in the $\phi_{+-}$ resulting from too high an experimental value for $\Delta m$. Note that the E731 results are competitive with these later results, even though the experiment was not optimized for these particular measurements. The good agreement between these experiments and the E731 results for neutral $K$ parameters lends additional credence to the reliability of the $\varepsilon'/\varepsilon$ measurement presented here.

## E. Summary remarks

Experiment E731 was designed to measure $\mathrm{Re}(\varepsilon'/\varepsilon)$. The final error quoted is a factor of 10 improvement over the best result prior to this effort, E617, a predecessor to this effort. In addition, the phase difference $\Delta\phi$ has been improved from an error of $6° - 1.2°$, and the best values of $\tau_S$ and $\phi_{+-}$ have been reported. The first measurment of $\Delta m$ in 20 years has also been made, and correcting previous determinations of $\phi_{+-}$ for this new value brings all experiments into agreement with each other and with $CPT$ symmetry. Additional rare decay modes have been studied with this data set. The question of direct $CP$ violation remains open.

[1] L. K. Gibbons, Ph.D. thesis, The University of Chicago, 1993.
[2] T. D. Lee and C. S. Wu, Annu. Rev. Nucl. Sci. **16**, 511 (1966).
[3] L. Wolfenstein, Nuovo Cimento A **63**, 269 (1969).
[4] V V. Barmin *et al.*, Nucl. Phys. **B347**, 293 (1984); **B254**, 747 (1984).
[5] J. W. Cronin, Acta Phys. Pol. B **15**, 419 (1984).
[6] R. G. Sachs, *The Physics of Time Reversal* (The University of Chicago Press, Chicago, 1987).
[7] K. Kleinknecht, in *CP Violation*, edited by C. Jarlskog (World Scientific, Singapore, 1989), p. 41.
[8] B. Winstein and L. Wolfenstein, Rev. Mod. Phys. **65**, 1113 (1993).
[9] T. T. Wu and C. N. Yang, Phys. Rev. Lett. **13**, 380 (1964).
[10] Particle Data Group, L. Montanet *et al.*, Phys. Rev. D **50**, 1173 (1994).
[11] L. K. Gibbons *et al.*, Phys. Rev. Lett. **61**, 2661 (1988).
[12] V. Papadimitriou *et al.*, Phys. Rev. Lett. **63**, 28 (1989).
[13] A. R. Barker *et al.*, Phys. Rev. D **41**, 3546 (1990).
[14] V. Papadimitriou *et al.*, Phys. Rev. D **44**, R573 (1991).
[15] G. E.Graham *et al.*, Phys. Lett. B **295**, 169 (1992).
[16] W. Ochs, Munich Report No. MPI-Ph/Ph91-35; $\pi N$ Newsletter, No. 3, 1991, p. 25.
[17] J. K. Black *et al.*, Phys. Rev. Lett. **54**, 1628 (1985).
[18] R. H. Bernstein *et al.*, Phys. Rev. Lett. **54**, 1631 (1985).
[19] M. Woods *et al.*, Phys. Rev. Lett. **60**, 1695 (1988).
[20] H. Burkhardt *et al.*, Phys. Lett. B **206**, 169 (1988).

[21] J. R. Patterson *et al.*, Phys. Rev. Lett. **64**, 1491 (1990).
[22] L. K. Gibbons *et al.*, Phys. Rev. Lett. **70**, 1203 (1993).
[23] G. D. Barr *et al.*, Phys. Lett. B **317**, 233 (1993).
[24] M. Kobayashi and A. I. Sanda, Phys. Rev. Lett. **69**, 3139 (1992).
[25] V. A. Kostelecky and Robertus Potting, Nucl. Phys. **B359**, 545 (1991); Phys. Rev. D **51**, 3923 (1995).
[26] M. Karlsson *et al.*, Phys. Rev. Lett. **64**, 2976 (1990).
[27] R. Carosi *et al.*, Phys. Lett. B **237**, 303 (1990).
[28] S. Gjesdal *et al.*, Phys. Lett. **52B**, 119 (1974).
[29] W. C. Carithers *et al.*, Phys. Rev. Lett. **34**, 1244 (1975).
[30] Particle Data Group, K. Hikasa *et al.*, Phys. Rev. D **45**, S1 (1992).
[31] L. K. Gibbons *et al.*, Phys. Rev. Lett. **70**, 1199 (1993).
[32] W. R. Molzon *et al.*, Phys. Rev. Lett. **41**, 1213 (1978).
[33] J. Ellis, M. K. Gaillard, and D. V. Nanopoulos, Nucl. Phys. **B109**, 213 (1976).
[34] Frederick J. Gilman, Phys. Rev. **171**, 1453 (1968).
[35] Roy A. Briere and Bruce Winstein, Phys. Rev. Lett. **75**, 402 (1995); **75**, 2070 (1995).
[36] J. R. Patterson, Ph.D. thesis, The University of Chicago, 1990.
[37] V. Papadimitriou, Ph.D. thesis, The University of Chicago, 1990.
[38] M. Karlsson, Ph.D. thesis, Princeton University, 1990.
[39] M. B.Woods, Ph.D. thesis, The University of Chicago, 1988.

[40] A. M. Eisner, R. J. Morrison, J. Cumalat, and C. Lauer, Nucl. Instrum. Methods **143**, 311 (1977).

[41] M. Asner *et al.*, Nucl. Instrum. Methods Phys. Res. A **291**, 577 (1990).

[42] E. Longo and I. Sestili, Nucl. Instrum. Methods **128**, 283 (1975).

[43] W. R. Nelson, H. Hirayama, and W. O. Rogers, ''The EGS4 code system,'' Report No. SLAC-Report-265, Stanford Linear Accelerator Center, 1985 (unpublished).

[44] A. Carroll *et al.*, Phys. Rev. Lett. **44**, 529 (1980).

[45] E. J. Ramberg *et al.*, Phys. Rev. Lett. **70**, 2525 (1993).

[46] W. R. Molzon, Ph.D. thesis, The University of Chicago, 1979.

[47] J. Roehrig *et al.*, Phys. Rev. Lett. **38**, 1116 (1977).

[48] G. J. Bock *et al.*, Phys. Rev. Lett. **42**, 350 (1979).

[49] A. Gsponer *et al.*, Phys. Rev. Lett. **42**, 13 (1979).

[50] A. J. Malensek, Report No. FN-341, Fermi National Accelerator Laboratory, 1981 (unpublished).

[51] R. A. Briere, Ph.D. thesis, The University of Chicago, 1995.

[52] A. Schiz *et al.*, Phys. Rev. D **21**, 3010 (1980).

[53] J. H. Hubbell, H. A. Gimm, and I. Øverbø, J. Phys. Chem. Ref. Data **9**, 1023 (1980).

[54] B. Rossi, *High Energy Particles* (Prentice-Hall, Englewood Cliffs, NJ, 1952).

[55] A. Gsponer *et al.*, Phys. Rev. Lett. **42**, 9 (1979).

[56] J. Roehrig, Ph.D thesis, The University of Chicago, 1977.

[57] E. C. Swallow, in *The Vancouver Meeting, Particles and Fields '91*, edited by D. Axen, D. Bryman, and M. Comyn (World Scientific, Singapore, 1992), p. 581.

[58] B. Schwingenheuer, Ph.D. thesis, The University of Chicago, 1995.

[59] D'Huart Industrie S. A., Certificat d'analyse chimique, Coulee No. 873, 1976 (unpublished).

[60] K. Kleinknecht and S. Luitz, Phys. Lett. B **336**, 581 (1994).

[61] J. M. Flynn and L. Randall, Phys. Lett. B **224**, 221 (1989).

[62] F. Abe *et al.*, Phys. Rev. Lett. **74**, 2626 (1995).

[63] S. Abachi *et al.*, Phys. Rev. Lett. **74**, 2632 (1995).

[64] M. Ciuchini, E. Franco, G. Martinelli, and L. Reina, Phys. Lett. B **301**, 263 (1993).

[65] M. Ciuchini, E. Franco, G. Martinelli, L. Reina and L. Silvestrini, Z. Phys. C **68**, 239 (1995).

[66] A. J. Buras, M. Jamin, and M. E. Lautenbacher, Nucl. Phys. **B408**, 209 (1993).

[67] R. D. Peccei, Report No. UCLA/93/TEP/19, University of California, Los Angeles, 1993 (unpublished).

[68] H. Burkhardt, Nucl. Instrum. Methods Phys. Res. A **268**, 116 (1988).

[69] J. W. Cronin, Rev. Mod. Phys. **53**, 373 (1981).

[70] B. Schwingenheuer *et al.*, Phys. Rev. Lett. **74**, 4376 (1995).

[71] R. A. Briere *et al.* (in preparation).

[72] R. Adler *et al.*, Phys. Lett. B **363**, 237 (1995).

[73] R. Adler *et al.*, Phys. Lett. B **363**, 243 (1995).

TABLE I. Recently published measurements of $Re(\varepsilon'/\varepsilon)$. Errors listed are statistical error first and the systematic error second, otherwise the combined error.

| Collaboration | Year | $Re(\varepsilon'/\varepsilon)$ $(10^{-4})$ |
|---|---|---|
| Yale–BNL [29] | 1985 | $17 \pm 82$ |
| Chicago–Saclay (FNAL E617) [30] | 1985 | $-46 \pm 53 \pm 24$ |
| Chicago–Elmhurst–FNAL–Princeton–Saclay (FNAL E731A) [31] | 1988 | $32 \pm 28 \pm 12$ |
| CERN–Dortmund–Edinburgh–Mainz–Orsay– Pisa–Siegen (CERN NA31) [17] | 1988 | $33 \pm 7 \pm 8$ |
| Chicago–Elmhurst–FNAL–Princeton–Saclay (FNAL E731 20%) [18] | 1990 | $-4 \pm 14 \pm 6$ |
| Chicago–Elmhurst–FNAL–Princeton–Saclay (FNAL E731 final result) [19] | 1993 | $7.4 \pm 5.2 \pm 2.9$ |
| CERN–Edinburgh–Mainz–Orsay–Pisa–Siegen (CERN NA31 final result) [20] | 1993 | $23 \pm 6.5$ |

TABLE II. The detector elements and their positions from target.

| Detector Element | z-location (meter) | Detector Element | z-location (meter) |
|---|---|---|---|
| Pinching Anti (PA) | 116.118 | Drift Chamber 1 | 159.292 |
| Sweeper Anti (SA) | 119.59 | Drift Chamber 2 | 165.867 |
| Sweeper Magnet | 119.59 | Magnet Anti (MA) | 166.836 |
| Active Mask (AM) | 121.893 | Analyzing Magnet | 168.865 |
| Regenerator | 123.550 | Drift Chamber 3 | 171.857 |
| Vacuum Anti 1 (VA1) | 127.855 | Drift Chamber 4 | 178.004 |
| Vacuum Anti 2 (VA2) | 132.819 | Lead Glass Anti (LGA) | 178.710 |
| V hodoscope | 137.792 | C Hodoscope | 179.502 |
| Lead sheet | 137.804 | B Hodoscope | 179.520 |
| T hodoscope | 137.815 | Collar Anti (CA) | 180.700 |
| DRAC veto counter | 137.826 | Lead Glass Array | 181.809 |
| DRAN veto counter | 137.866 | Lead Wall | 182.7 |
| Separator Magnet | 139.008 | Mu1 Hadron Veto | 183.996 |
| Vacuum Anti 3 (VA3) | 149.309 | Back Anti (BA) | 185.047 |
| Vacuum Anti 4 (VA4) | 158.291 | 3.2m Steel Muon Filter | 186.7 |
| Vacuum Window | 158.965 | Mu2 Muon Veto | 189.914 |

TABLE III. A list of the materials in the HDRA and their physical properties. The thicknesses are averaged over the beam region, while the radiation lengths are averaged over the illuminated region. The lead sheet was not always present (see text). $(f - \bar{f})/k$ is given at 70 GeV/c.

| Material | Thickness (mm) | Density (gm/cm$^3$) | Atomic Weight | $\frac{f-\bar{f}}{k}$ (mbarn) | $\frac{f+\bar{f}}{k}$ (mbarn) | Radiation Length (%) |
|---|---|---|---|---|---|---|
| Scintillator | 2.17 | 1.03 | 13.0 | 1.15 | 33.10 | 0.497 |
| Mylar | 0.11 | 1.39 | 96.1 | 8.29 | 239.57 | 0.044 |
| Aluminum | 0.05 | 2.70 | 27.0 | 2.07 | 59.21 | 0.058 |
| Paper | 0.38 | 0.63 | 94.1 | 10.89 | 229.51 | 0.066 |
| Lead | 0.515 | 11.35 | 207.2 | 9.71 | 326.28 | 8.9 |

TABLE IV. The characteristics of the $\pi^+\pi^-$ and $2\pi^0$ data subsets.

| Subset | Proton Beam Intensity (10^12 per spill) | Pb Sheet Installed | $2\pi^0$ Triggers to Tape (10^6) | $\pi^+\pi^-$ Triggers to Tape (10^6) |
|---|---|---|---|---|
| C1 | 0.3 | No | – | 16 |
| N1 | 2.0 | Yes | 44 | – |
| C2 | 0.3 | No | – | 70 |
| N2 | 2.0 | Yes | 36 | – |
| C3 | 0.3 | No | – | 82 |
| N3 | 2.0 | Yes | 22 | – |
| N4 | 2.0 | No | 8 | – |
| C4 | 0.3 | No | – | 75 |
| NC | 0.8 | No | 61 | 61 |

TABLE V. Rotation of the horizontal $y$ view sense wires away from the perpendicular $x$ view wires in each drift chamber. For a positive rotation, the horizontal $y$ wires are high on the $+x$ side of the chamber and low on the $-x$ side.

| Chamber | Rotation ($\mu$rad) |
|---|---|
| 1 | 0 |
| 2 | 47 |
| 3 | 198 |
| 4 | -150 |

TABLE VI. The fraction of coherent $\pi^+\pi^-$ decays lost as each analysis cut is applied sequentially, and when a cut is applied as the final cut. For the first sequential cut, the loss is relative to the number of $\pi^+\pi^-$ events which reconstruct within the fiducial energy and $z$ region used in the fits. Each cut thereafter is normalized to the number of kaons left after the preceding cut. Here "$K_L$" and "$K_S$" have been used as shorthand for the vacuum and regenerator beams, respectively. The two momentum ranges are given in GeV/c.

| Analysis cut | Sequential loss (%) | | | | Loss as Final Cut (%) | | | |
|---|---|---|---|---|---|---|---|---|
| | 40–160 | | 20–160 | | 40–160 | | 20–160 | |
| | $K_L$ | $K_S$ | $K_L$ | $K_S$ | $K_L$ | $K_S$ | $K_L$ | $K_S$ |
| Pions within calorimeter | 3.77 | 4.68 | 7.12 | 7.93 | 1.09 | 1.35 | 2.14 | 2.49 |
| Vacuum Window Aperture | 0.04 | 0.05 | 0.15 | 0.22 | 0.02 | 0.03 | 0.11 | 0.16 |
| Analysis Magnet Aperture | 0.55 | 0.74 | 1.16 | 1.62 | 0.30 | 0.40 | 0.73 | 1.16 |
| HDRA Aperture | 0.03 | 0.01 | 0.05 | 0.02 | 0.02 | 0.00 | 0.04 | 0.01 |
| Tracks Remain in Helium Volume | 0.02 | 0.09 | 0.30 | 0.44 | 0.02 | 0.07 | 0.29 | 0.47 |
| $\Lambda$ cuts | 2.71 | 1.98 | 2.38 | 1.75 | 0.56 | 0.34 | 0.48 | 0.30 |
| $p_\pi > 7$ GeV/c | 3.16 | 3.38 | 4.10 | 3.87 | 0.79 | 0.91 | 1.41 | 1.13 |
| Track $\chi^2$ [a] | 0.04 | 0.05 | 0.04 | 0.05 | 0.02 | 0.02 | 0.02 | 0.02 |
| Distance of Closest Approach | 0.95 | 0.94 | 0.90 | 0.91 | 0.86 | 0.89 | 0.79 | 0.83 |
| Track Separation at Magnet | 0.04 | 0.05 | 0.06 | 0.06 | 0.03 | 0.04 | 0.05 | 0.04 |
| $\pi \to \mu\nu$ decay veto | 1.86 | 2.09 | 2.29 | 2.41 | 2.23 | 2.47 | 2.69 | 2.80 |
| Mask Aperture | 1.00 | 0.01 | 0.92 | 0.01 | 1.06 | 0.00 | 0.95 | 0.00 |
| No pions in CA or beam hole | 21.99 | 21.05 | 19.68 | 18.84 | 19.38 | 18.54 | 17.23 | 16.50 |
| Chamber 2 Trigger Reverify | 0.01 | 0.00 | 0.01 | 0.00 | 0.01 | 0.00 | 0.01 | 0.00 |
| BC Hodoscope Trigger Reverify | 1.89 | 1.95 | 1.92 | 1.92 | 1.74 | 1.80 | 1.77 | 1.77 |
| $\pi^+\pi^-$ Mass | 1.36 | 1.39 | 1.47 | 1.54 | 0.39 | 0.40 | 0.40 | 0.42 |
| $p_t^2$ | 0.55 | 0.48 | 0.49 | 0.43 | 0.55 | 0.48 | 0.49 | 0.43 |

[a] Without $\delta - rays$. See text for loss estimates from $\pi^+\pi^-\pi^0$ studies.

TABLE VII. The number of coherent $\pi^+\pi^-$ decays after background subtraction, and the total background fraction subtracted in each 10 GeV/$c$ bin. The background levels are given in percent. Indicated errors include only statistical uncertainties.

| Momentum Range | Vacuum Beam | | Regenerator Beam | |
|---|---|---|---|---|
| (GeV/$c$) | Data | Background (%) | Data | Background (%) |
| 20-30 | 11712 | $0.31 \pm 0.05$ | 19059 | $0.158 \pm 0.029$ |
| 30-40 | 42092 | $0.34 \pm 0.03$ | 144363 | $0.165 \pm 0.011$ |
| 40-50 | 59701 | $0.37 \pm 0.02$ | 230593 | $0.160 \pm 0.008$ |
| 50-60 | 59983 | $0.40 \pm 0.03$ | 222405 | $0.157 \pm 0.008$ |
| 60-70 | 52227 | $0.37 \pm 0.03$ | 185010 | $0.153 \pm 0.009$ |
| 70-80 | 42380 | $0.34 \pm 0.03$ | 136064 | $0.150 \pm 0.010$ |
| 80-90 | 32525 | $0.32 \pm 0.03$ | 97159 | $0.145 \pm 0.012$ |
| 90-100 | 24702 | $0.28 \pm 0.03$ | 66862 | $0.144 \pm 0.015$ |
| 100-110 | 17689 | $0.27 \pm 0.04$ | 44144 | $0.143 \pm 0.018$ |
| 110-120 | 13241 | $0.26 \pm 0.04$ | 30246 | $0.143 \pm 0.022$ |
| 120-130 | 9704 | $0.26 \pm 0.05$ | 20461 | $0.142 \pm 0.026$ |
| 130-140 | 7056 | $0.25 \pm 0.06$ | 13414 | $0.142 \pm 0.033$ |
| 140-150 | 5486 | $0.25 \pm 0.07$ | 8656 | $0.141 \pm 0.040$ |
| 150-160 | 4286 | $0.24 \pm 0.08$ | 5654 | $0.141 \pm 0.050$ |
| 20-160 | 382783 | $0.340 \pm 0.009$ | 1224088 | $0.154 \pm 0.004$ |
| 40-160 | 328980 | $0.341 \pm 0.010$ | 1060667 | $0.152 \pm 0.004$ |

TABLE VIII. Reconstructed $2\pi^0$ mass shift $\delta m$ in MeV of data relative to Monte Carlo simulation in the five neutral subsets. Two of the subsets have been subdivided into time periods for which separate calibrations have been used. A negative shift implies the $2\pi^0$ mass in the data was lower than that in the Monte Carlo.

| $2\pi^0$ subset sample | N1a | N1b | N2 | N3 | N4 | NCa | NCb |
|---|---|---|---|---|---|---|---|
| $\delta m$ (no pipe block cluster) | −0.76 | −0.83 | −0.71 | −0.74 | −0.63 | −0.43 | −0.44 |
| $\delta m$ ($\geq 1$ pipe block clusters) | −1.07 | −1.40 | −0.90 | −0.94 | −0.82 | −0.65 | −0.60 |

TABLE IX. Photon veto cuts in minimum ionizing equivalents (MIPs) applied in the $2\pi^0$ sample.

| Veto Detectors | Low Intensity cut | High Intensity Cut |
|---|---|---|
| VA1 | 2.6 | none |
| VA2 | 1.3 | 6.0 |
| DRAC | 0.5 | 1.2 |
| DRAN | 0.6 | 1.5 |
| VA3 | 1.0 | 1.8 |
| VA4 | 1.5 | 3.0 |
| MA | 2.0 | 1.8 |
| LGA | 2.5 | 5.0 |

TABLE X. The fraction of coherent $2\pi^0$ decays in the regenerator beam lost after each analysis cut is applied as determined from the Monte Carlo simulation. In the "Sequential Loss" columns, the loss of the first cut is normalized to all $2\pi^0$ events which reconstructed within the fiducial energy and $z$ region used for the $Re(\varepsilon'/\varepsilon)$ fits. Each cut thereafter is normalized to the number of kaons left after the preceding cut. The precision in this table is approximately 0.03% (only a small portion of the MC was used).

| Analysis cut | Sequential loss (%) | | Loss as Final Cut (%) | |
|---|---|---|---|---|
| | Pb Sheet | No Pb Sheet | Pb Sheet | No Pb Sheet |
| Chamber and hodoscope hits | 21.37 | 1.12 | 15.49 | 0.06 |
| Ring number | 3.28 | 2.26 | 2.74 | 1.81 |
| Photon veto | 0.00 | 0.00 | 0.00 | 0.00 |
| Minimum cluster energy | 1.35 | 1.43 | 0.89 | 1.00 |
| Maximum cluster energy | 8.81 | 8.67 | 7.77 | 7.82 |
| Cluster fusion cuts | 0.90 | 0.80 | 0.90 | 0.79 |
| Best pairing $\chi^2$ | 3.09 | 2.50 | 2.76 | 2.21 |
| Mispairing cuts | 1.74 | 1.61 | 0.99 | 0.93 |
| $2\pi^0$ mass | 0.26 | 0.21 | 0.26 | 0.21 |

TABLE XI. The parameters for the photon energy scale corrections, and the average correction applied, in the each $2\pi^0$ subset.

| Subset | Slope $(E_K < 80~\mathrm{GeV})$ [% per GeV] | Slope $(E_K > 80~\mathrm{GeV})$ [% per GeV] | 80 GeV correction [%] | Average Correction [%] |
|---|---|---|---|---|
| N1a | $-1.7 \times 10^{-3}$ | $+0.4 \times 10^{-3}$ | -0.094 | -0.06 |
| N1b | $-4.2 \times 10^{-3}$ | $-2.9 \times 10^{-3}$ | -0.041 | 0.02 |
| N2 | $-4.2 \times 10^{-3}$ | $-6.5 \times 10^{-3}$ | +0.065 | 0.11 |
| N3 | $-4.3 \times 10^{-3}$ | $-2.8 \times 10^{-3}$ | +0.080 | 0.14 |
| N4 | $-4.5 \times 10^{-3}$ | $-7.0 \times 10^{-3}$ | +0.176 | 0.22 |
| NCa | $-5.0 \times 10^{-3}$ | $-3.3 \times 10^{-3}$ | +0.324 | 0.39 |
| NCb | $-3.2 \times 10^{-3}$ | $+0.9 \times 10^{-3}$ | +0.313 | 0.37 |

TABLE XII. The $2\pi^0$ background sources and fractions.

| Source | Vacuum Beam Fraction (%) | Regenerator Beam Fraction (%) |
|---|---|---|
| $3\pi^0$ background | $1.78 \pm 0.03$ | $0.049 \pm 0.003$ |
| Beam Interaction | $0.21 \pm 0.02$ | $0.027 \pm 0.004$ |
| Regenerator Noncoherent Scattering | $2.26 \pm 0.04$ | $2.53 \pm 0.04$ |
| HDRA Diffractive Scattering | $0.78 \pm 0.02$ | $0.027 \pm 0.002$ |
| HDRA Inelastic Scattering | $0.13 \pm 0.02$ | $0.027 \pm 0.011$ |

TABLE XIII. The number of coherent $2\pi^0$ decays after background subtraction and the total background fraction in each 10 GeV bin for the lead sheet and no lead sheet data samples. The background levels are given in percent.

| Momentum Range (GeV/$c$) | Lead | | | | No Lead | | | |
|---|---|---|---|---|---|---|---|---|
| | Vacuum | | Regenerator | | Vacuum | | Regenerator | |
| | Data | Bkg(%) | Data | Bkg(%) | Data | Bkg(%) | Data | Bkg(%) |
| 40-50 | 45812 | 4.8 | 45667 | 1.6 | 30096 | 3.5 | 34700 | 1.4 |
| 50-60 | 51102 | 5.0 | 83563 | 1.7 | 34659 | 3.8 | 62948 | 1.6 |
| 60-70 | 46171 | 5.5 | 93830 | 2.2 | 31852 | 4.3 | 70311 | 2.0 |
| 70-80 | 36369 | 6.2 | 83444 | 2.7 | 25862 | 5.0 | 61841 | 2.6 |
| 80-90 | 26301 | 6.3 | 63474 | 3.2 | 18617 | 5.5 | 47401 | 3.1 |
| 90-100 | 16965 | 6.6 | 41124 | 3.9 | 12106 | 5.9 | 30694 | 3.7 |
| 100-110 | 9869 | 6.8 | 24102 | 4.5 | 7043 | 6.1 | 17605 | 4.4 |
| 110-120 | 5267 | 6.6 | 12821 | 5.2 | 3855 | 6.0 | 9360 | 5.2 |
| 120-130 | 2682 | 5.9 | 6188 | 5.8 | 1898 | 6.1 | 4383 | 6.0 |
| 130-140 | 1348 | 4.7 | 2626 | 6.4 | 941 | 4.8 | 1766 | 7.1 |
| 140-150 | 618 | 3.2 | 955 | 7.2 | 424 | 2.9 | 675 | 7.4 |
| 150-160 | 277 | 1.6 | 308 | 7.8 | 195 | 0.6 | 215 | 7.8 |
| Total | 242779 | 5.6 | 458101 | 2.7 | 167547 | 4.5 | 341897 | 2.6 |

TABLE XIV. Probability and exponential slope for single elastic scattering of kaons in each of the absorber elements in the kaon beam.

| Absorber Component | Single Scattering Probability (%) | Exponential Slope ($[GeV/c^2]^2$) |
|---|---|---|
| Beryllium, Common Absorber | 8.6 | 65 |
| Lead, Common Absorber | 17.8 | 420 |
| Beryllium, Movable Absorber | 7.8 | 65 |

TABLE XV. Scattering and photon conversion locations and the thickness of material in radiation lengths.

| Detector Element | Location from Target ($m$) | Thickness (Radiation Lengths) |
|---|---|---|
| V hodoscope | 137.792 | $3.23 \times 10^{-3}$ |
| Pb sheet[a] | 137.804 | $9.36 \times 10^{-2}$ |
| T hodoscope | 137.815 | $3.43 \times 10^{-3}$ |
| Vacuum Window | 158.965 | $2.50 \times 10^{-3}$ |
| Drift Chamber 1 | 159.292 | $3.42 \times 10^{-3}$ |
| Drift Chamber 2 | 165.867 | $3.86 \times 10^{-3}$ |
| Drift Chamber 3 | 171.857 | $3.63 \times 10^{-3}$ |
| Drift Chamber 4 | 178.004 | $2.10 \times 10^{-3}$ |
| Chamber Field Wires[b] | — | $5.70 \times 10^{-3}$ |
| Chamber Sense Wires[c] | — | $6.43 \times 10^{-3}$ |
| C Hodoscope | 179.502 | $4.0 \times 10^{-2}$ |
| B Hodoscope | 179.520 | $4.0 \times 10^{-2}$ |

[a]Used only in $2\pi^0$ lead sheet subsets. Average radiation length is listed.

[b]This contribution is identical in all four chambers. Only the 9.9% of the tracks which hit these wires (per chamber) see this contribution.

[c]This contribution is identical in all four chambers. Only the 0.7% of the tracks which hit these wires (per chamber) see this contribution.

TABLE XVI. Regeneration parameters for the boron-carbide and lead in the regenerator used in the fits. For the boron-carbide, values of regeneration parameters which float in the fitting are presented.

| Material | Atomic Weight | Density (gm/cm³) | $(f - \bar{f})/k$ (mbarn) | Power-Law Slope | Phase (degrees) |
|---|---|---|---|---|---|
| $B_4C$ | 55.26 | 2.52 | 5.791 [a] | −0.604 [a] | −125.6 [b] |
| Pb | 207.19 | 11.35 | 9.71 ± 0.14 [c] | −0.654 ± 0.018 [d] | −122.2 ± 1.8 [d] |

[a] Always extracted as a parameter in the fits. This is a typical value.

[b] Always obtained via analyticity from the current value of $\alpha_{B_4C}$ in the fits. This is a typical value.

[c] Value obtained using the data in [47], with a correction for the change in $\eta_{+-}$. The error includes the error quoted in [47] added in quadrature with the contribution from the uncertainty of $\eta_{+-}$.

[d] From [47]. Although the analyticity of Lead is only good to a few degrees, the Lead is only a small contribution here.

TABLE XVII. Results of the unconstrained fits used to determine $Re(\varepsilon'/\varepsilon)$ which is fixed at 0 in the first four fits to the charged and neutral subsets so that the regeneration parameters from these sets may be compared. The cross section correction is quoted in terms of the correction to the carbon cross-section at 156 GeV/c.

| Fit | $Re(\varepsilon'/\varepsilon)$ (×10⁻⁴) | $\Delta f\|_{70}$ (mbarns) | $\alpha$ | $\Delta\sigma_T$ (mbarns) | $\chi^2/d.o.f$ |
|---|---|---|---|---|---|
| $\pi^+\pi^-$ | 0[a] | 5.786 ± 0.008 | −0.605 ± 0.007 | −3.1 ± 1.4 | 8.9/9 |
| $2\pi^0$(Pb Sheet) | 0[a] | 5.799 ± 0.009 | −0.598 ± 0.010 | −2.4 ± 2.8 | 8.2/9 |
| $2\pi^0$(No Pb Sheet) | 0[a] | 5.801 ± 0.011 | −0.609 ± 0.011 | −1.8 ± 3.2 | 6.2/9 |
| $2\pi^0$(Combined) | 0[a] | 5.800 ± 0.007 | −0.603 ± 0.007 | −2.1 ± 2.1 | 16.8/21 |
| Simultaneous $\pi^+\pi^-$ and $2\pi^0$ | 7.4 ± 5.2 | 5.791 ± 0.005 | −0.604 ± 0.005 | −2.8 ± 1.1 | 25.8/32 |

[a] Fixed at this value for this fit.

TABLE XVIII. Variation of the extracted value for $Re(\varepsilon'/\varepsilon)$ with the values of physical constants in the fit. The units assumed for each of the constants is given in square brackets in the first column. Here $\Delta Re(\varepsilon'/\varepsilon)$ is the change in $Re(\varepsilon'/\varepsilon)$ for an increase in the constant by one standard deviation. The correction to $Re(\varepsilon'/\varepsilon)$ as a function of the physical constants is presented in the last column.

| Parameter | Value | Error | $10^4 \times \Delta Re(\varepsilon'/\varepsilon)$ (+1σ variation) | $10^4 \times Re(\varepsilon'/\varepsilon)$ dependence |
|---|---|---|---|---|
| $\Delta m$ $[10^{10}\hbar s^{-1}]$ | 0.5286 | 0.0028 | +0.41 | $77.2(\frac{\Delta m - 0.5286}{0.5286})$ |
| $\tau_S$ $[10^{-10} s]$ | 0.8929 | 0.0016 | −0.26 | $-147(\frac{\tau_S - 0.8929}{0.8929})$ |
| $\tau_L$ $[10^{-8} s]$ | 5.17 | 0.004 | +0.05 | $5.8(\frac{\tau_L - 5.17}{5.17})$ |
| $|\varepsilon|$ $[10^{-3}]$ | 2.279 | 0.022 | −0.11 | $-11.4(\frac{|\varepsilon| - 2.279}{2.279})$ |
| $\phi_\varepsilon$ | 43.4° | 0.2° | −0.15 | $-0.75(\phi_\varepsilon - 43.4°)$ |
| $\phi_{\varepsilon'}$ | 47° | 6° | −0.11 | $-0.018(\phi_{\varepsilon'} - 47°)$ |

TABLE XIX. Summary of fits for $\Delta m$ and $\tau_S$ for both the $\pi^+\pi^-$ and $2\pi^0$ modes. Numbers in parentheses are the statistical errors to the least significant figure.

| Sample | z bin size | $\Delta m$ $(10^{10}\hbar s^{-1})$ | $\tau_S$ $(10^{-10} s)$ | $\Delta f\vert_{70}$ (mbarn) | $\alpha$ | $\chi^2/d.o.f.$ |
|---|---|---|---|---|---|---|
| $\pi^+\pi^-$ | 1 m | 0.5302(44) | 0.8952(15) | 5.774(9) | −0.590(3) | 157/160 |
| $\pi^+\pi^-$ | 2 m | 0.5319(45) | 0.8953(15) | 5.773(9) | −0.590(3) | 92/90 |
| $2\pi^0_{all}$ | 2 m | 0.5277(30) | 0.8911(16) | 5.804(11) | −0.602(7) | 335/302 |
| $2\pi^0_{all}$ | 3 m | 0.5274(30) | 0.8912(17) | 5.802(11) | −0.603(7) | 221/203 |
| $2\pi^0_{Pb}$ | 3 m | 0.5289(39) | 0.8904(22) | 5.803(15) | −0.604(10) | 118/99 |
| $2\pi^0_{NoPb}$ | 3 m | 0.5251(47) | 0.8920(25) | 5.803(17) | −0.601(11) | 100/99 |

TABLE XX. Results of the fits for $\Delta\phi$ and $\phi_{+-}$. Numbers in parentheses are the statistical errors to the least significant figure.

| fit | $\Delta\phi$ | $\phi_{+-}$ | $Re(\varepsilon'/\varepsilon)$ $(10^{-4})$ | $\Delta f\vert_{70}$ (mbarns) | Power $\alpha$ | $\Delta m$ $(10^{10}\hbar s)$ |
|---|---|---|---|---|---|---|
| $\Delta\phi$ (1m bins) | −1.7° ± 1.0° | 44.1° ± 0.9°[a] | 3.2 ± 6.7 | 5.787(7) | −0.592(3) | 0.5286[b] |
| $\Delta\phi$ (2m bins) | −1.4° ± 1.0° | 43.8° ± 0.9°[a] | 4.7 ± 6.7 | 5.785(7) | −0.592(3) | 0.5286[b] |
| $\phi_{+-}$ | −1.7° ± 1.0° | 42.2° ± 1.3° | 8.8 ± 6.7 | 5.781(9) | −0.592(3) | 0.5257(49) |

[a]Correlated with assumed values of $\Delta m$ and $\tau_S$ (see text).
[b]Held constant in this fit.

TABLE XXI. The measured regeneration phase and corresponding analyticity predictions in simultaneous fits to the $\pi^+\pi^-$ and $2\pi^0$ data. Numbers in parentheses are the statistical errors to the least significant figure.

| $\Delta m$ $(10^{10}\hbar s^{-1})$ | $\alpha$ | $\phi_{pred}$ (analyticity) | $\phi_{f-f}$ (measured) | $\phi_{f-f} - \phi_{pred}$ |
|---|---|---|---|---|
| 0.5286[a] | −0.5922(25) | −126.70° ± 0.23° | −125.92° ± 0.45° | 0.78° ± 0.51° |
| 0.5351[a] | −0.5912(24) | −126.79° ± 0.23° | −127.56° ± 0.45° | −0.77° ± 0.51° |
| 0.5275(47) | −0.5925(26) | −126.68° ± 0.23° | −125.6° ± 1.3° | 1.1° ± 1.3° |

[a]Fixed.

TABLE XXII. Shifts in $Re(\varepsilon'/\varepsilon)$ for changes in the fitting technique and for changes in the fiducial cuts. For the studies involving the change of a cut, the "allowed" shifts are the one standard deviation shifts expected from the change in statistics alone. For a change in methodology, the shift was predicted using Monte Carlo studies. The shift observed with the mass cut is discussed in the text.

| Analysis Change or Fit Modification | $\Delta Re(\varepsilon'/\varepsilon)$ $(\times 10^{-4})$ | "Allowed" Shift |
|---|---|---|
| Bin $2\pi^0$ data in 3 m × 10 GeV/c $pz$ bins | −2.48 | 2.21 |
| Reduce Momentum range to 40 − 150 GeV/c | +0.21 | 0.27 |
| Reduce Neutral z range to 110 − 137 m | +0.42 | 2.65 |
| Relax analyticity assumption | −0.22 | — |
| Loosen Ring Cut from 112 to 128 | +0.46 | 0.47 |
| Tighten Mass cut from ±24 MeV/c² to ±18 MeV/c² | +1.28 | 0.32 |
| Loosen Mass cut from ±24 MeV/c² to ±28 MeV/c² | −0.30 | 0.19 |
| Loosen charged mode cuts | −0.25 | 1.01 |

TABLE XXIII. Shifts in $Re(\varepsilon'/\varepsilon)$ for studies demonstrating the stability of $Re(\varepsilon'/\varepsilon)$ due to the simultaneous collection of $K_S$ and $K_L$ decays.

| Study | $\Delta Re(\varepsilon'/\varepsilon)$ $(\times 10^{-4})$ | "Allowed" Shift |
|---|---|---|
| Introduce 90% efficiency into 2 $B$ bank trigger counters, and 0% efficiency into 4 drift chamber wires, in the $\pi^+\pi^-$ Monte Carlo simulation | $-1.50$ | — |
| Loosen maximum photon energy cut in $2\pi^0$ analysis from 60 GeV to 90 GeV | $+2.00$ | 1.16 |
| Loosen maximum photon energy cut in $2\pi^0$ analysis from 90 GeV to 120 GeV | $+0.10$ | 0.27 |

TABLE XXIV. Shift in $Re(\varepsilon'/\varepsilon)$ induced by some of the systematic biases introduced into the photon energy reconstruction procedure. The resolution bias was discussed in the previous section.

| Reconstruction bias | $|\Delta Re(\varepsilon'/\varepsilon)|$ $(\times 10^{-4})$ |
|---|---|
| 0.5% energy smearing | 0.36 |
| 0.03% average energy scale change $(\Delta E = 3 \times 10^{-4} E)$ | 0.93 |
| Quadratic energy scale change $(\Delta E = q E^2)$ | 1.57 |
| "Pedestal" shift (20 MeV per cluster) | 0.46 |

TABLE XXV. Change in the single ratios and in $Re(\varepsilon'/\varepsilon)$ when the size of a limiting aperture is changed in the Monte Carlo. $\Delta R_{00}$ and $\Delta R_{+-}$ are the changes in the vacuum to regenerator beam ratios in the charged and neutral mode samples. In each case, the size of the apertures in the $x$ and $y$ were simultaneously changed by 70 $\mu$m in order to maximize the effect.

| Aperture adjustment | $\Delta R_{00}$ (percent) | $\Delta R_{+-}$ (percent) | $|\Delta Re(\varepsilon'/\varepsilon)|$ $(\times 10^{-4})$ |
|---|---|---|---|
| Change Mask Size by 70 $\mu$m | $-0.013$ | $-0.014$ | 0.02 |
| Change HDRA size by 70 $\mu$m | $-0.002$ | negligible | 0.03 |
| Change CA size by 70 $\mu$m | $-0.021$ | negligible | 0.35 |

TABLE XXVI. Contribution to the systematic uncertainty in $Re(\varepsilon'/\varepsilon)$ from backgrounds.

| Background Source | Uncertainty | |
|---|---|---|
| | $\pi^+\pi^-$ | $2\pi^0$ |
| Incoherent Regeneration (in regenerator) | $0.18 \times 10^{-4}$ | $0.84 \times 10^{-4}$ |
| Semileptonic Decays | $0.23 \times 10^{-4}$ | — |
| $3\pi^0$ Decays and Beam Interactions | — | $0.60 \times 10^{-4}$ |
| Total | $0.29 \times 10^{-4}$ | $1.03 \times 10^{-4}$ |

TABLE XXVII. Change in $Re(\varepsilon'/\varepsilon)$ for different modifications to the kaon flux shapes assumed in the fitting program. Note that these changes *are not* made in determining the acceptance, they only affect the relative contribution of the *predicted rate* of a 1 GeV/$c$ momentum bite to the total predicted rate in a 10 GeV/$c$ bin.

| Modification to beam spectrum | $\delta Re(\varepsilon'/\varepsilon)$ $(10^{-4})$ |
|---|---|
| Flat Incident spectrum ($F_v(p) = $ constant) | $-1.21$ |
| Quadratic distortion — both $2\pi^0$ and $\pi^+\pi^-$ samples ($F_v'(p) = F_v(p)\{1 + 0.1[(p - 60)/100]^2\}$) | $+0.12$ |
| Quadratic distortion, $\pi^+\pi^-$ sample only | $+0.04$ |
| Increase average regenerator beam transmission by 1 $\sigma$ ($t \to 1.005t$) | $-0.13$ |
| No shadow absorber scattering correction to regenerator beam flux | $-0.36$ |
| Use shadow absorber scattering correction determined for the $\pi^+\pi^-$ sample for all data sets[a] | $-0.27$ |
| Use shadow absorber scattering correction determined for the $2\pi^0$ lead sheet sample for all data sets | $-0.27$ |
| Change dilution factor used to calculate change in the relative flux shape between the regenerator and vacuum beam from regeneration in the shadow absorber | $+0.04$ |
| Ignore "sneakby" rate[b] | $-0.76$ |
| Correct for "sneakby" kaons, but ignore the rate of $K_L$ decay from these kaons | $-0.26$ |
| Use the "sneakby" rate determined for the $\pi^+\pi^-$ set for all of the subsets | $-0.47$ |
| Use the "sneakby" rate determined for the lead sheet $2\pi^0$ set for all of the subsets | $-0.46$ |

[a]See Section VIII A 2.
[b]That is, assume the entire flux of kaons observed in the vacuum beam passes through the regenerator.

TABLE XXVIII. Change in $\Delta m$, $\tau_S$, $\Delta\phi$ and $\phi_{+-}$ for different distortions of the vacuum and regenerator beam kaon momentum spectra.

| Modification to vacuum or regenerator beam spectrum | $\|\delta\Delta m\|$ $(10^{10}\hbar s^{-1})$ | $\|\delta\tau_S\|$ $(10^{-10}s)$ | $\|\delta\Delta\phi\|$ | $\|\delta\phi_{+-}\|$ |
|---|---|---|---|---|
| Flat Incident spectrum ($F_v(p) = $ constant) | 0.0038 | 0.0007 | $1.3°$ | $1.2°$ |
| Quadratic distortion: ($F_v'(p) = F_v(p)\{1 + 0.1[(p - 60)/100]^2\}$) | 0.0001 | 0.0001 | $0.3°$ | $0.5°$ |
| Change average regenerator beam transmission by 1 standard deviation: ($t \to 1.005t$) | 0.0004 | 0.0002 | $< 0.1°$ | $0.3°$ |
| No shadow absorber scattering correction to regenerator beam flux | 0.0007 | 0.0002 | $0.1°$ | $0.3°$ |
| Use the shadow absorber scattering correction determined for the $\pi^+\pi^-$ sample for all data sets | $< 0.0001$ | $< 0.0001$ | $< 0.1°$ | $< 0.1°$ |
| Ignore "sneakby" rate | 0.0003 | 0.0002 | $0.5°$ | $0.3°$ |
| Use the "sneakby" rate determined for the $\pi^+\pi^-$ set for all of the subsets | $< 0.0001$ | $< 0.0001$ | $< 0.1°$ | $< 0.1°$ |

TABLE XXIX. Sequential change in observed $2\pi^0$ vacuum beam to regenerator beam ratio due to accidental event loss as each analysis cut is applied. Events which would not have passed cuts except for the presence of the accidental activity are *not* included in these numbers.

| Analysis Cut | Change in Ratio (%) |
|---|---|
| 4 clusters | +0.065±0.021 |
| Best pairing $\chi^2 < 4$ | −0.137±0.013 |
| Cluster fusion | +0.234±0.048 |
| 2nd best $\chi^2$ cuts | −0.017±0.005 |
| Chamber, BC hodoscope hits | +0.099±0.028 |
| Collar Anti | −0.055±0.012 |
| Cluster energy cuts | −0.002±0.001 |
| Ring number | −0.001±0.003 |
| $2\pi^0$ mass | −0.032±0.004 |
| Total energy | −0.018±0.002 |
| $z$ fiducial cut | −0.051±0.002 |
| Total | +0.085±0.062 |

TABLE XXX. Summary of systematic uncertainties on $Re(\varepsilon'/\varepsilon)$, $\Delta m$ and $\tau_S$ measured in the $\pi^+\pi^-$ and $2\pi^0$ decay modes, $\Delta\phi$, and $\phi_{+-}$.

| Systematic Source | $Re(\varepsilon'/\varepsilon)$ $(10^{-4})$ | $\tau_S$ $(10^{-10} s)$ $2\pi^0$ | $\pi^+\pi^-$ | $\Delta m$ $(10^{10} \hbar s^{-1})$ $2\pi^0$ | $\pi^+\pi^-$ | $\Delta\phi$ | $\phi_{+-}$ |
|---|---|---|---|---|---|---|---|
| $\gamma$ energy | 1.61 | 0.0012 | — | 0.0014 | — | 0.5° | — |
| $\pi^+\pi^-$ acceptance | 0.65 | — | 0.0020 | — | 0.0009 | 0.4° | 0.35° |
| $2\pi^0$ acceptance | 1.00 | 0.0002 | — | 0.0001 | — | — | — |
| RA4 position | 0.59 | — | — | — | — | — | — |
| HDRA material | 1.22 | 0.0001 | — | 0.0008 | — | 0.2° | — |
| $2\pi^0$ backgrounds | 1.03 | — | — | — | — | — | — |
| $\pi^+\pi^-$ backgrounds | 0.29 | — | — | — | — | — | — |
| Kaon flux | 0.30 | 0.0002[a] | 0.0002[a] | 0.0004[a] | 0.0004[a] | 0.2° | 0.4° |
| Analyticity | — | — | 0.0003 | — | 0.0019 | — | 0.5° |
| Accidentals | 1.07 | — | — | 0.0004 | — | 0.1° | — |
| Totals | 2.87 | 0.0012 | 0.0020 | 0.0017 | 0.0021 | 0.7° | 0.7° |

[a]This error is completely correlated between the $\pi^+\pi^-$ and $2\pi^0$ samples, and is not included in the total error listed here.

TABLE XXXI. Our result for and previous best measurements of $\phi_{+-}$. We have corrected the previously reported value of $\phi_{+-}$ for the change in the assumed $\Delta m$ to our current result for $\Delta m$ using the reported experimental dependences.

| Experiment | $\phi_{+-}$ (degrees) | Internal Error (degrees) | Assumed $\Delta m$ ($\times 10^{10} \hbar s^{-1}$) | $\Delta\phi_{+-}$ for +1% $\delta\Delta m$ (degrees) | $\phi_{+-}$ (our $\Delta m$) (degrees) |
|---|---|---|---|---|---|
| C. Geweniger et al. [25] | 45.6 | 1.0 | 0.5338 | 3.05 | 43.0 |
| W.C. Carithers et al. [26] | 45.5 | 2.8 | 0.5348 | 1.20 | 44.1 |
| R. Carosi et al. [24] | 46.9 | 1.6 | 0.5351 | 3.10 | 43.4 |
| This experiment [28] | 42.2 | 1.4 | floated[a] | — | 42.2 |

[a]See Section IX C